Optical Design and Numerical Modeling of the AEI 10 m Prototype sub-SQL Interferometer

Von der Fakultät für Mathematik und Physik
der Gottfried Wilhelm Leibniz Universität Hannover
zur Erlangung des Grades

Doktor der Naturwissenschaften
Dr. rer. nat.

vorgelegte Dissertation
von

Dipl.-Phys. Christian Gräf

geboren am 8. Mai 1980 in Hannover

2013

Abstract

The core experiment that is planned to be realized in the scope of the AEI 10 m Prototype project is an interferometer which aims for reaching a mirror displacement sensitivity in the audio frequency band at the Standard Quantum Limit (SQL) for its 100 g test masses. After reaching this goal, the experiment is planned to serve as a testbed for advanced interferometry techniques which will enable measurements even below the SQL. The investigation and further development of these techniques is crucial to achieve the planned sensitivity improvements in future GW detectors, to further increase the scientific potential of these instruments from the astrophysical and cosmological point of view.

A necessary prerequisite for reaching the SQL is a sufficiently small influence of classical noise sources on the sensitivity of the interferometer. In particular, the reduction of Brownian thermal noise in the dielectric coatings of the mirrors is of central importance. In a conceptual design study for the planned experiment, possible, but very challenging and so far untested approaches to realizing an interferometer with sufficiently low coating thermal noise were delineated.

This work is focused on an in-depth investigation of the techniques proposed in the conceptual design for the reduction of coating Brownian thermal noise as well as on the formulation of a technical design for a practical implementation of the experiment. Moreover, within the scope of this work, an optical layout for the interferometer was developed which allows to stepwise approach the targeted configuration with extremely large beam spots on the interferometer mirrors, which give rise to marginal stability of the arm cavities. Implications of marginally stable arm cavities on the performance of the interferometer were studied with the aid of numerical models, and requirements for the quality of the interferometer optics' surfaces were derived. Furthermore, in this thesis, the "single arm test" experiment is introduced which was proposed as a stepping-stone toward the implementation of the sub-SQL interferometer. This experiment was designed to investigate essential technological aspects of the sub-SQL interferometer and will therefore provide crucial input on the way toward the world's first sub-SQL measurement at audio band frequencies. At the time of writing, this experiment is being set up, making optimal use of the technical infrastructure in the prototype which is already installed and operational.

In addition to these aspects, in the scope of this thesis, the squeezed-light laser for the GEO 600 gravitational wave detector was interfaced to a digital control system and fully automated operation of the experiment was realized. This enabled the long-term stable injection of squeezed vacuum states of light into the GEO interferometer and the associated continuous enhancement of the shot noise-limited sensitivity of the instrument.

Key words: Optical design, Standard Quantum Limit, Coating Brownian thermal noise

Kurzfassung

Als Kernexperiment des AEI 10 m Prototyp Projektes ist der Aufbau eines Laserinterferometers geplant, welches zum ersten Mal Messungen mit einer Empfindlichkeit am Standardquantenlimit (SQL) im Audiofrequenzband ermöglichen soll. Nach dem Erreichen dieses Ziels soll das Experiment in einem weiteren Schritt als Testumgebung für neue Technologien dienen, mit denen Messempfindlichkeiten unterhalb des SQL erreicht werden. Die Erforschung dieser Technologien ist von herausragender Bedeutung, um in zukünftigen Gravitationswellendetektoren die geplanten Empfindlichkeitssteigerungen zu realisieren und damit die Möglichkeiten astrophysikalischen und kosmologischen Erkenntnisgewinns zu verbessern.
Eine notwendige Voraussetzung zum Erreichen des SQL ist ein hinreichend kleiner Einfluss klassischer Rauschbeiträge auf die Empfindlichkeit des Interferometers. Insbesondere der Verminderung von Brown'schem Rauschen in den Spiegelbeschichtungen kommt eine zentrale Bedeutung zu. Für das geplante Experiment liegt eine Konzeptstudie vor, in der – basierend auf dem Einsatz neuartiger Technologien – Wege aufgezeigt werden, um ein Interferometer mit hinreichend kleinem thermischen Beschichtungsrauschen zu realisieren. Eine experimentelle Umsetzung dieser Technologien ist als außerordentlich anspruchsvoll zu betrachten.
Diese Arbeit knüpft an die genannte Konzeptstudie an und beinhaltet eine vertiefte Untersuchung der vorgeschlagenen Techniken zur Verminderung thermischen Beschichtungsrauschens, mit dem Ziel der Ausarbeitung eines technischen Designs, welches als Experiment umsetzbar ist. Ferner wurde im Rahmen dieser Arbeit ein optisches Layout für das geplante Experiment entwickelt, welches eine schrittweise Annäherung an die Zielkonfiguration mit extrem großen Strahlradien ermöglicht, welche mit marginaler Stabilität der Armresonatoren des Interferometers einhergehen. Der Einfluss marginal stabiler Armresonatoren auf die Leistungsfähigkeit des Interferometers wurde mithilfe numerischer Modelle untersucht und Anforderungen an die erforderliche Qualität der zu verwendenden Optiken im Hinblick auf ihre Oberflächengüte abgeleitet. Weiterhin wird in dieser Arbeit das "single arm test" Experiment vorgestellt, welches als Etappenziel zum Aufbau des sub-SQL Interferometers vorgeschlagen wurde. Dieses Experiment wird die Untersuchung zentraler technische Aspekte des Interferometers ermöglichen und damit den Weg hin zu dessen Realisierung ebnen. Das Experiment nutzt die bereits fertiggestellte Infrastruktur im Prototypen optimal aus und befindet sich derzeit im Aufbau.
Zusätzlich zu den genannten Aspekten ist im Rahmen dieser Arbeit der Quetschlichtlaser für den Gravitationswellendetektor GEO 600 an ein digitales Regelungssystem angebunden und vollständig automatisiert worden. Dies ermöglicht die langzeitstabile Injektion gequetschter Vakuumzustände in das GEO Interferometer und die damit verbundene Steigerung der schrotrauschlimitierten Empfindlichkeit.

Schlagworte: Optisches Design, Standardquantenlimit, Brown'sches Spiegelbeschichtungsrauschen

Contents

Acronyms and symbols **ix**

List of Figures **xv**

List of Tables **xix**

1 Introduction **1**
1.1 Gravitational waves 1
1.2 Direct detection of gravitational waves 2
1.3 Quantum noise and the Standard Quantum Limit 6
1.4 The AEI 10 m Prototype 10
1.4.1 Scientific goals 11
1.4.2 Vacuum system 12
1.4.3 Seismically isolated optical tables 14
1.4.4 Suspension platform interferometer 16
1.4.5 Laser system 18
1.4.6 Frequency reference cavity 19
1.5 Conceptual design of the 10 m sub-SQL interferometer 21
1.6 Aim and structure of the thesis 26

2 Laser beams and optical resonators **29**
2.1 Gaussian laser beams 29
2.2 Ray transfer matrices 31
2.3 Optical resonators 32
2.3.1 A matrix-based resonator model 33
2.3.2 Fabry-Perot cavities 33
2.3.3 Impedance matched, under coupled and over coupled resonators 36
2.3.4 Multi-mirror coupled cavities 37
2.3.5 Mode coupling efficiency 40
2.3.6 Cavity stability 42

3 On coating thermal noise reduction techniques 45
3.1 A coating Brownian thermal noise model 45
3.2 Increasing beam spot sizes 48
3.3 Anti-resonant end mirror cavities 50
3.3.1 The general concept 50
3.3.2 Aspects of length sensing and control 54
3.3.3 Optical layout of the coupled arm cavities 63
3.3.4 Options to relax the requirements 80
3.4 Alternative approaches to coating thermal noise reduction 84
3.4.1 Lower arm cavity mirror reflectivities and higher input power 84
3.4.2 Khalili etalons, waveguide mirrors and new coating materials 85
3.5 Summary 87

4 The tunable stability interferometer optical layout 89
4.1 Introduction 89
4.2 Challenges of operating the target configuration 91
4.2.1 Typical stabilities of the target configuration 91
4.3 Motivation for a stepwise approach 92
4.3.1 Direct measurement of coating Brownian noise 94
4.3.2 Potential impact on future gravitational wave detectors 95
4.4 Properties of the tunable stability configuration 96
4.4.1 Collimated interferometer input beam 96
4.4.2 Coupling efficiency of the flexible mode matching scheme . . 97
4.4.3 Further operational requirements 102
4.5 Estimation of the operational robustness 102
4.5.1 Initial laser beam waist radius and position 103
4.5.2 Collimating mirror ROC imperfections 103
4.5.3 Input mirror AR surface ROC 105
4.5.4 Cavity mirror HR-side ROC tolerances 106
4.6 Dissipative heating and thermal aberrations 107
4.7 Further implications of marginal stability 112
4.7.1 Modal degeneracy 112
4.7.2 Angular misalignment coupling to longitudinal phase 113
4.7.3 Input beam pointing noise 116
4.8 Summary 119

5 Modeling the sub-SQL interferometer with realistic mirrors 121
5.1 Mirror surface topography and optical losses 121
5.1.1 Sources of light scattering 123
5.1.2 Implications of light scattering in interferometers 125
5.2 Figures of merit for the mirror surface quality 127

5.2.1 Arm cavity imbalance, contrast defect and noise couplings . . 127
5.2.2 Round-trip loss and quantum noise reduction techniques . . . 129
5.3 The grid-based Fabry-Perot Michelson interferometer model 136
5.3.1 Grid parameter requirements 140
5.4 Modeling mirrors with realistic surface topography 142
5.4.1 Spectral approach to optical surface characterization 143
5.4.2 Polynomial description of optical surfaces 145
5.4.3 A hybrid mirror surface model 147
5.5 A parameter study with realistic mirror surfaces 151
5.6 Summary 159

6 The 10 m Prototype single arm test experiment 161
6.1 Introduction 161
6.2 Scientific and technical rationale 162
6.3 Technical approach 165
6.4 Required resources 168
6.4.1 Mirror specifications 168
6.4.2 Mode-matching optics 170
6.4.3 Further hardware requirements 171
6.5 Summary 173

7 Automation of the GEO squeezed-light laser 175
7.1 Squeezing enhancement of laser interferometers 176
7.2 Introduction to the GEO squeezed-light laser 177
7.3 The digital control system architecture 180
7.3.1 Hardware components 180
7.3.2 Control system software 182
7.4 Conceptual approach to squeezed-light laser automation 184
7.5 Interfacing of the squeezed-light laser with the digital control system 185
7.5.1 Hardware interfacing 186
7.5.2 Real-time software control of the optical stages 187
7.6 Remote control and control automation 198
7.7 Routine operation of the automated squeezer in the GEO detector . . 200
7.8 Summary 203

8 Summary and outlook 205

Bibliography 209

A Numerical simulation source code 231

B Interfacing electronics for the GEO squeezer 255

C GEO squeezer automation real-time code **269**

D Memorable whiteboard sketches **273**

Curriculum vitae **275**

Publications **277**

Acknowledgements **283**

Acronyms and symbols

Acronyms:

AR	Anti reflection
AC	Arm cavity
ADC	Analog to digital converter
ALS	Advanced LIGO arm length stabilization system
BHD	Balanced homodyne detection
BRDF	Bi-directional reflectance distribution function
CA	EPICS Channel Access protocol
CBTN	Coating Brownian thermal noise
CDS	LIGO Control and data system
DAC	Digital to analog converter
DC	Direct current
DAQ	Data acquisition
DFT	Discrete Fourier transform
DI	Digital interferometry
DOF	Degree of freedom
DR	Dual recycling
EETM	End mirror cavity end test mass
EM	End mirror
ESD	Electro static drive
ET	Einstein Telescope
ETM	End test mass
EOM	Electro-optic modulator
EPICS	Experimental Physics and Industrial Control System
FDT	Fluctuation-dissipation theorem

FPC	Fabry-Perot cavity
FS	Fused silica
FSR	Free spectral range
FFT	Fast Fourier transform
FWHM	Full width at half maximum
FI	Faraday isolator
FPMI	Fabry-Perot Michelson interferometer
GAS	Geometric anti-spring
GPS	Global positioning system
GW	Gravitational wave
HOM	Higher-order transverse mode
HR	High reflective
HV	High voltage
IBS	Ion-beam sputtering
IETM	Intermediate end test mass
IM	Input mirror
IOC	Input/output controller
IOP	I/O processor
IP	Inverted pendulum
ITM	Input test mass
KC	Khalili cavity
KE	Khalili etalon
LO	Local oscillator
LVDT	Linear variable differential transformer
MC	Mode cleaner
MZI	Mach-Zehnder interferometer
NDS	Network data server
NPRO	Non planar ring oscillator
NTP	Network time protocol
OMC	Output mode cleaner
OPL	Optical path length
OPO	Optical parametric oscillation

PDH	Pound-Drever-Hall scheme
PLL	Phase-locked loop
PPKTP	Periodically poled potassium titanyl phosphate
PMC	Pre mode cleaner
PSD	Power spectral density
PV	EPICS process variable
PZT	Piezo-electric transducer
QND	Quantum non-demolition
QPD	Quadrant photo detector
RCG	Real-time code generator
RF	Radio frequency
RMS	Root mean square
ROC	Radius of curvature
RTL	Round-trip loss
RTL_{00}	Fundamental mode round-trip loss
SAS	Seismic attenuation system
SHG	Second harmonic generator
SLS	Squeezed light source
SPI	Suspension platform interferometer
SR	Signal recycling
SD	Scratch/dig
SQL	Standard Quantum Limit
TIS	Total integrated scattering
TEM	Transverse electro magnetic mode
WFS	Wave front sensor

Physical symbols and constants:

α	Absorption per unit length
$\mathcal{A}$	Laser beam effective cross-sectional area
$A(x,y)$	Aperture function
$a_1(t)$	Input field amplitude quadrature

$a_2(t)$	Input field phase quadrature
A_n^m	Zernike amplitude
β	Thermo-optic coefficient
χ	Reduced radiation constant
c	Vacuum speed of light
η	Power mode coupling efficiency
$\mathcal{E}(\Omega)$	Net fractional photon loss
$E(t)$	Scalar electric field
$E(x, y, z)$	Electric field
$\mathcal{F}$	Finesse
f	Frequency
$F(f)$	Fourier transform of a periodic force F(t)
f_c	Cavity pole frequency
Γ	Modulation index
γ	Cavity bandwidth
G	Cavity resonant gain
g	Cavity stability parameter
$G(k_x, k_y, L)$	Momentum space propagator
$\hbar$	Reduced Planck constant
$H_n(x)$	Hermite polynomial of n-th order
h_{GW}	Gravitational wave strain amplitude
h_{SQL}	Strain SQL
$I(\vec{r})$	Laser beam intensity profile
I_0	Input laser power
$J_k(x)$	Bessel function of the first kind
κ	Thermal conductivity
$\mathcal{K}$	Kimble's coupling constant
k	Wave number
k_B	Boltzmann constant
Δ	Laplace operator
λ, λ_0	Wave length, carrier wave length
$\mathcal{L}$	Absorption and scattering loss per cavity round-trip

m	Mirror mass
Ω	Signal sideband angular frequency
ω, ω_0	Angular frequency, carrier field angular frequency
$\hat{P}$	Momentum operator
ϕ, φ	Phase
$\Phi^{\mathrm{CR}}, \Phi^{\mathrm{SB}}$	Carrier field, sideband field
Φ_{Gouy}	Gouy phase
$q(z)$	Complex beam parameter
ϱ, τ	Cavity amplitude reflectivity, amplitude transmittance
R, T	Power reflectivity, power transmittance
r, t	Amplitude reflectivity, amplitude transmittance
$R_c(z)$	Wave front radius of curvature
ΔS	Sagitta change
σ	Stefan-Boltzmann constant
$S_{\hat{F}}(f)$	Quantum back-action noise spectral density
$S_{\hat{x}}(f)$	Displacement power spectral density
$S_{\hat{x}}^{\mathrm{SQL}}(f)$	Displacement SQL spectral density
$\mathcal{T}_{\mathrm{in}}$	Arm cavity input mirror transmittance
T	Temperature
$w(z)$	Beam radius
w_0	Beam waist radius
W_{diss}	Dissipated power
$\hat{x}$	Position operator
$\hat{X}_1$	Amplitude quadrature
$\hat{X}_2$	Phase quadrature
ξ	Contrast defect
$x(f)$	Fourier transform of steady-state displacement response amplitude
$\mathbb{Y}$	Mechanical admittance
Y, Y'	Bulk, coating Young's moduli
$\mathbb{Z}$	Mechanical impedance
ζ	Homodyne phase
$Z_n^m(\rho, \Theta)$	Zernike function
z_R	Rayleigh range

List of Figures

1.1 Effects of differently polarized gravitational waves on free-falling test particles. 3
1.2 Advanced generation gravitational wave detector optical configuration and top-level noise budget. 5
1.3 Quantum noise in a Fabry-Perot Michelson interferometer with frequency-independent input squeezing. 8
1.4 Rendered image of a bird's-eye view of the AEI 10 m Prototype hall. . . 11
1.5 Rendered technical drawing of the AEI 10 m Prototype vacuum system. 13
1.6 Rendered technical drawing of an AEI-SAS optical table. 15
1.7 Schematic drawing of the SPI optical layout. 17
1.8 Schematic drawing of the main AEI 10 m Prototype laser system. 18
1.9 Schematic drawing of the frequency reference cavity control topology. . 20
1.10 Schematic layout of the sub-SQL interferometer target configuration. . . 22
1.11 Optimization of the mirror aspect ratio in the sub-SQL interferometer. . 23
1.12 Noise budget of the sub-SQL interferometer configuration proposed in the conceptual design. 24

2.1 Cross sections of Hermite-Gaussian transverse laser modes. 31
2.2 Frequency dependence of the optical gain of a two-mirror cavity. 35
2.3 Light transmitted and reflected at an over coupled, under coupled and impedance matched cavity. 36
2.4 Amplitude and phase of light reflected at an over coupled, under coupled and impedance matched cavity. 38
2.5 Simulated power transmittance map of a linear three mirror coupled cavity. 40
2.6 Sketch of a lens guide as a cavity equivalent. 42

3.1 Schematic drawing of the principle layout of a Khalili end mirror cavity. 51
3.2 Transfer functions for end mirror displacement to the main interferometer signal in configurations with and without Khalili end mirror cavities. . . 53
3.3 Simulated intra-cavity powers in the arm cavity and in the Khalili cavity. 54
3.4 Simulated power transmittance map of an arm cavity with Khalili end mirror cavity with sub-SQL interferometer parameters. 56

3.5 Generic simulated heterodyne length signals for the sub-SQL interferometer arm cavities. 57
3.6 Carrier and sideband resonance in the interferometer arm cavities with Khalili end mirror cavities. 58
3.7 Coupling of heterodyne length signals for optimized control sideband frequency. 60
3.8 Schematic drawing of an interferometer arm cavity with a Khalili end mirror cavity. 64
3.9 Total loss in the coupled interferometer arm cavity as a function of AC and KC round-trip loss. 66
3.10 Approximated fundamental mode loss of an unstable cavity. 67
3.11 Khalili end mirror cavity stability parameter versus IETM and EETM ROCs for the configuration with a beam waist in the KC. 70
3.12 Khalili end mirror cavity stability parameter versus IETM and EETM ROCs for the configuration with a nearly collimated beam in the KC. . . 71
3.13 Khalili cavity example configurations, with and without a beam waist in the end mirror cavity. 72
3.14 Estimation of the robustness of Khalili end mirror cavity design parameters, for the configuration with a nearly collimated beam in the KC. . . . 78
3.15 Coupling of EETM tilt to the longitudinal phase of the Khalili end mirror cavity. 81
3.16 Coating Brownian thermal noise and end mirror cavity-specific noise in the sub-SQL interferometer versus the beam spot size on the core optics. 83
3.17 Progression of the interferometer layout toward reducing coating thermal noise with Khalili etalons. 87

4.1 Schematic drawing of the sub-SQL interferometer target configuration. . 90
4.2 Schematic drawing of the principle approach to an interferometer with variable arm cavity stability and tunable beam sizes. 93
4.3 Beam size and stability parameter of a symmetric arm cavity of variable length. 94
4.4 Simplified displacement sensitivity of the initial sub-SQL interferometer configuration. 95
4.5 Schematic drawing of the interferometer configuration with tunable arm cavity lengths. 97
4.6 Mode matching efficiency maps of the interferometer arm cavities for the initial and for the marginally stable configuration. 98
4.7 Arm cavity eigenmodes at different cavity lengths. 100
4.8 Mode matching efficiency of one of the interferometer arms as a function of the cavity length. 101

4.9 Degradation of the mode matching due to deviations of the initial beam waist position and the ROC of the collimating mirror. 103
4.10 Degradation of the mode matching due to deviations of the initial beam waist radius and the IM AR-surface ROC. 105
4.11 Coating absorption-induced heating of the arm cavity mirrors. 110
4.12 Interferometer arm cavity modal degeneracy for different values of the stability parameter. 114
4.13 Coupling of mirror tilt to longitudinal arm cavity phase for different cavity stability parameter values. 116
4.14 Transfer functions for input beam jitter to fundamental mode modulation sidebands in the detection port for different arm cavity lengths. 118

5.1 Sources of cavity round-trip loss. 122
5.2 Definition of the cavity scattering threshold angle. 124
5.3 Specular reflection and Lambertian reflection at a mirror with an irregular surface. 125
5.4 Fabry-Perot Michelson interferometer with balanced homodyne readout. 130
5.5 Fractional sideband photon loss in the arm cavities of the sub-SQL interferometer. 132
5.6 Back-action evasion in the sub-SQL interferometer by means of balanced homodyne detection for different homodyne angles. 133
5.7 Flow chart of the computational steps carried out in the grid-based sub-SQL interferometer model. 137
5.8 Illustration of the iterative calculation for the cavity steady-state field in the grid-based sub-SQL interferometer model. 140
5.9 Surface plots of Zernike polynomials with unity amplitude up to second degree. 146
5.10 Example of a synthetic PSD-based mirror surface map. 149
5.11 Estimated power spectral densities of phase maps generated with the synthetic mirror surface model. 150
5.12 Simulated round-trip loss of the marginally stable sub-SQL interferometer arm cavities with realistic mirror surfaces. 154
5.13 Simulated round-trip loss projected to the fundamental mode of the marginally stable sub-SQL interferometer arm cavities. 155
5.14 Simulated contrast defect in the sub-SQL interferometer with marginally stable arm cavities and realistic mirror surfaces. 156
5.15 Fundamental mode round-trip loss and contrast defect probabilities for varied mirror RMS irregularities, with and without astigmatism. 157

6.1 Mock-up 3D model of the single arm test experiment. 162

6.2 Stability parameter and beam spot size in the single arm test cavity plotted versus the cavity length. 164
6.3 Rendered technical drawings of plate capacitor ESD actuator prototype designs. 165
6.4 Schematic drawing of the single arm test optical layout. 166
6.5 Single arm test input optics layout. 171

7.1 Schematic drawing of the GEO squeezed-light laser optical layout. . . . 178
7.2 Chart of the building blocks of a generic LIGO CDS digital control system hardware setup. 181
7.3 Chart of the steps and components involved in the generation of CDS real-time code. 183
7.4 Distribution of squeezed-light laser control automation tasks between the CDS real-time and EPICS layers. 185
7.5 Schematic drawing of the hardware interface of the squeezed-light laser analog control electronics to CDS. 186
7.6 Graphical real-time code model of the SHG component. 188
7.7 Flowchart of the real-time locking algorithm top-level execution layer. . 190
7.8 Flowchart of the real-time locking sequence one code branch. 195
7.9 Flowchart of the real-time locking sequence two code branch. 196
7.10 Flowchart of the real-time locking sequence three code branch. 197
7.11 Correction signal transients recorded during lock acquisition of the squeezed-light laser. 201
7.12 Time series diagram of GEO fully locked operation and science time with and without squeezing enhancement. 202

List of Tables

1.1 Conceptual design parameters of the proposed sub-SQL interferometer target configuration. 25

3.1 Parameters of optical layout examples for the two Khalili cavity configurations. 73
3.2 Radius of curvature tolerances and resulting optical parameters for the configuration with a beam waist in the Khalili cavity. 75
3.3 Radius of curvature tolerances and resulting optical parameters for the configuration with a nearly collimated beam in the Khalili cavity. 76
3.4 Mirror ROC specifications for arm cavities with Khalili end mirror cavities with relaxed spot size constraint. 77
3.5 Optical parameters for an arm cavity configuration with Khalili end mirror cavities with reduced beam spot size. 84
3.6 Comparison of the high finesse configuration with end mirror cavities with a low finesse alternative for the sub-SQL interferometer. 85

4.1 Typical stabilities of arm cavities in large-scale GW interferometers in comparison to the sub-SQL interferometer target configuration. 92
4.2 Thermal effects in the sub-SQL interferometer arm cavities. 111

5.1 Key parameters of the sub-SQL interferometer quantum noise model. . . 131
5.2 Round-trip loss estimated with the modal and the grid-based model. . . 141
5.3 First ten Zernike polynomials and their common names. 145

6.1 Comparison of technical features of the single arm test and the sub-SQL interferometer. 166
6.2 Specifications of the single arm test pilot mirrors. 169
6.3 Proposed specifications of the single arm test steering mirrors. 170
6.4 CDS channels count for the single arm test experiment. 172

7.1 Flags and variables used in the squeezing automation real-time code. . . 192
7.2 EPICS PVs defined in the squeezing automation real-time code model. . 194

CHAPTER 1

Introduction

Experimental tests of the general theory of relativity are among the most challenging endeavors of modern physics. The fact that the measurable effects are extraordinarily small requires the construction of extremely sensitive measurement apparatus.

In this chapter a brief introduction to gravitational waves is given. The suitability of laser interferometers to directly measure the tiny disturbances of space-time which are caused by passing gravitational waves is pointed out. This discussion is followed by an introduction to the notion of quantum noise and its role as a limiting noise source in future GW interferometers. The relation to current prototyping efforts aiming at investigating techniques for the reduction of quantum noise in interferometers is established. Finally, the AEI 10 m Prototype project is introduced and an outline of the planned interferometer aiming at reaching sub-SQL sensitivity at hundreds of Hertz for its 100 g mirror test masses is given.

1.1 Gravitational waves

Only a few months after *Albert Einstein* published his general theory of relativity in 1916 he himself proclaimed the existence of gravitational waves (GWs) [1]. Due to the fact that these waves exhibit extremely small amplitude Einstein believed that GWs would never be measured.

GWs are transverse quadrupole waves propagating at the speed of light and are emitted when heavy cosmological objects with a non-vanishing quadrupole moment are subject to acceleration. This occurs for instance in binary star systems, supernovae or colliding black holes. These GWs can be regarded as a direct consequence of the principle of causality which postulates that cause and effect are separated in time as the cause cannot propagate faster than the speed of light. The violation of this principle had been a known shortcoming of *Newton*'s theory of gravity in which every cause has an instantaneous effect.

Although GWs are in many respects analogous to electromagnetic waves which are described by *Maxwell*'s theory of electromagnetism, they play a special role in the scope of astronomy and astrophysics. The fact that they penetrate through all matter nearly without interaction opens up a new window to astronomers and the

observation of the universe. An important difference between these two phenomena, however, is the existence of only one "charge" in gravitation, contrasting the existence of positive and negative charge in electromagnetism.

The first indirect proof of the existence of GWs was given by the physicists *Hulse and Taylor* in the year 1974 when they investigated the Pulsar PSR 1913+16 which was part of a binary star system. Their analysis of radio astronomy data led to the conclusion that the orbital period of the observed system slowly decayed during the observation time. The resulting energy loss could, in excellent agreement, be explained by the emission of GWs. For this discovery Hulse and Taylor were awarded the Nobel prize in 1993.

The first direct detection of GWs is an ongoing effort and is yet to be accomplished. However, after the first successful direct detection of GWs it is intended to increase the number of detected events further and further until GWs are routinely observed. This would be the beginning of the era of GW astronomy which would give scientists a fascinating insight, e.g. in the inner structure of cosmological objects, the observation of dark objects in space but also the extraction of information about the universe in its early phase after the big bang which is encoded in the stochastic GW background [2]. For a comprehensive introduction to the theory of GWs we refer to [3].

For the further discussion the measurable effects of GWs are of primary interest. A passing GW changes the local metric of space time, i.e. in a setup with free falling test masses a passing GW causes a fluctuation of the relative distance of the masses. The amplitude of a GW is defined as

$$h_{\mathrm{GW}} = \frac{2\Delta L_{\mathrm{GW}}}{L} \tag{1.1}$$

which is referred to as the GW *strain*. The quantity ΔL_{GW} is the GW-induced length fluctuation between two events in space time with a spatial separation of L. The measurable strain amplitudes on earth caused by astronomical sources of GWs are typically very small. For instance, a supernova explosion at a distance of 10 kpc would result in a measurable strain of $h \sim 10^{-20}$ on the earth. Despite the large instantaneous energy flux the resulting strain amplitudes are tiny which is a direct consequence of the extremely large stiffness of space time. It is evident that it requires extremely sensitive instruments to resolve these tiny signals by direct measurement.

1.2 Direct detection of gravitational waves

The first attempts of a direct measurement of GWs were undertaken in the 1960s by the physicist *Joseph Weber* with so-called *resonant bars* [4]. These resonant bars were freely suspended massive mechanical resonators, typically made of aluminum or niobium, with a weight of several tons. It was expected that a passing GW would excite oscillations at the eigenfrequency of the bar which was read out with sensors attached to the resonant body. The modern variants of Weber's resonant bar antenna

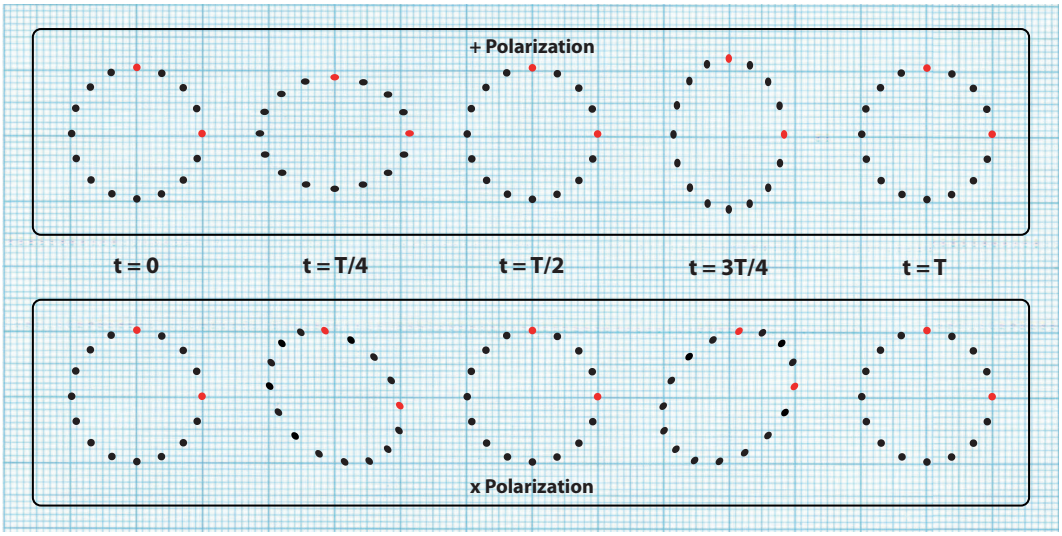

Figure 1.1: Effects of differently polarized gravitational waves on a ring of free-falling test particles. The wave propagating perpendicular to the plane of the test particles squeezes and stretches the space between these. By assuming that the red points represent the end mirrors of the perpendicular arms of a Michelson interferometer it becomes evident that a „plus" polarized GW excites the differential mode of the interferometer arms whereas a „cross" polarized GW excites the common mode of the interferometer arms.

had lengths of several meters and reached remarkable strain sensitivities of the order of $10^{-20}\,(\sqrt{\mathrm{Hz}})^{-1}$, with a bandwidth of approximately 100 Hz at a detection frequency of 1 kHz. Despite the continuous refinement of the resonant bar concept at numerous sites in the world no successful GW measurement could be accomplished with these.

Interferometric GW detectors are based on a fundamentally different concept. The principle which is common to all interferometric detectors is the measurement of the GW-induced change in the traveling time of light between free-falling test masses. The physical effect of a GW on light propagating between test masses can be described as either a modulation of the refractive index of the medium in which the light propagates or by a tidal force field acting on the test masses. Michelson interferometers with orthogonal arms in which the suspended mirrors act as test masses are particularly well suited for this purpose. In the picture of tidal forces acting on the interferometer mirrors gravitational waves cause deformations in the plane transverse to their direction of propagation which distort circles to ellipses while preserving the area of the original circle, cf. Figure 1.1. Similar to electromagnetic waves, GWs come in different polarizations, often referred to as "plus" polarization and "cross" polarization. Whereas the "plus" polarization poses the ideal case because it directly excites the differential mode of the interferometer arm lengths, the interferometer does not resolve GWs in "cross" polarization as these

solely excite the common mode of the arms. Only the excitation of the differential mode of the arms by a passing GW results in a signal in the detection port.

A GW incident on a laser interferometer causes a periodic differential change of the arm length which changes the phase at the beam splitter of the light returning from the arms by [5]

$$\Delta\phi_{\mathrm{GW}} = \frac{4\pi}{\lambda}\Delta L_{\mathrm{GW}} \,. \tag{1.2}$$

A fundamental property of the Michelson interferometer is the conversion of a phase change at the beam splitter which is caused by an excitation of the differential mode of the arms to a change in the amplitude of the fields in the symmetric and antisymmetric ports of the beam splitter. Hence, the information about the GW-induced arm length modulation can be read out from the interference pattern at the beam splitter using appropriate photo detection methods.

Since it was independently proposed to employ Michelson interferometers as broadband GW antennae by Weiss [6] and Forward [7] including the systematic identification of limiting noise sources, techniques for interferometric GW detection have been continuously improved and refined leading to the construction of large scale interferometers around the world with arm lengths of up to several kilometers. A decisive advantage of interferometric detectors over resonant bars is their larger bandwidth which typically ranges from approximately 10 Hz to 10 kHz. This enables the detection of GWs from a variety of cosmological sources. Besides optical bars and ground-based laser interferometry other approaches to directly measure GWs were conceived, e.g. space-borne laser interferometers such as the LISA gravitational wave observatory [8], spacecraft Doppler tracking [9], and pulsar timing experiments [10].

Currently, the world-wide network of ground-based GW detectors is in an upgrade phase towards what is commonly referred as the "second generation" of GW observatories. These observatories include the Advanced LIGO project [11], the French-Italian Advanced Virgo detector [12] and the German-British GEO-HF detector [13] and are complemented by the new Japanese observatory KAGRA [14], formerly referred to as LCGT.

The variants of the Michelson interferometer which are employed for GW detection are typically operated at the "dark fringe". Feedback control systems are employed to arrange for a dark signal port, in the case of heterodyne readout, or for a small amount of carrier light leaking into the signal port, in the case of "direct conversion" (DC) readout. In this case the laser light incident on the interferometer is fully reflected towards the laser source, the interferometer acts as a reflecting mirror and the detection port remains dark. Provided that the interferometer arms exhibit a high level of symmetry this gives rise to the rejection of common-mode fluctuations, e.g. of frequency noise of the input laser, which would otherwise couple into the interferometer signal and diminish the sensitivity of the instrument. Also, operating the interferometer on the dark fringe is required to make effective use of the techniques of *power recycling* and *signal recycling* [15], the combination of which will be employed in all second generation GW detectors (cf. Figure 1.2).

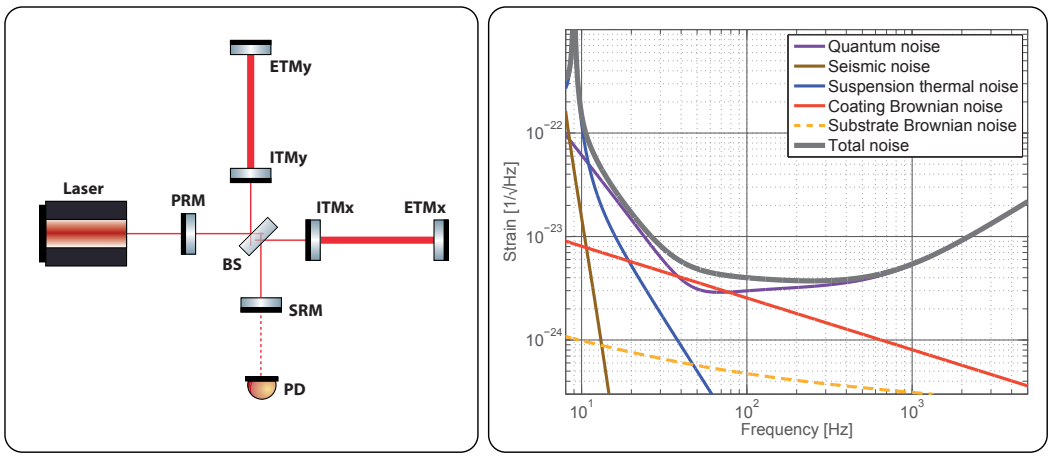

Figure 1.2: Left: Schematic layout of a Fabry-Perot Michelson interferometer with power recycling and signal recycling cavities. This configuration was adopted as baseline design for the Advanced LIGO [11] and Advanced Virgo [12] detectors, respectively, as well as for the KAGRA detector [14]. Cavities in the interferometer arms serve to increase the circulating power in the arms, to achieve higher shot noise-limited sensitivities. Furthermore, power recycling and signal recycling cavities are employed for resonant enhancement of the carrier and signal fields, respectively. **Right:** Anticipated top-level noise budget of the Advanced LIGO GW detectors, reproduced from [16]. Between 10 Hz and 200 Hz thermal noise sources limit the sensitivity of the detector and prevent reaching a sensitivity at the SQL.

It is the presence of noise in the detector that gives rise to the difficulty of detecting signals as small as GW-induced strain. To reach the targeted sensitivities, perturbations of the mirror positions need to be arranged for significantly smaller than the GW signal. A multitude of noise sources of classical as well as quantum mechanical origin can have a limiting effect on the achievable sensitivity of a GW detector. Classical noise sources that play a role in laser interferometers are e.g. frequency and amplitude noise of the input laser, noise in the electronics for sensing and control of the instrument, residual gas noise in the vacuum environment, seismic noise induced by vibrations of the ground of anthropogenic origin or caused e.g. by ocean waves. Once all technical noise sources are reduced by a sufficient amount the be negligible, three fundamental noise sources remain. First, gravity gradient noise at low frequencies, caused by mass distribution fluctuations in the vicinity of the interferometer resulting in forces exerted on the mirror test masses. Second, thermal noise in the optics and the suspension systems and third, quantum noise in the interferometer.

Hence, as the techniques for the reduction of classical noise in interferometers are further and further refined, quantum noise will be dominating in future high-precision laser interferometers and requires the application of sophisticated techniques to alleviate its impact on the sensitivities of the instruments.

1.3 Quantum noise and the Standard Quantum Limit

Quantum noise in laser interferometers arises from the quantum nature of the laser light and the photo-detection process. *Shot noise*, which is also referred to as photon counting noise, originates from fluctuations in the phase quadrature of the laser light in the interferometer. This gives rise to photon number fluctuations in the detection port of the interferometer resulting in a measurement error. *Quantum radiation pressure noise* is a result of random fluctuations in the amplitude quadrature entering through the dark port and beating against the carrier field which causes a fluctuating force acting on the interferometer mirrors. Whereas quantum radiation pressure noise dominates at lower frequencies, shot noise is the dominant quantum noise contribution at higher frequencies.

From the laws of quantum mechanics one can infer that if the position of a test mass in an interferometer is measured with high precision this measurement inevitably induces a random perturbation of the momentum of the test mass, which is a direct consequence of the *Heisenberg uncertainty principle*. The noise which stems from the perturbation of the test mass momentum is often referred to as *quantum back-action noise* and the higher the precision of the position measurement in a measurement apparatus, the more back-action noise is introduced by this measurement. This was expressed in [17] in the form of the uncertainty relation

$$S_{\hat{x}}(f)S_{\hat{F}}(f) - |S_{\hat{x}\hat{F}}(f)|^2 \geq \frac{\hbar^2}{4} \,. \tag{1.3}$$

In the above uncertainty relation $S_{\hat{x}}$ represents the noise spectral density of the intrinsic measurement noise, i.e. photon shot noise, and $S_{\hat{F}}$ represents the noise spectral density of the back-action noise, which occurs as quantum radiation pressure noise in an interferometer and $\hbar$ is the reduced Planck constant. In the general case the cross correlation term $|S_{\hat{x}\hat{F}}(f)|^2$ in Equation (1.3) vanishes. In this case the quadrature sum of the two quantum noise contributions enforces a quantum limit for the precision of a position measurement, the Standard Quantum Limit (SQL), which reads

$$S_{\hat{x}}^{\mathrm{SQL}}(f) = \frac{8\hbar}{m(2\pi f)^2} \tag{1.4}$$

for a Fabry-Perot Michelson interferometer. Obviously, the SQL scales with the interferometer mirror mass and heavier mirrors, which give rise to lower quantum radiation pressure noise, may be employed to reduce the impact of the SQL. However, as the strain-referred SQL scales with $m^{-1/2}$ it requires a factor of 100 increase in the mass of the mirrors to gain an order of magnitude in sensitivity. Extremely heavy test masses are the result which give rise to numerous technical difficulties.

By formulating electric fields in terms of field quadratures [18]

$$E(t) = \sqrt{\frac{4\pi\hbar\omega_0}{\mathcal{A}c}}\,[a_1(t)\cos(\omega_0 t) + a_2(t)\sin(\omega_0 t)] \tag{1.5}$$

the relations between incoming quadratures (a_1,a_2) and outgoing quadratures (b_1,b_2) can be given. The parameter ω_0 in equation (1.5) is the angular frequency of the

carrier field, $\mathcal{A}$ is the effective cross-sectional area of the laser beam, and $a_1(t)$, $a_2(t)$ are the input field amplitude and phase quadratures, respectively. In the presence of a GW with strain amplitude h_{GW} the output quadratures read

$$b_1 = a_1 \times \exp(2i\beta) \tag{1.6}$$

$$b_2 = \left[(a_2 - \mathcal{K}a_1) + \sqrt{2\mathcal{K}}\frac{h_{\mathrm{GW}}}{h_{\mathrm{SQL}}}\exp(-i\beta)\right] \times \exp(2i\beta) \ , \tag{1.7}$$

where $\exp(2i\beta)$ accounts for a time delay between incoming and outgoing fields caused by the arm cavities with $\beta = \arctan(2\pi f/\gamma)$ where γ is the arm cavity bandwidth. The constant $\mathcal{K}$ is a coupling constant which was first introduced in [18]

$$\mathcal{K} = \frac{2\gamma}{\Omega^2(\Omega^2+\gamma^2)}\frac{8\omega_0 I_0/\mathcal{T}_{\mathrm{in}}}{mLc} \ . \tag{1.8}$$

The parameter $\Omega = 2\pi f$ denotes the angular signal frequency, I_0 is the input laser power, $\mathcal{T}_{\mathrm{in}}$ is the arm cavity input mirror power transmittance and $h_{\mathrm{SQL}} = (S_{\hat{x}}^{\mathrm{SQL}})^{1/2}/L$, cf. Equation (1.4). According to Equation (1.7), the phase quadrature of the output field b_2 not only contains the GW signal, but also depends on the input field quadratures a_1 and a_2. Whereas the term proportional to a_2 represents shot noise, the term proportional to $\mathcal{K}$ gives rise to quantum radiation pressure noise. As pointed out previously it is noise in the a_1 quadrature quantum radiation pressure noise originates from.

In the case of b_2 quadrature detection in a conventional Fabry-Perot Michelson interferometer with uncorrelated quantum noise contributions, the strain-referred quantum noise spectrum of the interferometer can be written as

$$S_h = \frac{h_{\mathrm{SQL}}^2}{2}\left(\frac{1}{\mathcal{K}} + \mathcal{K}\right) \ . \tag{1.9}$$

The term proportional to $1/\mathcal{K}$ represents shot noise, which decreases with increasing laser power I_0. Quantum radiation pressure noise grows with increasing laser power and is thus represented by the second term proportional to $\mathcal{K}$. The SQL is reached at the frequency where S_h is minimal, i.e. at the point where the shot noise contribution to the total quantum noise is equal to the contribution by quantum radiation pressure noise.

Whereas the impact of quantum shot noise can in principle be reduced by increasing the circulating laser power, this approach is ultimately limited by thermo-elastic and thermo-refractive effects in the interferometer optics as well as other instabilities which occur at high laser power [19]. By increasing the circulating laser power quantum radiation pressure noise is increased and may reduce the low-frequency sensitivity of the detector. Even if the mirror test masses in an interferometer are made heavier, the low-frequency sensitivity will still be limited by the sharply increasing quantum radiation pressure noise which is proportional to f^{-2}. Cancellation of this noise contribution would therefore greatly enhance the low-frequency sensitivity of the detector resulting in increased binary inspiral

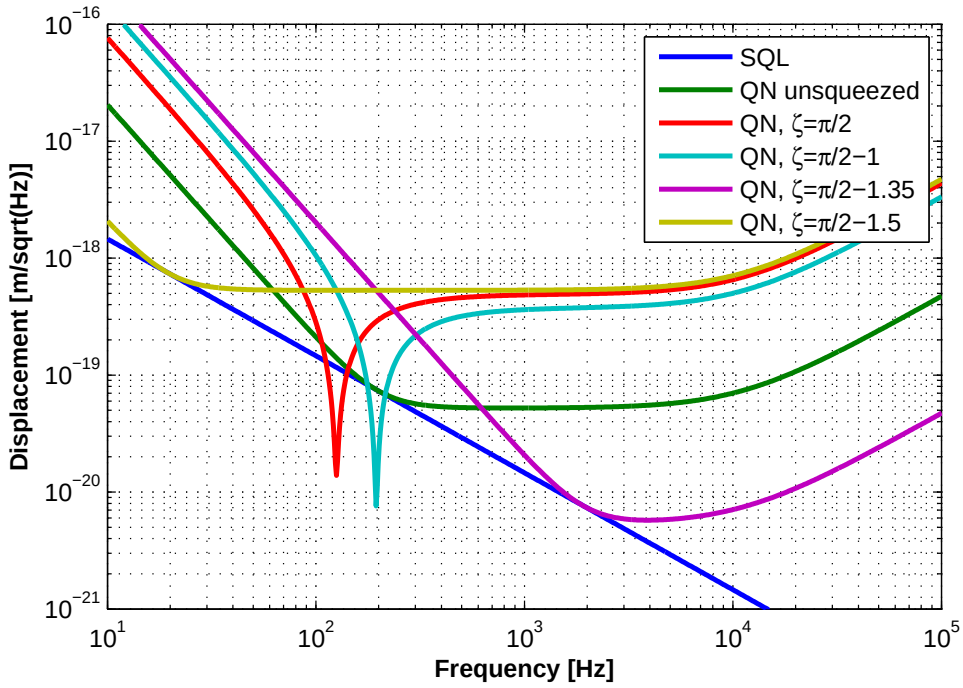

Figure 1.3: Quantum noise in a Fabry-Perot Michelson interferometer with frequency-independent input squeezing. The interferometer features 10 m arm cavities with a finesse of 670, 100 ppm round-trip loss. An input laser power of 5 W was chosen, resulting in an SQL touching frequency of approximately 200 Hz. The frequency independent squeezing with 10 dB quantum noise reduction is injected at different squeezing angles. By choosing the squeezing angle ζ appropriately, the SQL can be surpassed in a small frequency range.

ranges and would allow for the investigation of slower pulsars such as the Crab and Vela pulsars [20].

The only possible means to measure the test mass position in a given interferometer with a sensitivity below the SQL is the introduction of correlations between sensing noise and back-action noise in the instrument. This can be achieved by injecting squeezed states of light or by employing so-called "quantum non-demolition" (QND) techniques.

To surpass the SQL by input squeezing the appropriate *squeezing angle* needs to be chosen for the injected squeezed vacuum. The squeezing angle determines the squeezed and anti-squeezed quadratures and from Equation (1.7) it can be inferred that it is the $a_2 - \mathcal{K}a_1$ quadrature that needs to be squeezed to reduce the impact of quantum noise on the measurement. In fact, due to the frequency dependence of the coupling constant $\mathcal{K}$ the optimal squeezing angle is a function of the frequency. Quantum noise spectra of a Fabry-Perot Michelson interferometer with 10 m arm cavities with a finesse of ~ 670 and 5 W input power with frequency independent input squeezing are shown in Figure 1.3. With this approach the SQL can be surpassed in a small frequency range. Alternatively, by employing a

readout scheme which is capable of detecting a particular combination of the output quadratures

$$b_\zeta = b_1 \cos\zeta + b_2 \sin(\zeta) \ , \tag{1.10}$$

where ζ is the quadrature angle, quantum back-action noise can be canceled from the measurement. For a broadband reduction of quantum noise either of these two techniques needs to be employed in combination with detuned *filter cavities* [18], to provide a frequency-dependent rotation of the involved field quadratures upon reflection at these cavities. The resulting configurations are generally referred to as *frequency-dependent input squeezing* and *quantum variational readout*, respectively. Both techniques may be implemented in parallel in an interferometer to combine their respective strengths, resulting in what is referred to in the literature as a *squeezed-variational* interferometer.

Instead of modifying the input and output optics of a conventional Michelson interferometer, different interferometer configurations may be employed which are inherently capable of measuring QND variables. In conventional Michelson interferometers the measured observable is the test mass position, hence these interferometers are also referred to as *position meters*. Due to the non-commutativity of two subsequent position measurements

$$[\hat{x}(t), \hat{x}(t')] \neq 0 \tag{1.11}$$

an uncertainty relation exists for the corresponding observables which leads to the SQL. Obviously, to circumvent the SQL a quantity $\hat{P}$ of the mirrors needs to be measured which commutes at different times,

$$[\hat{P}(t), \hat{P}(t')] = 0 \ , \tag{1.12}$$

which could e.g. be the test mass momentum. Interferometer configurations in which a measurement of the momentum of the test masses is realized were initially proposed by *Braginsky* and *Khalili* [21] and are nowadays commonly referred to as *speed meters*. Other than in a conventional position meter, in which the non commuting test mass position is probed, in speed meter interferometers the relative speed of the test masses is measured. Technical realizations of speed meters are based e.g. on Michelson interferometers with a so-called *sloshing cavity* [22] or the *zero-area Sagnac* topology [23]. However, substantial research is necessary to evaluate the potential of speed meter configurations for an application in GW interferometry.

In future GW detectors QN is expected to be the limiting noise source in a broad frequency band. As can be seen in Figure 1.2, the sensitivity of the second generation Advanced LIGO GW detectors will be limited by quantum noise in the frequency band ranging from a few Hz to several kHz, except for a small region around 100 Hz in which coating Brownian thermal noise dominates over quantum noise. In particular, the anticipated sensitivity of Advanced LIGO is within a factor of ~ 2 near the SQL. To further increase the sensitivities of future detectors in a broad frequency band the employment of quantum noise reduction techniques will be inevitable. For instance, in the conceptual study for the third generation

observatory *Einstein Telescope* (ET) [24], techniques for the reduction of quantum noise are already part of the baseline design and are key to reaching the targeted sensitivity. Hence, the subject of quantum noise reduction in interferometers is an important subject of ongoing research. Prototype experiments such as the AEI 10 m Prototype are intended not only to serve as testbeds for the proposed QN reduction techniques but also to bring these techniques to a level of maturity which enables an application in large-scale interferometers. The role of quantum noise in future GW detectors is reviewed e.g. in [25, 26].

1.4 The AEI 10 m Prototype

Since the early days of interferometric gravitational wave detection, smaller scale interferometer prototypes played a pioneering role for the development and refinement of interferometry techniques which were later adopted by the large-scale instruments. Hence, these prototypes significantly contributed to the successful construction and operation of the first generation GW detectors as well as to the more sensitive, but also significantly more complex, second generation observatories and will pave the way also for the third generation of earth-bound GW detectors.

For instance, prior to its integration in the baseline design of the GEO 600 GW detector, the technique of *dual recycling* (DR) [15] was first thoroughly investigated in interferometer prototypes at Glasgow University [27] and the Max-Planck-Institut für Quantenoptik in Garching [28, 29]. Many of the interferometry techniques employed in the Advanced LIGO GW observatories were thoroughly tested within two prototype facilities operated by the LIGO project, namely the *LIGO advanced systems testing interferometer* (LASTI) at the Massachusetts Institute for Technology and the *Caltech 40 m prototype* at the California Institute for technology. Whereas the former is a testbed for full-scale infrastructure such as the aLIGO monolithic main suspensions and seismic isolation systems [30] the latter focuses on optical configuration, signal readout as well as sensing and control aspects [31, 32].

Novel concepts for the reduction of thermal noise such as for instance interferometry with diffractive optics [33, 34] and higher-order Laguerre-Gauss modes of light [35] have recently been investigated in the Glasgow 10 m prototype. Techniques for interferometry at cryogenic temperatures were tested in the scope of the Japanese *cryogenic laser interferometer observatory* (CLIO) project [36], which pioneered the construction of the *Kamioka gravitational wave detector* (KAGRA) [14].

In this section, an overview of the 10 m Prototype facility is given, which is under construction at the Albert-Einstein-Institute at University of Hannover. The discussion includes an introduction to its individual subsystems as well as an overview of the conceptual design of the *sub-SQL interferometer* experiment which is planned to be among the first experiments that will be carried out in the scope of this project.

The AEI 10 m Prototype facility is located in a dedicated hall at the Albert-Einstein-Institute. Whereas at surface level the facility provides lab space for auxiliary systems and includes a clean room environment for the assembly of mechanical

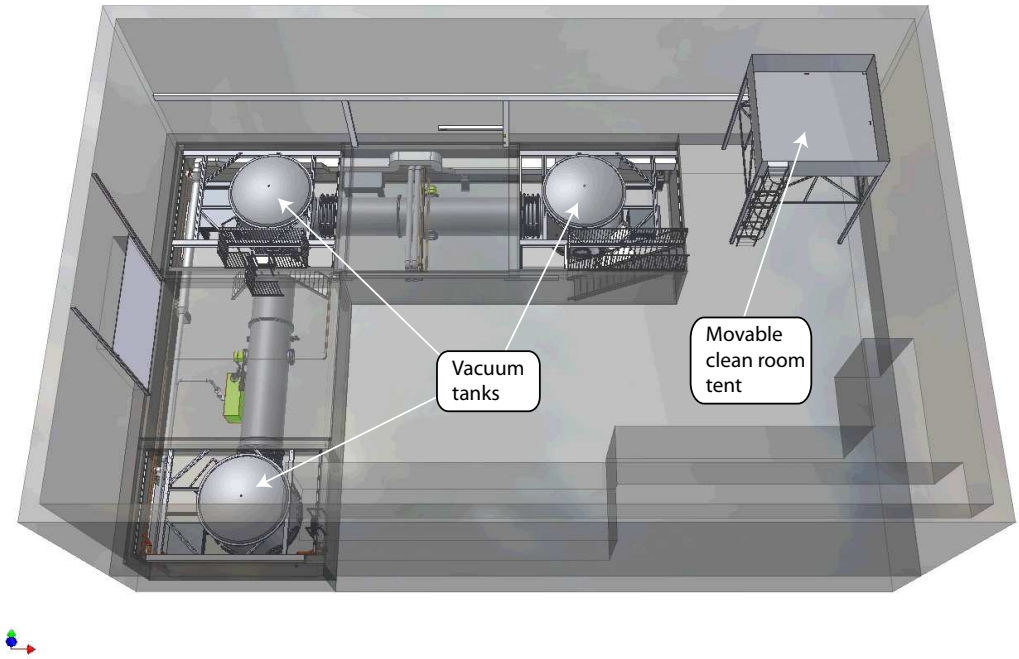

Figure 1.4: Rendered image of a bird's-eye view of the AEI 10 m Prototype hall. At ground surface level space is available for auxiliary systems and for the assembly of mechanical parts. The L-shaped vacuum system, which will house the planned interferometry experiments, is located at basement level.

parts, the actual vacuum system, which will house the planned experiments, was set up at basement level, cf. Figure 1.4. In this section an overview of the subsystems forming the prototype infrastructure is given. These include the vacuum system, seismic isolation tables, the suspension platform interferometer and the main laser system along with the reference cavity for laser frequency stabilization. The digital system control and data system, which is employed for the implementation of digital feedback controls required by the prototype infrastructure and future experiments and which provides data acquisition and long-term storage capabilities, is outlined in Chapter 7.

1.4.1 Scientific goals

Unlike previous prototype experiments built and operated by the GW community, which were often engineering prototypes dedicated to testing advanced technologies for a particular large-scale GW detector project, the AEI 10 m Prototype is more independent in the sense that it has a much wider scope with respect to planned experiments and the testing of innovative interferometry concepts, which will have a wide application in future ultra-high precision interferometers.

On the one hand the AEI prototype facility is intended to host experiments which aim at testing advanced interferometry technologies and at evaluating their viability as upgrades for second or third generation GW observatories [37]. On the other hand the AEI 10 m Prototype is meant to provide a testbed for experiments which require a certain infrastructure such as an ultra-high vacuum environment, excellent seismic isolation as well as optical infrastructure. Potential candidates for this type of experiments are e.g. not only LISA [38, 39] related experiments as well as tests of the interferometry infrastructure for future space-borne satellite geodesy missions, e.g. the GRACE follow-on mission [40], but also direct measurements of thermal noise.

Reaching the SQL has been a long standing goal of interferometry experiments. Among the first planned experiments in the AEI 10 m Prototype is an interferometer, commonly referred to as the sub-SQL interferometer, which is supposed to be exclusively limited in its sensitivity by photon shot noise and quantum back-action noise at approximately 200 Hz. Besides viewing the sub-SQL interferometer as a proof-of-principle demonstrator for sensitivities below the SQL this instrument may also be regarded as a testbed for advanced interferometry techniques aiming at quantum noise reduction, as for instance squeezing injection or back action evasion by means of balanced homodyne readout. The goal of directly measuring quantum radiation-pressure noise is closely related to the generation of *ponderomotive squeezing* [41]. Mathematically, the generation of ponderomotive squeezing is contained in Equations (1.6) and (1.7). Input field fluctuations of the amplitude quadrature are converted to phase fluctuations via coupling of the light field to the mirror position. Hence this opto-mechanical coupling gives rise to correlated phase and amplitude quadrature fluctuations of the light field which can be viewed as squeezing of its quantum noise. Furthermore, by arranging for a classical noise budget below the SQL the interferometer mirrors can be prepared into nearly quantum states, resulting in macroscopically entangled interferometer test masses [42].

1.4.2 Vacuum system

The vacuum system provides the ultra-high vacuum environment required by extremely sensitive interferometry experiments which will be carried out in the scope of the 10 m Prototype project. Its aim is to ensure that environmental noise sources, as for instance acoustic coupling and refractive index fluctuations, are reduced to a sufficiently low level such that these effects do not impede the precision of future measurements. The 10 m Prototype vacuum system was in-house designed to fit into the existing laboratory space and was set up in the basement of the Prototype hall at the AEI. A rendered image of the system is depicted in Figure 1.5.

The L-shaped vacuum system is composed of three stainless steel tanks with a height of 3.4 m and a diameter of 3 m which are interconnected by tubes with a diameter of 1.5 m. Owing to the generous dimensions the seismic isolation tables described in Section 1.4.3 fit in the tanks conveniently and leave enough room for the experimenter to enter the vacuum tanks to work on the mechanical or optical

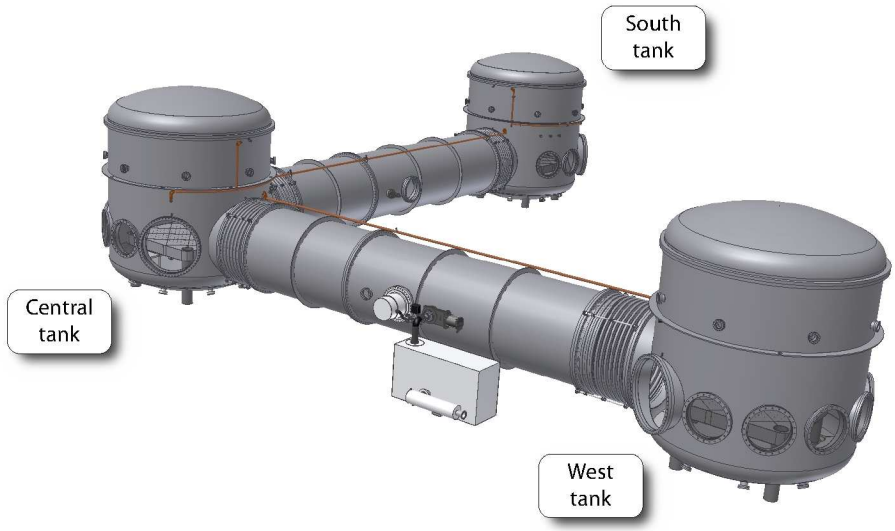

Figure 1.5: Rendered technical drawing of the AEI 10 m Prototype vacuum system. The three stainless steel tanks with a diameter of 3 m and a height of 3.4 m are interconnected with tubes with 1.5 m diameter. The tank center-to-center distance is 11.65 m.

infrastructure. The tank center-to-center distance is 11.65 m, the overall volume of the system is approximately 100 m^3 and the weight is approximately 22 t. Installation of the system was completed in February 2009 and it is fully operational since May 2009 with a residual gas pressure of $\sim 5 \times 10^{-8}$ mbar.

A generous number of flanges were included in the design to allow for routing of electronic signals into and out of the vacuum system. All smaller flanges with diameters ≤ 60 cm are sealed with copper gaskets. The larger flanges, i.e. the doors of the tanks with a diameter of 1 m, the flanges for the tubes with a diameter of 1.5 m and the flanges at the lids of the tanks with a diameter of 3 m are sealed with Viton® o-rings.

To reach the desired vacuum levels, an array of vacuum pumps is employed. For the roughing a screw pump with a pump power of 175 l/s is used which reduces the atmospheric pressure in the vacuum system to a level of approximately 5×10^{-2} mbar after about two hours of pumping. Once this pressure is reached, the screw pump is switched off and two scroll pumps take over. The purpose of the first one of these pumps is to further reduce the pressure achieved with the screw pump and backing of the turbo-molecular pumps. The second scroll pump is used for differential pumping of the gap between the o-rings used to seal the big vacuum flanges. To prevent vibrations of the scroll pumps from disturbing experiments carried out in the prototype, these pumps are located in a dedicated pump room, spatially separated from the vacuum system. Furthermore, they are set up on simple, yet effective, double stack isolators consisting of granite slabs and Sorbothane® hemispheres.

Once a pressure of $\leq$ 1 mbar is reached, two magnetically levitated turbomolecular pumps with a pump power of approximately 2400 l/s are activated. These are located directly at the tubes interconnecting the vacuum tanks. With this configuration it is possible to reach pressures as low as 10^{-6} mbar after 12 hours of pumping and 10^{-7} mbar after one week of pumping. Since the system was not baked, the vacuum pressure is limited by water vapor at approximately 5×10^{-8} mbar. It is worth noting that gate valves were not included in the design, i.e. it is necessary to vent the whole system to work on the infrastructure. However, as very low pressures can be reached after comparatively short pumping times, the configuration is well suited for prototype work requiring the system to be vented frequently.

1.4.3 Seismically isolated optical tables

In current high-precision laser interferometric experiments, seismic noise turns out to be the limiting noise source at low frequencies, below approximately tens of Hz. Seismic noise originates from the vibration of the ground which is caused by natural events such as plate tectonics or ocean waves hitting the coast but also by human activity such as transportation and industrial work. For instance, the ground motion in the AEI 10 m Prototype hall was measured to be approximately 300 nm RMS. If optical elements of interferometric experiments are not sufficiently well isolated, the ground motion may couple into the measurement and spoil the sensitivities of the instruments.

As the first stage of seismic isolation of the experiments carried out in the AEI 10 m Prototype a system based on the LIGO *seismic attenuation system* (SAS) [43] was adopted. The original system was re-designed to meet the specific requirements of the AEI 10 m Prototype baseline [44]. The revised design is commonly referred to as *AEI-SAS*. With these isolation tables it is aimed for a suppression of to the ground motion by up to 80 dB below 10 Hz.

The foundation of the SAS concept is the combination of two passive isolation techniques, the *inverted pendulum* (IP) legs [45] and *geometric anti-spring* (GAS) filters [46], for seismic isolation of all six degrees of freedom. A rendered technical drawing of an AEI-SAS table is shown in Figure 1.6. The virtue of this passive isolation approach lies in the fact that no feedback control with complex control schemes, which need to be adapted to the altered dynamical behavior whenever the payload on the tables changes, is required.

The three IP legs of the tables exploit the well-known roll-off of the frequency response of pendula above their resonance frequency and thus provide horizontal isolation of the tables. A stiff flexure at the bottom of the IP legs supports the intrinsically unstable IPs against gravity to ensure that they remain in an upright position. A soft flexure at the top of the IPs serves as a hinge between the legs and the spring box, the part of the table which contains the GAS filters, hence constraining its pitch and roll movement. The IPs exhibit resonance frequencies of approximately

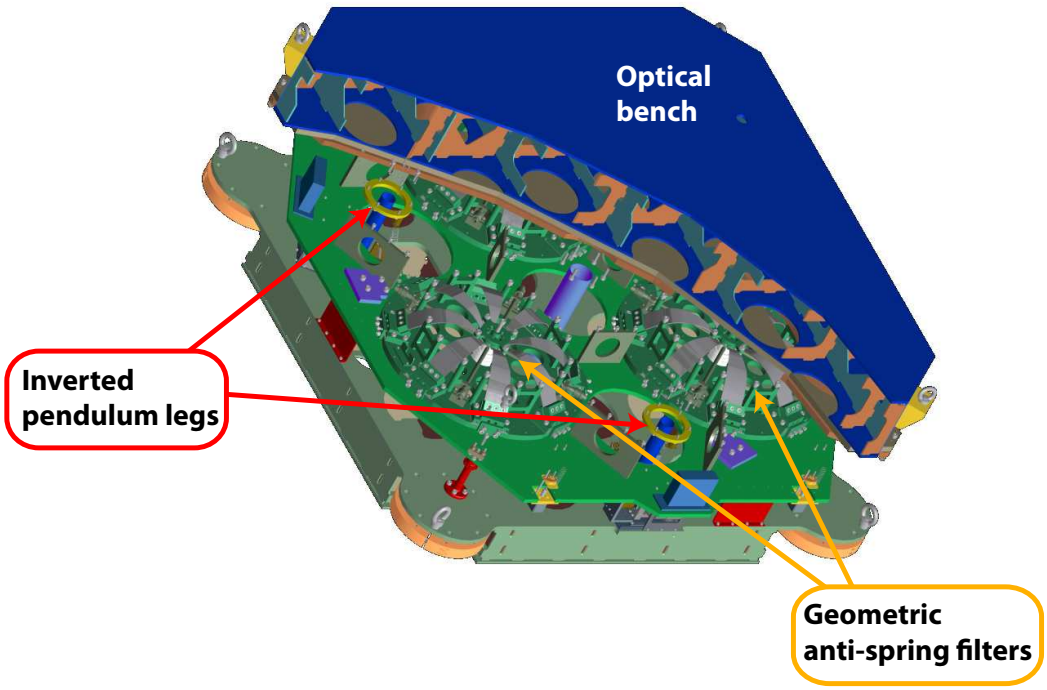

Figure 1.6: Rendered technical drawing of an AEI-SAS (seismic attenuation system) optical table. For passive horizontal and vertical seismic isolation the optical tables in the AEI prototype are equipped with inverted pendulum legs and geometric-anti spring filters. Above the so-called spring box which houses the GAS filters sits the 40 cm high optical bench, with a usable area of $1.75 \times 1.75\,m^2$ for optical assemblies.

50 mHz. Vibration attenuation of up to 70 dB – 90 dB can be achieved, limited by the inertia of the legs [44].

The three GAS filters consist of eight blade springs each, which are bent and radially compressed, forming a crown of curved blades. This serves to exploit the geometric anti-spring effect to achieve very low resonance frequencies of the vertical action oscillator. Additional so-called *magic wands* [43] are employed in the GAS filters to compensate for the inertia of the blade springs, to optimize the isolating action of the filter. The GAS filters exhibit mechanical resonance frequencies of about 200 mHz which can be further reduced with the aid of feedback control. Provided that the GAS filter is optimally aligned, vertical isolation of up to 60 dB – 80 dB can be achieved [44].

To improve the attenuation performance of the system, especially near its fundamental resonance frequencies, the tables are equipped with numerous co-located sensors and actuators enabling active damping of resonances. Three types of sensors are used for reading out the motion of the table: *linear variable differential transformers* (LVDTs) for position measurements relative to the ground, accelerometers for measuring horizontal inertial motion and geophones for measuring residual motion of the optical bench. Voice-coil actuators are used for damping of resonances and

for low-frequency positioning of the tables. Finally, stepper motors are employed for fine tuning of the table positions and for alignment.

The optical bench, which is the topmost stage shown in blue in the drawing in Figure 1.6, is 175 cm × 175 cm wide, 40 cm high and is made of stainless steel. A honeycomb structure provides stiffening while keeping the weight manageable. Each of the tables weighs approximately 950 kg. For a homogeneous mass distribution the tables are equipped with ballast rods, which are removed when the payload increases.

At the time of writing two of the seismic isolation tables were already installed in the central and the south tank of the vacuum system, respectively, and were operational. The construction of the third table had started. For further details on the seismic isolation tables see [47].

1.4.4 Suspension platform interferometer

To actively suppress the relative motion of the optical tables described in the previous section, an interferometric link by means of a *suspension platform interferometer* (SPI) is established between the central table and the two far tables. With the aid of the SPI, the relative position and orientation of the optical tables will be sensed and the extracted signals will be utilized for relative stabilization in all degrees of freedom except for roll about the optical axis of the SPI to which it is insensitive. The benefit from the SPI is that of relaxed control requirements for the planned interferometry experiments. Furthermore, it enables tests of techniques for space interferometry, such as the planned experiment for a GRACE follow-on mission [40].

For the SPI, the method of heterodyne Mach-Zehnder interferometry was adopted, which provides error signals over a wide operating range much larger than the optical wave length of the measurement laser. A schematic drawing of the SPI optical layout is shown in Figure 1.7. The main laser of the SPI, an *Innolight Prometheus* solid-state laser with an iodine frequency stabilization [49], sits on the modulation bench outside the vacuum system where two beams frequency-shifted by 80 MHz ±10 kHz are generated and guided into the vacuum system to the measurement bench on the central table via two optical fibers. The majority of optical components are set up on this measurement bench. To avoid drifts due to thermal expansion, these components are bonded to a CLEARCERAM®-Z HS base plate by means of hydroxide-catalysis bonding [50]. A single curved mirror is set up on each of the far tables. The purpose of these curved mirrors is to reflect the measurement beams which are launched at the far table mirrors from the central table assembly back to the central table.

Basically, the SPI consists of four interferometers: one reference interferometer, one diagnostic interferometer and two measurement interferometers. The reference interferometer is intended to measure common-mode fluctuations which are subtracted from the signals obtained from all other interferometers. The diagnostic interferometer is used for debugging purposes and for estimating the sensitivity of the SPI. Finally, the two measurement interferometers measure the distance and

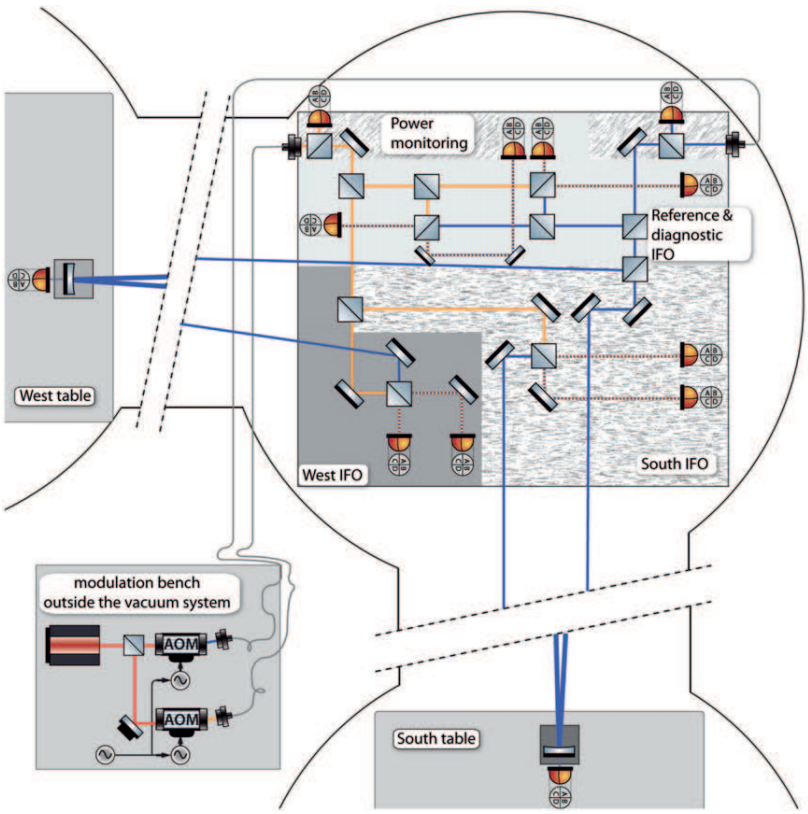

Figure 1.7: Schematic drawing of the optical layout of the suspension platform interferometer, reproduced from [48]. The laser source of the SPI sits on the modulation bench outside the vacuum system where two beams with a frequency shift of 80 MHz ±10 kHz are prepared and guided into the vacuum system via two optical fibers. The relative distance and orientation of the tables is sensed with the aid of two heterodyne Mach-Zehnder interferometers with one arm of each of the interferometers reaching to the west and the south table, respectively. © IOP Publishing. Reproduced by permission of IOP Publishing. All rights reserved.

orientation of the far tables relative to the central table. The curved mirrors on the far tables are in fact part of one of the measurement interferometers' folded arms.

Quadrant photo detectors (QPDs) are employed for reading out the measurement interferometer signals. The photo currents from each of the QPD quadrants are fed to a *phase meter* [51], which processes the measured signals and outputs a DC signal as well as real and imaginary parts of the complex amplitude of the QPD quadrant signal at the heterodyne frequency of $\sim$ 20 kHz. The phase meter output signals are sent to the digital control system via Ethernet where they are combined to yield error signals for feedback control of the optical tables. For actuation, the voice-coil actuators of the AEI-SAS tables are be utilized [44].

With the aid of the SPI, it is aimed for a stabilization of the relative distances of the tables to better than $10^{-10}\,\mathrm{m}/\sqrt{\mathrm{Hz}}$ in the frequency range of 10 mHz-100 Hz.

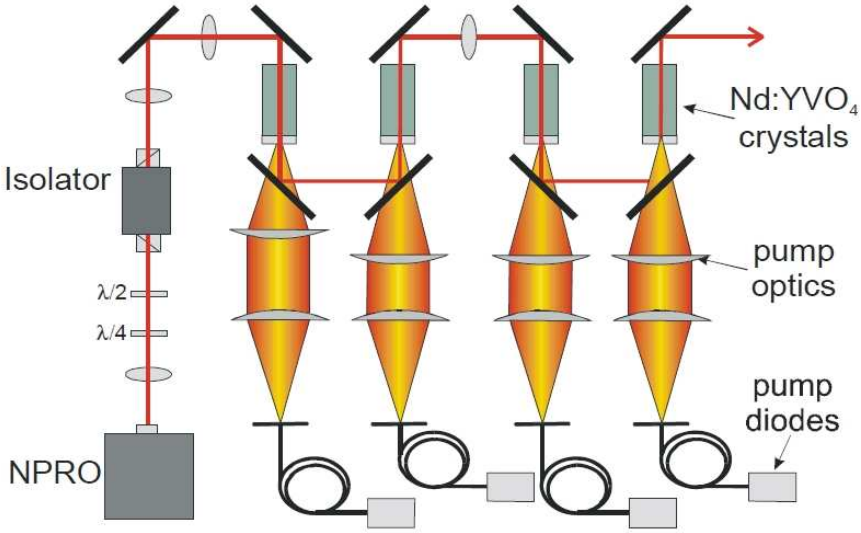

Figure 1.8: Schematic drawing of the main AEI 10 m Prototype laser system, based on the Advanced LIGO laser front end design. The output power of 2 W from an NPRO master laser is guided through an amplifier stage consisting of four consecutive diode laser-pumped Nd:YVO_4 crystals, yielding a nominal output power of 35 W with low frequency and intensity noise and excellent beam quality. © OSA. Image reproduced from [54] with kind permission of the Optical Society of America.

For angular fluctuations of the relative table orientation it is aimed for less than $10^{-8}\,\mathrm{rad}/\sqrt{\mathrm{Hz}}$ in the same frequency range.

At the time of writing the SPI was installed and being commissioned on the central and south optical tables. For further details on the SPI see [52, 53].

1.4.5 Laser system

The main laser source of the AEI 10 m Prototype is based on the first two stages, the so-called *front end*, of the three stage Advanced LIGO laser system design and is composed of a Nd:YAG solid-state *master* laser in its first stage followed by an amplifier forming the second stage. The master oscillator is a commercial *Innolight Mephisto* non-planar ring oscillator (NPRO) laser, which operates at a wave length of $\lambda_0 = 1064\,\mathrm{nm}$ with an output power of 2 W cw. The beam emitted by the master laser is directed through a four head Nd:YVO_4 amplifier stage [54], which is pumped with light from an array of diode lasers at a wave length of at 808 nm, resulting in a nominal output power of 35 W with approximately 95 % of the output power in the fundamental mode. A schematic drawing of the laser system is shown in Figure 1.8.

Approximately 10 W of laser light are guided into the vacuum system with a 4.5 m long photonic crystal fiber, which provides filtering of the spatial mode of the laser beam. Since the maximum transmitted power is limited by stimulated

Brillouin scattering free space coupling of the laser beam poses an option for future experiments requiring higher laser power.

An in-vacuum mode-cleaner (MC) cavity provides further spatial mode cleaning and filtering of high-frequency noise. It consists of three mirrors, two planar coupling mirrors and an end mirror with 1 m curvature radius, which were glued to a rigid spacer, forming a triangular cavity with a round-trip length of 53 cm. The spacer is made of *Super Invar* which exhibits a thermal expansion coefficient as low as $0.63 \times 10^{-6}\,\mathrm{K}^{-1}$. The cavity g-factor of 0.735 and the nominal value of ~ 1000 for the MC cavity Finesse ensure good suppression of higher-order transverse modes in the transmitted field. For length sensing and control of the MC cavity the *Pound-Drever-Hall* (PDH) scheme is employed [55].

A fraction of the beam transmitted by the MC cavity is directed to a photodetector, which is part of the laser intensity stabilization feedback loop, as well as to the frequency reference cavity for laser frequency stabilization which will be discussed in the following section. For further details on the laser system, fiber-coupling and the laser preparation stage see [56].

1.4.6 Frequency reference cavity

To further improve the frequency stability of the main laser system, a frequency reference cavity is employed. This cavity is formed by three suspended mirrors in a triangular configuration with a round-trip length of 21.2 m. Two planar cavity mirrors are located at the central table and the third curved one on the south table. The round-trip length of the cavity together with the chosen radii of curvature of the cavity mirrors results in a cavity g-factor of 0.72, yielding a 2.4 mm beam waist and a suppression of higher-order transverse modes in the laser beam by a factor of $\gtrsim 1000$ for modes up to sixth order.

Since the frequency fluctuations Δf, which are a consequence of the fluctuating length of the cavity ΔL, are proportional to the inverse of the cavity length L, i.e. $\Delta f \propto \Delta L / L$, under given spatial constraints a triangular configuration with its increased round-trip length is more favorable than e.g. a linear two mirror cavity. A mass of 850 g was chosen for the mirrors, based on noise performance considerations and tolerable loading of the optical tables. To keep classical radiation pressure noise and shot noise levels below the requirements an input power of 532 mW was chosen at the nominal Finesse of $\mathcal{F} = 4637$ of the reference cavity.

The coupling of seismic noise, which is already strongly attenuated by the isolation tables described in Section 1.4.3, is further reduced with the aid of suspensions for the mirrors. These are typically composed of multiple cascaded pendulum stages for horizontal seismic isolation, and blade springs for vertical seismic isolation, respectively. For excitations of the suspension point above their resonance frequencies, coupling to the position of the suspended optics is reduced proportional to f^{-2} per pendulum stage, where f is the frequency of the excitation. For the reference cavity mirror suspensions a design based on two stages of vertical isolation and triple-cascaded pendulum stages for horizontal isolation was assumed. The mirrors are suspended from the penultimate stage with 55 μm steel wires. A rendered image

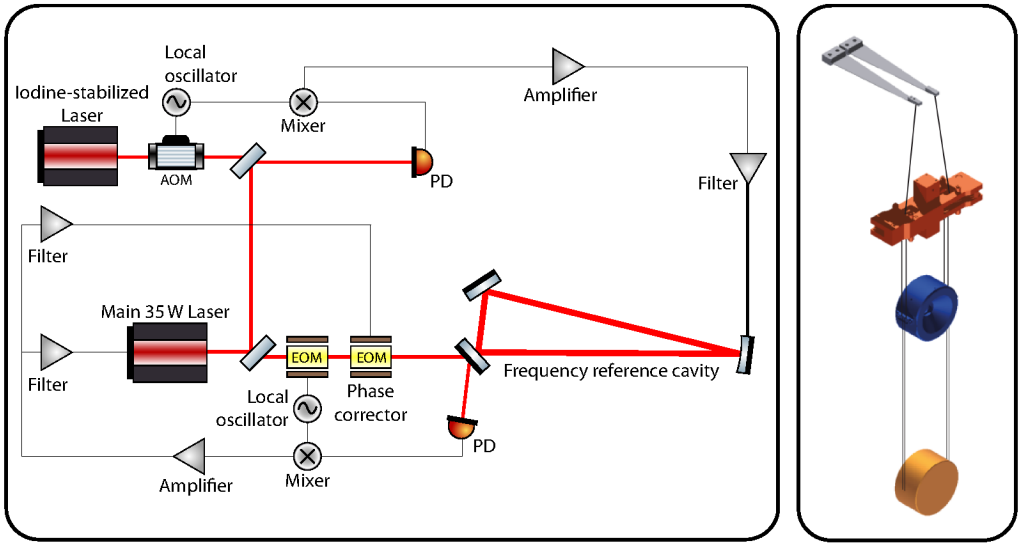

Figure 1.9: Left: Schematic drawing of the frequency reference cavity control topology. To improve the low-frequency stability of the reference cavity it will be locked to the frequency of the iodine-stabilized SPI laser at frequencies $\lesssim 4\,\mathrm{Hz}$. The Pound-Drever-Hall scheme is employed to obtain a length signal from the reference cavity which is used for feedback to the main laser frequency. **Right:** Rendered image of a reference cavity suspension. The design is based on triple-cascaded steel wire pendulum stages for horizontal isolation in combination with two stages of vertical isolation.

of this design is shown in the right frame in Figure 1.9. So-called *BOSEMs* [57] are employed at the top masses, enabling position measurements based on shadow sensors as well as active position control and damping of eigenmodes with coil-magnet actuators.

To ensure optimal performance of the system, a sophisticated control scheme based on several sensors and actuators with control authority in different frequency bands was developed. The control topology layout is shown in the schematic drawing in the left frame in Figure 1.9.

Below the pendulum resonances of the suspended reference cavity mirrors the scheme relies on the SPI-enhanced length stability. Above the resonance frequency, length fluctuations are reduced by the high frequency roll-off of the frequency response of the suspension system. For stabilization at frequencies $\lesssim 4\,\mathrm{Hz}$, the iodine-stabilized SPI laser provides a better reference than the suspended cavity. Hence, a feedback loop will be utilized which makes the length of the reference cavity follow the frequency of the SPI laser at low frequencies.

To obtain a length signal from the reference cavity, the *Pound-Drever-Hall* scheme is employed [55]. An electro-optic modulator in the beam path imprints phase modulation sidebands at 8 MHz on the laser beam which are anti-resonant in the reference cavity. The same phase modulation sidebands form the basis of the angular control scheme of the cavity.

The detected signal in reflection of the cavity is demodulated at the modulation frequency to obtain an error signal for laser frequency correction via actuation on the NPRO crystal length. For corrections below 1 Hz, the crystal is thermally actuated on. Mechanical actuation on the laser crystal by means of a piezo-electric transducer (PZT) is employed for corrections in the range of 1 Hz - 10 kHz and, finally, a phase correcting EOM is employed for actuation on the frequency in the 10 kHz - 250 kHz range. With this stabilization scheme it is aimed for a frequency noise level of $\sim 10^{-4}\,\mathrm{Hz}/\sqrt{\mathrm{Hz}}$ at 20 Hz rolling off to below $6 \times 10^{-6}\,\mathrm{Hz}/\sqrt{\mathrm{Hz}}$ above 1 kHz.

To ensure good alignment of the input laser beam to the reference cavity eigenmode, fast steering mirrors in the input optics train will be utilized, which will be part of an alignment control loop. Alignment signals for feedback control will be extracted with the aid of differential wave-front sensing. Additionally, spot position sensors will be employed to measure static misalignment in the ring cavity, which will be corrected for by directly actuating on the reference cavity mirrors. For further details on the frequency reference cavity see [58, 59].

1.5 Conceptual design of the 10 m sub-SQL interferometer experiment

One of the experiments which are planned to be carried out in the AEI 10 m Prototype environment is a Fabry-Perot Michelson interferometer which is intended to operate at a purely quantum noise limited sensitivity in its detection band at hundreds of Hertz. At a frequency of approximately 200 Hz this instrument will be capable of reaching the standard quantum limit (SQL) of optical interferometry for 100 g mirrors. By creating quantum correlations within this interferometer, e.g. by injecting squeezed vacuum, this limit can then even be surpassed. This will allow operating the interferometer at sub-SQL sensitivity, a state of operation which has to date not been reached by any interferometry experiment.

A conceptual design for the sub-SQL interferometer which is planned to be operated in the AEI 10 m Prototype facility was presented by *Somiya et al* in 2009 [60]. This conceptual design aims at answering the question of how in principle an interferometer with a sensitivity at the SQL can be realized in the given lab environment. In the conceptual design document Somiya points out that the approach of simply down-scaling the layout of, for instance, the Advanced LIGO gravitational wave detector, which will operate at a sensitivity which is separated by approximately a factor of two from the SQL, does not pose a viable option. In the following the line of reasoning is briefly recapitulated.

Since the SQL scales with $m^{-1/2}$ it appears natural to decrease the mass of the mirrors in the design of an interferometer aiming at reaching SQL sensitivity. However, in order to keep the level of thermal noise in the experiment sufficiently low, the aspect ratio of mirror thickness to mirror diameter needs to be optimized. As was shown in [61], coating Brownian thermal noise rapidly increases as the interferometer mirrors are made thinner and thinner. The reduction of the mass of the mirrors with fixed aspect ratio inevitably leads to smaller mirrors. If furthermore

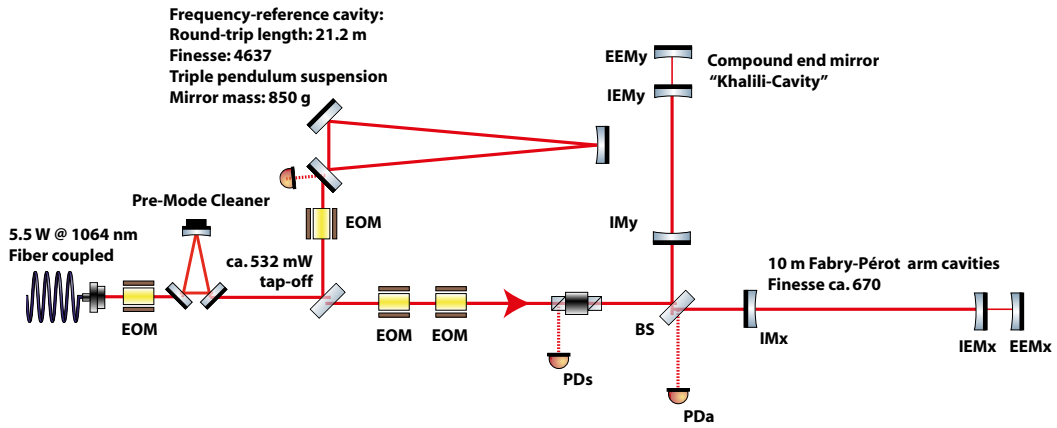

Figure 1.10: Schematic layout of the sub-SQL interferometer target configuration including the frequency reference cavity and the laser preparation stage, consisting of a single mode fiber and a metal spacer-mounted ring cavity for mode cleaning of the input beam. Configuration-wise the interferometer is planned to be a Fabry-Perot Michelson interferometer with an arm length of approximately 10 m. The interferometer will not employ any recycling techniques. For the reduction of coating Brownian thermal noise it is intended to replace the conventional highly reflective arm cavity end mirrors with short, strongly over coupled cavities which will be held on anti-resonance for the carrier light by means of feedback control.

an upper limit for the tolerable diffraction loss is postulated, the size of the laser beam spots on the mirrors needs to be reduced accordingly. Smaller beam spots, in turn, lead to an increase of coating thermal noise which is inversely proportional to the spot size on the mirrors [62]. With these boundary conditions the coating thermal noise can be expressed as a function of the mirror mass and it is found that coating Brownian thermal noise scales with $m^{-1/3}$. This means that if the mass of the mirrors is reduced, not only quantum noise but simultaneously also thermal noise increases and the overall gain of this approach is not more than $m^{-1/6}$. Hence, extremely light mirrors need to be employed to actually arrange for the level of quantum noise well above thermal noise.

It is obvious that a dedicated design of the interferometer is necessary to reach the targeted sensitivity under the given boundary conditions. Configuration-wise a Fabry-Perot Michelson interferometer with *Khalili cavities* [63] instead of conventional arm cavity end mirrors was proposed in the conceptual design. These end mirror cavities were proposed to reduce the level of coating Brownian thermal noise in the interferometer. A schematic drawing of the original interferometer conceptual design configuration, which in the following will be referred to as the *target configuration*, is shown in Figure 1.10.

For the mass of the mirrors in the interferometer arms a value of $m = 100\,\mathrm{g}$ was assumed. This allows to employ well-established methods of suspending the

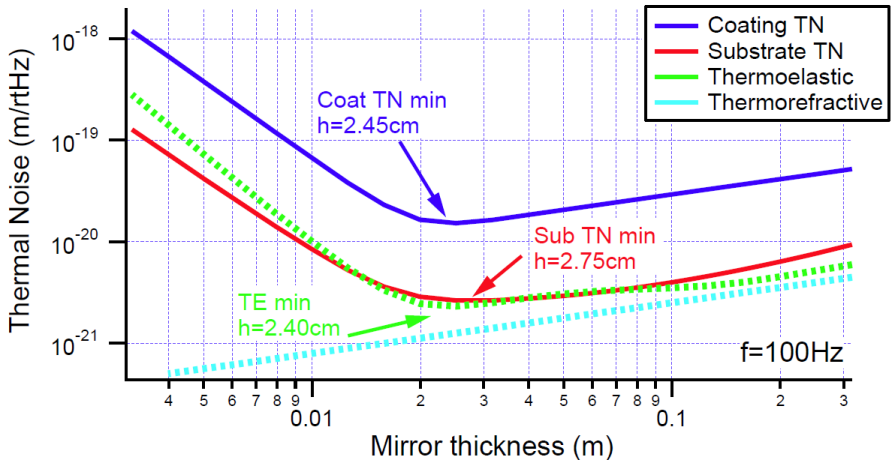

Figure 1.11: Aspect ratio dependence of coating Brownian, substrate thermal, thermo-refractive and thermo-elastic noise, taken from [60]. The minima of the curves in the plot correspond to optimal mirror aspect ratios with respect to minimizing the respective thermal noise contribution. The dominant contribution, coating Brownian thermal noise, is minimized by assuming an aspect ratio of mirror diameter to mirror thickness of $2a/h = 1.98$.

mirrors for better seismic isolation and to keep suspension thermal noise sufficiently low. The optimal aspect ratio of the mirror thickness and its diameter which allows for minimizing coating Brownian thermal noise was determined. In fact, three thermal noise contributions exhibit a dependence on the aspect ratio, namely coating Brownian, substrate Brownian, as well as thermo-optic noise. However, since coating Brownian thermal noise is the dominant contribution the aspect ratio of $2a/h = 1.98$ was assumed for the mirrors to minimize this type of thermal noise. A plot of the aspect ratio optimization is shown in Figure 1.11.

For a fused-silica mirror with a mass of 100 g this results in a mirror thickness of $h = 24.5$ mm and a mirror diameter of $2a = 48.6$ mm. The beam spot size was then maximized by setting an upper limit for the clipping loss of approximately 4 ppm. This results in a beam radius which is 1/2.5 times the radius of the mirror, corresponding to $w_m = 9.72$ mm.

Since the thickness of the coatings and hence the reflectivities of the mirrors are directly related to the level of coating Brownian thermal noise in the interferometer, these were also optimized with respect to minimizing thermal noise. As was shown in the conceptual design, the combination of 2 SiO_2/Ta_2O_5 double layers on the intermediate mirror, i.e. the Khalili cavity input mirror, and 15 double layers on the end mirror was found to be optimal in terms of minimizing coating Brownian thermal noise as well as thermo-refractive noise from the intermediate mirror substrate. For the arm cavity input mirror 8 double layers were chosen, resulting in a total loss of $1 - r_{\mathrm{arm}}^2 = 4.99\,\%$ in one interferometer arm, where r_{arm} is the amplitude

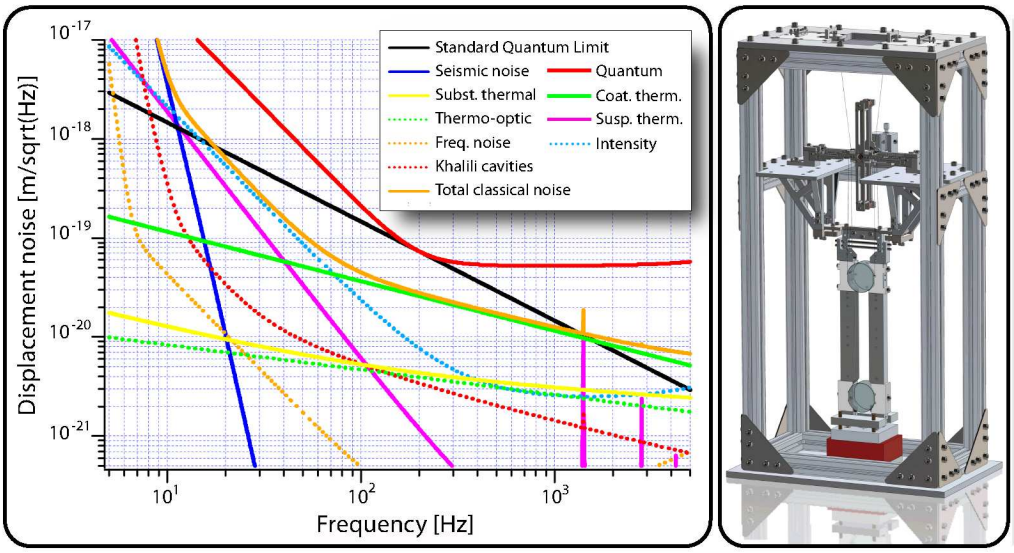

Figure 1.12: Left: Noise budget of the sub-SQL interferometer conceptual design configuration. At approximately 200 Hz the interferometer is capable of reaching SQL sensitivity. **Right:** Rendered image of the sub-SQL interferometer main suspension design. The design features two stages of vertical isolation in combination with triple cascaded pendulum stages with a monolithic last stage for horizontal isolation. The outer dimensions of the suspension frame are 200 mm × 350 mm × 700 mm.

reflectivity of the arm cavity at its operating point. These coating parameters result in a finesse of $\mathcal{F} \simeq 670$ of the interferometer arm cavities.

After coating Brownian thermal noise, laser intensity noise is identified as the second largest classical noise term in the interferometer. Stabilizing the laser intensity to the common mode of the interferometer arms which is excited by radiation pressure was pointed out as an option to decrease intensity noise in the range of $\sim$ 10 Hz to 100 Hz. This scheme may be combined with the traditional approach of picking-off a fraction of the input beam to obtain a correction signal for laser intensity stabilization.

Within the scope of the conceptual design a numerical model of the anticipated sensitivity of the interferometer was composed [64]. The noise budget of the target configuration is shown in Figure 1.12. Besides the use of end mirror cavities, the technique of titania-doping of the Ta_2O_5 thin film layers [65] and the optimization of the layer thickness [66] to reduce the total amount of lossy Ta_2O_5 were proposed. A comprehensive summary of the interferometer parameters derived in [60] is given in Table 1.1.

An important building block to reach the goals of the sub-SQL interferometer experiment are the suspensions for the core optics. One the one hand, sufficient isolation of the mirrors needs to be provided to reduce the impact of seismic noise on the measurement. On the other hand, it is necessary to ensure suspension thermal noise to be sufficiently low. Dedicated mirror suspensions were designed

Table 1.1: Conceptual design parameters of the proposed sub-SQL interferometer target configuration. The number of Ta_2O_5 and SiO_2 double layers to realize the respective reflectivity are given in brackets along with the power reflectivities of the cavity mirrors. Parameter values taken from [60].

Parameter	Value
Input laser power	5.5 W
Arm cavity mirror substrate thickness	24.5 mm
Arm cavity mirror substrate radius	24.3 mm
Beam spot radius on cavity mirrors	9.7 mm
Arm cavity input mirror reflectivity (coating doublets)	99.0696 % (8)
Arm cavity intermediate mirror reflectivity (coating doublets)	51.1510 % (2)
Arm cavity end mirror reflectivity (coating doublets)	99.9936 % (15)
Arm cavity finesse	≈ 670
Arm cavity length	≈ 10 m
End mirror cavity length	≈ 1 m

for the sub-SQL interferometer, based on two stages of vertical isolation and three cascaded triple pendulum stages for horizontal isolation, with outer dimensions of the suspension frame of 200 mm × 350 mm × 700 mm. A rendered image of the main suspension design is shown in Figure 1.12.

The reduction of mechanical dissipation is key to keeping thermal noise in the experiment at a sufficiently low level. This is why the suspension system for the sub-SQL interferometer features a monolithic all-silica final pendulum stage with the mirrors suspended from 20 µm fused-silica filaments. This small diameter is required to keep the vertical resonance frequency low, in order to prevent mechanical resonances in the measurement band of the interferometer.

For the realization of fibers with such a small diameter, a CO_2 laser-based fiber pulling technique is employed. In a first step, fused-silica rods are pulled down to a diameter of approximately 400 µm – 500 µm. Then, in a second step, the thin fibers with the targeted diameter are pulled, having larger diameters at the ends of the fibers, which can be conveniently attached to the interferometer mirrors. With this technique fiber diameters down to 15 µm have been successfully demonstrated [67]. The fibers are attached onto the mirrors' fused-silica ears by CO_2 laser welding.

For vertical isolation small blade springs with a length of approximately 6 cm and a thickness of 0.3 mm are used. Two vertical isolation stages were included in the sub-SQL interferometer suspension design. Finite-element models showed a vertical bounce mode at 2.9 Hz and the first internal mode at 369 Hz. These values could be confirmed in measurements [67].

For local damping of the suspended mirrors and for global control of the lengths in the interferometer different types of actuators will be employed. Whereas passive eddy-current damping and coil-magnet actuation will be employed at the uppermost stage and at the intermediate stage, respectively, special electro-static drives in a

plate capacitor setup will be employed for fast actuation on the final stage. These fast actuators will be designed and tested in the scope of the *single-arm test* experiment which will be introduced in Chapter 6.

1.6 Aim and structure of the thesis

The aim of this thesis is the further development of the sub-SQL interferometer design from the conceptual level towards a workable technical design. This includes the identification of an optical layout for the practical implementation of the experiment in the AEI 10 m Prototype.

Among the cornerstones of the proposed conceptual approach to reach the targeted sensitivity in the interferometer is the adoption of extremely large beam spots, in relation to the arm cavity length, on all core interferometer optics as well as the use of anti-resonant end mirror cavities. Both of these concepts aim at reducing the impact of coating Brownian thermal noise which would otherwise dominate over quantum noise in the instrument. However, neither of these two techniques was implemented in a high-precision laser interferometer experiment before, which gives rise to questions regarding the technical feasibility of their implementation and robust operation.

In the scope of this thesis, a detailed investigation of the aforementioned concepts for the reduction of coating Brownian thermal noise was carried out. Special emphasis was placed on technical aspects of the implementation of these concepts under realistic conditions, including the derivation of requirements for the main optics as well as the evaluation of implications for the robustness and operability of the experiment. To accomplish these objectives, a wide range of numerical modeling techniques were employed which were chosen situationally with respect to optimal performance and accuracy. Based on the results of these investigations an optical layout for the experiment was developed which specifically deals with the challenge of extremely large beam spots on the core optics, which come at the expense of poor geometric stability of the interferometer arm cavities.

This thesis is subdivided into eight chapters. In the first chapter, a general introduction to the field of gravitational waves and their interferometric detection is given, including an introduction to the notion of quantum noise in laser interferometers and the challenges imposed by quantum noise on the design of future interferometric detectors. Furthermore, the AEI 10 m Prototype project is introduced and an outline of its subsystems and planned experiments is presented.

The general introduction is followed by an overview of elementary theoretical models for the description of laser beams and optical resonators in chapter two. These methods are the foundation of the numerical modeling techniques utilized throughout the thesis and were made use of either implicitly, as part of the technically more complex numerical models which were employed, or explicitly, as for instance in the investigations presented in the fourth chapter.

In chapter three, the proposed techniques for coating Brownian thermal noise reduction – extremely large beam spots and anti-resonant end mirror cavities –

are reviewed and different layout options for an implementation in the AEI 10 m Prototype interferometer are derived. Results obtained from numerical simulations of these layout options are presented and their technical properties are discussed.

In chapter four, a detailed optical layout of a Fabry-Perot Michelson interferometer with tunable stability is presented. This configuration allows to stepwise approach the targeted extremely large beam size on the core interferometer optics. It was proposed not only to facilitate the initial commissioning but also to alleviate the risk of inoperability of the interferometer due to performance limitations imposed by the resulting poor arm cavity stability. Furthermore, requirements for the optical elements are presented which were derived in the scope of robustness evaluations.

Chapter five focuses on the investigation of interferometer performance limitations imposed by the unavoidable marginal arm cavity stability of the target configuration in conjunction with realistic mirror surface figure error. For these investigations, a mirror surface model based on measured spectral properties of state-of-the-art mirrors was combined with a grid-based simulation of the interferometer. A parameter study based on this compound model was carried out on a high-performance computer cluster. Suitable figures of merit were identified which relate the simulation output to interferometer performance measures, to determine the tolerable level of surface figure error in the marginally stable configuration.

To gain experience with the technical challenges of the sub-SQL interferometer prior to the completion of the full AEI 10 m Prototype infrastructure, the *single arm test* experiment was proposed. In chapter six this "stepping stone" experiment for the final interferometer is introduced which aims at operating a single cavity with sub-SQL interferometer-like parameters but less demanding technical and infrastructural requirements. The experiment is intended to serve as a test bed for testing novel hardware developed for the use in the sub-SQL interferometer and to gain early commissioning experience with operating a marginally stable 10 m arm cavity with suspended 100 g mirrors.

Besides the work on the optical layout for the 10 m sub-SQL interferometer, in the scope of this thesis the GEO squeezed light laser was in a first step interfaced to a digital control and data system and in a second step the fully automated operation of the experiment was realized. This enabled the intervention-free, long-term stable generation of squeezed vacuum states of light for the injection into the GEO 600 gravitational wave detector and the corresponding routine enhancement of its shot noise-limited sensitivity. In chapter seven, the concept of the GEO squeezed light laser digital interfacing and automation scheme is introduced and its practical implementation is described in detail.

Finally, in chapter eight the results of the thesis are summarized and an outlook is given.

CHAPTER 2

Laser beams and optical resonators

In this chapter, elementary concepts for the analysis of laser beams and optical resonators are recapitulated which serve as the foundation for the investigations presented in the following chapters. This chapter includes the derivation of transverse electromagnetic modes as solutions of the wave equation as well as the transformation of Gaussian laser beams with the aid of the ray transfer matrix formalism. Furthermore, important properties of optical resonators are delineated, including a discussion of the notion of geometric stability.

2.1 Gaussian laser beams

In general, the propagation of electric fields is described by the scalar wave equation

$$\left(\Delta + k^2\right) E(x,y,z) = 0 \,, \tag{2.1}$$

where Δ is the Laplace operator, $k = 2\pi/\lambda$ is the wave number and $E(x,y,z)$ is the complex electric field. For a beam propagating along the z axis it can be assumed that the plane wave variation of the field in the direction of propagation is much faster than the transverse variation of the field. This gives rise to the definition

$$E(x,y,z) = u(x,y,z) \times \exp\left(-ikz\right) \,, \tag{2.2}$$

with u slowly varying in z-direction. Inserting this expression into Equation (2.1) yields

$$\left(\partial_x^2 + \partial_y^2 + \partial_z^2 - 2ik\partial_z\right) u(x,y,z) = 0 \,. \tag{2.3}$$

Since the dependency on the second derivative in z-direction is mainly due to diffraction effects which are slow compared to transverse variations, this term may be omitted. In the limit of this so-called *paraxial approximation*, which holds for beams with divergence angles $\Theta \lesssim 30°$ [68], Equation (2.3) reads

$$\left(\partial_x^2 + \partial_y^2 - 2ik\partial_z\right) u(x,y,z) = 0 \,. \tag{2.4}$$

One possible solution for this equation can be written as

$$u(x,y,z) = u_m(x,z)u_n(y,z) \tag{2.5}$$

with

$$u_n(x,z) = \left(\frac{2}{\pi}\right)^{1/4} \left(\frac{1}{2^n n! w_0} \frac{q_0}{q(z)}\right)^{1/2} \left(\frac{q_0 q^*(z)}{q_0^* q(z)}\right)^{n/2} H_n\left(\frac{\sqrt{2}x}{w(z)}\right) \exp\left(-i\frac{kx^2}{2q(z)}\right), \tag{2.6}$$

where q is the complex beam parameter

$$\frac{1}{q(z)} = \frac{1}{R_c(z)} - i\frac{\lambda}{\pi w^2(z)}\,, \tag{2.7}$$

$q_0 = q(z_0)$ is the beam parameter at the beam waist, $w(z)$ is the beam radius

$$w(z) = \sqrt{\frac{\lambda}{\pi}\frac{|q|^2}{\mathrm{Im}\,\{q\}}}\,, \tag{2.8}$$

$w_0 = w(z_0)$ is the beam waist radius, $H_n(x)$ is the Hermite polynomial of order n which can be obtained from the recursion

$$H_{n+1}(x) = 2xH_n(x) - 2nH_{n-1}(x) \tag{2.9}$$

knowing that $H_0(x) = 1$ and $H_1(x) = 2x$. The resulting solutions of the wave equation are known as *Hermite-Gauss modes* of light. The transverse fields of the lowest-order Hermite-Gauss modes, up to up to order $m = n = 2$, are shown in Figure 2.1.

The wave front radius of curvature of a beam described by the complex parameter $q(z)$ is given by

$$R_c(z) = \frac{|q|^2}{\mathrm{Re}\,\{q\}}\,. \tag{2.10}$$

The complex beam parameter $q(z)$ can also be expressed in terms of the *Rayleigh range* z_R,

$$q(z) = iz_R + z - z_0\,, \tag{2.11}$$

where

$$z_R = \frac{\pi w_0^2}{\lambda}\,. \tag{2.12}$$

The divergence angle in the far field can be expressed as

$$\Theta = \tan^{-1}\left(\frac{\lambda}{\pi w_0}\right)\,. \tag{2.13}$$

The solutions of the wave equation of the form given in Equation (2.5) are referred to as *transverse electromagnetic modes* (TEM_{mn}). Furthermore, the eigenmodes of optical cavities with spherical mirrors are represented by transverse electromagnetic modes. Hence, for theoretical analyses of laser beams and resonators it is

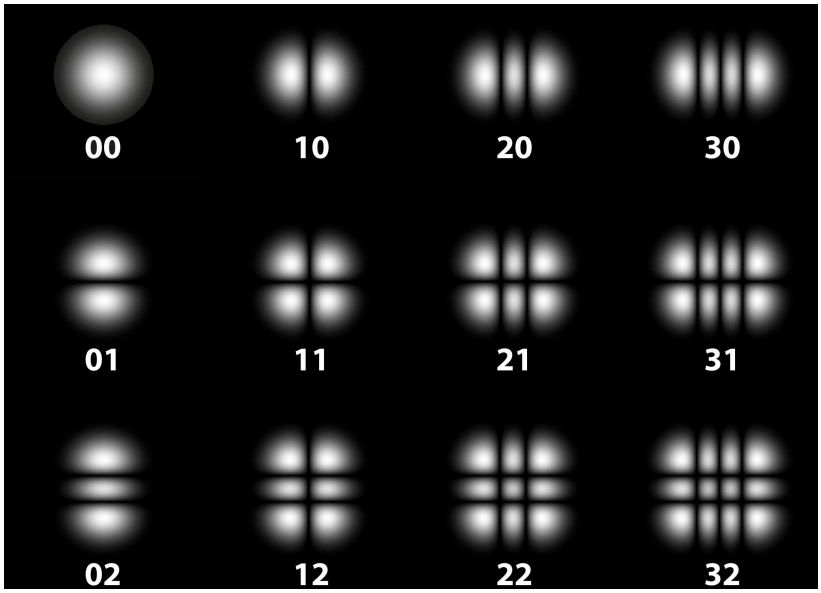

Figure 2.1: Cross sections of the intensity distribution of Hermite-Gaussian transverse laser modes, up to order $m = 3$ and $n = 2$. For each of the modes shown in the image, the first digit represents the index m and the second digit represents the index n. For increasing mode indices m, n the area occupied by the intensity distribution increases while the peak intensity decreases. The mode indices n, m define the number of dark stripes in x-direction and y-direction, respectively.

often convenient to decompose the beams in transverse modes. The TEM_{00} mode is typically referred to as a *Gaussian beam*.

In optical resonators, a distinction is made between longitudinal modes, which have different frequency and can be scanned by tuning the length of the cavity and transverse modes, which not only differ in frequency but also in the transverse amplitude pattern. Originally it was *Fox and Li* and *Boyd and Kogelnik* who described modes of optical resonators with orthonormal functions [69, 70]. Another complete set of solutions of Equation (2.4) are the *Laguerre-Gauss* modes. Other than Hermite-Gauss modes which are defined in Cartesian coordinates, Laguerre-Gauss modes are defined in a cylindrical coordinate system and are thus ideally suited for the description of systems with cylindrical symmetry. For the derivation of Laguerre-Gauss modes see e.g. [71].

2.2 Ray transfer matrices

Propagation of a laser beam described by the complex parameter q_{in} through an optical system is mathematically realized by applying the transformation [68]

$$q_{\mathrm{out}}/n_2 = \frac{Aq_{\mathrm{in}}/n_1 + B}{Cq_{\mathrm{in}}/n_1 + D} \,. \tag{2.14}$$

Here, n_1, n_2 are the refractive indices of the corresponding media at the input and the output of the optical system, respectively. A,B,C and D are the elements of a two dimensional *ray transfer matrix* of the system

$$M = \begin{pmatrix} A & B \\ C & D \end{pmatrix} . \tag{2.15}$$

Ray transfer matrices for the description of complex optical systems are composed of matrices representing elementary operations, by multiplication of these in "reverse" order, i.e. the matrix describing the first element that is encountered by the light ray traveling through the system is the rightmost matrix in the matrix product. In the following, a selection of elementary transfer matrices will be presented. For instance, beam propagation over a distance d, independent of the refractive index of the medium, is described by the matrix

$$M_{\text{prop}}(d) = \begin{pmatrix} 1 & d \\ 0 & 1 \end{pmatrix} . \tag{2.16}$$

The matrix

$$M_{\text{lens}}(f) = \begin{pmatrix} 1 & 0 \\ -1/f & 1 \end{pmatrix} . \tag{2.17}$$

represents a thin lens with a focal length f. A curved mirror with a focal length $f = R_c/2$ is represented by

$$M_{\text{mirror}}(R_c) = \begin{pmatrix} 1 & 0 \\ -2/R_c & 1 \end{pmatrix} , \tag{2.18}$$

where R_c is its radius of curvature. Refraction at a curved interface between two media is described by the matrix

$$M_{\text{refract}}(R_c, n_1, n_2) = \begin{pmatrix} 1 & 0 \\ \frac{n_1 - n_2}{R \cdot n_2} & \frac{n_1}{n_2} \end{pmatrix} , \tag{2.19}$$

where R_c is the radius of curvature of the interface and n_1 and n_2 are the refractive indices of the media. Besides these simple examples, matrix representations of numerous more complex optical elements exist, see e.g. [68, 72].

2.3 Optical resonators

Optical resonators are a versatile tool of laser optics with a wide scope of applications, ranging from frequency references for laser stabilization through spatial and temporal mode cleaners, nonlinear cavities for the conversion of laser light to different wave lengths, to arm cavities or recycling cavities in laser interferometers. Despite the few components required to build a simple cavity, these exhibit remarkable optical properties which will be discussed in the following.

2.3.1 A matrix-based resonator model

Typically, optical resonators consist of a number of partially transmissive mirrors which are orientated relative to each other in a way such that an incident laser beam may remain inside the cavity for multiple round trips. In a geometrically stable cavity the incident beam reproduces itself after one round-trip, cf. Section 2.3.6, which is a necessary prerequisite for the existence of low-loss cavity eigenmodes.

For the analysis of the frequency dependent behavior of an optical resonator the existence of only a single resonant spatial mode may be assumed without loss of generality. Furthermore, a stable geometry of the cavity as well as perfect matching of the input beam to the resonator eigenmode are assumed. With these assumptions the resonance condition solely depends on the cavity length or the frequency of the incident light, respectively.

For the case of mirrors lined up along a single optical axis the electromagnetic field in each point can be described as a superposition of two waves traveling back and forth,

$$a = a_1 e^{i(kz-\omega t)} + a_2 e^{i(kz+\omega t)} \ , \tag{2.20}$$

where z is a spatial coordinate along the optical axis, $k = 2\pi/\lambda$ is the wave number and ω is the angular frequency of the light wave. The amplitudes of these two waves can be written as a complex two-dimensional vector of the form $(a_1, a_2)^T$. Ordinary mirrors give rise to a coupling of the fields on each of their two optical surfaces which can be mathematically described as a linear operation. Thus, to account for the coupling of light fields in this simple model, a description based on 2×2 matrices is appropriate. Beam propagation over a finite stretch of space is the represented by the matrix [73]

$$S = \begin{pmatrix} e^{-(\alpha+ik)L} & 0 \\ 0 & e^{(\alpha+ik)L} \end{pmatrix} \ , \tag{2.21}$$

whereas L represents the propagation length and the coefficient α was introduced to account for propagation in an absorbing medium. Mirrors couple fields on their two surfaces, whereas the coupling is governed quantitatively by the mirrors' amplitude reflectivity coefficient r and transmission coefficient t. The resulting matrix reads

$$M = \frac{-1}{it} \begin{pmatrix} 1-\mathcal{L} & -r \\ r & -1 \end{pmatrix} \ . \tag{2.22}$$

The parameter $\mathcal{L}$ quantifies the power loss per reflection by absorption and scattering at the optical component.

2.3.2 Fabry-Perot cavities

The most elementary configuration of an optical cavity is the *Fabry-Perot cavity*. It consists of two mirrors at a distance of L which are aligned to an optical axis. Light which is incident on the cavity and transmitted through the coupling mirror experiences multiple reflections inside the resonator. The resulting internal field

is a superposition of fields after different numbers of reflections inside the cavity. The field reflected at the coupling mirror results from interference of the directly reflected field and the fraction of the internal field leaking out through the coupling mirror.

The matrix representation of this type of cavity can be obtained by calculating the product of two mirror matrices and a propagation matrix in the appropriate order,

$$\begin{aligned} M_2SM_1 &= \frac{-1}{t_1t_2}\begin{pmatrix} 1-\mathcal{L}_2 & -r_2 \\ r_2 & -1 \end{pmatrix}\begin{pmatrix} e^{-ikL} & 0 \\ 0 & e^{ikL} \end{pmatrix}\begin{pmatrix} 1-\mathcal{L}_1 & -r_1 \\ r_1 & -1 \end{pmatrix} \\ &= \frac{-1}{t_1t_2}\begin{pmatrix} -r_1r_2e^{ikL}+(1-\mathcal{L}_1)(1-\mathcal{L}_2)e^{-ikL} & r_2e^{ikL}-r_1(1-\mathcal{L}_2)e^{-ikL} \\ -r_1e^{ikL}+r_2(1-\mathcal{L}_1)e^{-ikL} & e^{ikL}-r_1r_2e^{-ikL} \end{pmatrix} . \end{aligned} \tag{2.23}$$

For the typical case of a laser beam incident on only one side of the cavity the relationship

$$\begin{pmatrix} a_{\text{trans}} \\ 0 \end{pmatrix} = M_2SM_1\begin{pmatrix} a_{\text{in}} \\ a_{\text{refl}} \end{pmatrix} , \tag{2.24}$$

holds for the field amplitudes, whereas a_{in}, a_{refl} and a_{trans} are the complex amplitudes of the incident and reflected and transmitted field, respectively. By taking the ratio of these amplitudes the reflectivity and the transmittance of a given cavity can be determined,

$$\varrho_{\text{FPC}}(\phi) = \frac{a_{\text{refl}}}{a_{\text{in}}} = \frac{r_1-(1-\mathcal{L}_1)r_2e^{-i2\phi}}{1-r_1r_2e^{-i2\phi}} \tag{2.25}$$

$$\tau_{\text{FPC}}(\phi) = \frac{a_{\text{trans}}}{ia_{\text{in}}} = \frac{it_1t_2e^{-i\phi}}{1-r_1r_2e^{-i2\phi}} , \tag{2.26}$$

whereas $\phi = kL = \omega L/c$ is the *tuning* of the cavity. The dependence of the amplitude and phase response on the resonator parameters will be discussed in the following section.

Various quantities are used in practice to characterize optical resonators. The *Finesse* $\mathcal{F}$ of a cavity is defined as the ratio of the *free spectral range* (FSR)

$$\text{FSR} = \frac{c}{2L} \tag{2.27}$$

and the cavity bandwidth represented by the *full width at half maximum* (FWHM) of its resonance peaks and is given by

$$\mathcal{F} = \frac{\text{FSR}}{\text{FWHM}} = \frac{\pi}{2\arcsin(\frac{1-r_1r_2}{2\sqrt{r_1r_2}})} \approx \frac{\pi\sqrt{r_1r_2}}{1-r_1r_2} . \tag{2.28}$$

The finesse is fully determined by the optical losses in a cavity, is closely related to the Q-factor of a resonant system and is a measure which can be used to estimate the resonant enhancement of the internal field

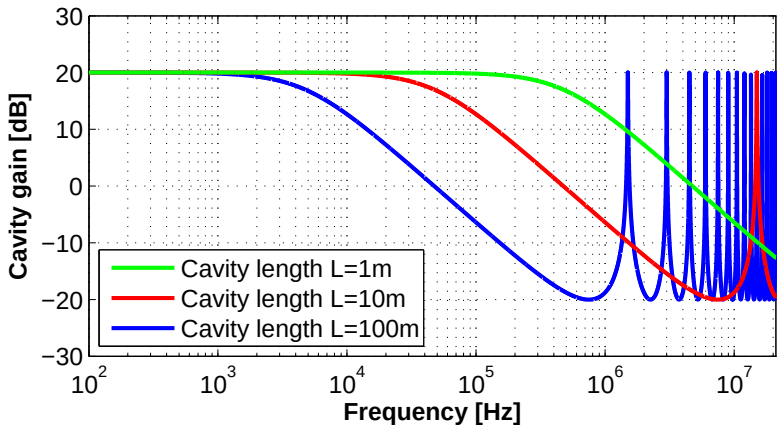

Figure 2.2: Frequency dependence of the optical gain of a two-mirror cavity. The three cavity configurations simulated for the plot exhibit an identical finesse of $\mathcal{F} \approx 50$ but different lengths. The frequency of the cavity pole is inversely proportional to the cavity length. The frequency spacing of the resonance peaks is determined by the free spectral range of the cavity, which decreases as the length is decreased.

Optical resonators can be regarded as filters acting on the incident field. The frequency response of a cavity may be extracted from the complex-valued functions ϱ_{FPC} and τ_{FPC}. Whereas the amplitude response for reflection or transmission is the absolute value of the respective coefficient, the phase response is given by the complex angle of ϱ_{FPC} and τ_{FPC}. For the transmitted field an optical resonator acts as a low pass filter with a pole frequency of

$$f_c = \frac{1}{2}\frac{FSR}{\mathcal{F}} \,. \tag{2.29}$$

The plot in Figure 2.2 illustrates the frequency dependence of the optical gain in a two mirror cavity for different cavity lengths.
The aforementioned resonant gain G of a cavity is given as

$$G = \frac{t_1^2}{(1 - r_1 r_2)^2} \,. \tag{2.30}$$

The resonant cavity gain is the reason for the adoption of arm cavities in high precision laser interferometers. Whereas in a Michelson interferometer without arm cavities a length change of one of the arms by ΔL gives rise to a phase change of $\Delta\phi = 2k\Delta L$ of the returning field, in an interferometer with arm cavities the phase change is amplified by the resonant gain thus making the instrument more sensitive.

Depending on the choice of the reflectivities of the input mirror and the end mirror, optical resonators exhibit distinctive properties with respect to reflected, transmitted and internal fields and are subdivided in three different classes. The differences between these classes, under coupled, over coupled and impedance matched cavities, will be delineated in the following section.

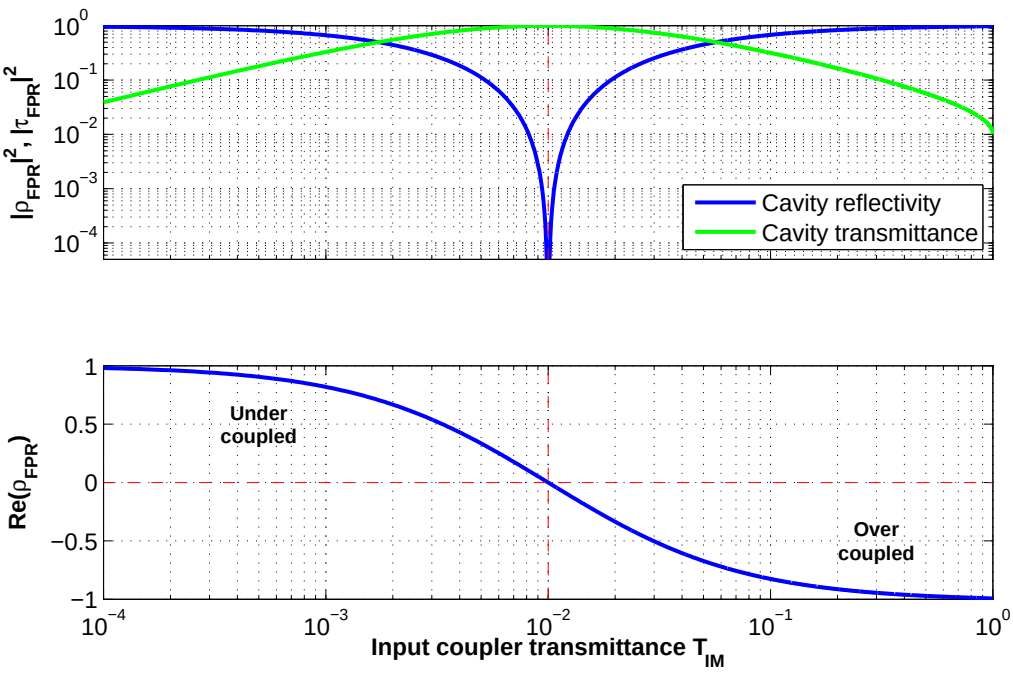

Figure 2.3: Light transmitted and reflected at an over coupled, under coupled and impedance matched cavity. The transmittance of the rear cavity mirror was held constant at $T_{EM} = 1\,\%$ while the input coupler transmittance was tuned. The upper plot shows the cavity power reflectivity $|\varrho_{FPC}|^2$ and transmittance $|\tau_{FPC}|^2$, respectively. The power transmitted through the cavity peaks in the impedance matched case, i.e. $T_{IM} = T_{EM}$, while the amplitude response drops to zero. The field reflected at the cavity vanishes, cf. lower plot. The amplitude response of the cavity is given by the real part of the amplitude reflectivity coefficient ϱ_{FPC}.

2.3.3 Impedance matched, under coupled and over coupled resonators

The relations derived so far are universally valid for Fabry-Perot cavities. It is common to further classify optical resonators as either *under coupled*, *impedance matched* or *over coupled* cavities, depending on their phase response, internal buildup and light reflection and transmission characteristics. In the lossless case of $\mathcal{L} = 0$, maximal transmission $\tau_{FPC} = 1$ can be observed for equal mirror reflectivities $r_1 = r_2$ which goes hand in hand with a vanishing reflection coefficient, $\varrho_{FPC} = 0$. This configuration represents the impedance matched case and for the more realistic scenario in which losses are present, $\mathcal{L} \neq 0$, the mirror reflectivities are to be chosen according to

$$r_1 = (1 - \mathcal{L})r_2 \tag{2.31}$$

to arrange for impedance matching. If now the reflectivity of one of the mirrors is reduced or increased, this results in a cavity reflectivity $|\rho_{FPC}| \neq 0$ and a transmission coefficient $|\tau_{FPC}| < 1$. The case $r_1 > (1 - \mathcal{L})r_2$ corresponds to an under coupled

cavity and $r_1 < (1-\mathcal{L})r_2$ is referred to as the over coupled case. The transition between these three cases in a cavity is illustrated in Figure 2.3. The expression for the reflectivity of an FPC can be re-written in the form

$$\varrho_{\text{FPC}} = \frac{r_1 - (1-\mathcal{L})r_2 e^{-i2\phi}}{1 - r_1 r_2 e^{-i2\phi}} = r_1 + r_2 \frac{(it_1)^2 e^{-i2\phi}}{1 - r_1 r_2 e^{-i2\phi}} \ . \tag{2.32}$$

The first term represents the fraction of light which is directly reflected at the coupling mirror and is obviously independent of the tuning of the cavity. The second term defines the fraction of the internal field which leaks out of the cavity through the coupling mirror. Amplitude and phase of this field depend on the tuning of the cavity.

Equation (2.32) can be interpreted in the phasor picture [74]. Whereas the first term is represented by a constant phasor, the second term is represented by a phasor which varies in magnitude and direction depending on the cavity tuning ϕ. The plots in Figure 2.4 illustrate the dependence of the magnitude and phase of the reflected field for cavities tuned through resonance. Plots for the over coupled, the under coupled and the impedance matched case are shown.

For under coupled cavities the variable phasor always has a smaller magnitude than the constant one. The vectorial sum of the two phasors will always remain in the right complex half plane. The phase of the resulting field, which is represented by the angle of the sum vector with respect to the real axis, will only change by a marginal amount when the cavity is tuned through resonance.

In the case of the resonant over coupled cavity the variable phasor has a larger magnitude than the constant one. The sum vector reaches the negative complex half plane and the phase of the resulting field experiences a shift by 2π when the cavity is tuned through resonance.

Reflectivities of mirrors in interferometer arm cavities are typically chosen to result in a strongly over coupled configuration. Practically this is achieved by choosing end mirror reflectivities close to unity, $R_{ETM} \sim 1$. The lower the reflectivity of the end mirror, the higher the amount of light which is transmitted through the cavity, which can be effectively regarded as lost for the measurement.

2.3.4 Multi-mirror coupled cavities

In close analogy to the simple matrix-based two mirror Fabry-Perot cavity model introduced in Section 2.3.2, coupled cavity systems can be described with the aid of the same formalism. An alternative approach to the description of multi-mirror cavities was e.g. introduced by *van de Stadt and Muller* [75].

For the special case of a linear coupled cavity composed of three mirrors, the model is composed of three matrices representing mirrors and two matrices representing spaces. One obtains a linear equation system for the complex field amplitudes of the form

$$\begin{pmatrix} a_{\text{trans}} \\ 0 \end{pmatrix} = M_3 S_2 M_2 S_1 M_1 \begin{pmatrix} a_{\text{in}} \\ a_{\text{refl}} \end{pmatrix} \ , \tag{2.33}$$

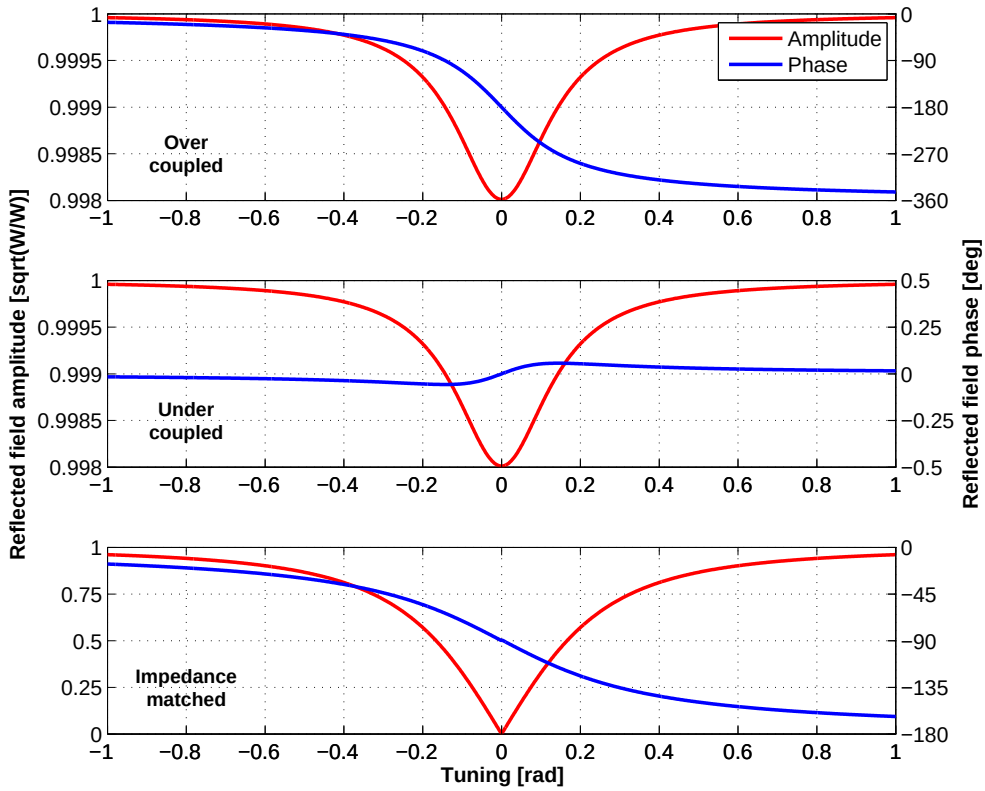

Figure 2.4: Amplitude and phase of light reflected at an over coupled, under coupled and impedance matched cavity. In all three cases an input field amplitude of $a_{\text{in}} = \sqrt{1\,W}$ was assumed and the mirror reflectivities were chosen such that a finesse of ≈ 625 of the cavities is achieved. The phase change of the reflected field is most pronounced in the case of the over coupled cavity (top plot) with $\Delta\phi_{\text{oc}} = 360°$, followed by the impedance matched case (bottom plot) with $\Delta\phi_{\text{im}} = 180°$. In the under coupled case (middle plot) the phase phase of the reflected field changes only marginally when the cavity length is tuned through resonance.

in which the full transformation matrix is given as the product of the matrices representing the three cavity mirrors, M_i, and two matrices representing the free space propagation between the mirrors, S_i. The elements of the resulting field transformation matrix $T = M_3 S_2 M_2 S_1 M_1$ are given as

$$\begin{aligned}
T_{11} &= -\frac{i}{\sigma}\left[\left(\zeta_2\zeta_3 e^{ikL_2} - r_2 r_3 e^{ikL_2}\right)\zeta_1 e^{-ikL_1} + \left(-r_2\zeta_3 e^{-ikL_2} + r_3 e^{ikL_2}\right) r_1 e^{ikL_1}\right] \\
T_{12} &= -\frac{i}{\sigma}\left[\left(\zeta_2\zeta_3 e^{ikL_2} - r_2 r_3 e^{ikL_2}\right) r_1 e^{-ikL_1} - \left(-r_2\zeta_3 e^{-ikL_2} + r_3 e^{ikL_2}\right) e^{ikL_1}\right] \\
T_{21} &= -\frac{i}{\sigma}\left[\left(\zeta_2 r_3 e^{-ikL_2} - \varrho e^{ikL_2}\right)\zeta_1 e^{-ikL_1} + \left(-r_2 r_3 e^{-ikL_2} + e^{ikL_2}\right) r_1 e^{ikL_1}\right] \\
T_{22} &= -\frac{i}{\sigma}\left[-\left(\zeta_2 r_3 e^{-ikL_2} - r_2 e^{ikL_2}\right) r_1 e^{-ikL_1} - \left(-r_2 r_3 e^{-ikL_2} + e^{ikL_2}\right) e^{ikL_1}\right]
\end{aligned} \tag{2.34}$$

with $\zeta_i = (1 - \mathcal{L}_i)$ and $\sigma = t_1 t_2 t_3$. With the matrix elements T_{mn} the linear system of equations for the field amplitudes can be written as

$$a_{\text{trans}} = T_{11} a_{\text{in}} + T_{12} a_{\text{refl}} \tag{2.35}$$

$$0 = T_{21} a_{\text{in}} + T_{22} a_{\text{refl}} \, . \tag{2.36}$$

To simplify matters, vanishing optical losses will be assumed for the further analysis, i.e. $\zeta_i = 0$. Again, the amplitude reflectivity and transmittance of the coupled cavity can be expressed as the ratio of the field amplitudes $a_{\text{refl}}/a_{\text{in}}$ and $a_{\text{trans}}/a_{\text{in}}$, respectively. This yields

$$\varrho(\phi_1, \phi_2) = -\frac{r_3 e^{-i\phi_2}(e^{-i\phi_1} - r_1 r_2 e^{i\phi_1}) - e^{i\phi_2}(r_2 e^{-i\phi_1} - r_1 e^{i\phi_1})}{r_3 e^{-i\phi_2}(r_2 e^{i\phi_1} - r_1 e^{-i\phi_1}) - e^{i\phi_2}(e^{i\phi_1} - r_1 r_2 e^{-i\phi_1})} \tag{2.37}$$

$$\tau(\phi_1, \phi_2) = \frac{\tau_1 \tau_2 \tau_3}{r_3 e^{-i\phi_2}(r_2 e^{i\phi_1} - r_1 e^{-i\phi_1}) - e^{i\phi_2}(e^{i\phi_1} - r_1 r_2 e^{-i\phi_1})} \, , \tag{2.38}$$

with the substitutions $\phi_1 = \omega L_1/c$ and $\phi_2 = \omega L_2/c$, with ϕ_1 representing the tuning of the partial resonator formed by M_1 and M_2 and ϕ_2 representing the tuning of the partial resonator formed by M_2 and M_3, respectively.

The occurrence of these two tuning parameters is a direct consequence of the two length degrees of freedom, in contrast to the single length degree of freedom of the conventional Fabry-Perot cavity and, accordingly, the occurrence of only one cavity tuning parameter. The power transmittance $T = |\tau(\phi_1, \phi_2)|^2$ of a three mirror coupled cavity plotted as a function of its two tunings is depicted in Figure 2.5, for an arbitrary set of amplitude reflectivities r_1, r_2, r_3 for the input mirror, the shared intermediate mirror and the end mirror, respectively. The choice of the mirror reflectivities fully determines the range of values the function $\tau(\phi_1, \phi_2)$ can take on. Each possible state of the three mirror coupled cavity is represented by a point in the ϕ_1-ϕ_2-plane.

A variation of the frequency of the incident laser light is equivalent to a simultaneous detuning of both partial resonators,

$$\Delta\phi_k = \Delta\omega L_k/c \, . \tag{2.39}$$

What follows is a proportionality of both tunings of the form $\Delta\phi_1/\Delta\phi_2 = L_1/L_2$. This relation represents a section of the ϕ_1-ϕ_2-plane with the slope L_1/L_2,

$$\phi_1 = \frac{L_1}{L_2}\phi_2 + \beta \, . \tag{2.40}$$

The intercept β is determined by the initial microscopic position of the cavity mirrors.

For the special case of $L_1/L_2 = 1$ and $\beta = 0$ it is found that the three mirror coupled cavity exhibits symmetric *resonance doublets*, centered about the carrier frequency. The *frequency splitting*, i.e. the "distance" of the transmission peaks in terms of frequency difference, is a function of the coupling of the three mirror cavity, determined by the reflectivity of the central mirror [76].

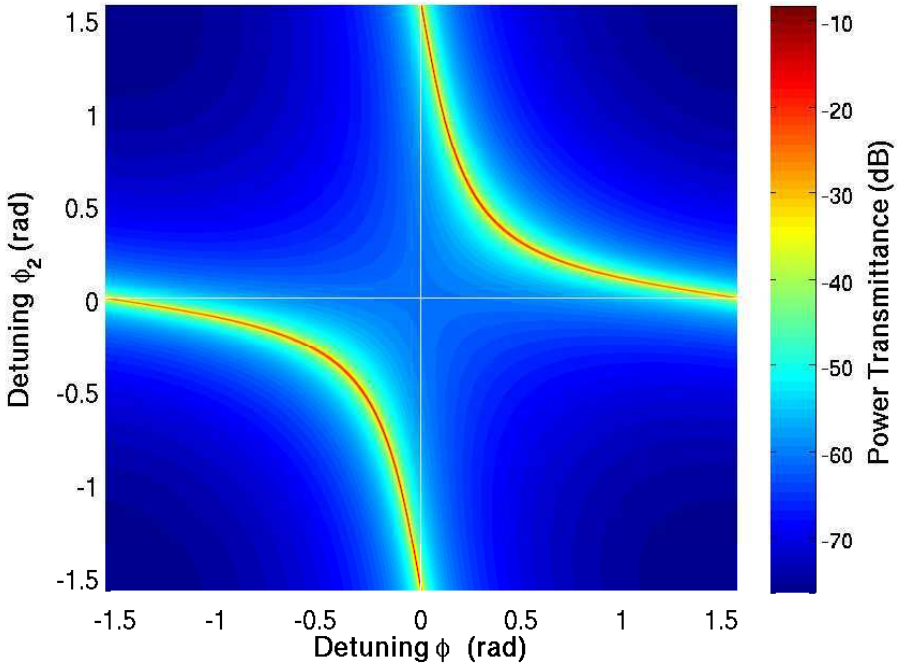

Figure 2.5: Linear three mirror coupled cavity simulated power transmittance, plotted as a function of the two tunings ϕ_1 and ϕ_2. The two resonance branches are a characteristic feature of this resonator type. The resonance branches exhibit a π-periodicity with respect to both tuning parameters. Other than in the case of the conventional two mirror cavity, zero detuning of the cavity lengths does not result in a resonant state of the cavity.

It is a remarkable property of three mirror coupled cavities that the fulfillment of the resonance condition $\phi_{1,2} = n\pi$ with $n \in \mathbb{N}_+^*$ by one or both cavities does not necessarily set the coupled cavity on resonance for the carrier field. However, by tuning the first one of the partial cavities to $\phi_1 = (2n+1)\pi/2$ and the second one to $\phi_2 = \phi_1 \pm \pi/2$ the coupled cavity system is set on resonance, with maximized transmittance of the cavity. For these tunings, the intra-cavity powers in either the first or the second partial cavity are maximized.

2.3.5 Mode coupling efficiency

To ensure optimal coupling of a laser beam into an optical resonator, the input field $\Psi(x,y,z)$ needs to be overlapped with the eigenmode of the cavity $\tilde{\Phi}(x,y,z)$. The mode coupling efficiency η is quantified by an overlap integral of the form

$$\eta = \frac{\left|\iint dx\,dy\,\Psi(x,y,z)\,\tilde{\Phi}^*(x,y,z)\right|^2}{\iint dx\,dy\,|\Psi(x,y,z)|^2 \times \iint dx\,dy\,\left|\tilde{\Phi}(x,y,z)\right|^2}\,. \tag{2.41}$$

It is useful to formulate the mode matching efficiency as a function of the beam parameters of the two beams under investigation, i.e. $\eta = \eta(q(z_0), \tilde{q}(z_0))$.

The mathematical description of the electric field of a Gaussian beam in its fundamental mode, as a function of a complex beam parameter, reads

$$E(x,y,z) = E_0 \cdot u_{00} \cdot \exp(-ikz) \tag{2.42}$$

$$= E_0 \cdot \frac{1}{q(z)} \cdot \exp\left(-ik\frac{x^2+y^2}{2q(z)}\right) \exp(-ikz) \ . \tag{2.43}$$

The integrals in the numerator and denominator can be solved as a function of the involved complex beam parameters. The product of the two modes reads

$$\Psi\tilde{\Phi}^* = E_0\tilde{E}_0^* \cdot \frac{1}{q(z)\tilde{q}^*(z)} \cdot \exp\left(-ik\left(x^2+y^2\right)\left[\frac{1}{2q(z)} - \frac{1}{2\tilde{q}^*(z)}\right]\right) \exp(-ikz+ikz) \ . \tag{2.44}$$

For the numerator Ξ, which is the actual overlap integral, the expression

$$\Xi = \left|\iint dx\,dy\,\Psi(x,y,z)\,\tilde{\Phi}^*(x,y,z)\right|^2 \tag{2.45}$$

$$= \left|E_0\tilde{E}_0^* \cdot \frac{1}{q(z)\tilde{q}^*(z)} \cdot \frac{\pi}{\alpha+\tilde{\alpha}^*}\right|^2$$

is found, with the abbreviation $\alpha := \frac{ik}{2q}$ and the solution to the well-known integral $\int \mathrm{d}x\, e^{-\gamma x^2} = \sqrt{\frac{\pi}{\gamma}}$, which holds for $\Re(\gamma) > 0$).

After some algebra (for brevity the dependence of q on the beam axis coordinate z is omitted from now on) the expression

$$\Xi = |E_0|^2 \left|\tilde{E}_0\right|^2 \frac{4\pi^2}{k^2} \frac{1}{|q|^2 + |\tilde{q}|^2 - q^*\tilde{q}^* - q\tilde{q}} \ . \tag{2.46}$$

is obtained. For the denominator Ω it is sufficient to solve one of the normalization integrals,

$$\Omega = \iint dx\,dy\Psi\Psi^* \tag{2.47}$$

$$= E_0^2 \cdot \frac{1}{|q|^2} \cdot \sqrt{\frac{\pi}{\alpha+\alpha^*}} \cdot \sqrt{\frac{\pi}{\alpha+\alpha^*}} \ .$$

Finally, the solution

$$\Omega = |E_0|^2 \cdot \frac{1}{|q|^2} \cdot \pi \cdot \frac{2qq^*}{ik(q^*-q)} \tag{2.48}$$

is obtained after some algebraic manipulation. The solutions for the numerator and the denominator can be combined to obtain the final solution, $\eta = \Xi/(\Omega\tilde{\Omega})$:

$$\eta = \frac{|E_0|^2 \left|\tilde{E}_0\right|^2 \frac{4\pi^2}{k^2} \frac{1}{|q|^2+|\tilde{q}|^2-q^*\tilde{q}^*-q\tilde{q}}}{|E_0|^2 \cdot \frac{1}{|q|^2} \cdot \pi \cdot \frac{2qq^*}{ik(q^*-q)} \times \left|\tilde{E}_0\right|^2 \cdot \frac{1}{|\tilde{q}|^2} \cdot \pi \cdot \frac{2\tilde{q}\tilde{q}^*}{ik(\tilde{q}^*-\tilde{q})}} \tag{2.49}$$

$$= \frac{i(q^*-q)\cdot i(\tilde{q}^*-\tilde{q})}{|q|^2+|\tilde{q}|^2-q^*\tilde{q}^*-q\tilde{q}} \ . \tag{2.50}$$

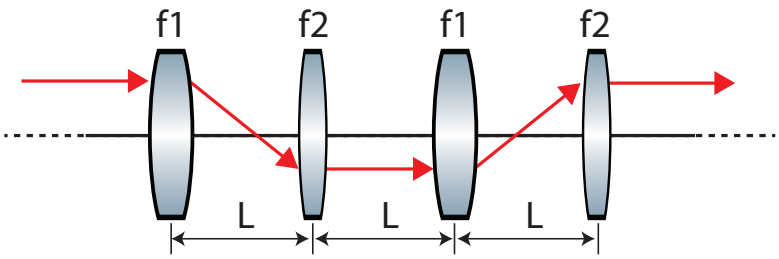

Figure 2.6: Lens guide as a cavity equivalent. A light ray in a stable cavity experiences periodic re-focusing and remains near the optical axis of the resonator, similar to a ray in a lens guide with the focal lengths of the lenses chosen appropriately.

Eventually, the power coupling efficiency can be written as

$$\eta(q,\tilde{q}) = \frac{q^*\tilde{q} + q\tilde{q}^* - q\tilde{q} - q^*\tilde{q}^*}{|q|^2 + |\tilde{q}|^2 - q^*\tilde{q}^* - q\tilde{q}} \,. \tag{2.51}$$

2.3.6 Cavity stability

Geometric stability of optical resonators is a necessary prerequisite for the existence of low-loss cavity eigenmodes. Assuming that a single round-trip through an arbitrary cavity is described by the transfer matrix M and a light ray at the input of the cavity is given by $\vec{r}_0 = (r,\alpha)^T$, the ray after n round-trips is given as

$$\vec{r}_n = M^n \vec{r} \,. \tag{2.52}$$

If it is further assumed that M can be diagonalized, $M' = PMP^{-1}$, where P is the corresponding transformation matrix. M' can be written in terms of its eigenvectors $\vec{x}_1$ and $\vec{x}_2$ with eigenvalues x_1 and x_2, respectively. It follows that

$$\vec{r}_n = P^{-1} \begin{pmatrix} x_1^n & 0 \\ 0 & x_2^n \end{pmatrix} P\vec{r} \,. \tag{2.53}$$

The cavity is stable if the light ray is periodically re-focused and remains near the optical axis, i.e. if upper bounds $|x_1| \leq 1$ and $|x_2| \leq 1$ exist. The picture of an equivalent infinite lens guide is often used to illustrate this condition, cf. Figure 2.6. Generally, the determinant of a ray transfer matrix is the ratio of the refractive indices n_1, n_2 of two reference planes where propagations starts and where it ends, respectively:

$$\det(M) = n_1/n_2 \,. \tag{2.54}$$

As these are identical after a cavity round-trip, $\det(M) = 1$ holds in this case. The determinant of the diagonal ray transfer matrix is given as the product of the complex eigenvalues $x_1 = |x_1| \cdot \exp(i\varphi_1)$ and $x_2 = |x_2| \cdot \exp(i\varphi_2)$. Hence, to fulfill the condition $|x_1| \leq 1$ and $|x_2| \leq 1$, i.e. to ensure that the resonator is geometrically

stable, the absolute values need to fulfill $x_1 x_2 = 1$ and the arguments need to fulfill the condition $\varphi_1 = -\varphi_2 \equiv \varphi$. For the trace of the ray transfer matrix

$$\begin{aligned} \mathrm{tr}(M) &= x_1 + x_2 \\ &= \exp(i\varphi) + \exp(-i\varphi) = 2\cos(\varphi) \end{aligned} \tag{2.55}$$

can be written. From this equality a stability criterion can be deduced which reads

$$-1 \leq \frac{\mathrm{tr}(M)}{2} \leq 1 \tag{2.56}$$

or equivalently

$$0 \leq \frac{\mathrm{tr}(M) + 2}{4} \leq 1 \,. \tag{2.57}$$

which is valid for an arbitrary cavity geometry, described by the transfer matrix M. The propagation matrix of a two-mirror optical resonator can be written as [72]

$$M_{\mathrm{cavity}} = \begin{pmatrix} 2g_1g_2 - 1 & 2Lg_2 \\ \frac{(2g_1g_2-1)^2-1}{2Lg_2} & 2g_1g_2 - 1 \end{pmatrix} \,, \tag{2.58}$$

with

$$g_i = 1 - \frac{L}{R_i} \,, \quad i \in \{1, 2\} \,. \tag{2.59}$$

For the stability term given above in Equation (2.57) the expression

$$\frac{\mathrm{tr}(M) + 2}{4} = g_1 g_2 \tag{2.60}$$

is obtained and it is easy to show that a stable two mirror cavity needs to fulfill the condition

$$0 \leq \left(1 - \frac{L}{R_1}\right)\left(1 - \frac{L}{R_2}\right) \leq 1 \tag{2.61}$$

or written in terms of the factors g_1 and g_2

$$0 \leq g_1 g_2 \leq 1 \tag{2.62}$$

which is the well-known two-mirror cavity stability criterion.

The same result can be deduced for Gaussian beams. In a stable cavity the beam parameter q of an eigenmode is reproduced after one round-trip,

$$q = \frac{Aq + B}{Cq + D} \quad \Leftrightarrow \quad q^2 + (D - A)/Cq - B/C = 0 \,. \tag{2.63}$$

The waist position z_0 and the Rayleigh range z_R expressed in terms of the propagation matrix elements read

$$z_0 = z_{\mathrm{in}} - \frac{A - D}{2C} \tag{2.64}$$

and

$$z_R = \frac{\sqrt{4-(A+D)^2}}{2\,|C|}\,, \tag{2.65}$$

respectively. The Rayleigh range is only defined if the radicand in the numerator of Equation (2.65) is larger than zero. Hence,

$$-1 < \frac{A+D}{2} < 1 \tag{2.66}$$

is to be fulfilled by a stable cavity which is equivalent to the criterion given in Equation (2.56).

Numerous alternative resonator stability criteria exist besides the criterion derived above. It is worth mentioning that the stability criterion

$$0 < AD < 1\,. \tag{2.67}$$

which was formulated by Baues [77] encompasses many of the less general criteria.

CHAPTER 3

On coating thermal noise reduction techniques

Thermal noise plays a crucial role in the field of optical precision metrology, e.g. in laser frequency stabilization [78], in microscopic opto-mechanical experiments probing at the quantum limit [79] but also in large-scale high-precision laser interferometers for GW detection [62].

In fact, in any experiment aiming to perform a measurement with quantum noise-limited sensitivity, thermal noise constitutes a serious obstacle which needs to be dealt with. In the case of the planned sub-SQL interferometer experiment, coating Brownian thermal noise is the dominant classical noise contribution to the noise budget of the sub-SQL interferometer in its measurement band at frequencies of hundreds of Hertz.

Two novel techniques which aim at the reduction of coating Brownian thermal noise were proposed to be implemented in the sub-SQL interferometer to increase the margin between the SQL and the total classical noise in the instrument. These techniques are extremely large beam spots – in relation to the length of the arm cavities – on the arm cavity mirrors and the use of anti-resonant end mirror cavities instead of conventional highly reflective arm cavity end mirrors.

In this chapter, a detailed investigation of these techniques is presented and technical implications are discussed.

3.1 A coating Brownian thermal noise model

Coating Brownian thermal noise originates from random motion of the reflecting surfaces of mirrors used in optical precision metrology experiments. In a massive body with temperature $T > 0$ the atoms are subject to a random oscillatory motion about their equilibrium points which is a consequence of their thermal excitation. Due to the strong coupling with neighboring atoms the internal fluctuations give rise to elastic waves. These are reflected at the surfaces of the body which gives rise to the formation of stationary waves corresponding to elastic normal modes. Atomic motion near the reflecting surface of a mirror distorts the surface which changes the

phase of the reflected light field and can thus be regarded as a source of phase noise with a distinctive noise spectrum.

According to the *fluctuation-dissipation theorem* (FDT), devised by *Callen et al* [80], thermal noise is a consequence of mechanical losses. This theorem reflects the relation between mechanical losses on microscopic scale and the resulting amplitude of macroscopic position fluctuations which in the case of a mirror in a laser interferometer gives rise to thermal noise. The noise power spectral density of thermally induced mirror surface fluctuations can be written as

$$S_{\hat{x}}(f) = \frac{k_B T}{\pi^2 f^2} \mathrm{Re}\{\mathbb{Z}^{-1}\} \ , \tag{3.1}$$

with the Boltzmann constant k_B, the temperature T of the mirror and the frequency f of the fluctuations. It is furthermore proportional to the inverse mechanical impedance of the mirror, $\mathbb{Z}^{-1}$, which is also referred to as the mechanical admittance $\mathbb{Y} = \mathbb{Z}^{-1}$. The mechanical admittance of a mirror can be written as [81]

$$\mathbb{Y}(f) = i2\pi f \frac{x(f)}{F(f)} \ . \tag{3.2}$$

The quantity $F(f)$ is the Fourier transform of a periodic driving force and $x(f)$ is the Fourier transform of the mirror's response to this force in terms of a displacement.

In the time domain the driving force can be written as an oscillatory pressure applied to the mirror surface,

$$P(\vec{r}, t) = F_0 \cos(2\pi f t) f(\vec{r}) \ , \tag{3.3}$$

with form factor $f(\vec{r})$ representing the transverse shape of the beam used for reading out the position of the mirror and $\vec{r}$ representing a point on the surface of the mirror. For a Gaussian beam Equation (3.3) takes on the form

$$P(\vec{r}, t) = P(r, t) = \frac{2F_0}{\pi w^2} \exp\left(-\frac{2r^2}{w^2}\right) \cos(2\pi f t) \tag{3.4}$$

with w the (amplitude) radius of the Gaussian laser beam, i.e. the radius at which the light intensity is $1/e^2$ times the maximum.

Following Levin's approach [81] the real part of the admittance, which describes the coupling of the driving force to mirror displacement and is a measure for the damping of the system, takes on the form

$$\mathrm{Re}\{\mathbb{Y}(f)\} = 2\frac{W_{\mathrm{diss}}}{F_0^2} \ , \tag{3.5}$$

with W_{diss} the power dissipated in the mirror and F_0 the amplitude of the periodic driving force. From this equation it can be inferred that the average power W_{diss} dissipated in the mirror as a result of the oscillatory pressure needs to be computed to determine the real part of the admittance which is the missing piece in Equation (3.1), to formulate the spectral density of the thermal fluctuations. For the case

of homogeneous dissipation, loss angles $\phi \ll 1$ and for frequencies below the first mirror normal mode W_{diss} can be expressed as

$$W_{\text{diss}} = 2\pi f U_{\text{max}} \phi \,, \tag{3.6}$$

with U_{max} the energy of elastic deformation when the mirror is maximally contracted or extended under the action of the driving force and ϕ the loss angle of the material. This description is based on the phenomenological model of so-called *structural damping* in the material [82]. Furthermore, in the limit of measurement frequencies much lower than the lowest resonance frequency of the mirror, Equation (3.4) can be approximated assuming a constant pressure

$$P(r) = \frac{2F_0}{\pi w^2} \exp\left(-\frac{2r^2}{w^2}\right) . \tag{3.7}$$

The task that remains to be solved is to calculate $U_{\text{max}}\ \phi(f)$ under the cyclic pressure in Equation (3.7), usually approximating the coated mirror as a half-infinite mass.

The model of coating Brownian thermal noise assuming independent dielectric coating layers on an infinite half-space substrate was investigated in detail by various authors, e.g. in [62, 83]. To estimate the expected level of coating Brownian thermal noise the spectral density can be written in the approximative form [84]

$$S_{\hat{x}}^{\text{CBTN}} = \frac{2k_B T}{\pi^2 f Y} \frac{d}{w_m^2} \left(\frac{Y'}{Y}\phi_{\parallel} + \frac{Y}{Y'}\phi_{\perp}\right) \tag{3.8}$$

The parameter T is the temperature of the mirror, k_B the Boltzmann constant, d is the thickness of the coating , w_m is the beam spot size on the mirror surface and f is the frequency of the fluctuations. The parameters Y and Y' Young's moduli of the bulk substrate and the coating, respectively. Finally, $\phi_{\parallel}$ and $\phi_{\perp}$ represent the mechanical loss angles for strains parallel and perpendicular to the surface of the mirror.

The reason why coating Brownian thermal noise usually dominates substrate Brownian thermal noise in precision interferometry experiments can be attributed on the one hand to larger mechanical losses. Loss angles in conventional SiO_2/Ta_2O_5 stacks were found to be of the order of approximately $\phi_{SiO_2} = 1 \times 10^{-4}$ and $\phi_{Ta_2O_5} = 4 \times 10^{-4}$ [62] and thus several orders of magnitude higher than reported loss angles in the bulk substrates of approximately $\phi = 5 \times 10^{-9}$ [85]. On the other hand fluctuations in the coatings, which are located near the surface of a mirror, have a larger influence on the displacement noise of the optic than fluctuations in the substrate material. As was shown in [81], coating Brownian thermal noise scales with $S_{\hat{x}}^{\text{CBTN}} \propto 1/w_m^2$ whereas substrate Brownian thermal noise scales with $S_{\hat{x}}^{\text{SBTN}} \propto 1/w_m$, with w_m representing the beam spot size on the mirror surface. Thus, if the beam spot size on a mirror is decreased, coating Brownian thermal noise grows faster than thermal noise due to bulk damping.

Evidently, the level of coating Brownian thermal noise in an experiment can be lowered by tuning the magnitude of one or a combination of parameters in Equation (3.8). A combination of approaches to reduce coating thermal noise in the

sub-SQL interferometer were proposed in [60]. To reduce the mechanical loss angle of the coatings it was proposed to employ titania-doped coatings [65]. Furthermore, an optimization of the thin film layer thickness to reduce the total amount of tantala [66] was proposed. In addition to this it is planned to operate the interferometer with extremely large beam spots w_m and to reduce the effective thickness of the end mirror coatings by employing strongly over coupled anti-resonant end mirror cavities instead of conventional highly reflective end mirrors with numerous coating layers [63].

3.2 Increasing beam spot sizes

The most straight-forward approach to coating Brownian thermal noise reduction is probably to increase the beam spot size on the mirrors in the interferometer arm cavities. A natural limitation to this approach is on the one hand imposed by the cavities' geometric stabilities and on the other hand by beam clipping loss at the apertures of the mirrors with given aspect ratio.

In precision interferometry experiments, laser beam spots on the relevant cavity mirrors are typically much larger than the thickness of the dielectric coatings. In this case it is fair to assume that coating Brownian thermal noise occurring at different positions of the mirror surface is uncorrelated, to good approximation. *Lovelace* devised a general scaling law for the power spectral density of coating Brownian thermal noise of the following form [86]

$$S_{\mathrm{x}}^{\mathrm{CBTN}} \propto \frac{\int_{\mathrm{S}} \mathrm{d}^2 r \, I^2(\vec{r})}{\left(\int_{\mathrm{S}} \mathrm{d}^2 r \, I(\vec{r})\right)^2} \, . \tag{3.9}$$

which expresses an inverse proportionality between an arbitrary intensity profile $I(\vec{r})$ of the laser beam employed to read out the mirror position and the resulting coating Brownian thermal noise spectral density, i.e. the larger the effective area of the optical mode, the smaller the coating Brownian thermal noise contribution.

To overcome the limitations of the commonly used Gaussian beam profile, which averages the thermally driven mirror displacement over a comparatively small region of the mirror, alternative beam shapes were proposed which exhibit an intensity distribution superior to the Gaussian shape.

However, these alternative beam shapes, namely conical beams [87], mesa beams [88] and higher order transverse modes such as the LG_{33} mode [89] impose substantial technical challenges. Whereas the former two beam shapes, conical and mesa, require special mirrors to be used in the experiment, LG_{33} beams can be used in conjunction with standard spherical optics. However, investigations have shown that interferometry with LG_{33} modes requires polishing of the mirror surfaces to be better by about one order of magnitude than what is currently achievable [90]. Hence, for the sub-SQL interferometer beams with standard Gaussian intensity profile will be used with extremely large spot sizes, cf. Section 1.5.

It was found by *Somiya and Yamamoto* that the infinite-mirror model overestimates coating Brownian thermal noise for the case of large beam spots. However, as the

authors point out in [61], their finite-mirror model is in very good agreement with the infinite-mirror model for spot sizes of interest in the sub-SQL interferometer.

The optimal configuration to reduce coating Brownian thermal noise in interferometer arm cavity is that of a symmetric linear cavity with equal radii of curvature of the mirrors and equal beam spot sizes on both mirrors. A further advantage of choosing the symmetric configuration is the reduction of the manufacturing costs for the mirrors since the same metrology can be used for all HR-side curvatures without the need for additional custom-made mirror metrology references.

With the assumption of perfectly spherical mirror surfaces the fundamental cavity eigenmode of a two-mirror cavity is completely determined by the radii of curvature of the mirrors and their spatial separation.

The *g–factor*

$$g_{1,2} = 1 - \frac{L}{R_{\mathrm{c}\,1,2}} \tag{3.10}$$

relates cavity length and radii of curvature of the mirrors forming the cavity to the existence of a stable, i.e. low-loss fundamental Gaussian eigenmode. For the beam spot size on the cavity mirrors one obtains [91]

$$w_{1,2}^2 = \frac{\lambda L}{\pi}\sqrt{\frac{g_{2,1}}{g_{1,2}(1-g_1 g_2)}}\,. \tag{3.11}$$

This equation can be inverted to yield

$$g_{1,2} = \pm\frac{w_{2,1}}{w_{1,2}}\sqrt{1-\frac{w_0^2}{w_1^2 w_2^2}}\,. \tag{3.12}$$

The waist size of this eigenmode can be expressed as a function of the g-factors of the cavity mirrors

$$w_0 = \frac{\lambda L}{\pi}\sqrt{\frac{g_1 g_2\,(1-g_1 g_2)}{(g_1+g_2-2g_1 g_2)^2}} \tag{3.13}$$

which can be approximated as

$$w_0 \approx \sqrt{\frac{\lambda L}{\pi}} \tag{3.14}$$

for long cavities. A boundary condition for the identification of an arm cavity configuration for the sub-SQL interferometer is the requirement for equal spot sizes on the mirrors, i.e. $w_m = w_1 = w_2$. Furthermore large beam radii of $w_m = 1/2.5a$, with a the radius of the mirror, are aimed for. The configurations which fulfill these requirements for a given cavity length of approximately $L = 10\,m$ are the near-planar configuration with $g_1 = g_2 \approx 1$ and the concentric cavity with $R_1 = R_2 = L/2$ and $g_1 = g_2 \approx -1$. The nearly concentric configuration is identified as the most suitable candidate since this configuration supports diffraction-limited beams with maximized beam spot sizes. By inserting Equation (3.14) into Equation (3.12) and further assuming $w_1 = w_2 =$ const. is found that the stability of the cavity, i.e. the product of its g-factors (cf. Section 2.3.6), improves as the length of the cavity is

increased. A further boundary condition which was also discussed in [60], is the aspect of angular instability of the arm cavities due to optical torques [92]. By adopting negative g-factors for the mirrors, which is fulfilled by the near concentric configuration, it can be arranged for an optical stiffness matrix with reduced opto-mechanical coupling in the unstable angular mode, which needs to be stabilized with the aid of the alignment control system.

3.3 Anti-resonant end mirror cavities

In this section, the concept of anti-resonant end mirror cavities for coating thermal noise reduction is reviewed and investigations of technical implications of their use in the AEI 10 m sub-SQL interferometer are presented. Special emphasis is placed on the specific properties and requirements of the optical layout candidates for the three mirror coupled arm cavity configuration.

3.3.1 The general concept

The concept of coating Brownian thermal noise reduction by replacing interferometer end mirrors with over coupled anti-resonant cavities was originally proposed by *F. Khalili* [63]. Often these end mirror cavities are simply referred to as "Khalili cavities" (KC).

As pointed out previously, the coating Brownian thermal noise spectral density is proportional to the number of dielectric coating layers of a mirror, cf. Section 3.1. Hence, the largest coating thermal noise contribution stems from the arm cavity end mirrors which are typically made highly reflective, with reflectivities close to unity. This is achieved by applying a comparatively large number of thin film layers to the mirror substrates.

A highly reflective optical coating composed of numerous layers can be thought of as a series of short, anti-resonant cavities. The resulting phase fluctuations of a reflected beam are equal to the wave number $k = 2\pi/\lambda$ multiplied with twice the motion of the mirror surface which is composed of the mostly coherent motion of the individual coating layers. By replacing the single highly-reflective coating stack with two stacks and arranging for a mechanical separation between these, equal to an anti-resonant tuning, coating Brownian thermal noise can be reduced, provided that the number of coating layers is chosen appropriately.

Khalili cavities cleverly implement this idea and exploit the property of phase noise suppression in an optical resonator tuned to an anti-resonant working point. The principle layout of a KC as part of an interferometer arm is shown in Figure 3.1. If conventional interferometer end mirrors are replaced with cavities one can arrange for a comparatively low reflectivity of the input mirror but at the same time preserve high reflectivity of the end mirror cavity by tuning its length to (or close to) an odd integer multiple of a quarter wavelength. The laser field circulating in the arm predominantly senses the reduced number of coating layers on the IETM and is thus subject to lower coating thermal noise. Nonetheless, a fraction of the light leaks

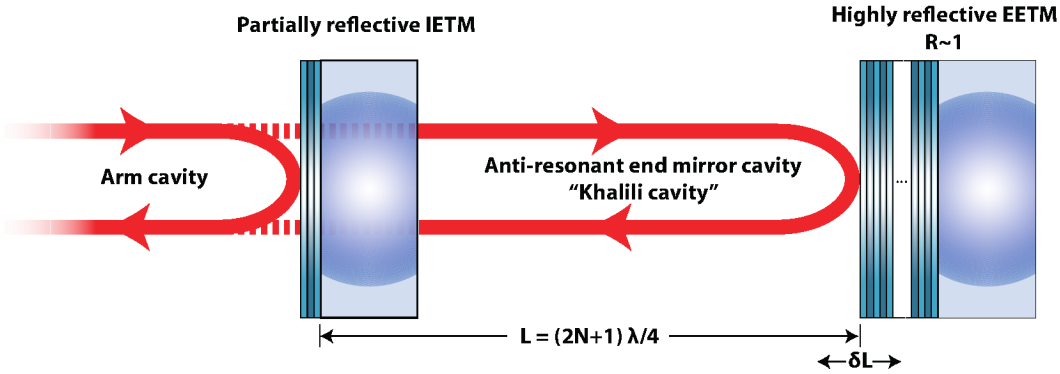

Figure 3.1: Schematic drawing of the principle layout of a Khalili end mirror cavity. Whereas the intermediate mirror is coated for a comparatively low reflectivity, the rear mirror is made highly reflective. By tuning the length of the cavity to anti-resonance, suppression of phase noise originating from a displacement δl of the rear mirror can be achieved. It must be noted that in the drawing the thickness of the coating layers is strongly exaggerated for illustrative purposes and is not to scale with the substrates. The real thickness of the dielectric coating layers is in the order of the wavelength of the laser light.

into the end mirror cavity and senses the highly reflective EETM. In his paper [63], *Khalili* shows that displacement noise from the EETM is effectively suppressed and in effect the net phase fluctuations of the beam reflected at the KC are reduced.

The calculations presented in [63] result in a complex reflection factor for a beam incident on an end mirror cavity of

$$\varrho_{\mathrm{KC}} \approx -r_{\mathrm{KC}} \cdot \exp\left(i\phi_{\mathrm{KC}}\right) \tag{3.15}$$

with

$$r_{\mathrm{KC}} = 1 - \frac{(1 - r_{\mathrm{IETM}})(1 - r_{\mathrm{EETM}} \left|t_{\mathrm{IETM}}^{\mathrm{bulk}}\right|^2)}{1 + r_{\mathrm{IETM}} r_{\mathrm{EETM}} \left|t_{\mathrm{IETM}}^{\mathrm{bulk}}\right|^2} \tag{3.16}$$

and

$$\phi_{\mathrm{KC}} \approx \frac{2 r_{\mathrm{EETM}} \left|t_{\mathrm{IETM}}^{\mathrm{bulk}}\right|^2 t_{\mathrm{IETM}}^2}{(r_{\mathrm{EETM}} \left|t_{\mathrm{IETM}}^{\mathrm{bulk}}\right|^2 + r_{\mathrm{IETM}})(1 + r_{\mathrm{IETM}} r_{\mathrm{EETM}} \left|t_{\mathrm{IETM}}^{\mathrm{bulk}}\right|^2)} k \cdot \delta l \,, \tag{3.17}$$

where r_{IETM}, r_{EETM} are the amplitude reflectivities of the IETM and the EETM, respectively, $t_{\mathrm{IETM}}^{\mathrm{bulk}}$ is the amplitude reflectivity of the bulk substrate, δl is the longitudinal displacement of the EETM surface and $k = 2\pi/\lambda$ is the wave number.

The plot shown in Figure 3.2 illustrates the attenuation of EETM displacement in the interferometer signal compared to the displacement transfer function of an interferometer with a conventional end mirror. The numerical model serves to validate the predictions of the analytic model in terms of suppression of EETM fluctuations. With the mirror reflectivities proposed for the sub-SQL interferometer,

cf. Section 1.5, one obtains an attenuation factor of ≈ 6 for EETM displacement-induced phase fluctuations of the beam reflected at the KC. More details on this configuration are given later in this chapter. This attenuation factor is in excellent agreement with the ratio of the modeled transfer functions for ETM displacement in an interferometer with conventional end mirrors and EETM displacement in an interferometer with Khalili cavities. The analytic model, however, does not take the input mirrors of the arm cavities into account and therefore lacks the characteristic roll-up of the attenuation factor toward higher frequencies which is due to the finite bandwidth of the arm cavity. The reflectivity of the IETM affects the magnitude of noise contributions from both, the IETM and the EETM and thus needs to be chosen carefully. On the one hand it determines the direct coating thermal noise contribution of the IETM. The larger the number of coating layers on the IETM, and consequently its reflectivity, the larger the fluctuations of its coating thickness. On the other hand, the IETM reflectivity determines the suppression of surface fluctuations from the EETM. The suppression of phase fluctuations induced by EETM surface displacement δl, as given in Equation (3.17), is proportional to the power transmittance of the IETM. The reflectivity of the IETM also determines the level of other noises, e.g. thermorefractive noise in the IETM substrate. The lower the IETM reflectivity is chosen, the higher the transmitted light power and consequently the thermorefractive noise contribution.

Thus, by optimizing the number of coating layers on the IETM a trade off between noise contributions from the IETM and the EETM and thermorefractive noise from the IETM substrate needs to be identified. This optimization was carried out for the sub-SQL interferometer in [60] with the result of optimal numbers of SiO_2-Ta_2O_5 double layers of 8, 2 and 15 on the reflective sides of the ITM, IETM and EETM, respectively. With the aid of the sensitivity model [64] it is found that the margin between coating Brownian thermal noise and the SQL is increased by approximately 30 % in the configuration with end mirror cavities, compared to an interferometer with conventional two mirror arm cavities with input mirror and end mirror reflectivities identical to the reflectivities of the ITM and EETM, respectively (cf. Figure 3.16). In a realistic interferometer arm configuration the power in the KC is much lower than the power circulating in the arm. From a plane-wave model with sub-SQL interferometer parameters and an injected power of $I_0 = 5.5\,\mathrm{W}$ one obtains, for the reflectivities given above and with the assumption of 50 ppm loss per mirror due to scattering and absorption, a circulating power of approximately 1.2 kW in the arm cavities and approximately 200 W in the KCs, cf. Figure 3.3. It is obvious that the power in the interferometer arm exhibits a lower dependence on the tuning of the KC than on the arm cavity tuning which is due to the working point of the end mirror cavity. An immediate advantage of including KCs in an interferometer is the possibility to compensate for a finesse imbalance of the arms by changing the tuning of the end mirror cavities. Also, it is worth noting that the ratio of powers in the arm cavity and in the KC corresponds to the ratio of the low-frequency limit of the conventional ETM and the EETM displacement transfer functions in Figure 3.2.

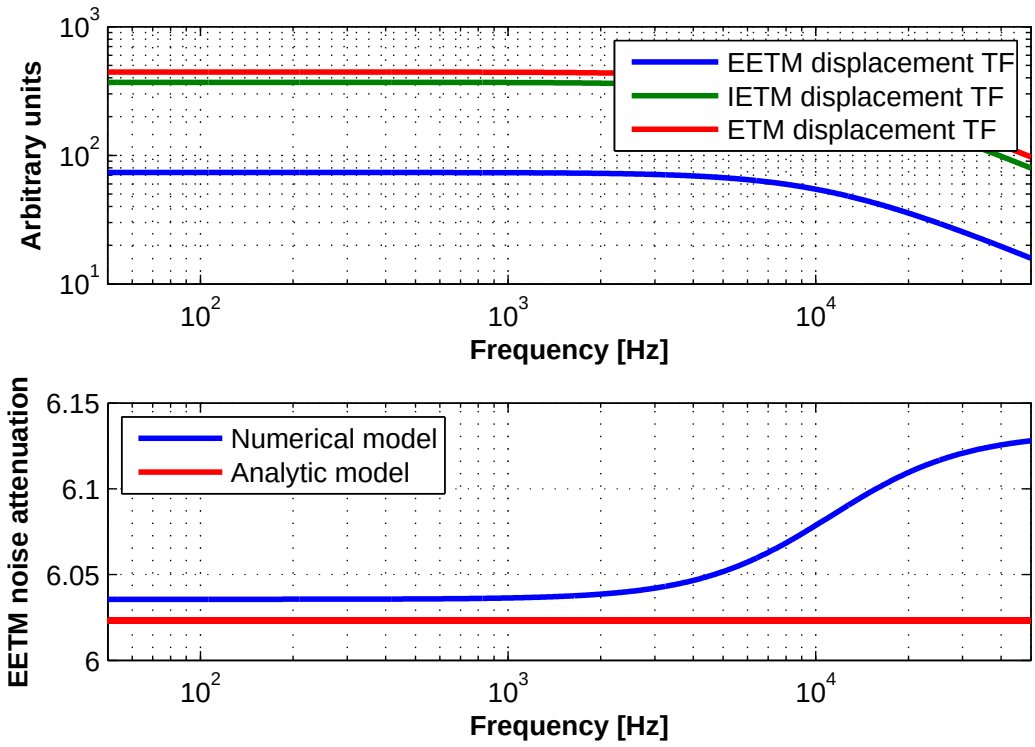

Figure 3.2: Transfer functions for end mirror displacement to the main interferometer signal for a configuration with 10 m sub-SQL interferometer parameters, with and without Khalili end mirror cavities. The upper plot shows the modeled transfer functions of a differential excitation of the Khalili cavity end mirrors (EETM) in the two interferometer arms and of the Khalili cavity input mirrors (IETM), respectively. The transfer function of a differential excitation of conventional end mirrors (ETM) to the main interferometer signal is shown for comparison. The lower plot shows a comparison of the ratio of the transfer functions for ETM and EETM excitation obtained from the numerical model with an analytic result. The analytic result, as obtained from Equation (3.17), is in very good agreement with the numerical model. However, the analytical result does not exhibit the frequency dependence of the suppression factor as in the case of the numerically modeled curve. This frequency dependence originates from the cavity poles which are accounted for in the numerical simulation but not in the analytical model. It is obvious that the pole frequencies are slightly different for the ETM and the EETM displacement transfer functions which is mainly due to different cavity lengths.

Despite the slightly lowered requirements for the EETM e.g. in terms of seismic isolation due to the suppression of fluctuations by the KC, the optical design of the KC needs to fulfill the same requirements as any cavity which is part of a high precision laser interferometer. In particular a sophisticated control scheme needs to be employed to lock the KCs on their designated operating points.

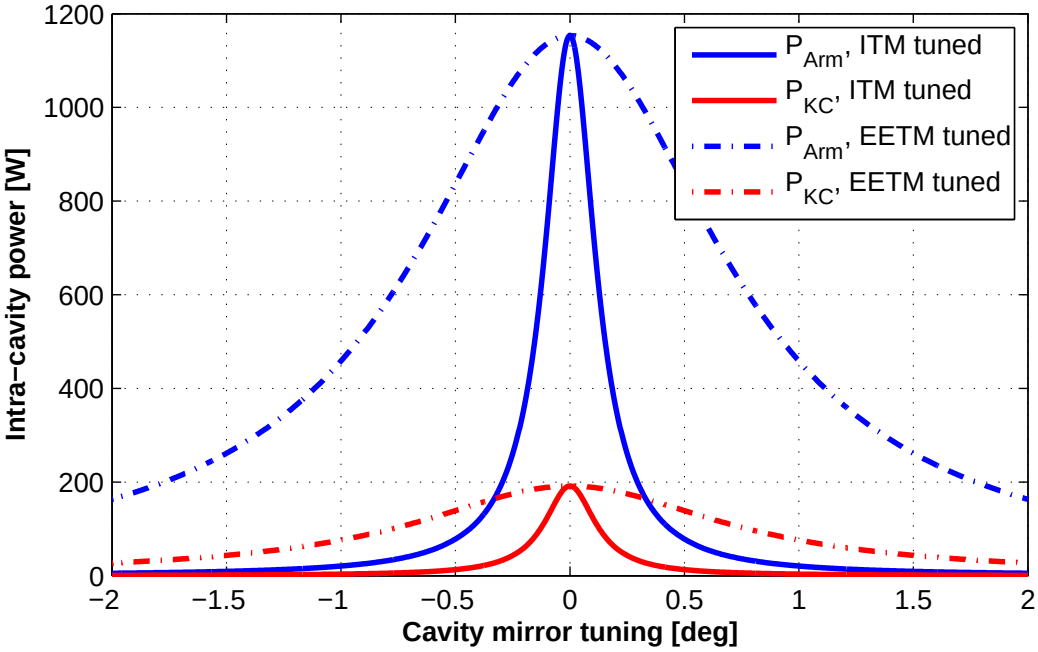

Figure 3.3: Simulated intra-cavity powers in the arm cavity and the Khalili cavity for the proposed sub-SQL interferometer mirror reflectivities and an input laser power of $P_{\text{in}} = 5.5\,\text{W}$. The reflectivities were set to 99.0696 %, 51.151 % and 99.9936 % for the ITM, IETM and EETM, respectively. A loss of 50 ppm per mirror was assumed to account for light scattering and absorption. Intra cavity powers are approximately 1.2 kW and 200 W for the AC and the KC, respectively. Due to the chosen KC working point, changes in the KC tuning have a lower impact on the power stored in the arm than changes of the arm cavity tuning of the same magnitude.

3.3.2 Aspects of length sensing and control

An important prerequisite for operating a high-precision laser interferometer is that the multitude of longitudinal and angular degrees of freedom in the optical setup are held tightly at their designated operating points, to ensure full power buildup and to suppress disturbances of any kind which might introduce additional noise into the differential mode signal of the interferometer arms. In this section, aspects of length sensing and control of Khalili end mirror cavities are discussed.

To solve the task of controlling the longitudinal DOF in an interferometer it is necessary to extract signals which can be utilized as error signals for feedback control, i.e. linear, time invariant signals which are proportional to the deviation of a DOF from its working point. A requirement which is commonly applied in the design of interferometer controls is to postulate the stabilization of a primary length DOF in the interferometer to less than 1 % RMS deviation from its corresponding line width. Assuming sub-SQL interferometer parameters this translates to a deviation of the length of the arm cavity (AC), i.e. the cavity formed by the input test mass (ITM) and the intermediate end test mass (IETM) , from its operating point by less

than 4×10^{-12} m. For the end mirror cavity it was determined that it needs to be held to within 2.4×10^{-11} m of its operating point, i.e. the requirement for stabilizing the length of the KC is almost as stringent as the one for the arm cavity and it needs to be orders of magnitude more stable than for instance the central Michelson length degree of freedom in an interferometer, cf. [93]. This means that the end mirror cavities will exhibit strong coupling to the differential arm length channel of the interferometer and thus require great carefulness regarding their control in order not to degrade the sensitivity, e.g. by introducing low-frequency noise to the main interferometer signal.

These numbers illustrate the fundamental difference between an isolated anti-resonant cavity and a cavity tuned to $\phi = 90°$ which is part of a three mirror coupled cavity. In fact, the EETM tuning has a substantial effect on the resonance state of the three mirror coupled cavity as a whole, cf. Figure 3.3. Thus, the end mirror cavity, formed by the IETM and EETM, cannot be treated independently of the arm cavity formed by the ITM and the IETM. In this respect the intuitive approach of thinking of the three mirror coupled cavity in terms a resonant two mirror cavity coupled to an anti-resonant two mirror cavity fails since an anti-resonant cavity can be tuned over a wide range with only little effect on the phase and amplitude of the reflected light.

For the following investigations aiming at obtaining length signals for the end mirror cavities with reduced coupling, the widespread approach of using a plane wave model was adopted, realized with FINESSE [94]. To obtain length signals for controlling the two longitudinal DOF of the coupled cavity, a variant of the *Pound-Drever-Hall* technique [55] with phase modulation sidebands imprinted on the input laser is usually employed.

Phase modulation of the input laser field is typically achieved with an electro optic modulator (EOM) and results in an electric field

$$\Phi_{\text{in}} = \Phi_{\text{Laser}} \cdot \exp\left(i\Gamma \cos\left(\omega t\right)\right) \ , \tag{3.18}$$

where ω is the angular frequency of the phase modulation. For small modulation indices Γ this expression can be approximated as

$$\begin{aligned} \Phi_{\text{in}} \approx J_0(\Gamma)\Phi_{\text{Laser}} + iJ_1(\Gamma)\Phi_{\text{Laser}} \exp\left(+i\omega t\right) + \\ +iJ_1(\Gamma)\Phi_{\text{Laser}} \exp\left(-i\omega t\right) \ , \end{aligned} \tag{3.19}$$

where $J_k(\Gamma)$ are the Bessel functions of the first kind. In the sideband picture this first order approximation can be decomposed in a carrier field and the upper (+) and lower (-) phase modulation sideband fields,

$$\Phi_{\text{in}} = \Phi_{\text{in}}^{\text{CR}} + \Phi_{\text{in}}^{\text{SB+}} \exp\left(+i\omega t\right) + \Phi_{\text{in}}^{\text{SB-}} \exp\left(-i\omega t\right) \ . \tag{3.20}$$

To analyze the resonance properties of coupled cavities the power transmittance plotted as a function of the two cavity tunings has proven as a useful tool. A transmittance map of a three mirror coupled cavity with sub-SQL interferometer arm

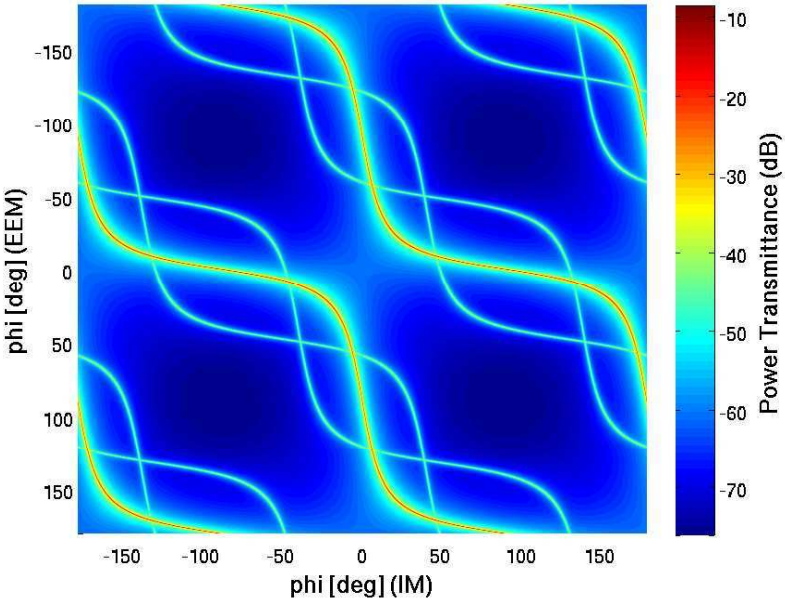

Figure 3.4: Power transmittance map of an arm cavity with Khalili end mirror cavity with sub-SQL interferometer parameters in the presence of phase modulation sidebands at 40 MHz. Whereas the wider lines in the plot represent resonant states of the carrier field, the finer lines correspond to sideband resonance states. At tunings where one of the finer lines intersects with the carrier resonance branch, both, the carrier field and one of the sideband fields are simultaneously resonant in the three mirror coupled cavity.

cavity parameters in the presence of phase modulation sidebands at an arbitrarily chosen frequency of 40 MHz is shown in Figure 3.4. At the desired working point $(\phi_{\mathrm{AC}}, \phi_{\mathrm{KC}}) = (0°, 90°)$ the phase modulation sidebands at the chosen frequency are not resonant in the three mirror cavity and due to the coupling of the longitudinal DOF in the linear three mirror cavity the extracted heterodyne signals likewise, are coupled. The plot shown in Figure 3.5 illustrates the length signal coupling of the same coupled geometry for 40 MHz control sidebands. For an arbitrarily chosen sideband frequency not only detunings of the AC degree of freedom but also KC detunings result in a heterodyne signal in reflection of the cavity with considerable optical gain. Generally, the effect of AC detunings dominates over KC detunings in terms of heterodyne signal slope. A consequence of optical couplings between longitudinal DOF is that the PDH signal extraction scheme does not always provide reliable signals during lock acquisition when the cavities are far from their nominal working points [95]. This coupling can often be reduced by choosing a prudent design for the optical plant and the sensing scheme parameters. The foundation of the approach discussed in the following is the use of two pairs of phase modulation sidebands with optimized frequencies imprinted on the input laser.

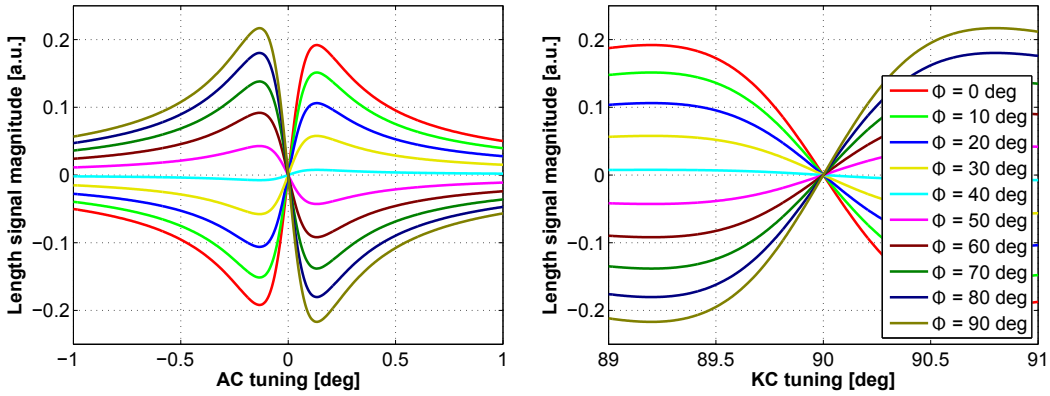

Figure 3.5: Generic heterodyne length signals for the interferometer arm cavities at different demodulation phases Φ, plotted versus the frequency and the tuning of the ITM and the EETM, respectively. Parameters of the 10 m sub-SQL interferometer arm cavities were assumed. Phase modulation sidebands at an arbitrarily chosen frequency of 40 MHz were imprinted on the input laser beam with a modulation index of 0.3 and were demodulated in reflection of the coupled cavity. For each plot the second DOF which was not tuned was assumed to be held at its designated operating point. The signals which arise from AC detuning (left) dominate over KC detuning signals (right) in terms of the error signal slope.

For the reflectivities of the mirrors the optimized values given in [60] were assumed. Generally, macroscopic spacings in the optical setup are subject to spatial constraints imposed by e.g. optical table dimensions, conflicting payload of neighboring sub-systems, load balancing, etc. A length of $L_{\mathrm{AC}} = 10.4\,\mathrm{m}$ was assumed for the arm cavity and $L_{\mathrm{KC}} = 1\,\mathrm{m}$ for the end mirror cavity which complies with the spatial constraints calculated for the Prototype environment while retaining some flexibility for on-the-fly changes of the optical layout such as changes in the optical readout system.

The following boundary conditions for the RF length signal extraction scheme can be formulated:

- The extracted signals need to exhibit zero crossings at $\phi_{\mathrm{AC}} = 0°$ and $\phi_{\mathrm{KC}} = 90°$ for AC and KC longitudinal control, respectively.
- To independently control the two length degrees of freedom the extracted error signals need to be at least linearly independent.
- If possible, RF modulation frequencies should be arranged for below approximately 100 MHz. This is because modulation frequencies above 100 MHz require more complicated designs for RF electronics and photo detectors. Furthermore, small active area diodes with low capacitance are required for fast photo detection. These are more susceptible to noise and optical losses due to

beam pointing instabilities and are more likely to get damaged during lock loss events.

If the RF modulation frequency for the end-mirror cavity length signal is chosen appropriately, the extracted signal exhibits reduced coupling to changes of the AC tuning. The plots shown in Figure 3.6, in which the carrier and sideband resonance is plotted versus the tunings of the AC and KC degrees of freedom, illustrate the cause of this reduced coupling of the KC length signal to the AC DOF.

The operating point of the coupled three mirror cavity is represented by the intersection of the two white lines in the plot and corresponds to a tuning of the AC of $\phi_{\mathrm{AC}} = 0°$ and a KC tuning of $\phi_{\mathrm{KC}} = 90°$. Whereas the wide curves in the plot represent resonance states of the carrier field in the coupled three mirror cavity, the finer curves represent resonance states of modulation sidebands. As can be seen at the chosen working point, the resonance condition for the RF modulation sideband exhibits much stronger dependence on the tuning of the EETM, i.e. the length of the KC, than on changes of the AC length. Carrier resonance, however, is preserved for small changes of the KC length. In reflection of the three mirror cavity arm, at the operating point, this results in a comparatively steep change of the phase of the reflected sidebands whereas the carrier phase remains mostly stable for small KC length changes. Thus, the reflected carrier field acts as a reference for the reflected sidebands with varied phase, resulting in a beat between the two fields which partly converts phase modulation to amplitude modulation of the reflected field. By demodulating this field one can obtain an error signal for the KC length which exhibits little coupling to the AC degree of freedom. An arbitrarily chosen phase modulation frequency does generally not yield an intersection with the operating point in the resonance map, cf. Figure 3.4. This means that the resulting heterodyne signal originates from phase changes of the reflected carrier field beating against the reflected sidebands which act as the reference in this case. Since tunings of both length degrees of freedom, the AC length as well as the KC length, have an influence on the phase of the reflected carrier field, in this case the obtained length signal cannot be unambiguously brought in line with the degree of freedom which caused the phase change of the carrier field. Nevertheless, by choosing the second modulation frequency to be nearly anti-resonating in the coupled cavity in order to reduce cavity-induced phase shifts, a linearly independent length signal for the

Figure 3.6 ***(following page)*****:** Carrier and sideband resonance in the three mirror coupled arm cavity. The upper plot shows the resonance map of a three mirror coupled arm cavity with sub-SQL interferometer parameters. A pair of RF phase modulation sidebands at a frequency of 77.73 MHz is present on the carrier field. The intersection of the white lines in the plot marks the designated operating point which is represented by the tunings of $\phi_{\mathrm{AC}} = 0°$ and $\phi_{\mathrm{KC}} = 90°$. Whereas the wider curves correspond to resonant states of the carrier, the finer ones represent tunings for which the control sidebands are resonant. It is evident that the chosen working point represents a resonant state of the three mirror arm cavity. The lower plot shows the zoomed area for tunings around the chosen operating point.

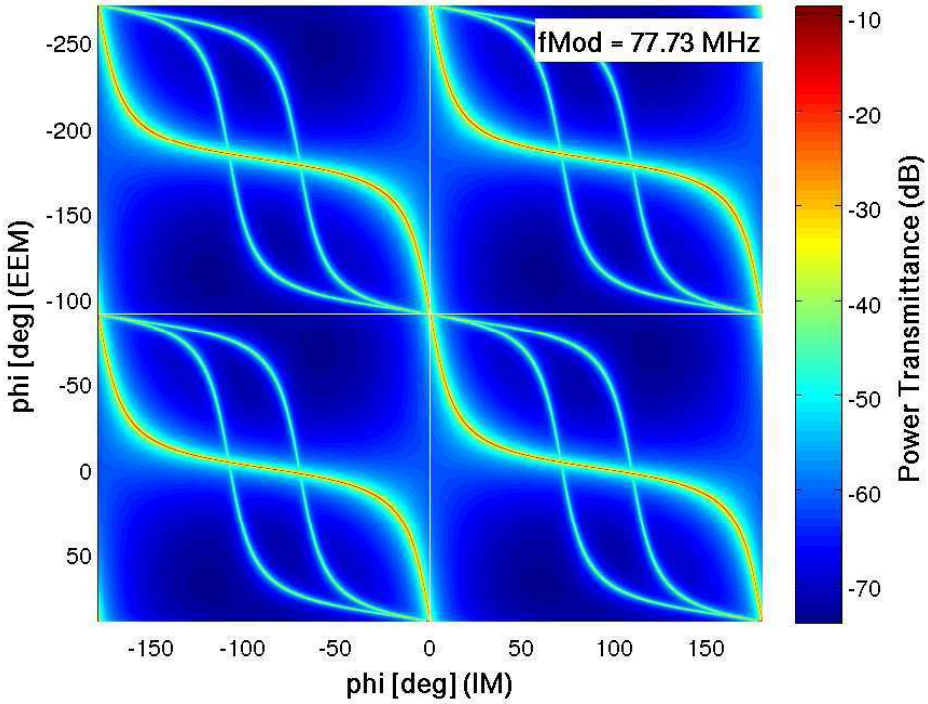
fMod = 77.73 MHz
phi [deg] (EEM)
phi [deg] (IM)
Power Transmittance (dB)
-250
-200
-150
-100
-50
0
50
-150
-100
-50
0
50
100
150
-10
-20
-30
-40
-50
-60
-70

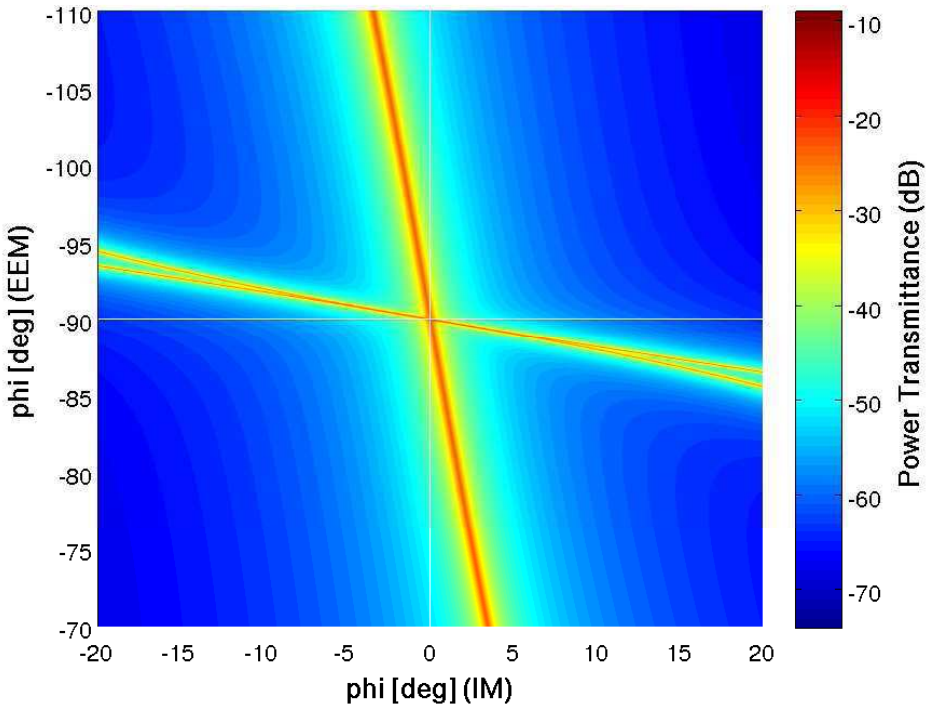
phi [deg] (EEM)
phi [deg] (IM)
Power Transmittance (dB)
-110
-105
-100
-95
-90
-85
-80
-75
-70
-20
-15
-10
-5
0
5
10
15
20
-10
-20
-30
-40
-50
-60
-70

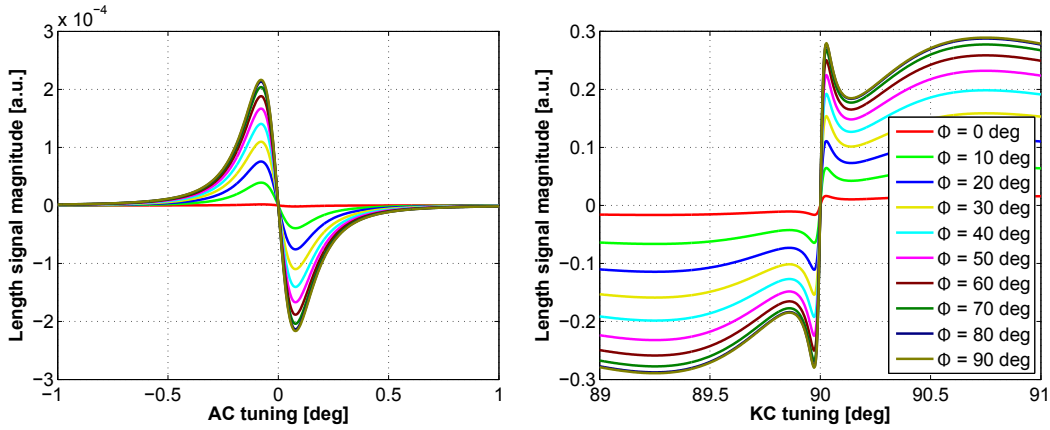

Figure 3.7: Heterodyne length signals for the interferometer arm cavities at different demodulation phases Φ, plotted versus the frequency and the tuning of the ITM and the EETM, respectively. Parameters of the 10 m sub-SQL interferometer arm cavities were assumed. Phase modulation sidebands at the optimized frequency of 77.73 MHz were imprinted on the input laser beam with a modulation index of 0.3 and were demodulated in reflection of the coupled cavity. For each plot the second DOF which was not tuned was assumed to be held at its designated operating point. Other than in the generic case illustrated in Figure 3.5, the optimized phase modulation sideband frequency results in a large heterodyne signal with a steep slope for detunings of the end mirror cavity (right) and shows only little susceptibility to length changes of the ITM–IETM cavity (left).

AC degree of freedom can be obtained. It is worth noting that frequency responses of three mirror coupled cavities differ from those of their two-mirror pendants, cf. [76]. Thus, optimal modulation frequencies for length sensing in a three mirror coupled cavity differ from frequencies determined as optimal for its "constituents". For the given setup, an optimal modulation frequency of $f_{\mathrm{mod}}^{\mathrm{KC}} \approx 77.73\,\mathrm{MHz}$ was identified which yields a heterodyne length signal with minimized dependence of the ITM–IETM length, characterized by a sensing matrix row or column with a negligibly small element representing the optical gain for AC length fluctuations. The corresponding simulated heterodyne length signal for different demodulation phases Φ are shown in Figure 3.7.

A common approach for controlling optical plants with linearly independent but non-orthogonal error signals, i.e. with a length DOF causing large signals in two or more extraction ports, is the application of the concept of gain hierarchy [96]. The underlying principle of this concept is that strong coupling of DOFs can be reduced by closing a control loop around a DOF which couples into extraction ports associated with other DOFs. This results in a suppression of the coupling proportional to the gain of the closed loop. In the present case, the KC length loop would be closed first, to eliminate coupling to the AC signal port resulting from KC length fluctuations.

A known shortcoming of the PDH technique is the fact that reliable length signals can only be extracted near the operating point of the optical plant. A very simplistic approach to lock acquisition is to wait for the ground motion to drive the mirrors coincidentally within the linear regions of their error signals near the operating points to then engage feedback control. However, in an interferometer with as many as five longitudinal DOF which are partially coupled this strategy is prone to result in a very poor duty cycle. In the case of the sub-SQL interferometer the presence of optical springs which occur in detuned cavities may further complicate the task of bringing the interferometer to the locked state.

To ensure deterministic lock acquisition of an interferometer with KCs, systems such as the *arm length stabilization system* (ALS) [97] or *digital interferometry* (DI) [98] may be employed in conjunction with a classical frontal phase modulation scheme. While the former system is based on a PDH configuration with frequency doubled auxiliary lasers which limits its effectiveness to a single DOF and requires modifications of the interferometer optics, the latter approach can also be used for independent sensing of the DOFs in coupled cavity systems [99].

As it was demonstrated e.g. in [100], once one length DOF in a coupled three mirror cavity is locked on an arbitrary operating point with the carrier being resonant, the length actuator will make the locked DOF follow the unlocked one. The whole system will remain in the resonant state and drift along the carrier resonance branch unless the actuation range is exceeded.

With one of the above systems, lock acquisition could be realized in the following way:

1 | The KC length is stabilized by means of the auxiliary locking system, reducing KC length fluctuations which deteriorate the AC length signal.

2 | The AC is locked on carrier resonance of the three mirror coupled cavity with an error signal obtained from the conventional frontal phase modulation scheme.

3 | The KC is tuned to its designated operating point with control authority still with the auxiliary locking system. The AC will follow the KC along the carrier resonance branch of the three mirror coupled cavity system.

4 | Once the KC has reached its operating point, control authority is handed over to the low-noise frontal phase modulation-based sensing and control system.

A rudimentary conceptual layout for a frontal phase modulation-based sensing scheme for the five length DOF of the sub-SQL interferometer was presented in [60] and may serve as a basis for the implementation of the above considerations.

3.3.2.1 Stability implications for length sensing

In the following, the aspect of stability of the coupled cavity system will be discussed as it turns out that marginally stable cavities need to be adopted for the AC and KC, respectively, to fulfill the requirement for large beam spots formulated in [60].

Heterodyne length sensing of a marginally stable coupled cavity system has a number of subtleties that do not occur in a plane wave model but in more realistic models taking transverse modes into account. First, the situation encountered in the case of arm cavities with conventional end mirrors will be reviewed [101].

The starting point for the following investigations is the expression for the phase modulated light field given in Equation (3.20). In the picture of spatial modes of the light one can think of this expression as co-linearly propagating beams with a separation of the sidebands from the carrier by $\pm\omega$ in frequency. For the longitudinal control of conventional two mirror arm cavities it is sufficient to utilize a pair of phase modulation sidebands that are well outside the bandwidth of the arms. Thus, the sidebands are promptly reflected and basically do not sense the cavity internals. The carrier, however is usually made resonant in the cavity and hence, in the case of marginally stable cavities, is subject to the modal degeneracy. This can be expressed as [101]

$$\Phi_{\text{refl}}^{\text{CR}} = D\Phi_{\text{in}}^{\text{CR}} \tag{3.21}$$

$$\Phi_{\text{refl}}^{\text{SB+}} = -\Phi_{\text{in}}^{\text{SB+}} \tag{3.22}$$

$$\Phi_{\text{refl}}^{\text{SB-}} = -\Phi_{\text{in}}^{\text{SB-}}\,, \tag{3.23}$$

where D is a linear operator which represents the effect of the cavity on the reflected carrier field. This operator depends on the parameters of the cavity, including the properties of the used mirrors such as their surface topography, etc. The resonating carrier may, for instance, experience light scattering in higher-order transverse modes which is amplified in the case of marginal stability by the modal degeneracy of the cavity. As a consequence the reflected field at the cavity may not be a pure TEM_{00} mode anymore but may contain higher order modes. The power of the reflected field can then be written as

$$P_{\text{refl}} = \int_S \mathrm{d}S \left|\Phi_{\text{refl}}^{\text{CR}} + \Phi_{\text{refl}}^{\text{SB+}} + \Phi_{\text{refl}}^{\text{SB-}}\right|^2 \tag{3.24}$$

with an integral over an area S much larger than the area of the beam. The error signal for the cavity V_I can be obtained by demodulating the signal from the photo detector obtained from detecting the reflected field

$$V_I \approx \alpha \int_S \mathrm{d}S \int_0^T \mathrm{d}t \frac{P_{\text{refl}}\cos(\omega t)}{T} \tag{3.25}$$

$$= \alpha \int_S \mathrm{d}S\, \mathrm{Re}\left(\Phi_{\text{refl}}^{\text{CR}}\Phi_{\text{refl}}^{\text{SB-}*} + \Phi_{\text{refl}}^{\text{SB+}}\Phi_{\text{refl}}^{\text{CR}*}\right) \tag{3.26}$$

From Equation (3.26) one can infer that only the component of the carrier field which is in the same mode as the sideband fields will contribute to the signal. This is a consequence of the fact that transverse modes with different mode indices are orthogonal. Within the boundaries of the validity of the model, no corruption of length signals is expected in the case of phase modulation sidebands at frequencies which are anti-resonant in the cavities.

For the case of modulation sidebands which are resonant in the cavity, i.e.

$$\Phi_{\text{refl}}^{\text{CR}} = D\Phi_{\text{in}}^{\text{CR}} \tag{3.27}$$
$$\Phi_{\text{refl}}^{\text{SB+}} = D^{+}\Phi_{\text{in}}^{\text{SB+}} \tag{3.28}$$
$$\Phi_{\text{refl}}^{\text{SB-}} = D^{-}\Phi_{\text{in}}^{\text{SB-}}\,, \tag{3.29}$$

the sidebands will experience a transformation D^{+} or D^{-}, similar to the transformation D on the carrier. The differences in the operations on carrier and sidebands are due to different optical gains in the cavity for fundamental and higher-order transverse modes at carrier and sideband frequencies, respectively. Hence, under these circumstances in a realistic cavity not only the carrier but also the sidebands are subject to modal degeneracy effects in the cavity. In particular, deformation of the spatial mode by light scattering into HOMs at aberrated mirror surfaces is amplified for both, carrier and sideband fields. In degenerate cavities, such as the sub-SQL interferometer arm cavities, for sidebands within the bandwidth of the cavity the "mode selective" behavior for the fundamental mode encountered in the previous case is not present. This implies that corruption of length signals due to higher-order mode content of the sideband fields is likely which may severely impede the robustness of the control system of the interferometer.

As pointed out previously, in order to extract length information about the end mirror cavities it is necessary to transmit the heterodyne sidebands for sensing of the rear cavity through the front cavity. Hence, these sidebands will experience the marginally stable, modally degenerate arm cavity which may result in the possible length signal corruption pointed out above.

A similar situation was encountered in the case of marginally stable power recycling cavities in the initial LIGO and Virgo detector generation. A significant difference is that in the gravitational wave detectors the marginally stable recycling cavities experience a stabilizing effect by the much more stable arm cavities, i.e. the stable arm cavities define the mode that resonates in the coupled cavity [101, 102]. However, as the stable reference is missing in the present case, such an effect is not expected.

3.3.3 Optical layout of the coupled arm cavities

In contrast to a conventional interferometer arm cavity design, where the eigenmode of the cavity determines the beam geometry which needs to be arranged for by the input optics chain, Khalili cavities need to be designed "around" their input beam. This is the beam transmitted through the KC input mirror IETM, which is defined by the beam parameter of the input beam matched to the eigenmode of the arm cavity. In other words, the KC geometry needs to be "matched" to the arm cavity mode which is fully determined by the length of the arm cavity and the radii of curvature of the HR-coated sides of the ITM and the IETM.

The challenge is to find a cavity geometry for the KC which fulfills the requirements of

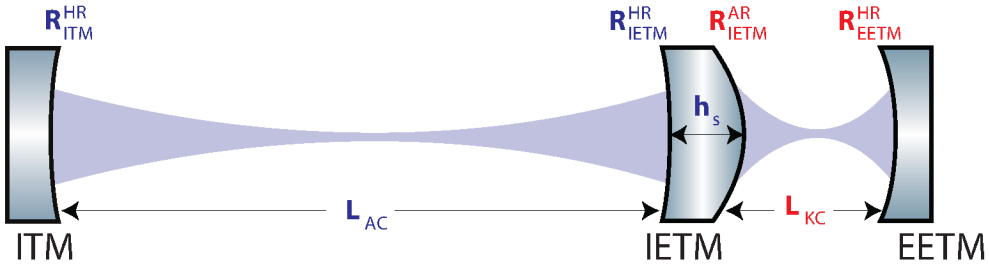

Figure 3.8: Schematic drawing of an interferometer arm cavity with a Khalili end mirror cavity. The Khalili cavity geometry needs to be matched to the IETM transmitted beam which is determined by the geometry of the arm cavity, i.e. its length and the ITM and IETM HR-side radii of curvature. The length of the KC, L_{KC}, and the radii of curvature of the IETM AR-side and the EETM HR-side, $R^{\mathrm{AR}}_{\mathrm{IETM}}$ and $R^{\mathrm{HR}}_{\mathrm{EETM}}$, respectively, are free parameters for the optical design of the end mirror cavity if no further constraints exist.

- Geometric stability: the beam in the KC is required to reproduce itself after one round trip, cf. Section 2.3.6.
- Optimal mode matching to the arm cavity transmitted beam: a cavity geometry is preferred which does not require the introduction of additional mode matching optics.
- Designated beam spot size on the arm cavity mirrors: in the case of the sub-SQL interferometer it is aimed for an optimized beam spot size of $w_m = 9.7\,\mathrm{mm}$ on all HR-coated cavity mirror surfaces, to bring down coating Brownian thermal noise, cf. Section 3.2.

Generally, three parameters are available for tuning to reach these goals: the curvature of the rear (AR-coated) side of the IETM, the length of the Khalili cavity and, finally, the ROC of the HR-coated surface of the EETM. A schematic drawing of a three mirror arm with Khalili end mirror cavity is shown in Figure 3.8.

For the arm cavity, which is also subject to the requirement for a particular beam size and geometric stability, a set of parameters which result in the desired cavity eigenmode under the given boundary conditions and spatial constraints is assumed. The mode matching aspect does not necessarily need to be addressed here since the required beam geometry can generally be arranged for by the input optics chain. Motivated by the minimization of coating Brownian thermal noise the symmetric case with identical radii of curvature of the ITM and IETM HR-surfaces was assumed, cf. Section 3.2. For the arm cavity length a value of $L = 10.4\,\mathrm{m}$ is assumed which conveniently fits into the prototype infrastructure and leaves approximately one meter space for the end mirror cavity and some additional headroom, e.g. for later adaptation of the absolute positions of the suspended cavity optics. By choosing radii of curvature of $R^{\mathrm{HR}}_{\mathrm{ITM}} = R^{\mathrm{HR}}_{\mathrm{IETM}} = 5.2\,\mathrm{m}$ the problem is further constrained such that the symmetric beam spot size on the ITM and IETM surfaces is solely a

function of the cavity length. With these curvatures it is found that a cavity length of $L = 10.396\,\mathrm{m}$ results in the desired beam spot radii $w_0 = 9.72\,\mathrm{mm}$, of $1/2.5$ of the radius of the cavity mirrors with $r = 24.3\,\mathrm{mm}$. The IETM HR-side curvature is common to both cavities but in was chosen to utilize this parameter exclusively to arrange for the optimal geometry of the arm cavity. This curvature is thus not available as a free parameter for the design of the KC.

3.3.3.1 Optical losses and stability implications

Even though cavities on anti-resonance are sometimes treated as analogous to a reflective mirror there is a subtle difference between these two. The reflectivity of a mirror is independent of the beam parameter of the beam that is launched at it. This is, however, not the case for a cavity used as a reflector. If the ingoing beam is not properly matched to the cavity eigenmode the consequence is a non-optimal overlap of the promptly reflected beam and the internal beam exiting the cavity through the input mirror. Furthermore, the internal beam will not be self-reproducing after a round trip, i.e. a fraction of the beam will e.g. experience angular spread and will be diffracted out of the cavity. In effect, this will increase the effective optical losses. If this picture is transferred to the interferometer arm with an end-mirror cavity, one can infer that an imperfectly mode-matched KC acts as a lossy mirror, which will result in increased optical losses in the interferometer arm cavity. Hence, optimal mode matching of the KCs is crucial to ensure low-loss operation and to maintain high circulating powers in the interferometer arm cavities.

Generally, optical losses, such as diffraction or absorption losses, play a less pronounced role in anti-resonant cavities compared to resonant ones [103]. It is intuitively clear that a cavity with a low internal buildup, i.e. only very few round trips of the internal fields, is lacking the strong "amplification" of the role of losses which is present in resonant cavities with high finesse. If a field experiences multiple bounces from a lossy optic the absolute effect strongly gains significance.

The plot shown in Figure 3.9 illustrates the dependence of the total losses in an interferometer arm with Khalili end mirror cavity on round trip losses due to diffraction and absorption by the mirrors in the AC and the KC, respectively. The plot was derived from a plane wave model based on the coupled cavity matrix formalism introduced in Section 2.3.4. The total losses are defined as $\mathcal{L} = 1 - R_{\mathrm{arm}}$ where R_{arm} is the power reflectivity of the arm cavity locked to its resonant working point. While one of the cavities was assumed to be lossless, the losses in the second cavity were varied. As can be seen, absorption or scattering loss in the AC has a more pronounced effect on the total losses in the arm than KC losses. Nevertheless, end mirror cavity losses contribute substantially to the total losses in the arm and need to be controlled to avoid degradation of the interferometer performance.

Furthermore, stability of the cavities needs to be maintained to ensure low-loss operation. Unstable cavities lack the feature of self-reproducibility of the beam after one round trip, cf. Section 2.3.6. Therefore, unstable optical cavities typically exhibit much higher losses than stable resonators.

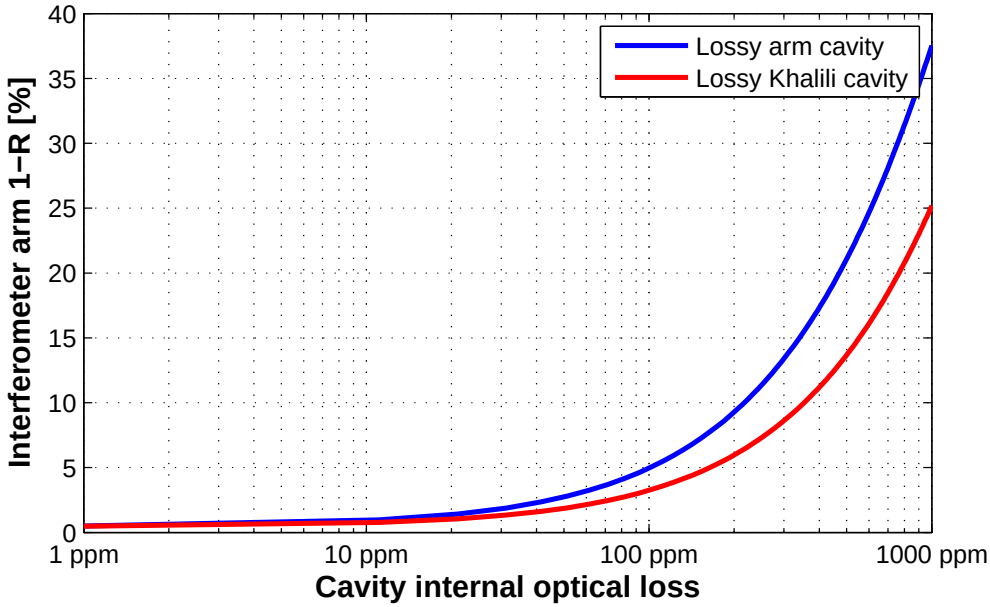

Figure 3.9: Fraction of the light incident on the coupled interferometer arm cavity which is not reflected, i.e. the total loss, plotted as a function of round-trip optical loss in the arm cavity and the Khalili cavity, respectively. For the blue curve a lossless Khalili cavity was assumed and for the red curve a lossless arm cavity. Only the fraction of input light which is reflected by the interferometer arm cavity contributes to the measurement of the differential arm length. Due to energy conservation the light which is not reflected is either transmitted through the end mirror of the arm cavity or it is subject to absorption or scattering.

The fundamental mode optical loss of an unstable resonator is to first order independent of the geometry of the cavity under investigation and can be approximated as [104]

$$\lambda_{00} = 1 - \frac{1 - \sqrt{1 - g^{-1}}}{1 + \sqrt{1 - g^{-1}}} \,. \tag{3.30}$$

This approximation is in good agreement with the average losses of the TEM_{00} mode obtained e.g. by solving diffraction integrals representing unstable cavity systems [69]. The relation between the g-factor of an unstable cavity and the resulting loss given in Equation (3.30) is plotted in Figure 3.10. It is obvious that surpassing the stability boundary at $g = 1$ results in a dramatic increase of the diffraction loss in the cavity. As discussed previously, this leads to strongly increased total optical losses in the interferometer arm. Hence, it must be arranged for stability of both partial cavities, the arm cavities as well as the Khalili cavities.

3.3.3.2 Example configurations

The goal for the identification of candidate configurations for the end mirror cavities is a set of parameters for the IETM AR curvature, the EETM HR curvature and the

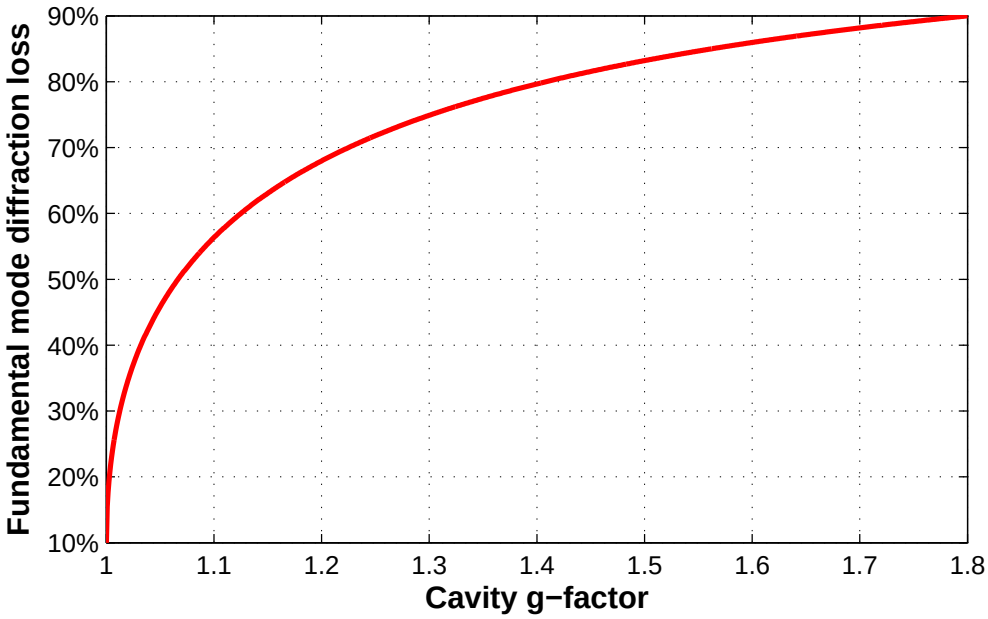

Figure 3.10: Approximated fundamental mode loss of an unstable cavity, as given by Equation (3.30). Above the stability boundary at $g = 1$ no low-loss eigenmode exists in the cavity. As a consequence diffraction loss of the cavity shoots up dramatically. Thus, an unstable Khalili end mirror cavity will strongly increase the total losses in the coupled interferometer arm cavity.

distance between these two optical surfaces. Boundary conditions are a given beam parameter in transmission of the IETM HR surface and the requirements for stability, optimal mode matching and, in the present case, a beam spot radius on the EETM HR-surface of $w^{\mathrm{HR}}_{\mathrm{EETM}} = 9.72\,\mathrm{mm}$. Furthermore an upper limit of $L_{\mathrm{KC}} \approx 1\,\mathrm{m}$ exists for the length of the end mirror cavity. For all cavity mirrors a radius of $r = 24.3\,\mathrm{mm}$ and a thickness of $h = 24.5\,\mathrm{mm}$ is assumed.

To find a solution to the design task, different scenarios can be conceived. It is evident that, with the given boundary conditions, it is unavoidable to have a lens polished into the IETM AR surface. The beam in transmission of the IETM HR-surface is strongly divergent and needs to be focused to keep the clipping losses at the mirror apertures at a tolerable level. In fact, to achieve the required spot size at the EETM, geometric considerations lead to the insight that there are basically two different options for beam forming. The beam either needs to be focused down strongly, to arrange for a beam waist in the end mirror cavity or the beam can be arranged for to be nearly collimated, with a small amount of convergence to compensate for the beam expansion over the distance between the IETM HR surface and the lens polished into the IETM AR surface, which is given by the substrate thickness requirement.

In the former case the waist of the KC eigenmode is extremely small and hence the beam in the KC is strongly divergent. This is not surprising as only one tenth

of the length of the arm cavity is available to focus the beam down and to let it diverge again to achieve the same beam spot size on the far mirror as in the case of the already marginally stable arm cavity. This ratio also reflects in the waist sizes of the two cavities which turns out approximately a factor of ten smaller in the KC than in the AC.

The latter configuration, with its nearly collimated beam, bears similarity to the near-planar resonator geometry, which is a classic representative of boundary-stable optical cavities. Plane-parallel resonators are known to be difficult to align and exhibit strong modal degeneracy, i.e. the fundamental mode and higher order transverse modes are simultaneously resonant [105]. Based on the given arguments the two configurations are expected to exhibit very poor geometric stability with a stability margin even lower than that of the arm cavities.

To estimate the geometric stability of candidate Khalili cavity layouts a model based on the propagation matrix formalism introduced in Chapter 2 was used. For the Khalili cavities a beam propagation matrix of the following form was obtained:

$$M_{\mathrm{KC}} = M_{\mathrm{IETM}} M_{\mathrm{L}} M_{\mathrm{EETM}} M_{\mathrm{L}} M'_{\mathrm{IETM}} \tag{3.31}$$

with a matrix representing the IETM, i.e. the intermediate end mirror

$$M_{\mathrm{IETM}} = \begin{pmatrix} 1 & 0 \\ -1/R^{\mathrm{HR}}_{\mathrm{IETM}} & 1 \end{pmatrix} \begin{pmatrix} 1 & h_{\mathrm{S}} \\ 0 & 1 \end{pmatrix} \begin{pmatrix} 1 & 0 \\ \frac{n_1 - n_2}{n_2 \cdot R^{\mathrm{AR}}_{\mathrm{IETM}}} & n_1/n_2 \end{pmatrix} , \tag{3.32}$$

a matrix representing free space beam propagation in the Khalili end mirror cavity

$$M_{\mathrm{L}} = \begin{pmatrix} 1 & L_{\mathrm{KC}} \\ 0 & 1 \end{pmatrix} , \tag{3.33}$$

a matrix representing the EETM, i.e. the end mirror of the Khalili cavity

$$M_{\mathrm{EETM}} = \begin{pmatrix} 1 & 0 \\ -2/R^{\mathrm{HR}}_{\mathrm{EETM}} & 1 \end{pmatrix} \tag{3.34}$$

and, finally, a matrix representing the intermediate end mirror for the reverse direction of beam propagation

$$M'_{\mathrm{IETM}} = \begin{pmatrix} 1 & 0 \\ \frac{n_2 - n_1}{-n_1 \cdot R^{\mathrm{AR}}_{\mathrm{IETM}}} & n_2/n_1 \end{pmatrix} \begin{pmatrix} 1 & h_{\mathrm{S}} \\ 0 & 1 \end{pmatrix} \begin{pmatrix} 1 & 0 \\ -1/R^{\mathrm{HR}}_{\mathrm{IETM}} & 1 \end{pmatrix} . \tag{3.35}$$

The ray transfer matrix M_{IETM} in Equation (3.32) that represents focusing and propagation from one surface of the IETM to the other is actually composed of three matrices: a reflection at the HR-surface of the IETM, a matrix for the propagation in the IETM substrate over the distance h_s and a matrix which models the transition of the beam from the substrate to vacuum at the curved interface on the AR-coated side of the IETM. The matrix M_{L} in Equation (3.33) propagates the beam in vacuum over the length L in the end mirror cavity. Reflection at the KC end mirror is represented by the matrix M_{EETM} in Equation (3.34). Finally, the matrix M'_{IETM} in Equation (3.35) describes the same beam focusing and propagation steps as the matrix M_{IETM} but in reverse direction.

A result of the theory of optical resonators with internal lenses is that they exhibit the same ray transfer matrix for the transit as an equivalent empty cavity defined by the equivalent g-factors g_1^*, g_2^* and length L^* [72]. The Gaussian beam radii on the mirrors, which are solely a function of the resonator matrix elements, are identical for the cavity with internal optical elements and the equivalent empty cavity. However, the beam geometry *inside* the two resonators is different. Stability of the lens resonator can be inferred from the g-factors g_1^*, g_2^* obtained from the equivalent empty resonator [106]. the geometric stability of the Khalili cavity can thus be determined from the trace of the matrix M_{KC}:

$$g_{\mathrm{KC}}(R^{\mathrm{HR}}_{\mathrm{IETM}}, R^{\mathrm{AR}}_{\mathrm{IETM}}, R^{\mathrm{HR}}_{\mathrm{EETM}}, L_{\mathrm{KC}}) \equiv g_1^* g_2^* = \frac{\mathrm{tr}(M_{\mathrm{KC}}) + 2}{4}\,, \tag{3.36}$$

which results in a stable cavity if $0 < g_{\mathrm{KC}} < 1$, cf. Section 2.3.6. The KC stability parameter is plotted as a function of the radii of curvature of the IETM AR-side and the EETM HR-side in Figure 3.11 for the configuration with a waist in the KC and in Figure 3.12 for the configuration with a nearly collimated beam. The colored regions represent parameter sets for the mirror curvatures which result in a stable end mirror cavity. However, stability does not imply that the cavity is well matched to the transmitted beam of the arm cavity and, furthermore, the targeted beam spot size on the EETM HR surface is not necessarily achieved.

For the configuration with a beam waist in the cavity shown in Figure 3.11 it was found that only a comparatively narrow range of curvature radii of the IETM AR-side exists which result in a stable end mirror cavity with a sharp cut off in the stability region for IETM AR-side curvatures larger than approximately 0.35 m. As can be seen, the end mirror cavity g-factor exhibits less sensitivity to changes of the EETM HR-side curvature than to IETM AR-side curvature changes.

The configuration with a nearly collimated beam in the KC, for which the stability diagram is shown in Figure 3.12, exhibits comparatively low sensitivity to variations in the EETM HR-side ROC which increases for $g \to 1$. Again, a steep cut off of the stability is observed for IETM AR-side radii of curvature larger than approximately 1.6 m. If a beam entering the end mirror cavity experiences less focusing here, its propagation will not be confined to the cavity.

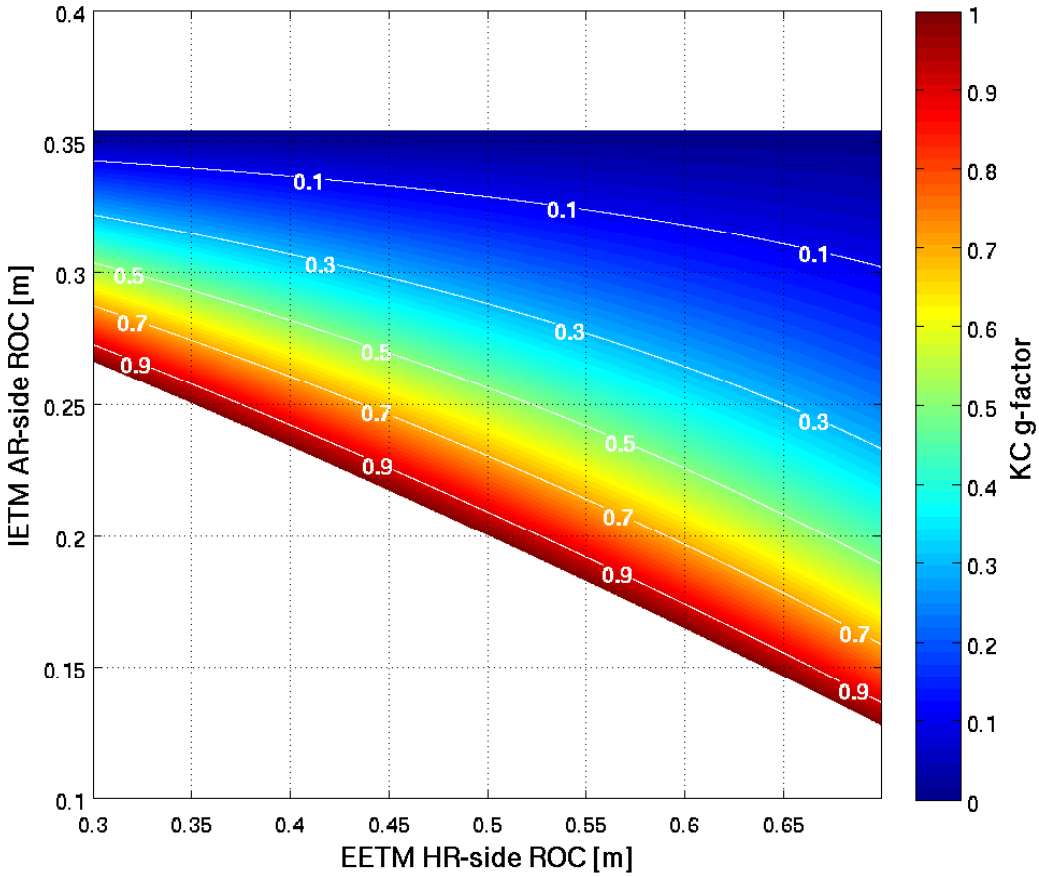

Figure 3.11: Khalili end mirror cavity stability parameter as a function of the IETM and EETM ROCs for the configuration with a strongly curved IETM AR-surface and a beam waist in the KC. Implicitly, a length of the end mirror cavity of $L = 1.007435$ m was assumed. The colored region represents combinations of IETM and EETM curvatures which result in a stable end mirror cavity and, correspondingly, the white regions represent parameter sets that result in instability. Even though stability is provided in the colored region, the corresponding curvatures do not necessarily result in a well mode matched end mirror cavity, to the mode defined by the arm cavity. Moreover, the spot size boundary condition for the HR-coated surface of the EETM is not necessarily fulfilled. A derivation of the corresponding beam spot sizes shows that the requirement for 9.7 mm spots on the mirrors is fulfilled in the region near the stability boundary with $g_{\mathrm{KC}} \simeq 1$.

Both configurations have in common that in order to arrange for the nominal beam spot size of $w_m = 9.7$ mm they need to be operated extremely close to the stability boundary with $g_{\mathrm{KC}} \sim 1$.

In the following discussion representative layouts of the two configuration options will be reviewed. A numerical model based on the software FINESSE [94] was employed to identify parameters which fulfill the optical design requirements.

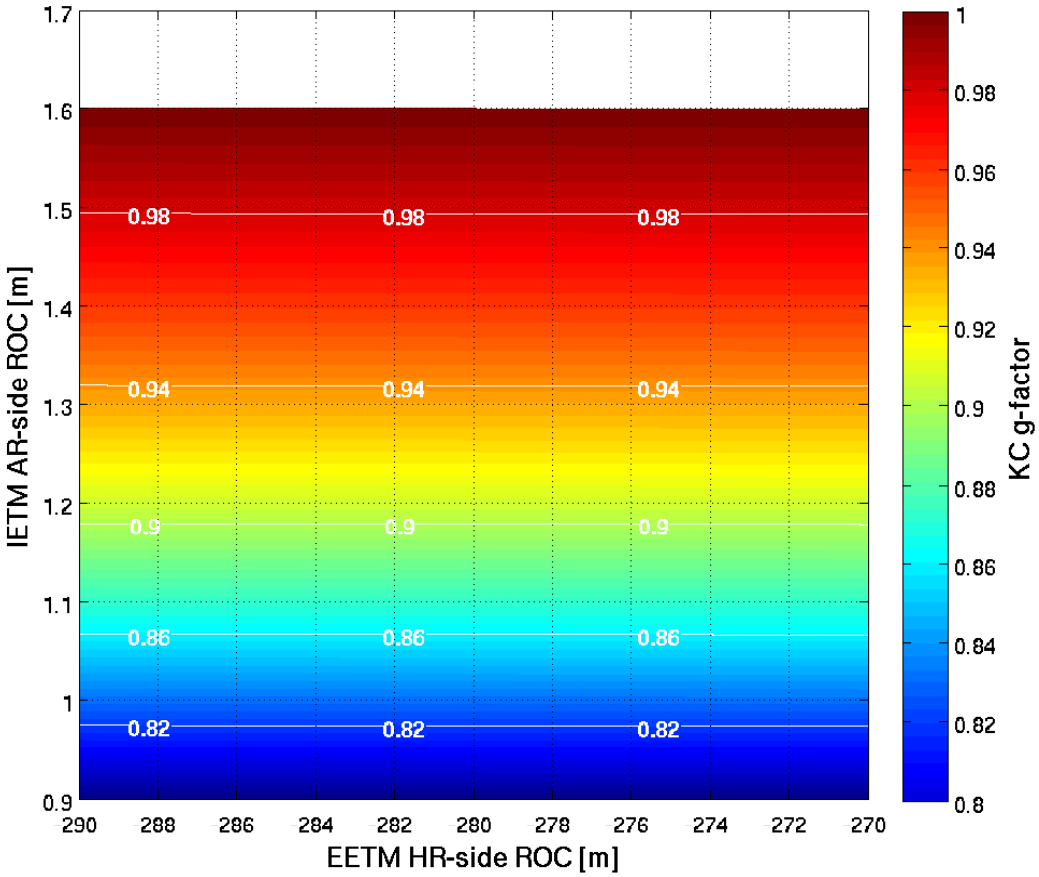

Figure 3.12: Khalili end mirror cavity stability parameter as a function of the IETM and EETM ROCs for the configuration with a nearly collimated beam in the KC. Implicitly, a length of the end mirror cavity of $L = 0.9791\,\mathrm{m}$ was assumed. The curvature of the EETM HR-coated surface is convex. The colored region represents combinations of IETM and EETM curvatures which result in a stable end mirror cavity and, correspondingly, the white regions represent parameter sets that result in instability. Even though stability is given in the colored region, the corresponding curvatures do not necessarily result in a well mode matched end mirror cavity, to the mode defined by the arm cavity. Furthermore, the spot size boundary condition for the HR-coated surface of the EETM is not necessarily fulfilled. Calculations of the corresponding beam spot sizes on the cavity mirrors show that the nominal beam size is achieved near the stability boundary with $g_{\mathrm{KC}} \simeq 1$.

The investigated configurations are depicted in Figure 3.13 and the corresponding parameters are given in Table 3.1.

To realize the configuration with a beam waist in the KC – from now on referred to as configuration 1 – the IETM AR-surface was chosen to be strongly curved with a ROC of $R^{\mathrm{AR}}_{\mathrm{IETM}} = 0.2\,\mathrm{m}$. This yields a beam waist which is approximately centered

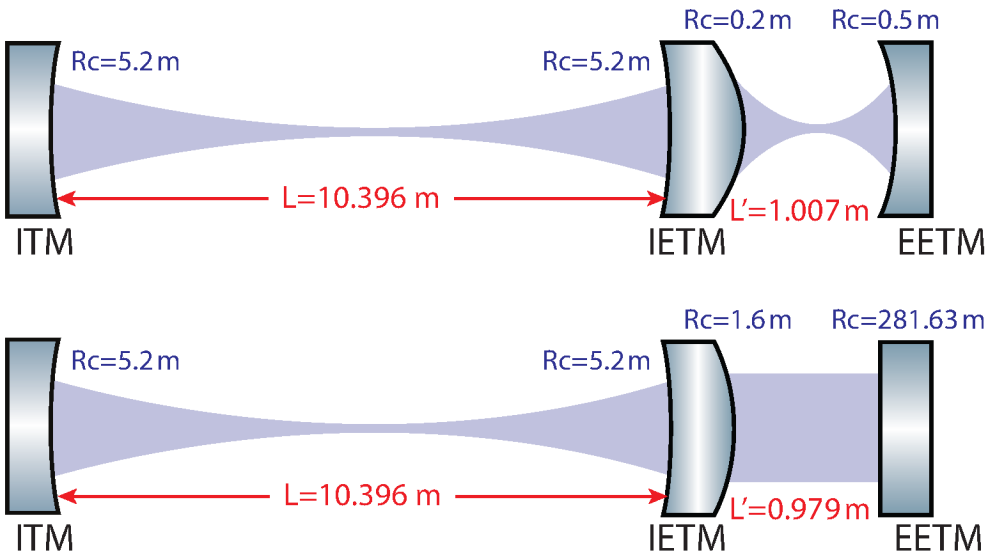

Figure 3.13: Khalili cavity example configurations, with and without a beam waist in the end mirror cavity, which fulfill the boundary condition of stability, mode matching and the requirement for the nominal beam spot size on the cavity mirrors. The configuration with a beam waist in the end mirror cavity requires strong focusing of the beam at the IETM AR-coated surface and a comparatively strongly curved EETM to match the wavefront of the beam after about one meter of propagation. The configuration without a waist in the KC requires a less strongly curved IETM AR-coated surface to produce a nearly collimated beam and a large convex curvature radius at the EETM to match the wave front of the beam.

in the KC. By choosing an EETM HR-side curvature of $R^{\mathrm{HR}}_{\mathrm{EETM}} = 0.5\,\mathrm{m}$ and slightly increasing the length of the KC by approximately 7.4 mm one obtains a configuration which is well mode-matched and exhibits beam spots of $w_m = 9.7\,\mathrm{mm}$ on all HR surfaces. However, the stability margin $1 - g_{\mathrm{KC}}$ of this configuration is found to be extremely small and is of the order of $\sim 10^{-5}$.

The configuration with a nearly collimated beam in the KC (configuration 2) can be realized by focusing the AC transmitted beam less strongly, i.e. by arranging for a larger ROC at the IETM AR-surface than in the previous case. An IETM AR-side curvature of $R^{\mathrm{AR}}_{\mathrm{IETM}} = 1.6\,\mathrm{m}$ was chosen. Since the beam needs to be arranged for to slightly converge, to compensate for the expansion of the beam from propagation in the IETM substrate, the wave front at the end mirror will exhibit a finite, yet large, curvature radius. By decreasing the length of the end mirror cavity by approximately 2.1 cm and choosing a mirror curvature radius of $R^{\mathrm{HR}}_{\mathrm{EETM}} \approx -281.63\,\mathrm{m}$ that matches the wave front curvature one obtains a well-matched cavity with nominal beam spots. Similar to the configuration discussed previously, this configuration for the end mirror cavity exhibits a stability margin also of the order of $\sim 10^{-5}$.

Table 3.1: Parameters of optical layout examples for the two Khalili cavity configurations. The configuration with a strongly curved IETM AR surface and a beam waist in the Khalili cavity is referred to as "configuration 1" here and the configuration with the nearly collimated beam in the KC is referred to as "configuration 2". The FINESSE-based numerical model, which was used to determine the presented parameters, is based on the assumption of perfectly spherical, fully aligned optics. The input laser beam is perfectly mode matched to the arm cavity. Light in higher-order modes originates from a small mismatch between the arm cavity and the end mirror cavity. The intra-cavity powers are given for an input beam incident on the arm cavity with a power of $P_{\text{in}} = 1\,\text{W}$.

Parameter	Configuration 1	Configuration 2
IETM AR-side ROC	0.2 m	1.6 m
EETM HR-side ROC	0.5 m	−281.626254 m
Distance IETM–EETM	1.007434 m	0.9791 m
KC g-factor	0.999987	0.999987
Mode matching efficiency	>99 %	>99 %
Normalized KC intra-cavity power	69.1544 W	69.1544 W
KC Power in HOMs	87.7 μW	4.7037 mW
Waist radius	17.5628 μm	6.9 mm
Waist position rel. to EETM	0.5 m	-137.7770 m
Rayleigh range	910.7383 μm	140.7804 m
Beam radius on EETM HR	9.7 mm	9.7 mm
Arm cavity length	10.3964 m	10.3964 m
ROC arm cavity mirrors	5.2 m	5.2 m
Arm cavity g-factor	0.9986	0.9986
Normalized AC intra-cavity power	416.4575 W	416.4575 W

3.3.3.3 Discussion of robustness of the configurations

In order to reliably operate the interferometer arm cavities with Khalili end mirror cavities the parameters, which are relevant for the optical properties of the KC, need to be sufficiently robust under deviations from their nominal values. The radii of curvature of the cavity mirrors for example can only be manufactured up to a certain accuracy. Even for mirrors polished with the required extreme precision, the dielectric coatings impose stress on the optic which may result in an unintended deformation of the surfaces [107]. Light absorption in the substrates or the coatings may result in thermoelastic expansion of the mirrors or the formation of a thermo-refractive index field in the optics [108]. Both of these effects change the optical properties of the cavity and may degrade the performance of the interferometer or – regarding the marginal stability of the cavities – even render the instrument unstable and thus inoperable.

To estimate the robustness of the two configurations with respect to deviations of mirror ROCs from their nominal values a FINESSE-based model of the three mirror coupled interferometer arm cavity was employed. In this model the coupled cavity system is defined by six parameters, four radii of curvature and two lengths.

Boundary conditions exist for seven output parameters of the model: three beam radii on the HR surfaces of the mirrors, two mode matching efficiencies and two cavity stabilities, of the AC and the KC, respectively. For the first ROC tolerancing analysis the boundary conditions were assumed that both cavities, the AC and the KC, remain at least boundary stable and it was aimed for maintaining an intra-cavity power in both cavities of $\geq$ 99 % relative to the perfectly matched case. As pointed out previously, other than in the case of matching a laser beam to a conventional two mirror cavity, in the case of a coupled cavity system additionally good overlap of the field transmitted from one cavity to the other with the respective eigenmodes needs to be ensured. Since the fraction of light which is not matched to the cavities' fundamental eigenmodes is lost for the measurement, high mode coupling efficiencies are crucial to ensure the desired buildup of light power inside the cavities.

In a cavity with sufficiently high finesse the circulating laser light will generally match the eigenmode of the cavity. If in the course of the tolerancing analyses one of the radii of curvature of the AC mirrors is changed, the mode matching of the input beam to the AC will nevertheless be arranged for to be perfect in the numerical model. Assuming a pure TEM_{00} input laser beam this means that all of the light power incident on the AC is coupled to its fundamental eigenmode, cf. section 2.3.5. However, since the AC is part of a three mirror coupled cavity, even if the input beam is perfectly mode matched to the AC, a mismatch of the AC and KC eigenmodes among each other reduces the circulating power in both cavities. Thus, if the coupling efficiency η is, as in the present case, derived from the intra-cavity powers, perfect mode matching of the input beam to the AC does not necessarily result in a perfectly mode matched three mirror coupled cavity.

Since in the nominal case with ideal parameters the KC geometry was matched to the nominal AC eigenmode, the deviation of curvatures in the AC from their designated values will result in an imperfect matching of the beam defined by the changed AC eigenmode which is transmitted to the KC. Also, the field returning from the KC will in this case not be perfectly matched to the changed AC eigenmode. Similarly, if the KC geometry deviates from the nominal case due to ROC error, the field transmitted by the AC will not perfectly match the changed KC eigenmode. Likewise, the field returning from the KC with non-nominal parameters will not be matched to the AC eigenmode anymore. In both cases this mutual mismatch gives rise to a reduction of the circulating power in the whole coupled cavity system.

The results of the first tolerancing analysis are summarized in Table 3.2 for configuration 1 and in Table 3.3 for configuration 2, respectively. The coupling efficiencies of the two cavities determined with the aid of the numerical model are typically of the same order, i.e. if the intra cavity power drops in one cavity, the power in the second one is reduced by approximately the same factor. It was found that in most cases the mode matching efficiency is strongly reduced before the cavity becomes unstable, i.e. the mode matching efficiency limits the tolerable ROC deviations in the first place. The strong susceptibility of the beam spot size on

Table 3.2: Radius of curvature tolerances and resulting optical parameters for the configuration with a beam waist in the KC (configuration 1). For all four curved surfaces which are part of the arm cavity with Khalili end mirror cavities the tolerable deviations from the nominal ROC were calculated. The cavity lengths were held at their designated values defined in Table 3.1. Boundary conditions were to retain a mode matching efficiency of $\eta \geq 99\,\%$ and stability or boundary stability, i.e. $g \leq 1$, for the arm cavity and the Khalili cavity, respectively.

	ROC deviation	w_{ITM} [mm]	w_{IETM} [mm]	w_{EETM} [mm]	η	g_{AC}	g_{KC}
$\mathrm{R_{ITM}} = 5.2\,\mathrm{m}$	+0.295 %	6.4	6.4	9.7	99 %	0.99274	0.99999
	-0.057 %	15.0	15.0	9.7	99 %	0.99975	0.99999
$\mathrm{R_{IETM}} = 5.2\,\mathrm{m}$	+0.004 %	9.6	9.6	15.5	99 %	0.99854	1
	-0.01 %	10.1	10.1	7.2	99 %	0.99882	0.99996
$\mathrm{R^{AR}_{IETM}} = 0.2\,\mathrm{m}$	+0.001 %	9.7	9.7	7	99 %	0.99862	0.99995
	> -0.001 %	9.7	9.7	15.7	99 %	0.99862	1
$\mathrm{R_{EETM}} = 0.5\,\mathrm{m}$	+0.002 %	9.7	9.7	7	99 %	0.99862	0.99995
	>-0.001 %	9.7	9.7	15.7	99 %	0.99862	1

the cavity mirrors to ROC error is a consequence of the marginal stability of the AC and of the KC.

For configuration 1, for which the results are summarized in Table 3.2 it was found that the curvatures of all mirrors, except for the ITM, are almost similarly critical. Furthermore, it was found that for the most critical ROCs even tiniest deviations result in a strong magnification of the beam spot on the EETM which, even though the cavity remains nominally operable, gives rise to strongly increased diffraction loss. The reduction of the beam spot on the EETM which occurs e.g. in the case of already quite small positive ROC error of the IETM AR-surface gives rise to increased coating Brownian thermal noise and reduces the benefit from the end mirror cavities.

The results of the investigations of configuration 2 are summarized in Table 3.3. It was found that negative curvature error of the IETM HR surface and positive curvature error of the IETM AR surface are most critical. Again the beam spot size on the EETM exhibits high susceptibility to deviations in these two curvatures, potentially leading to strongly increased diffraction loss in the KC. It must be noted that even though the tolerances given for the EETM substrate in this case are considerably larger than for the other mirrors, the numbers need to be seen in relation to the large curvature radius.

Generally, the estimated requirements in terms of curvature accuracy can be regarded as extremely challenging. The curvature accuracies that can be attained by manufacturers strongly depend on the employed metrology method. With the standard method of comparing the curvature of the work piece with a test plate, tolerances for curvatures of the order of one meter are typically in the range of approximately $\pm 0.5\,\%$ to $\pm 1\,\%$ [109–112]. Higher accuracies of approximately $\pm 0.05\,\%$ for meter-scale radii of curvature can be achieved with the aid of customized

Table 3.3: Radius of curvature tolerances and resulting optical parameters for the configuration with a nearly collimated beam in the KC (configuration 2). For all four curved surfaces which are part of the arm cavity with Khalili end mirror cavities the tolerable deviations from the nominal ROC were calculated. The cavity lengths were held at their designated values defined in Table 3.1. Boundary conditions were to retain a mode matching efficiency of $\eta \geq 99\,\%$ and stability or boundary stability, i.e. $g \leq 1$, for the arm cavity and the Khalili cavity, respectively.

	ROC deviation	w_{ITM} [mm]	w_{IETM} [mm]	w_{EETM} [mm]	η	g_{AC}	g_{KC}
$\mathrm{R_{ITM}} = 5.2\,\mathrm{m}$	+0.302 %	6.4	6.4	9.7	99 %	0.99260	0.99999
	-0.055 %	14.5	14.5	9.7	99 %	0.99972	0.99999
$\mathrm{R_{IETM}} = 5.2\,\mathrm{m}$	+0.014 %	9.3	9.3	6.7	99 %	0.99834	0.99995
	-0.004 %	9.9	9.9	16.1	99 %	0.99870	1
$\mathrm{R^{AR}_{IETM}} = 1.6\,\mathrm{m}$	+0.004 %	9.7	9.7	15.8	99 %	0.99862	1
	-0.011 %	9.7	9.7	7.1	99 %	0.99862	0.99996
$\mathrm{R_{EETM}} = -281.63\,\mathrm{m}$	+0.895 %	9.7	9.7	7.1	99 %	0.99862	0.99996
	-0.317 %	9.7	9.7	15.8	99 %	0.99862	1

test plates which were manufactured with the aid of interferometric metrology [113]. Finally, if interferometers are employed to directly measure the curvature of the work piece during the manufacturing process, accuracies of approximately $\pm 0.005\,\%$ – $\pm 0.01\,\%$ can be reached [114], typically requiring an investment in custom-made reference spheres for the interferometer used for the measurement. Better accuracies than those stated above may be achieved with the aid of even more sophisticated surface metrology techniques. It must be noted that for large radii of curvature, i.e. the ROC of the end mirror for the second configuration in Table 3.1, the tolerances differ from the numbers given above. This is due to the fact that the sagitta of a mirror with large curvature radius is comparatively small. As a consequence, the tolerances for large curvature radii are generally larger than those for small curvatures. For instance, for the kilometer scale curvatures of GW detector test masses, curvature errors are typically of the order of $\sim 1\,\%$, cf. e.g. [115].

So far only the stability and the mode coupling efficiency of the coupled cavity were used as additional boundary conditions for the coupled cavity layout. Since the targeted beam spot size of $w = 9.7\,\mathrm{mm}$ is a corner stone of the design to reduce coating Brownian thermal noise it is obvious to further constrain the range of tolerable spot sizes on the mirrors. Besides the new constraint of beam spot radius deviations of $\leq \pm 10\,\%$, corresponding to $\Delta w \approx \pm 1\,\mathrm{mm}$, for the following investigations stability or at least boundary stability of the cavities is assumed as a boundary condition, as well as mode coupling of $\eta \geq 99\,\%$ of the coupled cavity.

The parameters of the investigated configurations are summarized in Table 3.4. It must be noted that allowing for 10 % tolerance in the beam spot radii comes at the expense of increased coating thermal noise for smaller than nominal beams, according to the scaling law in Equation (3.9), or diffraction loss for beams with larger than nominal spot size. A common model to estimate optical loss due to

Table 3.4: Mirror ROC specifications for the two investigated three mirror coupled arm cavity configurations. Besides the requirements for a mode matching efficiency of $\eta \geq 99\,\%$ and stability or at least boundary stability of the cavities, deviations of the beam spot radii on the mirrors are postulated to be smaller than $\pm 10\,\%$ with respect to the optimum.

Radius of curvature	Configuration 1	Configuration 2
ITM HR-side ROC	5.2 m +0.0375 %/−0.0215 %	5.2 m +0.0375 %/−0.0215 %
IETM HR-side ROC	5.2 m +0.0015 %/−0.0022 %	5.2 m +0.0023 %/−0.0016 %
IETM AR-side ROC	0.2 m +0.0003 %/−0.0002 %	1.6 m +0.0015 %/−0.0023 %
EETM HR-side ROC	0.5 m +0.0003 %/−0.0002 %	−281.63 m +0.1832 %/−0.1218 %

diffraction at apertures is the *clipping approximation*. In this approximation the loss due to beam clipping is given as [116]

$$\mathcal{L}_{\text{clip}}(w, \varrho, z) = 1 - \int_0^{2\pi} \mathrm{d}\phi \int_0^{\varrho} \mathrm{d}r\, r\, |u(w, r, \phi, z)|^2 \tag{3.37}$$

where w denotes the radius of the beam spot on the mirror surface, ϱ the radius of the coated mirror aperture and $u(w, r, \phi, z)$ the field distribution of the transverse mode of the laser beam. In the case of Gaussian beams one obtain the expression [117]

$$P_{\text{clip}} = P \cdot \exp(-2r^2/w^2) \tag{3.38}$$

for the light power lost due to clipping at the mirror aperture. For increasing the beam radius by 10 % the loss increases from approximately 4 ppm to 31 ppm. However, in a strict sense this model is only poorly suited for estimating losses that occur in a cavity since the distortion of the reflected field is not accounted for. Nevertheless, the increased clipping losses add to the round-trip losses of the interferometer arm and increase the total losses of the arm cavity, cf. Figure 3.9.

In the case of the first configuration with an intra-cavity waist the spot size constraint results in a reduction of the tolerable ROC deviations for all four curved surfaces. This is most striking for the IETM AR-side ROC and the EETM HR-side ROC. As can be seen, the tolerances drop below the values given above for maximally feasible ROC accuracy of approximately $\pm 0.005\,\%$ in this curvature range. For the second configuration one observes, likewise, tolerances lower than what is feasible to manufactured by standard means.

A number of measures are available to compensate for deviations of curvatures. A comparatively simple approach is the attempt to compensate for curvature error by changing the cavity length which is, compared to tuning radii of curvature, an easily accessible parameter in this case. To estimate the viability of this approach a tolerancing analysis was performed in which the individual radii of curvature in the coupled cavity arm were deliberately offset from their designated values. Where the system was driven into instability it was attempted to recover stable operation by varying the length of the cavities.

The geometric stability of configuration 1 with the strongly curved AR-coated side of the IETM was found to be extremely susceptible to cavity length changes.

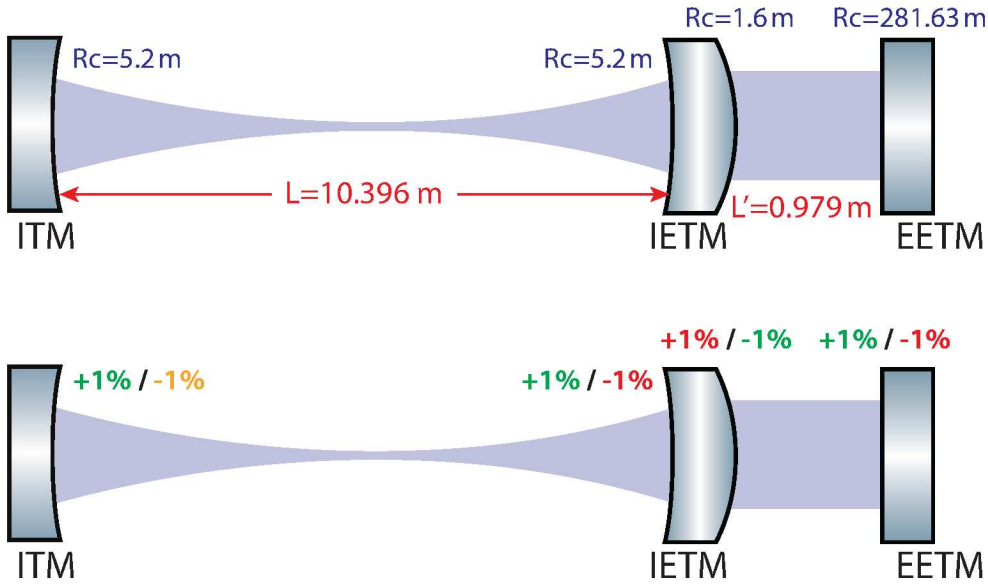

Figure 3.14: Estimation of the robustness of Khalili end mirror cavity design parameters, for the configuration with a nearly collimated beam in the KC. A design is considered to be sufficiently robust if a deviation of the radii of curvature of the cavity mirrors from their specified values can be compensated for by changing the length of either cavity. The four intra-cavity radii of curvature were offset by $\pm 1\,\%$ and it was attempted to compensate for this deviation by changing the lengths of the arm cavity and the Khalili end mirror cavity, respectively. For the deviations printed in green the cavity remained stable, yellow deviations drove the KC into instability but could be compensated for by changing cavity lengths. The offsets printed in red resulted in instability of the KC and could not be compensated for by changing the cavity lengths.

With the stability model introduced in Section 3.3.3.2 it was found that changing the cavity length by only a few micron was sufficient to drive the KC into instability, even with nominal values for the radii of curvature. This is regarded as a severe shortcoming and leads to the conclusion that this configuration is not recommended for the implementation in the interferometer.

The situation is more subtle in the case of the second configuration with a nearly collimated beam in the KC. The result of the tolerancing analysis is illustrated in Figure 3.14. The four intra-cavity radii of curvature were offset by $\pm 1\,\%$ and it was attempted to compensate for this deviation by changing the lengths of the arm cavity and the end mirror cavity. For the deviations printed in green the cavity remained stable, the deviations printed in yellow drove the AC into instability but could be compensated for by changing the AC length. The offsets printed in red resulted in instability of the KC and could not be compensated for by changing the cavity length.

It is noteworthy that a ROC error of 1 % for the curvatures in the range of a few meters is already quite large. However, it can be shown with the stability model that in the case of the IETM HR and IETM AR side ROCs deviations of $\Delta R^{\mathrm{HR}}_{\mathrm{IETM}} = -0.01\,\%$ and $\Delta R^{\mathrm{AR}}_{\mathrm{IETM}} = +0.01\,\%$ are already too large to be compensated by varying the length of the KC. For the considerably larger EETM HR-side curvature, deviations of $\Delta R^{\mathrm{HR}}_{\mathrm{EETM}} > 0.5\,\%$ exceed the range of what can be compensated for by KC length variation. It is worth noting that even though smaller ROC error can be compensated for by changing the length of the KC this will generally not result in well mode matched cavities or beam spots with nominal radii. However, whereas the mode matching is comparatively robust under length changes, the beam spot sizes are comparatively sensitive to the length.

Another option is the use of a thermal compensation system [118, 119]. The principle of these systems is to locally heat mirrors to deterministically deform these and thereby, to some extent, achieve tunability of curvatures. Downsides of this approach are e.g. limited actuation range and heating of nearby infrastructure which may result in undesired thermal expansion of the environment of the experiment. Furthermore, it is questionable whether a system of this kind should be included in the baseline design of a prototype interferometer. As it may turn out in a later stage of the experiment that thermal actuation is required to ensure a less fundamental operability requirement than cavity stability, for instance to compensate for differential asymmetries in the arms, it appears more advisable to save this technique for later use.

Generally, thermal actuation does not pose a suitable option for direct adjustment of IETM curvatures. This is because in the case of the doubly curved IETM, which is part of two cavities, actuation on one of the mirror surfaces would simultaneously lead to an unwanted deformation of the opposite surface. Thus, thermal actuation on the IETM is prone to compromise the eigenmode of the arm cavity, which is undesired. A potential alternative to achieve IETM ROC error compensation is thermal actuation on the EETM ROC. With the aid of the numerical model it was found that compensation of curvature error of the critical IETM ROCs is possible for deviations $|\Delta R| \leq 0.05\,\%$ and requires a tuning range of the EETM curvature of the order of tens of meters. With these boundary conditions thermal adjustment of the EETM curvature makes it possible to recover stability, mode matching and the desired beam spot size in the KC. However, if spot size deviations on the EETM of $\Delta w_m = \pm 0.1\,\mathrm{mm}$ from the nominal value are tolerated it turns out that in order to compensate for a ROC error of $\Delta R^{\mathrm{HR}}_{\mathrm{IETM}} = -0.05\,\%$ and $\Delta R^{\mathrm{AR}}_{\mathrm{IETM}} = +0.05\,\%$ the EETM HR ROC needs to be tuned from $R^{\mathrm{HR}}_{\mathrm{EETM}} = -281.63\,\mathrm{m}$ to $\hat{R}^{\mathrm{HR}}_{\mathrm{EETM}} = -305.76\,\mathrm{m}$ $\pm 0.5\,\mathrm{m}$, corresponding to $\pm 0.16\,\%$ tolerance. Even though the curvature error requirements are relaxed in this scenario, mirrors with the given curvatures and ROC accuracies of better than $\pm 0.05\,\%$ are still challenging to manufacture, the adoption of a thermal compensation system in the baseline design introduces significant additional complexity to the experiment and only little tolerances are allowed for the thermally adjusted EETM radius. A related question is to what extent the homogeneity of the EETM surface figure is affected, i.e. if mirror surface aberrations of the EETM are introduced by the thermal actuation system. These potentially

distort the wave front of the field circulating in the arm and may e.g. lead to increased scattering of fundamental mode light to higher order transverse modes which has implications for the performance of the interferometer.

3.3.3.4 Angular misalignment

To estimate the susceptibility of the three mirror coupled arm cavity to mirror misalignment in the KC, the coupling of EETM tilt to the longitudinal phase of the end mirror cavity was modeled. The plots shown in Figure 3.15 illustrate the dependence of the intra-cavity power in the arm cavity and in the end mirror cavity on an angular misalignment of the EETM and on the longitudinal phase of the KC. Both configurations, with and without a beam waist in the KC, exhibit almost identical behavior regarding the coupling of EETM misalignment to longitudinal phase and the degradation of the mode matching of the cavities among each other. As can be seen for increasing angular misalignment of the end mirror the length servo loop needs to compensate for by acting on the length of the cavity to keep the three mirror cavity on resonance. At the same time the end mirror misalignment gives rise to a change of the eigenmode of the end mirror cavity. Whereas the input beam is at all times perfectly mode matched to the AC the matching of the AC transmitted beam to the KC is degraded as the EETM misalignment increases. This, in turn, also affects the field in the AC as the beam returning from the KC is not matched to the AC eigenmode anymore. For an angular misalignment of 5 µrad the length servo needs to tune the cavity by approximately 5° to keep the system on resonance. Nevertheless, due to mode mismatch, the power buildup in the AC and the KC is reduced by approximately 35 %.

If it is again assumed that the three mirror cavity needs to be stabilized to within a residual RMS deviation of less the 1 % of its line width it is found that the static misalignment of the EETM needs to be arranged for lower than 1.3×10^{-7} rad. This holds for both configurations, with and without a beam waist in the KC.

3.3.4 Options to relax the requirements

Quite generally, the stringent requirements presented in the previous section can be attributed to the poor stability of the cavities. Two different options come to mind to relax the requirements of the cavity parameters: either the stability of the cavities is left unchanged and it is attempted to cure the implications or, alternatively, it can be attempted to improve the stability of the cavities.

The spot size requirement, for instance, could be relaxed without changing the stability of the cavities. It was already pointed out that for the given mirror dimensions tolerating larger deviations from the nominal spot size results either in increased coating Brownian thermal noise, which reduces the sensitivity of the interferometer in general and efficiency of the KCs in particular, or in increased diffraction loss which may impede the performance of the instrument, especially in conjunction with squeezing injection or QND techniques such as the implementation

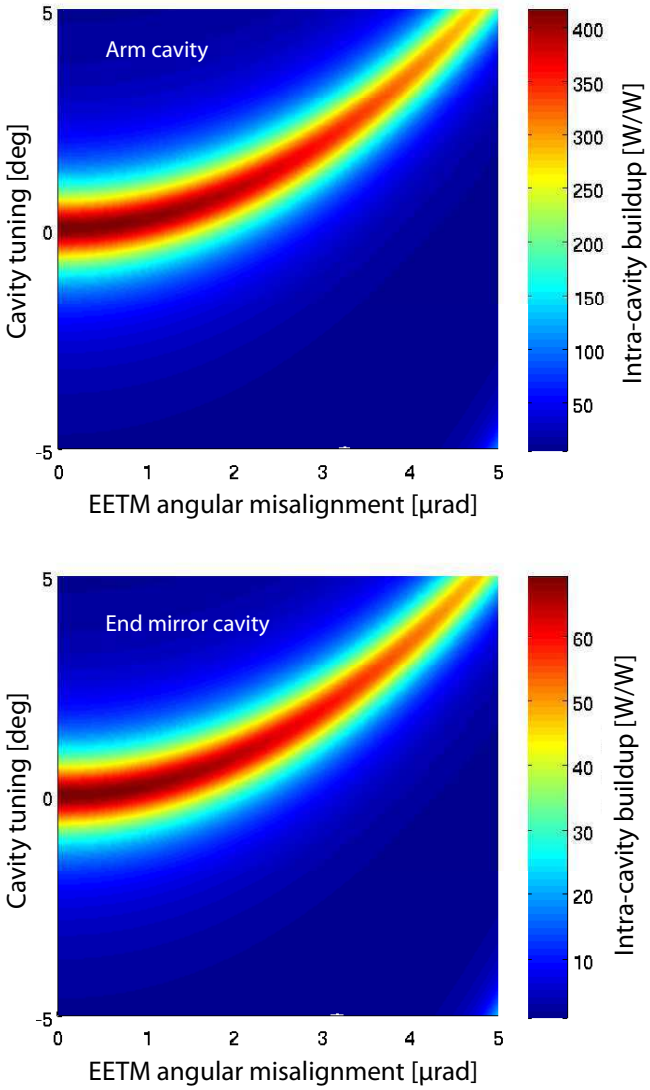

Figure 3.15: Coupling of EETM tilt to the longitudinal phase of the Khalili end mirror cavity and the reduction of the intra-cavity power buildup due to a degradation of the mode matching of the cavities among each other. The power buildup in the AC and in the KC is shown in the top and in the bottom plot, respectively. Parameters that were swept in the simulation are the misalignment angle β_x of the EETM and the longitudinal phase of the KC. The modeled configuration is the one with a nearly collimated beam in the KC.

of back-action evasion schemes, which are planned for later stages of the experiment. A straightforward way to reduce diffraction loss at the EETM would be to use e.g. a mirror with a larger diameter. If the aspect ratio requirement given in [60], aiming at the minimization of thermal noise contributions, are obeyed, this inevitably results in heavier mirrors. However, the mirror mass is critical for reaching the

scientific goals of the experiment as changing the mass of one of the mirrors in the interferometer gives rise to changed dynamical properties. Besides this, there is also a technical implication of larger EETMs which is the need for different suspensions for the larger and heavier mirrors.

It is evident that the more promising option is a modification of the optical layout aiming at increasing the stability margin. A straight forward approach is to increase the length of cavities with poor stability to make them more stable. In the case of the nearly concentric ACs, if the cavity lengths were increased, less strongly curved mirrors could be employed to obtain the same beam spot radius on the mirrors, which reduces the magnitude of the g-factors of the cavity. Even a configuration with a relatively stable AC, coupled to a marginally stable KC would be more beneficial than two coupled marginally stable cavities since the more stable cavity has in this case a stabilizing effect on the coupled cavity system, which was e.g. pointed out in [101]. However, the size of the vacuum system imposes a constraint on the length of the arm cavities which cannot be significantly extended beyond a length of approximately 11.5 m.

Another possibility to improve the stability of the coupled cavity system would be to go for smaller beam spot radii on the cavity mirrors than those postulated in the sub-SQL interferometer conceptual design [60]. By doing so one would basically trade coating thermal noise reduction for less stringent requirements and better operability of the interferometer. However, arranging for smaller beam spots than proposed would not only increase the coating Brownian thermal noise in the interferometer but also at some "break even" spot size diminish the benefit from the end mirror cavities. The plot shown in Figure 3.16 further illustrates this argument.

If in the interferometer configuration with three mirror coupled cavity arms the beam spot size is reduced to 75 % of the nominal size, the combined coating Brownian thermal noise and a number of specific noise terms originating from the end mirror cavity reaches the same magnitude as the coating Brownian thermal noise one would encounter in a Fabry-Perot Michelson interferometer with sub-SQL interferometer parameters but without end mirror cavities.

In Table 3.5 the parameters for a three mirror coupled arm cavity configuration with beam spot sizes reduced by 25 % are summarized. In the underlying model in the first step the parameters defining the arm cavity eigenmode were changed to reduce the spot sizes on the ITM and IETM. It is worth noting that regardless of which variant is chosen for changing the beam spot size here, either changing the length of the arm cavity or changing the radii of curvature of the ITM and the IETM, results in almost identical stabilities of the coupled cavity system. The curvature of the EETM was then fitted to the wave front curvature of the transmitted beam at one meter distance behind the IETM.

A reduction of the beam size by 25 % was found to result only in a moderate improvement of the stability of the AC and the KC, respectively. Further reduction of the beam size is necessary to significantly improve the stability. Since the coating thermal noise level in an interferometer with end mirror cavities and beam spots

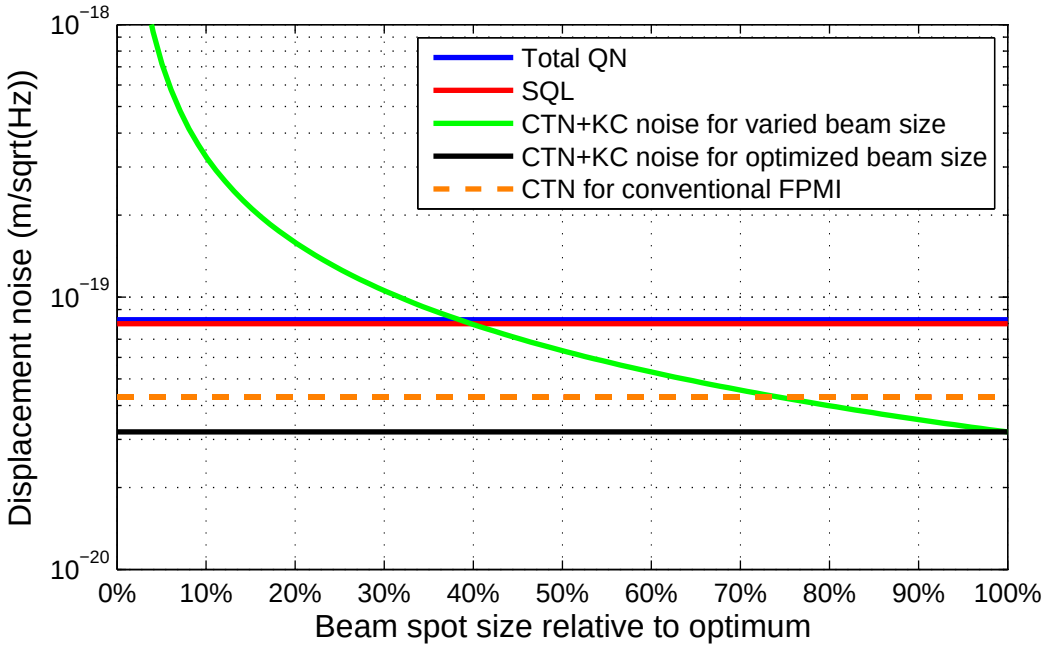

Figure 3.16: Combined coating thermal and additional end mirror cavity related noise in the sub-SQL interferometer, plotted for varied beam spot sizes on the cavity mirrors at a fixed frequency of 183 Hz. The noise spectral density data was obtained from the sub-SQL interferometer sensitivity model [64] and includes the coating Brownian thermal noise contribution also from the ITMs. The orange dashed line represents the coating Brownian thermal noise in a Fabry-Perot Michelson interferometer with identical parameters and large beam spots but without end mirror cavities.

reduced by approximately 25 % is equivalent to that of a considerably simpler Fabry-Perot Michelson interferometer with sub-SQL interferometer parameters but without end mirror cavities, it is worth considering if an equivalent sensitivity could, from the technical point of view, be more easily achieved with a marginally stable interferometer without end mirror cavities than with a slightly more stable one with end mirror cavities.

Finally, the introduction of additional optical elements into the end mirror cavities poses another option to alter the cavity geometry and, as a consequence to possibly, improve the stability of the interferometer arm. However, it must be noted that generally the introduction of lenses into cavities of laser interferometers for ultra-high precision measurements as the sub-SQL interferometer is barely favorable. To avoid back reflections from lenses these are typically not introduced into the optical setup with the beam perpendicular to the surface but deliberately tilted by some small angle. This, however, is prone to introduce wave front aberrations such as astigmatism to the circulating laser field with downstream effects such as reduced circulating power and increased round trip optical losses. A common approach to intra-cavity beam shaping which is e.g. employed in the recycling cavities of GW detectors [102, 120] is the use of additional curved mirrors. To avoid wave front

Table 3.5: Optical parameters for smaller-than-nominal spot sizes on the HR surfaces of the mirrors in a sub-SQL interferometer arm cavity with end-mirror cavities. Even though this configuration exhibits 25 % smaller beam spots than the configuration with nominal beam spots of $w_m = 9.7$ mm, the stability of the arm cavity and the Khalili cavity is only moderately improved. Note that instead of shortening the arm cavity the radii of curvature of the ITM and the IETM could have been increased instead. However, both approaches result in basically the same improvement of the stability margin for the AC and the KC, respectively.

	Configuration 1	Configuration 2
$R_{\mathrm{ITM}}^{\mathrm{HR}}$	5.2 m	5.2 m
$R_{\mathrm{IETM}}^{\mathrm{HR}}$	5.2 m	5.2 m
$R_{\mathrm{IETM}}^{\mathrm{AR}}$	0.19785 m	1.593 m
$R_{\mathrm{EETM}}^{\mathrm{HR}}$	0.49879 m	−209.72 m
L_{AC}	10.3886 m	10.3886 m
L_{KC}	1.0 m	1.0 m
w	7.29 mm	7.29 mm
g_{AC}	0.9956	0.9956
g_{KC}	0.99996	0.99996

deformation of the circulating laser beam, in the optical layouts of these cavities it is typically arranged for beam angles of incidence deviating only by a small amount from normal incidence, i.e. the beam paths are horizontally or vertically folded. Folding mirrors will give rise to additional phase noise due to path length fluctuations. As they are part of the interferometer arm cavities, folding mirrors need to be suspended to avoid the introduction of additional seismic noise. Since the intra-cavity field is reflected at the folding mirrors twice per round-trip, their noise contribution is larger than that of mirrors in an unfolded cavity configuration. Furthermore, as pointed out previously, additional reflective optical elements may give rise to altered dynamical properties of the interferometer which may conflict with the scientific goals of the experiment.

3.4 Alternative approaches to coating thermal noise reduction

A number of alternatives to anti-resonant end mirror cavities for coating thermal noise reduction in the sub-SQL interferometer were conceived. In the following, a selection of these will be briefly reviewed as options for a future implementation in the experiment.

3.4.1 Lower arm cavity mirror reflectivities and higher input power

By adopting conventional two mirror arm cavities with reduced reflectivities of the mirrors and compensation of the lower finesse by increasing the input laser power,

a clearance between quantum noise and coating Brownian thermal noise can be achieved which is similar to that of the configuration proposed in the conceptual design with high finesse and end mirror cavities. It was, however, pointed out by *Somiya* that the two mirror low-finesse cavity configuration, while maintaining the SQL touching frequency of the high finesse configuration with end mirror cavities, requires large input laser powers up to several kW. It was shown in [121] that this approach is prone to increase the impact of laser intensity noise on the main signal, which couples by radiation pressure imbalances in the arms, to a level above coating Brownian thermal noise in the frequency range of interest. A variant which requires less input power was proposed by *Khalili* [122]. He showed that by assuming $N_{\mathrm{ITM}} = 6$ and $N_{\mathrm{ITM}} = 8$ coating double layers for the input mirrors and end mirrors, respectively, and an input power of approximately 30 W, one obtains a configuration with an SQL touching frequency of approximately 100 Hz, with similar headroom with respect to coating Brownian thermal noise than in the case of the high finesse arm cavity with an end mirror cavity, cf. Table 3.6.

Table 3.6: Comparison of the key parameters of the high finesse configuration with end mirror cavities [60] and a low finesse configuration [122] with a reduced number of coating layers on the input and end mirrors.

	High Finesse w/ KCs	Low finesse w/o KCs
ITM coating double layers N_{ITM}	8	6
EM coating double layers N_{EM}	2 + 15	8
Effective double layers N_{eff}	~ 12	14
Arm cavity finesse	670	130
Input power I_{in}	5.5 W	30 W
Arm cavity circulating power I_c	~ 1.2 kW	~ 1 kW
SQL touching frequency f_{SQL}	~ 200 Hz	~ 100 Hz

Since the maximally available laser power is expected to be limited by stimulated Brillouin scattering in the optical fiber employed to couple the light into the vacuum system [123], the adoption of *power recycling* was suggested to achieve the required powers at the beam splitter. However, it must be noted that due to the comparatively high losses in the arm cavity the potential benefit from squeezing injection or the application of QND techniques is limited. Further investigation of this configuration is necessary to evaluate the viability for its implementation in the sub-SQL interferometer, e.g. with respect to the role of seismic noise in the measurement band at lower frequencies.

3.4.2 Khalili etalons, waveguide mirrors and new coating materials

As an alternative to end mirror cavities, formed by spatially separated mirrors, *Khalili etalons* (KEs) were proposed. Other than Khalili cavities, these do not re-

quire longitudinal and angular control but yield a comparable reduction of coating Brownian thermal noise [124]. In contrast to conventional highly reflective mirrors, KEs exhibit only few coating layers on the front surface and a much larger number of coating layers on the rear surface to ensure high reflectivity of the etalon. The substrate thickness is arranged for such that the carrier field is anti-resonant in the substrate. Tunability of the etalon length is e.g. achieved by heating. As was shown in [84], if conventional mirrors in the sub-SQL interferometer are replaced with KEs, these need to be slightly thicker and, due to the mass constraint, smaller in diameter for optimal coating Brownian thermal noise reduction.

The following progression was proposed for adopting KEs in the sub-SQL interferometer optical layout [125]:

1 | Stable FPMI

2 | Marginally stable FPMI

3 | Marginally stable FPMI with Khalili etalons as end mirrors

4 | Marginally stable FPMI with Khalili etalons as input and end mirrors

These four configurations are schematically illustrated in Figure 3.17. Whereas the first configuration is expected to pose only minor technical challenges the second configuration already constitutes an experiment which is – due to the marginal stability of the interferometer arm cavities – deemed challenging to operate. An approach which makes the step from the first configuration, the stable FPMI, to the second one, the FPMI with marginally stable arm cavities, much less invasive is presented in Chapter 4. Additionally, this approach allows to determine the limitations of marginally stable operation of the interferometer as the stability of the arm cavities can be tuned over a large range in a comfortable way. Despite the mitigation of the technical complexity in terms of sensing and controls by employing KEs instead of end mirror cavities, it is expected that KEs are required to be manufactured with extremely high precision of curvatures and the parallelism of the optical surfaces [93].

Another option for the reduction of coating Brownian thermal noise, proposed by *Bunkowski et al* [126], is the use of waveguide gratings at normal incidence which provide high reflectivity while requiring much less coating material than conventional mirrors. However, recent work suggests that at room temperature the benefit from wave guide mirrors in terms of coating thermal noise reduction will be comparatively modest [127].

Finally, another approach for coating Brownian thermal noise reduction is the use of better coatings. For instance, crystalline coatings based one epitaxially grown Al_xGaAs_{1-x} stacks [128] are one such candidate. Besides loss angles of $\phi_{\text{cryst}} \sim 2.5 \times 10^{-5}$ determined from ring-down measurements at room temperature for a free-standing sample, which about one order of magnitude smaller than those of Ta_2O_5, for these coatings surface roughness of $1 - 2\,\mathring{A}$, absorption of $A \sim 10\,\text{ppm}$

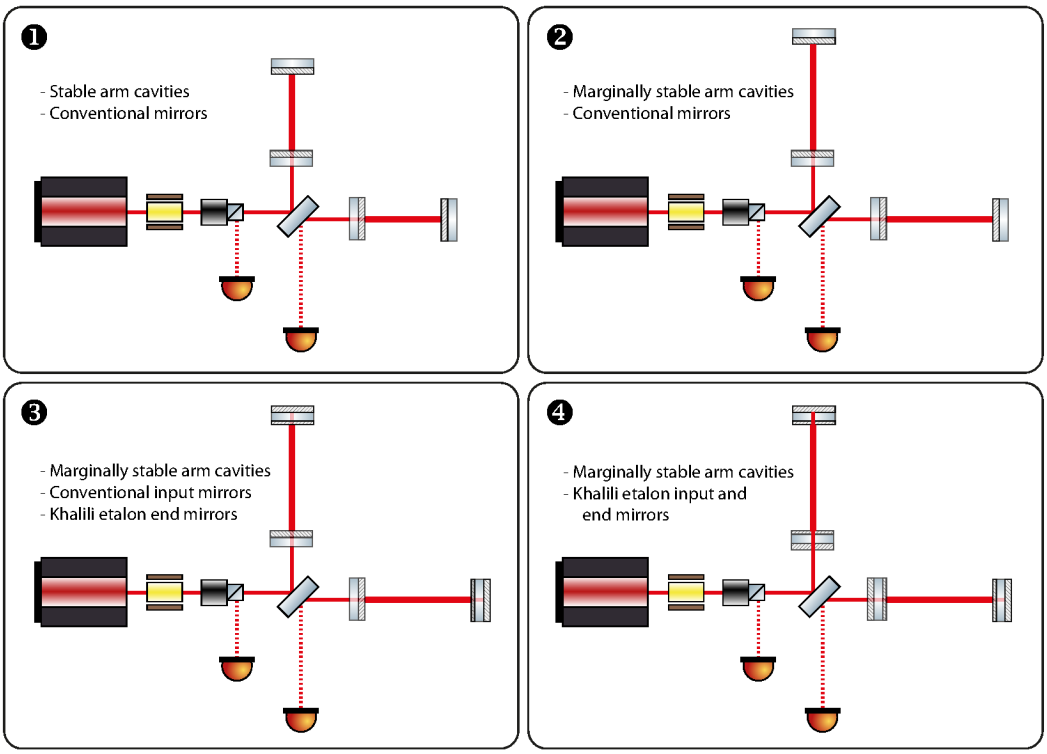

Figure 3.17: Progression of the interferometer layout toward reducing coating thermal noise with Khalili etalons. After initially operating the interferometer with stable arm cavities ❶ the optical layout is changed to arrange for marginally stable arm cavities ❷. This can e.g. be achieved by swapping arm cavity mirrors or extending the cavity lengths. Once the target sensitivity of the marginally stable FPMI is reached, the end mirrors are replaced with Khalili etalons ❸. In the last upgrade step of the interferometer also the arm cavity input mirrors are replaced with Khalili etalons ❹, to further reduce coating thermal noise.

and reflectivities $R > 99.99\,\%$ were reported [129]. A downside of this material is that it is not grown on optical substrates but needs to be transferred e.g. to a fused silica substrate which can then be used as a mirror. However, the loss angles reported for free standing samples are yet to be confirmed for crystalline coating stacks mounted to mirror substrates [130].

3.5 Summary

In this chapter, the role of coating Brownian thermal noise in precision interferometry experiments was recapitulated and detailed investigations of the novel techniques which were proposed in the conceptual design study for the reduction of coating thermal noise in the AEI 10 m sub-SQL interferometer were presented.

Large beam spots can in principle be arranged for in a straight-forward way, by choosing lengths and curvatures of the arm cavities accordingly. However, besides the obvious increased optical loss due to diffraction at the mirror apertures,

extremely large beam spots in a configuration with relatively short cavities come at the expense of marginal geometric stability of the cavities. A consequence of marginally stable arm cavities are extremely stringent requirements regarding the optical design and control of the interferometer, to ensure robust operation of the experiment.

The introduction of Khalili cavities, likewise, requires great care in terms of optical and control design, especially in conjunction with the requirement for large beam sizes which results in cavity geometries with stability margins significantly smaller than in the case of the arm cavities with similar beam spot sizes on the mirrors. In the scope of the investigations toward a possible optical layout, two candidate configurations were identified, with and without a beam waist in the end mirror cavity, respectively. It was found that both of the investigated configurations pose substantial challenges in terms of meeting the required precision of the parameters of the optics to be used as well with regard to sensing and control of the additional degrees of freedom in the interferometer. In the case of the configuration with an intra-cavity beam waist, a strong susceptibility of the geometric stability on the length of the cavity was found. Length changes in the micron range potentially drive the cavity into instability which renders this configuration – even if all mirror requirements were perfectly met – extremely challenging to operate in the actual sub-SQL interferometer. For the configuration with a nearly collimated beam in the end mirror cavity, a strong dependence of the chosen figures of merit (stability, mode coupling efficiency and spot size on the mirrors' HR surfaces) on the radii of curvature of the IETM, of the AR-coated and HR-coated surface, respectively, was identified. Deviations of these curvatures from their nominal values cannot be compensated for by varying the length of the end mirror cavity and direct thermal actuation on the IETM is prone to simultaneously affect the eigenmode in the arm cavity, which is undesired. However, it was found that, if all other curvature requirements were perfectly met, small curvature error of the order of less than $\pm 0.05\,\%$ of the IETM HR-coated and AR-coated surfaces could be compensated for by thermally adjusting the EETM curvature radius in the range of tens of meters. Nevertheless, optics requirements remain extremely stringent and a practical implementation of this configuration is expected to be experimentally highly challenging. Hence, the results of the investigations suggest that it is advisable to postpone the adoption of end mirror cavities to a later stage of the experiment and to concentrate on the implementation and commissioning of the marginally stable Fabry-Perot Michelson interferometer with extremely large beams in the first place, which is expected to be already challenging to operate by itself.

Alternative approaches for the reduction of coating Brownian thermal noise such as Khalili etalons or better coatings are the subject of ongoing research by several groups. Once these techniques have reached a sufficient level of maturity they may be considered for an implementation in the experiment, as an alternative to end mirror cavities, to further reduce coating Brownian thermal noise in the fully commissioned Fabry-Perot Michelson interferometer with marginally stable arm cavities.

CHAPTER 4

The tunable stability interferometer optical layout

A straight-forward approach to reducing coating thermal noise in interferometry experiments is to arrange for the laser beam spots to cover an area as large as possible on the highly reflective surfaces on the mirrors of the optical resonators forming the interferometer arms. However, the stability of the resonators and their optical performance often imposes a limit on the maximally feasible beam size. In this chapter, the optical design of a 10 m Fabry-Perot Michelson interferometer with tunable stability is described. The proposed design will allow initial commissioning to be carried out with arm cavities of high stability, while afterwards the arm cavity length can be increased stepwise towards the final, marginally stable configuration. Requiring only minimal hardware changes, with respect to a comparable "static" layout, the proposed technique will not only enable the investigation the stability limits of an optical resonator with realistic mirrors exhibiting inevitable surface imperfections, but also gives the opportunity to measure coating Brownian noise at frequencies as low as a few hundred Hertz. A detailed optical design of the tunable interferometer is presented and requirements for the optical elements are derived from robustness evaluations.

Part of the investigations presented in this chapter were published in [131]

> "Optical layout of a 10 m Fabry-Perot Michelson interferometer with tunable stability", C Gräf, S Hild, H Lück, B Willke, K A Strain, S Goßler, and K Danzmann, Class. Quantum Grav. **29**, 075003 (2012).

4.1 Introduction

It is evident that in the design of an instrument to reach the SQL, quantum noise must dominate over the sum of classical contributions which must be minimized. The employment of advanced technologies, such as monolithic all-silica suspensions and ultra-low loss optics, as well as a rigorous optimization of all relevant parameters is obligatory to reduce the individual types of thermal noise to a tolerable level. As

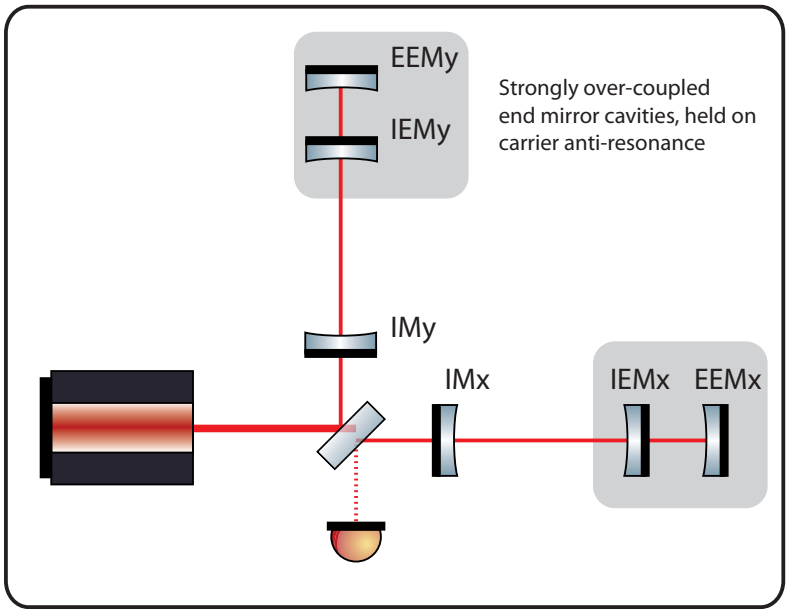

Figure 4.1: Schematic drawing of the AEI 10 m sub-SQL interferometer target configuration, as proposed in [60]. Configuration-wise the interferometer is planned to be a Fabry-Perot Michelson Interferometer with an arm length of approximately 10 m. The interferometer will not employ any recycling techniques. For the reduction of coating Brownian thermal noise it is intended to replace the conventional highly reflective arm cavity end mirrors with short, strongly over coupled cavities which will be held on anti-resonance for the carrier light by means of feedback control cf. [63]. See Chapter 1, Section 1.5 for details on the proposed target configuration, including the anticipated noise in the instrument.

in the case of large-scale advanced gravitational wave detectors, coating Brownian thermal noise is identified to be the most prominent classical noise source in the noise budget of the AEI 10 m sub-SQL interferometer. See Chapter 1, Section 1.5 for a detailed introduction to the proposed configuration, including the anticipated noise budget of the instrument.

Techniques aiming at the reduction of coating Brownian thermal noise have been developed to further increase the sensitivity of future GW detectors. These techniques, which are the subject of ongoing research, include modifications of the optics (e.g. TiO_2-doping of tantala/silica coatings [65], or the use of waveguides instead of dielectric mirrors [126]), changes in the optical technologies (e.g. interferometry with higher order optical modes such as the LG_{33} mode [89, 116]), and cryogenic cooling of the optics.

In this chapter, a stepwise approach to reducing coating thermal noise is introduced by iteratively enlarging the beam spots on the interferometer's arm cavity optics towards the technically feasible maximum. This goes hand in hand with pushing the arm cavities toward their geometric stability boundary.

Typically, the radii of the laser beams on the interferometer optics are chosen much smaller than optics' radii to avoid excessive diffraction loss, and to ensure stability of the optical mode. However, the larger the mirror surface area which is illuminated, the smaller the resulting coating thermal noise contribution. This reflects in the coating thermal noise theoretical model given in [62]. The use of extremely large laser beam spots, in relation to the length of its arm cavities, is a key feature in the target configuration of the AEI 10 m sub-SQL interferometer to reduce coating thermal noise below quantum noise level. This instrument is planned to be operated with beam spots with an equal radius of $w \approx 9.7$ mm on all cavity mirrors, which have a radius of $a = 24.3$ mm. In this sense the configuration with tunable stability proposed in this chapter can be regarded as an intermediate, simplified setup to pave the way to eventually building and operating the target configuration described in [60].

4.2 Challenges of stably operating the target configuration

The attempt to operate a Fabry-Perot Michelson interferometer with extremely large beam spots on the cavity mirrors inevitably comes at the expense of poor resonator stability if the arm cavities are comparatively short. The notion of stability of an optical resonator is closely connected to the existence of low-loss cavity eigenmodes. With the aid of the formalism introduced in Chapter 2, in Sections 2.2 and 2.3.6, which was originally devised in [132], one can quantify the stability of an optical resonator as a function of the mirrors' radii of curvature and their spatial separation. This measure is commonly referred to as the cavities' *g-factor* or *stability parameter*.

In marginally stable (i.e. $g \simeq 1$) optical resonators even small-scale length perturbations or mirror curvature error can render the instrument unstable. Implications of this are e.g. a dramatic increase of optical losses and a deterioration of heterodyne signals [101], which are extracted for interferometer feedback control. As a consequence, poor stability may prevent the instrument from reaching its sensitivity goal and may severely impede its operability, respectively.

4.2.1 Typical stabilities of the target configuration

The AEI Prototype facility, in particular the vacuum system, imposes space constraints on the minimum and maximum arm length of the sub-SQL interferometer. In this respect, for the target configuration shown in Figure 4.1, typical arm cavity lengths are of the order $L_{\mathrm{arm}} \approx 10.4$ m.

Another boundary condition with an impact on cavity lengths and mirror radii of curvature is the requirement for beam spots with a designated radius of $w = 9.7$ mm, which stems from a trade-off between low coating thermal noise and diffraction loss. Obeying these boundary conditions, calculations yield an arm cavity stability parameter value of typically $g = 0.999$. It must be noted that all stability estimates are approximate in the sense that they are based on the assumption of perfectly spherical optics. For more meaningful predictions of the stability, realistically imperfect optics need to be taken into account. In the experiment it will be possible

Table 4.1: Comparison of arm cavity lengths and radii of curvature of cavity mirrors and the resulting cavity g-factors for large scale second and third generation GW observatories and the planned AEI 10 m sub-SQL interferometer. Whereas second generation observatories exhibit a generous safety margin in their cavity stabilities, which is planned to be considerably smaller in the third generation detectors, the AEI sub-SQL interferometer arm cavities will eventually be operated extremely close to the stability boundary.

		Radius of curvature		
	Cavity length	Input mirror	End mirror	Cavity g-factor
Advanced LIGO [133]	3996 m	1934 m	2245 m	0.832
Advanced Virgo [115]	3000 m	1420 m	1683 m	0.871
ET-B [134]	10000 m	5070 m	5070 m	0.945
Sub-SQL IFO simplified design:				
Initial configuration	10.8 m	5.7 m	5.7 m	0.8
Marginally stable configuration	11.3952 m	5.7 m	5.7 m	0.998

to obtain surface maps of the actual mirrors, and to simulate the effect on stability. For such a configuration, a cavity length or a radius of curvature error of only a few mm would be sufficient to render the cavity unstable.

For the purpose of comparison, typical arm cavity stabilities of large scale interferometric GW detectors and the AEI 10 m sub-SQL interferometer are summarized in Table 4.1.

4.3 Motivation for a stepwise approach towards the final beam size

In this chapter, a *stepwise approach towards the final beam size* is proposed, in order to ease the commissioning of the AEI 10 m sub-SQL interferometer. With this approach it will be possible to initially learn how to operate the interferometer with relatively small beam spots on the cavity optics and therefore more comfortable arm cavity stability. After having established stable operation in the initial configuration and gathering the required experience, the marginally stable configuration can then be approached by iteratively enlarging the beam size on the main mirrors towards its design value, cf. Figure 4.2.

For this stepwise approach to be feasible, it is crucial to find a way of increasing the beam size that does not require any major hardware changes, such as for instance replacing main optics. It would for example be impractical and too cost intensive to adjust the beam size in the arm cavities by swapping the main mirrors with ones with a different ROC, especially as the mirrors feature monolithic suspension systems. Systems to thermally actuate on mirror curvatures have been successfully demonstrated [118, 119] but provide insufficient actuation range for the application in the sub-SQL interferometer, to replace the approach of tuning cavity lengths. A tuning range of the cavity stability parameter similar to the approach of changing

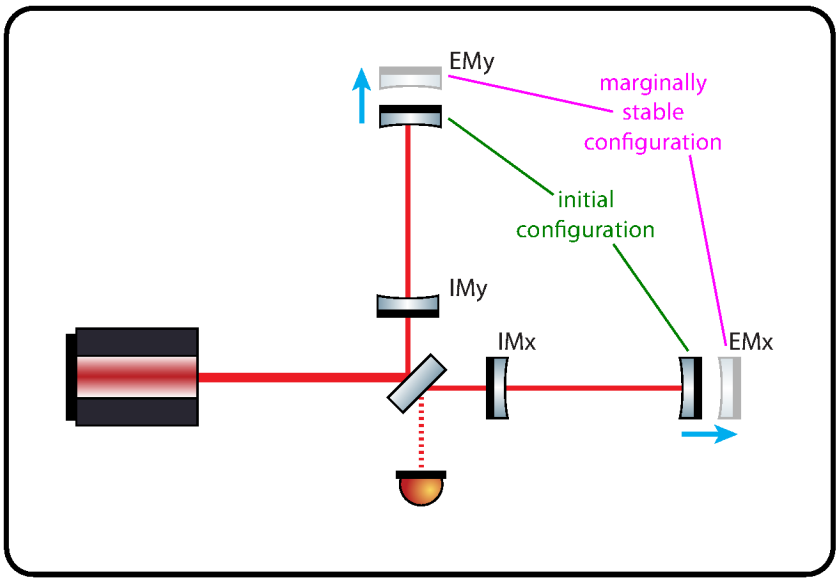

Figure 4.2: Schematic drawing of the principle approach to an interferometer with variable arm cavity stability and tunable beam sizes. The beam size on the arm cavity mirrors is determined by the lengths of the cavities and the radii of curvature of the cavity mirrors. Changing the mirror curvatures, e.g. by exchanging the monolithically suspended optics or by means of thermal actuation, requires great effort and is technically very challenging. It is, however, comparatively easy to change the cavity length by shifting the positions of the arm cavity end mirrors. In this approach the interferometer layout is optimized for marginally stable operation but the initial commissioning is carried out with shorter arm cavities with increased stability margin. After the initial commissioning phase the cavity lengths are stepwise increased towards the targeted marginally stable configuration.

the length of the cavities would require to change the sagitta of the arm cavity mirrors in the order of microns. To achieve this, the mirrors would have to be heated by hundreds of Kelvins.

However, as the AEI Prototype infrastructure provides sufficient space to shift the positions of the main mirrors by up to about 1 m or 10 % of the arm cavity length, it is possible to reduce the beam size on the optics without adjusting the main mirror ROC, but by initially shortening the arm cavity length. For the following investigations design values for the arm cavity length of $L_{\mathrm{arm}} = 11.395\,\mathrm{m}$ and radii of curvature of the input mirrors' (IM) and end mirrors' (EM) high reflective-coated (HR) surfaces of $R_{IM}^{HR} = R_{EM}^{HR} = 5.7\,\mathrm{m}$ shall be assumed. Such an arm cavity would have a stability parameter value of $g \approx 0.998$. As shown in Figure 4.3, a comfortable g-factor of $g = 0.8$ can be achieved with exactly the same mirrors by just shortening the distance between the input and end mirror by about 0.6 m to a total arm cavity length of $L_{\mathrm{arm}} = 10.8\,\mathrm{m}$. Such a shortening of the arm cavity length corresponds to

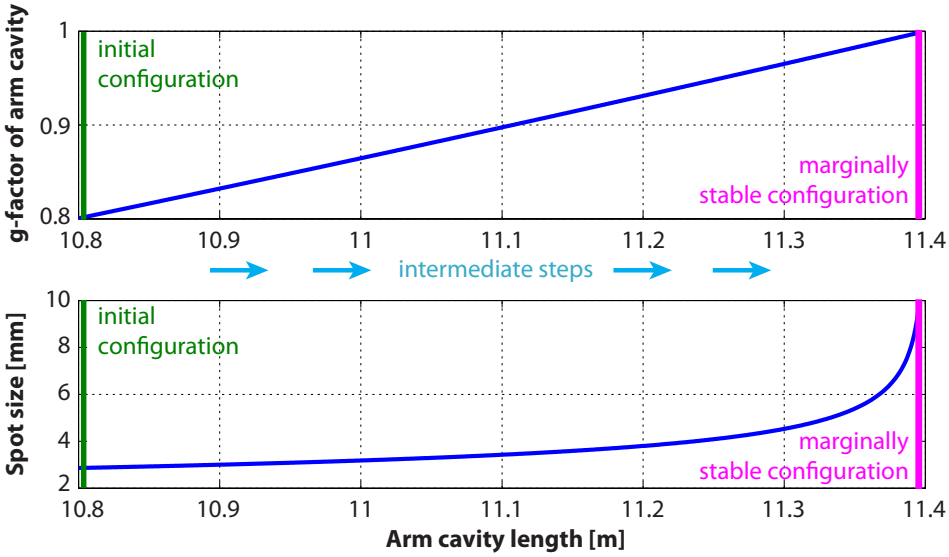

Figure 4.3: Beam size and stability parameter (g-factor) of a symmetric arm cavity of variable length, with input mirror and end mirror curvature of the HR (high reflective-coated) surfaces of $R_{IM}^{HR} = R_{EM}^{HR} = 5.7\,\mathrm{m}$. The right end of the plot represents the marginally stable configuration of the AEI 10 m sub-SQL interferometer which features extremely large beam spots and a g-factor close to instability. However, by using exactly the same mirrors, but an arm cavity length shortened to $L_{\mathrm{arm}} = 10.8\,\mathrm{m}$ the g-factor can be reduced to a comfortable value of $g = 0.8$ while at the same time reducing the beam size of $w = 9.72\,\mathrm{mm}$ to $w = 2.86\,\mathrm{mm}$.

reducing the beam size on the main mirrors from the targeted value of $w = 9.72\,\mathrm{mm}$ to an initial beam size of only $w = 2.86\,\mathrm{mm}$ (see lower plot of Figure 4.3).

4.3.1 Direct measurement of coating Brownian noise

Starting with the $L_{\mathrm{arm}} = 10.8\,\mathrm{m}$ configuration will not only be advantageous for commissioning of the interferometer and noise hunting, but will also enable direct measurements of coating Brownian thermal noise. Figure 4.4 shows the fundamental noise limits of the simplified AEI 10 m sub-SQL interferometer design for the marginally stable configuration with $L_{\mathrm{arm}} = 11.395\,\mathrm{m}$ arm length and the initial configuration with $L_{\mathrm{arm}} = 10.8\,\mathrm{m}$ long arm cavities. Since the beam size on all main mirrors is different by about a factor 3.5 between the two arm cavity lengths, the coating Brownian noise will scale accordingly, thus offering the possibility to directly measure coating Brownian noise at frequencies between about 100 Hz and 1 kHz with the initial configuration. This is an interesting opportunity to verify the coating Brownian noise level at frequencies around 200 Hz, which is the frequency range

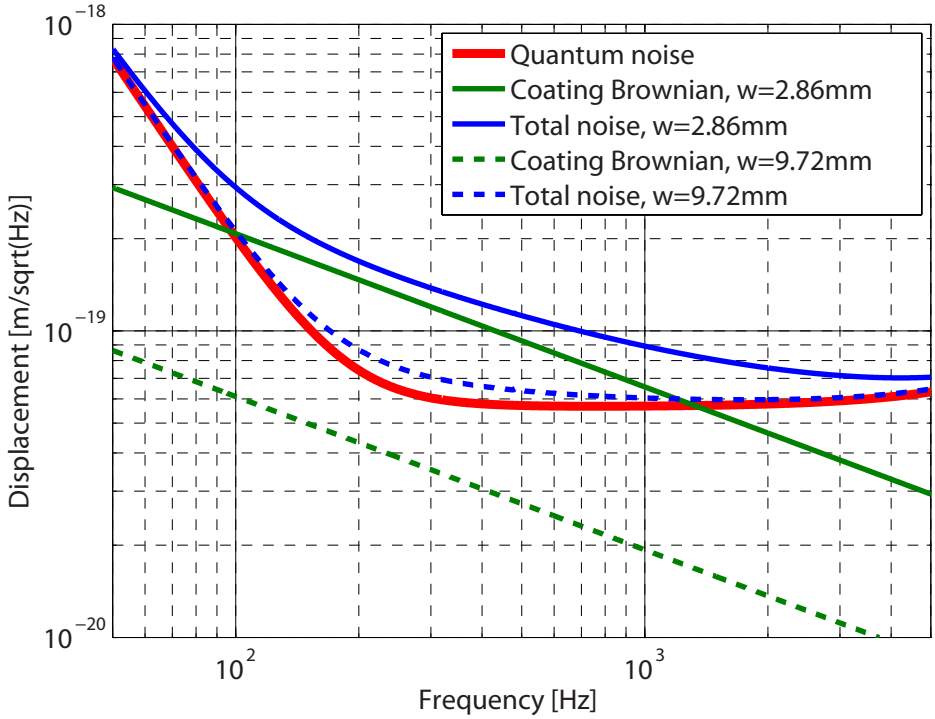

Figure 4.4: Simplified displacement sensitivity graph for the AEI 10 m sub-SQL interferometer only including the quantum noise and coating Brownian noise contributions for the initial configuration of 10.8 m arm cavity length (solid traces) and the marginally stable configuration (dashed traces) with $L_{\text{arm}} = 11.395$ m arm cavity length. The quantum noise (red) is independent of the arm cavity length. With the initial configuration it will be possible to directly measure coating Brownian thermal noise in the frequency range between 100 Hz and 1 kHz, while in the marginally stable configuration with large beam spots thermal noise contributions will be significantly below the quantum noise.

where coating Brownian noise is most important for the advanced GW detectors, and which has so far not been accessible by direct measurement [135, 136].

4.3.2 Potential impact on future gravitational wave detectors

One of the major steps for improving the sensitivity from the first to second generation GW detectors was to significantly increase the beam size on the main test masses, especially at the input mirrors. If larger mirror substrates become available, future upgrades to these advanced detectors might include even further increased beam sizes on the mirrors in order to reduce the influence of thermal noise contributions. This would require to operate the arm cavities with g-factors even higher than the ones stated in Table 4.1.

The experience that will be gained from the AEI 10 m sub-SQL interferometer by step-wise approaching the cavity g-factor of $g = 0.998$, will permit detailed studies

of destabilizing effects and stability limitations for related experiments. These results combined with reliable simulations can be at least partially transferred to upgrades of second generation GW detectors as well as to third generation GW detectors and may provide guidance in determining maximally feasible beam sizes for these instruments.

4.4 Properties of the optical configuration with tunable stability

Unlike the typical scenario in which Fabry-Perot Michelson interferometers are applied, in which the arm cavity geometry is not changed during the lifetime of the experiment, the primary goal for the AEI 10 m sub-SQL interferometer optical design is to identify a configuration which fulfills the requirement of tunable arm cavity stability or, synonymously, which can be operated equally well for different beam spot sizes on the cavity mirrors, cf. Section 4.3.

Owing to the fact that each iteration step, at discrete arm cavity lengths, will feature distinct cavity eigenmodes, it follows that the implementation of a flexible mode matching scheme is the most elegant approach to solving this problem. The performance goals of the instrument require close to optimal mode matching of the cavities at all times.

The starting point for the proposed optical configuration is the generation of a collimated laser beam with tunable radius. This forms the input beam to the interferometer and is matched into the arm cavity eigenmodes by curved rear (antireflection coated) surfaces on the substrates of the input mirrors. A schematic drawing of this concept is depicted in Figure 4.5.

4.4.1 Collimated interferometer input beam

From the technical point of view, a collimated beam can easily be prepared by including a curved mirror into the input optics chain and by choosing the mirror's ROC and its distance to the input beam waist appropriately. To minimize the astigmatism introduced by the collimating mirror, the opening angle between the incident and the reflected beam should be as small as possible. This can be achieved by increasing the distance of beam propagation of the incoming and outgoing beam, e.g. by positioning the collimating mirror near one of the interferometer arm cavity end mirrors.

Using a collimated input beam has a number of advantages over using a diverging beam. It is generally desired to have a high level of symmetry of the interferometer arms because this has a high impact on the intrinsic cancellation of common mode perturbations at the beam splitter. On the other hand, to provide transmission of RF control sidebands to the detection port of the interferometer, which is typically locked on or very close to a dark fringe, it is necessary to introduce a macroscopic offset in the path lengths between the two arm cavity input mirrors

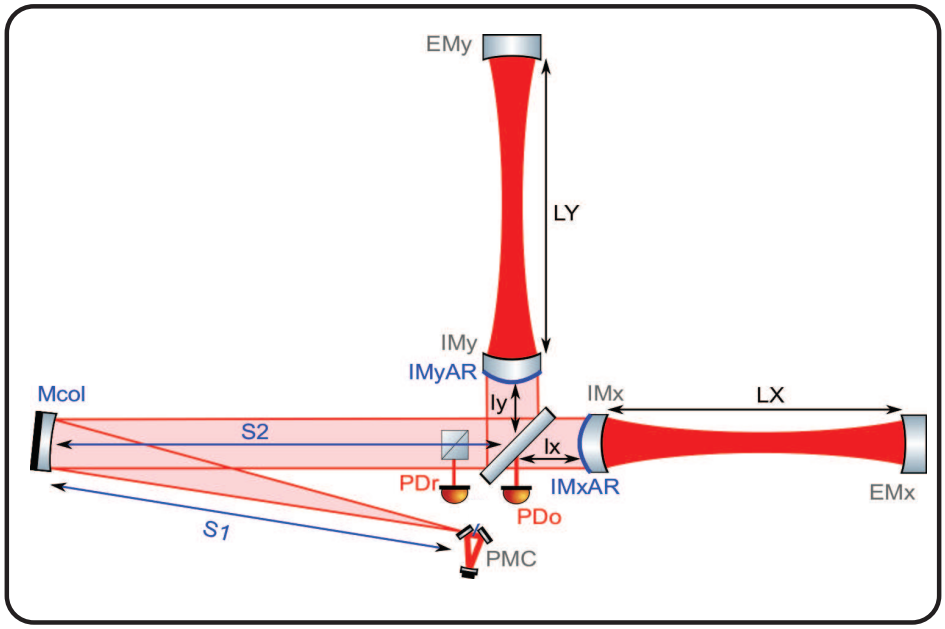

Figure 4.5: Simplified schematic drawing of the building blocks of the tunable arm cavity length interferometer configuration. The beam with a waist defined by the triangular pre-mode cleaner cavity (PMC) propagates to a curved collimating mirror at a distance of about 12 m. The reflected beam is directed into the interferometer where it is matched to the arm cavities' fundamental eigenmodes by means of curved arm cavity input mirror AR-coated surfaces.

and the beam splitter. This offset is referred to as the *Schnupp asymmetry* [137]. For a non-collimated input beam the propagation over unequal path lengths would lead to beam parameters which were different on the parallel and the perpendicular arm cavity IMs. If perfect mode matching were to be achieved for both arm cavities, this configuration would require either to include additional optics, or to have different radii of curvatures for the AR surfaces on the input mirrors. A further benefit of using a collimated input beam is reduction of astigmatism introduced at the beam splitter. However, a possible downside of this approach may be a potentially higher susceptibility to beam pointing noise, cf. Section 4.7.3.

4.4.2 Coupling efficiency of the flexible mode matching scheme

A natural measure to benchmark the proposed layout, especially with respect to the flexibility of the mode matching scheme, is the theoretical mode coupling efficiency for the extreme cases, i.e. the initial configuration and the marginally stable configuration. The mode matching efficiency η,

$$\eta = \frac{\left|\iint dx\,dy\,\Psi(x,y,z)\,\hat{\Phi}^*(x,y,z)\right|^2}{\iint dx\,dy\,|\Psi(x,y,z)|^2 \times \iint dx\,dy\,\left|\hat{\Phi}(x,y,z)\right|^2} \quad , \tag{4.1}$$

which is referred to several times throughout this chapter, is a measure of the coupling of optical power into a fundamental cavity eigenmode. It is defined as the normalized overlap integral of the TEM_{00} mode of the laser beam Ψ and the fundamental cavity eigenmode $\hat{\Phi}$. The modes Ψ and $\hat{\Phi}$ are fully determined by the complex beam parameters $q(z)$ and $\hat{q}(z)$ of the input beam and eigenmode at an arbitrary position $z = z_0$ along the beam axis of propagation.

The mode coupling efficiency of two beams described by beam parameters q and $\tilde{q}$ can be written as

$$\eta(q, \tilde{q}) = \frac{q^*\tilde{q} + q\tilde{q}^* - q\tilde{q} - q^*\tilde{q}^*}{|q|^2 + |\tilde{q}|^2 - q^*\tilde{q}^* - q\tilde{q}}\,, \tag{4.2}$$

where q^* is the complex conjugate of the beam parameter q. See Chapter 2, Section 2.3.5 for the derivation of this formula.

The mode coupling efficiencies calculated in the course of the following investigations can be regarded as upper bounds to the practically achievable mode matching quality. The marginally stable configuration is considered as the reference, meaning that in the analysis all relevant parameters are chosen with respect to achieving perfect mode matching for this configuration. By keeping all parameters, except for the arm cavity length, constant the degradation of the mode matching can be quantified and possibilities for the recovery of the mode matching can be identified as well as limits to the degree by which it is recoverable.

In the underlying case, the mode matching efficiency is determined by two parameters: the radius of the collimated input beam as well as the ROC of the arm cavity input mirrors' AR surfaces. For the marginally stable configuration with an arm cavity length of $L_{\text{arm}} = 11.3952\,\text{m}$ and mirror high reflectivity (HR) surface radii of curvature of $R_{IM}^{HR} = R_{EM}^{HR} = 5.7\,\text{m}$ it was found that an input beam radius of $w \approx 9.74\,\text{mm}$ and an IM AR surface ROC of $R_{IM}^{AR} \approx 1.776\,\text{m}$ result in a perfect mode matching to the arm cavities.

Ideally, in the real interferometer the arm cavity length is changed in each iteration step by moving the end mirrors only; this is adopted as a further boundary

Figure 4.6 ***(following page)*****:** Mode matching efficiency maps of the interferometer arm cavities. The top plot corresponds to the marginally stable configuration with an arm cavity length of $L_{\text{arm}} = 11.395\,\text{m}$, the bottom plot illustrates the situation for the starting configuration with a reduced arm cavity length of $L_{\text{arm}} = 10.8\,\text{m}$. In both plots the mode matching efficiency is color coded as a function of the radius of the collimated interferometer input beam and the ROC of the AR-coated surface of the arm cavity input mirrors. By holding the IM AR-coated surface ROC constant and changing the input beam radius only a mode matching efficiency for the short arm cavity configuration can be obtained which is degraded by approximately 1 % of the (theoretically perfect) matching efficiency of the marginally stable configuration. All numerical investigations were carried out by means of the matrix formalism introduced in [132] as well as the interferometer simulation software *FINESSE* [94].

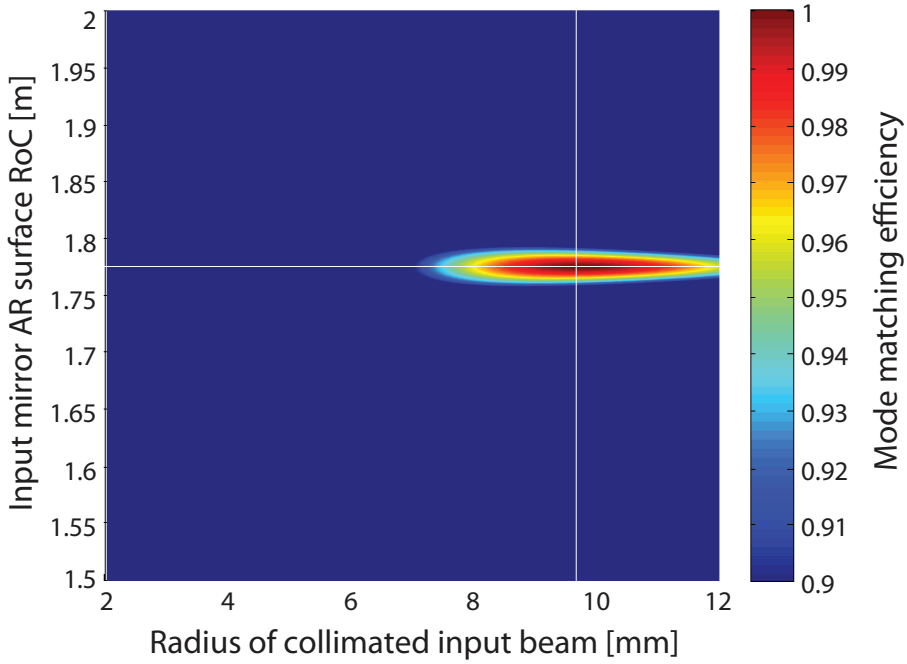
Input mirror AR surface RoC [m]
2
1.95
1.9
1.85
1.8
1.75
1.7
1.65
1.6
1.55
1.5
2
4
6
8
10
12
Radius of collimated input beam [mm]
1
0.99
0.98
0.97
0.96
0.95
0.94
0.93
0.92
0.91
0.9
Mode matching efficiency

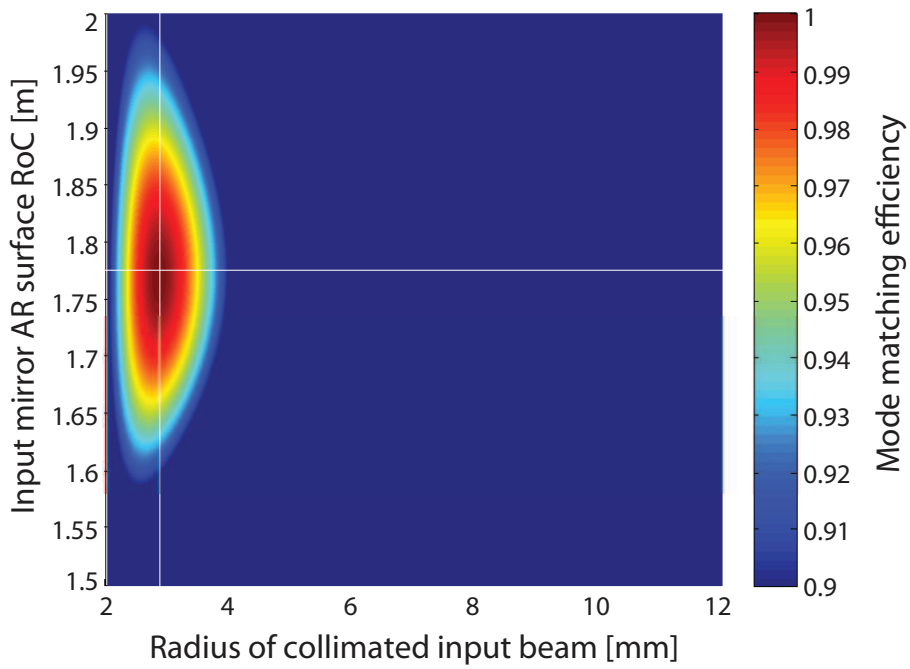
Input mirror AR surface RoC [m]
2
1.95
1.9
1.85
1.8
1.75
1.7
1.65
1.6
1.55
1.5
2
4
6
8
10
12
Radius of collimated input beam [mm]
1
0.99
0.98
0.97
0.96
0.95
0.94
0.93
0.92
0.91
0.9
Mode matching efficiency

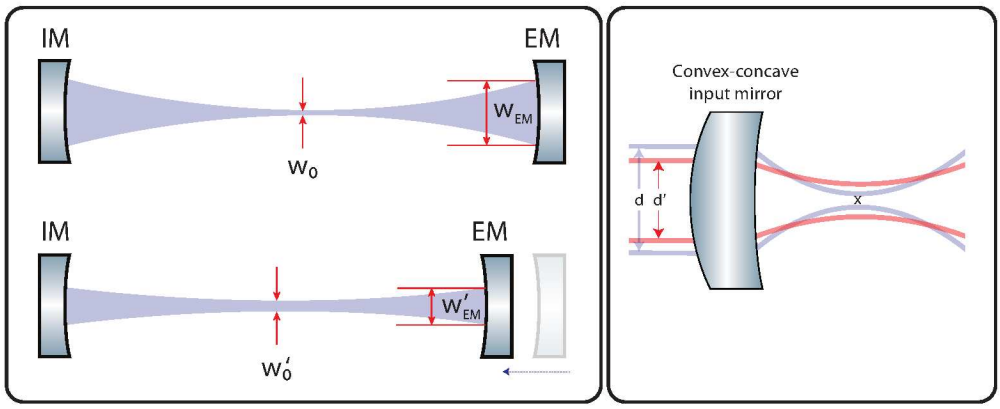

Figure 4.7: Left: Moving the end mirrors of the arm cavities alters the fundamental arm cavity eigenmode geometry. For the starting configuration, which features shorter arm cavities than the marginally stable design configuration, a larger beam waist at a shorter distance from the input mirror are observed as well as smaller beam spots on both cavity mirrors. **Right:** Collimated beam focusing by the convex-concave input mirror. By tuning the radius of the collimated input beam the beam waist radius inside the cavity can be adjusted. Input beam radius and waist radius are inversely proportional, the larger input beam diameter d will result in a smaller beam waist than the beam with diameter d'. The distance of the waist from the input mirror is constrained by the choice of the input mirror curvatures.

condition for the stepwise cavity length tuning. If now the optimal values of the marginally stable configuration are kept the same for all parameters, except for the arm cavity length which is reduced to a value of $L_{\text{arm}} = 10.8\,\text{m}$ by shifting the end mirror towards the input mirror, one can observe a substantial decrease of the mode matching efficiency. This scenario corresponds to setting up the initial configuration with improved stability with optics that are optimized for marginally stable operation.

Owing to the fact that the ROC of the IM AR surfaces cannot be easily changed in practice, this value is to be considered a constant for all length iteration steps. On the contrary, the radius of the collimated input beam can be tuned to recover the beam matching to the cavities' eigenmodes. According to this, by tuning the radius of the collimated input beam down to $w \approx 2.88\,\text{mm}$ the matching efficiency for the configuration with shortened arms can be $\eta > 99\,\%$, albeit the limitation of the radius of the collimated input beam being the only parameter available for optimization. Aspects of the technical realization of a tunable collimated input beam are addressed in Section 4.4.3.

Based on experience gained from earlier experiments, a degradation of the mode matching efficiency of not more than 1 % (with respect to the perfectly matched case) is considered as tolerable in the sense that this is likely to have a negligible impact on the performance of the instrument. A more elaborate estimation of this requirement based on a detailed noise analysis is subject to future work.

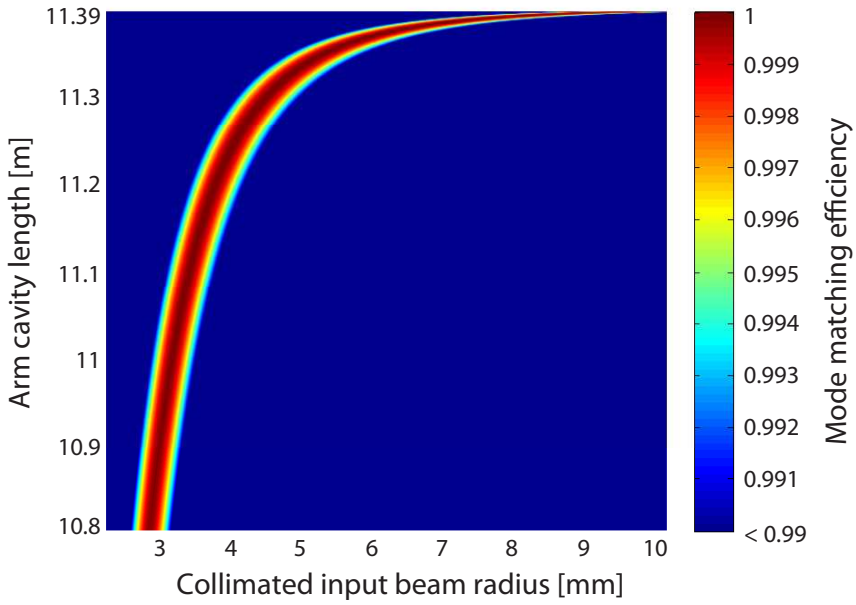

Figure 4.8: Mode matching efficiency of the interferometer arm in the reflected port of the beam splitter (with respect to the input beam) as a function of the radius of the collimated input beam and the arm cavity length. For the ROC of the arm cavity input mirror AR surface a value of $R_{IM}^{AR} = 1.776\,\mathrm{m}$ was implicitly assumed. Whereas in theory perfect mode matching can be achieved for the marginally stable design configuration, a mode matching efficiency of up to 99 % is theoretically feasible for the starting configuration with shorter arm cavities.

The mode matching efficiency as a function of the radius of the collimated input beam and the ROC of the arm cavity input mirror AR surfaces for the two arm cavity length extremes is shown in Figure 4.6. The residual degradation in the short arm cavity case can be attributed to a waist position mismatch within the cavities, which cannot be compensated by tuning the input beam radius. This is due to the fact that the focal distance of the curved IM AR surface for the collimated input beam is constant whereas the position of the waist of the arm cavity eigenmode is a function of the cavity length. Due to the symmetry of the configuration, the waist position moves towards the IMs by half the length change. This is illustrated in Figure 4.7.

The pivotal point of this approach is that only one parameter – the radius of the collimated input beam – needs to be tuned to adapt the beam to cavity eigenmodes corresponding to different cavity lengths. Keeping in mind that the mode coupling efficiency strongly depends on the matching of the beam waist radius while being less susceptible to waist position mismatch between input beam and cavity eigenmode [138], it is arranged for the possibility to achieve the best possible matching of the beam waist radius while a certain mismatch of the position of the beam waist is tolerated.

The evolution of the mode matching efficiency as a function of the collimated input beam radius and the arm cavity length is shown in Figure 4.8.

4.4.3 Further operational requirements

In the present case, besides the introduction of the curved collimating mirror, the input optics chain needs to be extended by optics to implement the required feature of radius tunability of the collimated beam. The notion of *input optics* commonly summarizes the optical elements which serve the purpose to deliver a pure, well-aligned beam with the optimal geometry to the interferometer. For conciseness further optical elements such as electro-optic modulators, isolators, etc. which are usually required elements of the input optics chain, are omitted in this discussion.

It is possible to conceive various approaches to implementing adjustable mode-matching in the input chain. Obvious examples include exchanging the collimating mirror in each iteration step and introducing a beam expanding telescope in the collimated beam path, but these turn out to be poor choices. Whereas the former option depends on the time-consuming task of replacing a suspended optic and gives rise to a complicated re-alignment procedure in each iteration step, the latter, likewise, requires frequent swapping of optics and may furthermore be an additional source of optical aberrations.

The preferred method of input beam shaping is to tune the waist radius of the *initial* beam, while keeping the waist position constant, prior to its reflection at the collimating mirror. This can, for instance, be accomplished by means of a beam telescope in combination with a beam expander, which consist of lenses or mirrors. These can easily be shifted on the optical table for fine tuning. The use of active optics may help to avoid the need to exchange fixed focal length optical elements.

A matter closely related to the stable operation of the tunable length interferometer is the sub-area of sensing and control of the optical degrees of freedom of the instrument. Typically, RF modulation based heterodyne length signal extraction schemes are employed, which require one or more electronic local oscillators as signal sources, whose frequencies are optimized with respect to cavity lengths within the interferometer to be controlled [55]. In the present case the cavity length tunability may require a flexible RF modulation scheme.

However, a detailed treatment of this topic, which can be regarded as a technical issue, will be subject to future work.

4.5 Estimation of the operational robustness

Parameters in the optical layout may deviate from their designated values for a variety of reasons, e.g. due to fabrication tolerances, environment-induced drifts or the nature of the experimental apparatus itself. Ideally, the interferometer design should exhibit a high level of immunity to tolerances in its constituting parameters. Practically, imperfections in the optical elements and inaccuracies in the optical setup degrade the performance of the interferometer or, in the worst case, may even render the instrument inoperable.

On the basis of the schematic drawing shown in Figure 4.5, design parameters can be identified which have a direct impact on the maximally achievable mode matching efficiency. These are: the initial beam waist radius w_0 as well as its position z_0 (defined by the eigenmode of the triangular cavity in Figure 4.5), the ROC of the collimating mirror as well as its position on the table and the ROC of the IMs' AR surfaces.

In this section, the impact of deviations of these parameters from their design values will be investigated. This knowledge can in turn be utilized to formulate specifications for the required manufacturing precision for the optics.

4.5.1 Initial laser beam waist radius and position

Provision of an initial beam with well-defined beam parameters is crucial to meet the requirement for a well-collimated interferometer input beam with a specific radius for each cavity length iteration step. A mismatch of the actual parameters of the initial beam with respect to the ideal ones is likely to have a direct impact on the mode matching quality.

The dependence of the arm cavity mode matching efficiency on the initial beam waist position z_0 is depicted in the top plot in Figure 4.9. Clearly, a deviation of the waist position along the optical axis can be compensated by shifting the position of the collimating mirror by the same amount.

It is important to keep in mind that shifting the collimating mirror position simultaneously alters the length of the incoming as well as the outgoing beam path. Nevertheless, due to the reflected beam being collimated, this coupling of the two lengths is neutralized in first order. Consequently, the quality of the mode matching is mostly insensitive to length changes in this path.

Small deviations of the initial beam waist radius from the optimum can be found to have a negligible effect on the mode coupling efficiency, cf. left plot in Figure 4.10. A deviation of $\pm 5\,\%$ in w_0 results in a degradation of the mode matching efficiency of less than $0.5\,\%$.

4.5.2 Collimating mirror ROC imperfections

The effect of ROC imperfections of the collimating mirror as well as a possible workaround is illustrated in the bottom plot in Figure 4.9.

Figure 4.9 ***(following page)*:** Degradation of the theoretically achievable mode matching efficiency due to deviations of the initial beam waist position and the ROC of the collimating mirror from their designated values, and the compensation of these deviations via the position of the collimating mirror. **Top:** A mismatch in the input beam waist position z_0 can be compensated by shifting the position of the collimating mirror on the table. **Bottom:** Likewise, imperfections of the collimating mirror ROC can be compensated by shifting the collimating mirror's position.

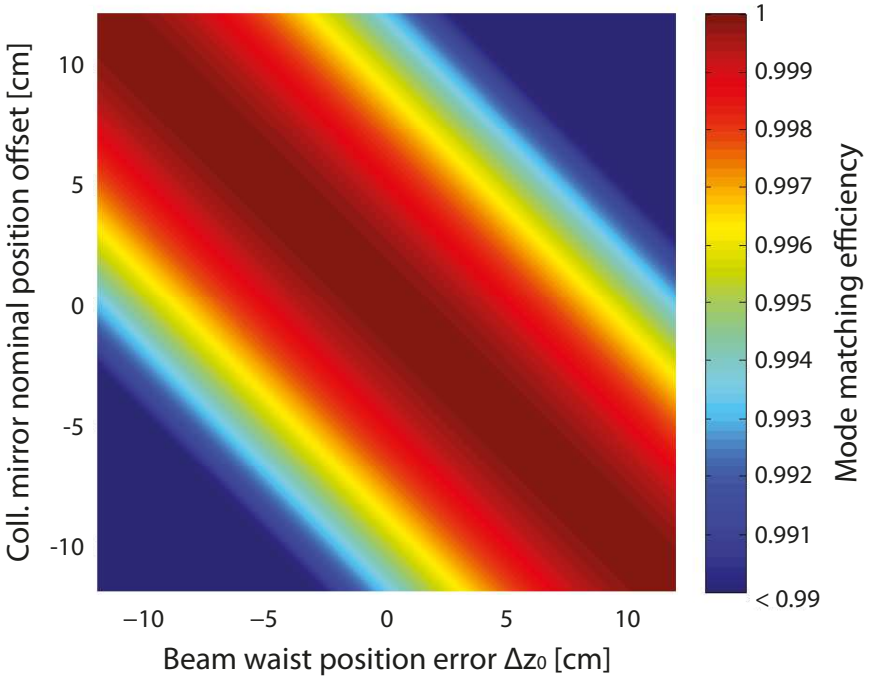
Coll. mirror nominal position offset [cm]
10
5
0
-5
-10
−10
−5
0
5
10
Beam waist position error Δz0 [cm]
1
0.999
0.998
0.997
0.996
0.995
0.994
0.993
0.992
0.991
< 0.99
Mode matching efficiency

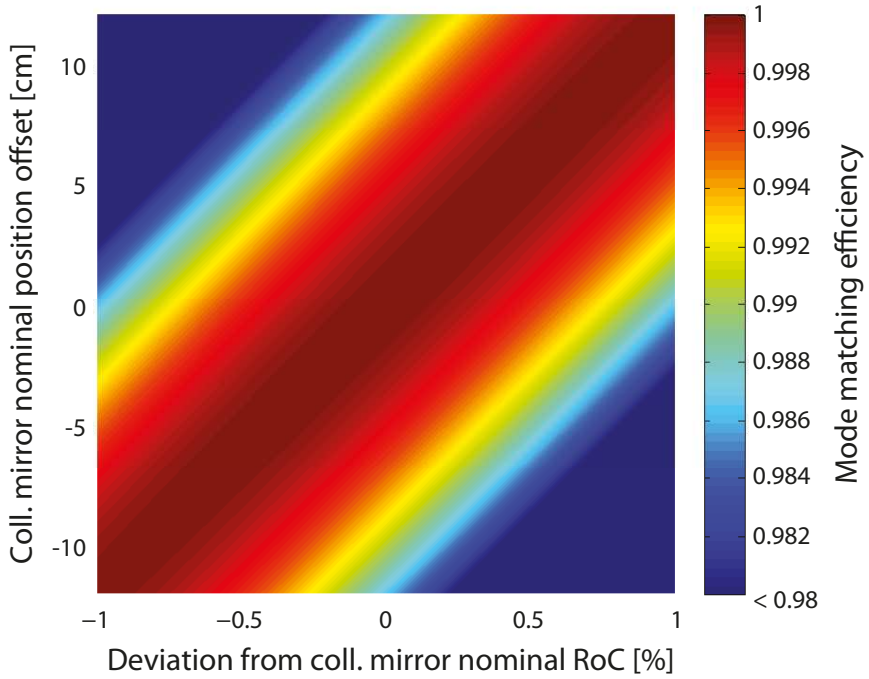
Coll. mirror nominal position offset [cm]
10
5
0
-5
-10
−1
−0.5
0
0.5
1
Deviation from coll. mirror nominal RoC [%]
1
0.998
0.996
0.994
0.992
0.99
0.988
0.986
0.984
0.982
< 0.98
Mode matching efficiency

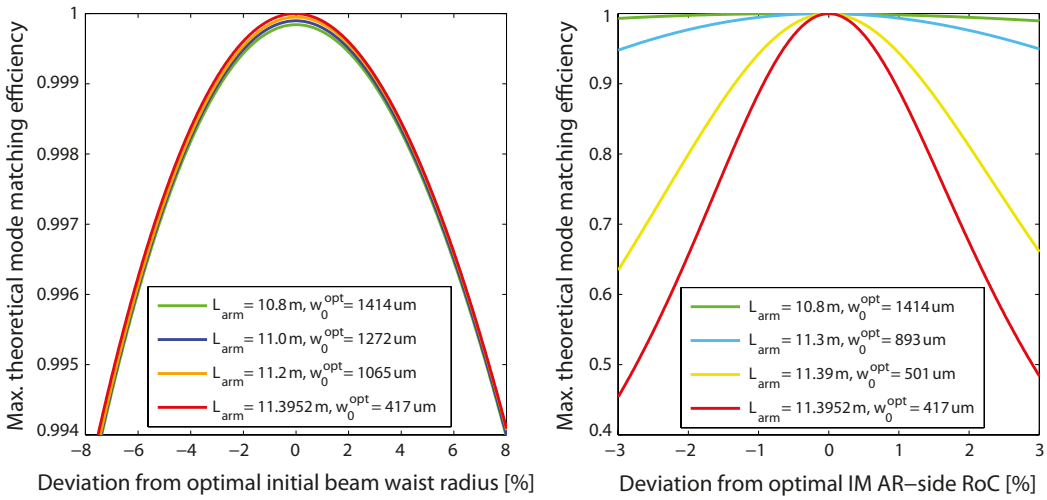

Figure 4.10: Degradation of the theoretically achievable mode matching efficiency due to deviations of the initial beam waist radius and the IM AR-surface ROC from their designated values. **Left:** The mode matching efficiency exhibits fairly low susceptibility to deviations from the optimal initial beam waist radius w_0. A deviation of $\pm 5\,\%$ in w_0 results in a mode matching efficiency degradation of less than $0.5\,\%$. Note that none of the configurations, except for the marginally stable one, reaches perfect mode matching. **Right:** The susceptibility to IM AR-surface ROC error increases with the arm cavity length approaching the marginally stable case. In the marginally stable configuration a deviation of $\pm 1\,\%$ comes at the expense of a mode matching efficiency degradation of $\approx 11.2\,\%$.

A ROC error results in a non-optimal focal length of the mirror. The focal length, in turn, is required to match the distance to the initial beam waist to perfectly collimate the beam in reflection. Again, the collimating mirror position can be shifted to compensate this type of imperfection. The same argument of length offsets in the reflected beam path being negligible (see previous section) holds here, too. Alternatively, instead of shifting the mirror position, the ROC could e.g. be thermally actuated upon.

4.5.3 Input mirror AR surface ROC

The susceptibility of the mode matching efficiency to ROC imperfections of the IMs' AR surfaces is illustrated in the right plot in Figure 4.10. It becomes evident that whereas for the starting setup the arm cavity mode matching shows comparatively low susceptibility to this type of imperfection, the effect increases as the marginally stable configuration arm cavity length is approached. While for the initial configuration it takes a ROC error of $\pm 3.2\,\%$ to degrade the mode matching by $\approx 1\,\%$, for the marginally stable setup a ROC deviation of $\pm 1\,\%$ was found to result in a mode matching efficiency degradation of $\approx 11.2\,\%$. A mode matching efficiency of $\eta \gtrsim 99\,\%$ for all configurations, including the marginally stable one, could be

achieved by means of an IM AR surface ROC error lower than $\pm 0.28\,\%$, which corresponds to an absolute ROC error of $\pm 5\,\mathrm{mm}$.

For meter-scale radii of curvature tolerances of approximately $\pm 0.05\,\%$ are routinely achieved if for example test plates which were manufactured with the aid of interferometric surface metrology equipment are used for the fabrication of the mirrors [113]. Even better accuracies of approximately $\pm 0.005\,\% - 0.01\,\%$ can be reached if interferometers are employed for directly measuring the workpiece during the fabrication process [114].

Unlike the cases discussed previously, for the IM AR-surface ROC there is no well-decoupled degree of freedom in the instrument available that can be utilized to easily compensate an error in this parameter. Direct thermal actuation does not pose a suitable solution as the radii of curvature on both sides of the mirror would be affected simultaneously, leading to an unwanted distortion of the cavity eigenmode. However, depending on its nature, a residual ROC error in both IM AR surfaces could be tackled by different means:

A "common mode" ROC error (i.e. the sign of both ROC deviations, for the parallel and the perpendicular interferometer arm IM, is identical) of both IMs could be compensated by slightly tuning the divergence angle of the interferometer input beam. This could be achieved by means of shifting the collimating mirror from its optimal position or actuating on its ROC (e.g. thermally). The pivotal point of this approach is to trade waist radius error for waist position error, the latter of which the cavity mode matching efficiency is generally less susceptible to. If, for instance, in the marginally stable configuration the actual IM AR surface ROC turns out to be smaller by $1\,\%$ with respect to its optimal value of $R_{IM}^{AR} = 1.776\,\mathrm{m}$, the mode matching efficiency can be recovered to $\eta \gtrsim 99\,\%$ by increasing the ROC of the collimating mirror. For typical beam path lengths in the collimating stage the required change of the collimating mirror ROC would be of the order of tens of centimeters. Alternatively, the same can be achieved by shifting the initial beam waist out of the focal point of the collimating mirror, with an offset of the same order as the previously described collimating mirror ROC change.

A "differential" ROC error is in general harder to handle but could, if absolutely necessary, be compensated by introducing additional optical elements in the central Michelson arms, i.e. between the beam splitter and the arm cavity IMs.

As mentioned previously, first and foremost these compensation techniques are relevant for configurations very close or at the marginally stable arm cavity length, only if mirror AR surface ROC fabrication errors turn out to be larger than desired. For the larger part of the operation modes, in terms of different cavity lengths, no such measures need to be taken.

4.5.4 Cavity mirror HR-side ROC tolerances

The tolerable level of ROC error of the HR-coated surfaces of the cavity mirrors follows immediately from the requirement for a stable, well mode matched cavity with the designated beam spot size. On the one hand, setting tight specifications for the cavity mirror HR-side ROC error will ensure that the requirements for stability,

mode matching and nominal beam spot sizes are well met. On the other hand, extremely stringent specifications will dramatically increase the required effort and hence the costs for fabricating the mirrors. It is thus indicated to determine an upper limit for the tolerable ROC error that can still be compensated for by standard means, such as adapting lengths in the optical setup or by tuning the radius of the collimated input beam.

On the one hand, mirrors with a ROC error specification of $\pm 0.1\,\%$ can be fabricated with reasonable effort e.g. with test plates that were manufactured with the aid of interferometric metrology equipment [113]. On the other hand, numerical simulations showed that ROC deviations of up to $\pm 0.1\,\%$ can be compensated in the critical case of the marginally stable configuration by a combination of changing the length of the cavity and tuning the beam radius of the collimated input beam.

In the case of a "common" ROC deviation of the mirrors in one arm cavity of $(\Delta R_{\mathrm{IM}}^{\mathrm{HR}}, \Delta R_{\mathrm{EM}}^{\mathrm{HR}}) = (+0.1\,\%, +0.1\,\%)$ or $(\Delta R_{\mathrm{IM}}^{\mathrm{HR}}, \Delta R_{\mathrm{EM}}^{\mathrm{HR}}) = (-0.1\,\%, -0.1\,\%)$, the length of the cavity needs to be tuned to $L_{\mathrm{AC}} = 11.4066\,\mathrm{m}$ or $L_{\mathrm{AC}} = 11.3838\,\mathrm{m}$, respectively, to recover stability of the cavity and to arrange for beam spots of $w_m \approx 9.7\,\mathrm{mm}$ on both cavity mirrors. In the latter case of negative common ROC error it was found that additional tuning of the radius of the collimated input beam to $w_{\mathrm{coll}} = 9.75\,\mathrm{mm}$ slightly improved the theoretical mode matching efficiency of the cavity. For both types of common ROC error, mode matching efficiencies of $\eta \approx 99.9\,\%$ could be achieved.

An immediate consequence of differential ROC error is a shift of the beam waist of the cavity eigenmode toward the mirror with the smaller ROC, which results in different beam spot sizes on the cavity mirrors. However, for the cases of $(\Delta R_{\mathrm{IM}}^{\mathrm{HR}}, \Delta R_{\mathrm{EM}}^{\mathrm{HR}}) = (\pm 0.1\,\%, \mp 0.1\,\%)$ the beam radii on the mirror surfaces were found to differ by only $\Delta w < 0.1\,\mathrm{mm}$. In the case of differential ROC error of $\pm 0.1\,\%$, mode matching efficiencies of $\eta \approx 99.9\,\%$ are maintained without the need for tuning the length of the cavity.

Relaxing the ROC specification to, for example, $\pm 0.5\,\%$ has the consequence that the mode matching efficiency can be recovered only partially by means of changing the cavity length or tuning the input beam radius. For instance, for the case of a common ROC deviation of $+0.5\,\%$ it was found that the achievable theoretical mode matching efficiency is limited to $\eta \approx 97\,\%$ after an optimization of the cavity length aimed at recovering cavity stability and the nominal spot size on the mirrors and an optimization of the radius of the collimated input beam. This limitation of the mode matching efficiency is a consequence of the waist position mismatch caused by the fixed focal length of the convex-concave IM substrate. This effect is negligible in the case of a smaller ROC deviation of up to $\pm 0.1\,\%$.

4.6 Dissipative heating and thermal aberrations

Another class of potentially performance-degrading effects, relevant for interferometric systems close to instability in particular, are *thermal aberrations*. These are driven by thermal gradients in the optical elements that, in turn, are a conse-

quence of bulk and coating absorption of laser light. Absorption coefficients of $\epsilon_b < 1\,\mathrm{ppm/cm}$ have been reported for high-performance synthetic fused silica material [139]. For coatings composed of SiO_2-TaO_5 double stacks an absorption coefficient of $\epsilon_c = 0.5\,\mathrm{ppm}$ was determined with absorption measurements of state-of-the art *ion-beam sputtered* (IBS) dielectric coatings [140].

The types of thermal aberrations considered here can be subdivided into thermo-elastic expansion of optics, resulting e.g. in a change of the effective radii of curvature, and thermo-refractive index fields in the locally heated optic, an effect which is commonly referred to as *thermal lensing*. In this respect, thermal aberrations have the potential to distort cavity eigenmodes as well as laser beams interacting with the affected optical element, by means of locally different refractive indices or the introduction of mirror surface form error. Due to the fact that the circulating power in the sub-SQL interferometer arm cavities with $P_{\mathrm{circ}} \sim 1\,\mathrm{kW}$ is much larger than the power of $\sim 2.5\,\mathrm{W}$ transmitted through the input mirror substrates, heating due to coating absorption is the dominant effect in the present case.

The first effect, thermally induced surface deformation, potentially reduces the coupling efficiency of the input field to the cavity eigenmode since the eigenbeam of the cavity is changed. The transverse shape of the beam resonating in the cavity is primarily determined by the shape of the mirror surfaces. Hence, the deformation of the mirror surfaces gives rise to light conversion into higher-order transverse modes and thus changes the modal composition of the internal field. The perturbed field may be subject to higher diffraction loss than the field in the cavity without thermal deformation of the mirror surfaces. The presence of higher order modes in the field returning from the cavity gives rise to imperfect contrast at the beam splitter of the interferometer.

The second effect, the formation of a thermal lens in the input mirror, changes the transverse shape of the input beam entering the cavity. Hence, the coupling efficiency of the input beam to the cavity eigenmode is reduced. Likewise, the light field leaving the cavity through the input mirror is affected which may result in reduced contrast at the Michelson beam splitter and degraded purity of the signal.

To estimate the absorption-induced heating of the sub-SQL interferometer arm cavity mirrors in the nominal state of operation, an analytical model based on the approach introduced by *Hello and Vinet* in [141] was employed. This model yields the steady-state temperature field of a cylindrical mirror created by absorption in the coating for an impinging Gaussian beam.

Mathematically, in the absence of internal heat sources, the stationary temperature field can be obtained by solving the Laplace equation

$$\Delta T(r,z) = 0\,, \tag{4.3}$$

which can in cylindrical coordinates be written as

$$\left(\partial_r^2 + \frac{1}{r}\partial_r + \partial_z^2\right) T(r,z) = 0\,. \tag{4.4}$$

The approach followed in [141] is to assume a *Fourier-Bessel* series expansion for the solution of Equation (4.4), i.e.

$$T(r,z) = \sum_n J_0(k_n r)\left[A_n \exp(k_n z) + B_n \exp(-k_n z)\right] \ , \tag{4.5}$$

with J_0 the zeroth-order Bessel function of the first kind. The coefficients $k_n = \zeta_n/a$, where a is the radius of the mirror, are obtained by solving

$$\zeta_n J_1(\zeta_n) - \chi J_0(\zeta_n) = 0 \tag{4.6}$$

for ζ. J_1 is the first order Bessel function of the first kind. The constant $\chi = 4\sigma' T_0^3 a/\kappa$ is the reduced radiation constant with $\sigma' = 5.67 \times 10^{-8}\,\mathrm{Wm^{-2}K^{-4}}$ the Stefan-Boltzmann constant with an emissivity correction, T_0 the ambient temperature and κ the thermal conductivity of the mirror material. The boundary condition that at the edges of the mirror the temperature only changes due to radiation losses is implicitly contained in Equation (4.6).

Further boundary conditions for the rear and front surface of the mirror are included in the model. Whereas at the rear surface heat is only radiated away from the mirror, the front surface is actively heated by absorption of light of the impinging laser beam. These surface boundary conditions are implicitly contained in the coefficients A_n and B_n in Equation (4.5) which read

$$A_n = \frac{\epsilon_c p_n a}{\kappa} \exp\left(-\frac{3\zeta_n h}{2a}\right) \frac{\zeta_n - \chi}{(\zeta_n+\chi)^2 - (\zeta_n-\chi)^2 \exp(-2\zeta_n h/a)} \tag{4.7}$$

and

$$B_n = \frac{\epsilon_c p_n a}{\kappa} \exp\left(-\frac{\zeta_n h}{2a}\right) \frac{\zeta_n + \chi}{(\zeta_n+\chi)^2 - (\zeta_n-\chi)^2 \exp(-2\zeta_n h/a)} \tag{4.8}$$

with κ the thermal conductivity of the substrate material, h the substrate thickness and

$$p_n = \frac{P}{\pi a^2} \frac{\zeta_n^2}{(\zeta_n^2+\chi^2) J_0(\zeta_n)^2} \exp\left(-\frac{w^2\zeta_n^2}{8a^2}\right) \tag{4.9}$$

with P the power and w the spot radius on the mirror surface of the incident laser beam.

By inserting the above coefficients A_n and B_n in Equation (4.5) one obtains the solution for the temperature field which reads

$$T(r,z) = \sum_n \frac{\epsilon_c p_n a}{\kappa} e^{-\zeta_n h/(2a)} \frac{(\zeta_n-\chi)e^{-\zeta_n(h-z)/a} + (\zeta_n+\chi)e^{-\zeta_n z/a}}{(\zeta_n+\chi)^2 - (\zeta_n-\chi)^2 e^{-2\zeta_n h/a}} J_0\left(\frac{\zeta_n r}{a}\right) \ . \tag{4.10}$$

The temperature field in a sub-SQL interferometer arm cavity mirror due to coating absorption is plotted in Figure 4.11. A thermal conductivity of $\kappa = 1.38\,\mathrm{Wm^{-1}K^{-1}}$ was assumed for the fused silica material and spot sizes of $w = 2.86\,\mathrm{mm}$ and $w = 9.72\,\mathrm{mm}$ for the initial and the marginally stable configuration, respectively. For the circulating power in the cavity a value of $P_{\mathrm{circ}} = 1.16\,\mathrm{kW}$ was assumed.

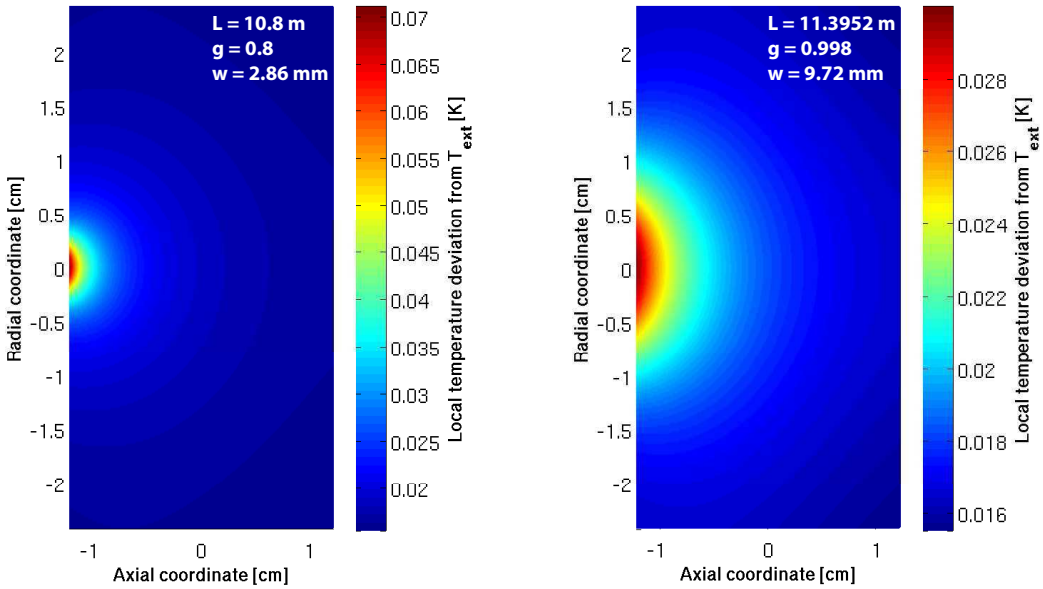

Figure 4.11: Coating absorption-induced heating of the arm cavity mirrors in the initial configuration (left) and the marginally stable configuration (right). A circulating light power of $P_{\text{circ}} \sim 1\,\text{kW}$ and a coating absorption of $\epsilon_c = 0.5\,\text{ppm}$ were assumed. In both cases light absorption causes only a modest increase of the local temperature in the mirror substrates.

Due to the smaller beam spot size in the initial configuration the heated volume of the mirror is more concentrated around the center of the mirror. In the case of the marginally stable configuration the spot size on the mirror surface is increased and consequently the temperature increase with respect to the ambient temperature spreads out vertically. At the same time the peak temperature decreases. However, for the given optical properties and circulating laser power the temperature increases only modestly, with peak values of ΔT smaller than a tenth of a Kelvin. Hence, only weak refractive index fields $\Delta n(r,z) = \mathrm{d}n/\mathrm{d}T \times T(r,z)$ will form and thermo-elastic deformation of the mirror will be small.

Based on the approximative formulas given in [108] the implications of thermo-elastic deformation of the interferometer arm cavity mirrors as well as the formation of refractive index fields can be estimated. The change of the sagitta as a consequence of thermo-elastic deformation of a mirror which is subject to coating absorption can be approximated as

$$\Delta S \sim -\alpha/(4\pi\kappa)\epsilon_c P_{\text{circ}} \tag{4.11}$$

with $\alpha = 5.5 \times 10^{-7}\,\text{K}^{-1}$ the coefficient of thermal expansion of fused silica. The optical path length change in the substrate as a consequence of coating absorption is approximately given as

$$\Delta\text{OPL} \sim \beta/(4\pi\kappa)\epsilon_c P_{\text{circ}} \tag{4.12}$$

Table 4.2: Thermal effects in the sub-SQL interferometer arm cavities in the marginally stable configuration. Implicitly, values of $\varepsilon_c = 0.5\,\text{ppm}$ and $\varepsilon_b = 1\,\text{ppm/cm}$ were assumed, for silica/tantala coating absorption and for fused silica bulk absorption, respectively. An input power of $P_{\text{in}} \sim 5\,\text{W}$ yields a power circulating in each of the arm cavities of $P_{\text{circ}} \approx 1\,\text{kW}$. For the anticipated input power of $P_{\text{in}} \sim 5\,\text{W}$ a degradation of the mode coupling efficiency of $\lesssim 0.1\,\%$ is expected.

Substrate absorption – thermo-refractive index field		
Optical path length change	δs_{STR}	$3.811 \times 10^{-14}\,\text{m}$
Effective lens focal length	$\hat{f}_{STR}$	$6.172 \times 10^{8}\,\text{m}$
Coating absorption – thermo-elastic expansion		
Sagitta change	δs_{CTE}	$1.586 \times 10^{-11}\,\text{m}$
Resulting ROC change	δR_{CTE}	$1.095 \times 10^{-5}\,\text{m}$
Resulting beam spot radius change	δw	$1.102 \times 10^{-5}\,\text{m}$
Resulting cavity g-factor change	δg_{arm}	7.676×10^{-6}
Coating absorption – thermo-refractive index field		
Optical path length change	δs_{CTR}	$2.393 \times 10^{-10}\,\text{m}$
Effective lens focal length	$\hat{f}_{CTR}$	$9.829 \times 10^{4}\,\text{m}$
Resulting mode matching degradation	$\Delta\eta$	$\lesssim 0.1\,\%$

with $\beta = \mathrm{d}n/\mathrm{d}T = 8.3 \times 10^{-6}\,\text{K}^{-1}$ the thermo-optic coefficient of fused silica. Absorption of light transmitted through the input mirror substrate results in an approximate optical path length change of

$$\Delta\text{OPL} \sim 1.3 \times \beta/(4\pi\kappa) h \epsilon_b P_{\text{trans}} \tag{4.13}$$

where h is the thickness of the substrate. Regarding the relative strengths of these effects, it is found for the case of fused silica optics that the thermo-refractive effect dominates the thermo-elastic effect by approximately one order of magnitude [142].

Since thermoelastic deformation changes the effective radius of curvature of an optic, this effect is also relevant for stability considerations in optical cavities. However, as the radius of curvature of a heated mirror is locally increased, HR coating absorption-induced thermo-elastic deformation of a mirror in a near concentric cavity has in fact a stabilizing effect. Consequently, due to the relation between beam radii and cavity g-factors, the spot sizes of the eigenbeam on the cavity mirrors are reduced which may, in extreme cases, result in increased coating Brownian thermal noise. The change of the stability of a cavity as a consequence of mirror dissipative heating was for instance accounted for in the marginally unstable recycling cavities of the initial LIGO interferometers by specifying the radii of curvature with the effects of dissipative heating in mind. The curvatures were chosen such that stable operation was provided once the optics had sufficiently deformed by dissipative heating to form a stable power recycling cavity [101].

With the anticipated mirror reflectivity and absorption specifications for the interferometer optics, and with typical input laser powers, as stated in [60], the

thermally induced changes in optical path lengths and mirror curvature sagitta can be estimated, based on Equations (4.11), (4.12) and (4.13). Furthermore, the impact on cavity stability and mode matching efficiency can be deduced. The results for the marginally stable configuration are summarized in Table 4.2.

For the nominal input laser power of $P_{\text{in}} \sim 5\,\text{W}$, a power of $\sim 2.5\,\text{W}$ is transmitted through the IM substrates of each arm cavity and a power of $\approx 1\,\text{kW}$ is found to be resonating in each cavity. As expected, due to the comparatively low transmitted light power the change of the optical path length due to substrate absorption is negligibly small. The change of the effective radius of curvature of the mirrors results in a change of the beam spot size on the HR surfaces of approximately 10 μm which is negligible in terms of an increase of coating Brownian thermal noise. Finally, the refractive index field caused by coating absorption gives rise to an optical path length difference of the order of approximately 0.24 nm. If the changed effective radii of curvature and the changed optical path length in the IM substrate are included in the numerical model of the interferometer, it is found that thermal effects give rise to a reduction of the coupling efficiency of $\Delta\eta \lesssim 0.1\,\%$.

It can be concluded that for the nominal input power of $P_{\text{in}} \sim 5\,\text{W}$ thermal effects are not expected to have a significant effect on the performance of the interferometer. In particular, neither the mode matching efficiency, nor the level of coating Brownian thermal noise in the interferometer is significantly affected.

4.7 Further implications of marginal stability

In the following, consequences of the marginal stability of the interferometer arm cavities for the performance of the instrument will be discussed. Among the discussed effects are the degeneracy of transverse modes in the arm cavities, the susceptibility to mirror misalignment and the coupling of input beam pointing fluctuations to the main interferometer signal.

4.7.1 Modal degeneracy

Typically, Michelson interferometers with Fabry-Perot arm cavities are operated with a generous stability margin which, as one consequence, gives rise to a strong suppression of higher order modes. Simultaneous resonance of the fundamental mode and higher-order transverse modes occurs in cavities in which higher-order modes accumulate only little round-trip *Gouy phase* [68]. The one-way Gouy phase shift $\Delta\Phi_{\text{Gouy}}$ can be expressed as a function of the cavity g-factor which also quantifies the stability of the cavity,

$$\Delta\Phi_{\text{Gouy}} = \arccos(\pm\sqrt{g})\ . \tag{4.14}$$

The Gouy phase of a stable cavity can be identified as a significant fraction of π. Transverse mode spacings of fundamental and higher order Hermite-Gauss modes can be obtained from the expression

$$\Delta\nu_{mn} = \frac{\text{FSR}}{\pi}(m+n)\Delta\Phi_{\text{Gouy}} \tag{4.15}$$

and for the spacings of fundamental and higher-order Laguerre-Gauss modes from

$$\Delta\nu_{lm} = \frac{\mathrm{FSR}}{\pi}(2l+m)\Delta\Phi_{\mathrm{Gouy}}\ , \tag{4.16}$$

where $\mathrm{FSR} = c/(2L)$ corresponds to the free spectral range of the cavity in Hertz.

The optical gains of fundamental and higher-order transverse modes in the cavity can be written as [102]

$$G_{mn}(t_{\mathrm{IM}}, r_{\mathrm{IM}}, r_{\mathrm{EM}}, \Delta\Phi_{\mathrm{Gouy}}) = \left|\frac{t_{\mathrm{IM}}}{1 - r_{\mathrm{IM}} r_{\mathrm{EM}} \exp[-2i(m+n+1)\Delta\Phi_{\mathrm{Gouy}}]}\right|^2\ , \tag{4.17}$$

in the exemplary case of Hermite-Gauss modes. As the stability of the arm cavities is decreased, the Gouy phase shift decreases. This results in a decreasing separation of fundamental mode and higher order mode resonance frequencies, giving rise to lower suppression of higher order modes generated inside the arm cavities, e.g. by light scattering at irregular mirror surfaces or mirror misalignment, or which are injected into the cavity as higher-order modes contained in the input beam. The resulting eigenbeam of the cavity is, as opposed to a cavity operating on a single transverse mode, not diffraction limited anymore. This is due to the fact that in cavities in which the resonance frequencies of HOMs coincide with that of the fundamental mode, the amplitude contributions of degenerate HOMs from several round-trips add coherently. This results in the accumulation of high intra-cavity powers of degenerate higher-order modes [143]. Consequences are e.g. increased optical losses due to clipping of higher order modes at the mirror apertures but also deformed beams returning from the arm cavities, causing a degradation of the beam splitter contrast. Poor beam splitter contrast gives rise to additional shot noise and increased coupling of input laser noises to the main readout interferometer signal. These effects are discussed in detail in Chapter 5.

The normalized gains of the fundamental mode and HOMs up to tenth order in the sub-SQL interferometer arm cavities as a function of the frequency are shown in Figure 4.12. As the targeted stability of $g = 0.998$ is approached, corresponding to an arm cavity length of $L = 11.3952\,\mathrm{m}$, the higher order mode spacing is decreased. At the same time the gains of the low order HOMs are increased.

However, the plot shown in Figure 4.12 is based on the assumption of perfectly spherical mirrors. In the presence of irregular mirror surfaces the degeneracy of higher-order modes of the same order is broken. Differently shaped transverse modes of identical mode order experience different phase shifts upon reflection at the irregular surface. This gives rise to a slight shift of their resonance frequency which manifests in a frequency splitting of modes. Implications of realistic mirrors on the performance of the interferometer with marginally stable arm cavities are discussed in Chapter 5.

4.7.2 Angular misalignment coupling to longitudinal phase

A well-known property of marginally stable cavities is their susceptibility to fluctuations of the alignment of the cavity mirrors. Cavities approaching the degenerate

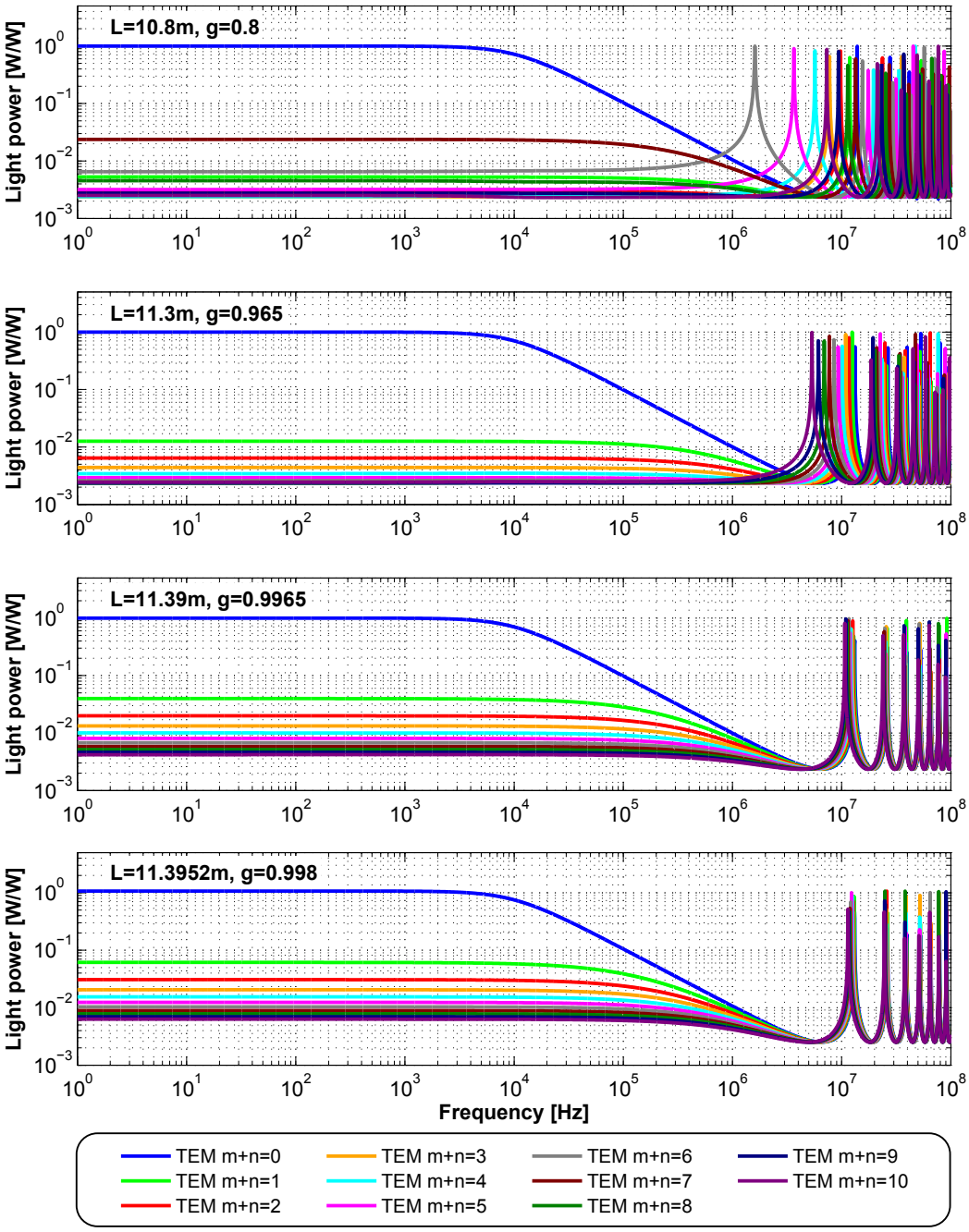

Figure 4.12: Modal degeneracy of the interferometer arm cavities for different values of the stability parameter. Modes of the same order experience the same Gouy phase shift per cavity round-trip and are therefore, in a model with perfectly spherical mirrors, degenerated. Whereas in the initial configuration with g= 0.8 most higher-order modes are well suppressed on fundamental mode resonance, the relative contribution of HOMs increases toward the marginally stable configuration with a cavity stability parameter of g= 0.998.

case of $g \simeq 1$ share the property that their alignment is critical in terms of the required accuracy [144]. For a misaligned degenerate cavity no optical axis exists, which is defined as a ray which retraces itself after one round-trip. The required alignment accuracy scales with the finesse of the cavity. In this section, the coupling of cavity mirror misalignment to fluctuations of the longitudinal phase of the cavity is quantified for different values of the stability parameter.

The tuning ϕ of a cavity is its microscopic deviation from the resonance condition and is defined as the length of the cavity modulo the wavelength of the used laser light, which is conveniently expressed in degrees,

$$\phi = 360^\circ \times (L_{\text{arm}} \bmod \lambda_0) \; . \tag{4.18}$$

From a geometrical standpoint it becomes clear that by tilting a cavity mirror the phase accumulated per round trip by the intra-cavity field changes. Hence, to ensure resonance of the cavity, a servo controller needs to actuate on the cavity length, thus changing the tuning of the cavity. Besides this, if a perfectly mode matched cavity is subject to angular misalignments of its mirrors, the mode matching efficiency will be reduced. The eigenmode of the cavity with tilted mirrors will, likewise, be tilted and will thus exhibit less overlap with the injected beam, resulting in a reduction of the light power circulating in the cavity.

Figure 4.13 illustrates the relationship between angular misalignment of one of the cavity mirrors and the resulting fluctuation of the longitudinal phase as well as the effect on the intra-cavity power.

It is evident that the coupling steeply increases as the marginally stable configuration is approached. Whereas the initial configuration with shorter arm cavities and a stability parameter of $g = 0.8$ exhibits comparatively small angular to longitudinal coupling and also little susceptibility of the circulating power to angular misalignment, in the case of the marginally stable configuration with $g = 0.998$ it was found that an angular misalignment of the end mirror of $\beta = 1\,\mu$rad requires a longitudinal detuning of the cavity of $\Delta\phi = 1^\circ$ by the servo controller to compensate for the phase change. At the same time the change of the eigenmode of the cavity with tilted mirrors and the resulting mismatch with the input beam results in a substantial reduction of the power circulating in the cavity to approximately 50 % of the power resonating in the perfectly aligned cavity.

If the common requirement of postulating that arm cavity fluctuations need to be suppressed to less than 1 % of the cavity line width is assumed, the corresponding fluctuations in the circulating power of $\Delta P \approx 110\,$mW can be related to the reduction of the intra-cavity power resulting from mirror misalignment. Whereas in the initial configuration with $g = 0.8$ an RMS angular misalignment of $\lesssim 3.5 \times 10^{-7}$ rad is necessary to fulfill this condition, in the case of the marginally stable configuration with a stability parameter value of $g = 0.998$ a mirror misalignment of $\lesssim 1.4 \times 10^{-8}$ rad RMS needs to be maintained.

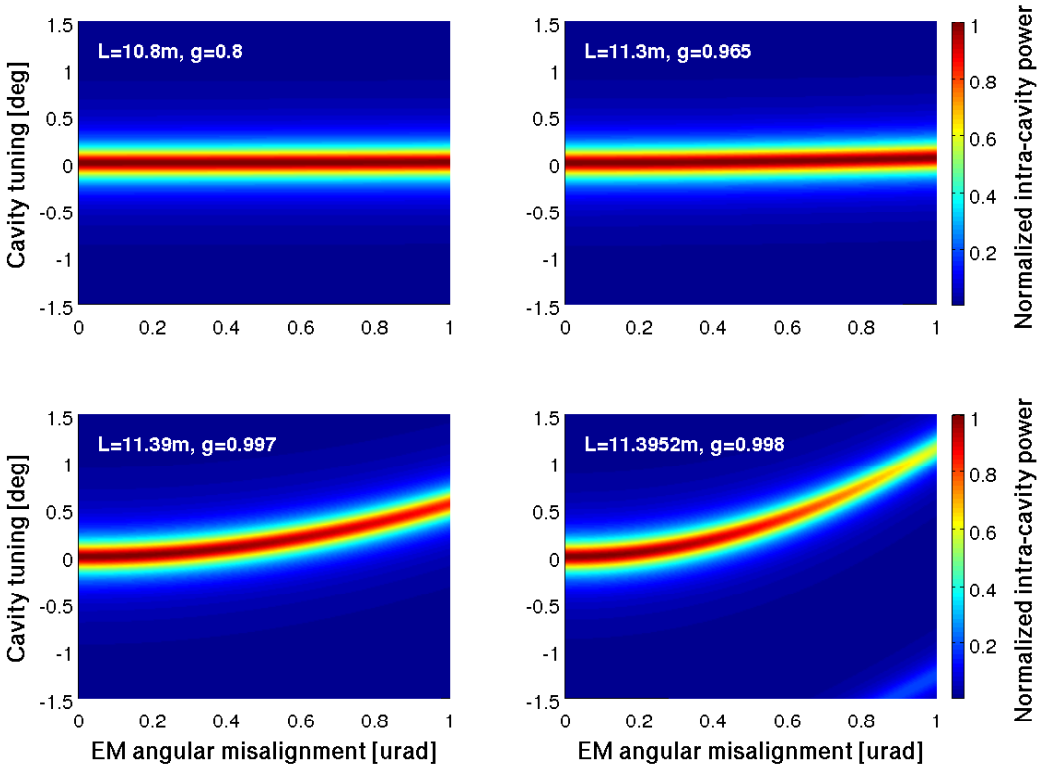

Figure 4.13: Coupling of mirror tilt to longitudinal arm cavity phase for different cavity stability parameter values. Whereas the initial configuration with an arm cavity length of $L = 10.8\,\mathrm{m}$ and $g = 0.8$ exhibits little coupling of misalignment to longitudinal phase, this effect becomes more and more pronounced the further the marginally stable configuration with $L = 11.3952\,\mathrm{m}$ and $g = 0.998$ is approached. An angular misalignment of the marginally stable arm cavity end mirror of $\beta = 1\,\mu\mathrm{rad}$ results in a shift of the resonance condition by approximately $\Delta\phi = 1^\circ$ which the length control loop needs to compensate for. Nevertheless, despite the correcting action of the length servo the circulating power drops to about 50 % of the power circulating in the perfectly aligned cavity due to a change of the cavity eigenmode and the resulting mode mismatch.

4.7.3 Input beam pointing noise

Angular fluctuations of laser beams and interferometer mirrors give rise to noise couplings to the main interferometer signal. Both, coupling of high-frequency beam jitter with the RMS angular motion of the mirrors and high-frequency angular mirror motion with beam mis-centering couple quadratically to the detection port [145].

In the modal picture, geometric beam jitter can be described as first order spatial mode sidebands which are subject to amplitude modulation. In a perfect interferometer locked on the dark fringe this first order mode light would be reflected and had no influence on the measurement in the asymmetric port of the interferometer. Input beam jitter becomes an issue in the presence of misalignments of interferometer

mirrors and asymmetries in the arms. These give rise to a partial conversion of first order mode modulation sidebands to the fundamental mode. Input beam jitter may thus couple to the asymmetric port in the form of spurious modulation sidebands and may potentially impede the sensitivity of the interferometer. In Fabry-Perot Michelson interferometers it is found that differential misalignment of the arm cavity mirrors is, compared to misalignments of the other angular degrees of freedom, the strongest contributor to light conversion from first order mode content in the input beam to the fundamental mode light in the asymmetric port [146].

It is expected that beam pointing noise will play a significant role in the sub-SQL interferometer. On the one hand this is due to the fact that the marginal stability of the arm cavities gives rise to a partial degeneracy of first order transverse modes which results in increased coupling of beam pointing fluctuations to the interferometer signal. This coupling also scales with the size of the beam spots on the cavity mirrors, which are required to be comparatively large in the sub-SQL interferometer. On the other hand large beam spots in the input optics train give rise to increased generation of jitter sidebands on the interferometer input beam.

Since in the interferometer layout with tunable stability the beam spot sizes on the cavity mirrors as well as the cavity g-factors are changed in each step toward the targeted arm cavity length, this results in changing transfer functions for beam jitter noise coupling. Plots of transfer functions for jitter sidebands to fundamental mode modulation sidebands in the detection port of the interferometer are shown in Figure 4.14 for different arm cavity lengths.

The transfer functions were extracted from a FINESSE-based model of the tunable stability interferometer. The model can be found in Appendix A. To simulate the coupling of input beam pointing fluctuations, a pure first order mode beam was modulated in amplitude to generate jitter sideband fields. These were propagated through the virtual interferometer in which the arm cavity mirrors were subject to static misalignments. For all transfer functions shown in Figure 4.14, a differential static misalignment of 10^{-8} rad was assumed for the arm cavity input mirrors and end mirrors, respectively. To estimate the magnitude of first order mode sidebands converted to fundamental mode modulation sidebands the fundamental mode amplitude was detected in the asymmetric port and demodulated at the amplitude modulation frequency of the input beam.

The frequency response represented by the transfer functions is a consequence of the superposition of modulation sideband fields promptly reflected at the arm cavities and sidebands leaking out of the cavities. Since upper and lower jitter sidebands are symmetrically arranged around the carrier frequency their frequency spacings, with respect to first order mode resonance in the arm cavities, are different. Hence the different frequency responses of upper and lower sidebands.

As can be seen, the g-factor of the arm cavities has a significant impact on the magnitude of jitter sideband coupling to the interferometer signal and increases by almost two orders of magnitude in the course of the stepwise approach to the marginally stable configuration.

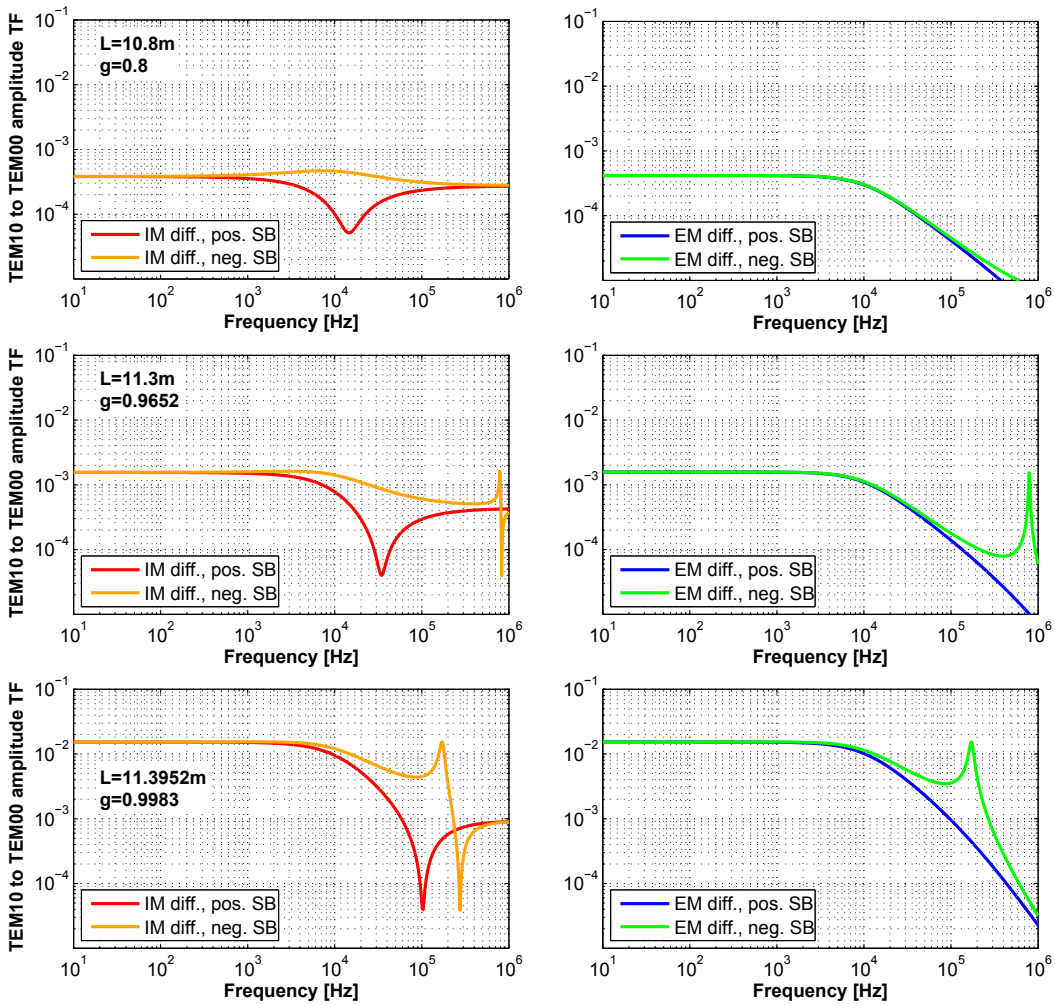

Figure 4.14: Transfer functions for input beam jitter to fundamental mode modulation sidebands in the detection port, for different arm cavity lengths and, correspondingly, different cavity stability parameter values. In each row in the figure the left-hand side and right-hand side plot shows the upper and lower sideband transfer functions for differentially misaligned arm cavity input mirrors and end mirrors, respectively, for a given cavity length. The magnitude of the transfer functions and hence the coupling of input beam pointing fluctuations to the main readout channel increases as the arm cavities approach the marginally stable configuration.

The noise in the interferometer signal caused by beam pointing needs to be arranged for below the targeted sensitivity of the interferometer, including sufficient margin. A requirement for beam pointing in the target configuration, based on a tentative readout scheme for the main interferometer signal, was given in [56].

Possible measures to reduce beam pointing are the introduction of additional means of mode cleaning of the input beam, for the conversion of beam geometry fluctuations to intensity fluctuations which are suppressed by the common-mode

rejection in the interferometer. Since the mode cleaner cavity may be driven by seismic motion itself and give rise to additional beam pointing fluctuations, suspending the cavity mirrors is an option to reduce this effect. In addition to this, better isolation of the input optics for steering and beam shaping, the reduction of the static misalignment of the interferometer optics and the reduction of the beam spot size on the input optics pose further options for keeping beam jitter noise manageable. Finally, active suppression of beam pointing based on wave-front sensing, as described in [147], may be considered as an option.

Measurements to characterize the pointing stability of the main laser in the AEI 10 m Prototype are planned to be carried out in the future. These will serve as a basis for further considerations aiming at reducing the impact of beam pointing in the interferometer. The role of beam pointing noise in the tunable stability scheme in particular will be clarified in the scope of the planned *single arm test* experiment which is introduced in Chapter 6.

4.8 Summary

In this chapter, a detailed optical layout for the AEI 10 m sub-SQL interferometer, based on a robust procedure to bring the interferometer to its final configuration with marginally stable arm cavities, was described. Starting with the arm cavities set to be shorter than eventually required, but with all other parameters unchanged, significantly increased stability of the arm cavity eigenmode can be realized. This is desirable to allow initial commissioning of the AEI 10 m sub-SQL interferometer. A step-by-step approach to the final, marginally stable cavity mode was proposed.

In order to realize a close-to-optimal mode matching to the arm cavities, over the whole range of spot sizes, a collimated beam of variable size is employed in combination with arm cavity input mirror substrates with curved front and rear sides. It was found that the mode matching for different arm cavity lengths can be nearly completely recovered by changing the size of the incident laser beam, while the associated change of the eigenmode waist position only degrades the mode matching on the sub-percentage level.

The robustness analysis that was performed shows that the most stringent requirements for manufacturing accuracy are imposed by the curvatures of the input mirror rear surfaces, while deviations from all other design parameters are either mostly uncritical or can easily be compensated for by changing of free parameters in the optical setup.

It was furthermore pointed out that several aspects of the work presented in this chapter are of interest for the wider community, such as for instance the possibility to directly measure coating Brownian noise with the AEI 10 m sub-SQL interferometer at frequencies around 200 Hz. Moreover, the proposed optical layout will allow to determine how close to instability one can realistically operate the arm cavities of a Fabry-Perot Michelson interferometer, which is one of the key-questions for future GW detectors.

CHAPTER 5

Modeling the sub-SQL interferometer with realistic mirrors

A fundamental question which needs to be addressed when constructing a high precision optical experiment is the required quality of the mirrors to be used. Especially optics which serve as cavity mirrors for the arm resonators of a laser interferometer need to meet stringent requirements in terms of surface irregularity, in order not to impede the performance of the instrument by giving rise to excessive optical losses or a strong deformation of the geometry of the laser mode.

In the present case of the 10 m sub-SQL interferometer the marginal stability of the arm cavities and large beam spots on the mirrors potentially result in partial degeneracy of higher-order transverse modes and increased diffraction loss and give rise to particularly challenging requirements.

In this chapter investigations of the impact of realistic mirror surface deformations on the performance of the sub-SQL interferometer with marginally stable arm cavities are presented. To evaluate the dependence of the interferometer performance on mirror surface quality it is necessary to identify meaningful figures of merit. The optical round-trip loss in the arm cavities and the interferometer contrast defect are motivated as suitable figures of merit in the present case.

A grid-based numerical model of the sub-SQL interferometer with realistic mirrors which provides high modal resolution to account for the marginal stability of the interferometer arm cavities is introduced. With the aid of spectral methods phase maps representing the surface topography of realistic mirrors were generated and integrated into the model.

A detailed parameter study with this model was carried out on a high-performance computer cluster. The extracted information can be used, for instance, to infer the required surface figure for the actual interferometer mirrors.

5.1 Mirror surface topography and optical losses

In order to reach the sensitivity goals in high-precision laser interferometers high laser powers and low optical losses need to be maintained. Common sources of

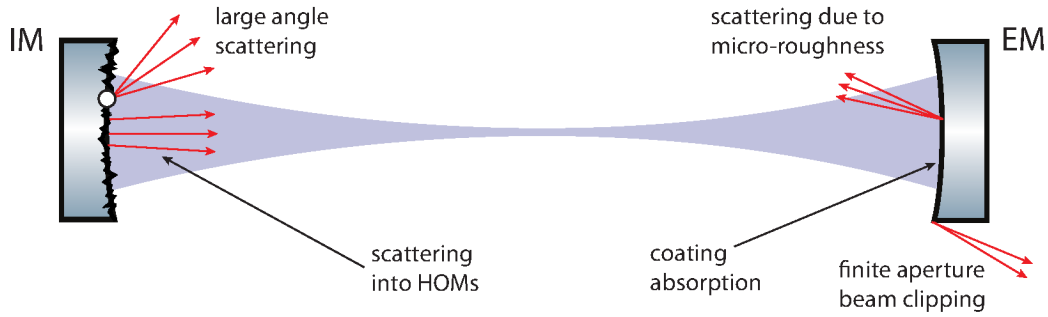

Figure 5.1: Sources of cavity round-trip loss. Long and short wavelength surface distortions correspond to small and large scattering angles, respectively. Light scattered at small angles may remain in the cavity and can be viewed as fundamental mode light converted to HOMs. The larger the beam size of the cavity eigenmode, the larger the fraction of light which is subject to loss due to diffraction at the mirror apertures. Point defects give rise to light scattered at large angles. Finally, besides diffraction effects, light absorption in the optical coatings also contributes to the round-trip loss.

optical losses are e.g. imperfect matching of the input beam to the eigenmodes of the cavities in the interferometer, absorption of light in coatings and substrates of optical elements, light transmission through the interferometer end mirrors, scattering and light diffraction at apertures in the optical setup. Especially scattering and absorption which occurs in arm cavities needs to be controlled since their effect on the circulating fields is amplified by the finesse of the cavity. Besides a reduction of the finesse of the cavity and consequently lower circulating laser power the loss mechanisms mentioned above may also affect the modal purity of the reflected and transmitted fields which gives rise e.g. to non-perfect interference of the fields at the beam splitter and additional noise in the detection port. The notion of *round-trip loss* (RTL) describes the power which is lost in each cavity round-trip of the circulating light. Loss mechanisms that contribute to the RTL of a cavity are coating absorption, scattering and diffraction loss, cf. Figure 5.1.

The round-trip loss in the arm cavities of state-of-the-art interferometers is typically dominated by scattering loss. A detailed introduction to the sources of scattered light is given in Section 5.1.1. However, in cavities with large beam sizes, as in the case of the sub-SQL interferometer, diffraction at the mirror apertures gains significance. A commonly used model to predict diffraction loss at mirror apertures is the *clipping approximation* which is based on the assumption that diffraction loss stems from the portion of light falling out of the mirrors' apertures which is simply clipped [148]. It turns out that diffraction loss is typically underestimated by this model. Higher losses are to be expected in an actual cavity due to the fact that in this approximation the deformation of the reflected mode is not accounted for [149].

Numerical models of realistically apertured arm cavities confirmed this shortcoming of the clipping model [150].

Coating absorption plays a less significant role since very low absorption can be achieved with contemporary ion-beam sputtered coatings. For instance, coating absorption in the sub-ppm range for coatings optimized for $\lambda_0 = 1064\,\mathrm{nm}$ was reported on in [140].

5.1.1 Sources of light scattering

In this section the sources of scattering in laser interferometers are reviewed. Purely specular reflection of light occurs at a perfectly smooth boundary between two media with different refractive indices. In a microscopic picture the macroscopic material constants reflectivity, transmittance and refractive index are revealed as statistical properties averaged over a large quantity of coupled scatter events on a microscopic scale, i.e. a reflected laser beam can be regarded as the summation over many scatter components that are similar in direction and phase. Light which is scattered out of a reflected laser beam is the result of fluctuations in the homogeneity of the reflective surface. The dominance of either specular or *Lambertian* reflection, i.e. diffusely reflected light, is determined by the topography of the reflecting surface.

In the following, beam angles of incidence will be limited, without loss of generality, to near normal incidence. The theory of scattering at a sinusoidal diffraction grating relates the scattering angle $\Theta_{\mathrm{scatter}}$ with the spatial frequency f_{sp} of the grating, and can for small angles of incidence be approximated as

$$\Theta_{\mathrm{scatter}} = f_{\mathrm{sp}} \times \lambda \,, \tag{5.1}$$

where λ is the laser wavelength. Obviously, low spatial-frequency fluctuations of optical surfaces result in small scattering angles and vice versa. What follows immediately from this relation is that only beams with diameters larger than the spatial wavelength $\Lambda := 1/f_{\mathrm{sp}}$ will sense a sinusoidal surface distortion with spatial frequency f_{sp}. In practice, diffraction will occur for beams which are larger than the spatial wavelength Λ by a factor of approximately three to five [151].

Furthermore, for optical cavities a distinction can be made between light that is scattered at small angles below a specific threshold angle, such that it remains within the mirrors' apertures, and light scattered a angles larger than this threshold, cf. Figure 5.2. Light which is scattered at angles larger than the threshold angle Θ_{th} can be regarded escaping the cavity, i.e. it is lost for good. For an arm length of approximately 11.4 m and a mirror diameter of 48.6 mm one obtains a threshold angle of $\Theta_{\mathrm{th}} \approx 2.1\,\mathrm{mrad}$ which is related via Equation (5.1) to a spatial frequency of the surface fluctuations of $f_s \approx 2000\,\mathrm{m}^{-1}$.

Light which is scattered at smaller angles is likely to remain within the cavity. As was shown by *Winkler et al* in [152], fundamental mode scattering at small angles can be described as scattering of light from the TEM_{00} mode into higher-order transverse modes. Implications of fundamental mode scattering into HOMs

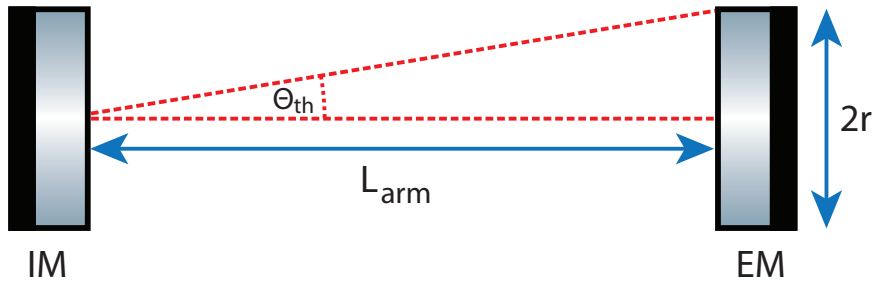

Figure 5.2: Definition of the cavity scattering threshold angle. By assuming that most of the light power is concentrated at the center of the mirror it is found that in a marginally stable sub-SQL interferometer arm cavity with $L \approx 11.4\,\mathrm{m}$ and mirror diameters of 48.6 mm the light is lost for good if it is diffracted by mirror surface fluctuations with a spatial frequency higher than $f_s \approx 2000\,\mathrm{m}^{-1}$.

in marginally stable, near-degenerate cavities will be discussed in the following section.

The scattered light power is related to the amplitude of the fluctuations of the scattering surface. Opposed to the comparatively simple relationship for the dependence of the scattering angle on the spatial frequency of the surface fluctuations, predicting the amplitude of the scattered fields is considerably more difficult and requires the application of diffraction theory. Since exact solutions are available only for special cases, numerical solutions prove a useful tool to obtain solutions for more general scenarios and will hence form the basis of the investigations presented later in this chapter.

A commonly used quantity to describe the total scattered light power, integrated over all solid angles, is the *total integrated scattering* (TIS) which is given as [153]

$$\mathrm{TIS} = \frac{P_{\mathrm{specular}}}{R P_{\mathrm{inc}}} \simeq \left(\frac{4\pi\sigma_{\mathrm{surf}}}{\lambda}\right)^2 , \tag{5.2}$$

with P_{inc} the incident light power, P_{specular} the power of the light subject to specular reflection, R the power reflectivity of the surface and σ_{surf} the RMS deviation of the surface figure from the ideal form (cf. Figure 5.3). The equation holds for sufficiently smooth surfaces with $\lambda \gg 4\pi\sigma_{\mathrm{surf}}$. Furthermore, it was pointed out by *Yamamoto* in [154] that this equation is valid for surfaces with a power spectral density (PSD) proportional to f_s^{-1}. To quantitatively describe the properties of optical surfaces, the use of spectral densities is widespread throughout the field of optical surface metrology. A PSD represents an infinite number of actual optical surfaces which have the same statistical properties with respect to their surface topography, cf. Section 5.4.1.

So far it has been assumed that scattering occurs at a single surface of an optical element. However, highly reflective mirrors are composed of polished substrates to

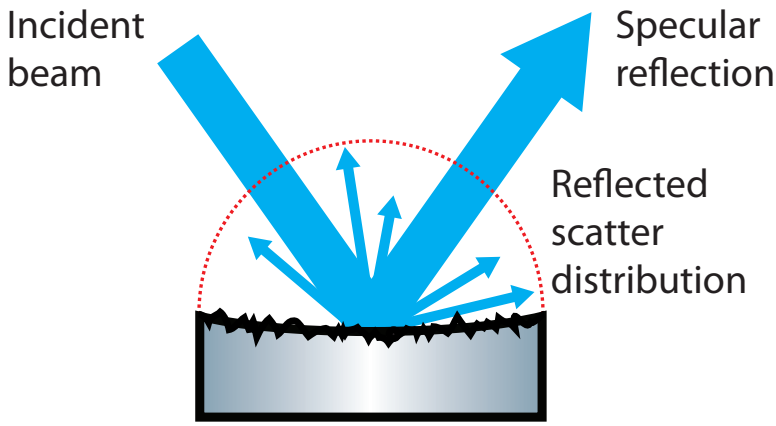

Figure 5.3: Specular reflection and Lambertian reflection at a mirror with an irregular surface. The total integrated scattering, cf. Equation (5.2), is obtained by integrating the scattered light power over all scattering angles in the half-sphere facing the surface of the mirror.

which numerous dielectric coating layers are applied. Whereas in coatings which are applied with standard methods, e.g. electron beam deposition, additional scattering from the dielectric layers can be observed, in high-quality coatings such as ion-beam sputtered coatings the surface topography of the coating layers follows the mirror substrate surface figure [155]. This means that for mirrors with good polishing and IBS coatings the quality of the substrate surface determines the scattering characteristics of the optic and the model of a single scattering surface holds to very good approximation. However, for fluctuations with very large spatial wavelength Λ also IBS coatings exhibit inhomogeneities, which demands for more elaborate models to investigate scattering effects.

Finally, an important source of scattering at large angles are sporadically distributed impurities and point defects of any kind. These are expected to strongly increase the overall scatter [156] and need to be controlled to ensure low optical losses. Due to their small dimensions and the resulting large scattering angles point defects are not resolved by conventional optical models which are based on the paraxial approximation. However, diffraction theory can be employed to estimate point defect-induced scattering loss [157].

For a comprehensive discussion of the subject of light scattering see e.g. [151].

5.1.2 Implications of light scattering in interferometers

An immediate consequence of scattering in laser interferometers are increased optical losses. As pointed out previously, in order to maintain good performance of optical cavities it is required that optical losses are sufficiently low. The round-trip loss of an optical cavity is defined as the fraction of the circulating light field that is lost on each round-trip, i.e. for a linear two mirror resonator after two reflections at

the input mirror and at the end mirror, respectively, and twice the propagation of the distance between the two mirrors.

To quantitatively assess the round-trip loss of a cavity, energy conservation can be utilized [158]. The light power incident on a cavity equals the sum of reflected and transmitted power and the light which is lost,

$$P_{\text{inc}} = P_{\text{refl}} + P_{\text{trans}} + P_{\text{loss}} \,. \tag{5.3}$$

By dividing this expression by the circulating power P_{circ} one obtains

$$\frac{P_{\text{inc}}}{P_{\text{circ}}} = \frac{P_{\text{refl}} + P_{\text{trans}} + P_{\text{loss}}}{P_{\text{circ}}} \,. \tag{5.4}$$

This can be re-arranged to obtain the light power lost per Watt of circulating power in the cavity,

$$\frac{P_{\text{Loss}}}{P_{\text{circ}}} = \frac{P_{\text{inc}} - P_{\text{refl}} - P_{\text{trans}}}{P_{\text{circ}}} := \text{RTL} \,, \tag{5.5}$$

which is the definition of the cavity round-trip power loss.

Especially for numerical investigations it has proven useful to formulate the round-trip loss as a function of the powers of the incident, reflected, transmitted and circulating fields since these quantities are often easy to extract from the models.

Similar to the definition given above, energy conservation can be utilized for the fraction of the fields in the fundamental mode to obtain the fundamental mode round-trip loss (RTL_{00}), which is given as

$$\text{RTL}_{00} := \frac{P_{\text{inc}} - P^{00}_{\text{refl}} - P^{00}_{\text{trans}}}{P^{00}_{\text{circ}}} \,, \tag{5.6}$$

where P^{00}_{refl}, P^{00}_{trans} and P^{00}_{circ} are the powers of the reflected, transmitted and circulating light in the fundamental mode, respectively. In contrast to the round-trip loss defined in Equation (5.5) the fundamental mode round-trip loss also accounts for light converted to HOMs as losses. This is justified since light returning from the arm cavities which is not in the fundamental mode may not interfere destructively in the dark port of the interferometer, i.e. it is lost for the measurement.

For interferometers with stable high-finesse arm cavities it was found that, to very good approximation, the round-trip losses obtained from numerical simulations were equivalent to the round-trip loss projected to the fundamental mode [159]. This is a convenient finding since in simulations which are based on a representation of the light fields by numerical grids calculating the RTL_{00} requires the additional effort of projecting fields in the perturbed case to reference fields obtained from a simulation with unperturbed cavities. However, for the sub-SQL interferometer with marginally stable, near-degenerate arm cavities this simplification does not hold, cf. Section 4.7.1 in Chapter 4.

If HOMs experience significant buildup in the cavity this will result in a deformation of the cavity eigenbeam which is no longer a pure TEM_{00} field. This new

eigenbeam is a superposition of the fundamental mode with spot size w_0 on the cavity mirrors and HOMs with approximated spot sizes [152]

$$w_n \approx \sqrt{n} w_{n=0} \ , \tag{5.7}$$

which holds for large mode orders n. Since the distorted eigenbeam will exhibit larger beam sizes on the cavity mirrors, increased light loss due to diffraction at the mirror apertures is a likely consequence. *Klaassen et al* showed that small-angle scattering due to mirror surface irregularity in frequency-degenerate cavities gives rise to transverse mode coupling and changed eigenbeams and eigenfrequencies which results in inhomogeneous broadening of the measured cavity resonance [160].

Due to the fact that the surfaces of the mirrors in each arm will be differently aberrated the laser beam will be differently distorted resulting in a non-perfect overlap at the beam splitter of the fields reflected at the arm cavities. This gives rise to a larger contrast defect which potentially decreases the performance of the instrument and needs to be controlled. The role of contrast defect in the sub-SQL interferometer will be discussed in Section 5.2.1.

Besides giving rise to optical losses, scattered light may also degrade the sensitivity of the instrument by recombining with the measurement beam and introducing modulation signals. These false signals are a consequence of reflection of the scattered light at unsuspended infrastructure driven by seismic motion [161]. However, a detailed investigation of this phenomenon is not within the scope of this work.

5.2 Figures of merit for the mirror surface quality

To set a limit on the tolerable deviations of the interferometer mirrors' surfaces from the ideal shape it is necessary to identify meaningful figures of merit, i.e. quantitative relationships between the mirror surface quality and the performance of the interferometer. Roughly speaking, the mirrors need to be manufactured with sufficiently high quality to ensure that the scientific goals of the experiment can be reached. Since the first intermediate goal of the interferometer is to reach a purely quantum noise-limited sensitivity in its detection band at hundreds of Hertz, it is required that classical noise terms are not increased as a result of poor mirror surface figure. In the next phase of the experiment it is planned to employ advanced techniques aiming at the reduction of quantum noise and to demonstrate measurements with sub-SQL sensitivity. Effective use of advanced techniques for quantum noise reduction requires optical losses to be sufficiently low.

For the investigations presented in the following the contrast defect ζ at the beam splitter of the interferometer and the round-trip loss in the arm cavities as figures of merit.

5.2.1 Arm cavity imbalance, contrast defect and noise couplings

The contrast defect is a measure for how well the beams returning from the two arm cavities interfere at the beam splitter of the interferometer, which depends on their

relative deformation after reflection at the interferometer arms. The contrast defect at the beam splitter is defined as

$$\xi := 1 - C = 1 - \frac{P_{\text{sym}} - P_{\text{asy}}}{P_{\text{sym}} + P_{\text{asy}}} , \tag{5.8}$$

where P_{sym} is the power of the light reflected by the interferometer tuned to the dark fringe, measured in the symmetric port, and P_{asy} the light power measured in the asymmetric port, i.e. the detection port of the interferometer. In a perfect interferometer with identical arm cavities which is locked to the dark fringe, no light leaks into the detection port. The interferometer exhibits a contrast of $C = 1$, i.e. $\xi = 0$. In a realistic interferometer the maximally achievable contrast is reduced as a consequence of imbalances in the arm cavities.

These imbalances need to be controlled because they give rise to the coupling of laser noise to the main interferometer signal [162]. For instance, laser intensity noise, which is the dominant classical noise contribution to the sub-SQL interferometer noise budget after coating Brownian thermal noise, couples to the interferometer signal via imbalances in the mirror masses, the arm cavities' finesse, loss imbalance, imperfect splitting ratio of the beam splitter and a mismatch of the relative arm cavity length, assuming homodyne readout and sufficiently large laser powers or low mirror mass such that radiation pressure plays a role [163]. For the loss imbalance of the sub-SQL interferometer a targeted value of $\Delta\varepsilon = \pm 15\,\text{ppm}$, i.e. a difference in RTL of the arm cavities, was given in [60]. The loss imbalance can be related to the contrast defect of the interferometer via [163]

$$\xi = \frac{2\Delta\varepsilon}{T} , \tag{5.9}$$

where T is the power transmittance of the arm cavity input mirrors, which yields a tolerable contrast defect of $\xi \leq 3.2 \times 10^{-3}$ for the sub-SQL interferometer.

For the initial LIGO and enhanced LIGO GW detectors, for example, contrast defects of $\xi_{\text{iLIGO}} \lesssim 3 \times 10^{-3}$ and $\xi_{\text{eLIGO}} \lesssim 1 \times 10^{-3}$, respectively, were assumed as requirements [164]. A contrast defect as low as $\xi \sim 10^{-4}$ was determined experimentally in the LIGO Hanford interferometer [165].

The most elegant solution to keep the degradation of the contrast at a tolerable level is, naturally, to avoid it in the first place by arranging for sufficiently low phase front distortion in the arm cavities, e.g. by employing mirrors with sufficiently low surface irregularity. To alleviate the effects of a given contrast defect, two options come to mind immediately. The effect of *mode healing*, which can be encountered in interferometers with signal recycling (SR) [15] cavities, has the potential to cure modal deformation of laser beams [166]. However, SR is not part of the baseline design of the sub-SQL interferometer but may be adopted as a future upgrade of the experiment. Another option is the use of an output mode cleaner (OMC) cavity [94]. These are employed to strip light in HOMs and RF sidebands from the field in the detection port prior to photo detection. By choosing the round-trip Gouy phase of the OMC cavity accordingly, it can be arranged for carrier resonance while HOMs

are suppressed to a large degree. In this way light which would not contribute to the signal but increase shot noise can be prevented from reaching the photo detector. However, coupling of input laser noise via the fundamental mode to the interferometer signal cannot be reduced with this approach.

5.2.2 Round-trip loss and quantum noise reduction techniques

After reaching the first intermediate goal of a purely quantum noise-limited sensitivity at frequencies in the detection band centered at about 200 Hz, the sub-SQL interferometer experiment aims at surpassing the SQL for its 100 g test masses. To achieve this, different scenarios based on squeezing injection [167], balanced homodyne detection (BHD) [168] as well as combinations of both techniques [18] were proposed in the past.

Squeezing injection and back-action evasion schemes share the property that they are highly susceptible to optical losses. Wherever losses occur in the optical train, squeezed fields are replaced with conventional, i.e. unsqueezed vacuum fields which increases the noise in the measurement [169]. Therefore, it is evident that optical losses need to be controlled to optimize the benefit from these techniques for the sensitivity of the interferometer.

In the following, as a realization of a back-action evasion measurement, the narrow band cancellation of quantum radiation pressure noise by means of frequency independent balanced homodyne detection is discussed, cf. Figure 5.4. This back-action evasion technique, in particular, was proposed for an application in the sub-SQL interferometer in [170]. With BHD an arbitrary quadrature of the interferometer output field can be read out. For a coherent amplitude of the dark port field much smaller than the coherent amplitude of the LO field, $\alpha_{\mathrm{DP}} \ll \alpha_{\mathrm{LO}}$, one obtains a difference signal of the photo currents i_Δ of the form

$$i_\Delta(\phi) \propto \alpha_{\mathrm{LO}} \left(\hat{X}_1 \cos(\phi) + \hat{X}_2 \sin(\phi)\right) \ , \tag{5.10}$$

i.e. the difference signal is obtained from a quadrature $\hat{X}(\phi)$ which is composed of a superposition of $\hat{X}_1$ and $\hat{X}_2$, the amplitude and phase quadrature of the output field, respectively. The quadrature angle can be chosen by adjusting the phase ϕ of the LO field. Compared to DC readout [171], balanced homodyne detection with an external LO has the advantage that in principle no dark fringe offset needs to be introduced to the interferometer, resulting in better common mode rejection of input laser noise of the interferometer.

Balanced homodyne detection could be made effective use of already in early iteration steps of the initial configuration since quantum radiation pressure is limiting at frequencies $\lesssim 100$ Hz, cf. Figure 4.4 in Chapter 4. In the marginally stable configuration with conventional end mirrors, classical noise is reduced to the shot noise level at $\simeq 100$ Hz, increasing the headroom for back-action evasion demonstrations. Optionally, in order to "artificially" increase quantum radiation-pressure noise the interferometer input power could be increased.

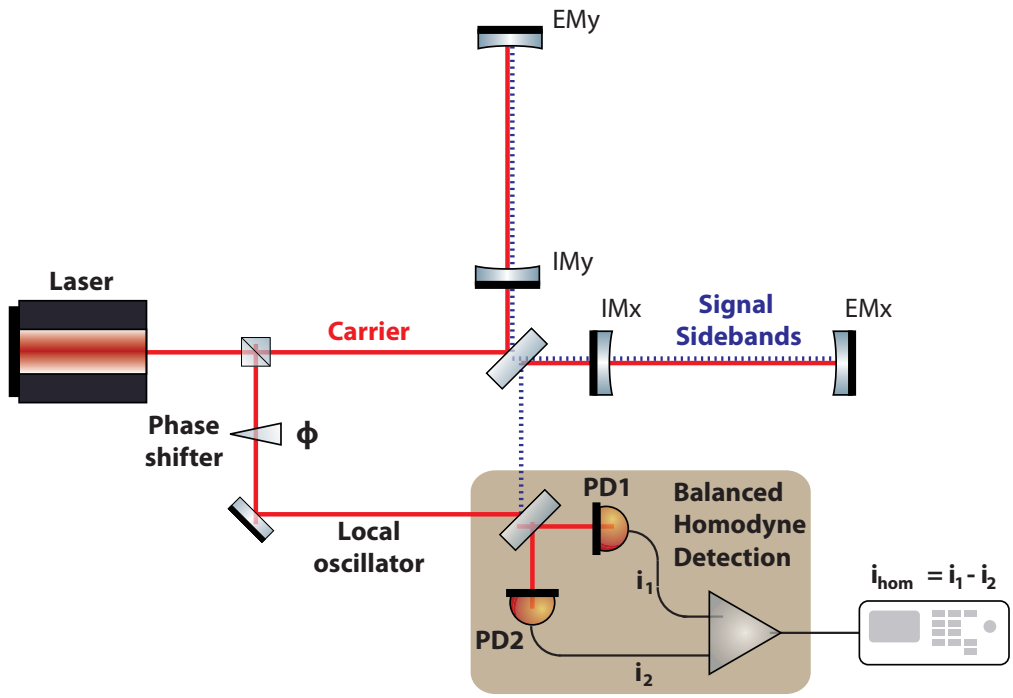

Figure 5.4: Schematic drawing of an interferometer with balanced homodyne readout. The interferometer is kept at the dark fringe by means of feedback control of the differential arm length longitudinal degree of freedom. A local oscillator (LO) beam is picked off from the interferometer input beam and is superimposed with the signal field exiting the interferometer. By adjusting the phase ϕ of the local oscillator field the signal quandrature for readout can be selected.

From the targeted total loss in the interferometer arm cavities of $1 - r_c^2 = 4.99\,\%$ [60] the maximum round-trip loss can be inferred by solving

$$r_c = \frac{r_{\mathrm{IM}} - \sqrt{1 - t_{\mathrm{EM}}^2 - \mathcal{A}}}{1 - r_{\mathrm{IM}}\sqrt{1 - t_{\mathrm{EM}}^2 - \mathcal{A}}} \tag{5.11}$$

for the average losses per mirror, $\mathcal{A}$. The result is a value of $\mathcal{A} = 55\,\mathrm{ppm}$, i.e. $110\,\mathrm{ppm}$ for the round-trip power loss.

In the following, a quantum noise model for the sub-SQL interferometer with balanced homodyne detection will be presented. The parameters in this model are based on the initial sub-SQL interferometer configuration with conventional arm cavities, cf. Chapter 4. The model includes lossy arm cavities and the option to set an arbitrary homodyne phase in the readout stage. Since the impact of arm cavity losses on the performance of the back-action evasion capabilities is of primary interest, optical losses in the output optics train including the beam splitter were omitted. A selection of parameters relevant for the noise model is given in Table 5.1.

Table 5.1: Key parameters of the sub-SQL interferometer relevant for estimating the quantum noise in the instrument.

Parameter	Symbol	Value
Mirror mass	m	100 g
Arm length	L	$\sim 10\,\mathrm{m}$
Arm cavity half bandwidth	γ	$\frac{T_{\mathrm{IM}}c}{4L} \simeq 2\pi \cdot 11 \times 10^3\,\mathrm{s}^{-1}$
Carrier frequency	ω_0	$1.8 \times 10^{15}\,\mathrm{s}^{-1}$
Signal frequency	Ω	—
Light power at the beam splitter	I_0	$\sim 5.5\,\mathrm{W}$
Light power to reach SQL	I_{SQL}	$\frac{mL^2\gamma^4}{4\omega_0} \simeq 2.24 \times 10^4\,\mathrm{W}$
Strain SQL	h_{SQL}	$\sqrt{\frac{8\hbar}{m\Omega^2L^2}} \simeq 1.5 \times 10^{-22}\frac{\gamma}{\Omega}\mathrm{Hz}^{-1/2}$
Opto-mechanical coupling	$\mathcal{K}$	$\frac{I_0/I_{\mathrm{SQL}}2\gamma^4}{\Omega^2(\gamma^2+\Omega^2)}$

The quantum noise spectral density of a lossless Fabry-Perot Michelson interferometer with homodyne detection reads [172]

$$S_h = \frac{h_{\mathrm{SQL}}^2}{2}\frac{1+(\mathcal{K}-\cot(\zeta))^2}{\mathcal{K}}\,, \tag{5.12}$$

where ζ is the homodyne phase,

$$h_{\mathrm{SQL}} = \sqrt{\frac{8\hbar}{m\Omega^2L^2}} \tag{5.13}$$

is the strain SQL and

$$\mathcal{K} = \frac{2(I_0/I_{\mathrm{SQL}})\omega_c^4}{\Omega^2(\omega_c^2+\Omega^2)} \tag{5.14}$$

is the coupling constant first introduced in [18]. Here, ω_c is the angular frequency of the carrier field, Ω is the signal frequency, I_0 is the laser power at the beam splitter of the interferometer and

$$I_{\mathrm{SQL}} = \frac{mL^2w_c^4}{4\omega_0}$$

is the laser power required in a conventional interferometer to reach the SQL. Optical losses can be accounted for in Equation (5.12) by introducing the loss-modified coupling constant $\mathcal{K}_*$ which reads [18]

$$\mathcal{K}_* = \mathcal{K}\left(1-\frac{1}{2}\mathcal{E}(\Omega)\right)\,. \tag{5.15}$$

The quantity $\mathcal{E}(\Omega)$ represents the net fractional loss of sideband photons in the arm cavities and reads

$$\mathcal{E}(\Omega) = \frac{2\epsilon}{1+\frac{\Omega^2}{\omega_c^2}}\,. \tag{5.16}$$

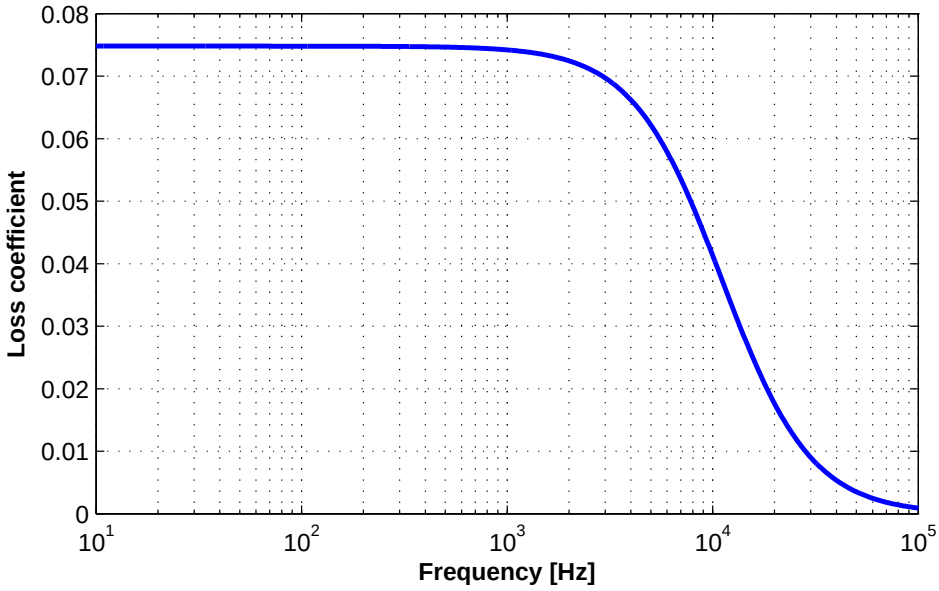

Figure 5.5: Fractional sideband photon loss in the sub-SQL interferometer arm cavities, assuming a round-trip loss of 110 ppm. The loss coefficient is weighted with the arm cavity pole to account for larger losses experienced by resonant sideband fields that undergo multiple reflections in the lossy cavity.

Equation (5.16) is obtained by weighting the net fractional loss of photons in the arm cavities,

$$\epsilon = \frac{2(2\mathcal{A} + T_{\mathrm{EM}})}{T_{\mathrm{IM}}} \,, \tag{5.17}$$

with the arm cavity pole. This is due to the fact that sideband fields that undergo multiple reflections inside the cavities experience larger losses than fields that are not resonant in the cavity. The net fractional sideband photon loss of the sub-SQL interferometer arm cavities, assuming a round-trip loss of 110 ppm, is shown in Figure 5.5. With the loss-modified coupling constant in Equation (5.15) one can write

$$\begin{aligned} S_{\mathrm{h}} = \frac{h_{\mathrm{SQL}}^2}{2\mathcal{K}_*} \Bigg[& \left(\left(1 - \frac{\mathcal{E}(\Omega)}{2} \right) \cdot \cot(\zeta) - \mathcal{K}_* \right)^2 + \\ & + \left(1 - \frac{\mathcal{E}(\Omega)}{2} \right)^2 + \mathcal{E}(\Omega) + \mathcal{E}(\Omega) \cot^2(\zeta) \Bigg] \end{aligned} \tag{5.18}$$

for the noise spectral density of a FPMI with homodyne readout with homodyne phase ζ and lossy arm cavities.

In the following, the benefit from back-action evasion by means of BHD in three different configurations will be compared: a hypothetical lossless sub-SQL inter-

ferometer, a configuration with the targeted round-trip losses given in [60] and a configuration approximately twice as lossy. The resulting quantum noise of these scenarios is shown in the plots in Figure 5.6 for different homodyne angles ζ. As expected, optical loss sets an upper limit to the benefit from balanced homodyne detection, in terms of the achievable back-action noise cancellation. In the case of lossless arm cavities it is worth noting that with the aid of balanced homodyne detection quantum radiation-pressure noise can be fully removed from the interferometer signal at a single frequency, below the SQL touching frequency, which can be selected via the phase of the local oscillator field. The quantum noise that remains at this frequency is shot-noise which was buried under radiation-pressure noise before. As can be seen in the top plot in Figure 5.6, the minima of the spectra for different homodyne angles reach the level of quantum shot-noise, if it is extrapolated from higher frequencies, where it dominates, to lower frequencies. Assuming lossless arm cavities, the model predicts theoretical SQL beating factors of ≈ 4.08, 2.83 and 2.04 at 70 Hz, 100 Hz and 150 Hz, respectively.

In the case of lossy arm cavities, quantum radiation-pressure noise cannot be completely removed from the measurement. Approximated to first order in the round-trip loss, the input field is attenuated by $\mathcal{E}(\Omega)$ in the interferometer arms. The fraction of the field which is lost is replaced with ordinary vacuum fluctuations at the output of the interferometer. The quantum radiation-pressure noise acting on the interferometer mirrors is increased by $\mathcal{E}(\Omega)/2$ in power, which originates from the noise field leaking into the lossy interferometer [18]. This additional loss-induced radiation pressure noise component cannot be removed from the measurement by means of BHD. For assuming a round-trip loss of each of the arm cavities of 110 ppm the model predicts theoretical SQL beating factors of ≈ 1.6, 1.87 and 1.66 at 70 Hz, 100 Hz and 150 Hz, respectively. Due to the fact that the loss-induced additional radiation pressure noise component is proportional to $1/\Omega^2$, the peak sensitivity is affected more strongly at homodyne angles resulting in cancellation of back action noise at lower frequencies. Finally, for a round-trip loss of each of the arm cavities of 250 ppm the model predicts theoretical SQL beating factors of ≈ 1.22, 1.54 and 1.52 at 70 Hz, 100 Hz and 150 Hz, respectively.

If the round-trip loss of both arm cavities is further increased by a factor of two, the model predicts that surpassing the SQL at frequencies $\lesssim 100$ Hz is barely possible. Hence, a round-trip loss of ~ 500 ppm is clearly too high to be tolerable. It can be concluded that the targeted round-trip loss of ≈ 100 ppm due to light scattering and absorption in the arm cavities is acceptable in terms of sufficient

Figure 5.6 ***(following page)*:** Back-action evasion in the sub-SQL interferometer by means of balanced homodyne detection. The resulting quantum noise spectral densities are plotted for different homodyne angles. The upper plot ❶ shows the lossless case, the middle plot ❷ is based on the targeted arm cavity round-trip loss of 110 ppm and in the bottom plot ❸ a round-trip loss of 250 ppm was assumed.

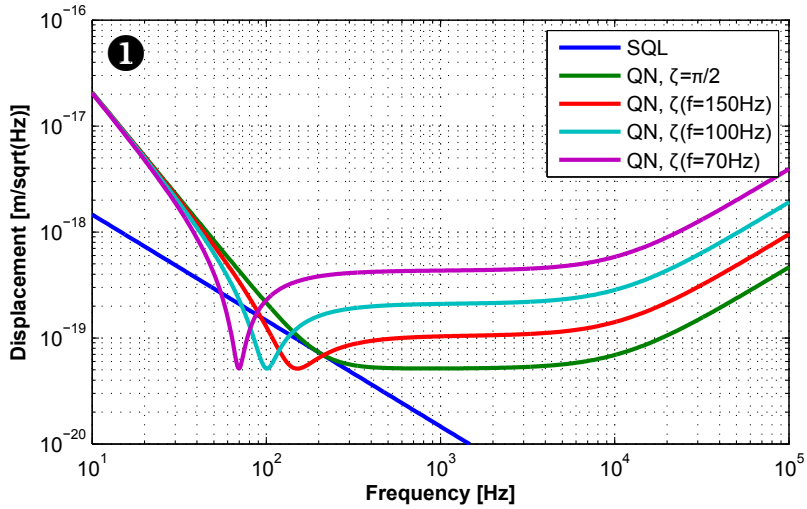
❶
SQL
QN, ζ=π/2
QN, ζ(f=150Hz)
QN, ζ(f=100Hz)
QN, ζ(f=70Hz)
Displacement [m/sqrt(Hz)]
Frequency [Hz]

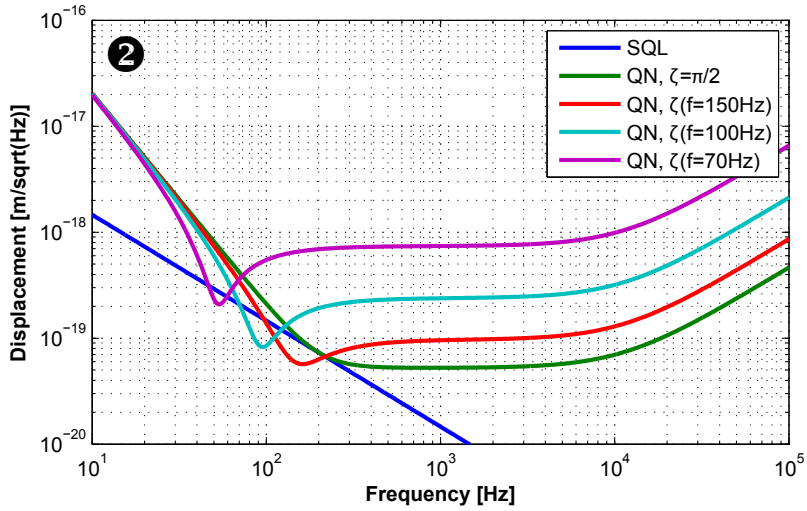
❷
SQL
QN, ζ=π/2
QN, ζ(f=150Hz)
QN, ζ(f=100Hz)
QN, ζ(f=70Hz)
Displacement [m/sqrt(Hz)]
Frequency [Hz]

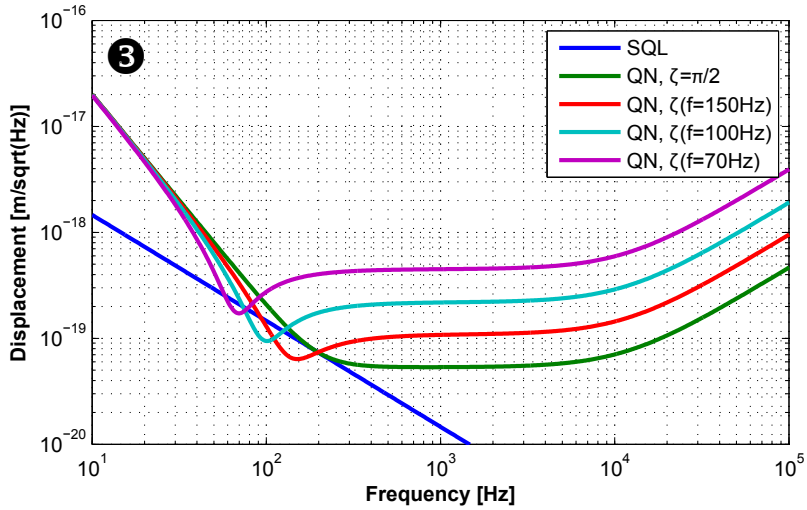
❸
SQL
QN, ζ=π/2
QN, ζ(f=150Hz)
QN, ζ(f=100Hz)
QN, ζ(f=70Hz)
Displacement [m/sqrt(Hz)]
Frequency [Hz]

headroom for the application of back-action evasion techniques, as one option to achieve a sensitivity in the interferometer below the SQL.

As was pointed out previously, in the case of marginally stable arm cavities the difference between round-trip loss and round-trip loss projected to the fundamental mode is – as opposed to the case of stable arm cavities – not negligible. It was shown in [173] that round-trip loss of the fundamental mode in a cavity is modeled equivalently by an increased end mirror transmittance. Since the end mirror transmittance directly contributes to the net fractional photon loss in the back-action evasion model, cf. Equation 5.17, it can be concluded that in fact the RTL_{00} is the quantity that is relevant for estimating the benefit from back-action evasion schemes. Hence, from the viewpoint of beating the SQL by means of back-action evasion, a value of $\mathrm{RTL}_{00} \lesssim 110\,\mathrm{ppm}$ can be confirmed as reasonable target for the round-trip loss of the interferometer arm cavities.

For the above discussions, scattering and absorption in the arm cavities were assumed as the only sources of loss present in the experiment. However, further sources of optical loss exist, which have an influence on the performance. These are e.g. losses at the Michelson beam splitter, non-perfect contrast at the homodyne beam splitter which is determined by the mode overlap of the local oscillator (LO) field and the signal field as well as the non-perfect quantum efficiency of the homodyne photo diodes.

Practical requirements for using balanced homodyne detection for interferometer readout are yet to be formulated. Whereas classical laser noise is suppressed by the balanced homodyne detector due to its property of common mode rejection, beam pointing noise, for instance, may lead to losses due to reduced overlap of the local oscillator field with the signal field as well as to noise originating from inhomogeneities in the active areas of the photo detectors. The need for good homodyne contrast gives rise to a requirement for relative beam pointing fluctuations of the signal field and the LO beam. The work presented in [174] relates the pointing stability of a laser beam to a time dependent overlap integral between a beam which is subject to pointing and a perfectly stable one. If this picture is transferred to balanced homodyne detection it becomes clear that beam pointing fluctuations cause frequency dependent losses which reduce the performance of the detector. A detailed discussion of noise sources in BHD and methods aiming at their mitigation can be found in [175].

As shown in the schematic drawing of a Michelson interferometer with BHD signal readout in Figure 5.4 the whole setup can be regarded as a Mach-Zehnder interferometer with a Michelson interferometer in one of its arms. It is thus clear that not only the Michelson degrees of freedom but also the Mach-Zehnder degrees of freedom need to be controlled to ensure stable operation at the designated working points, including the desired homodyne phase, which determines the detected quadrature of the signal field from the Michelson interferometer. A control scheme for balanced homodyne readout of a bench-top Michelson interferometer was successfully demonstrated in [176] and may serve as a basis for the development of a suitable control scheme for the application of this technique in the sub-SQL interferometer.

5.3 The grid-based Fabry-Perot Michelson interferometer model

It was first shown by *Sziklas and Siegman* [177] that propagation of light fields can be modeled with the aid of the *Huygens-Fresnel integral* with a simple algorithm involving Fourier transforms. This is extremely valuable for the practical application in numerical studies since solving the general Kirchhoff integral is computationally costly. A necessary condition for the application of the Huygens-Fresnel formula is the validity of the paraxial approximation, i.e. the modeled laser beams propagate under small angles with respect to the optical axis, cf. Section 2.1 in Chapter 2. This is the domain of scalar diffraction theory in which the effect of polarization is not modeled and magnetic fields are not explicitly calculated.

Vinet et al suggested to use this modeling technique for the design of laser interferometers [178] and pointed out its wide area of applicability, e.g. to accurately model effects such as mirror misalignments, curvature error, surface irregularity or substrate inhomogeneities. Ever since, grid-based simulations have, besides modal models, served as a basis for numerous modeling studies in the design and commissioning phases of laser interferometers, cf. e.g. [179–183].

With this method, propagation of a light field can be broken down into three steps, involving Fourier transforms of the fields:

- Calculation of the Fourier transform of the complex field $\Phi(x, y, z = 0)$ representing the light field of a cross section of the beam at an initial reference plane located at $z = 0$:

$$\tilde{\Phi}(k_x, k_y, 0) = \frac{1}{2\pi} \int_{-\infty}^{\infty} \int_{-\infty}^{\infty} \mathrm{d}x\mathrm{d}y \, \Phi(x, y, 0) \exp(i[k_x x + k_y y]) \, . \tag{5.19}$$

- Multiplication of the Fourier-transformed field with a momentum-space "propagator" $G_k(k_x, k_y, L)$, which propagates the field $\tilde{\Phi}$ by the distance L by acting on its phase:

$$\begin{aligned} \tilde{\Phi}(k_x, k_y, L) &= \tilde{\Phi}(k_x, k_y, 0) \times G_k(k_x, k_y, L) \\ &= \tilde{\Phi}(k_x, k_y, 0) \times \exp(i[k - \lambda\pi\{k_x^2 + k_y^2\}]L) \, . \end{aligned} \tag{5.20}$$

- Inverse Fourier transform of the field $\tilde{\Phi}(k_x, k_y, L)$ to obtain the propagated field in position-space:

$$\Phi(x, y, L) = \frac{1}{2\pi} \int_{-\infty}^{\infty} \int_{-\infty}^{\infty} \mathrm{d}k_x \mathrm{d}k_y \tilde{\Phi}(k_x, k_y, L) \exp(-i[k_x x + k_y y]) \, . \tag{5.21}$$

By discretizing the fields and the propagator and by replacing integrals with discrete summation, the method can be implemented as a computer algorithm in a straight-forward way. In particular, the use of the *Fast Fourier Transform* (FFT) algorithm, as was motivated in [177], significantly enhances the computational performance of the method.

The FFT algorithm, originally devised by *Cooley and Tukey* [184], is a particularly efficient variant of the discrete Fourier transform (DFT). The working principle of the FFT is to recursively compute a rank N DFT – which can be decomposed into two rank $N/2$ DFTs – from a series of rank 2 DFTs. Thus, a practical implications of the FFT algorithm is that the rank of the input vector needs to be an integer power of two. Whereas the computational cost of a rank N DFT are $O(N^2)$, the FFT scales significantly better with $O(N \log_2 N)$. For a two dimensional FFT, as encountered in the grid-based interferometer model, the speedup s is

$$s \propto \left(\frac{N}{\log_2 N} \right)^2 . \tag{5.22}$$

According to this formula, in the case of a two-dimensional grid with a rank of $N = 1024$ the FFT performs a factor of more than 10^4 better than the naive DFT.

For beam reflection, transmission or refraction at an optical element, each grid point of the field $\Phi(x, y)$ can be propagated independently, i.e. these operations are realized by adding phase factors to the complex grid points in position space [178]. Provided that the occurring optical path length differences $\Delta\mathrm{OPL}(x, y)$ are sufficiently small, the field after interaction with an optical component reads

$$\Phi_{\mathrm{out}}(x, y) = \Phi_{\mathrm{in}}(x, y) \times \exp(-ik\,\Delta\mathrm{OPL}(x, y)) . \tag{5.23}$$

Here, the right-hand side is, in the discretized form, mathematically treated as an element-wise multiplication of two arrays. To model the effect of finite apertures, the outgoing field is multiplied with an aperture function $A(x, y)$, i.e.

$$\Phi^{\mathrm{A}}_{\mathrm{out}}(x, y) = \Phi_{\mathrm{out}}(x, y) \times A(x, y) \tag{5.24}$$

where the aperture function for an optical element with circular aperture radius R is defined as

$$A(x, y) = \begin{cases} 1 & \sqrt{x^2 + y^2} \leq R \\ 0 & \text{otherwise} . \end{cases} \tag{5.25}$$

The grid-based interferometer model of the sub-SQL interferometer, that was used for the investigations presented later in this chapter, is based on the object-oriented optical FFT simulation library *OSCAR* [185]. This library was adapted and extended in many aspects to suit the requirements of the present simulation task. Numerous checks of the validity of results obtained with the OSCAR simulation were performed in the past, e.g. cross-checks against the modal simulation *FINESSE* [94], which were documented in [186]. Also, the OSCAR package was extensively used throughout the optical design of the Advanced Virgo GW detector [115], in

Figure 5.7 ***(following page)*****:** Flow chart of the computational steps carried out in a simulation run of the grid-based sub-SQL interferometer model.

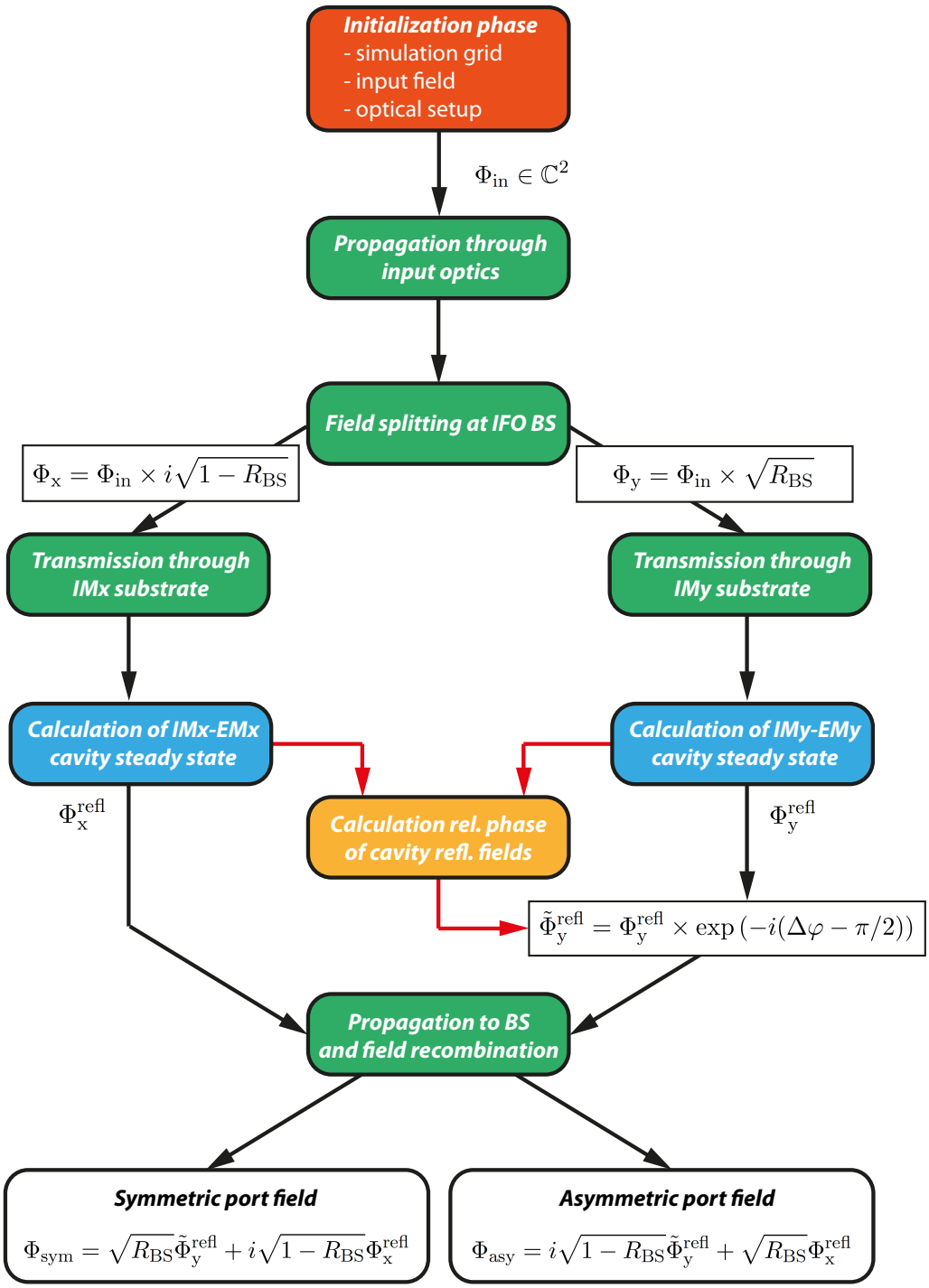
Initialization phase
- simulation grid
- input field
- optical setup
$\Phi_{\mathrm{in}} \in \mathbb{C}^2$
Propagation through input optics
Field splitting at IFO BS
$\Phi_{\mathrm{x}} = \Phi_{\mathrm{in}} \times i\sqrt{1 - R_{\mathrm{BS}}}$
$\Phi_{\mathrm{y}} = \Phi_{\mathrm{in}} \times \sqrt{R_{\mathrm{BS}}}$
Transmission through IMx substrate
Transmission through IMy substrate
Calculation of IMx-EMx cavity steady state
Calculation of IMy-EMy cavity steady state
$\Phi_{\mathrm{x}}^{\mathrm{refl}}$
Calculation rel. phase of cavity refl. fields
$\Phi_{\mathrm{y}}^{\mathrm{refl}}$
$\tilde{\Phi}_{\mathrm{y}}^{\mathrm{refl}} = \Phi_{\mathrm{y}}^{\mathrm{refl}} \times \exp\left(-i(\Delta\varphi - \pi/2)\right)$
Propagation to BS and field recombination
Symmetric port field
$\Phi_{\mathrm{sym}} = \sqrt{R_{\mathrm{BS}}}\tilde{\Phi}_{\mathrm{y}}^{\mathrm{refl}} + i\sqrt{1 - R_{\mathrm{BS}}}\Phi_{\mathrm{x}}^{\mathrm{refl}}$
Asymmetric port field
$\Phi_{\mathrm{asy}} = i\sqrt{1 - R_{\mathrm{BS}}}\tilde{\Phi}_{\mathrm{y}}^{\mathrm{refl}} + \sqrt{R_{\mathrm{BS}}}\Phi_{\mathrm{x}}^{\mathrm{refl}}$

particular to model the implications of aberrated mirror surfaces on the detector performance and to derive mirror polishing requirements.

In the following, the computational steps which are carried out in a simulation run of the grid-based sub-SQL interferometer model will be described:

1 | Initialization of the model.

2 | Propagation of the input laser field through the input optics chain.

3 | Splitting of the input field at the (idealized) beam splitter into two components, $\Phi_x = \Phi_{in} \times i\sqrt{1 - R_{BS}}$ propagating towards the arm in line with the input beam and $\Phi_y = \Phi_{in} \times \sqrt{R_{BS}}$ propagating towards the arm perpendicular to the input laser beam.

4 | Both fields are transmitted through the input mirror substrates, to the reference plane coinciding with the HR-coated surface of the arm cavity input mirrors.

5 | The steady state of both arm cavities is calculated. Arbitrary phase maps can be applied to the HR-coated surfaces of the input mirror and end mirror of the arm cavity to model realistic surface irregularities.

6 | The relative phase $\Delta\varphi$ of the field reflected at the arm cavities is calculated, the field reflected at the perpendicular arm cavity is multiplied with a phase factor $\tilde{\Phi}_y^{refl} = \Phi_y^{refl} \times \exp\left(-i(\Delta\varphi - \pi/2)\right)$ to account for the phase difference.

7 | The reflected fields are propagated to the beam splitter where they are superimposed, resulting in the field $\Phi_{sym} = \sqrt{R_{BS}}\tilde{\Phi}_y^{refl} + i\sqrt{1 - R_{BS}}\Phi_x^{refl}$ in the symmetric port and $\Phi_{asy} = i\sqrt{1 - R_{BS}}\tilde{\Phi}_y^{refl} + \sqrt{R_{BS}}\Phi_x^{refl}$ in the asymmetric port of the interferometer

A flow chart of the "top level" steps carried out in the grid-based simulation of the marginally stable Fabry-Perot Michelson interferometer is depicted in Figure 5.7.

For the calculation of the steady-state intra-cavity field an iterative scheme is employed [187], based calculating the resulting fields after multiple cavity round-trips, cf. Figure 5.8. In each round-trip, the initial field is subject to losses due to transmission at the cavity mirrors as well as optical losses due to diffraction, i.e. its amplitude decays in the course of the iteration scheme. The required number of round-trips depends on the finesse of the cavity and the desired accuracy of the solution. For instance, to achieve an accuracy of the simulation result of 10^{-5} in power, in the case of a sub-SQL interferometer arm cavity with a finesse of ≈ 670, the computation of ≈ 2600 round-trips is necessary before the iteration algorithm terminates. Prior to the computation of the steady-state field the resonance phase of the cavity is determined with an algorithm originally devised in [188]. For a more detailed technical exposition of the model see [186].

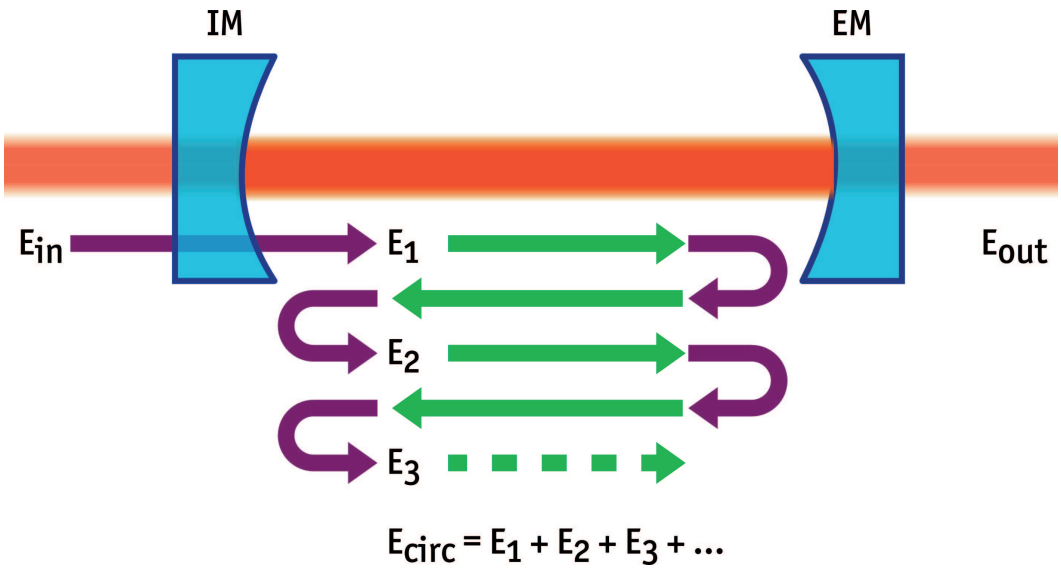

Figure 5.8: Illustration of the iterative calculation of the cavity steady-state field in the grid-based sub-SQL interferometer model. The green arrows represent propagation of the field in momentum-space, the violet arrows represent interaction with optical elements, i.e. transmission or reflection at cavity mirrors. To obtain the cavity steady-state field, multiple round-trips of the initial field E_1 are calculated. This results in the field E_{k+1} where k is the number of round-trips the field has undergone. Summing over these fields yields the steady-state circulating field in the cavity. Image © IOP Publishing Ltd. Reproduced from [185] with kind permission of IOP Publishing.

5.3.1 Grid parameter requirements

Due to the fact that in grid-based optical models phase and amplitude of the modeled laser beams are projected on discrete grids, it is evident that the accuracy of the simulation results depends on the choice of the grid parameters. The square simulation grid is fully determined by two parameters: the length of the edges of the simulation window F and the number of grid points N^2, whereas N is typically referred to as the rank of the (square) grid. From these two numbers, the resolution ρ of one pixel of the grid can be deduced,

$$\rho = \frac{F}{N} \,. \tag{5.26}$$

To prevent failure of the propagation algorithm it is necessary to ensure that on the one hand the window is large enough to accommodate the largest beam radius in the modeled setup. On the other hand the resolution needs to be fine enough such that the smallest beam radius, typically at a beam waist, is still represented by at least one pixel of the grid.

For the model of the Fabry-Perot interferometer with marginally stable arm cavities a window size of $F = 11\,\text{cm}$ was chosen which includes a generous margin with respect to the largest occurring beam spot radii of $w \sim 1\,\text{cm}$. For the rank of

Table 5.2: Round-trip loss of an unperturbed marginally stable interferometer arm cavity, simulated with a modal (FINESSE) model, for different maximum mode order sums $n + m$ of the Hermite-Gauss modes used in the simulation. The simulated powers and the resulting round-trip loss obtained from the grid-based model are given for comparison.

n+m	P_{in} [W]	P_{refl} [W]	P_{trans} [W]	P_{circ} [W]	RTL [ppm]
10	2.75	2.6679064	0.0741875	1159.1066	6.82
15	2.75	2.6693778	0.0742079	1159.4244	5.53
20	2.75	2.6706683	0.0742257	1159.7278	4.30
25	2.75	2.6706683	0.0742257	1159.7031	4.40
30	2.75	2.6709604	0.0742297	1159.7662	4.15
FFT	2.75	2.6709298	0.0742281	1159.8168	4.18

the grids a value of $N = 1024$ was assumed, resulting in a resolution of one pixel of $\rho \approx 107\,\mu\text{m}$. The smallest beam sizes that occur in the simulation, which are the beams waists in the cavities with diameters of $2w_0 \sim 400\,\mu\text{m}$, are sufficiently well resolved.

The importance of these parameters stems from the fact that they are directly related to the occurrence of *aliasing* in the simulation, both, in position-space and in momentum-space. Aliasing is a consequence of the violation of the *Nyquist–Shannon sampling theorem* and occurs in discrete sampling of functions which have power at frequencies above the *Nyquist frequency*, which is half the sampling frequency [189]. In systems which are subject to aliasing, power at high frequencies is shifted to lower frequencies which gives rise to erroneous modeling results. In [164] five criteria were formulated which need to be fulfilled in a grid-based optical FFT model to either avoid or suppress aliasing, in order to ensure that the simulation results are not corrupted. The grid parameters of the Fabry-Perot Michelson interferometer model were chosen to meet all of these criteria.

For well-chosen grid parameters the model results are, within reasonable boundaries, expected to be robust under changes of the parameters. The robustness of the grid-based interferometer model was verified in a number of trial runs. Furthermore, very good agreement was found between results obtained from the grid-based model and a modal model with apertured mirrors based on FINESSE, of the same optical setup of a marginally stable interferometer arm cavity.

It was found that in the unperturbed modal model of the marginally stable sub-SQL interferometer arm cavity a comparatively large number of transverse modes is required for the results to converge to those obtained from the grid-based model, cf. Table 5.2. As can be seen in the table, for a modal simulation with $n + m = 15$ the resulting round-trip loss deviates by $\approx 25\,\%$ from the value obtained from the grid-based model. Mode orders of $n + m = 20$ are required to ensure deviations of lower than $\approx 3\,\%$ between results from the two different models. This behavior can be explained with the deformation of the transverse beam shape upon reflection at the cavity mirrors. Due to the comparatively large beam spots in the marginally stable

cavity, and hence increased clipping of the beam at the mirror apertures, this effect is more pronounced than in the common case of arm cavities with mirror dimensions and beam sizes chosen to result in only little beam clipping. To properly resolve this "sharp" effect, which occurs comparatively far from the beam center, many higher-order modes with large effective radius need to be included in the simulation. Due to the fact that a simulation run of the modal interferometer model with mode orders $n + m \sim 25$ may easily take more than a day on a modern multi-core work station to terminate, the grid-based model appears to be the computationally more efficient option to simulate diffraction effects in the interferometer with marginally stable arm cavities in a larger scale parameter study.

5.4 Modeling mirrors with realistic surface topography

An ideal cavity mirror would exhibit a perfectly smooth, spherical surface with a radius of curvature matching the curvature of the phase front of the incident beam. Realistic mirrors, however, are subject to different types of surface irregularities which are often a consequence of the manufacturing process, giving rise to local deviations of the surface from the desired shape. An electromagnetic field $\Phi(x, y, z)$ representing a laser beam which is reflected off a mirror with a distorted surface can be written as

$$\Phi_{\text{refl}}(x, y, z) = r \cdot \Phi(x, y, z) \cdot \exp(2ikZ(x, y)) \ , \tag{5.27}$$

with r representing the uniform amplitude reflectivity of the surface. Obviously, the mirror surface height function $Z(x, y)$ locally changes the phase of the incident field upon reflection.

The surface height information $Z(x, y)$ of an actual mirror can be obtained by different means. For a given mirror it is straight forward to extract this information from direct measurements of the surfaces. Fizeau interferometers, for instance, are commonly employed to assess the surface topography of optical components [190]. From the digitized surface measurement data, *phase maps* can be composed which may be included in numerical interferometer models. This approach is valuable e.g. in the commissioning phase of a laser interferometer as it allows to greatly enhance the realism of interferometer models and may help to track down performance limitations which are related to the properties of the interferometer optics' surfaces.

For interferometers in the design phase, for which surface requirements are yet to be determined, including realistic mirror surface information in simulations poses a viable option to identify potential performance limitations that originate from the properties of the mirrors. Based on the results of these simulations, mirror polishing requirements may be formulated. However, since in most cases the actual mirrors do not yet exist in the design phase, phase maps for simulations may alternatively be generated with the aid of synthetic mirror surface models.

In order for synthetic mirror surface models to be useful they need to be parameterized such that the quality of the mirrors' surfaces can be easily tuned, e.g. in the scope of numerical parameter studies. Ideally, the parameters are directly related to

"real world" quantities which can be given to mirror manufacturers as specifications for the desired optics.

In the following, two common approaches of modeling optical surfaces will be introduced, namely a statistical model based on spectral densities for describing surface fluctuations and a polynomial approach based on Zernike functions.

5.4.1 Spectral approach to optical surface characterization

A common approach to quantitatively describe the surface finish of optics, which was also adopted as an international standard [191], is the statistical description of surface fluctuations by means of the power spectral density (PSD). The PSD yields the distribution in spatial frequencies of the squared amplitude of the surface fluctuations and is closely related to the angle-dependent scattering properties of an optical surface. The PSD of an optical surface can e.g. be estimated from direct measurements of the surface topography or indirectly from angle-resolved scattering measurements [192], e.g. of the *bi-directional reflectance distribution function* (BRDF).

Two equivalent approaches for the calculation of the PSD from measured surface topography data are commonly employed: either the calculation of the squared Fourier transform of the spatial distribution of surface fluctuations or the calculation of the Fourier transform of the auto-covariance of the surface error distribution function [193]. Often, for the practical reason of different surface metrology methods resolving different spatial frequency bands, a distinction is made between low-frequency fluctuations of a surface with spatial frequencies $f_{\mathrm{sp}} \lesssim 10^3\,\mathrm{m}^{-1}$ and high-frequency fluctuations with $f_{\mathrm{sp}} \gtrsim 10^3\,\mathrm{m}^{-1}$. These are commonly referred to as *surface irregularity* and *micro-roughness*, respectively.

It was pointed out by Church [194] that the surface of highly polished optical surfaces was frequently fractal-like and well described by a one-sided power spectral density of the form

$$S_{1D}(f_x) = \frac{K_n}{f_x^n} \quad \text{with } 1 < n < 3\,, \tag{5.28}$$

where f_x is the spatial frequency and K_n is a normalization constant. Especially for generating synthetic phase maps for simulations in the design phase of interferometers, aiming at the derivation of mirror requirements, the approximation given in Equation (5.28) has proven useful, cf. e.g. [195].

For an isotropically rough surface the two dimensional power spectral density of the surface topography can be written as

$$S_{2D}(f_r) = \frac{\Gamma[(n+1)/2]}{2\Gamma(1/2)\Gamma(n/2)} \times \frac{K_n}{f_r^{n+1}}\,, \tag{5.29}$$

where $f_r = \sqrt{f_x^2 + f_y^2}$ is the radial spatial frequency and Γ is the special gamma function. It is worth noting that the two dimensional form falls off one power of the spatial frequency faster than the one dimensional form given in Equation (5.28).

By integrating over the two-dimensional PSD $S_{2D}(f_r, \phi)$ of an isotropic surface, where $\phi = \arctan(f_y/f_x)$, the corresponding one-dimensional radial PSD

$$S_{1D}(f_r) = \int_0^{2\pi} \mathrm{d}\phi \, f_r S_{2D}(f_r, \phi) \ , \tag{5.30}$$

is obtained.

Conversely to the approach described above, i.e. the extraction of the PSD from discrete surface measurement data, the PSD may be used as a basis for generating artificial surfaces with topographies whose spectral properties are determined by the PSD the model is based on. It was pointed out by *Bondu* that, based on a given two-dimensional PSD, synthetic mirror surface maps with different surface topography can be generated which are spectrally identical [196].

One of the cornerstones of this approach is a complex matrix $\tilde{M}(f_x, f_y)$ with elements equal to the square root of the two-dimensional PSD $S(f_r)$, which was chosen to spectrally represent the surface,

$$\left|\tilde{M}(f_x, f_y)\right| = \begin{cases} 0 & f_r = 0 \\ \sqrt{S(f_r)} & f_r > 0 \ . \end{cases} \tag{5.31}$$

In a numerical implementation the matrix $\left|\tilde{M}(f_x, f_y)\right|$ is represented by a grid, with the element corresponding to $f_x = f_y = 0$ located at its center. To add randomness to the surface topography, each grid cell is multiplied with a random phase which is drawn from a uniform distribution in the interval $\psi \in [0, 2\pi)$.

$$\tilde{M}^r(f_x, f_y) = \left|\tilde{M}(f_x, f_y)\right| \dot{\times} \exp(i\Psi) \ , \tag{5.32}$$

where $\dot{\times}$ denotes element-wise multiplication and Ψ is a matrix with the same dimensions as $\tilde{M}$ and random elements ψ. The actual synthetic surface map is the inverse two-dimensional Fourier transform of the matrix in Equation (5.32),

$$M(x, y) = \mathcal{FT}^{-1}\left\{\tilde{M}^r(f_x, f_y)\right\} \ . \tag{5.33}$$

The result is a topographical model with the spectral content determined by the initial two-dimensional PSD. The resulting surface can then be normalized and scaled, to obtain a surface with a particular RMS irregularity. The RMS irregularity σ can be obtained from the PSD via

$$\sigma_{\mathrm{RMS}}^2 = \int_{f_{\min}}^{f_{\max}} \mathrm{d}f_r \, S_{1D}(f_r) \ , \tag{5.34}$$

where the boundaries of the integral, $f_{\min}$ and $f_{\max}$, are the lowest and the highest spatial frequency, respectively, contained in the surface map. In the case of a discretized surface map, $f_{\min}$ depends on the width of the map and $f_{\max} = N/(2F)$ depends on the chosen resolution. The value of σ_{RMS} given in Equation (5.34) can alternatively be obtained by calculating the standard deviation of the phase map in

Table 5.3: First ten Zernike polynomials and their common names [198].

$Z_0^0(\rho,\Theta)$	1	piston
$Z_1^{-1}(\rho,\Theta)$	$2\rho\cdot\cos(\Theta)$	x-tilt
$Z_1^1(\rho,\Theta)$	$2\rho\cdot\sin(\Theta)$	y-tilt
$Z_2^{-2}(\rho,\Theta)$	$\sqrt{6}\rho^2\cdot\cos(2\Theta)$	primary astigmatism
$Z_2^0(\rho,\Theta)$	$\sqrt{3}(2\rho^2-1)$	defocus
$Z_2^2(\rho,\Theta)$	$\sqrt{6}\rho^2\cdot\sin(2\Theta)$	primary astigmatism
$Z_3^{-3}(\rho,\Theta)$	$\sqrt{8}\rho^3\cdot\cos(3\Theta)$	trefoil
$Z_3^{-1}(\rho,\Theta)$	$\sqrt{8}(3\rho^3-2\rho)\cos(\Theta)$	primary x-coma
$Z_3^1(\rho,\Theta)$	$\sqrt{8}(3\rho^3-2\rho)\sin(\Theta)$	primary y-coma
$Z_3^3(\rho,\Theta)$	$\sqrt{8}\rho^3\cdot\sin(3\Theta)$	trefoil

Equation (5.33). The normalized map is scaled to an arbitrary RMS irregularity σ' simply by multiplication with the desired value

$$M'(x,y) = \frac{\sigma'}{\sigma}M(x,y)\,. \tag{5.35}$$

The advantage of this approach is that, for a given PSD, the number of parameters that need to be tuned to alter the topography of the synthetic mirrors can be reduced to only the RMS irregularity of the surfaces. This parameter is also a common quantity used for mirror surface figure specification and is readily accepted by optics manufacturers.

5.4.2 Polynomial description of optical surfaces

A powerful tool in optics design, to analytically represent optical aberrations, are the so-called *Zernike polynomials*. These polynomials are defined over the unit circle, form a complete orthogonal basis and are closely related to the classical optical aberrations [197]. Hence, Zernike functions are well suited to model deviations of circular optical surfaces from the ideal shape. Their property of orthogonality makes it possible to study surface deformations individually and to even subtract a specific aberration contained in the surface under study without affecting the remaining ones.

The Zernike functions Z_n^m are a product of the radial Zernike polynomials $R_n^m(\rho)$ and sine or cosine functions which depend on the azimuthal parameter Θ,

$$Z_n^m(\rho,\Theta) = R_n^m(\rho)\cdot\sin(m\Theta) \tag{5.36}$$

and

$$Z_n^{-m}(\rho,\Theta) = R_n^m(\rho)\cdot\cos(m\Theta)\,, \tag{5.37}$$

where $\rho = r/a$ is the radial parameter for a given mirror with a radius a and Θ is the azimuthal coordinate and $R_n^m(\rho)$ is the so-called radial polynomial.

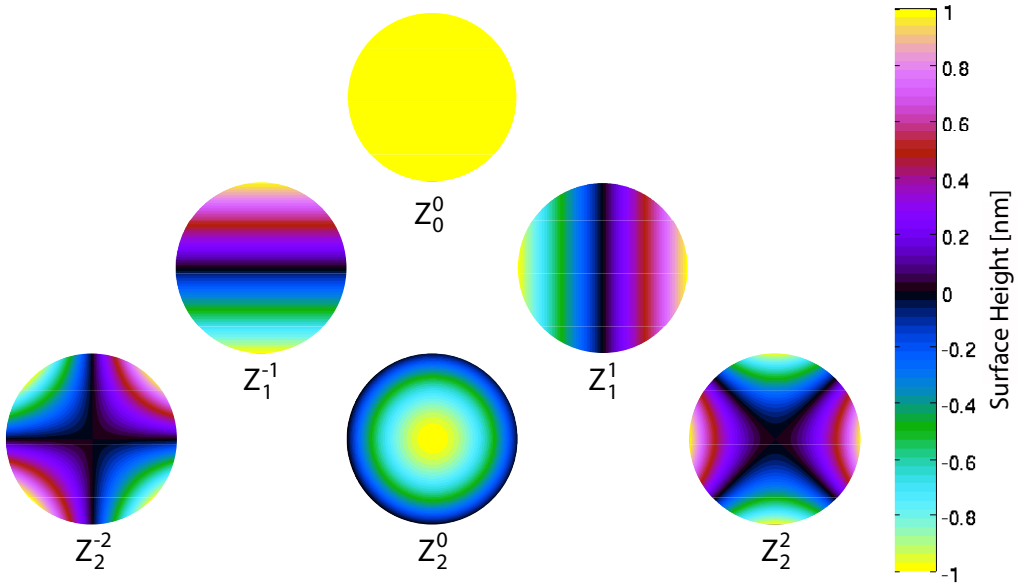

Figure 5.9: Surface plots of Zernike polynomials with unity amplitude up to second degree. It is obvious that polynomials with the same absolute value of the azimuthal index m, i.e. the same order, are identical except for a rotation.

The index $n = 0, 1, 2, \ldots$ is referred to as the *degree* of the polynomial, while $m = -n \ldots n$ with $(n - m)$ even, is called the *order* of the function. Obviously, the polynomial of order $m = -k$ is identical to the polynomial of k-th order except for a rotation, i.e. polynomials with orders $m = \pm k$ describe the same type of aberration with a magnitude

$$\bar{A}_n^m = \sqrt{\left(A_n^{-m}\right)^2 + \left(A_n^{+m}\right)^2}\,, \tag{5.38}$$

which is the RMS of the amplitudes of the two corresponding polynomials [199].

The radial polynomial is typically given in the form of a series expansion as a finite sum of powers of ρ [200],

$$R_n^m(\rho) = c_{mn} \sum_{q=0}^{(n-m)/2} \frac{(-1)^q (n-q)!}{q!(\frac{n+m}{2} - q)!(\frac{n-m}{2} - q)!} \rho^{n-2q} \tag{5.39}$$

where c_{mn} is a normalization constant given as

$$c_{mn} = \sqrt{\frac{2(n+1)}{\pi(1+\delta_{m0})}}\,. \tag{5.40}$$

The first ten Zernike polynomials along with their common names are listed in Table 5.3. Surface plots of the Zernike functions up to second degree are shown in Figure 5.9.

To decompose a given circular optical surface Z_s in a Zernike polynomial basis, a convolution of the form

$$A_n^m = \int_0^{2\pi} \int_0^1 \mathrm{d}\Theta \, \mathrm{d}\rho \cdot \rho \cdot Z_s(\rho, \Theta) \cdot Z_n^m(\rho, \Theta) \tag{5.41}$$

is carried out, yielding the polynomial amplitudes A_n^m. Conversely, for a given set of Zernike amplitudes A_n^m an optical surface can be reconstructed via

$$Z_s = \sum_{n=0}^{\infty} \sum_{m=-n}^{n} A_n^m \cdot Z_n^m(\rho, \Theta) \; . \tag{5.42}$$

As was shown in [199] the PSD of a reconstructed Zernike surface matches that of the original surface up to a certain frequency which depends on the maximum Zernike order, i.e. the higher the maximum order of the Zernike polynomials included in the analysis, the higher the maximum spatial frequencies in the surface that are resolved by the Zernike model. A comprehensive summary of numerical methods for Zernike decomposition of optical surfaces can be found e.g. in [201].

5.4.3 A hybrid mirror surface model

Of the surface modeling approaches introduced in the previous sections, each one has its distinctive strengths and weaknesses. A well-known shortcoming of surface models solely based on the PSD method introduced in Section 5.4.1 is that low-order aberrations, in particular astigmatism, are potentially underestimated [202]. Also, it is worth questioning to what extent a single PSD-based map with randomized topography is a good representative of an actual mirror surface. Since deviations from the perfect spherical shape are the result of imperfect mechanical processing and measurement error of the surfaces, which is deterministic and repeatable, it may be concluded that a statistical approach does not account for these effects sufficiently well. However, for a large number of simulation runs with mirror surface maps based on the same PSD but with different surface topographies it can be expected that for an output quantity such as the round-trip loss an accumulation of values within a particular interval will occur. From the distribution of the simulation results one can then e.g. deduce probabilities for the occurrence of a particular value as an upper limit. It is obvious that in order for this approach to yield meaningful results, a large number of simulation runs is necessary to ensure good statistics. A spectral approach for modeling interferometers with realistic optical surfaces was successfully employed in the past, for setting polishing requirements for advanced generation GW detectors, cf. e.g. [115, 203].

For a realistic surface model based on Zernike polynomials, a set of meaningful sampled amplitudes A_n^m is required as a starting point. These can e.g. be extracted from measurements of actual mirrors with comparable surface properties. Ideally, if a large set of measured data is available, intervals for the amplitudes of the individual aberrations can be deduced. These intervals may serve as a basis for tolerancing studies to determine upper limits for tolerable magnitudes of surface aberrations.

The Zernike amplitudes extracted from the measured data of a mirror surface will generally depend on the surface processing techniques that were employed to produce this particular mirror. This means that mirrors manufactured under different conditions will generally exhibit different Zernike content. If, for instance the surface "footprint" of a particular manufacturer was characterized by means of Zernike amplitudes and used for simulations, it is not straight forward to transfer simulation results to mirrors manufactured under different circumstances. However, other than in a PSD-based model, in a polynomial model the deterministic effects of the surface processing steps will be accurately represented, allowing to extract meaningful information even from a single simulation run. The orthogonality of the Zernike polynomials allows to tune the magnitude of individual aberration terms, thus making it possible to study the effect of individual aberrations on the performance of the instrument. In this way, performance-critical aberrations may be identified and tolerances for these may be formulated as appropriate. It is obvious that, compared to the PSD-based model, the polynomial model possesses a much larger number of degrees of freedom. In order to accurately represent surface fluctuations at higher spatial frequencies an extremely large number of polynomials needs to be included, cf. [199]. Although this gives full control of the surface model, at the same time this significantly complicates its practical application for the formulation of surface polishing specifications. Further practical downsides of this approach are the potential susceptibility of complicated specifications based on a multitude of parameters to misinterpretation and the fact that complete specifications based on Zernike amplitudes have not yet gained full acceptance by mirror vendors. However, since standard surface metrology instruments such as commercial Fizeau interferometers often directly output the amplitudes of low-order Zernike amplitudes, formulating upper limits for these as a supplement to a conventional specification are a feasible option.

To overcome the individual shortcomings of the PSD-based approach and the polynomial model, it was chosen to combine these to form a hybrid mirror surface model. The resulting surface model is a combination of randomized surfaces generated from a given PSD and separately modeled primary astigmatism, accounted for by means of the corresponding Zernike polynomials.

A power spectral density of the form

$$S(f) \propto \frac{1}{1 + (0.04f)^2} \tag{5.43}$$

was chosen to serve as the foundation of the PSD-based component of the mirror surface model. This PSD is based on measurements of the Advanced LIGO test mass surface spectra [90] and has served as the foundation of numerous numerical studies e.g. related to the compatibility of potential future upgrades of the aLIGO detector with the current mirror surface quality, for instance compatibility with LG_{33} beams. Hence, the present model is based on the assumption of high surface polishing quality, comparable to the surface quality of mirrors employed in aLIGO. Initial LIGO mirror surface spectra, for instance, were found to be in good agreement with

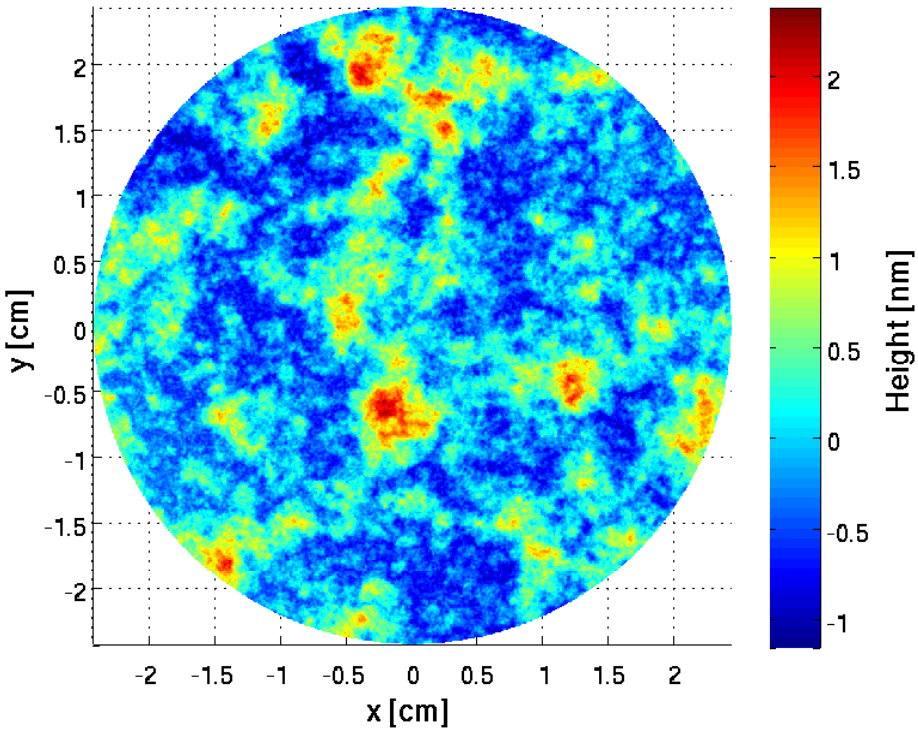

Figure 5.10: Example of a synthetic mirror surface map, based on the analytic PSD in Equation (5.43). The surface topography was randomized by multiplying the two dimensional power spectral density matrix elements with uniformly distributed phase factors from the interval $\phi \in [0, 2\pi)$, cf. Section 5.4.1. Before the map was scaled to 0.5 nm RMS surface irregularity in this case, low-order aberration terms (piston, tilt, curvature and primary astigmatism) were removed.

a PSD $\propto f^{-1.5}$ [193]. For the derivation of specifications for the mirrors of the VIRGO interferometer, a power law $\propto f^{-1.7}$ was assumed [204].

To generate surface maps based on the PSD in Equation (5.43), the framework introduced in Section 5.4.1 is employed. The resulting synthetic mirror surfaces contain undesired information which is usually removed in a post-processing step. This is also common practice when working with measured mirror surface maps, cf. [193]. If $Z_r(x)$ is a raw output surface profile and $Z(x)$ is the desired profile, one can write

$$Z_r(x) = Z(x) + \left(A + Bx + Cx^2\right) \ , \tag{5.44}$$

with coefficients A, B and C representing unwanted contributions of piston, tilt and curvature in the surface. Piston and tilt of the mirror surface is in a real interferometer compensated for by the longitudinal and angular control loops, respectively. To save the effort of implementing these in the numerical model, contributions of these terms are identified and subtracted from the surface map

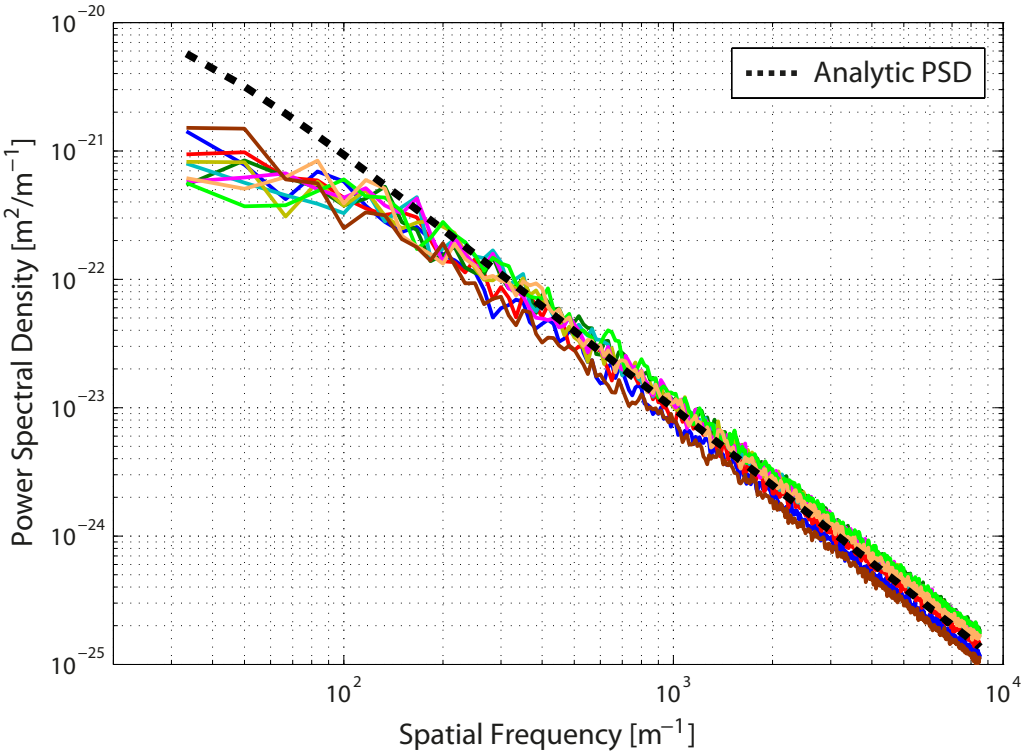

Figure 5.11: Estimated power spectral densities of synthetic mirror maps with randomized topography. The generated synthetic maps are based on the analytic PSD given in Equation (5.43), which was included in the plot as the black dashed curve. The deviation of the analytic and the extracted PSDs at low spatial frequencies is due to the subtraction of low-order aberration terms, i.e. piston, tilt, curvature and primary astigmatism.

data. This also applies to residual curvature which may be contained in the map. Curvature of the mirrors is a parameter which is generally desired to be known and to be manually fully adjustable in interferometer models. So, likewise, this term is subtracted from the map data. To remove these unwanted contributions, typically either an appropriate polynomial is fitted to the data using a least-squares algorithm or the corresponding Zernike content is removed. Besides piston, tilt and curvature also primary astigmatism is fully removed from the synthetic maps to be added again in a later step with a deliberate magnitude and random orientation. An example of a synthetic surface map after the post-processing steps is shown in Figure 5.10. As an example, a number of PSDs, which were extracted from the generated synthetic surfaces, are plotted in Figure 5.11, along with the analytic PSD given in Equation (5.43) the model is based on.

As mentioned previously, astigmatism is typically underestimated in PSD-based synthetic mirror surface maps. To model the effects of astigmatic mirrors it is possible to manually add the corresponding Zernike aberrations to the generated

PSD-based surface maps. Astigmatism with arbitrary orientation and amplitude can be expressed as a superposition of the Zernike terms Z_2^{-2} and Z_2^2, cf. Table 5.3, with amplitudes A_2^{-2} and A_2^2.

As was shown in Equation (5.38), the magnitude of a Zernike aberration can be given as the RMS of the amplitudes of the pair of polynomials, i.e. the even and odd polynomials, describing this type of aberration. By choosing different Zernike amplitudes A_n^{-m} and A_n^{+m} while maintaining the value for their square sum, the orientation of the resulting aberration can be selected while the aberration magnitude is preserved. With this side condition the squared sum of the Zernike amplitudes can be written as

$$(\bar{A}_n^m)^2 = \left(A_n^{-m}\right)^2 + \left(A_n^{+m}\right)^2 \tag{5.45}$$

$$= c\,(\bar{A}_n^m)^2 + [1-c]\,(\bar{A}_n^m)^2 \ , \tag{5.46}$$

where $c \in [0,1]$. The even and odd Zernike amplitudes can be associated with the resulting weighted amplitudes,

$$A_n^{-m} = \pm\sqrt{c\,(\bar{A}_n^m)^2} \tag{5.47}$$

$$A_n^{+m} = \pm\sqrt{[1-c]\,(\bar{A}_n^m)^2}\,. \tag{5.48}$$

By choosing an arbitrary value for $\bar{A}_n^m$, assigning a value to c drawn from a uniform distribution and randomizing the signs in Equations (5.47) and (5.48), the resulting Zernike amplitudes A_n^{-m} and A_n^{+m} describe a randomly orientated mirror surface aberration with given peak RMS amplitude. After inserting the resulting amplitudes in the Z_2^{-2} and Z_2^2 polynomials, randomly orientated astigmatism with a particular RMS amplitude can be added to the PSD-based synthetic map from which residual astigmatism was previously subtracted. For manipulating Zernike terms in the mirror surface model, numerical routines from the *Simtools* library are used [205].

The resulting model is based on a combination of the spectral and the polynomial approach, with two degrees of freedom. Namely these are the RMS irregularity of the surface without astigmatism and the peak-valley amplitude of the sum of the Z_2^{-2} and Z_2^2 polynomials. This model was used to generate synthetic mirror surfaces, including astigmatism, for the numerical parameter studies which are discussed in the following section.

5.5 A parameter study with realistic mirror surfaces

In order to quantitatively assess the effect of realistic mirror surface irregularity on the performance of the interferometer with marginally stable arm cavities a parameter study with a large number of different synthetic mirror surface maps was carried out. For this parameter study the grid-based model introduced in Section 5.3 was combined with synthetic arm cavity mirrors. These were represented by surface maps which were generated according to the method described in Section 5.4.

The large number of simulations that were carried out per parameter set was meant to compensate for the fact that PSD-based mirror maps with randomized surface topography only to some extent resemble the features found in real mirror surfaces, which exhibit the deterministic footprint of the employed surface processing techniques. However, it is expected that, provided that the number of simulation runs is large enough, average results obtained with this method come close to results from simulations based on measured mirror surface maps which were obtained from real mirrors with comparable spectral properties.

The concept of running a large number of deterministic simulations of a real-world system with one or more of the input parameters being subject to randomization is often referred to as *Monte-Carlo studies*. In fact, the used model exhibits the typical Monte-Carlo pattern. A number of input parameters are available which are, in the present case, the ones for which tolerable upper limits are to be derived. The model inputs are the PSD of the mirror surfaces – the one given in Equation (5.43) is used throughout the presented investigations – and two model steering parameters, namely the RMS irregularity of the PSD-based surfaces, with piston, tilt, curvature and primary astigmatism subtracted, and the peak-valley amplitude of the $\bar{Z}_2^2$ term, representing astigmatism in the modeled surface. For both parameters arbitrary values may be chosen but these will generally be held fixed within a single Monte-Carlo run, consisting of a multitude of model runs with different random surface topographies. Based on these input parameters for the algorithm described in the previous section a set of synthetic surface maps is generated for each run of the grid-based interferometer model.

The randomness in the input parameters, which is a key ingredient in Monte-Carlo studies, is in the present case introduced in the surface map generation process. The topography of the PSD-based mirror maps is randomized by multiplication of the two-dimensional PSD with random phase factors, cf. Section 5.4.1. The resulting surface map is then post-processed and scaled to the desired RMS irregularity and in the next step primary astigmatism with random orientation is added to the map. Whereas the magnitudes are determined by the input parameters, the distribution of surface features is totally random in this model.

Then, in the next step the randomized maps are included in the grid-based interferometer model and a deterministic computation is performed. What is deterministic about this stage in the Monte-Carlo study is the fact that for two identical sets of surface maps the simulation results will always be the same. Among the outputs of the model are the electric fields at various locations in the interferometer from which e.g. cavity round-trip loss or beam splitter contrast can be inferred. These serve, in the present case, as figures of merit for the performance of the interferometer, cf. Section 5.2.

Finally, in the last step of a model run the results are aggregated. In the present case, for a large number of model runs with the same input parameters, a distribution of values of the chosen output quantities is obtained. Based on this distribution it is possible to deduce probabilities for the figures of merit to assume particular values, for a given set of input parameters.

Regarding the computational effort, the performed parameter study may be considered as computationally quite demanding. On the one hand this is due to the fact that a large number of hundreds of simulation runs per parameter set needs to be carried out to obtain statistically significant results. It is clear that tremendous "wall clock" computation times are required if these simulations are run serially on a single work station. On the other hand, the computational requirements of the grid-based model itself, which are a consequence of the marginally stable, nearly concentric cavity geometry and the necessity to prevent position and momentum space aliasing, add to the computational effort per simulation run, cf. Section 5.3.1. A single run of the FPMI model with the chosen grid resolution takes approximately 2.5 - 4 hours on a modern work station computer with eight CPU cores.

To meet the computational requirements, it was decided to run the parameter study on a high-performance computer cluster system. For practical reasons the compute cluster system provided by the *Regionales Rechenzentrum Niedersachsen* (RRZN) at the Leibniz University of Hannover [206] was chosen. The grid-based interferometer model was adapted to the cluster environment and the generation of simulation runs and submission to the cluster batch system *Torque* was automated by means of batch scripts written in the *Python* programming language [207]. To speed up the computations, eight CPU cores were reserved on the cluster system for each instance of the model. This allowed to make use of the built-in thread parallelism of the MATLAB® language, in which the interferometer model was implemented. The top-level source code of the grid-based interferometer as well as the framework for automated job generation and submission can be found in Appendix A.

In the first round of simulations, with the synthetic mirror surfaces scaled to different RMS irregularities, a number of output quantities were extracted from the model, e.g. round-trip loss, fundamental mode round-trip loss and beam splitter contrast defect. In the plot in Figure 5.12, the modeled arm cavity round-trip loss is shown for a large number of simulations with different RMS mirror surface irregularity. The RMS irregularity was tuned from 0.1 nm to 2 nm RMS in steps of 0.01 nm. For each RMS irregularity value the marginally stable arm cavities were simulated with 20 different pairs of surface maps on the cavity mirrors, resulting in 4000 data points in total. For all runs identical RMS surface irregularities for the input mirrors and end mirrors were assumed. Surface topographies were random but their spectral content was based on the PSD given in Equation (5.43).

As can be seen in the plot, the targeted round-trip loss of $\sim$ 100 ppm, cf. Section 5.2, is reached at surface an RMS irregularity of approximately 0.9 nm. It is worth noting that the increase of the spread of the round-trip loss with increasing RMS irregularity is typical for this type of simulation, depends on the surface topography of the modeled mirror surfaces and was observed previously e.g. in [202].

The plot in Figure 5.13 shows the round-trip loss projected to the fundamental mode as a function of the mirrors' RMS irregularity. To assess the fundamental mode round-trip loss, the overlap between the fields in the distorted cavities and unperturbed reference fields was calculated. In this way the powers of the trans-

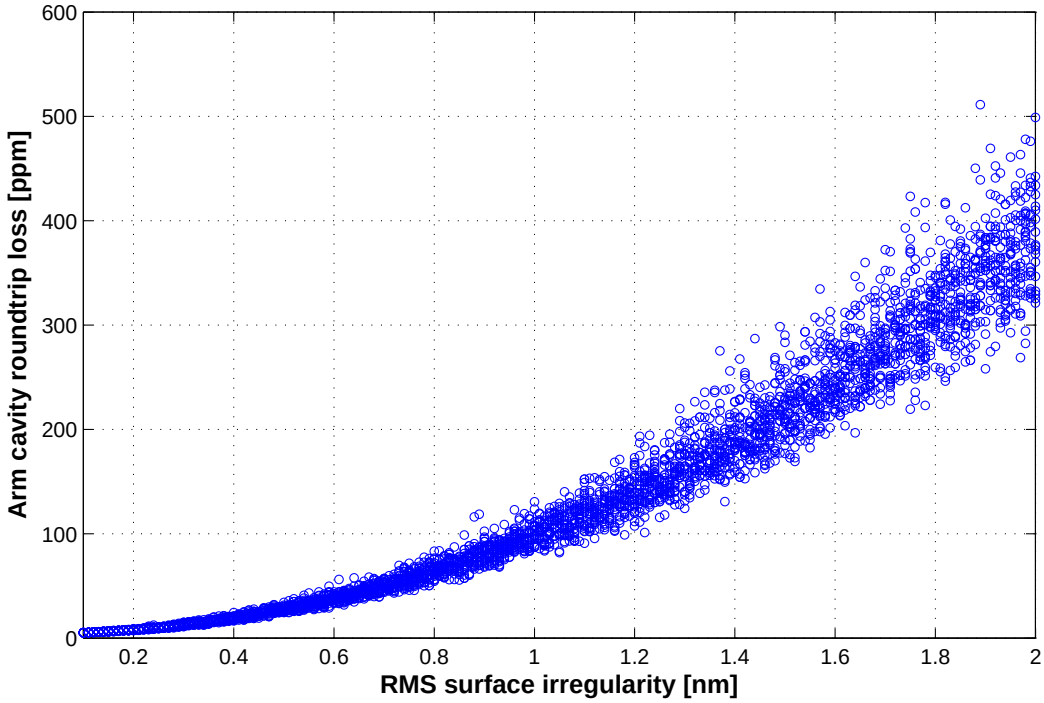

Figure 5.12: Simulated round-trip loss of the marginally stable sub-SQL interferometer arm cavities with realistic mirror surfaces. The RMS surface irregularity of the cavity mirrors was varied in the range of 0.1 nm - 2 nm in 0.01 nm steps. Astigmatism was fully removed from the surface maps over the full mirror aperture. For each surface irregularity value, 20 marginally stable arm cavities with different mirror surface topography were simulated, with identical RMS irregularity of the input and end mirrors. The increasing spread of the round-trip loss values toward larger RMS surface irregularity is typical for this type of simulation.

mitted, reflected and circulating light in the fundamental mode were obtained, cf. Section 5.1.2. The data was extracted from the same model runs as the data shown in the plot in Figure 5.12.

Obviously, for a given RMS irregularity the fundamental mode projected round-trip loss turns out larger than the conventional round-trip loss. Assuming RTL_{00} as the figure of merit for optical losses in the arm cavities, the targeted sub-SQL interferometer arm cavity round-trip loss of ~ 100 ppm is already reached at a surface irregularity of approximately 0.7 nm RMS. This observation can be explained by the marginal stability of the interferometer arms and the resulting partial degeneracy of higher order modes. The fact that the arm cavities, to some extent, support higher-order transverse modes gives rise to a deformation of the eigenmode of the perturbed cavity. Other than in the commonly encountered case of interferometers with generous stability margin of the arm cavities, in which the resonating mode in the perturbed arm cavities is mostly identical with the hypothetical unperturbed

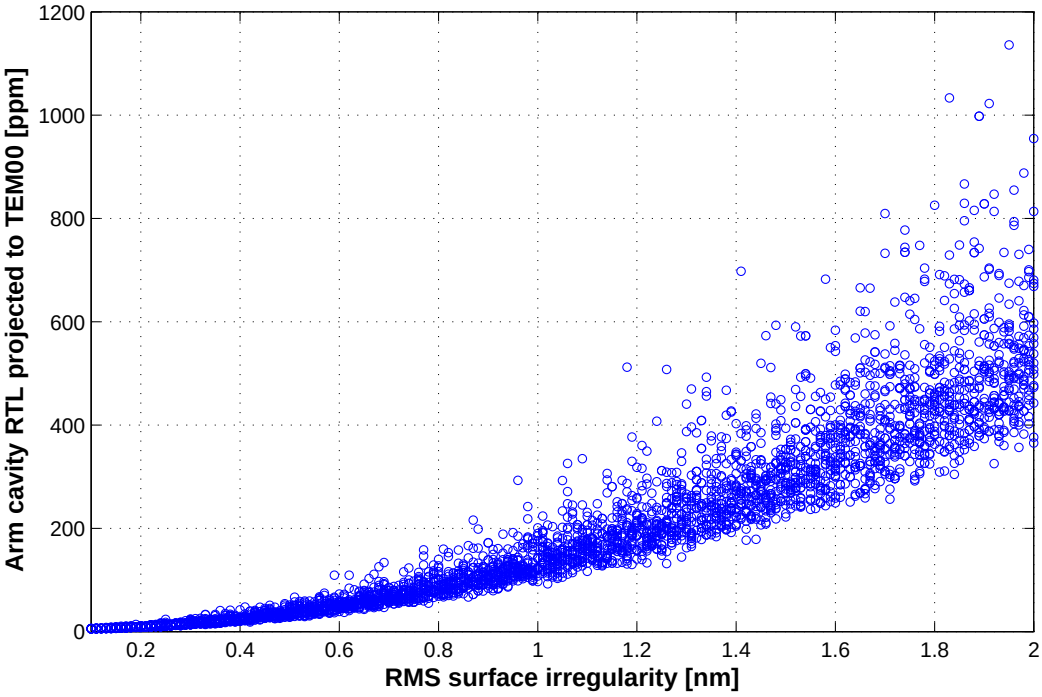

Figure 5.13: Simulated round-trip loss projected to the fundamental mode of the marginally stable sub-SQL interferometer arm cavities. The RMS surface irregularity of the cavity mirrors was varied in the range of 0.1 nm - 2 nm in 0.01 nm steps. In each simulation run the surfaces of all mirrors in the model were scaled to the same surface irregularity value. The data was obtained from the same model runs as the data plotted in Figure 5.12. It can be seen that the fundamental mode projected round-trip loss turns out to be considerably larger than the conventional round-trip loss. This is a consequence of light transferred inside the cavities from the fundamental mode to HOMs due to scattering at the irregular mirror surfaces in combination with the partial degeneracy of HOMs in the marginally stable arm cavities.

arm cavity mode, the perturbed and unperturbed arm cavity eigenmodes differ in the modeled marginally stable interferometer. As pointed out previously in Section 5.1.2, in the present case of marginally stable arm cavities the fundamental mode projected round-trip loss is the more adequate quantity for the estimation of optical losses in the interferometer and, furthermore, it is also the relevant quantity for the estimation of the benefit from squeezing injection or the application of back-action evasion schemes on the quantum noise limited sensitivity.

The contrast defect data shown in the plot in Figure 5.14 was obtained from the same model runs from which the round-trip loss data shown previously was extracted. Again, the surface irregularity was varied in the range of 0.1 nm to 2 nm RMS in 0.01 nm steps. The number of data points is halved since the reflected fields from two simulated cavities with mirrors with different surface topographies but identical RMS irregularity were combined to obtain the beam splitter contrast.

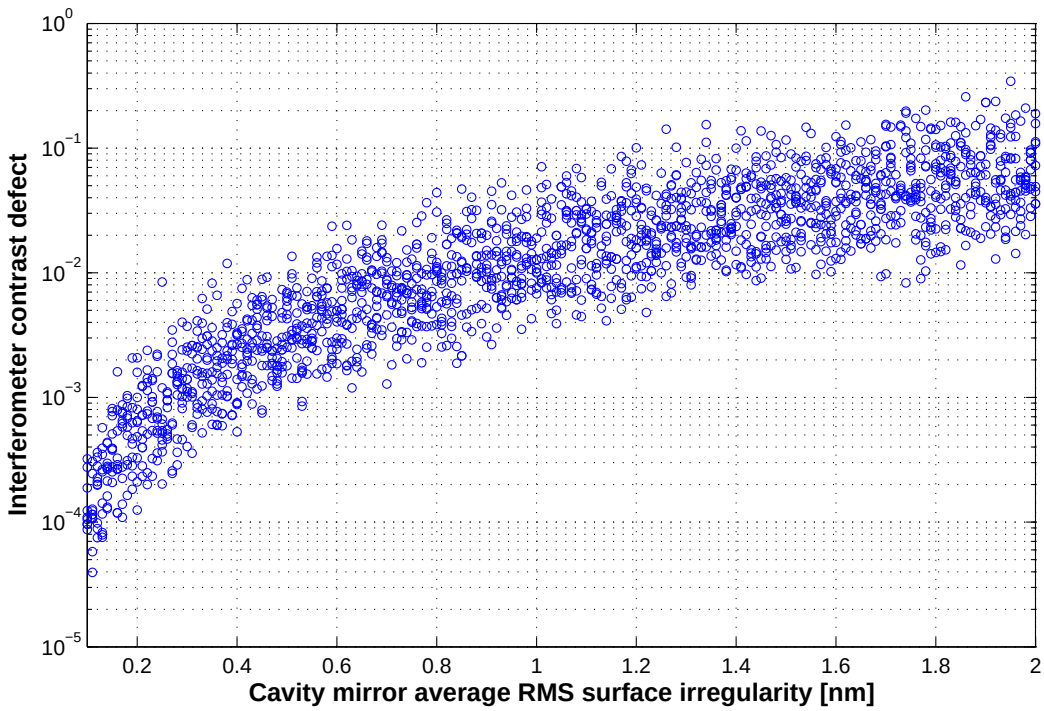

Figure 5.14: Simulated contrast defect in the sub-SQL interferometer with marginally stable arm cavities with realistic mirror surfaces. The RMS surface irregularity of the cavity mirrors was varied in the range of 0.1 nm - 2 nm in 0.1 nm steps. In each simulation run the surfaces of all mirrors in the model were scaled to the same surface irregularity value. The data was obtained from the same model runs as the data plotted in Figure 5.12. For each data point in the plot the interference contrast of the fields reflected at the two marginally stable arm cavities in the interferometer was calculated.

A contrast defect indicates non-perfect destructive interference at the beam splitter at the interferometer and gives rise to spurious light leakage into the detection port of the interferometer, as pointed out previously in Section 5.2. This light does not carry usable signal but contributes to the level of shot noise in the main readout channel, thus degrading the sensitivity of the interferometer. Moreover, poor contrast is known to increase the coupling of input laser noise to the main interferometer signal and also potentially affects the operability of the instrument in terms of compromising the robustness of longitudinal and angular controls.

From the plot in Figure 5.14 it can be inferred that the targeted upper limit for the contrast defect of $\xi \lesssim 3 \times 10^{-3}$, cf. Section 5.2, imposes more stringent requirements on the mirror surface figure than the round-trip loss requirement. The targeted upper limit for the contrast defect is already reached at a surface irregularity of approximately 0.3 nm RMS, compared to the value of approximately 0.7 nm RMS which represents the tolerable upper limit to meet the requirement of the targeted round-trip loss. Hence, this means that it is the targeted contrast at the beam splitter in the interferometer that determines the mirror surface irregularity requirement.

An alternative, more seizable way to interpret the results from the parameter study with the numerical interferometer model are the loss and contrast defect probabilities shown in Figure 5.15. For each of the plotted curves, 300 simulation runs of the grid-based Fabry-Perot Michelson interferometer model with marginally stable arm cavities were carried out. This resulted in 600 data points for the cavity round-trip loss (two data points per simulation run for the two arm cavities in the interferometer) and 300 data points for the contrast defect at the interferometer beam splitter. Based on this data, probabilities were calculated for the occurrence of a particular value of the round-trip loss and the contrast defect for a given value for the RMS surface irregularity. In each simulation run the RMS irregularity of all cavity mirror surfaces was identical. Due to the nature of the numerical simulation, the resulting data points representing the probabilities exhibit statistical variance which decreases with an increasing number of simulation runs. A smoothing algorithm was applied to the probability data to obtain a data set with less variance. Both, the original probability data, represented by the circles, as well as the smoothed data, represented by solid curves, are shown in the plots in Figure 5.15. Whereas astigmatism was fully removed over the full mirror aperture from the underlying synthetic mirror surface maps of the upper plots, in the middle plots and the lower plots astigmatism with random orientation was included, with a peak-valley amplitude of $\bar{Z}_2^2 = 1\,\mathrm{nm}$ and $\bar{Z}_2^2 = 2\,\mathrm{nm}$, respectively.

Obviously, in the cases where astigmatism is present in the mirror surface maps the round-trip loss is only moderately increased but the resulting deformation of the fields reflected at the astigmatic arm cavities gives rise to an increased deterioration of the Michelson beam splitter contrast, especially at low values for the RMS irregularity of the mirror surfaces. Assuming that it is aimed for achieving the targeted upper limit for the beam splitter contrast defect with a probability of at least 90 %, the uppermost plot in Figure 5.15 indicates that a surface irregularity of $\lesssim 0.3\,\mathrm{nm}$ RMS needs to be arranged for, in the case that primary astigmatism was fully removed from the surfaces of the mirrors. Whereas astigmatism with $\bar{Z}_2^2 = 1\,\mathrm{nm}$ has an almost negligible effect on the contrast defect for mirrors with 0.3 nm RMS irregularity, cf. middle plots in 5.15, the presence of astigmatism with $\bar{Z}_2^2 = 2\,\mathrm{nm}$ requires the surface irregularity – excluding astigmatism – to be approximately 0.2 nm RMS to reach the targeted upper limit for the contrast defect with 90 % probability. Since the RMS irregularity value of 0.3 nm RMS is already quite challenging to reach, it is advisable to prevent astigmatism from significantly increasing the contrast defect any further.

Figure 5.15 ***(following page)*****:** Fundamental mode round-trip loss and contrast defect probabilities for varied mirror RMS irregularities, with and without astigmatism. For the uppermost plots ❶ astigmatism was fully removed from the surface maps. In the middle plots ❷ and the lower plots ❸ astigmatism was present in the maps with $\bar{Z}_2^2 = 1\,\mathrm{nm}$ and $\bar{Z}_2^2 = 2\,\mathrm{nm}$, respectively.

❶

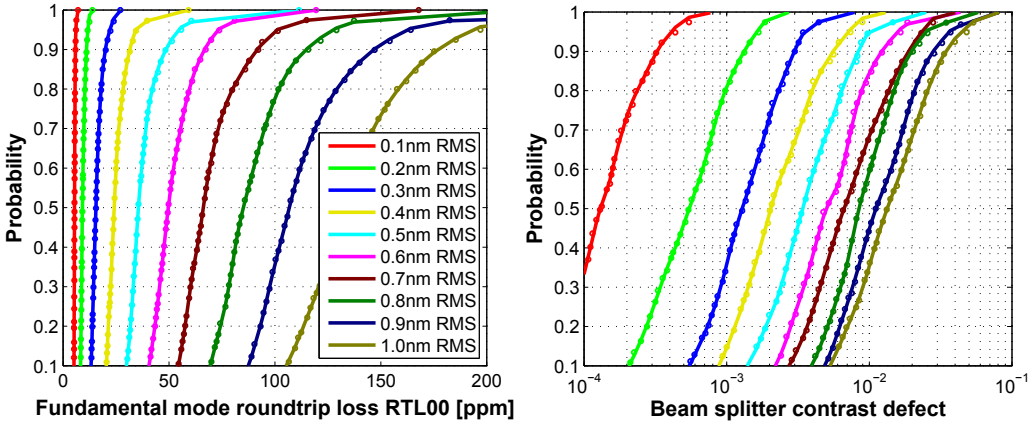
Probability
Fundamental mode roundtrip loss RTL00 [ppm]
Beam splitter contrast defect
0.1nm RMS
0.2nm RMS
0.3nm RMS
0.4nm RMS
0.5nm RMS
0.6nm RMS
0.7nm RMS
0.8nm RMS
0.9nm RMS
1.0nm RMS

❷

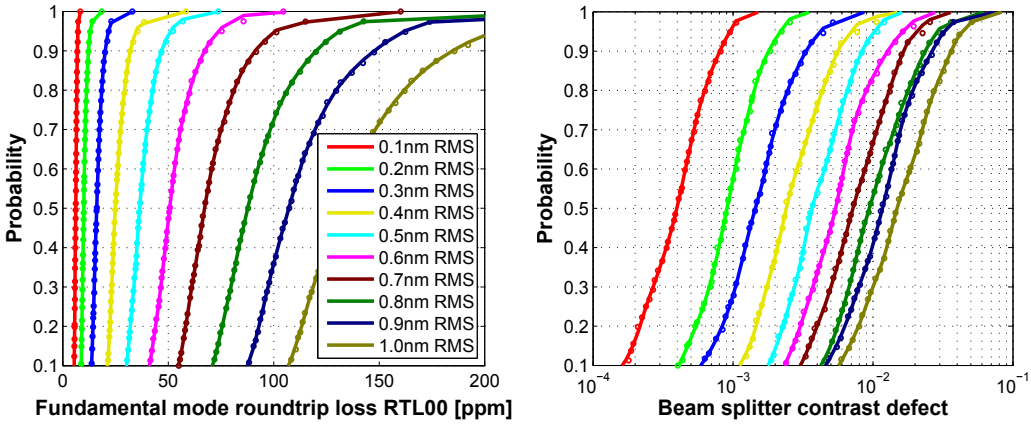
Probability
Fundamental mode roundtrip loss RTL00 [ppm]
Beam splitter contrast defect
0.1nm RMS
0.2nm RMS
0.3nm RMS
0.4nm RMS
0.5nm RMS
0.6nm RMS
0.7nm RMS
0.8nm RMS
0.9nm RMS
1.0nm RMS

❸

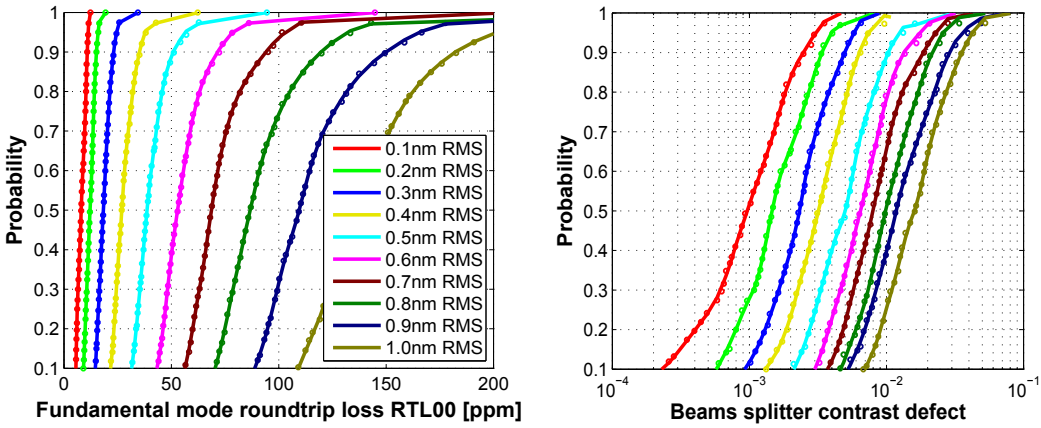
Probability
Fundamental mode roundtrip loss RTL00 [ppm]
Beams splitter contrast defect
0.1nm RMS
0.2nm RMS
0.3nm RMS
0.4nm RMS
0.5nm RMS
0.6nm RMS
0.7nm RMS
0.8nm RMS
0.9nm RMS
1.0nm RMS

It is concluded that in order to reach the targeted beam splitter contrast defect of $\lesssim 3 \times 10^{-3}$, cf. Section 5.2, the mirror surfaces should exhibit an RMS irregularity of $\lesssim 0.3\,\mathrm{nm}$ excluding astigmatism and a peak-valley amplitude of the Zernike terms representing astigmatism of $\bar{Z}_2^2 = \sqrt{(Z_2^{-2})^2 + (Z_2^2)^2} \lesssim 1\,\mathrm{nm}$.

It should be noted that the numbers stated above do not apply universally since implicitly a particular spectral model was assumed for the mirror surfaces. For mirrors with a spectral footprint that strongly deviates from the PSD given in Equation (5.43), additional modeling will be necessary. For mirrors, which were polished under similar conditions as those the PSD in Equation (5.43) was extracted from, the numbers stated above will give a good indication for what level of surface polishing will be necessary to meet the requirements for arm cavity round-trip loss projected to the fundamental mode and beam splitter contrast defect in the sub-SQL interferometer with marginally stable arm cavities.

Other than in the case of the studies toward mirror surface requirements for interferometry with higher-order Laguerre-Gauss modes in GW detectors, which resulted in surface irregularity requirements approximately one order of magnitude below what is currently achievable [90, 199], it was found that the required surface quality of the mirrors for the marginally stable sub-SQL interferometer arm cavities with extremely large beam spots can in fact be realized with current polishing techniques. However, reaching sub-nanometer surface irregularity requires the application of surface processing techniques more elaborate than those typically employed for conventional mirror surface finishing. Nevertheless, surface RMS irregularity in the sub-nanometer range is routinely achieved e.g. with *ion beam figuring* of optical surfaces [208, 209], which would be a viable option to ensure sufficiently low irregularity of the mirror surfaces in the sub-SQL interferometer.

5.6 Summary

In this chapter, a detailed discussion of mirror surface irregularity-induced scattering was presented and the importance of employing high-quality mirrors in the marginally stable 10 m Fabry-Perot Michelson interferometer under study was pointed out.

To assess the required mirror surface quality, two figures of merit were identified, namely the arm cavity round-trip loss of laser light in the fundamental mode and the contrast of the beams interfering at the main beam splitter of the interferometer. Whereas the former determines e.g. the achievable benefit from the application of non-classical interferometry techniques, the latter is relevant not only for keeping the level of input laser noise coupling to the main readout channel sufficiently low but also to prevent the introduction of additional shot noise into the measurement. By relating the output of a numerical interferometer model to upper limits for the chosen figures of merit, which were derived from the targeted noise budget of the experiment, requirements for mirror surface figure error were formulated.

For this purpose, a grid-based high-resolution numerical model of the Fabry-Perot Michelson interferometer with marginally stable arm cavities was developed.

To account for the effects of realistic surface irregularity of the mirrors in the simulated interferometer, a synthetic mirror surface model was employed. For a given surface fluctuation spectral density this model generates synthetic mirror surfaces with random topography, yet identical spectral properties. Since astigmatism is typically underrepresented in this approach, the model was parameterized to include realistic levels of astigmatism, described by means of the corresponding Zernike aberration polynomials.

With the numerical interferometer model with realistic mirror surfaces, a detailed parameter study was carried out on a high-performance computer cluster. In a large number of simulation runs the fundamental mode round-trip loss and the beam splitter contrast defect were evaluated for different RMS surface irregularities and astigmatism amplitudes of the mirrors in the marginally stable interferometer configuration. Probabilities were derived for given sets of mirror surface parameters to result in a particular round-trip loss and contrast defect in the interferometer.

It was found that in order to fulfill the requirements for the chosen figures of merit, mirrors with sub-nanometer RMS surface irregularity and astigmatism in the lower nanometer range need to be employed in the arm cavities of the interferometer. The treatment of the optical surfaces of the interferometer mirrors in the manufacturing process with the technique of *ion beam figuring* was pointed out as a potential option to reach the required levels of surface irregularity and astigmatism predicted by the numerical model.

CHAPTER 6

The 10 m Prototype single arm test experiment

As a stepping-stone toward the sub-SQL interferometer, an experiment aiming at operating a single marginally stable cavity with parameters similar to a sub-SQL interferometer arm cavity was proposed [210]. This *single arm test* experiment will enable first tests of the key technical infrastructure of the sub-SQL interferometer and will help to gain early experience with the challenges of marginally stable interferometry. In this chapter an overview of the single arm test experiment is given.

6.1 Introduction

The sub-SQL interferometer experiment at the AEI 10 m prototype facility requires relatively large beam spot sizes in the arm cavities in order to reduce the contribution of coating thermal noise which would otherwise limit the sensitivity of the interferometer [60]. As pointed out previously in Chapter 4, the large spot sizes lead to arm cavities with marginal stability, introducing several technical challenges, as delineated below. To gain early experience with these significant technical challenges, it was proposed to first build a single arm cavity using lower-quality mirrors than will be used in the actual interferometer. This early configuration will be called the *single arm test*.

The single arm test is motivated in part by the long lead time of the final-quality core optics. Instead of waiting until a vendor for the optics is identified, then waiting for the optics to be fabricated, and then building the sub-SQL interferometer in its "final form", the single arm test will allow to use this time to gain valuable experience meeting the technical challenges of the marginally stable configuration. Furthermore, a single arm test can be completed with the two seismic isolation tables that are already installed and operational, without waiting for the completion of the third table.

It is envisioned that all infrastructure developed for the single-arm test (input optics, electronics, suspensions, etc.) will follow the baseline design [131] of the sub-

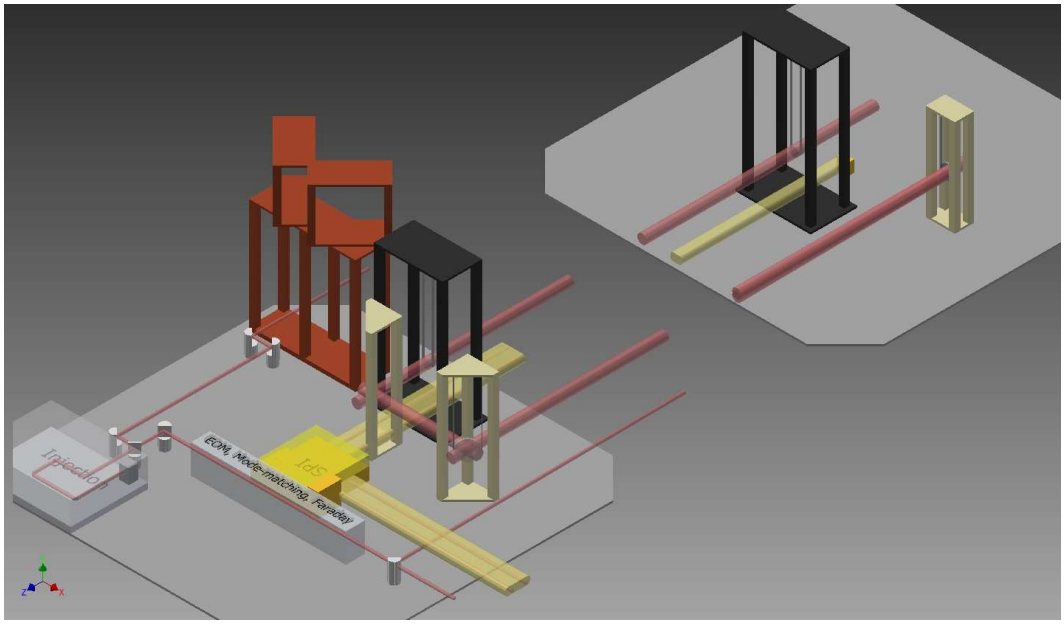

Figure 6.1: Mock-up 3D model of the single arm test experiment. The black cages represent the suspensions of the single arm test mirrors on the central table and on the south optical table. The smaller white cage on the south table represents the suspension for the collimating mirror. The white cages with the triangular base on the central table represent the steering mirror suspensions, for steering of the collimated beam into the single arm test cavity. For completeness, the SPI (yellow) and the reference cavity suspension cage (brick red) on the central table were included in the drawing.

SQL interferometer. Thus, the sub-SQL interferometer with the final high-quality mirrors will be a "drop-in replacement" of the single-arm configuration. A three dimensional mock-up model of the single arm test is shown in Figure 6.1.

6.2 Scientific and technical rationale

High-quality mirrors are required for the sub-SQL interferometer for several reasons. Due to the marginal stability of the sub-SQL interferometer arm cavities an increased contrast defect due to higher-order mode buildup in the cavities is expected. This results in a deviation of the transverse shape of the fields returning from the arm cavities from that of the desired fundamental mode. Non-perfect interference of these distorted fields at the beam splitter of the interferometer gives rise to couplings of input laser noise to the interferometer signal, cf. Chapter 5. Another consequence is increased shot noise on the detection photo diodes due to higher order modes, which contribute shot noise but not optical gain. Furthermore, the quality of the mirrors has a direct impact on optical losses, both due to scattering out of the cavity and due to higher order mode generation. Vacuum field will enter the interferometer through these losses, limiting the ability to surpass the SQL via non-

classical interferometry techniques. Another implication are potentially corrupted error signals due to higher-order modes on the detection PD. With other resonances very near the fundamental resonance, it may be difficult to lock to the desired mode. Because higher-order-modes become resonantly enhanced as the cavities are moved towards $g \to 1$, the most elegant means of excluding them is to prevent them from being generated in the first place. Radius of curvature error on the mirrors has a strong impact on the mode-matching into the cavities. Again, curvature mismatch reduces the coupling of the laser beam and gives rise to optical loss. With the single arm test it will not be attempted to reach the SQL, and thus optical losses are less of a concern. Hence, lower quality mirrors may be used. The tunable stability scheme introduced in Chapter 4 will be adopted for the single arm test, allowing to stepwise approach the marginally stable state of operation, cf. Figure 6.2. In the following, the aspects which are planned to be investigated in the scope of the single arm test experiment will be delineated.

Control of marginally stable cavities In marginally stable cavities even small-scale length perturbations, mirror rotation or curvature error may render the cavity unstable. This results in excessive optical losses and has the potential to severely impede the operability of the interferometer.

The single arm test will help to determine whether the marginally stable arm cavities of the sub-SQL interferometer can be stably controlled in all relevant degrees of freedom with the desired accuracy.

Cavity lock acquisition, coping with optical springs With the combination of very light mirrors (100 g), circulating laser powers in the kW range, and marginal stability, lock acquisition of the sub-SQL interferometer arm cavities is expected to be a non-trivial task. The occurrence of optical springs during the acquisition phase may be a source of further complications. A potential way to overcome these would be e.g. the implementation of a guided lock acquisition scheme in the real-time digital control system.

With the aid of the single arm test experiment, it will be possible to carry out a detailed study of the problem of lock acquisition of a marginally stable sub-SQL interferometer-type cavity. The procedures that will be developed in the course of the single arm test can later be transferred to the sub-SQL interferometer and will serve as a starting point for locking the full interferometer.

Testing of the new ESD concept A new concept for electro-static actuation was proposed for the sub-SQL interferometer [211] which has the advantage of leaving the free aperture of the cavity mirrors unaffected. These ESDs each consist of two capacitor plates facing each other, either below and above the mirrors or on both sides of the mirrors. Rendered images of first prototype designs are shown in Figure 6.3. By applying a voltage in the kV range a force is generated which drags the mirror inside the plate capacitor configuration. Whereas the first experimental

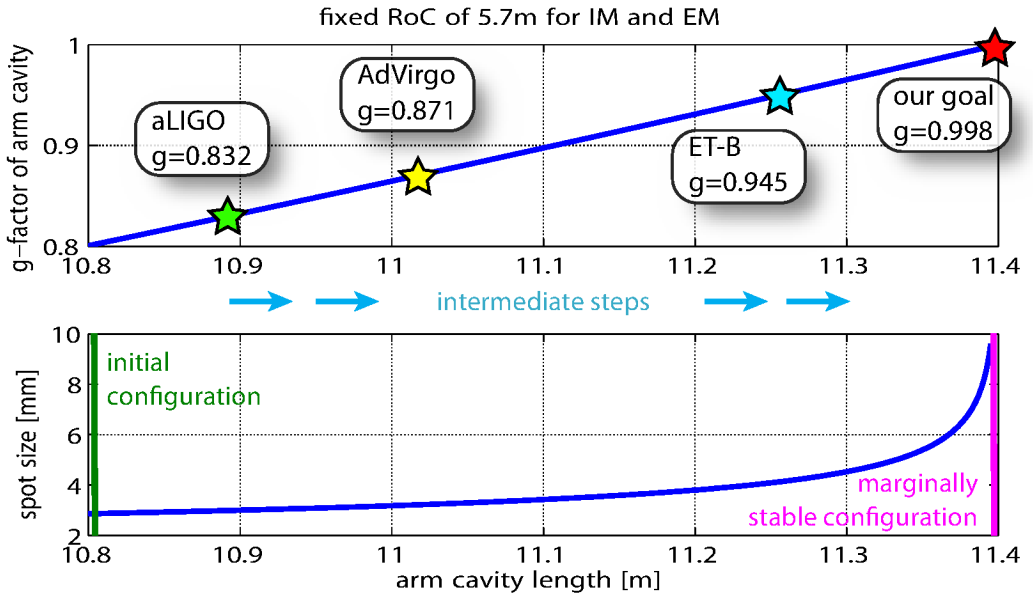

Figure 6.2: Stability parameter and beam spot size in the single arm test cavity plotted versus the cavity length. The tunable stability scheme introduced in Chapter 4 has been be adopted for the single arm test, allowing to stepwise approach the marginally stable state of operation. The experience gained from building and commissioning the single arm test experiment will set the stage for building and operating the sub-SQL interferometer. Furthermore, results obtained from interferometry experiments with marginally stable cavities will also be of interest for designs of future GW detectors.

demonstration has yet to be provided, encouraging results were obtained from first finite-element simulations and a comprehensive simulation study taking into account nearby conducting infrastructure is under way.

The single arm test will provide the first experimental demonstration of the plate capacitor ESD for the sub-SQL interferometer and will also shed light on aspects as e.g. actuation force and range, linearity, influence of parasitic charge, etc.

Investigation of beam jitter coupling Input beam jitter has the potential to limit the sensitivity of interferometer experiments. In the modal picture, fluctuations in the pointing of a laser beam can be described as first order mode content which is subject to amplitude modulation. At misaligned optical elements this first order mode light is converted to the fundamental mode, thus resulting in increased noise in the signal extraction port.

In the single arm test the susceptibility of the optical setup to coupling of input beam jitter to the signal readout will be investigated. Based on this knowledge it will be possible, if necessary, to adapt e.g. the input optics chain to further suppress input beam jitter to a tolerable level.

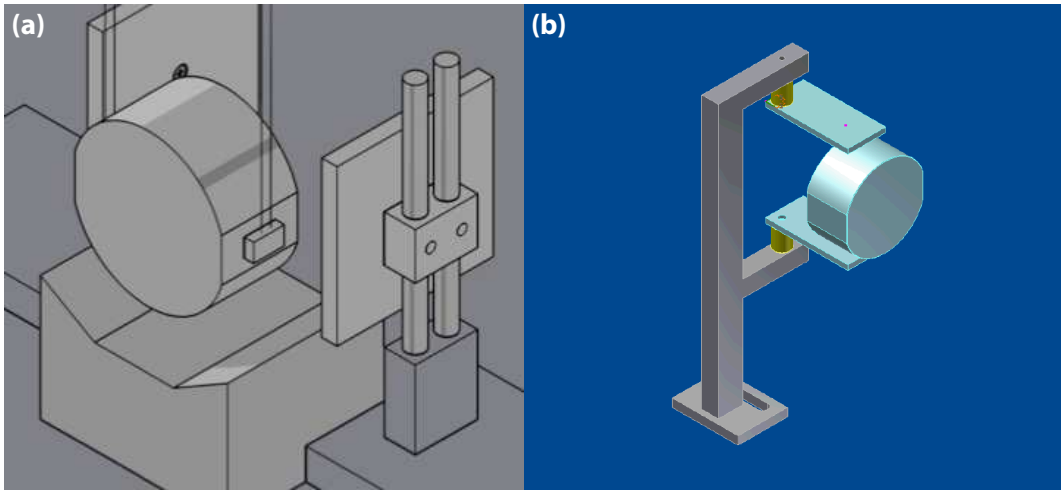

Figure 6.3: Rendered technical drawings of plate capacitor ESD actuator prototype designs. The principle layout is based on to two high-voltage electrodes facing each other, either (a) on both sides of the mirrors or (b) below and above the mirrors. By applying high-voltage to the electrodes a force is generated which drags the mirror inside the plate capacitor configuration.

6.3 Technical approach

For the single arm test it was proposed to set up a linear Fabry-Perot cavity with parameters based on the planned arm cavity configuration of the sub-SQL interferometer experiment. As the single arm test is aiming at gaining early experience with technical aspects of marginal cavity stability it was further proposed to relax a number of requirements on the infrastructure for this experiment:

- For the cavity mirrors it was proposed to use "standard grade" optics. For the single arm test it is not intended to use mirrors with the exceptionally precise curvature, extremely good surface figure, and best-available coating quality that will be ultimately be required for low-loss operation of the sub-SQL interferometer. In the further discussion it will be referred to the single arm test cavity optics as the *pilot mirrors*.
- Because suspension thermal noise is not a concern for the single arm test, the pilot mirrors will be suspended via metal wires (but otherwise use the baseline suspension design, allowing early testing of the suspensions).
- Glass break-off rods with about 3 mm diameter and grooves for the wires will be glued to the sides of the mirrors. The pilot mirrors will come without flats on their sides.

A comparison of selected technical features of the single arm test experiment and the planned sub-SQL interferometer is given in Table 6.1. and a sketch of the

Table 6.1: Comparison of technical features of the single arm test experiment and the planned sub-SQL interferometer.

	Sub-SQL interferometer	**Single Arm Test**
mirror substrate shape	cylindrical + polished flats	cylindrical
mirror surface figure	critical	not critical
mirror coatings	IBS w/ doping and optimization, multiple coating runs	conventional IBS, single HR + AR run
mirror substrate material	synthetic FS, highest grade	synthetic FS, standard grade
mirror ear construction	triangular prism	cylindrical rod
mirror ear attachment	hydroxy-catalysis bonding	glue
number of optics required	5 + spares	2 + spares
suspension	fused silica fiber	steel wire
subsystem dependence	laser + refcav + SPI	laser
SAS tables required	Central + South + West	Central + South

optical layout is shown in Figure 6.4. The purpose of the electro-optic modulator in the beam path is to generate RF control sidebands for cavity sensing and control. The Faraday isolator will prevent the back-reflected cavity field from reaching the laser. Part of the back reflected field will be guided out of the vacuum system to the nearby detection bench for length and alignment sensing purposes. As proposed in [131] the cavity input beam will be collimated by reflecting it off a curved mirror on the far table whose radius of curvature is equal to two times its distance to the waist of the incoming beam. The convex surface of the input mirror of the cavity acts as a mode matching lens and focusses the collimated input beam down such that it matches the cavity eigenmode. A set of rail-mounted lenses serves to tune the radius of the beam waist which is the only parameter that needs to be adapted to match the input beam to the cavity eigenmodes at different lengths, cf. Chapter 4. Input beam steering is accomplished by means of two suspended steering mirrors on the central table. Large substrate diameters are required for these mirrors to avoid clipping of the input beam. Additional beam position sensors behind these two mirrors are desirable.

The cavity length will be stabilized by Pound-Drever-Hall reflection locking. A photo detector in reflection of the cavity serves to extract heterodyne length signals

Figure 6.4 ***(following page)*****:** Schematic drawing of the single arm test optical layout. After phase modulation side bands were imprinted on the input laser beam it is guided through an optical isolator. An adjustable lens telescope serves to project the beam waist to the focal point of the collimating mirror on the far table. The diverging beam propagates to the far table and is collimated in reflection of the collimating mirror. With the aid of two suspended steering mirrors on the central table the collimated beam is directed into the single arm test cavity. Several optical sensors serve to extract signals for controlling the cavity as well as signals for diagnostics purposes.

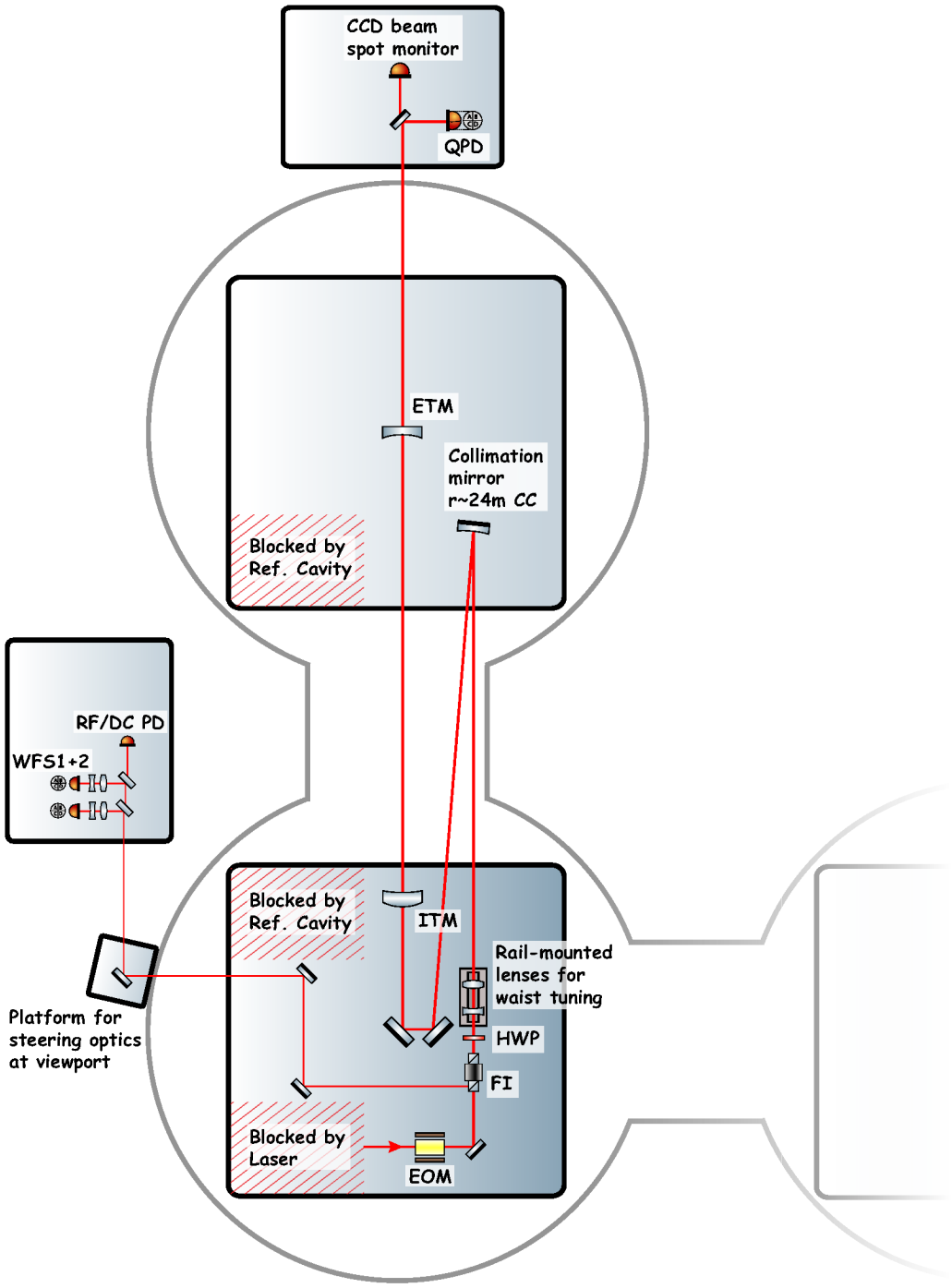
CCD beam
spot monitor
QPD
ETM
Collimation
mirror
r~24m CC
Blocked by
Ref. Cavity
RF/DC PD
WFS1+2
Blocked by
Ref. Cavity
ITM
Rail-mounted
lenses for
waist tuning
HWP
FI
Platform for
steering optics
at viewport
Blocked by
Laser
EOM

for longitudinal control as well as a DC signal proportional to the reflected light power. Two RF wave front sensors (WFS) in reflection of the cavity provide error signals for alignment control. A quadrant photo detector in transmission of the end mirror of the cavity will provide an absolute reference for the beam position. A CCD camera will serve to monitor the cross section of the transmitted beam.

The strength of the actuators of the triple-suspensions may be insufficient in the early stages, with the SPI not being fully commissioned. In this case first tests can be carried out by locking the laser frequency to the single arm cavity instead.

6.4 Required resources

To a large extent the technical infrastructure required for the single arm test experiment can be drawn from existing resources. This includes existing designs e.g. for electronics but also actual hardware such as a Faraday isolator (FI) and an electro-optic modulator. An in-vacuum FI is required for attenuation of the back-reflected field and to pick off light for length and alignment sensing. A unit which was formerly used in GEO is available for the single arm test. An EOM is required for imprinting phase modulation sidebands on the input laser beam for the extraction of length and alignment sensing signals. A spare unit for the reference cavity is available and can be employed. Hardware and electronics which will be built for the single arm test will be transferable to the sub-SQL interferometer experiment in most cases.

6.4.1 Mirror specifications

Custom-made pilot optics for the single arm test were acquired. The technical parameters of these optics are summarized in Table 6.2. The pilot cavity mirror substrates were made of *Corning 7980 0-F* synthetic fused silica with 27 mm thickness and 46.45 mm diameter, resulting in a weight of 100 g. Fabrication tolerances in the substrate dimensions of -0.05 mm in diameter and $\leq \pm 0.2$ mm in thickness were specified. No flats were polished into the sides of the pilot mirror substrates. The mirrors will be suspended by means of steel wires and glass rods with a diameter of 3 mm will serve as break-off rods for the suspension wires. The rods will be glued just above the mid-line on each side of the mirrors with epoxy. Two of the sub-SQL interferometer triple stage suspensions, cf. Section 1.5, will be employed for suspending the single arm test cavity mirrors.

The input mirror substrate is convex-concave with a radius of curvature of 1.776 m on the convex side and 5.700 m on the concave side. The end mirror substrate is a plano-concave one with a radius of curvature of 5.700 m on the concave side. The wedge of these substrates was specified as $\lesssim 5'$. For the uncoated substrates ROC tolerances of $\lesssim 1\,\%$ were specified and a surface form error of $3/0.2$, corresponding to $\lesssim \lambda/10$ peak-valley. Surface quality for a clear aperture $> 80\,\%$ was specified as $5/3 \times 0.025$ and surface roughness as < 0.3 nm RMS.

Table 6.2: Specifications of the single arm test pilot mirrors. The letters A and S in the coating specification denote absorption and scattering, respectively. The surface specifications are given for an aperture of $> 80\,\%$.

Cavity mirrors	
Substrate material	Corning 7980 0-F synthetic FS
Mirror dimensions	46.45 mm -0.05 mm diameter 27 mm ± 0.2 mm thickness
Input mirror curvature (CX-CC)	CX +1776.3 mm $\pm 1\,\%$ CC -5700 mm $\pm 1\,\%$
End mirror curvature (PL-CC)	CC -5700 mm $\pm 1\,\%$
Surface form error	$3/0.2$ ($\lesssim \lambda/10$)
Surface quality	$5/3 \times 0.025$
Surface roughness	< 0.3 nm RMS
Wedge	$< 5'$
IBS HR coating (CC surfaces)	R=99.5 %; A < 10 ppm; S < 10 ppm
IBS AR coating	R=0.1 %; A < 20 ppm; S < 1 ppm
Collimating mirror	
Substrate material	Corning 7980 0-F synthetic FS
Mirror dimensions	76.2 mm -0.1 mm diameter 25.4 mm ± 0.2 mm thickness
Mirror curvature (PL-CC)	CC -24000 mm $\pm 1\,\%$
Surface form error	$3/0.2$ ($\lesssim \lambda/10$)
Surface quality	$5/3 \times 0.063$
Surface roughness	< 0.5 nm RMS
Wedge	$< 5'$
IBS HR coating (CC surface)	R=99.5 %; A < 10 ppm; S < 10 ppm
IBS AR coating	R=0.1 %; A < 20 ppm; S < 1 ppm

For the collimating mirror substrates dimensions of 76.2 mm in diameter and 25.4 mm in thickness were chosen. Tolerances for the diameter were specified -0.1 mm and for the thickness as ± 0.2 mm. As in the case of the cavity mirrors the substrate material is *Corning 7980 0-F* synthetic fused silica. A curvature radius of 24 m was chosen for the concave surface of the plano-concave substrate. The curvature tolerance was specified as $\pm 1\,\%$. Surface form error, surface quality and roughness were specified as $3/0.2$, $5/3 \times 0.063$ and < 0.5 nm RMS, respectively.

The substrates were coated for a wave length of $\lambda_0 = 1064$ nm at normal incidence. For coating deposition the technique of *Ion beam sputtering* was chosen. The convex surface of the input mirror and the plane surfaces of the end mirror and the collimating mirror substrates were AR coated (R<0.1 %). The concave surface of the collimating mirror and the cavity mirrors were coated for a power reflectivity of R=99.5 %. Hence, the single arm test cavity will be impedance matched (cf. Section 2.3.3) with a finesse of $\mathcal{F}_{\mathrm{SAT}} \approx 628$ which is close to the targeted finesse of the sub-SQL interferometer arm cavities of $\mathcal{F} \approx 670$.

Table 6.3: Proposed specifications of the single arm test steering mirrors. The surface specifications are given for an aperture of $> 80\,\%$.

Large steering mirrors (PL-PL)	
Substrate material	UV-grade synthetic FS
Mirror dimensions	4″ diameter, $\sim$ 1″ thickness
Wedge	$< 5'$
S1: Surface form error surface quality surface roughness	$3/0.2$ ($\lesssim \lambda/10$), $5/5 \times 0.040$ ($\sim$SD 10-5), < 0.3 nm RMS
S2: Surface form error surface quality surface roughness	$3/0.5$ ($\lesssim \lambda/4$), $5/5 \times 0.063$ ($\sim$SD 20-10), < 0.5 nm RMS
S1: IBS HR coating	R=99.9 %, 45 deg, s-pol, λ_0=1064nm
S2: IBS AR coating	R<0.1 %, s-pol, λ_0=1064nm

Due to the fact the beams with a radius of up to a centimeter need to be handled, for the two steering mirrors on the central table a diameter of 4″ was chosen to avoid beam clipping. Since a non-optimal aspect ratio in combination with coating stress gives rise to a deformation of the optical surface, a thickness of approximately 1″ was proposed for these mirrors. A summary of proposed specifications for the steering mirrors is given in Table 6.3. Other than the pilot mirrors for the single arm cavity, the large steering mirrors are intended to be used also in the sub-SQL interferometer experiment. A design for the steering suspensions is available and adaptation of the design to larger steering mirrors is underway. Besides the large custom-made steering mirrors various small steering mirrors along with vacuum-compatible as well as standard mirror mounts for use in air are needed. For the extraction of beams from the vacuum system for length and alignment sensing the viewports which were welded in in the first round can be used. For beam steering an auxiliary optical platform will be attached to the viewport in the central tank facing south-east direction. This will be shared with the reference cavity.

6.4.2 Mode-matching optics

Additional mode matching optics are required for the single arm test experiment. A schematic drawing of the proposed single arm test mode matching optics layout is shown in Figure 6.5. The purpose of the mode matching optics is to arrange for a beam waist with a particular radius which depends on the chosen length of the cavity at the focal point of the collimating mirror. Quite generally, curved mirrors for mode matching are preferred over lenses. This is due to the fact that in order to avoid back-reflection lenses need to introduced into the beam path at a small tilt angle with respect to the optical axis. This, however, gives rise to a deformation of the transverse shape of the transmitted beam which potentially

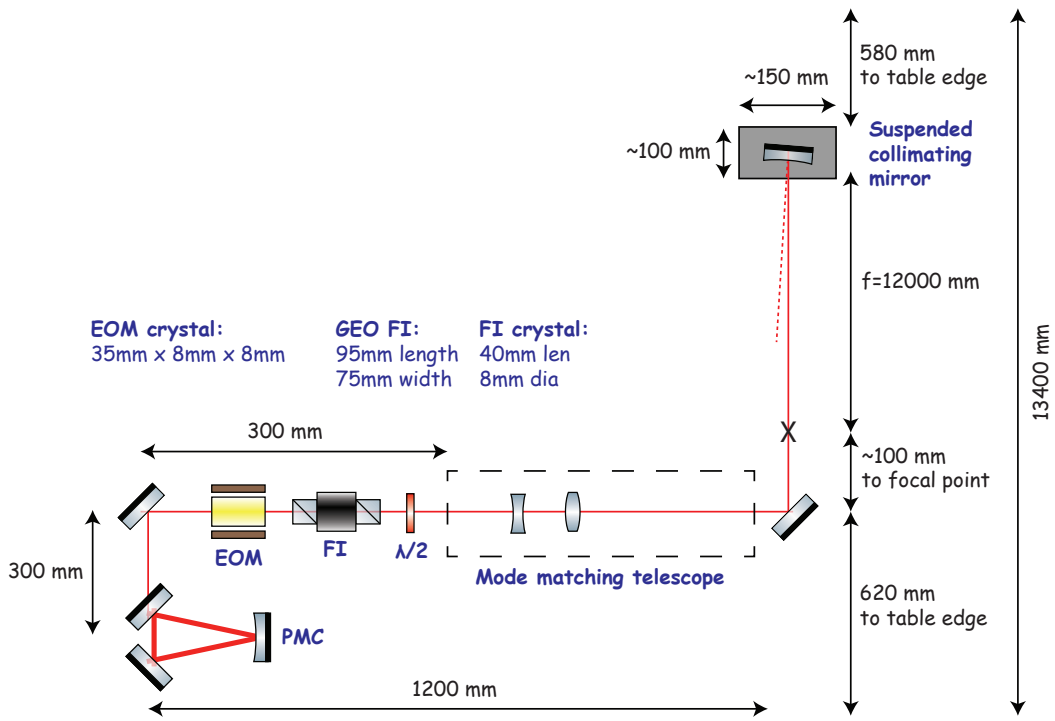

Figure 6.5: Schematic drawing of the input optics layout for the single arm test. For simplicity a conventional lens telescope was proposed for mode matching of the input beam which will be replaced with a mirror-based telescope for the final sub-SQL interferometer. A waveplate serves to rotate the polarization coming out of the Faraday isolator back into the nominal *s*-pol.

reduces the coupling efficiency to the cavities in the interferometer. Since for the single arm test the coupling efficiency is not an extremely critical parameter a mode matching scheme based on a simple lens telescope on the central table was proposed. This could be rail-mounted or, alternatively, piezo-driven positioning stages could be employed for in-situ shifting of the lens positions. Mode matching telescope parameters were identified, based on standard lenses with focal lengths in the range of ± 100 mm to ± 1000 mm, aiming at coupling efficiencies $> 99\,\%$ [212]. To realize the tunable stability scheme introduced previously in Chapter 4, lenses may need to be exchanged to ensure optimal mode matching at all cavity lengths in the targeted range of 10.8 m to 11.3952 m.

6.4.3 Further hardware requirements

For data acquisition and sensing and control of the single arm test cavity the CDS digital control system will be employed. The required CDS channels are summarized in Table 6.4. According to the channel count three 32-channel ADC boxes and two 16-channel DAC boxes are needed as well as associated anti-aliasing an anti-imaging filter units.

Table 6.4: CDS channels count for the single arm test experiment.

ADC channel count	*per unit*	*units*	*total*	*comment*
Main suspensions				
Shadow sensors	6	2	12	required
Coil current monitors	6	2	12	recommended
LED current monitors	6	2	12	optional
Electrostatic drive mon	1-2	2	2-4	recommended
Steering mirrors				
Shadow sensors	4	2	8	recommended
Coil current monitors	4	2	8	recommended
Optical Sensing				
QPD	4	1	4	required
WFS (I, Q, DC $\times$ 4)	6-12	2	12-24	required
RF PD (I, Q, DC)	3	1	3	required
Total			$\sim$ **100**	

DAC channel count	*per unit*	*units*	*total*	*comment*
Main suspensions				
Coil drives	6	2	12	required
Electrostatic drive	1-2	2	2-4	required
Steering mirrors				
Coil drives	4	2	8	required
IFO sensing				
Phase adjuster	1	3	6	required
Total			**30**	

Additional analog electronics will be needed for sensing and control of the single arm test experiment and diagnostics. These include:

- High-voltage ESD drive ($\sim \pm 1$ kV) along with special vacuum feedthroughs
- Coil driver electronics for mirror actuation
- RF oscillator/function generator
- RF/DC photo detectors
- Wave-front sensors
- RF demodulation electronics
- DC spot position sensors
- CCD camera

As pointed out previously, most of the circuit designs are readily available. Besides this, it will be possible to transfer most of the electronics built for the single arm test to the sub-SQL interferometer experiment. The high-voltage ESD drive will be designed and built in the course of the development of the first ESD actuator prototypes.

6.5 Summary

In this chapter, the single arm test experiment was introduced, which was proposed as a stepping stone toward the realization of the AEI 10 m Prototype sub-SQL interferometer. A detailed overview of the optical layout of the experiment was given, including core optics specifications, proposed parameters for the input optics layout as well as required hardware resources for sensing and control.

The single arm test was devised to enable the investigation of key technical aspects of the sub-SQL interferometer, prior to the finalization of the technical infrastructure in the AEI Prototype. Among the goals of the experiment are, for instance, the investigation of lock acquisition and robust control of a marginally stable cavity with 100 g mirrors and circulating powers in the kW range as well as the investigation of noise couplings, such as increased coupling of beam pointing fluctuations to the main signal port and its dependence on the chosen cavity stability. Furthermore, the tunable stability scheme introduced in Chapter 4 will be put to a test in the single arm experiment.

The single arm test experiment was designed to make best use of the existing and operational hardware in the AEI Prototype facility, including e.g. the vacuum system, the two fully installed seismic isolation tables, the SPI and the digital control infrastructure, and will enable the early testing and optimization of hardware for the sub-SQL interferometer, such as for instance the main suspensions and the novel ESD actuators. Most of the opto-mechanical and electronic infrastructure that will be developed for the single arm test is directly transferable to the planned sub-SQL interferometer experiment. Thus, upon the completion of the third seismic isolation table, the single arm test experiment can be gradually extended to the full Fabry-Perot Michelson interferometer.

At the time of writing, the single arm test is being set-up and will provide essential input on the way toward the realization of the sub-SQL interferometer, paving the way for the first audio-frequency band measurement below the SQL for its 100 g test masses.

CHAPTER 7

Automation of the GEO squeezed-light laser

One of the key advanced interferometry technologies which will be employed in future interferometric GW detectors is the injection of squeezed vacuum states of light for the enhancement of the quantum noise-limited sensitivities of these instruments.

The GEO detector was in fact the first large-scale GW interferometer to successfully demonstrate squeezing injection and the corresponding enhancement of its shot noise-limited sensitivity at audio frequencies [213]. Also, in enhanced LIGO squeezing injection was successfully tested and is considered as a prospective upgrade for the Advanced LIGO detectors [214]. In forthcoming generations of ground-based detectors, as for instance the currently envisaged Advanced LIGO upgrades or the Einstein Telescope GW observatory, the injection of frequency-dependent squeezed vacuum is an integral part of the baseline designs [215].

In the scope of this thesis a scheme for the integration of the GEO squeezed-light laser in a digital control system environment was developed and realized. Based on this scheme, the GEO squeezed-light laser was fully automated which enabled for the first time the continuous and long-term stable generation of squeezed vacuum for the routine sensitivity enhancement of a full-scale GW wave detector.

In this chapter an introduction to the GEO squeezed-light laser is given, along with an outline of the LIGO digital control and data system which was employed to digitally interface and automate the squeezed-light laser. The introduction is followed by a detailed discussion of the interfacing of the squeezing experiment to the digital system and the realization of its automation for intervention-free long-term stable operation. As figures of merit for the effectiveness of the automation scheme lock-acquisition transients are presented as well as the duty cycle of the squeezed GEO detector recorded over a period of nearly one year.

7.1 Squeezing enhancement of laser interferometers

The injection of squeezed vacuum into laser interferometers to enhance their shot noise-limited sensitivity was first proposed by *Caves* [216] more than two decades ago. Since then, extensive research efforts were undertaken to bring this technique to maturity, to enable its reliable application in high precision laser interferometers for GW detection in the audio frequency band.

The principle approach to the generation of squeezed states of light is the interaction of an intense laser beam with a non-linear medium, resulting in correlated quantum noise sidebands. Whereas in a conventional interferometer unsqueezed vacuum enters through the open detection port and gives rise to increased noise in the measurement, in a squeezing-enhanced interferometer conventional vacuum is replaced with squeezed vacuum with less noise in one quadrature. By arranging for a suitable orientation of the squeezing ellipse of the injected squeezed vacuum, the impact of quantum noise on the measurement can be reduced.

The first experimental observation of squeezed light was reported in the year 1985 by *Slusher et al* [217] and was closely followed by other experiments. Two years later, in 1987, *Wu et al* reported on the successful generation of squeezed light by means of optical parametric oscillation (OPO) [218]. Their experiment was based on a non-linear crystal enclosed in an optical cavity, which has become the most successful approach to generating continuous-wave squeezed states of light. Ever since, squeezed-light lasers were continuously optimized and squeezing factors further increased.

An important milestone was the first observation of 10 dB squeezing which was reported on by *Vahlbruch et al* in 2008 [219]. The current upper limit in terms of observed squeezing strength is a quantum noise suppression of almost 13 dB which was reported by *Eberle et al* [220]. Besides increasing the squeezing strength it was furthermore necessary to experimentally demonstrate the generation of squeezing at audio frequencies, in order to enable the enhancement of the sensitivity of ground-based GW detectors in their detection band. This task required substantial research and development and remained an unsolved challenge for years. The first successful demonstration of squeezing generation down to frequencies of hundreds of Hz was reported by *McKenzie et al* in 2004 [221]. An important breakthrough for the generation of low-frequency squeezing was the development and experimental demonstration of the concept of *coherent control* of squeezed light sources by *Vahlbruch et al* in 2006 [222] which enabled the generation of squeezing in the frequency range of 10 Hz to 10 kHz for the first time.

A few years after a squeezing-enhanced power recycled Michelson interferometer was reported on by *McKenzie et al* in 2002 [223], which can be regarded as a proof-of-principle demonstration of squeezing compatibility with the interferometer configuration adopted for initial LIGO, *Vahlbruch et al* successfully demonstrated squeezing enhancement of a Michelson interferometer with power recycling and detuned signal recycling in 2005 [224]. Later, in 2008, *Goda et al* successfully demonstrated the squeezing enhancement of a suspended prototype Fabry-Perot Michelson interferometer with power recycling [225], at frequencies above the audio band.

In 2010, squeezing injection and the associated sensitivity improvement at audio frequencies was realized in GEO 600 which was the first demonstration of squeezing enhancement of a full-scale GW detector in the relevant frequency band [213].

Generally, squeezed-light lasers are highly complex laser systems with a multitude of phase sensitive optical stages. These need to be tightly controlled to ensure the reliable generation of strong squeezing. Squeezed light lasers are typically not operated in vacuum and are thus subject to environmental disturbances which may compromise the stability of the squeezed light generation. This includes transient disturbances on a short time scales, which cannot be sufficiently suppressed by the control systems, but also low-frequency variations of parameters such as laser frequency drifts due to thermal fluctuations. Compensation of these variations may exceed the dynamic range of the actuators in the optical setup, resulting in lock-loss. Under typical laboratory conditions these disturbances require frequent intervention of the experimenter, to re-acquire full lock of the experiment. The goal of the work described in this chapter was the full automation of the GEO squeezed-light laser, to enable its long-term stable, intervention free operation in the GEO GW detector.

7.2 Introduction to the GEO squeezed-light laser

In the following, an introduction to the GEO squeezed-light laser optical layout will be given and the role of its individual optical stages and their interaction will be recalled. The conceptual design of the GEO squeezed-light laser was proposed by *Vahlbruch* in 2008 [226]. A schematic drawing of the optical layout is depicted in Figure 7.1. The squeezed-light laser was fully assembled and characterized in the clean room facilities at the Albert-Einstein-Institute. The optical components were mounted on a 1.13 m $\times$ 1.35 m aluminum bread board with a steel bottom plate to maintain transportability of the experiment. After the finalization of the optical assembly and the characterization of the experiment the analog electronics for coherent control were modified to enable interfacing to the digital control system, remote control of the experiment and finally full control automation. The fully assembled and automated squeezed-light laser was then taken to the GEO 600 site and integrated in the detector.

Three commercial *Innolight Mephisto* Nd:YAG NPRO-lasers were used as light sources for the experiment. Whereas the main laser generates an output power of 2 W cw at $\lambda_0 = 1064$ nm, the two auxiliary lasers, which are in the following referred to as *Aux1* and *Aux2*, have a nominal output power of 200 mW at the same wave length.

The heart of the GEO squeezed-light laser is the squeezed light source (SLS) resonator stage which is formed by a plano-convex periodically-poled potassium titanyl phosphate (PPKTP) crystal together with a convex-concave coupling mirror. The HR coated convex surface of the crystal forms a cavity with the coupling mirror, with a finesse of $\mathcal{F} \approx 75$ at 1064 nm [227]. The non-linear crystal and the coupling mirror are enclosed in a quasi-monolithic housing which also includes a piezo-

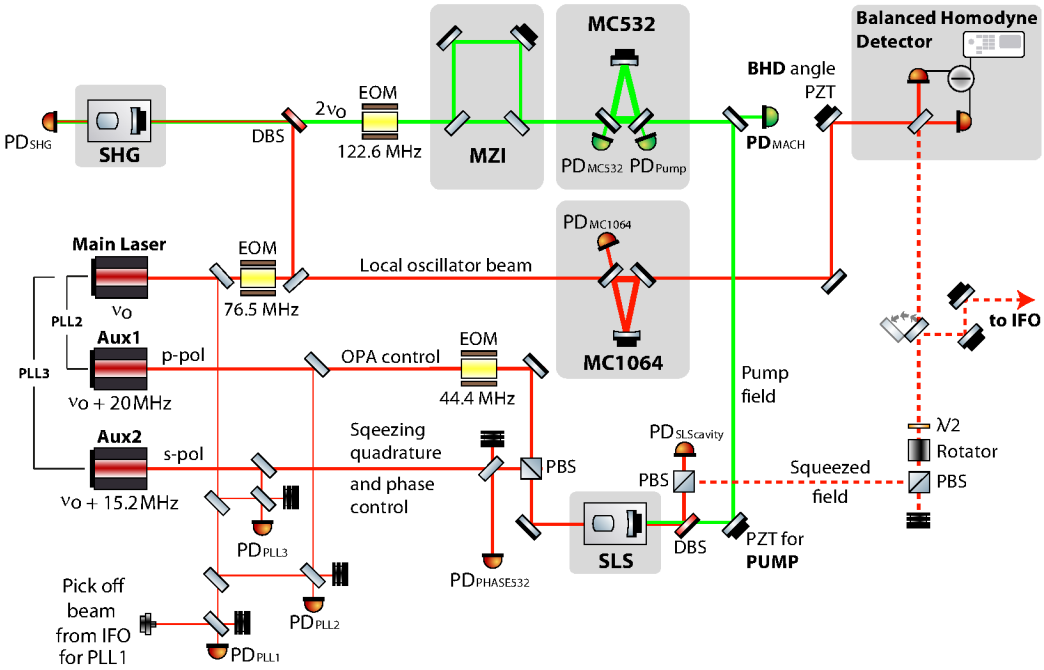

Figure 7.1: Schematic drawing of the GEO squeezed-light laser optical layout. Stages of the experiment that require control automation are the second-harmonic generator (SHG), the squeezed light source cavity (SLS), the Mach-Zehnder interferometer (MZI) for intensity stabilization of the pump field, the ring cavity for filtering of the pump field (MC532) and, finally, the phase of the harmonic pump field (PUMP). In diagnostics mode, control automation is extended to the mode cleaner cavity for the fundamental field (MC1064) and the phase of the local oscillator beam, to lock the readout quadrature at the balanced homodyne detector (BHD).

electric transducer and a Peltier element for actuation on the cavity length and the crystal temperature, respectively, as well as thermistor temperature sensors for sensing of the temperature of the non-linear crystal [228]. An analog control loop is employed to ensure that the phase-matching temperature of the crystal is maintained.

A fraction of the laser light generated by the main laser is directed to the second harmonic generator (SHG) for the generation of the pump field for the squeezing process at 532 nm. The SHG resonator layout is mostly identical to that of the SLS, with the difference that a plano-convex, 7 % doped $MgO:LiNbO_3$ crystal is used as non-linear medium. The finesse of the cavity for the fundamental wave length is arranged for as $\mathcal{F} \approx 59$ [227]. The SHG resonator is kept on resonance with the aid of the *Pound-Drever-Hall* (PDH) technique [55]. The error signal for the corresponding feedback loop is obtained from the photo detector in transmission of the SHG cavity,

by demodulating the signal at 76.5 MHz. The frequency-doubled SHG output field is phase modulated at 122.6 MHz, passes through a Mach-Zehnder Interferometer (MZI) before it is transmitted through an aluminum spacer-mounted ring cavity, for spatial mode cleaning as well as filtering of high frequency phase and amplitude noise. As high-frequency phase noise is known to reduce the achievable squeezing level, its attenuation is crucial to ensure the generation of strongly squeezed vacuum states of light. The PDH error signal for locking the mode cleaner length is obtained in reflection of the cavity. By shifting the phase in one of its arms, the MZI serves as an actuator for the power of the pump field. It is part of an intensity stabilization feedback loop to stabilize the power of the filtered pump field. The pump power is measured in transmission of the mode cleaner cavity and serves to generate an error signal for feedback to the MZI phase. Finally, to provide adjustability of the phase of the pump field a piezo-actuated mirror is included in the optical path.

For the stabilization of the SLS cavity length, an orthogonally polarized auxiliary beam is utilized to avoid the introduction of technical noise into the squeezed field at the fundamental frequency. The beam of the auxiliary laser *Aux1* is p-polarized, shifted in frequency to be simultaneously resonant with the s-polarized field in the squeezing source and phase modulated at 44.4 MHz before it is guided into the squeezing resonator. The *Aux1* laser is locked to the main laser by means of a phase locking loop (PLL). The light detected in transmission of the squeezing resonator is demodulated at 44.4 MHz to obtain an error signal for the cavity length.

For diagnostics purposes a balanced homodyne detector was included in the optical setup. A fraction of the main laser beam with phase modulation sidebands at 76.5 MHz is picked off and guided through a triangular mode cleaner cavity which is locked in reflection with the PDH technique. The transmitted beam serves as a optical local oscillator and can be shifted in phase with the aid of a piezo-actuated mirror in the beam path.

The second auxiliary laser *Aux2* is also phase locked to the main laser and shifted in frequency and serves to control the squeezing angle of the generated squeezed vacuum, implementing the *coherent control* scheme [222]. With the aid of the *Aux2* laser, error signals for the phase of the pump field and for the optical local oscillator phase can be obtained. The former signal is extracted from the photo detector signal in reflection of the squeezing resonator, by demodulating at twice the *Aux2* laser offset frequency. The latter signal is extracted from the difference photo current of the balanced homodyne detector by demodulating at the *Aux2* laser offset frequency. In the GEO detector, the *Aux2* laser is utilized to control the squeezing angle such that it matches the detected quadrature at the interferometer output. Furthermore, the *Aux2* laser serves to extract signals for alignment control of the squeezed field injected into the dark port of the interferometer [229]. To ensure a well-defined phase relation between the main GW observatory laser and the squeezed-light laser, the main laser on squeezing bread board is locked to the main laser of the interferometer with the aid of a third PLL. For further details on the GEO squeezed-light laser experiment see e.g. [226, 227, 230].

7.3 The digital control system architecture

In the course of the *GEO-HF* upgrade program the LIGO real-time digital *Control and Data System* (CDS) [231] was adopted for the realization of digital controls in the GEO detector. Furthermore, LIGO CDS is employed in the AEI 10 m Prototype and is intended to serve as the primary platform for data acquisition and the realization of the majority of feedback loops required for controlling the infrastructure as well as planned interferometry experiments.

The CDS platform was originally developed by the LIGO project, as an alternative to commercial digital control systems which did not meet the requirements for performance and scalability for controlling large laser interferometric GW detectors. Besides its real-time control and data acquisition capabilities CDS also provides long term data storage of the extracted data for later analysis. Furthermore, user interfaces are available for online steering of control parameters and for remote control of experiments, based on the *Experimental Physics and Industrial Control System* (EPICS) architecture [232]. Instead of making use of special hardware, CDS is to a large extent based on "off-the-shelf" components which greatly improves the scalability of the system.

7.3.1 Hardware components

Other than many commercial solutions, CDS is not a monolithic system but it is composed of a multitude of hardware components. A chart of the hardware components that make up a generic CDS system is depicted in Figure 7.2. At the heart of the CDS hardware setup sits the so-called *front end*. It is the machine which runs the real-time application code and is at the time of writing typically based on a standard Intel® Xeon® multi-core processor system. The fact that the number of front ends can simply be increased if more computational power or signal channels are required reflects the excellent scalability of CDS. The front ends are connected via Gigabit Ethernet to a local area network which serves a variety of purposes. Operator work stations, usually remotely located from the experiment in a control room, are part of this network for online steering of the real-time code running on the front end machines. Furthermore, permanent data storage units, the so-called *frame builders* are connected to this network. These frame builders are not necessarily dedicated computer systems but can optionally be operated as tasks running on the front end computers. A *Network Time Protocol* (NTP) server, which obtains the current time from a *Global Positioning System* (GPS) signal receiver, is also part of this network to ensure accurate time stamping of stored data.

The actual signal input/output hardware is housed in *expansion chassis* units which are connected to the front ends via PCI Express® bus. To ensure high transmission rates over distances of up to several hundreds of meters an optical fiber link is employed and serves to spatially extend the PCI Express® bus. The advantage of this approach is that expansion chassis can be set up in the direct vicinity of the experiment to keep the distances of analog signal transmission at a minimum while

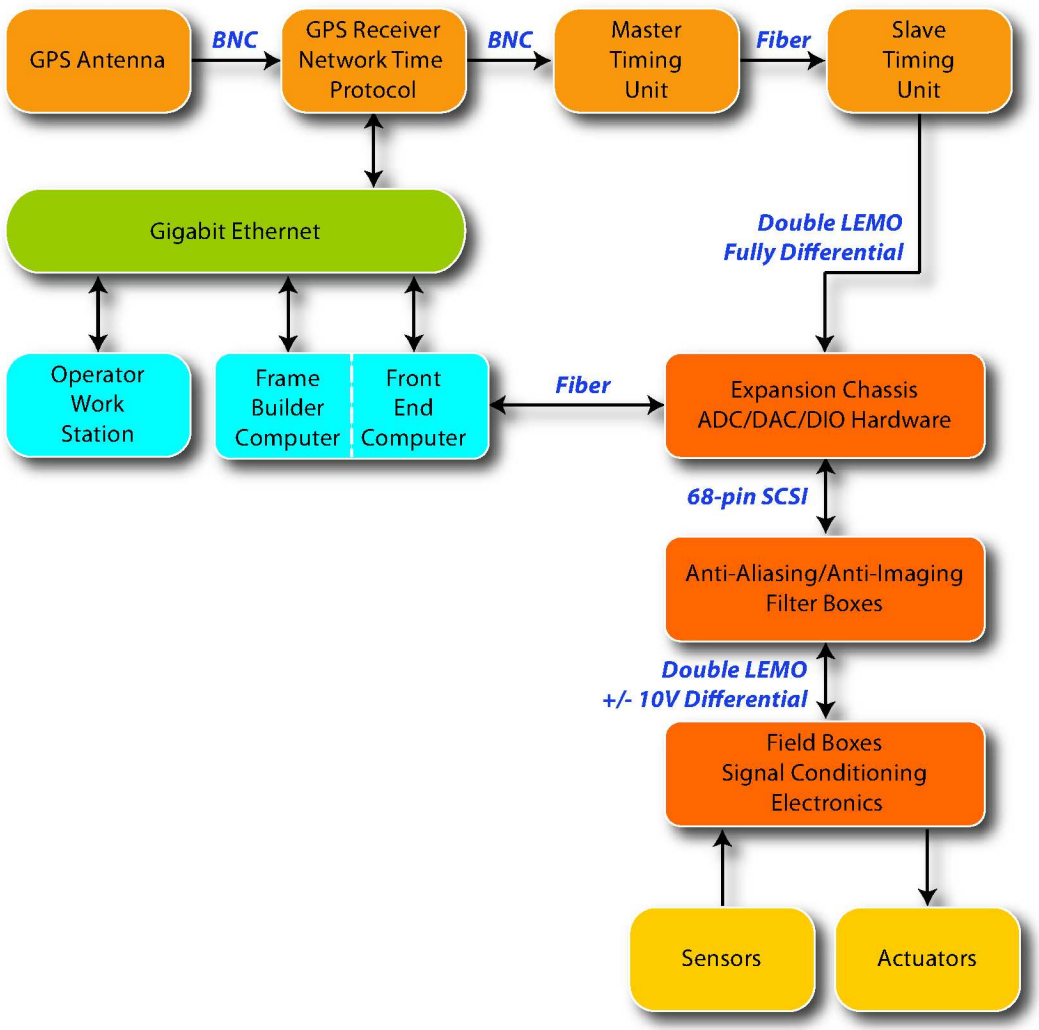

Figure 7.2: Chart of the building blocks of a generic LIGO CDS digital control system hardware setup. The system is composed of a multitude of "off-the-shelf" hardware components which interact via analog signals, Ethernet and a fast optical fiber link, respectively. At the heart of the setup sits the front end computer, which executes the real-time control application code. Operator workstations allow for online-steering of real-time code running on the front end machines.

the front end machines can be set up remotely, e.g. in a centralized server rack. The expansion chassis are equipped with commercial analog to digital (ADC) and digital to analog (DAC) signal conversion hardware. To ensure deterministic sampling intervals the expansion chassis are connected to a timing unit which triggers the ADCs and DACs at a rate of 65536 Hz. This timing unit receives the trigger signal from a timing master which is, again, locked to the GPS time.

Analog filter units are connected to the ADC and DAC cards to provide anti-aliasing and anti-imaging of signals, respectively. Both of these are based on fourth order Butterworth filters with a cut-off frequency of approximately 10 kHz and an additional high-Q notch filter at 65 kHz which suppresses aliased signals that would otherwise appear at DC. The purpose of anti-imaging low pass filtering is to smoothen the stepped output signal of the DACs. The *field boxes* are the link between the sensors and actuators in the plant which is to be monitored or controlled. These boxes contain signal conditioning electronics such as for instance analog whitening/de-whitening filters to make best use of the dynamic range of the digital system. For the transmission of analog signals fully differential signaling is employed, for better immunity to electromagnetic interference.

With this hardware setup with sampling rates of up to 65536 Samples/sec and corresponding latencies of a few microseconds hard real-time requirements are fulfilled. Hence, CDS allows for deterministic operation which is a prerequisite for implementing digital filters with bandwidths required for controlling interferometry experiments.

7.3.2 Control system software

The control system software environment is composed of various existing and specifically developed software components. These range from graphical tools for the formulation of the control algorithm through the automated generation of real-time code based on these graphical models to software to run the real-time application code and to enable online steering of the real-time software from operator work stations.

To provide a means of intuitive creation of real-time models the visual programming capabilities of MATLAB® Simulink® are made use of. To set up a real-time application, the control logic is defined in a block diagram. A library of custom CDS function blocks is provided which includes digital filters, simple mathematic operations, communication with EPICS channels as well as inter process communication, to enable interaction of two or more real-time models. Connections between inputs and outputs of these blocks define the signal flow in the real-time application.

The graphical model is converted to executable real-time code by the *Real-time code generator* (RCG). The core RCG application is a collection of Perl scripts which parse the graphical model and generate real-time C source code which implements the functions and the signal flow defined in the Simulink® block diagram. Based on this code a Linux kernel object is created, including standard RCG wrapper software to ensure proper code timing and sequencing, diagnostics, input/output drivers and connections to the data acquisition system. In parallel to the generation of the real-time code, an EPICS sequencer application and a channel database, the EPICS *input/output controller* (IOC), is built, to later provide operator access to the real-time process via Ethernet. Additionally, a set of configuration files is generated to define data channels as well as diagnostics test point information in the real-time model. A set of basic EPICS operator screens is generated for use as graphical user interfaces to the steerable components in the real-time model. A schematic of the automated

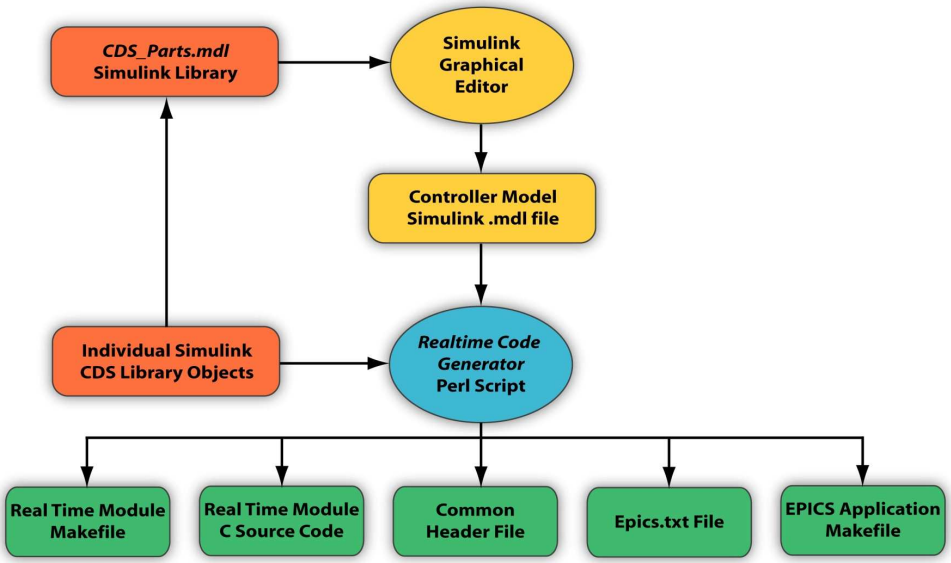

Figure 7.3: Chart of the steps and components involved in the generation of CDS real-time code by the *Real Time Code Generator* (RCG) application. MATLAB® Simulink® is used to create a block diagram representing the desired signal flow and control logic of the real-time application. A custom library contains function blocks representing e.g. digital filters, I/O operations or simple mathematical functions. The RCG parses the graphical model and outputs the real-time code implementing the logic of the block diagram, an EPICS application to enable operator access during runtime as well as software to automatically build these applications.

generation of real-time code by the RCG application is depicted in Figure 7.3. To ensure deterministic operation of the software, CDS was designed to run on a special operating system with real-time capabilities. To meet hard real-time requirements a Linux operating system with a specific LIGO-developed patch, inspired by the Preemptive Linux patch [233], is employed. With this patch it is possible to run the real-time application on a cpu core which is fully isolated from the rest of the system, i.e. it is also detached from the Linux scheduler which could interrupt the code execution. Hence this approach requires code scheduling to be taken care of manually which is realized by a special *I/O processor* (IOP) real-time model which needs to run in parallel to the real-time application.

The so-called *data acquisition daemon* software running on the frame builders provides data acquisition (DAQ) functionality. If requested by the user, this software continuously writes digitized data it receives from the front-end computers to storage media in a special frame data format. Finally, the *network data server* (NDS) provides data distribution functionality by retrieving and sending stored data to work station computers upon user request.

7.4 Conceptual approach to squeezed-light laser automation

Whereas in typical lab-scale squeezing experiments the duty cycle is usually of the order of minutes to hours, reliable squeezing generation on long time scales ranging from weeks to months with down times as short as possible is a crucial prerequisite for an implementation in a GW detector. Hence, full automation of the experiment, enabling intervention-free operation is required. The digital system was intended to take over the tasks which would normally be taken care of by the experimenter, i.e. surveillance of the experiment, adjustment of set points of the analog controls and ensuring fully locked operation at all times. Also the acquisition of the numerous monitor signals of the squeezed-light laser and their storage for later use was aimed for.

Even though CDS is capable of implementing digital filters for feedback control a different approach was favored for controlling and automating the squeezed-light laser experiment. It was intended that the control authority of the optical stages remained with the analog servo electronics which were already part of the experiment, as these were highly optimized and e.g. in terms of control bandwidth superior to a digital implementation of the controllers. Hence, to automate the experiment the existing analog control electronics were modified to enable digital system interfacing. However, it was intended to retain the option to later switch to a purely digital implementation, if desired. This approach was proposed in the conceptual design of the squeezed-light laser experiment in [226].

A central question regarding the principle approach is how to make best use of the capabilities of the digital system since CDS does not provide a standard method to realize process automation. However, the execution of custom code in the real-time layer and the EPICS scripting capabilities pose options to solve this task. Whereas EPICS layer scripting is convenient in terms of code development and testing, a real-time code implementation is much less comfortable but substantially faster in terms of digital system interaction with the experiment and hence well-suited for simple but time-critical tasks. Initially, it was experimented with a pure EPICS-based approach but it was found that the latencies were comparatively large, rendering this approach less useful for an application aiming at high duty cycle. For the automation of the squeezed-light laser a combined approach was chosen to take advantage of the individual strengths of a fast real-time code implementation and EPICS-layer scripting, to achieve optimal performance as well as code maintainability. A schematic illustrating this approach is depicted in Figure 7.4.

In the first step each component in the experiment that requires surveillance or full automation is mapped to a software representative, implemented in the real-time layer for fast interaction. These software modules encapsulate a number of functions and signals which are accessible from user space via EPICS channels. In a second step high-level representatives in the form of software objects are created in user space which communicate with the real-time representatives via EPICS and hence provide convenient but indirect access to the squeezed-light laser. Human operators

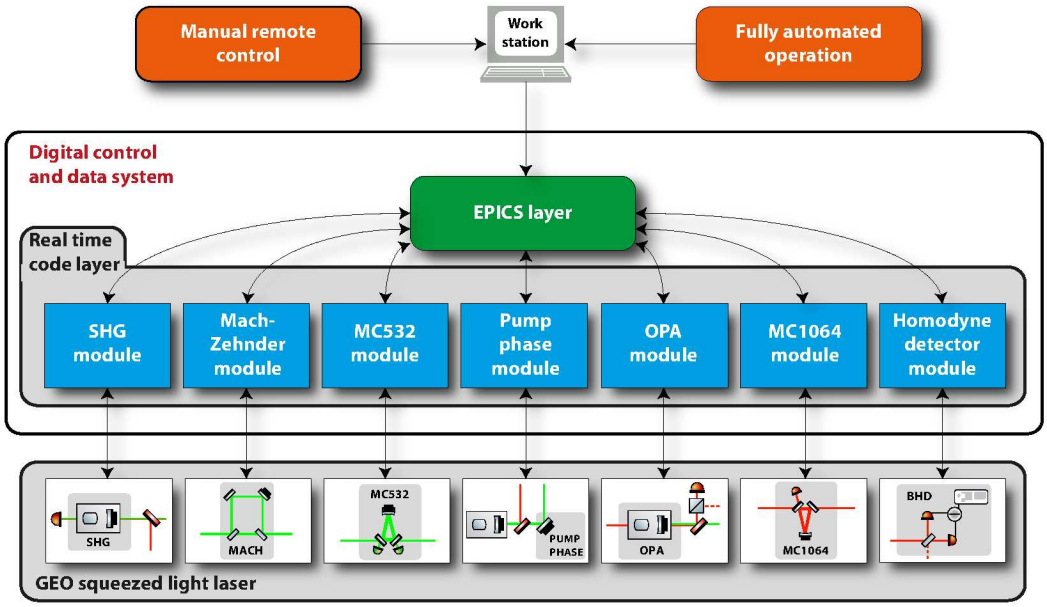

Figure 7.4: Distribution of squeezed-light laser control automation tasks between the CDS real-time and EPICS layers. In the first step each stage in the squeezed-light laser is mapped to a software module in the real-time layer. The functionality of the stage in the experiment can be accessed via the inputs and outputs of the real-time software representative via EPICS channels. In a second step, additional high-level objects are created in user space, which communicate with the real-time code representatives via an EPICS communication protocol. Human operators or automation scripts interact with the objects in user space and access the squeezed-light laser experiment indirectly, in a secure and controlled way.

or automation software communicates with these high-level objects and requests of e.g. a state change are forwarded via EPICS to the real-time layer representatives which take the necessary actions. Low-level network communication and interaction with the experiment is thus fully handled internally by the software, invisible to the user. This approach of granting controlled access to the experiment hence provides a convenient interface for manual operator steering or software extensions and the fact that the hardware in the experiment is accessed in a controlled way helps to prevent exceptions in the squeezed-light laser operation.

7.5 Interfacing of the squeezed-light laser with the digital control system

For remote control of the squeezed-light laser it was necessary to establish a hardware link between the digital system and the analog electronics as well as a low-level software interface capable of fast interaction with the optical stages in the experiment. In the following section a detailed description of the chosen approach to these two aspects will be given.

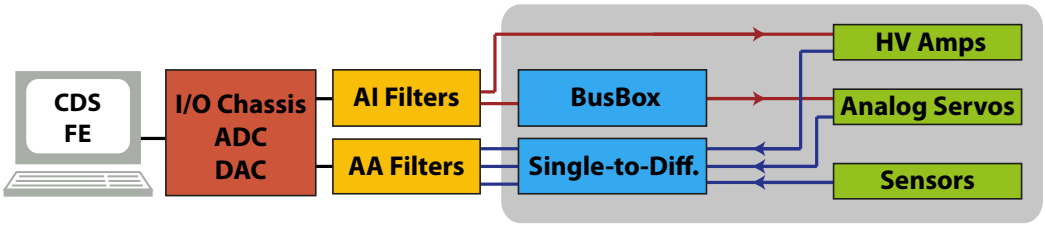

Figure 7.5: Schematic drawing of the hardware interface of the squeezed-light laser analog control electronics to CDS. Conventional ADC and DAC hardware in conjunction with AA and AI filters is employed to sample output signals of the sensors in the experiment and generate steering signals for the analog electronics, respectively. Whereas in the case of the sensor and monitor signals the single-ended analog outputs are converted to differential signals prior to transmission to the signal sampling hardware, the steering signals are directly fed to the analog electronics without an intermediate signal conversion stage. The *BusBox*, which is all passive and leaves the signals unmodified, serves as an interface to an existing hardware bus in the electronics rack over which the steering signals for the analog servo controllers are routed.

7.5.1 Hardware interfacing

As pointed out in Section 7.4, the feedback control authority was intended to remain with the analog electronics of the experiment. Hence, the control circuits of the GEO squeezed-light laser were modified to enable their remote steering and readout of monitor signals with the digital system.

A diagram illustrating the hardware interfacing scheme of the squeezed-light laser analog electronics to the digital system is depicted in Figure 7.5. Conventional ADC and DAC hardware was used for sampling of analog sensor signals and to synthesize steering signals for remote control of the analog hardware, respectively. Digital I/O hardware, which could have been employed as an alternative to DAC hardware for remote switching, was not available at the time of the squeezed-light laser automation. For this reason, and additionally with the option in mind to switch to purely digital control of the squeezed-light laser at a later point, it was chosen to employ DAC hardware for all digital system output channels. The signal input and output hardware was followed by AA and AI filter boxes, respectively.

Whereas the signals which were synthesized in the digital system to be fed to the HV-amplifiers were directly routed to the individual units, the remote steering signals for the servo controller electronics were routed over an existing hardware bus which is part of the electronics racks. Interface boxes ("BusBox") were employed for this purpose. Leaving the signals unaffected, the sole purpose of these is to provide an interface for the digital system outputs to the hardware bus in the electronics rack. Sensor signals from the experiment as well as monitor signals from the servo controllers (error signal monitor) and the HV-amplifiers (HV output monitor) were provided as single-ended signals. Prior to their transmission to the analog inputs of the digital system these were converted to differential signals with the aid of a

converter box ("Single-to-Diff"), with a circuit based on a differential line driver amplifier.

The modification of the servo controller electronics allowed to remotely close the feedback loops, to engage or disengage the integrator stages which were part of the controllers and to remotely adjust the proportional gains in the closed loops. Nevertheless, the option to switch to fully manual operation was retained. The high-voltage amplifiers of the squeezed-light laser, which serve the purpose of amplifying the control signals to provide a HV drive for the PTZ length actuators in the optical setup, were equipped with an additional input and a summing amplifier. With this modification it was possible to apply offsets generated by the digital system to the HV output signal. This allowed remote sweeping of lengths within the squeezed-light laser stages by the digital control system which was a necessary building-block for automated lock acquisition. For the schematics of the used analog electronics see Appendix B.

A vast number of sensor outputs and monitor signals from the squeezed-light laser were interfaced to the digital system for surveillance and diagnostics purposes but also to serve as trigger signals for actions defined in the automation code. Besides the demodulated RF signals which serve as error signals for the feedback loops, the measured DC signals of all photo detectors are digitized. The PLLs which are used to lock the phase of the auxiliary lasers to the main laser and the main laser the master laser of the interferometer require no remote steering or manual intervention except for sporadic resets of the PLL controllers. However, the outputs of the PLL controllers are interfaced with the digital system to make this information centrally available for diagnostics.

7.5.2 Real-time software control of the optical stages

As pointed out previously in Section 7.4, for the low-level software control of the stages in the squeezed-light laser a real-time layer implementation was chosen, to ensure low-latency interaction with the experiment. Whereas a signal graph generated with Simulink® (cf. Section 7.3.2) served as the foundation for this software, the graphical model needed to be extended with custom real-time code to account for the specific functionality of the optical stages and to combine simple instructions to realize more complex algorithms involving trigger events and state changes.

Besides the three PLLs which simply need to be activated for closed loop operation there are in total five lockable components which compose the GEO squeezed-light laser and which require control automation. These are

- the second harmonic generator (SHG),
- the Mach-Zehnder interferometer (MZI),
- the mode cleaner for the 532 nm pump field (MC532),
- the squeezed light source cavity (SLS),
- the phase of the pump beam (PUMP).

In diagnostics mode two more stages require attention by the digital system,

- the mode cleaner for the 1064 nm (MC1064) local oscillator beam,
- the local oscillator phase which determines the homodyne angle for balanced homodyne detection (BHD).

In the following the structure of the SHG graphical model, which is depicted in Figure 7.6, will be discussed in detail as a representative example. A similar model was developed for each of the lockable components listed above, with slight differences to account for specific properties of the corresponding stage in the squeezed-light laser.

Generally, three input signals which serve for monitoring and for steering of the corresponding component of the squeezed-light laser are routed to each of the real-time code sub-modules. These are the demodulated RF signal, which serves as the error signal for the control of the component, a DC signal representing the light power reflected at or transmitted through the optical stage and a monitor signal picked off at the respective HV amplifier. The HV monitor signal is an exact copy of the control signal fed to the actuator of the corresponding stage in the optical setup. For the SHG and SLS components, which require a temperature stabilization to ensure phase matching of the fundamental and the harmonic field, two additional signals are digitized and made available in the real-time application. These are the error signal of the respective temperature servo controller and a voltage which is proportional to the resistance of an NTC thermistor which is used to sense the temperature of the non-linear crystals. The real-time software representative of the diagnostic homodyne detector includes an additional monitor channel of the difference signal generated from the two homodyne photo diodes. This signal can e.g. be used for extracting squeezing spectra in diagnostics mode. In the software module for the Mach-Zehnder interferometer the DC signal which is measured in reflection of the pump field mode cleaner is made available in addition to the standard set of signals. Since in the automated locking sequence (cf. Section 7.6) the MC532 is locked prior to the MZI this auxiliary signal is required to tune the MZI such that sufficient light is transmitted to allow for locking of the MC532 component. After the MZI is tuned to maximum transmission with the aid of the auxiliary DC signal as a reference and the MC532 is stably locked, the signal from the MZI photo detector in transmission of the MC532 is used to lock the MZI on its operating point by means of a "side-fringe lock". Generally, all electronic signals that are

Figure 7.6 ***(following page)*****:** Graphical real-time code model of the SHG component as a representative example. The block diagram drawn in Simulink® serves to define the signal flow and the interaction of signals with predefined or custom functions represented by different blocks in the model. The real-time code generator application, which is part of CDS, parses the graphical model and converts it into real-time C code which is in turn compiled and executed on the front end computer.

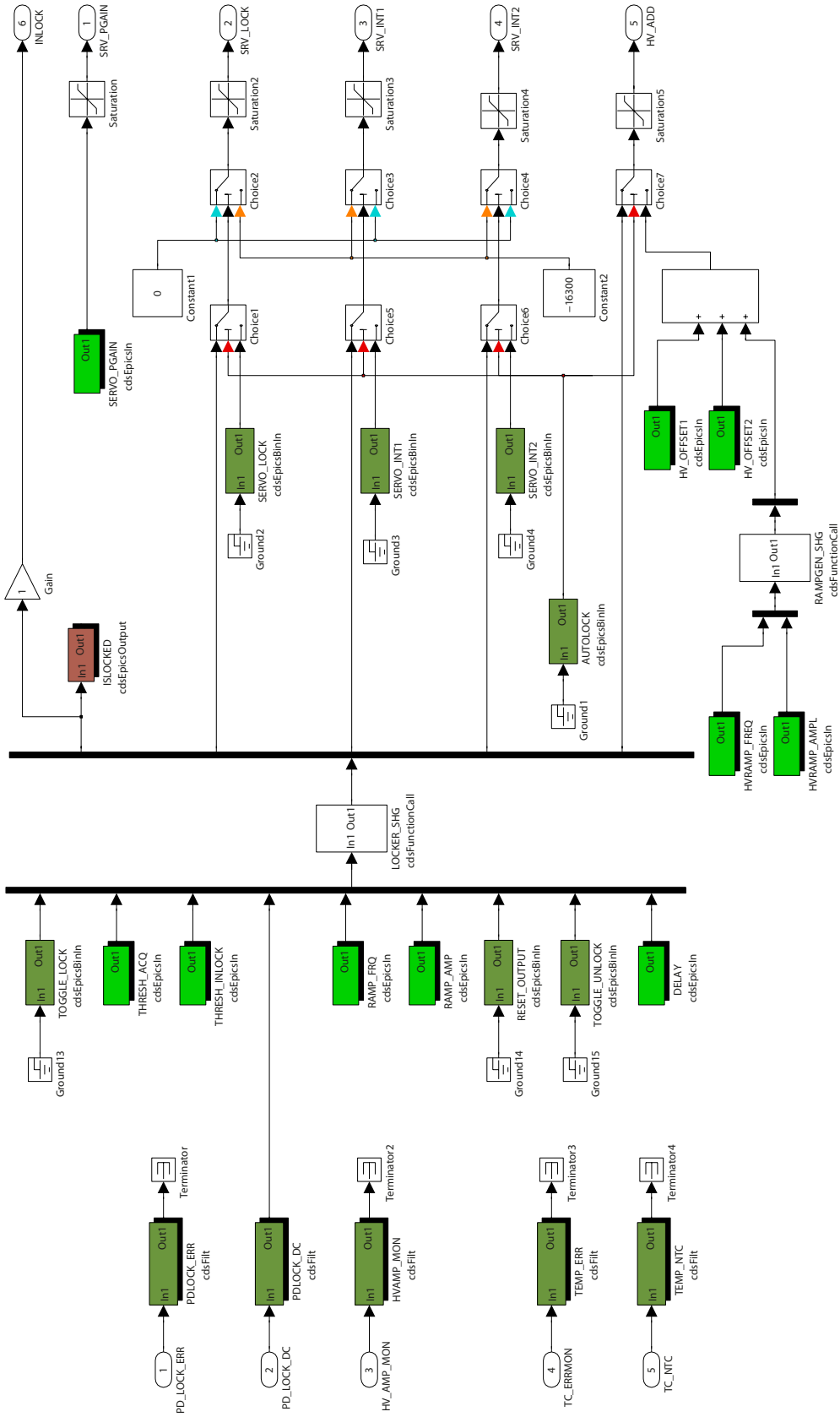
6 INLOCK
1 SRV_PGAIN
2 SRV_LOCK
3 SRV_INT1
4 SRV_INT2
5 HV_ADD
Saturation
Saturation2
Saturation3
Saturation4
Saturation5
Choice2
Choice3
Choice4
Choice7
0
Constant1
−16300
Constant2
Choice1
Choice5
Choice6
Out1 SERVO_PGAIN cdsEpicsIn
In1 Out1 SERVO_LOCK cdsEpicsBinIn
In1 Out1 SERVO_INT1 cdsEpicsBinIn
In1 Out1 SERVO_INT2 cdsEpicsBinIn
Out1 HV_OFFSET1 cdsEpicsIn
Out1 HV_OFFSET2 cdsEpicsIn
Ground2
Ground3
Ground4
Ground1
1 Gain
In1 Out1 ISLOCKED cdsEpicsOutput
In1 Out1 AUTOLOCK cdsEpicsBinIn
In1 Out1 RAMPGEN_SHG cdsFunctionCall
Out1 HVRAMP_FREQ cdsEpicsIn
Out1 HVRAMP_AMPL cdsEpicsIn
In1 Out1 LOCKER_SHG cdsFunctionCall
In1 Out1 TOGGLE_LOCK cdsEpicsBinIn
Out1 THRESH_ACQ cdsEpicsIn
Out1 THRESH_INLOCK cdsEpicsIn
Out1 RAMP_FRQ cdsEpicsIn
Out1 RAMP_AMP cdsEpicsIn
In1 Out1 RESET_OUTPUT cdsEpicsBinIn
In1 Out1 TOGGLE_UNLOCK cdsEpicsBinIn
Out1 DELAY cdsEpicsIn
Ground13
Ground14
Ground15
Terminator
Terminator2
Terminator3
Terminator4
In1 Out1 PDLOCK_ERR cdsFilt
In1 Out1 PDLOCK_DC cdsFilt
In1 Out1 HVAMP_MON cdsFilt
In1 Out1 TEMP_ERR cdsFilt
In1 Out1 TEMP_NTC cdsFilt
1 PD_LOCK_ERR
2 PD_LOCK_DC
3 HV_AMP_MON
4 TC_ERRMON
5 TC_NTC

routed from the squeezed-light laser to the digital control system can be accessed in real-time and, if necessary, recorded for long-term storage.

The core functionality of the real-time automation code is contained in a custom code block which is included in the real-time kernel module during compile time. The purpose of this code block is to perform the necessary steps to lock the associated stage if acquisition was requested and to continuously monitor the locked stage to detect exceptional behavior. The corresponding real-time code was customized for each of the components in the experiment. The algorithmic steps defined in this code block, referred to as the *locking algorithm* in the following discussion, are illustrated in the flow chart depicted in Figure 7.7.

The locking algorithm implements the concept of a Mealy-type finite state machine [234], i.e. the decisions this code makes in terms of the output signals it generates and changes of the internal state depend on the current inputs and on the internal state of the previous code cycle. For the realization of this concept it is necessary to provide a means of non-volatile memory for the internal state of the locking algorithm, to make the state information available in consecutive code cycles. Technically, the locking algorithm is realized as a C function which is called once in each code cycle of the real-time module. The lifetime of local variables defined within the scope of this function is limited to the duration of the function call, hence the information is lost once the function code execution ends. This can be circumvented with the aid of static variables which outlive the temporal scope of a single call of the locking algorithm function, i.e. these variables are not deallocated after the execution of the function in which they are defined. Thus, static variables were used for storing state information in the algorithm. Important variables and flags in this code are summarized in Table 7.1. The associated EPICS PVs which are defined in the real-time code model for user-space communication are summarized in Table 7.2.

In the following a single execution cycle of the real-time locking algorithm will be discussed. In general, the locking algorithm can take on five different states which are represented by the value of the variable `lock_state` in the real-time code. These states range from the unlocked, freely fluctuating state of a component to the fully locked state in which the corresponding servo loop is closed and both integrator stages are activated. To switch from manual operation to locking automation the binary EPICS PV `AUTOLOCK` needs to be set first. If the `AUTOLOCK` PV is unset the

Figure 7.7 ***(following page)*****:** Flowchart of the top-level execution layer of the real-time locking algorithm. This algorithm is part of each of the squeezer components' real-time modules and is represented in the graphical model by the *LOCKER* block. The locking algorithm is executed in each code cycle of the real-time code and, if requested by the user, attempts to bring the unlocked component to the fully locked state. Furthermore it continuously monitors the component and reports state information via specific monitor channels.

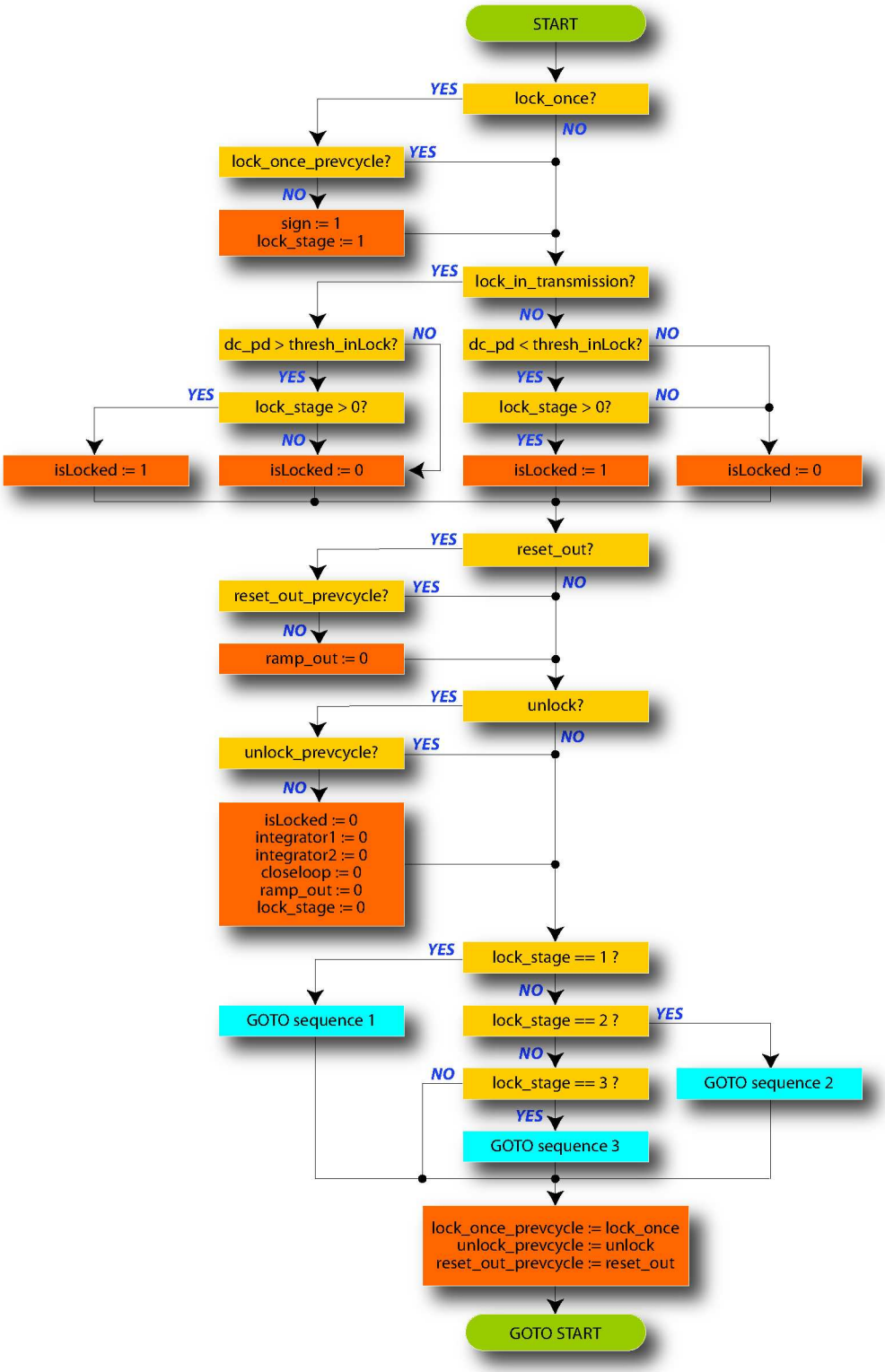
START
lock_once?
YES
NO
lock_once_prevcycle?
YES
NO
sign := 1
lock_stage := 1
lock_in_transmission?
YES
NO
dc_pd > thresh_inLock?
NO
dc_pd < thresh_inLock?
NO
YES
lock_stage > 0?
YES
NO
lock_stage > 0?
NO
YES
isLocked := 1
isLocked := 0
isLocked := 1
isLocked := 0
reset_out?
YES
NO
reset_out_prevcycle?
YES
NO
ramp_out := 0
unlock?
YES
NO
unlock_prevcycle?
YES
NO
isLocked := 0
integrator1 := 0
integrator2 := 0
closeloop := 0
ramp_out := 0
lock_stage := 0
lock_stage == 1 ?
YES
NO
GOTO sequence 1
lock_stage == 2 ?
YES
NO
lock_stage == 3 ?
NO
YES
GOTO sequence 2
GOTO sequence 3
lock_once_prevcycle := lock_once
unlock_prevcycle := unlock
reset_out_prevcycle := reset_out
GOTO START

Table 7.1: Flags and variables used in the squeezing automation real-time code.

Name	Range of values	Purpose
`lock_once`	$\{0,1\}$	request stage to lock
`lock_once_prevcycle`	$\{0,1\}$	static variable to arm or disarm `lock_once`
`unlock`	$\{0,1\}$	request stage to unlock
`unlock_prevcycle`	$\{0,1\}$	static variable to arm or disarm `unlock`
`lock_stage`	$\{0,1,2,3,4\}$	current status of the acquisition process: (0) unlocked; (1) ramping; (2) loop closed; (3) first integrator engaged; (4) full lock acquired
`lock_in_transmission`	$\{0,1\}$	true if monitor PD is in transmission of the component, false otherwise
`islocked`	$\{0,1\}$	reflects whether or not a component is locked
`dc_pd`	$[-32767, 32768]$	digitized locking monitor PD output output voltage in digital 'counts'
`thresh_acq`	user def'd	while in acquisition mode the feedback controller is engaged once `dc_pd` exceeds the acquisition threshold
`thresh_inLock`	user def'd	lock loss is assumed if `dc_pd` crosses this threshold
`reset_out`	$\{0,1\}$	request to set the ramp output signal to zero
`reset_out_prevcycle`	$\{0,1\}$	static variable to arm or disarm `reset_out`
`sign`	$\{-1,1\}$	sign of the slope of the generated ramp signal
`amp`	user def'd	Peak amplitude of the ramp signal in units of 'counts'
`freq`	user def'd	Frequency of the ramp signal
`FE_RATE`	user def'd	Real-time code clock rate, i.e. number of RT code cycles per second
`ramp_out`	{`-amp`,`amp`}	ramp signal which is HV amplified and fed to the PZT actuator of the component
`closeloop`	$\{0,1\}$	Reflects whether the feedback control loop is closed
`integrator1` `integrator2`	$\{0,1\}$	Reflects whether the integrating gain of the feedback controller is engaged
`switch_delay`	user def'd	delay in code cycles to avoid simultaneous switching of the integrators
`int1_delay_cnt` `int2_delay_cnt`	[0, `switch_delay`]	counter for code cycles between request and switching of the integrators

locking algorithm outputs are disconnected from the remote servo steering channels and the HV offset channel, respectively.

The execution of the real-time locking automation code starts with reading out the EPICS process variable (PV) `TOGGLE_LOCK` which can be set by the operator to request automated lock acquisition of the corresponding component, cf. Figure

7.6. If lock was requested, the flag `lock_once` is set locally in the real-time module for further reference. To avoid that lock acquisition starts over again and again in consecutive code cycles a second static variable is introduced which prevents a restart of the acquisition until the PV `TOGGLE_LOCK` is reset by the user for the duration of a least one code cycle. In effect this means that lock acquisition is started whenever a state change of the `TOGGLE_LOCK` PV from `false` to `true` is detected between two consecutive code cycles. In this case a ramp signal with user-defined amplitude and frequency and rising slope is generated by the locking algorithm. This digital ramp signal is converted by the DAC hardware to an analog voltage and fed to the summing input of the HV amplifier of the associated optical stage. Furthermore, to account for the state change, the variable `lock_state` is set to `lock_state`=1 which represents the state in which the length of the component in the squeezed-light laser is scanned to determine its operating point.

The principle idea of the locking algorithm is based on comparing a digitized DC voltage measured with a photo detector which is part of the component in the optical setup with a user-defined threshold. Depending on the result of this comparison the software infers whether the component is near its designated operating point. A distinction is made in the code for stages that are locked in reflection and in transmission, respectively. For instance, for a photo detector in transmission of a component in the squeezed-light laser the measured voltage will increase as the operating point is approached, provided that the sign of the signal is preserved in the analog electronics. Equivalently, for a component which is monitored in reflection the measured signal magnitude will decrease as the operating point is approached. In the next step in the code it is checked whether the component is locked in transmission or in reflection by reading the value of the hard-coded constant `lock_in_transmission` which exists for each optical stage.

In the real-time algorithm the variables `dc_pd`, which represents the measured photo detector DC voltage, and `thresh_inLock` are compared in each code cycle. The value of `thresh_inLock` represents the threshold for the measured DC voltage above or below which the component is considered to be in lock, for locking in transmission or reflection, respectively. The value of the real-time variable `thresh_inLock` is read from the EPICS PV `THRESH_INLOCK` in every real-time code cycle and needs to be provided by the user. If, in the case of locking in transmission, the measured value of `dc_pd` exceeds the threshold `thresh_inLock` and the component is in acquisition mode or in the fully locked state (i.e. `lock_stage`$\in \{1,2,3,4\}$), the `isLocked` flag is set, i.e. the component is considered to be in lock. Otherwise, if the measured DC photo detector value is below the set value of `thresh_inLock` the component is considered not to be in lock and the `isLocked` flag is unset. The same holds in the case of a component which is locked in reflection with the difference that for `dc_pd` values below the value of `thresh_inLock` the component is considered to be in the locked state. Besides `thresh_inLock` a second threshold is defined in the code to which the DC photo detector signal is compared in the acquisition phase. The user-defined value for this threshold is read from the PV `THRESH_ACQ` and stored in the real-time code in the variable `thresh_acq` and differs from `thresh_inLock`. The approach to set different thresholds active, depending on whether the component is

Table 7.2: EPICS PVs defined in the squeezing automation real-time code model for user-space communication.

Name	In/out range	Purpose
TOGGLE_LOCK	Binary in	request stage to lock
THRESH_ACQ	Integer in	lock acquisition threshold
THRESH_INLOCK	Integer in	threshold to distinguish locked from unlocked state
RAMP_FRQ	Integer in	frequency of the software-generated ramp signal for sweeping of the control variable in acquisition mode
RAMP_AMP	Integer in	peak amplitude of the software-generated ramp signal for sweeping of the control variable in acquisition mode
RESET_OUTPUT	Binary in	request ramp output of LOCKER block to be set to zero
TOGGLE_UNLOCK	Binary in	request unlocking of optical stage
DELAY	Integer in	number of code cycles to wait before integrators are engaged
HVRAMP_FREQ	Integer in	frequency of the ramp signal from ramp generator for manual operation
HVRAMP_AMPL	Integer in	peak amplitude of the ramp signal from ramp generator for manual operation
HV_OFFSET1	Integer in	high-voltage amplifier offset, coarse
HV_OFFSET2	Integer in	High-voltage amplifier offset, fine
AUTOLOCK	Binary in	Toggle between manual operation and automated locking
ISLOCKED	Binary out	monitor channel for diagnostics, true if the optical stage is fully locked
SERVO_PGAIN	Integer in	proportional gain of the servo controller
SERVO_LOCK	Binary in	open/close the feedback loop manually
SERVO_INT1	Binary in	engage/disengage integrator manually
SERVO_INT2	Binary in	engage/disengage integrator manually
PDLOCK_ERR_OUT16	Float out	slow error signal monitor channel
PDLOCK_DC_OUT16	Float out	slow DC signal monitor channel
HVAMP_MON_OUT16	Float out	slow HV amplifier control signal monitor channel
TEMP_ERR_OUT16	Float out	slow temperature control error signal monitor channel
TEMP_NTC_OUT16	Float out	slow NTC thermistor signal monitor channel

in the locked state or not, is basically a software emulation of a *Schmitt trigger* [235]. Stringent thresholds `thresh_inLock` are required to reliably determine lock loss of a component. Contrasting this, in acquisition mode it is sufficient to tune the control parameter to within the linear region of the corresponding error signal, the „capture range" of the servo electronics, before feedback control is engaged. Hence, to ensure rapid acquisition, less stringent values are chosen for `thresh_acq`. Details on the role of the acquisition threshold are given below.

In the next section of the code the locking algorithm checks whether a reset of the ramp signal generator or an unlock of the component was requested. Again, as in the case of the lock request, these actions are triggered by changes of the state of the corresponding flag. Once a reset of the ramp output or an unlock is requested, these channels are disarmed by setting a flag represented by a static variable, to prevent repeated unlocks of a component or ramp signal resets in consecutive code

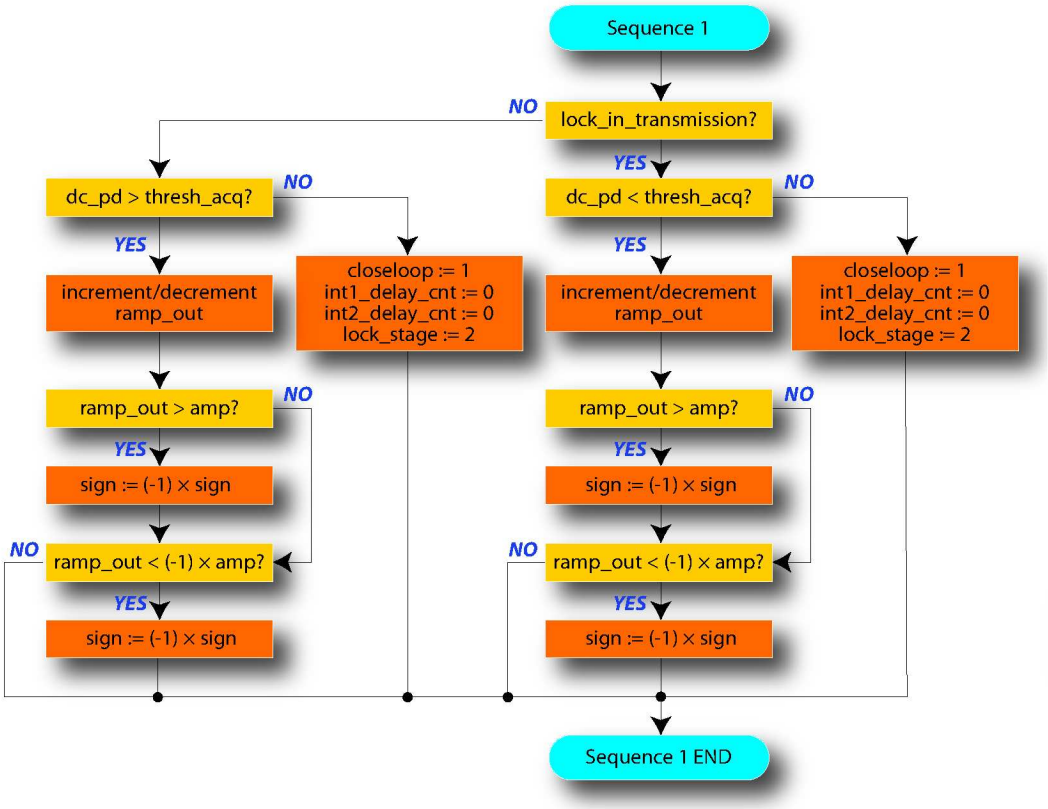

Figure 7.8: Flowchart of the real-time *locking sequence one*. In this code branch it is determined whether the control variable, which is swept by applying a HV ramp signal to the corresponding actuator, is within the capture range of the extracted error signal. If this condition is fulfilled, the control loop is closed and the acquisition stage of the component is set to lock_stage=2. If the ramp signal amplitude hits a pre-defined rail the code toggles between rising or falling slope, respectively.

cycles. Ramp signal resets are requested by the user via the PV `RESET_OUTPUT` and are accounted for in the code by setting the variable `ramp_out` to zero. Unlocking of the optical stage is requested via the PV `TOGGLE_UNLOCK` and initiates the real-time application to consider the optical stage unlocked, disengage analog servo control, reset the ramp output and set the state to "not locked" by setting `islocked`, `integrator1`, `integrator2`, `closeloop`, `ramp_out` and `lock_stage` to zero.

Depending on the current `lock_stage` of the component, code execution continues in different branches. In case that the generation of the ramp signal was engaged to sweep the control variable of the component to its operating point, a state which is represented by `lock_stage`=1, the code block of *locking sequence one* is executed, cf. Figure 7.8 Locking sequence one is further sub-divided in two different code branches, depending on whether the component is locked in transmission or in reflection with respect to the photo detector which is used to read out the signal

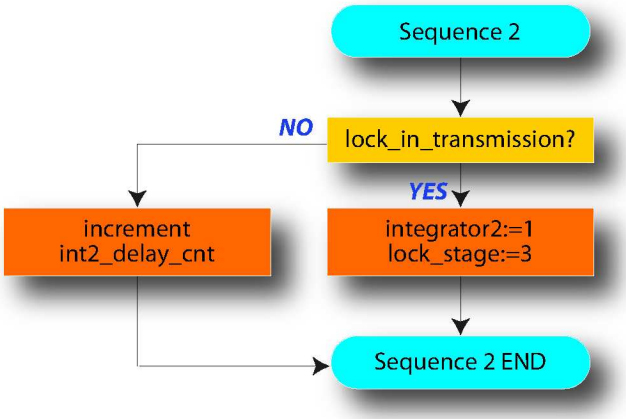

Figure 7.9: Flowchart of the real-time *locking sequence two*. In this code branch the locking algorithm waits for a user-defined number of code cycles before the first integrator stage of the analog servo controller is engaged and the acquisition stage is set to lock_stage=3.

stored in the variable `dc_pd`. To determine whether a swept component is within the capture range of the extracted error signal, the measured DC photo detector signal is compared with a user-defined acquisition threshold, as was already noted above. For locking in transmission, the component is considered to be near its designated operating point if the digitized DC voltage stored in `dc_pd` exceeds the pre-set value in the variable `thresh_acq`. For components locked in reflection these are considered to be within the capture range if `dc_pd` drops below `thresh_acq`. If the respective condition is fulfilled, the internal flag `closeloop` is set which indicates whether the feedback loop is closed. Besides this, a signal is generated by the locking algorithm which remotely toggles an electronic switch in the analog servo electronics which closes the physical control loop. Two counters which serve to introduce a switching delay for the two integrator stages in the analog servo are reset and the `lock_stage` flag reflecting the current status of the acquisition process is set to `lock_stage=2`.

If no crossing of the acquisition threshold was detected in the current code cycle the locking algorithm proceeds with sweeping the control variable of the optical stage. The locking algorithm continuously checks whether the ramp signal hits a user-defined rail, determined by the value of the variable `amp` which represents the peak amplitude of the generated signal. The value of this variable is read from the PV `RAMP_AMP`. The frequency of the generated ramp signal is read from the PV `RAMP_FRQ` and locally stored in the real-time application in the variable `freq`. If signal railing is detected the sign of the ramp increment, which is added to the signal amplitude of the previous code cycle, is flipped. This results in a falling slope if the ramp signal was rising before railing was detected and vice versa.

If the locking algorithm assumes a lock acquisition state of the optical component of `lock_stage=2`, i.e. the component was successfully taken near its operating point and the feedback loop was already closed, the code execution branches into the

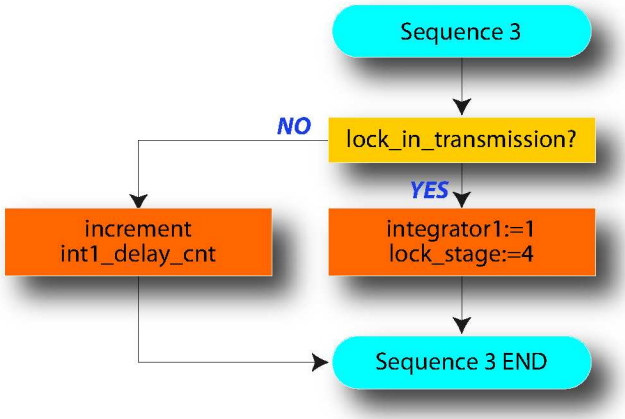

Figure 7.10: Flowchart of the real-time *locking sequence three*. Again, in this code branch the locking algorithm waits for a user-defined number of code cycles before the second integrator stage of the analog servo controller is engaged and the acquisition stage is set to lock_stage=4, corresponding to the fully locked state of the optical stage.

code block of *locking sequence two*, cf. Figure 7.9. In this code branch the real-time code waits for a user-defined number of code cycles before the first one of the two integrator stages – the one with higher corner frequency – is engaged. The switching delay was introduced to avoid nearly simultaneous closing of the feedback loop and engaging of the integrator stage which led to instabilities in the experiment. The number of cycles to wait are read from the EPICS PV `DELAY` and is stored in the variable `switch_delay` in the real-time code. Finally, at the end of the code branch, the acquisition stage of the component is set to `lock_stage`=3.

The code in the branch of *locking sequence three* is basically identical to the previous locking sequence. A flowchart is depicted in Figure 7.10. As in the previously described code branch, to allow the servo loop to settle the code waits for `switch_delay` cycles before the second integrator stage with lower corner frequency is engaged. As observed in the previous case, nearly simultaneous switching of the integrators led to instabilities in the feedback loop. After setting the acquisition stage of the component to `lock_stage`=4, meaning that the component is fully locked with both integrator stages engaged, the code branch is left. A code listing of the of the real-time locking algorithm is given in Appendix C.

There are two different ways of how a stage in the experiment can make the transition from the locked state to the unlocked state. Either the unlock was requested by the user or the unlock was caused by an exceptional event in the experiment. Lock loss may occur, e.g. as a consequence of drifts which the control loops cannot compensate for because of a lack of dynamic range of the actuators. Also transient disturbances which the servo controllers cannot sufficiently suppress due to limited gain may cause lock loss.

For manual remote control of the experiment an additional stage to add arbitrary offsets to the HV outputs and a second independent software ramp generator which is fully controlled via four EPICS PVs, namely `HV_OFFSET1`, `HV_OFFSET2`, `HVRAMP_FREQ` and `HVRAMP_AMPL` were included. Also remote control of the proportional gain of the analog servo controllers was realized which can be adjusted by the user via the PV `SERVO_PGAIN`. In each squeezer component sub-module the binary `islocked` output of the LOCKER block is multiplied with a unique value which is a power of two. The sum of these outputs is recorded and serves to unambiguously determine which of the optical stages were in lock at a particular point in time.

The presented software implementation can be viewed in the light of different abstraction layers for controlling the experiment. In the most basic mode of operation this real-time module can be used to manually control all relevant electronic settings of the squeezed-light laser experiment and to analyze electronic signals for diagnostics from a remote location by means of manipulating EPICS PVs. The automated locking algorithm significantly adds to the functionality of the module. By mapping the necessary steps for the repetitive task of lock acquisition and surveillance of the locked component to a software algorithm, the user solely needs to send a request to the real-time module via EPICS to trigger the automated locking of a stage in the squeezed-light laser which is typically achieved in less than a second. On the basis of this real-time software interface to the squeezed light laser, global control of the experiment can be easily achieved e.g. by means of user-space software scripts which communicate with the real-time module via EPICS *Channel Access* (CA) [232]. A realization of this concept is discussed in the following section.

7.6 Remote control and control automation

In this section, the chosen approach to realize an additional abstraction layer with software object representatives linked to the real-time code modules of the squeezed-light laser stages described in the previous section will be discussed. Furthermore, based on this high-level object representation the concept of the automation application will be introduced, in which the individual software components are combined and treated as a whole to enable intervention-free operation of the squeezed-light laser.

As already pointed out in Section 7.4 is was intended that control automation of the full experiment was not implemented in the real-time kernel module. For the sake of better maintainability and extensibility a "user space" implementation was preferred. With this approach it is possible to run the automation software on any workstation which is part of the local CDS network. For the object-oriented realization of the high-level representatives of the stages in the squeezed-light laser the programming language *Python* [207, 236] was chosen. On the one hand this choice was motivated by the flexibility of the language and its intuitive usage which makes it easy to read and extend even for non-experts. On the other hand the language is well-supported by the EPICS community and numerous libraries are available for the integration of applications in the EPICS environment. For the

communication of the automation application with EPICS PVs by means of the EPICS Channel Access protocol the *EpicsCA* [237] library was used.

The major difference between this new abstraction layer and the real-time software layer described in the previous section is that, whereas the real-time application implements all necessary functionality to remotely control the squeezed-light laser and provides low-level access to this functionality in the form of EPICS communication, the user space application aims at creating a high-level interface by making the functionality of the component available for comfortable operator interaction with the experiment. Tasks like establishing a connection to the EPICS IOC or communication with the experiment via the EPICS CA protocol are encapsulated in the high-level software component and need no explicit attention from the operator, i.e. the squeezed-light laser can be remotely controlled without in-depth knowledge of CDS and the EPICS software. The Python shell environment can be used for "online" manipulation of objects representing stages in the squeezed-light laser and hence serves as a control interpreter for the experiment. The corresponding Python objects can be loaded in this shell and comfortably manipulated by the operator, by changing attributes or calling methods. Complex tasks which involve e.g. communication with multiple EPICS PVs can be efficiently bundled and treated by a single method of the class.

Based on this new abstraction layer the software for the fully automated operation of the experiment could be comfortably realized. The principal idea of the automation algorithm is to continuously monitor the current state of the individual components by reading and processing the information obtained from the associated diagnostics channels. This information is internally obtained from the corresponding real-time module via EPICS PVs which are not disclosed to the user. Furthermore, decisions about necessary actions, triggered by state changes, are made by the automation code, based on predefined patterns implemented in the algorithm. In case exceptional behavior of the squeezed-light laser is detected, such as a lock loss, the automation code sends requests to the object representation of the squeezed-light laser component to initiate re-locking of the component. These request are also internally processed and forwarded to the real-time code module via the control channels realized as EPICS PVs.

The use of an instance of a so-called *container class* allows for efficient storage of the Python objects representing the components in the squeezed-light laser and furthermore makes it possible to iterate over these components. In the present case an instance of the built-in Python *tuple* class was used. The objects representing stages in the experiment are stored in the container object in the order of lock acquisition: (1) The PLL that locks the squeezed-light laser to the GEO master laser (PLL1), (2) the coherent control PLL (PLL3), (3) the p-polarized auxiliary laser PLL (PLL2), (4) the SLS component, (5) the SHG component, (6) the mode cleaner for the green field (MC532), (7) the Mach-Zehnder interferometer (MZI), (8) the phase of the pump field (PUMP) and in diagnostics mode also (9) the mode cleaner for the local oscillator field (MC1064) and (10) the homodyne angle of the balanced homodyne detector (BHD).

To provide a means of iterating over the container object and acting on the stored objects representing squeezed light laser components it is necessary that these objects share a common interface. This means that the classes these objects are instances of implement a set of particular methods which can be called by the automation software in the course of the lock acquisition process. In the present case this was realized by means of the concept of *code inheritance*, i.e. the different component classes inherit code from a "controller" super class. It was chosen to implement the controller class in the special form of an *abstract base class*. On the one hand this class directly implements methods to initiate locking and unlocking of a component and to request the status of the component. On the other hand, further methods are defined in the super class but are left to be implemented by the sub class, i.e. the super class only contains declarations of these methods and hence acts as an interface. It is thus ensured that each of the component classes implements a minimal set of methods which are required by the automation software for remote control of the stages in the experiment.

When lock automation is engaged for the first time, the algorithm starts with unlocking all ten components in reverse order to ensure that the squeezed-light laser is in a well-defined initial state. Then, starting with the first component, all components are sequentially brought to the locked state. Once full lock of the experiment is acquired, the automation algorithm continuously iterates over the list and checks the status of each of the components. If lock-loss of one of the components is detected, the first component in the locking sequence is determined which is not in lock anymore. All components in the list after the first unlocked component are unlocked in reverse order and re-locking starts with the component that caused the exception in the squeezed-light laser.

Locking of the components MC532 and MZI requires special attention by the automation script. Even though in the squeezed-light laser the MZI is located "upstream" of the MC532, the mode cleaner is brought to the locked state first. To ensure that a sufficient fraction of the green field is transmitted through the MZI, the MZI phase is swept to maximize the transmitted power prior to MC532 lock acquisition. To achieve this, the DC photo detector signal in reflection of the MC532 is used to measure the power transmitted through the MZI, cf. Section 7.5.2.

The implementation of the locking automation script was discussed in depth by Nico Lastzka in his doctoral thesis. For further details on this code see [238].

7.7 Routine operation of the automated squeezer in the GEO detector

In this section measurements which quantify the performance of the automated lock acquisition of the GEO squeezed-light laser as well as its long-term duty cycle in the GEO detector will be presented.

For the documentation of the locking automation functionality a selection of digitized monitor signals were recorded. In Figure 7.11 an exemplary measurement of the correction signals which are generated by the servo controllers, amplified to

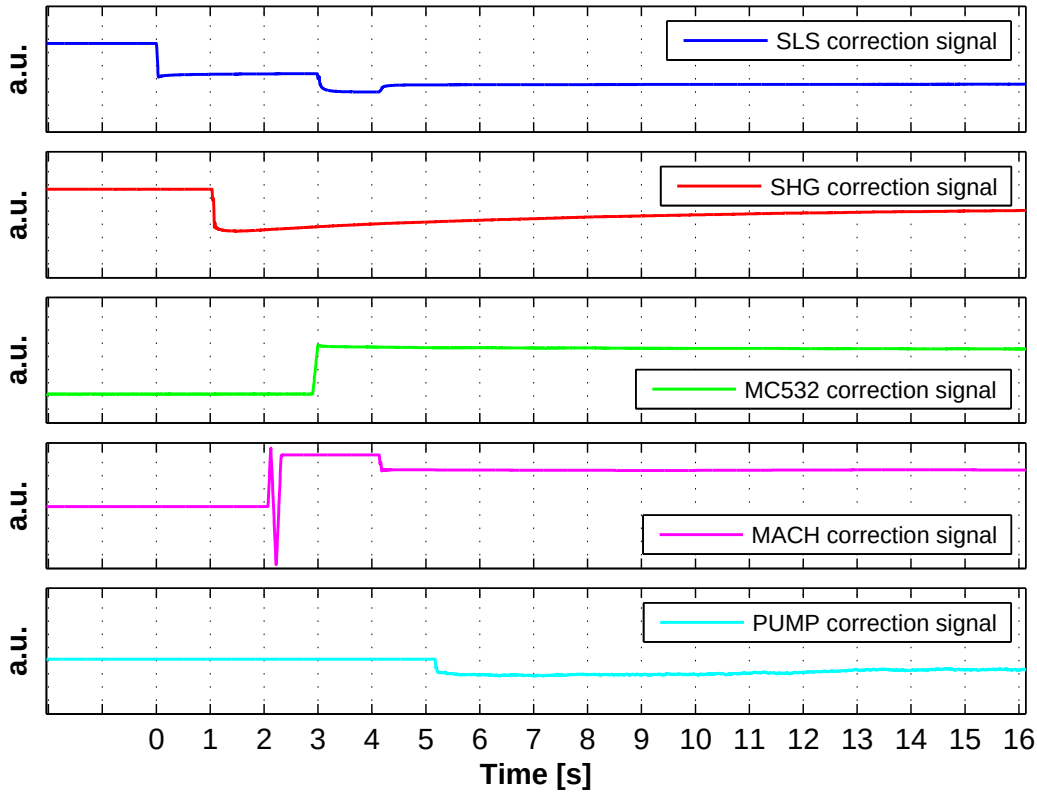

Figure 7.11: Correction signal transients recorded during lock acquisition of the squeezed-light laser. The plot shows the subset of signals for the optical stages in the squeezed light laser which are relevant for routine squeezing injection into the GEO detector. Lock acquisition starts at $t = 0\,\mathrm{s}$ with the SLS cavity (blue trace). The SHG cavity (red trace) is locked approximately one second later. Prior to locking the mode cleaner cavity for the pump field (MC532) the phase of the Mach-Zehnder interferometer (MACH) is ramped to maximize the transmission of the green field (magenta trace). A fringe lock of the Mach-Zehnder interferometer is established shortly after the mode cleaner for the green pump field (MC532) is brought to the locked state (green trace). Finally the servo loop for the phase of the pump field (PUMPE), which was already near its operating point, is closed (cyan trace). After approximately 5 seconds the optical components of the squeezed-light laser are fully locked. The two steps in the correction signal of the locked SLS cavity can be attributed to variations in the power of the green pump field incident on the SLS which affect the error signal for the SLS length locking loop.

high voltage and finally applied to the length actuators in the optical components is shown. The signals were extracted from the squeezed-light laser in its mode of operation in the GEO detector, i.e. with the squeezed light source, the second harmonic generator, the mode cleaner for the green pump field, the Mach-Zehnder interferometer and the phase lock for the green pump field in operation. The three phase locking loops which require no special attention during the acquisition phase

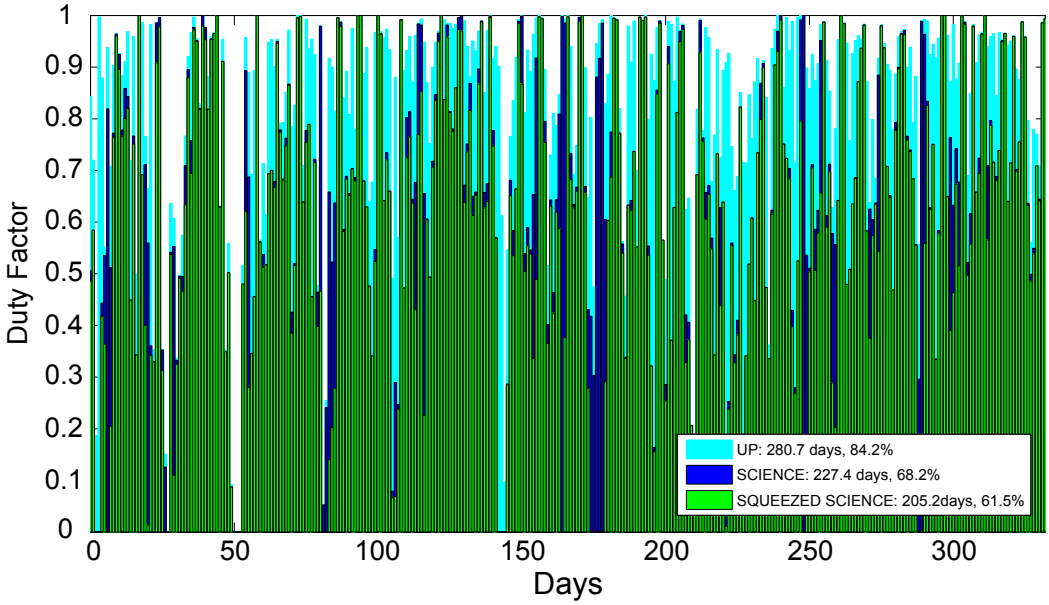

Figure 7.12: Time series diagram of GEO fully locked operation and science time with and without squeezing enhancement in the period from November 17, 2011 to October 15, 2012. The 'UP' status (84.2 % of the time) represents a fully locked and operational GEO detector. When the detector status was reported as 'SCIENCE', the taken data was flagged to have science quality (68.2 % of the time). Finally, 'SQUEEZED SCIENCE' status was reported when scientifically relevant data was taken and squeezed vacuum was injected into the detector (61.5 % of the time). For 90.2 % of the time when science data was taken the sensitivity of the detector was enhanced by squeezing injection.

(the controllers only need to be activated or reset sporadically) were not included in the plot.

Lock acquisition starts at $t = 0\,\mathrm{s}$ with the SLS cavity (blue trace). The SHG cavity (red trace) is locked approximately one second later. Prior to locking the mode cleaner cavity for the pump field (MC532) the phase of the Mach-Zehnder interferometer (MACH) is ramped to maximize the transmission of the green field (magenta trace). A fringe lock of the Mach-Zehnder interferometer is established shortly after the mode cleaner for the green pump field (MC532) is brought to the locked state (green trace). Finally the servo loop for the phase of the pump field (PUMP), which was already near its operating point, is closed (cyan trace). After approximately 5 seconds the relevant optical components of the squeezed-light laser are fully locked. The two steps in the correction signal of the locked SLS cavity at $t = 3\,\mathrm{s}$ and $t = 4\,\mathrm{s}$, respectively, can be attributed to variations in the power of the green pump field incident on the SLS cavity which affect the error signal for the SLS length locking loop.

A first demonstration of the long-term stable operation of the GEO squeezed-light laser and the generation of strongly squeezed vacuum was reported on in [239].

With the aid of the diagnostic homodyne detector which is part of the squeezed-light laser optical setup a suppression of quantum noise by 9 dB in the frequency range of 10 Hz to 10 kHz over a period of 20 hours was measured. During this measurement eight lock-losses occurred in the experiment. These were detected by the locking automation system which successfully relocked the experiment within less than 15 seconds. In the GEO detector the squeezed-light laser is routinely operated to enhance the shot noise-limited sensitivity of the interferometer. The plot in Figure 7.12 illustrates the duty cycle of the squeezed light laser for a data-taking run which lasted for about 11 months, from November 17, 2011 to October 15, 2012. In this period of time the GEO detector was fully locked and operational with a duty cycle of 84.2 %. Science quality data was taken with a duty cycle of 68.2 %. The duty cycle of the squeezing enhanced interferometer generating science quality data was 61.5 %. This means that during the time the detector produced science quality data the squeezed-light laser was fully operational for 90.2 % of the time and resulted in an improvement of the shot noise-limited sensitivity of the GEO detector by 2 dB on average [229].

7.8 Summary

In this chapter, the automation concept for the GEO squeezed light laser and its practical realization were described. For a seamless integration of the squeezed light laser in the control environment of the GEO detector the LIGO Control and Data System was chosen as the platform for interfacing and remote control of the squeezing experiment. In the first step the existing analog control electronics were modified to electronically interface the experiment with the digital system. In the second step a custom real-time software environment was set up to arrange for fast interaction of the control system with the experiment. To trigger actions of the real-time software performed on the experiment, EPICS-based user communication with the real-time module was implemented, effectively realizing a client-server pattern. To provide low-latency remote control of the experiment, algorithms to solve repetitive, yet time-critical tasks were encapsulated in this real-time module and can, likewise, be invoked via EPICS communication channels from within the local operator network. Based on this combination of real-time functionality and EPICS-based user interaction the state of the experiment is continuously monitored and, if necessary, relocked by means of a software script running on an arbitrary work station computer. Details on the implementation of these software scripts were given in [238].

The automation of the GEO squeezed light laser enabled, for the first time, the intervention-free operation of a squeezing experiment on timescales required for an application in a large-scale GW detector over long data-taking periods. By fully automating the squeezed-light laser a long-term stable injection of squeezed vacuum into the GEO detector and the associated enhancement of the shot noise-limited sensitivity were ensured. Also, the routine squeezing injection puts the GEO observatory in the position of the first large-scale interferometer in the world-wide

detector network in which techniques are developed and tested in the course of the ongoing commissioning which aim for the optimization of the squeezing enhancement of the instrument, such as automatic alignment schemes. The knowledge gained from these experiments is to be regarded of high significance not only with respect to the adoption of squeezed vacuum injection as an upgrade for advanced generation detectors but also to pave the way for the investigation of more advanced concepts such as frequency dependent squeezing injection, which is part of the baseline designs of all currently envisaged GW interferometers beyond the advanced detector generation.

CHAPTER 8

Summary and outlook

In the scope of this thesis, detailed investigations of key elements of the planned AEI 10 m sub-SQL interferometer experiment were carried out. Based on the results of these investigations, a workable technical design for the experiment was developed which constitutes an important step toward the realization of the sub-SQL interferometer in the AEI 10 m Prototype facility.

In the foregoing conceptual study for the sub-SQL interferometer, the adoption of novel technologies for the reduction of coating Brownian thermal noise in the experiment was proposed, which is a necessary prerequisite for reaching the targeted exclusively quantum noise-limited sensitivity. However, these technologies have not yet been tested experimentally and are to be regarded as extremely challenging with respect to their implementation and robust operation in an ultra-high precision interferometer experiment.

The approach proposed in the conceptual study for the reduction of coating Brownian thermal noise is based on the adoption of extremely large beam spots on the core interferometer optics in combination with anti-resonant end-mirror cavities instead of conventional highly-reflective end mirrors in the interferometer arms. In Chapter 3 of this thesis, these techniques were discussed in detail with special emphasis on implications of their practical implementation in the sub-SQL interferometer.

For the given spatial constraints, the realization of the targeted extremely large beam spot size does not only result in an obvious increase of diffraction loss at the mirror apertures, but also comes at the expense of marginal stability of the interferometer arm cavities. A consequence of this mode of operation are extremely stringent optical design requirements, e.g. with respect to specifications of the core optical components, as well as highly challenging control requirements.

Generally, candidate optical layouts for the sub-SQL interferometer need to fulfill a number of boundary conditions. These include spatial constraints, requirements for mirror dimensions and beam sizes as well as geometric stability and a sufficiently high theoretically achievable mode coupling efficiency. For the interferometer configuration with end mirror cavities, two layout options were identified – with or

without a beam waist in the end mirror cavity – and an in-depth analysis of their optical properties was carried out with the aid of numerical models.

From the sensing and control point of view it was found that control requirements for the end mirror cavities are almost as demanding as those for the arm cavities. Nevertheless, simulations showed that despite the optical coupling, sufficiently well-isolated heterodyne length signals, based on frontal phase modulation, can be extracted for independent length control of the two partial cavities in the interferometer arms.

The requirement for extremely large beam spots results in stability parameters for both end mirror cavity candidate configurations with even less stability margin than in the case of the arm cavities. Further investigations showed that in both configurations the stability parameter and the theoretical mode coupling efficiency are extremely susceptible to deviations of cavity lengths and mirror curvatures from their nominal values. In order to ensure stable, low-loss operation of the coupled arm cavities, extremely stringent specifications for tolerable curvature error of the cavity optics need to be assumed. These were found to be beyond typical manufacturing precisions that can currently be achieved, even if highly sophisticated interferometric surface metrology equipment is employed in the manufacturing process. Furthermore, it was found that, assuming parameters representative for an implementation in the AEI 10 m Prototype, deviations of the end mirror cavity length in the micron range are sufficient to drive the configuration with a beam waist in the end mirror cavity into instability. However, in the configuration with a nearly collimated beam in the end mirror cavity, larger-than-specified curvature error could, to some extent, be compensated for by means of adapting lengths in the optical setup in combination with thermally actuating on the curvature of the coupled-cavity end mirror.

Owing to the fact that the Fabry-Perot Michelson interferometer with marginally stable arm cavities will be challenging to operate taken by itself, it appears advisable to concentrate on the commissioning of the marginally stable interferometer without end mirror cavities in the first place and to keep these as an option for a future upgrade.

Motivated by these findings, the tunable stability interferometer layout for the AEI 10 m Prototype sub-SQL interferometer, which was presented in Chapter 4 of this thesis, was developed. This layout allows to initially operate the interferometer in a configuration with stable arm cavities to then stepwise approach the targeted critical beam size. Tunability of the arm cavity stability is achieved by means of a flexible mode matching scheme which is optimized for the marginally stable configuration but yields close-to-optimal mode coupling efficiencies also in the initial stable configuration. Hence, the tunable stability layout does not only significantly facilitate the initial commissioning of the experiment but also prevents inoperability of the interferometer due to poor arm cavity stability which could occur in a "static" marginally stable configuration. In this design, in the initial stable configuration coating Brownian thermal noise will dominate over quantum noise, which will enable direct coating thermal noise measurements at hundreds of Hertz. As the marginally stable configuration is approached, quantum noise will

become the dominant noise contribution, allowing e.g. a direct measurement of quantum radiation pressure noise. Furthermore, the experience gained by operating an interferometer with extremely large beam spots may be partially transferred to the designs of future GW detectors.

One of the consequences of arm cavities with marginal stability is the occurrence of an extremely small round-trip Gouy phase which leads to partial degeneracy of higher-order transverse modes with the fundamental cavity mode. This partial degeneracy potentially amplifies the effect of beam distortion inside the interferometer arm cavities due to irregular mirror surfaces. Investigations of the influence of realistic mirror surface irregularity on the performance of the sub-SQL interferometer were presented in Chapter 5 of this thesis.

To gain deeper insight into the role of mirror surface irregularity in the experiment, a grid-based high-resolution numerical model of the interferometer with marginally stable arm cavities and realistic mirror surfaces was developed. With this model, a detailed parameter study was carried out on a high-performance computer cluster. Two figures of merit, arm cavity round-trip loss and contrast defect at the beam splitter of the interferometer, for which upper limits were derived from the targeted noise budget of the experiment, were chosen to relate the simulation output to the performance of the instrument. It was found that the targeted upper limit for the contrast defect imposes more stringent requirements on the quality of the mirror surfaces than the upper limit for the tolerable round-trip loss in the arm cavities. In order to operate the interferometer with a sufficiently small contrast defect, the numerical model predicts a required RMS surface irregularity of the cavity mirrors in the sub-nanometer range in combination with astigmatism RMS amplitudes in the lower nanometer range. This can be achieved e.g. by a treatment of the core optics' surfaces with the technique of *ion beam figuring*.

In Chapter 6 of this thesis, the "single arm test" experiment was introduced, which was proposed as a stepping-stone toward the realization of the sub-SQL interferometer. This experiment was devised to enable the early investigation of key technical aspects prior to the full completion of the AEI Prototype infrastructure, which are essential for the successful operation of the sub-SQL interferometer. Hence, the single arm test will pave the way for the world's first measurement below the SQL for 100 g test masses in the audio-frequency band.

Among the aspects that will be addressed by the single arm test experiment are, for instance, longitudinal and angular control of a marginally stable cavity with suspended 100 g mirrors and circulating powers in the kW range, including lock-acquisition, tests of the effectiveness of the novel electro-static actuators and also investigations of the influence of marginal stability on noise coupling mechanisms, e.g. the coupling of input beam pointing fluctuations to the main signal readout. Due to the large infrastructural overlap, it will be possible to extend the single arm test experiment to the full interferometer once the third seismic isolation table has been installed in the vacuum system and set into operation.

The core optics for the single arm test were delivered in March 2013 and, at the time of writing, the experiment is being set up. In parallel to the construction of the opto-mechanical hardware and the installation of the single arm test cavity,

further work will be aimed e.g. at additional modeling, design and testing of the new ESD actuator concept as well as investigations toward sensing and control of the experiment.

Additionally, within the scope of this thesis, the squeezed light laser for the GEO 600 detector was interfaced to a digital control system and fully automated operation was realized. The automation concept as well as its practical realization were outlined in Chapter 7. The automation of the experiment ensured the continuous generation of squeezed-vacuum states of light without the need for human intervention, which is a necessary prerequisite for the adoption of this technique in a large-scale GW detector, for the enhancement of its shot noise-limited sensitivity over long data-taking periods. Furthermore, the routine application of squeezing puts the GEO detector into the position of the first large-scale interferometer in the world-wide detector network in which techniques for the integration and optimization of the squeezed vacuum injection can be developed. The gained experience will be extremely valuable for the integration and commissioning of squeezing in second as well as third generation GW observatories. The effectiveness of the automated squeezed-light laser was demonstrated in a data taking run in the period from November 2011 to October 2012 in which squeezed vacuum was injected into the GEO interferometer with a duty cycle of 90.2 % while the detector was taking science quality data.

To realize a measurement in the 10 m Prototype interferometer with a sensitivity below the SQL, one option is the injection of squeezed vacuum states of light into the instrument, generated with a squeezed-light laser similar to the one operated in the GEO detector. Due to the fact that in the AEI 10 m Prototype the same digital control system is utilized as in the GEO detector, the automation scheme developed for the GEO squeezed-light laser can be seamlessly transferred to the prototype, enabling the long-term stable generation of squeezed-vacuum states of light for the squeezing enhancement of the sub-SQL interferometer.

Future work toward the realization of the core interferometer in the AEI 10 m Prototype will be aimed at gaining experience with essential building blocks of the sub-SQL interferometer in the scope of the single arm test experiment introduced in this thesis. Once the prototype infrastructure has been completed, the single arm test experiment will be extended to the full sub-SQL interferometer with its monolithically suspended extremely high-quality optics. The sub-SQL interferometer will not only open up the path toward measurements at the SQL for its 100 g mirror test masses, enabling experiments in the domain of macroscopic quantum mechanics, but it will also serve as a testbed for advanced interferometry techniques to go below the SQL, which are important cornerstones in the designs of future gravitational wave detectors. Hence, the sub-SQL interferometer will make a key contribution to pave the way for the next generation of ground-based gravitational wave observatories and their substantially increased scientific potential with respect to astrophysical and cosmological observations.

Bibliography

[1] A. Einstein, "Approximative integration of the field equations of gravitation," *Preuss. Akad. Wiss. Berlin – Sitzungsber.*, p. 688, 1916.

[2] H. Lück, "Detecting gravitational waves," in *Gravitational wave and particle astrophysics detectors* (J. Hough and G. Sanders, eds.), Bellingham, Wash.: SPIE, 2004.

[3] B. Schutz, *A First Course in General Relativity*. Cambridge University Press, 2nd ed., 2009.

[4] J. Weber, "Gravitational-Wave-Detector Events," *Phys. Rev. Lett.*, vol. 20, pp. 1307–1308, 1968.

[5] P. R. Saulson, *Fundamentals of Interferometric Gravitational Wave Detectors*. World Scientific, 1994.

[6] R. Weiss, "Electromagetically Coupled Broadband Gravitational Antenna," *Quarterly Progress Report, Research Laboratory of Electronics, MIT*, vol. 105, pp. 54–76, 1972.

[7] R. L. Forward, "Wideband laser-interferometer graviational-radiation experiment," *Phys. Rev. D*, vol. 17, pp. 379–390, 1978.

[8] K. Danzmann and A. Rüdiger, "LISA technology – concept, status, prospects," *Class. Quantum Grav.*, vol. 20, no. 10, p. S1, 2003.

[9] J. W. Armstrong, "Low-Frequency Gravitational Wave Searches Using Spacecraft Doppler Tracking," *Living Rev. Relativity*, vol. 9, no. 1, 2006.

[10] D. R. Lorimer, "Binary and Millisecond Pulsars," *Living Rev. Relativity*, vol. 11, no. 8, 2008.

[11] G. M. Harry and the LIGO Scientific Collaboration, "Advanced LIGO: the next generation of gravitational wave detectors," *Class. Quantum Grav.*, vol. 27, no. 8, p. 084006, 2010.

[12] T. Accadia, F. Acernese, F. Antonucci, P. Astone, G. Ballardin, F. Barone, M. Barsuglia, A. Basti, T. S. Bauer, M. Bebronne, M. G. Beker, A. Belletoile,

S. Birindelli, M. Bitossi, M. A. Bizouard, M. Blom, F. Bondu, L. Bonelli, R. Bonnand, V. Boschi, L. Bosi, B. Bouhou, S. Braccini, C. Bradaschia, M. Branchesi, T. Briant, A. Brillet, V. Brisson, R. Budzyński, T. Bulik, H. J. Bulten, D. Buskulic, C. Buy, G. Cagnoli, E. Calloni, B. Canuel, F. Carbognani, F. Cavalier, R. Cavalieri, G. Cella, E. Cesarini, O. Chaibi, E. C. Mottin, A. Chincarini, F. Cleva, E. Coccia, P.-F. Cohadon, C. N. Colacino, J. Colas, A. Colla, M. Colombini, A. Corsi, J.-P. Coulon, E. Cuoco, S. D'Antonio, V. Dattilo, M. Davier, R. Day, R. D. Rosa, G. Debreczeni, W. D. Pozzo, M. del Prete, L. D. Fiore, A. D. Lieto, M. D. P. Emilio, A. D. Virgilio, A. Dietz, M. Drago, V. Fafone, I. Ferrante, F. Fidecaro, I. Fiori, R. Flaminio, L. A. Forte, J.-D. Fournier, J. Franc, S. Frasca, F. Frasconi, M. Galimberti, L. Gammaitoni, F. Garufi, M. E. Gáspár, G. Gemme, E. Genin, A. Gennai, A. Giazotto, R. Gouaty, M. Granata, C. Greverie, G. M. Guidi, J.-F. Hayau, A. Heidmann, H. Heitmann, P. Hello, D. Huet, P. Jaranowski, I. Kowalska, A. Królak, N. Leroy, N. Letendre, T. G. F. Li, N. Liguori, M. Lorenzini, V. Loriette, G. Losurdo, E. Majorana, I. Maksimovic, N. Man, M. Mantovani, F. Marchesoni, F. Marion, J. Marque, F. Martelli, A. Masserot, C. Michel, L. Milano, Y. Minenkov, M. Mohan, N. Morgado, A. Morgia, S. Mosca, V. Moscatelli, B. Mours, F. Nocera, G. Pagliaroli, L. Palladino, C. Palomba, F. Paoletti, M. Parisi, A. Pasqualetti, R. Passaquieti, D. Passuello, G. Persichetti, M. Pichot, F. Piergiovanni, M. Pietka, L. Pinard, R. Poggiani, M. Prato, G. A. Prodi, M. Punturo, P. Puppo, D. S. Rabeling, I. Rácz, P. Rapagnani, V. Re, T. Regimbau, F. Ricci, F. Robinet, A. Rocchi, L. Rolland, R. Romano, D. Rosińska, P. Ruggi, B. Sassolas, D. Sentenac, L. Sperandio, R. Sturani, B. Swinkels, M. Tacca, L. Taffarello, A. Toncelli, M. Tonelli, O. Torre, E. Tournefier, F. Travasso, G. Vajente, J. F. J. van den Brand, C. V. D. Broeck, S. van der Putten, M. Vasuth, M. Vavoulidis, G. Vedovato, D. Verkindt, F. Vetrano, A. Viceré, J.-Y. Vinet, S. Vitale, H. Vocca, R. L. Ward, M. Was, M. Yvert, and J.-P. Zendri, "Status of the Virgo project," *Class. Quantum Grav.*, vol. 28, no. 11, p. 114002, 2011.

[13] B. Willke, P. Ajith, B. Allen, P. Aufmuth, C. Aulbert, S. Babak, R. Balasubramanian, B. W. Barr, S. Berukoff, A. Bunkowski, G. Cagnoli, C. A. Cantley, M. M. Casey, S. Chelkowski, Y. Chen, D. Churches, T. Cokelaer, C. N. Colacino, D. R. M. Crooks, C. Cutler, K. Danzmann, R. J. Dupuis, E. Elliffe, C. Fallnich, A. Franzen, A. Freise, I. Gholami, S. Goßler, A. Grant, H. Grote, S. Grunewald, J. Harms, B. Hage, G. Heinzel, I. S. Heng, A. Hepstonstall, M. Heurs, M. Hewitson, S. Hild, J. Hough, Y. Itoh, G. Jones, R. Jones, S. H. Huttner, K. Kötter, B. Krishnan, P. Kwee, H. Lück, M. Luna, B. Machenschalk, M. Malec, R. A. Mercer, T. Meier, C. Messenger, S. Mohanty, K. Mossavi, S. Mukherjee, P. Murray, G. P. Newton, M. A. Papa, M. Perreur-Lloyd, M. Pitkin, M. V. Plissi, R. Prix, V. Quetschke, V. Re, T. Regimbau, H. Rehbein, S. Reid, L. Ribichini, D. I. Robertson, N. A. Robertson, C. Robinson, J. D. Romano, S. Rowan, A. Rüdiger, B. S. Sathyaprakash, R. Schilling, R. Schnabel, B. F. Schutz, F. Seifert, A. M. Sintes, J. R. Smith, P. H. Sneddon, K. A. Strain, I. Taylor, R. Taylor, A. Thüring, C. Ungarelli, H. Vahlbruch, A. Vecchio, J. Veitch, H. Ward, U. Weiland, H. Welling,

L. Wen, P. Williams, W. Winkler, G. Woan, and R. Zhu, "The GEO-HF project," *Class. Quantum Grav.*, vol. 23, no. 8, p. S207, 2006.

[14] K. Somiya, "Detector configuration of KAGRA–the Japanese cryogenic gravitational-wave detector," *Class. Quantum Grav.*, vol. 29, no. 12, p. 124007, 2012.

[15] B. J. Meers, "Recycling in laser-interferometric gravitational-wave detectors," *Phys. Rev. D*, vol. 38, p. 2317, 1988.

[16] S. J. Waldman, "The Advanced LIGO Gravitational Wave Detector," *arXiv:1103.2728 [gr-qc]*, 2011.

[17] V. Braginsky, F. Khalili, and K. Thorne, *Quantum Measurement*. Cambridge University Press, 1995.

[18] H. J. Kimble, Y. Levin, A. B. Matsko, K. S. Thorne, and S. P. Vyatchanin, "Conversion of conventional gravitational-wave interferometers into quantum nondemolition interferometers by modifying their input and/or output optics," *Phys. Rev. D*, vol. 65, p. 022002, 2002.

[19] C. Zhao, L. Ju, J. Degallaix, S. Gras, and D. G. Blair, "Parametric Instabilities and Their Control in Advanced Interferometer Gravitational-Wave Detectors," *Phys. Rev. Lett.*, vol. 94, p. 121102, 2005.

[20] Y. Chen, "Quantum Non-Demolition Gravitational-Wave Detectors: The Future of LIGO." Talk given at CaJAGWR seminar, 2005.

[21] V. B. Braginsky and F. Y. Khalili, "Quantum nondemolition measurements: the route from toys to tools," *Rev. Mod. Phys.*, vol. 68, p. 1, 1996.

[22] P. Purdue and Y. Chen, "Practical speed meter designs for quantum nondemolition gravitational-wave interferometers," *Phys. Rev. D*, vol. 66, p. 122004, 2002.

[23] Y. Chen, "Sagnac interferometer as a speed-meter-type, quantum-nondemolition gravitational-wave detector," *Phys. Rev. D*, vol. 67, p. 122004, 2003.

[24] M. Punturo, M. Abernathy, F. Acernese, B. Allen, N. Andersson, K. Arun, F. Barone, B. Barr, M. Barsuglia, M. Beker, N. Beveridge, S. Birindelli, S. Bose, L. Bosi, S. Braccini, C. Bradaschia, T. Bulik, E. Calloni, G. Cella, E. C. Mottin, S. Chelkowski, A. Chincarini, J. Clark, E. Coccia, C. Colacino, J. Colas, A. Cumming, L. Cunningham, E. Cuoco, S. Danilishin, K. Danzmann, G. D. Luca, R. D. Salvo, T. Dent, R. D. Rosa, L. D. Fiore, A. D. Virgilio, M. Doets, V. Fafone, P. Falferi, R. Flaminio, J. Franc, F. Frasconi, A. Freise, P. Fulda, J. Gair, G. Gemme, A. Gennai, A. Giazotto, K. Glampedakis, M. Granata, H. Grote, G. Guidi, G. Hammond, M. Hannam, J. Harms, D. Heinert, M. Hendry, I. Heng, E. Hennes, S. Hild, J. Hough, S. Husa, S. Huttner, G. Jones, F. Khalili,

K. Kokeyama, K. Kokkotas, B. Krishnan, M. Lorenzini, H. Lück, E. Majorana, I. Mandel, V. Mandic, I. Martin, C. Michel, Y. Minenkov, N. Morgado, S. Mosca, B. Mours, H. Müller–Ebhardt, P. Murray, R. Nawrodt, J. Nelson, R. Oshaughnessy, C. D. Ott, C. Palomba, A. Paoli, G. Parguez, A. Pasqualetti, R. Passaquieti, D. Passuello, L. Pinard, R. Poggiani, P. Popolizio, M. Prato, P. Puppo, D. Rabeling, P. Rapagnani, J. Read, T. Regimbau, H. Rehbein, S. Reid, L. Rezzolla, F. Ricci, F. Richard, A. Rocchi, S. Rowan, A. Rüdiger, B. Sassolas, B. Sathyaprakash, R. Schnabel, C. Schwarz, P. Seidel, A. Sintes, K. Somiya, F. Speirits, K. Strain, S. Strigin, P. Sutton, S. Tarabrin, A. Thüring, J. van den Brand, C. van Leewen, M. van Veggel, C. van den Broeck, A. Vecchio, J. Veitch, F. Vetrano, A. Vicere, S. Vyatchanin, B. Willke, G. Woan, P. Wolfango, and K. Yamamoto, "The Einstein Telescope: a third-generation gravitational wave observatory," *Class. Quantum Grav.*, vol. 27, no. 19, p. 194002, 2010.

[25] Y. Chen, S. Danilishin, F. Khalili, and H. Müller-Ebhardt, "QND measurements for future gravitational-wave detectors," *General Relativity and Gravitation*, vol. 43, pp. 671–694, 2011.

[26] D. McClelland, N. Mavalvala, Y. Chen, and R. Schnabel, "Advanced interferometry, quantum optics and optomechanics in gravitational wave detectors," *Laser & Photonics Reviews*, vol. 5, no. 5, pp. 677–696, 2011.

[27] K. A. Strain and B. J. Meers, "Experimental Demonstration of Dual Recycling for Interferometric Gravitational-Wave Detectors," *Phys. Rev. Lett.*, vol. 66, p. 1391, 1991.

[28] G. Heinzel, J. Mizuno, R. Schilling, W. Winkler, and A. Rüdiger, "An experimental demonstration of resonant sideband extraction for laser-interferometric gravitational wave detectors," *Phys. Lett. A*, vol. 217, p. 305, 1996.

[29] G. Heinzel, K. A. Strain, J. Mizuno, K. D. Skeldon, and B. Willke, "Experimental Demonstration of a Suspended Dual Recycling Interferometer for Gravitational Wave Detection," *Phys. Rev. Lett.*, vol. 81, p. 5493, 1998.

[30] N. A. Lockerbie, L. Carbone, B. Shapiro, K. V. Tokmakov, A. Bell, and K. A. Strain, "First results from the 'Violin-Mode' tests on an advanced LIGO suspension at MIT," *Class. Quantum Grav.*, vol. 28, no. 24, p. 245001, 2011.

[31] R. L. Ward, R. Adhikari, B. Abbott, R. Abbott, B. D., R. Bork, T. Fricke, V. Frolov, J. Heefner, A. Ivanov, O. Miyakawa, K. McKenzie, M. Slagmolen, B. Smith, R. Taylor, S. Vass, S. Waldman, and A. Weinstein, "DC readout experiment at the caltech 40 m prototype interferometer," *Class. Quantum Grav*, vol. 25, p. 114030, 2008.

[32] K. Izumi, K. Arai, B. Barr, J. Betzwieser, A. Brooks, K. Dahl, S. Doravari, J. C. Driggers, W. Z. Korth, H. Miao, J. Rollins, S. Vass, D. Yeaton-Massey, and R. X. Adhikari, "Multicolor cavity metrology," *J. Opt. Soc. Am. A*, vol. 29, no. 10, pp. 2092–2103, 2012.

[33] D. Friedrich, B. W. Barr, F. Brückner, S. Hild, J. Nelson, J. Macarthur, M. V. Plissi, M. P. Edgar, S. H. Huttner, B. Sorazu, S. Kroker, M. Britzger, E.-B. Kley, K. Danzmann, A. Tünnermann, K. A. Strain, and R. Schnabel, "Waveguide grating mirror in a fully suspended 10 meter Fabry-Perot cavity," *Opt. Express*, vol. 19, no. 16, pp. 14955–14963, 2011.

[34] B. W. Barr, M. P. Edgar, J. Nelson, M. V. Plissi, S. H. Huttner, B. Sorazu, K. A. Strain, O. Burmeister, M. Britzger, D. Friedrich, R. Schnabel, K. Danzmann, J. Hallam, A. Freise, T. Clausnitzer, F. Brückner, E.-B. Kley, and A. Tünnermann, "Translational, rotational, and vibrational coupling into phase in diffractively coupled optical cavities," *Opt. Lett.*, vol. 36, no. 14, pp. 2746–2748, 2011.

[35] B. Sorazu, P. J. Fulda, B. W. Barr, A. S. Bell, C. Bond, L. Carbone, A. Freise, S. Hild, S. H. Huttner, J. Macarthur, and K. A. Strain, "Experimental test of higher-order Laguerre–Gauss modes in the 10 m glasgow prototype interferometer," *Class. Quantum Grav.*, vol. 30, no. 3, p. 035004, 2013.

[36] K. Yamamoto, T. Uchiyama, S. Miyoki, M. Ohashi, K. Kuroda, H. Ishitsuka, T. Akutsu, S. Telada, T. Tomaru, T. Suzuki, N. Sato, Y. Saito, Y. Higashi, T. Haruyama, A. Yamamoto, T. Shintomi, D. Tatsumi, M. Ando, H. Tagoshi, N. Kanda, N. Awaya, S. Yamagishi, H. Takahashi, A. Araya, A. Takamori, S. Takemoto, T. Higashi, H. Hayakawa, W. Morii, and J. Akamatsu, "Current status of the CLIO project," *Journal of Physics: Conference Series*, vol. 122, p. 012002, 2008.

[37] H. Lück, C. Affeldt, J. Degallaix, A. Freise, H. Grote, M. Hewitson, S. Hild, J. Leong, M. Prijatelj, K. A. Strain, B. Willke, H. Wittel, and K. Danzmann, "The upgrade of GEO 600," *Journal of Physics: Conference Series*, vol. 228, no. 1, p. 012012, 2010.

[38] O. Jennrich, "LISA technology and instrumentation," *Class. Quantum Grav.*, vol. 26, no. 15, p. 153001, 2009.

[39] P. Amaro-Seoane, S. Aoudia, S. Babak, P. Binétruy, E. Berti, A. Bohé, C. Caprini, M. Colpi, N. J. Cornish, K. Danzmann, J.-F. Dufaux, J. Gair, O. Jennrich, P. Jetzer, A. Klein, R. N. Lang, A. Lobo, T. Littenberg, S. T. McWilliams, G. Nelemans, A. Petiteau, E. K. Porter, B. F. Schutz, A. Sesana, R. Stebbins, T. Sumner, M. Vallisneri, S. Vitale, M. Volonteri, and H. Ward, "Low-frequency gravitational-wave science with eLISA/NGO," *Class. Quantum Grav.*, vol. 29, no. 12, p. 124016, 2012.

[40] M. Dehne, F. G. Cervantes, B. Sheard, G. Heinzel, and K. Danzmann, "Laser interferometer for spaceborne mapping of the Earth's gravity field," *Journal of Physics: Conference Series*, vol. 154, no. 1, p. 012023, 2009.

[41] T. Corbitt, Y. Chen, F. Khalili, D. Ottaway, S. Vyatchanin, S. Whitcomb, and N. Mavalvala, "Squeezed-state source using radiation-pressure-induced rigidity," *Phys. Rev. A*, vol. 73, p. 023801, 2006.

[42] H. Müller-Ebhardt, H. Rehbein, R. Schnabel, K. Danzmann, and Y. Chen, "Entanglement of Macroscopic Test Masses and the Standard Quantum Limit in Laser Interferometry," *Phys. Rev. Lett.*, vol. 100, p. 013601, 2008.

[43] A. Stochino, B. Abbot, Y. Aso, M. Barton, A. Bertolini, V. Boschi, D. Coyne, R. DeSalvo, C. Galli, Y. Huang, A. Ivanov, S. Marka, D. Ottaway, V. Sannibale, C. Vanni, H. Yamamoto, and S. Yoshida, "The Seismic Attenuation System (SAS) for the Advanced LIGO gravitational wave interferometric detectors," *Nuclear Instruments and Methods in Physics Research Section A: Accelerators, Spectrometers, Detectors and Associated Equipment*, vol. 598, no. 3, pp. 737 – 753, 2009.

[44] A. Wanner, G. Bergmann, A. Bertolini, T. Fricke, H. Lück, C. M. Mow-Lowry, K. A. Strain, S. Goßler, and K. Danzmann, "Seismic attenuation system for the AEI 10 meter Prototype," *Class. Quantum Grav.*, vol. 29, no. 24, p. 245007, 2012.

[45] A. Takamori, P. Raffai, S. Márka, R. DeSalvo, V. Sannibale, H. Tariq, A. Bertolini, G. Cella, N. Viboud, K. Numata, R. Takahashi, and M. Fukushima, "Inverted pendulum as low-frequency pre-isolation for advanced gravitational wave detectors," *Nuclear Instruments and Methods in Physics Research Section A: Accelerators, Spectrometers, Detectors and Associated Equipment*, vol. 582, no. 2, pp. 683 – 692, 2007.

[46] A. Bertolini, G. Cella, R. DeSalvo, and V. Sannibale, "Seismic noise filters, vertical resonance frequency reduction with geometric anti-springs: a feasibility study," *Nuclear Instruments and Methods in Physics Research Section A: Accelerators, Spectrometers, Detectors and Associated Equipment*, vol. 435, no. 3, pp. 475 – 483, 1999.

[47] A. Wanner, *Seismic Attenuation System for the AEI 10 m Prototype*. PhD thesis, Leibniz Universität Hannover, 2013.

[48] K. Dahl, T. Alig, G. Bergmann, A. Bertolini, M. Born, Y. Chen, A. V. Cumming, L. Cunningham, C. Gräf, G. Hammond, G. Heinzel, S. Hild, S. H. Huttner, R. Jones, F. Kawazoe, S. Köhlenbeck, G. Kühn, H. Lück, K. Mossavi, P. Oppermann, J. Pöld, K. Somiya, A. A. van Veggel, A. Wanner, T. Westphal, B. Willke, K. A. Strain, S. G. ler, and K. Danzmann, "Status of the AEI 10m prototype," *Class. Quantum Grav.*, vol. 29, no. 14, p. 145005, 2012.

[49] Innolight GmbH.
`http://www.innolight.de`.

[50] E. J. Elliffe, J. Bogenstahl, A. Deshpande, J. Hough, C. Killow, S. Reid, D. Robertson, S. Rowan, H. Ward, and G. Cagnoli, "Hydroxide-catalysis bonding for stable optical systems for space," *Class. Quantum Grav.*, vol. 22, no. 10, p. S257, 2005.

[51] G. Heinzel, V. Wand, A. García, O. Jennrich, C. Braxmaier, D. Robertson, K. Middleton, D. Hoyland, A. Rüdiger, R. Schilling, U. Johann, and K. Danzmann, "The LTP interferometer and phasemeter," *Class. Quantum Grav.*, vol. 21, no. 5, p. S581, 2004.

[52] K. Dahl, A. Bertolini, M. Born, Y. Chen, D. Gering, S. Goßler, C. Gräf, G. Heinzel, S. Hild, F. Kawazoe, O. Kranz, G. Kühn, H. Lück, K. Mossavi, R. Schnabel, K. Somiya, K. A. Strain, J. R. Taylor, A. Wanner, T. Westphal, B. Willke, and K. Danzmann, "Towards a Suspension Platform Interferometer for the AEI 10m Prototype Interferometer," *J. Phys.: Conf. Ser.*, vol. 228, p. 012027, 2010.

[53] K. Dahl, G. Heinzel, B. Willke, K. A. Strain, S. Goßler, and K. Danzmann, "Suspension platform interferometer for the AEI 10 m prototype: concept, design and optical layout," *Class. Quantum Grav.*, vol. 29, no. 9, p. 095024, 2012.

[54] M. Frede, B. Schulz, R. Wilhelm, P. Kwee, F. Seifert, B. Willke, and D. Kracht, "Fundamental mode, single-frequency laser amplifier for gravitational wave detectors," *Opt. Express*, vol. 15, no. 2, pp. 459–465, 2007.

[55] R. W. P. Drever, J. L. Hall, F. V. Kowalski, J. Hough, and G. M. Ford, "Laser Phase and Frequency Stabilization Using an Optical Resonator," *Appl. Phys. B*, vol. 31, p. 97, 1983.

[56] T. Alig, "Charakterisierung und Unterdrückung der Strahlgeometriefluktuationen des fasergekoppelten 35 W Lasers für das AEI 10 m Prototypinterferometer," Master's thesis, Leibniz Universität Hannover, January 2013.

[57] L. Carbone, S. M. Aston, R. M. Cutler, A. Freise, J. Greenhalgh, J. Heefner, D. Hoyland, N. A. Lockerbie, D. Lodhia, N. A. Robertson, C. C. Speake, K. A. Strain, and A. Vecchio, "Sensors and actuators for the Advanced LIGO mirror suspensions," *Class. Quantum Grav.*, vol. 29, no. 11, p. 115005, 2012.

[58] F. Kawazoe, J. R. Taylor, A. Bertolini, M. Born, Y. Chen, K. Dahl, D. Gering, S. G. ler, C. Gräf, G. Heinzel, S. Hild, O. Kranz, G. Kühn, H. Lück, K. Mossavi, R. Schnabel, K. Somiya, K. Strain, A. Wanner, T. Westphal, B. Willke, and K. Danzmann, "Designs of the frequency reference cavity for the AEI 10 m Prototype interferometer," *Journal of Physics: Conference Series*, vol. 228, no. 1, p. 012028, 2010.

[59] F. Kawazoe, G. Bergmann, A. Bertolini, M. Born, Y. Chen, A. V. Cummning, L. Cunningham, K. Dahl, C. Gräf, G. Hammond, G. Heinzel, S. Hild, S. H. Huttner, R. Jones, S. Köhlenbeck, G. Kühn, H. Lück, K. Mossavi, J. H. Pöld, K. Somiya, A. M. van Veggel, A. Wanner, T. Westphal, B. Willke, K. Strain, S. Goßler, and K. Danzmann, "The AEI 10 m Prototype interferometer frequency control using the reference cavity and its angular control," *Journal of Physics: Conference Series*, vol. 363, no. 1, p. 012012, 2012.

[60] K. Somiya, J. Breyer, Y. Chen, K. Dahl, K. Danzmann, A. Freise, S. Goßler, H. Grote, G. Heinzel, M. Hewitson, F. Kawazoe, G. Kühn, J. Kullmann, H. Lück, K. Mossavi, H. Müller-Ebhardt, H. Rehbein, H. Ryll, R. Schnabel, K. A. Strain, B. Taylor, C. Torrie, A. Wanner, A. Weidner, and B. Willke, "Conceptual design of an interferometer with sub-SQL sensitivity, Ver. 2," *LIGO Document Control Center, T0900069*, 2009.

[61] K. Somiya and K. Yamamoto, "Coating thermal noise of a finite-size cylindrical mirror," *Phys. Rev. D*, vol. 79, p. 102004, 2009.

[62] G. M. Harry, A. M. Gretarsson, P. R. Saulson, S. E. Kittelberger, S. D. Penn, W. J. Startin, S. Rowan, M. M. Fejer, D. R. M. Crooks, G. Cagnoli, J. Hough, and N. Nakagawa, "Thermal noise in interferometric gravitational wave detectors due to dielectric optical coatings," *Class. Quantum Grav.*, vol. 19, no. 5, pp. 897–917, 2002.

[63] F. Y. Khalili, "Reducing the mirrors coating noise in laser gravitational-wave antennae by means of double mirrors," *Phys. Lett. A*, vol. 334, pp. 67–72, 2005.

[64] K. Somiya, "AEI 10 m sub-SQL interferometer sensitivity model." `https://arran.physics.gla.ac.uk/svn/AEI-PT-locking`, March 2011.

[65] G. M. Harry, M. R. Abernathy, A. E. Becerra-Toledo, H. Armandula, E. Black, K. Dooley, M. Eichenfield, C. Nwabugwu, A. Villar, D. R. M. Crooks, G. Cagnoli, J. Hough, C. R. How, I. MacLaren, P. Murray, S. Reid, S. Rowan, P. H. Sneddon, M. M. Fejer, R. Route, S. D. Penn, P. Ganau, J.-M. Mackowski, C. Michel, L. Pinard, and A. Remillieux, "Titania-doped tantala/silica coatings for gravitational-wave detection," *Class. Quantum Grav*, vol. 24, p. 405, 2007.

[66] A. E. Villar, E. D. Black, R. DeSalvo, K. G. Libbrecht, C. Michel, N. Morgado, L. Pinard, I. M. Pinto, V. Pierro, V. Galdi, M. Principe, and I. Taurasi, "Measurement of thermal noise in multilayer coatings with optimized layer thickness," *Phys. Rev. D*, vol. 81, p. 122001, 2010.

[67] A. Cumming, L. Cunningham, S. Gossler, G. Hammond, R. Jones, K. Strain, M. van Veggel, and T. Westphal, "Suspension systems for the AEI 10 m prototype." LIGO DCC, G1200916-v1, Sep 2012.

[68] A. Siegman, *Lasers*. University Science Books, 1986.

[69] A. G. Fox and T. Li, "Resonant Modes in a Maser Interferometer," *Bell System Tech. J.*, vol. 40, p. 453, 1961.

[70] G. D. Boyd and H. Kogelnik, "Generalized confocal resonator theory," *Bell Sys. Tech. J.*, vol. 41, p. 1347–1369, 1962.

[71] A. Freise and K. A. Strain, "Interferometer Techniques for Gravitational-Wave Detection," *Living Rev. Relativity*, vol. 13, 2010.

[72] N. Hodgson and H. Weber, *Optical Resonators: Fundamentals, Advanced Concepts and Applications*. Springer Series in Optical Sciences, Springer, 2005.

[73] J. Mizuno, *Comparison of optical configurations for laser-interferometric gravitational-wave detectors*. PhD thesis, Fachbereich Physik der Universität Hannover, 1995.

[74] M. Malec, *Commissioning of advanced, dual-recycled gravitational-wave detectors: simulations of complex optical systems guided by the phasor picture*. PhD thesis, Fachbereich Physik der Universität Hannover, 2006.

[75] H. van de Stadt and J. M. Muller, "Multimirror Fabry-Perot interferometers," *J. Opt. Soc. Am. A*, vol. 2, no. 8, pp. 1363–1370, 1985.

[76] A. Thüring, *Investigations of coupled and Kerr non-linear optical resonators*. PhD thesis, Albert-Einstein-Institut Hannover, 2009.

[77] P. Baues, "Huygens' principle in inhomogeneous, isotropic media and a general integral equation applicable to optical resonators," *Opto-electronics*, vol. 1, pp. 37–44, 1969.

[78] K. Numata, A. Kemery, and J. Camp, "Thermal-Noise Limit in the Frequency Stabilization of Lasers with Rigid Cavities," *Phys. Rev. Lett.*, vol. 93, p. 250602, 2004.

[79] T. J. Kippenberg and K. J. Vahala, "Cavity Optomechanics: Back-Action at the Mesoscale," *Science*, vol. 29, no. 321, pp. 1172–1176, 2008.

[80] H. B. Callen and R. F. Greene, "On a Theorem of Irreversible Thermodynamics," *Phys. Rev.*, vol. 86, pp. 702–710, 1952.

[81] Y. Levin, "Internal thermal noise in the LIGO test masses: A direct approach," *Phys. Rev. D*, vol. 57, pp. 659–663, 1998.

[82] P. R. Saulson, "Thermal noise in mechanical experiments," *Phys. Rev. D*, vol. 42, pp. 2437–2445, 1990.

[83] A. Gurkovsky and S. Vyatchanin, "The thermal noise in multilayer coating," *Physics Letters A*, vol. 374, no. 33, pp. 3267 – 3274, 2010.

[84] T. P. B. Gregory Harry and R. DeSalvo, *Optical Coatings and Thermal Noise in Precision Measurement*. Cambridge University Press, 2012.

[85] A. Ageev, B. C. Palmer, A. De Felice, S. D. Penn, and P. R. Saulson, "Very high quality factor measured in annealed fused silica," *Class. Quantum Grav.*, vol. 21, p. 3887, 2004.

[86] G. Lovelace, "The dependence of test-mass thermal noises on beam shape in gravitational-wave interferometers," *Class. Quantum Grav.*, vol. 24, no. 17, p. 4491, 2007.

[87] M. Bondarescu, O. Kogan, and Y. Chen, "Optimal light beams and mirror shapes for future LIGO interferometers," *Phys. Rev. D*, vol. 78, p. 082002, 2008.

[88] M. Bondarescu and K. S. Thorne, "New family of light beams and mirror shapes for future LIGO interferometers," *Phys. Rev. D*, vol. 74, p. 082003, 2006.

[89] B. Mours, E. Tournefier, and J.-Y. Vinet, "Thermal noise reduction in interferometric gravitational wave antennas: using high order TEM modes," *Class. Quantum Grav.*, vol. 23, no. 20, p. 5777, 2006.

[90] T. Hong, J. Miller, H. Yamamoto, Y. Chen, and R. Adhikari, "Effects of mirror aberrations on Laguerre-Gaussian beams in interferometric gravitational-wave detectors," *Phys. Rev. D*, vol. 84, p. 102001, 2011.

[91] O. Svelto and D. Hanna, *Principles of Lasers*. Springer, 4th ed., 1998.

[92] J. A. Sidles and D. Sigg, "Optical torques in suspended Fabry–Perot interferometers," *Phys. Lett. A*, vol. 354, p. 167–172, 2005.

[93] A. G. Gurkovsky, D. Heinert, S. Hild, R. Nawrodt, K. Somiya, S. P. Vyatchanin, and H. Wittel, "Reducing thermal noise in future gravitational wave detectors by employing Khalili etalons," *Physics Letters A*, vol. 375, no. 46, pp. 4147 – 4157, 2011.

[94] A. Freise, G. Heinzel, H. Lück, R. Schilling, B. Willke, and K. Danzmann, "Frequency-domain interferometer simulation with higher-order spatial modes," *Class. Quantum Grav.*, vol. 21, no. 5, p. S1067, 2004.

[95] M. Evans, N. Mavalvala, P. Fritschel, R. Bork, B. Bhawal, Gustafson, Kells, Landry, Sigg, Weiss, Whitcomp, and Yamamoto, "Lock acquisition of a gravitational-wave interferometer," *Opt. Lett.*, vol. 27, p. 598, 2002.

[96] K. A. Strain, G. Müller, T. Delker, D. H. Reitze, D. B. Tanner, J. E. Mason, P. A. Willems, D. A. Shaddock, M. B. Gray, C. Mow-Lowry, and D. E. McClelland, "Sensing and control in dual-recycling laser interferometer gravitational-wave detectors," *Appl. Opt.*, vol. 42, p. 1244, 2003.

[97] A. J. Mullavey, B. J. J. Slagmolen, J. Miller, M. Evans, P. Fritschel, D. Sigg, S. J. Waldman, D. A. Shaddock, and D. E. McClelland, "Arm-length stabilisation for interferometric gravitational-wave detectors using frequency-doubled auxiliary lasers," *Opt. Express*, vol. 20, no. 1, pp. 81–89, 2012.

[98] D. A. Shaddock, "Digitally enhanced heterodyne interferometry," *Opt. Lett.*, vol. 32, no. 22, pp. 3355–3357, 2007.

[99] J. Miller, S. Ngo, A. J. Mullavey, B. J. J. Slagmolen, D. A. Shaddock, and D. E. McClelland, "Control and tuning of a suspended Fabry-Perot cavity using digitally enhanced heterodyne interferometry," *Opt. Lett.*, vol. 37, no. 23, pp. 4952–4954, 2012.

[100] A. Thüring. *Lineare mehrfach Spiegel-Resonatoren für Gravitationswellendetektoren*. Diplomarbeit, Fachbereich Physik der Universität Hannover, 2004.

[101] A. M. Gretarsson, E. D'Ambrosio, V. Frolov, B. O'Reilly, and P. K. Fritschel, "Effects of mode degeneracy in the LIGO Livingston Observatory recycling cavity," *J. Opt. Soc. Am. B*, vol. 24, no. 11, pp. 2821–2828, 2007.

[102] M. Granata, M. Barsuglia, R. Flaminio, A. Freise, S. Hild, and J. Marque, "Design of the Advanced Virgo non-degenerate recycling cavities," *Journal of Physics: Conference Series*, vol. 228, no. 1, p. 012016, 2010.

[103] E. D'Ambrosio, "Study of the different responsive behaviour of the sidebands in LIGO I," *Class. Quantum Grav.*, vol. 21, p. S1113, 2004.

[104] A. Siegman, "Unstable optical resonators for laser applications," *Proceedings of the IEEE*, vol. 53, no. 3, pp. 277 – 287, 1965.

[105] D. C. Sinclair, "Choice of Mirror Curvatures for Gas Laser Cavities," *Appl. Opt.*, vol. 3, no. 9, pp. 1067–1071, 1964.

[106] P. Muys and H. Vanherzeele, "Pitfalls in the use of equivalent resonators," *Appl. Opt.*, vol. 21, no. 22, pp. 3983–3984, 1982.

[107] N. Kaiser and H. Pulker, *Optical Interference Coatings*. Springer Series in Optical Sciences, Springer, 2003.

[108] W. Winkler, K. Danzmann, A. Rüdiger, and R. Schilling, "Heating by optical absorption and the performance of interferometric gravitational-wave detectors," *Phys. Rev. A*, vol. 44, no. 11, pp. 7022–7036, 1991.

[109] D. Feige, "LASEROPTIK GmbH." Personal communication, August 2012.

[110] B. Herdt, "LASER COMPONENTS GmbH." Personal communication, August 2012.

[111] S. Götz, "Layertec GmbH." Personal communication, August 2012.

[112] U. Rädel, "TOPAG Lasertechnik GmbH." Personal communication, August 2012.

[113] F. Knutsen, "Photon LaserOptik GmbH." Personal communication, August 2012.

[114] J. Tardif, "Coastline Optics, Inc." Personal communication, April 2012.

[115] The Virgo Collaboration, "Advanced Virgo Technical Design Report," *Virgo TDS, VIR-0128A-12*, 2012.

[116] S. Chelkowski, S. Hild, and A. Freise, "Prospects of higher-order Laguerre-Gauss modes in future gravitational wave detectors," *Phys. Rev. D*, vol. 79, p. 122002, 2009.

[117] A. Freise, *FINESSE 0.99.8 Manual*. 2010.

[118] H. Lück, A. Freise, S. Goßler, S. Hild, K. Kawabe, and K. Danzmann, "Thermal correction of the radii of curvature of mirrors for GEO 600," *Class. Quantum Grav.*, vol. 21, no. 5, p. S985, 2004.

[119] R. Day, "Central Heating Radius of Curvature Correction System (CHRoCC) used in Virgo," *Virgo TDS, VIR-0479A-11*, 2011.

[120] M. A. Arain and G. Mueller, "Design of the Advanced LIGO recycling cavities," *Opt. Express*, vol. 16, no. 14, pp. 10018–10032, 2008.

[121] K. Somiya, "Thermal noise and laser intensity noise of a low-finesse cavity." Unpublished note, June 2010.

[122] F. Khalili. Personal communication, July 2012.

[123] H. Ryll. *Transmission hoher Laserleistung durch optische Fasern*. Diplomarbeit, Fachbereich Physik der Leibniz Universität Hannover, 2008.

[124] K. Somiya, A. G. Gurkovsky, D. Heinert, S. Hild, R. Nawrodt, and S. P. Vyatchanin, "Reduction of coating thermal noise by using an etalon," *Physics Letters A*, vol. 375, no. 11, pp. 1363 – 1374, 2011.

[125] K. Somiya. Personal communication, May 2011.

[126] A. Bunkowski, O. Burmeister, D. Friedrich, K. Danzmann, and R. Schnabel, "High reflectivity grating waveguide coatings for 1064 nm," *Class. Quantum Grav.*, vol. 23, no. 24, p. 7297, 2006.

[127] D. Heinert, S. Kroker, D. Friedrich, S. Hild, E.-B. Kley, S. Leavey, I. W. Martin, R. Nawrodt, A. Tünnermann, S. P. Vyatchanin, , and K. Yamamoto, "Calculation of thermal noise in grating reflectors," *in preparation*.

[128] G. D. Cole, S. Groblacher, K. Gugler, S. Gigan, and M. Aspelmeyer, "Monocrystalline Al_x Ga_{1-x} as heterostructures for high-reflectivity high-Q micromechanical resonators in the megahertz regime," *Applied Physics Letters*, vol. 92, no. 26, p. 261108, 2008.

[129] G. D. Cole, "Recent Progress in Substrate-Transferred Crystalline Mirrors." LIGO DCC, May 2012.

[130] G. H. Steven Penn, "Mechanical Loss in Aluminum Gallium Arsenide Crystal Coatings." LIGO DCC, September 2012. Poster at LVC meeting Rome.

[131] C. Gräf, S. Hild, H. Lück, B. Willke, K. A. Strain, S. Goßler, and K. Danzmann, "Optical layout for a 10 m Fabry–Perot Michelson interferometer with tunable stability," *Class. Quantum Grav.*, vol. 29, no. 7, p. 075003, 2012.

[132] H. Kogelnik and T. Li, "Laser Beams and Resonators," *Applied Optics*, vol. 5, p. 1550, 1966.

[133] G. M. Muzammil A. Arain, "Optical Layout and Parameters for the Advanced LIGO Cavities," *LIGO Document Control Center, T0900043*, 2009.

[134] A. F. Stefan Hild, Simon Chelkowski, "Pushing towards the ET sensitivity using 'conventional' technology," *arXiv:0810.0604 [gr-qc]*, 2008.

[135] K. Numata, M. Ando, K. Yamamoto, S. Otsuka, and K. Tsubono, "Wide-Band Direct Measurement of Thermal Fluctuations in an Interferometer," *Phys. Rev. Lett.*, vol. 91, p. 260602, 2003.

[136] E. D. Black, A. Villar, K. Barbary, A. Bushmaker, J. Heefner, S. Kawamura, F. Kawazoe, L. Matone, S. Meidt, S. R. Rao, K. Schulz, M. Zhang, and K. G. Libbrecht, "Direct observation of broadband coating thermal noise in a suspended interferometer," *Physics Letters A*, vol. 328, no. 1, pp. 1 – 5, 2004.

[137] L. Schnupp, "Presentation given at the European Collaboration Meeting on Interferometric Detection of Gravitational Waves in Sorrento, Italy," 1988.

[138] N. Uehara, E. K. Gustafson, M. M. Fejer, and R. L. Byer, "Modeling of efficient mode matching and thermal-lensing effect on a laser-beam coupling into a mode-cleaner cavity," *Proc. SPIE*, vol. 2989, p. 57, 1997.

[139] Heraeus Quarzglas GmbH & Co. KG, "Suprasil and Infrasil – Material Grades for the Infrared Spectrum." `http://heraeus-quarzglas.com/media/webmedia_local/downloads/broschren_mo/Suprasil_and_Infrasil__Material_Grades_for_the_Infrared_Spectrum.pdf`.

[140] R. Flaminio, J. Franc, C. Michel, N. Morgado, L. Pinard, and B. Sassolas, "A study of coating mechanical and optical losses in view of reducing mirror thermal noise in gravitational wave detectors," *Class. Quantum Grav.*, vol. 27, no. 8, p. 084030, 2010.

[141] P. Hello and J.-Y. Vinet, "Analytical models of thermal aberrations in massive mirrors heated by high power laser beams," *J. Phys. France*, vol. 51, pp. 1267–1282, 1990.

[142] R. Lawrence, *Active Wavefront Correction in Laser Interferometric Gravitational Wave Detectors*. PhD thesis, Massachusets Institute of Technology, 2003.

[143] R. Paschotta, "Beam quality deterioration of lasers caused by intracavity beam distortions," *Optics Express*, vol. 14, pp. 6069–6074, 2006.

[144] J. A. Arnaud, "Degenerate Optical Cavities," *Appl. Opt.*, vol. 8, no. 1, pp. 189–195, 1969.

[145] F. Acernese, P. Amico, M. Al-Shourbagy, S. Aoudia, S. Avino, D. Babusci, G. Ballardin, R. Barillé, F. Barone, L. Barsotti, M. Barsuglia, F. Beauville, M. A. Bizouard, C. Boccara, F. Bondu, L. Bosi, C. Bradaschia, S. Braccini, A. Brillet, V. Brisson, L. Brocco, D. Buskulic, E. Calloni, E. Campagna, F. Cavalier, R. Cavalieri, G. Cella, E. Chassande-Mottin, C. Corda, A.-C. Clapson, F. Cleva, J.-P. Coulon, E. Cuoco, V. Dattilo, M. Davier, R. D. Rosa, L. D. Fiore, A. D. Virgilio, B. Dujardin, A. Eleuteri, D. Enard, I. Ferrante, F. Fidecaro, I. Fiori, R. Flaminio, J.-D. Fournier, S. Frasca, F. Frasconi, A. Freise, L. Gammaitoni, A. Gennai, A. Giazotto, G. Giordano, L. Giordano, R. Gouaty, D. Grosjean, G. Guidi, S. Hebri, H. Heitmann, P. Hello, L. Holloway, S. Kreckelbergh, P. L. Penna, V. Loriette, M. Loupias, G. Losurdo, J.-M. Mackowski, E. Majorana, C. N. Man, M. Mantovani, F. Marchesoni, F. Marion, J. Marque, F. Martelli, A. Masserot, M. Mazzoni, L. Milano, C. Moins, J. Moreau, N. Morgado, B. Mours, A. Pai, C. Palomba, F. Paoletti, S. Pardi, A. Pasqualetti, R. Passaquieti, D. Passuello, B. Perniola, F. Piergiovanni, L. Pinard, R. Poggiani, M. Punturo, P. Puppo, K. Qipiani, P. Rapagnani, V. Reita, A. Remillieux, F. Ricci, I. Ricciardi, P. Ruggi, G. Russo, S. Solimeno, A. Spallicci, R. Stanga, R. Taddei, D. Tombolato, M. Tonelli, A. Toncelli, E. Tournefier, F. Travasso, G. Vajente, D. Verkindt, F. Vetrano, A. Viceré, J.-Y. Vinet, H. Vocca, M. Yvert, and Z. Zhang, "The Virgo automatic alignment system," *Class. Quantum Grav.*, vol. 23, no. 8, p. S91, 2006.

[146] G. Mueller, "Beam jitter coupling in Advanced LIGO," *Opt. Express*, vol. 13, no. 18, pp. 7118–7132, 2005.

[147] G. Müller, "Pointing requirements for Advanced LIGO." LIGO DCC, T0900142-v2, 2009.
`https://dcc.ligo.org/LIGO-T0900142-v2`.

[148] E. D'Ambrosio, "Nonspherical mirrors to reduce thermoelastic noise in advanced gravitational wave interferometers," *Phys. Rev. D*, vol. 102004, p. 1, 2003.

[149] A. P. Lundgren, R. Bondarescu, D. Tsang, and M. Bondarescu, "Finite mirror effects in advanced interferometric gravitational wave detectors," *Phys. Rev. D*, vol. 77, p. 042003, 2008.

[150] P. Barriga, B. Bhawal, L. Ju, and D. Blair, "Numerical calculations of diffraction losses in advanced interferometric gravitational wave detectors," *J. Opt. Soc. Am. A*, vol. 24, pp. 1731–1741, 2007.

[151] J. C. Stover, *Optical Scattering – Measurement and Analysis*. SPIE Optical Engineering Press, 1995.

[152] W. Winkler, R. Schilling, K. Danzmann, J. Mizuno, and A. Rüdiger, "Light scattering described in the mode picture," *Appl. Opt.*, vol. 33, p. 7547, 1994.

[153] H. Davies, "The reflection of electromagnetic waves from rough surface," *Proc. Inst. Electr. Eng.*, vol. 101, p. 209–214, 1954.

[154] H. Yamamoto, "LIGO I mirror scattering loss by microroughness." LIGO DCC T070082-v1, April 2009.

[155] S. E. Watkins, J. P. Black, and B. J. Pond, "Optical scatter characteristics of high-reflectance dielectric coatings and fused-silica substrates," *Appl. Opt.*, vol. 32, no. 28, pp. 5511–5518, 1993.

[156] W. Kells, "Scattered Light Loss from LIGO Arm Cavity Mirrors." LIGO DCC, March 2009.

[157] H. Yamamoto, "Optics, Cavity and Loss: What we learned in aLIGO." LIGO DCC, G1100857, August 2011.

[158] J. Degallaix, M. Galimberti, R. Bonnand, and Q. Benoit, "Defining the arm cavity loss for Advanced Virgo." Virgo TDS, December 2010.

[159] R. Bonnand and J. Degallaix, "Advanced Virgo arm mirror flatness specification, RTL or RTL00?." Virgo TDS, January 2012.

[160] T. Klaassen, J. de Jong, M. van Exter, and J. P. Woerdman, "Transverse mode coupling in an optical resonator," *Opt. Lett.*, vol. 30, no. 15, pp. 1959–1961, 2005.

[161] D. J. Ottaway, P. Fritschel, and S. J. Waldman, "Impact of upconverted scattered light on advanced interferometric gravitational wave detectors," *Opt. Express*, vol. 20, no. 8, pp. 8329–8336, 2012.

[162] J. Camp, H. Yamamoto, S. Whitcomb, and D. McClelland, "Analysis of light noise sources in a recycled Michelson interferometer with Fabry–Perot arms," *J. Opt. Soc. Am. A*, vol. 17, pp. 120–128, 2000.

[163] K. Somiya, Y. Chen, S. Kawamura, and N. Mio, "Frequency noise and intensity noise of next-generation gravitational-wave detectors with RF/DC readout schemes," *Phys. Rev. D*, vol. 73, p. 122005, 2006.

[164] B. Bochner, *Modelling the Performance of Interferometric Gravitational-Wave Detectors with Realistically Imperfect Optics*. PhD thesis, Massachusetts Institute for Technology, 1998.

[165] S. W. Ballmer, *LIGO interferometer operating at design sensitivity with application to gravitational radiometry*. PhD thesis, Massachusetts Institute of Technology, 2006.

[166] B. J. Meers and K. A. Strain, "Wave-front distortion in laser-interferometric gravitational-wave detectors," *Phys. Rev. D*, vol. 43, pp. 3117–3130, 1991.

[167] M. T. Jaekel and S. Reynaud, "Quantum Limits in Interferometric Measurements," *Europhys. Lett.*, vol. 13, p. 301, 1990.

[168] A. M. S.P. Vyatchanin, "Quantum limit on force measurements," *Sov. Phys. JETP*, vol. 77, p. 218, 1993.

[169] S. L. Danilishin and F. Y. Khalili, "Quantum Measurement Theory in Gravitational-Wave Detectors," *Living Rev. Relativity*, vol. 15, no. 5, 2012.

[170] K. Somiya, "The AEI 10 m Prototype Interferometer." Poster at QUEST international advisory-board meeting, 2009.

[171] S. Hild, H. Grote, J. Degallaix, S. Chelkowski, K. Danzmann, A. Freise, M. Hewitson, J. Hough, H. Luck, M. Prijatelj, K. A. Strain, J. R. Smith, and B. Willke, "DC-readout of a signal-recycled gravitational wave detector," *Class. Quantum Grav.*, vol. 26, no. 5, p. 055012 (10pp), 2009.

[172] K. Somiya, "Photodetection method using unbalanced sidebands for squeezed quantum noise in a gravitational wave interferometer," *Phys. Rev. D*, vol. 67, p. 122001, 2003.

[173] F. Bondu, M. Laval, and J.-Y. Vinet, "From mirror maps to TEM00 model: evaluation of effective losses." Virgo TDS, December 2007.

[174] M. Morin, P. Bernard, and P. Galarneau, "Moment definition of the pointing stability of a laser beam," *Opt. Lett.*, vol. 19, no. 18, pp. 1379–1381, 1994.

[175] M. S. Stefszky, C. M. Mow-Lowry, S. S. Y. Chua, D. A. Shaddock, B. C. Buchler, H. Vahlbruch, A. Khalaidovski, R. Schnabel, P. K. Lam, and D. E. McClelland, "Balanced homodyne detection of optical quantum states at audio-band frequencies and below," *Class. Quantum Grav.*, vol. 29, no. 14, p. 145015, 2012.

[176] S. Sakata, S. Kawamura, S. Sato, K. Somiya, K. Arai, M. Fukushima, and A. Sugamoto, "Development of a control scheme of homodyne detection for extracting ponderomotive squeezing from a Michelson interferometer," *Journal of Physics: Conference Series*, vol. 32, no. 1, p. 464, 2006.

[177] E. Sziklas and A. Siegman, "Diffraction calculations using fast Fourier transform methods," *Proceedings of the IEEE*, vol. 62, no. 3, pp. 410 – 412, 1974.

[178] J.-Y. Vinet, P. Hello, C. N. Man, and A. Brillet, "A high accuracy method for the simulation of non-ideal optical cavities," *J. Phys. I France*, vol. 2, no. 7, pp. 1287 – 1303, 1992.

[179] R. Mavaddat, D. E. McClelland, P. Hello, and J. Y. Vinet, "Dual recycling laser interferometer gravitational wave detectors: simulating the performance with imperfect mirrors," *Journal of Optics*, vol. 26, no. 4, p. 145, 1995.

[180] B. Petrovichev, M. Gray, and D. McClelland, "Simulating the Performance of Michelson- and Sagnac-based Laser Interferometric Gravitational Wave Detectors in the Presence of Mirror Tilt and Curvature Errors," *General Relativity and Gravitation*, vol. 30, pp. 1055–1074, 1998.

[181] B. Bochner, "Simulating a Dual-Recycled Gravitational Wave Interferometer with Realistically Imperfect Optics," *General Relativity and Gravitation*, vol. 35, no. 6, pp. 1029–1057, 2003.

[182] B. Bochner and Y. Hefetz, "Grid-based simulation program for gravitational wave interferometers with realistically imperfect optics," *Phys. Rev. D*, vol. 68, p. 082001, 2003.

[183] A. Brillet, J.-Y. Vinet, V. Loriette, J.-M. Mackowski, L. Pinard, and A. Remillieux, "Virtual gravitational wave interferometers with actual mirrors," *Phys. Rev. D*, vol. 67, p. 102006, 2003.

[184] J. W. Cooley and J. W. Tukey, "An algorithm for the machine calculation of complex Fourier series," *Math. Comp.*, vol. 19, pp. 297–301, 1965.

[185] J. Degallaix, "OSCAR – A Matlab based optical FFT code," *Journal of Physics: Conference Series*, vol. 228, no. 1, p. 012021, 2010.

[186] J. Degallaix, "OSCAR software package." MATLAB® File Exchange, http://www.mathworks.com/matlabcentral/fileexchange/20607, February 2013.

[187] P. Saha, "Fast estimation of transverse fields in high-finesse optical cavities," *J. Opt. Soc. Am. A*, vol. 14, no. 9, pp. 2195–2202, 1997.

[188] A. G. Fox and T. Li, "Computation of optical resonator modes by the method of resonance excitation," *IEEE J. Quantum Electron.*, vol. 4, pp. 460–465, 1968.

[189] W. H. Press, S. A. Teukolsky, W. T. Vetterling, and B. P. Flannery, *Numerical Recipes – The Art of Scientific Computing*. Cambridge University Press, 2007.

[190] D. Malacara, *Optical Shop Testing*. Wiley Series in Pure and Applied Optics, 3rd ed., 2007.

[191] International Organization for Standardization, ""Optics and optical instruments—indications in optical drawings," in Draft International Standard ISO 10110 Part 8: Surface Texture." ISO/TC 172/SC 1/WG 2, Geneva, Switzerland.

[192] A. Duparre, J. Ferre-Borrull, S. Gliech, G. Notni, and J. Steinert, "Surface characterization techniques for determining the root-mean-square roughness and power spectral densities of optical components," *Appl. Opt.*, vol. 41, p. 154, 2002.

[193] C. J. Walsh, A. J. Leistner, and B. F. Oreb, "Power Spectral Density Analysis of Optical Substrates for Gravitational-Wave Interferometry," *Appl. Opt.*, vol. 38, no. 22, pp. 4790–4801, 1999.

[194] E. L. Church, "Fractal surface finish," *Appl. Opt.*, vol. 27, no. 8, pp. 1518–1526, 1988.

[195] M. Galimberti, "Characterization and simulation of mirror surfaces." Virgo TDS, VIR-0038A-11, January 2011.

[196] F. Bondu, "Large virtual mirror maps." Virgo TDS, VIR-0271A-10, May 2010.

[197] M. Born and E. Wolf, *Principles of Optics: Electromagnetic Theory of Propagation, Interference and Diffraction of Light*. Cambridge University Press, 7th ed., Oct. 1999.

[198] V. N. Mahajan, "Zernike Circle Polynomials and Optical Aberrations of Systems with Circular Pupils," *Appl. Opt.*, vol. 33, no. 34, pp. 8121–8121, 1994.

[199] C. Bond, P. Fulda, L. Carbone, K. Kokeyama, and A. Freise, "Higher order Laguerre-Gauss mode degeneracy in realistic, high finesse cavities," *Phys. Rev. D*, vol. 84, p. 102002, 2011.

[200] The Virgo Collaboration, *Virgo Physics Book Vol. II*. The Virgo Collaboration, 2006.
`https://wwwcascina.virgo.infn.it/vpb/`.

[201] J. Y. Wang and D. E. Silva, "Wave-front interpretation with Zernike polynomials," *Appl. Opt.*, vol. 19, no. 9, pp. 1510–1518, 1980.

[202] R. Bonnand, J. Degallaix, M. Galimberti, R. Flaminio, and L. Pinard, "Simulations for the specifications of mirror flatness for Advanced Virgo." Virgo TDS, VIR-0104A-11, February 2011.

[203] H. Yamamoto, "LCGT test mass surface specification," February 2011.
Available at `http://gwdoc.icrr.u-tokyo.ac.jp/DocDB/0003/T1100351/001/JGW-T1100351.pdf`.

[204] J. Mackowski, L. Pinard, L. Dognin, P. Ganau, B. Lagrange, C. Michel, and M. Morgue, "VIRGO mirrors: wavefront control," *Optical and Quantum Electronics*, vol. 31, pp. 507–514, 1999.

[205] A. Freise and C. Bond, "Simtools – A collection of Matlab tools for optical simulations."
`http://www.gwoptics.org/simtools/`.

[206] "RRZN cluster system at the Leibniz University of Hannover, Germany."

[207] Python Software Foundation., "Python Language Reference, version 2.7."
`http://www.python.org`.

[208] T. Hänsel, F. Frost, A. Nickel, and T. Schindler, "Ultra-precision Surface Finishing by Ion Beam Techniques," *Vakuum in Forschung und Praxis*, vol. 19, no. 5, pp. 24–30, 2007.

[209] T. Haensel, A. Nickel, and A. Schindler, "Ion Beam Figuring of Strongly Curved Surfaces with a (X, Y, Z) Linear Three-Axes System," *Plasmonics and Metamaterials*, p. JWD6, 2008.

[210] C. Gräf and T. Fricke, "Proposal for a single arm cavity test experiment," *Internal Note, AEI 10 m Prototype Logbook*, p. 814, Sep 2012.

[211] H. Wittel, S. Hild, and K. A. Strain, "Design ideas for the electrostatic drives of the AEI 10 m," *Internal Note, AEI 10 m Prototype Logbook*, p. 693, June 2012.

[212] C. Gräf, "Preliminary SAT matching telescope design data," *AEI 10 m Prototype Logbook*, p. 884, Nov 2012.

[213] Roman Schnabel for the LIGO Scientific Collaboration, "A gravitational wave observatory operating beyond the quantum shot-noise limit," *Nature Physics*, vol. 7, pp. 962–965, 2011.

[214] L. Barsotti for the LIGO Scientific Collaboration, "Enhancing the astrophysical reach of the LIGO gravitational wave detector by using squeezed states of light," *to be published*.

[215] S. Hild, M. Abernathy, F. Acernese, P. Amaro-Seoane, N. Andersson, K. Arun, F. Barone, B. Barr, M. Barsuglia, M. Beker, N. Beveridge, S. Birindelli, S. Bose, L. Bosi, S. Braccini, C. Bradaschia, T. Bulik, E. Calloni, G. Cella, E. C. Mottin, S. Chelkowski, A. Chincarini, J. Clark, E. Coccia, C. Colacino, J. Colas, A. Cumming, L. Cunningham, E. Cuoco, S. Danilishin, K. Danzmann, R. D. Salvo, T. Dent, R. D. Rosa, L. D. Fiore, A. D. Virgilio, M. Doets, V. Fafone, P. Falferi, R. Flaminio, J. Franc, F. Frasconi, A. Freise, D. Friedrich, P. Fulda, J. Gair, G. Gemme, E. Genin, A. Gennai, A. Giazotto, K. Glampedakis, C. Gräf, M. Granata, H. Grote, G. Guidi, A. Gurkovsky, G. Hammond, M. Hannam, J. Harms, D. Heinert, M. Hendry, I. Heng, E. Hennes, J. Hough, S. Husa, S. Huttner, G. Jones, F. Khalili, K. Kokeyama, K. Kokkotas, B. Krishnan, T. G. F. Li, M. Lorenzini, H. Lück, E. Majorana, I. Mandel, V. Mandic, M. Mantovani, I. Martin, C. Michel, Y. Minenkov, N. Morgado, S. Mosca, B. Mours, H. Müller–Ebhardt, P. Murray, R. Nawrodt, J. Nelson, R. Oshaughnessy, C. D. Ott, C. Palomba, A. Paoli, G. Parguez, A. Pasqualetti, R. Passaquieti, D. Passuello, L. Pinard, W. Plastino, R. Poggiani, P. Popolizio, M. Prato, M. Punturo, P. Puppo, D. Rabeling, P. Rapagnani, J. Read, T. Regimbau, H. Rehbein, S. Reid, F. Ricci, F. Richard, A. Rocchi, S. Rowan, A. Rüdiger, L. Santamaría, B. Sassolas, B. Sathyaprakash, R. Schnabel, C. Schwarz, P. Seidel, A. Sintes, K. Somiya, F. Speirits, K. Strain, S. Strigin, P. Sutton, S. Tarabrin, A. Thüring, J. van den Brand, M. van Veggel, C. van den Broeck, A. Vecchio, J. Veitch, F. Vetrano, A. Vicere, S. Vyatchanin, B. Willke, G. Woan, and K. Yamamoto, "Sensitivity studies for third-generation gravitational wave observatories," *Class. Quantum Grav.*, vol. 28, p. 094013, 2011.

[216] C. M. Caves, "Quantum-mechanical noise in an interferometer," *Phys. Rev. D*, vol. 23, p. 1693, 1981.

[217] R. E. Slusher, L. W. Hollberg, B. Yurke, J. C. Mertz, and J. F. Valley, "Observation of Squeezed States Generated by Four-Wave Mixing in an Optical Cavity," *Phys. Rev. Lett.*, vol. 55, p. 2409, 1985.

[218] L.-A. Wu, M. Xiao, and H. J. Kimble, "Squeezed states of light from an optical parametric oscillator," *J. Opt. Soc. Am. B*, vol. 4, p. 1465, 1987.

[219] H. Vahlbruch, M. Mehmet, S. Chelkowski, B. Hage, A. Franzen, N. Lastzka, S. Goßler, K. Danzmann, and R. Schnabel, "Observation of Squeezed Light with 10-dB Quantum-Noise Reduction," *Phys. Rev. Lett.*, vol. 100, p. 033602, 2008.

[220] T. Eberle, S. Steinlechner, J. Bauchrowitz, V. Händchen, H. Vahlbruch, M. Mehmet, H. Müller-Ebhardt, and R. Schnabel, "Quantum Enhancement of the Zero-Area Sagnac Interferometer Topology for Gravitational Wave Detection," *Phys. Rev. Lett.*, vol. 104, p. 251102, 2010.

[221] K. McKenzie, N. Grosse, W. P. Bowen, S. E. Whitcomb, M. B. Gray, McCelland, and Lam, "Squeezing in the Audio Gravitational-Wave Detection Band," *Phys. Rev. Lett.*, vol. 93, p. 161105, 2004.

[222] H. Vahlbruch, S. Chelkowski, B. Hage, A. Franzen, K. Danzmann, and R. Schnabel, "Coherent Control of Vacuum Squeezing in the Gravitational-Wave Detection Band," *Phys. Rev. Lett.*, vol. 97, p. 011101, 2006.

[223] K. McKenzie, D. A. Shaddock, and D. E. McClelland, "Experimental Demonstration of a Squeezing-Enhanced Power-Recycled Michelson Interferometer for Gravitational Wave Detection," *Phys. Rev. Lett.*, vol. 88, p. 231102, 2002.

[224] H. Vahlbruch, S. Chelkowski, B. Hage, A. Franzen, K. Danzmann, and R. Schnabel, "Demonstration of a Squeezed-Light-Enhanced Power- and Signal-Recycled Michelson Interferometer," *Phys. Rev. Lett.*, vol. 95, p. 211102, 2005.

[225] K. Goda, O. Miyakawa, E. E. Mikhailov, S. Saraf, R. Adhikari, K. McKenzie, R. Ward, S. Vass, A. J. Weinstein, and N. Mavalvala, "A quantum-enhanced prototype gravitational-wave detector," *Nature Physics*, vol. 4, pp. 1745–2473, 2008.

[226] H. Vahlbruch, *Squeezed Light for Gravitational Wave Astronomy*. PhD thesis, Fachbereich Physik der Universität Hannover, 2008.

[227] A. Khalaidovski, *Beyond the quantum limit – a squeezed light laser for GEO 600*. PhD thesis, Fachbereich Physik der Leibniz Universität Hannover, 2011.

[228] C. Gräf. *PPKTP-Quetschlichtquelle und Twin-Signal-Recycling*. Diplomarbeit, Fachbereich Physik der Leibniz Universität Hannover, 2008.

[229] H. Grote, K. Danzmann, K. L. Dooley, R. Schnabel, J. Slutsky, and H. Vahlbruch, "First Long-Term Application of Squeezed States of Light in a Gravitational-Wave Observatory," *Phys. Rev. Lett.*, vol. 110, p. 181101, 2013.

[230] H. Vahlbruch, A. Khalaidovski, N. Lastzka, C. Gräf, K. Danzmann, and R. Schnabel, "The GEO 600 sqeezed light source," *Class. Quantum Grav.*, vol. 27, p. 084027, 2010.

[231] R. Bork, "Advanced LIGO CDS Design Overview." LIGO Document Control Center, 2009.
`https://dcc.ligo.org/public/0007/T0900612/002/`.

[232] Experimental Physics and Industrial Control System (EPICS).
`http://www.aps.anl.gov/epics`.

[233] Linux real time Preempt patch.
`https://rt.wiki.kernel.org`.

[234] G. H. Mealy, "A Method for Synthesizing Sequential Circuits," *Bell System Tech. J.*, vol. 34, p. 1045–1079, 1955.

[235] O. H. Schmitt, "A thermionic trigger," *Journal of Scientific Instruments*, vol. 15, no. 1, p. 24, 1938.

[236] G. van Rossum, "Python tutorial." Technical Report CS-R9526, Centrum voor Wiskunde en Informatica (CWI), May 1995.

[237] M. Newville, "EpicsCA. Python interface to EPICS Channel Access protocol."
`http://cars9.uchicago.edu/~newville/Epics/Python/EpicsCA.html`.

[238] N. Lastzka, *Numerical modelling of classical and quantum effects in non-linear optical systems*. PhD thesis, Fachbereich Physik der Leibniz Universität Hannover, 2010.

[239] A. Khalaidovski, H. Vahlbruch, N. Lastzka, C. Gräf, K. Danzmann, H. Grote, and R. Schnabel, "Long-term stable squeezed vacuum state of light for gravitational wave detectors," *Class. Quantum Grav.*, vol. 29, no. 7, p. 075001, 2012.

APPENDIX A

Numerical simulation source code

In this appendix, source code listings of selected numerical simulations are given, which were developed for the investigations presented in this thesis.

Sub-SQL interferometer parameters

Listing A.1: MATLAB® function which returns a "struct" containing the most relevant parameters of the optical layout of the sub-SQL interferometer.

```
function [ parmStruct ] = getSSIGlobalParms()
%getSSIGlobal_Parms Returns global parameters for the SubSQL IFO
%
%    Usage: ps = getSSIGlobalParms()
%
%    Parameters can be accessed from the caller of the function using the
%    dot notation, e.g. x = ps.IM.R to store the IM power reflectivity in
%    the variable x.
%
%    All numbers, if not explicitly noted, taken from Kentaro's
%    "Conceptual design of an interferometer with a sub-SQL
%         sensitivity ver. 2.0"
%
%
%     For non-pure Matlab-based usage keep an eye on potential
%          TRUNCATION ERROR!
%     (e.g. for passing small numbers to Finesse via SimTools).
%     Matlab displays numbers at lower precision than they are handled
%     internally. It is advisable to enforce the desired precision e.g.
%     with a command in the style of
%                    num2str(RoC_IM_HR,'% 10.8f');
%     i.e. by using format specifiers to export the constant RoC_IM_HR to
%     a .kat file via SimTools or similar applications.
%


    % Fundamental laser wave length
    parmStruct.lambda0 = 1064e-9;

    % Laser input power
    parmStruct.Pin = 5.5;

    % Refractive index FS
```

```
parmStruct.nFusedSilica = 1.4496309898590634;

% Thickness of main suspension substrates
parmStruct.SubstrateThickness = 0.0245;

% Radius of main suspension substrates
parmStruct.SubstrateRadius = 0.0243;

% optimal spot radius on IFO mirrors, a/2.5 to keep diffraction loss
% at a tolerable level of ~ 2.25ppm
parmStruct.w_optim = parmStruct.SubstrateRadius / 2.5;

% optical pathlength in IEM substrate
parmStruct.L_optical_IEM = parmStruct.SubstrateThickness * parmStruct.
    nFusedSilica;

% mirror/bs power reflectivities
parmStruct.IM.R = 0.990696;
parmStruct.IEM.R = 0.511510;
parmStruct.EEM.R = 0.999936;
parmStruct.EM.R = 0.999936;
parmStruct.BS.R = 0.5;

% mirror/bs power loss
%%% A value of 50ppm loss/mirror was assumed in the conceptual design
parmStruct.IM.L = 50e-6;
%parmStruct.IEM.L = 50e-6;
%parmStruct.EEM.L = 50e-6;
parmStruct.EM.L = 50e-6;
parmStruct.BS.L = 50e-6;

% mirror/bs power transmittances
parmStruct.IM.T = 1 - parmStruct.IM.R - parmStruct.IM.L;
parmStruct.EM.T = 1 - parmStruct.EM.R - parmStruct.EM.L;
parmStruct.BS.T = 1 - parmStruct.BS.R - parmStruct.BS.L;

%%%%%%%%%%%%%%%%%%%%%%%%%%%%%%%%%%%%%%%%%%%%%%%%%%%%%%%%%%%%%%%%%
%  Parameters above this block are considered to be stable  %%%%%
%%%%%%%%%%%%%%%%%%%%%%%%%%%%%%%%%%%%%%%%%%%%%%%%%%%%%%%%%%%%%%%%%
%%%%%%%%%%%%%%%%%%%%%%%%%%%%%%%%%%%%%%%%%%%%%%%%%%%%%%%%%%%%%%%%%
% Parameters given below are subject to changes %%%%%%%%%%%%%%%%%
%%%%%%%%%%%%%%%%%%%%%%%%%%%%%%%%%%%%%%%%%%%%%%%%%%%%%%%%%%%%%%%%%

% AR power reflectivities
parmStruct.IM_AR.R = 10e-6;
parmStruct.EM_AR.R = 10e-6;
parmStruct.BS_AR.R = 100e-6;

% AR power loss
parmStruct.IM_AR.L = 5e-6;
parmStruct.EM_AR.L = 5e-6;
parmStruct.BS_AR.L = 5e-6;

% Lengths
parmStruct.LX = 11.3952;
parmStruct.LY = 11.3952;
parmStruct.lx = 0.4;
parmStruct.ly = 0.6;
parmStruct.lin = 12;
parmStruct.lin2 = 12;

% ROCs
parmStruct.IMx.ROC = 5.7;
```

```
    parmStruct.EMx.ROC = 5.7;
    parmStruct.IMx_AR.ROC = 1.7755;
    parmStruct.IMy.ROC = 5.7;
    parmStruct.EMy.ROC = 5.7;
    parmStruct.IMy_AR.ROC = 1.7755;
    parmStruct.Mcol.ROC = 24;

    % Thickness of BS substrates
    parmStruct.SubstrateThickness_BS = 0.0245;

    % Size of dark fringe offset applied to BS
    parmStruct.BS.phi = 2; % [deg]

    % Angle of collimating mirror in modematching telescope
    parmStruct.Mcol.ang = 1; % [deg]

    % Pre-mode-cleaner waist size
    parmStruct.PMC.w = 0.000420;

    % RF Modulation 1
    parmStruct.fm1.freq = 20440400;
    parmStruct.fm1.midx = 0.3;

    % imbalances, imperfections and offsets, p.12 conceptual design
    parmStruct.Delta.epsilon = 15*1E-6; % +/- 15ppm arm cavity loss imbalance
    parmStruct.Delta.finesse = 0.01; % Arm cavity finesse imbalance
    parmStruct.Delta.mass = 0.01; % Mass imbalance between the arms
    parmStruct.BS.sigma = 0.01; % sigma = (r_BS)^2 - (t_BS)^2,

end
```

End mirror cavity modeling

Listing A.2: MATLAB® function which makes use of Simtools routines to model a single sub-SQL interferometer arm with a Khalili end mirror cavity. The function depends on the skeleton file SSI_OptParms.kat in which the basic optical layout is defined.

```
function [ opticalParms, Run1 ] = getSSIOpticalParms( L_AC, L_KC, RoC_IM_HR,
    RoC_IEM_HR, RoC_IEM_AR, RoC_EEM_HR, CavityStr )
% getSSIOpticalParms Calculates optical parameters from a basic set of
%                        variables, i.e. lengths and curvatures for a
%                        5-DOF AEI 10m SubSQL interferometer arm
%
%   Written by Christian Graef for the AEI 10m Prototype Team
%
%   Takes:
%     L_AC:       Arm cavity length
%     L_KC:       Khalili cavity length
%     RoC_IM_HR:  Radius of curvature of IM HR side (neg. for concave mirror)
%     RoC_IEM_HR: Radius of curvature of IEM HR side (pos. for concave mirror)
%     RoC_IEM_AR: Radius of curvature of IEM AR side, positive for focussing
    lens (pos. for focussing lens)
%     RoC_EEM_HR: Radius of curvature of EEM HR side (pos. for concave mirror)
%     CavityStr:  'AC', 'KC', 'both' or '' -- determines which cavities to set
     via Finesse "cav" command
%
%   Returns:      Struct containing optical parameters at all relevant optics
    surfaces as well as cavity parameters
%
```

```
%   Example call:   op=getSSIOpticalParms(10.3964, 0.9791, -5.2, 5.2, 1.6,
    -281.63, 'both')
%                   Calculates optical parameters for a SubSQL arm type
%                   3MCC for nearly collimated KC mode configuration and saves
     all data in the struct 'op'
%
%   Dependencies:   Finesse Ver. > 0.99.8 + SimTools Ver. > 0.6
%                   SSI_OptParms.kat
%                   getSSIGlobalParms.m
%                   getAcStability.m
%                   getKcStability.m
%
%
%   Please note:  -- Radii of curvature of the optics input is expected to
%                     follow the Finesse RoC convention
%                 -- Entries given in the resulting parameter struct are
    always
%                     related to the *beam*, not to the optics! This is
%                     evident for the IEM-AR case, where the calculated beam
%                     RoC naturally deviates from the RoC of the optic, as
%                     it is an intra-cavity object. For unstable cavities
%                     beam RoC and corresponding optic RoC generally don't
%                     match.
%
%
%   Revision history:   2011-04-18 Refactored from get_SubSQL_OpticalParms()
%                       2011-04-19 Cleaned up, extended, tested
%                       2011-05-10 Feature added to enable/disable
%                                  individual cavities, cavity read out
%                                  moved from .kat file to this one
%
%

format long;

setSimEnvironment;

FT=FT_init_Finesse('name','kat','path',getenv('KATBINARY'))

%% Parse global parameters
globalParms = getSSIGlobalParms();

%% Initialize SimTools run
readkat = 'SSI_OptParms.kat';
writekat = 'SSI_OP_out.kat'

myBlock=FT_read_blocks_from_file(readkat);

outbl(1) = FT_copy_block(myBlock, 'Constants');
outbl(2) = FT_copy_block(myBlock, 'Gauss');
outbl(3) = FT_copy_block(myBlock, 'Laser');
outbl(4) = FT_copy_block(myBlock, 'OptSetup');
%outbl(5) = FT_copy_block(myBlock, 'RoC');
outbl(12) = FT_copy_block(myBlock, 'Readout');
%outbl(7) = FT_copy_block(myBlock, 'xaxis');

%%% --- Block: Constants
outbl(1) = FT_write_kat_constant(outbl(1), 'subThick', num2str(globalParms.
    SubstrateThickness, '% 16.14f'));
outbl(1) = FT_write_kat_constant(outbl(1), 'nFS', num2str(globalParms.
    nFusedSilica, '% 16.14f'));
outbl(1) = FT_write_kat_constant(outbl(1), 'L_AC', num2str(L_AC, '% 16.14f'));
outbl(1) = FT_write_kat_constant(outbl(1), 'L_KC', num2str(L_KC, '% 16.14f'));
```

```
%%% --- Block: Optics radii of curvature ---
outbl(8) = FT_create_new_block('RadiusOfCurvature');
outbl(8) = FT_add_line_to_block(outbl(8), strcat('attr IM.HR Rc',{' '},
    num2str(RoC_IM_HR,'% 16.14f')));
outbl(8) = FT_add_line_to_block(outbl(8), strcat('attr IEM.HR Rc' ,{' '},
    num2str(RoC_IEM_HR, '% 16.14f')));
outbl(8) = FT_add_line_to_block(outbl(8), strcat('attr IEM.AR Rc', {' '},
    num2str(RoC_IEM_AR,'% 16.14f')));
outbl(8) = FT_add_line_to_block(outbl(8), strcat('attr EEM.HR Rc', {' '},
    num2str(RoC_EEM_HR,'% 16.14f')));

%%% --- Block: Finesse xaxis
outbl(9) = FT_create_new_block('xaxis_ST');
outbl(9) = FT_add_line_to_block(outbl(9), 'noxaxis');

%%% --- Block: Finesse yaxis
outbl(10) = FT_create_new_block('yaxis_ST');
outbl(10) = FT_add_line_to_block(outbl(10), 'yaxis re:im');

%%% --- Block: Cavity settings
outbl(11) = FT_create_new_block('Cavities');

switch CavityStr
    case 'AC',
        outbl(11) = FT_add_line_to_block(outbl(11), 'cav AC IM.HR nIMhr IEM.HR
             nIEMhr');
        outbl(11) = FT_add_line_to_block(outbl(11), '#cav KC IEM.HR nIEMs1 EEM
            .HR nEEMhr');
    case 'KC',
        outbl(11) = FT_add_line_to_block(outbl(11), '#cav AC IM.HR nIMhr IEM.
            HR nIEMhr');
        outbl(11) = FT_add_line_to_block(outbl(11), 'cav KC IEM.HR nIEMs1 EEM.
            HR nEEMhr');
    case ''
        outbl(11) = FT_add_line_to_block(outbl(11), '#cav AC IM.HR nIMhr IEM.
            HR nIEMhr');
        outbl(11) = FT_add_line_to_block(outbl(11), '#cav KC IEM.HR nIEMs1 EEM
            .HR nEEMhr');
    case 'both'
        outbl(11) = FT_add_line_to_block(outbl(11), 'cav AC IM.HR nIMhr IEM.HR
             nIEMhr');
        outbl(11) = FT_add_line_to_block(outbl(11), 'cav KC IEM.HR nIEMs1 EEM.
            HR nEEMhr');
end

outbl(11) = FT_add_line_to_block(outbl(11), '#trace 4');
outbl(11) = FT_add_line_to_block(outbl(11), '#ad myAD 0 nEEMhr');

%%% --- Block: Cavity parameters readout
if strcmp(CavityStr,'AC') || strcmp(CavityStr,'both')
        outbl(12) = FT_add_line_to_block(outbl(12), 'cp AC x w');
        outbl(12) = FT_add_line_to_block(outbl(12), 'cp AC x w0');
        outbl(12) = FT_add_line_to_block(outbl(12), 'cp AC x z');
        outbl(12) = FT_add_line_to_block(outbl(12), 'cp AC x r');
        outbl(12) = FT_add_line_to_block(outbl(12), 'cp AC x q');
        outbl(12) = FT_add_line_to_block(outbl(12), 'cp AC x finesse');
        outbl(12) = FT_add_line_to_block(outbl(12), 'cp AC x loss');
        outbl(12) = FT_add_line_to_block(outbl(12), 'cp AC x length');
        outbl(12) = FT_add_line_to_block(outbl(12), 'cp AC x FSR');
        outbl(12) = FT_add_line_to_block(outbl(12), 'cp AC x FHWM');
        outbl(12) = FT_add_line_to_block(outbl(12), 'cp AC x pole');
end
```

```
if strcmp(CavityStr,'KC') || strcmp(CavityStr,'both')
        outbl(12) = FT_add_line_to_block(outbl(12), 'cp KC x w');
        outbl(12) = FT_add_line_to_block(outbl(12), 'cp KC x w0');
        outbl(12) = FT_add_line_to_block(outbl(12), 'cp KC x z');
        outbl(12) = FT_add_line_to_block(outbl(12), 'cp KC x r');
        outbl(12) = FT_add_line_to_block(outbl(12), 'cp KC x q');
        outbl(12) = FT_add_line_to_block(outbl(12), 'cp KC x finesse');
        outbl(12) = FT_add_line_to_block(outbl(12), 'cp KC x loss');
        outbl(12) = FT_add_line_to_block(outbl(12), 'cp KC x length');
        outbl(12) = FT_add_line_to_block(outbl(12), 'cp KC x FSR');
        outbl(12) = FT_add_line_to_block(outbl(12), 'cp KC x FHWM');
        outbl(12) = FT_add_line_to_block(outbl(12), 'cp KC x pole');
end
if strcmp(CavityStr,'KC') || strcmp(CavityStr,'both')
        outbl(12) = FT_add_line_to_block(outbl(12), 'pd PowAC nIEMhr');
        outbl(12) = FT_add_line_to_block(outbl(12), 'pd PowKC nEEMhr');
        outbl(12) = FT_add_line_to_block(outbl(12), 'pd HomPowAC nIEMhr');
        outbl(12) = FT_add_line_to_block(outbl(12), 'mask HomPowAC 0 0 0');
        outbl(12) = FT_add_line_to_block(outbl(12), 'pd HomPowKC nEEMhr');
        outbl(12) = FT_add_line_to_block(outbl(12), 'mask HomPowKC 0 0 0');
end
%% Perform SimTools kat run
FT_write_blocks_into_file(outbl, writekat);

Run1=FT_create_new_kat_run();
Run1.filename = writekat;
Run1=FT_run_kat_simulation(FT,Run1);

%%%%%%%%%%%%%%%%%%%%%%%%%%%%%%%%%%%%%%%%%%%%%%%%%%%%%%
% Readout of simulation results
%%%%%%%%%%%%%%%%%%%%%%%%%%%%%%%%%%%%%%%%%%%%%%%%%%%%%%

%% IM HR-side
opticalParms.IM_HR.w_x = Run1.y(1,1) + 1i*Run1.y(1,2);
opticalParms.IM_HR.w_y = Run1.y(1,3) + 1i*Run1.y(1,4);
opticalParms.IM_HR.w0_x = Run1.y(1,5) + 1i*Run1.y(1,6);
opticalParms.IM_HR.w0_y = Run1.y(1,7) + 1i*Run1.y(1,8);
opticalParms.IM_HR.z_x = Run1.y(1,9) + 1i*Run1.y(1,10);
opticalParms.IM_HR.z_y = Run1.y(1,11) + 1i*Run1.y(1,12);
opticalParms.IM_HR.zr_x = Run1.y(1,13) + 1i*Run1.y(1,14);
opticalParms.IM_HR.zr_y = Run1.y(1,15) + 1i*Run1.y(1,16);
opticalParms.IM_HR.g_x = Run1.y(1,17) + 1i*Run1.y(1,18);
opticalParms.IM_HR.g_y = Run1.y(1,19) + 1i*Run1.y(1,20);
opticalParms.IM_HR.q_x = Run1.y(1,21) + 1i*Run1.y(1,22);
opticalParms.IM_HR.q_y = Run1.y(1,23) + 1i*Run1.y(1,24);
opticalParms.IM_HR.RoC_x = opticalParms.IM_HR.z_x + (opticalParms.IM_HR.zr_x)
    ^2/opticalParms.IM_HR.z_x;

%% IEM HR-side
opticalParms.IEM_HR.w_x = Run1.y(1,25) + 1i*Run1.y(1,26);
opticalParms.IEM_HR.w_y = Run1.y(1,27) + 1i*Run1.y(1,28);
opticalParms.IEM_HR.w0_x = Run1.y(1,29) + 1i*Run1.y(1,30);
opticalParms.IEM_HR.w0_y = Run1.y(1,31) + 1i*Run1.y(1,32);
opticalParms.IEM_HR.z_x = Run1.y(1,33) + 1i*Run1.y(1,34);
opticalParms.IEM_HR.z_y = Run1.y(1,35) + 1i*Run1.y(1,36);
opticalParms.IEM_HR.zr_x = Run1.y(1,37) + 1i*Run1.y(1,38);
opticalParms.IEM_HR.zr_y = Run1.y(1,39) + 1i*Run1.y(1,40);
opticalParms.IEM_HR.g_x = Run1.y(1,41) + 1i*Run1.y(1,42);
opticalParms.IEM_HR.g_y = Run1.y(1,43) + 1i*Run1.y(1,44);
opticalParms.IEM_HR.q_x = Run1.y(1,45) + 1i*Run1.y(1,46);
opticalParms.IEM_HR.q_y = Run1.y(1,47) + 1i*Run1.y(1,48);
opticalParms.IEM_HR.RoC_x = opticalParms.IEM_HR.z_x + (opticalParms.IEM_HR.
    zr_x)^2/opticalParms.IEM_HR.z_x;
```

```
%% IEM AR-side
opticalParms.IEM_AR.w_x = Run1.y(1,49) + 1i*Run1.y(1,50);
opticalParms.IEM_AR.w_y = Run1.y(1,51) + 1i*Run1.y(1,52);
opticalParms.IEM_AR.w0_x = Run1.y(1,53) + 1i*Run1.y(1,54);
opticalParms.IEM_AR.w0_y = Run1.y(1,55) + 1i*Run1.y(1,56);
opticalParms.IEM_AR.z_x = Run1.y(1,57) + 1i*Run1.y(1,58);
opticalParms.IEM_AR.z_y = Run1.y(1,59) + 1i*Run1.y(1,60);
opticalParms.IEM_AR.zr_x = Run1.y(1,61) + 1i*Run1.y(1,62);
opticalParms.IEM_AR.zr_y = Run1.y(1,63) + 1i*Run1.y(1,64);
opticalParms.IEM_AR.g_x = Run1.y(1,65) + 1i*Run1.y(1,66);
opticalParms.IEM_AR.g_y = Run1.y(1,67) + 1i*Run1.y(1,68);
opticalParms.IEM_AR.q_x = Run1.y(1,69) + 1i*Run1.y(1,70);
opticalParms.IEM_AR.q_y = Run1.y(1,71) + 1i*Run1.y(1,72);
opticalParms.IEM_AR.RoC_x = opticalParms.IEM_AR.z_x + (opticalParms.IEM_AR.
    zr_x)^2/opticalParms.IEM_AR.z_x;

%% EEM HR-side
opticalParms.EEM_HR.w_x = Run1.y(1,73) + 1i*Run1.y(1,74);
opticalParms.EEM_HR.w_y = Run1.y(1,75) + 1i*Run1.y(1,76);
opticalParms.EEM_HR.w0_x = Run1.y(1,77) + 1i*Run1.y(1,78);
opticalParms.EEM_HR.w0_y = Run1.y(1,79) + 1i*Run1.y(1,80);
opticalParms.EEM_HR.z_x = Run1.y(1,81) + 1i*Run1.y(1,82);
opticalParms.EEM_HR.z_y = Run1.y(1,83) + 1i*Run1.y(1,84);
opticalParms.EEM_HR.zr_x = Run1.y(1,85) + 1i*Run1.y(1,86);
opticalParms.EEM_HR.zr_y = Run1.y(1,87) + 1i*Run1.y(1,88);
opticalParms.EEM_HR.g_x = Run1.y(1,89) + 1i*Run1.y(1,90);
opticalParms.EEM_HR.g_y = Run1.y(1,91) + 1i*Run1.y(1,92);
opticalParms.EEM_HR.q_x = Run1.y(1,93) + 1i*Run1.y(1,94);
opticalParms.EEM_HR.q_y = Run1.y(1,95) + 1i*Run1.y(1,96);
opticalParms.EEM_HR.RoC_x = opticalParms.EEM_HR.z_x + (opticalParms.EEM_HR.
    zr_x)^2/opticalParms.EEM_HR.z_x;

%% AC
if strcmp(CavityStr,'AC') || strcmp(CavityStr,'both')
    opticalParms.AC.w_x = Run1.y(1,97) + 1i*Run1.y(1,98);
    opticalParms.AC.w0_x = Run1.y(1,99) + 1i*Run1.y(1,100);
    opticalParms.AC.z_x = Run1.y(1,101) + 1i*Run1.y(1,102);
    opticalParms.AC.r_x = Run1.y(1,103) + 1i*Run1.y(1,104);
    opticalParms.AC.q_x = Run1.y(1,105) + 1i*Run1.y(1,106);
    opticalParms.AC.Finesse = Run1.y(1,107) + 1i*Run1.y(1,108);
    opticalParms.AC.Loss = Run1.y(1,109) + 1i*Run1.y(1,110);
    opticalParms.AC.Length = Run1.y(1,111) + 1i*Run1.y(1,112);
    opticalParms.AC.FSR = Run1.y(1,113) + 1i*Run1.y(1,114);
    opticalParms.AC.FWHM = Run1.y(1,115) + 1i*Run1.y(1,116);
    opticalParms.AC.Pole = Run1.y(1,117) + 1i*Run1.y(1,118);
    opticalParms.AC.g1 = 1 - L_AC / abs(opticalParms.IM_HR.RoC_x);
    opticalParms.AC.g2 = 1 - L_AC / abs(opticalParms.IEM_HR.RoC_x);
    opticalParms.AC.g1g2 = opticalParms.AC.g1 * opticalParms.AC.g2;
end

% Get AC stability information from ABCD matrix, note that RoC_IM_HR
% definition is different for this and requires a factor (-1)
[~ , opticalParms.AC.g1g2_ABCD, opticalParms.AC.state_ABCD] = getAcStability(
    L_AC, (-1)*RoC_IM_HR, RoC_IEM_HR);
switch opticalParms.AC.state_ABCD
    case 0,
        opticalParms.AC.stateStr = 'stable';
    case 1,
        opticalParms.AC.stateStr = 'boundary-stable';
    case 2,
        opticalParms.AC.stateStr = 'unstable';
end;
```

```
%% KC
if strcmp(CavityStr,'KC') || strcmp(CavityStr,'both')
    opticalParms.KC.w_x = Run1.y(1,119) + 1i*Run1.y(1,120);
    opticalParms.KC.w0_x = Run1.y(1,121) + 1i*Run1.y(1,122);
    opticalParms.KC.z_x = Run1.y(1,123) + 1i*Run1.y(1,124);
    opticalParms.KC.r_x = Run1.y(1,125) + 1i*Run1.y(1,126);
    opticalParms.KC.q_x = Run1.y(1,127) + 1i*Run1.y(1,128);
    opticalParms.KC.Finesse = Run1.y(1,129) + 1i*Run1.y(1,130);
    opticalParms.KC.Loss = Run1.y(1,131) + 1i*Run1.y(1,132);
    opticalParms.KC.Length = Run1.y(1,133) + 1i*Run1.y(1,134);
    opticalParms.KC.FSR = Run1.y(1,135) + 1i*Run1.y(1,136);
    opticalParms.KC.FWHM = Run1.y(1,137) + 1i*Run1.y(1,138);
    opticalParms.KC.Pole = Run1.y(1,139) + 1i*Run1.y(1,140);
end
if strcmp(CavityStr,'both')
    opticalParms.AC.Power = Run1.y(1,141);
    opticalParms.KC.Power = Run1.y(1,143);
    opticalParms.AC.HOM_Power = Run1.y(1,145);
    opticalParms.KC.HOM_Power = Run1.y(1,147);
end

% Get KC stability information from ABCD matrix, note that RoC_IEM_AR
% definition is different for this and requires a factor (-1)
[~ , opticalParms.KC.g1g2_ABCD, opticalParms.KC.state_ABCD] = getKcStability(
    L_KC, (-1)*RoC_IEM_HR, RoC_IEM_AR, RoC_EEM_HR);
switch opticalParms.KC.state_ABCD
    case 0,
        opticalParms.KC.stateStr = 'stable';
    case 1,
        opticalParms.KC.stateStr = 'boundary-stable';
    case 2,
        opticalParms.KC.stateStr = 'unstable';
end;

% Tidy up before finishing
FT_kat_clean(Run1);
delete('SSI_OP_out.*');

end
```

Listing A.3: Skeleton FINESSE file for the MATLAB® /Simtools-based model of a single sub-SQL interferometer arm with a Khalili end mirror cavity. The function getSSIOpticalParms(.) merges the skeleton FINESSE model with additional parameter and component definitions and runs a FINESSE simulation based on the resulting model.

```
#
# Finesse skeleton file, defining the optical layout
# of a sub-SQL interferometer arm cavity with a
# Khalili end mirror cavity.
#
# Intended to be used with MATLAB/Simtools function
#      'getSSIOpticalParms.m'
#
# written by Christian Graef for the AEI 10m Prototype
#
# last changed 2010-05-10
#

%%% FTblock Constants
const lambda    0.0
const w_opt     0.0
```

```
const nFS        0.0
const subThick   0.0

const L_AC       0.0
const L_KC       0.0

const T_IM.HR    9.304E-3
const T_IEM.HR   488.49E-3
const T_EEM.HR   64.0E-6

const Loss_IM.HR 50E-6
const Loss_IEM.HR 50E-6
const Loss_EEM.HR 50E-6

%%% FTend

%%% FTblock Gauss
maxtem 10
#gauss myBeam IEM nIEM1
%%% FTend

%%% FTblock Laser
l laser 1 0 n0
%%% FTend

%%% FTblock OptSetup
s s1 1 n0 nIMar

m1 IM.AR 1.0 0 0 nIMar nIMs1
s IM.sub $subThick $nFS nIMs1 nIMs2
m1 IM.HR $T_IM.HR $Loss_IM.HR 0 nIMs2 nIMhr

s AC.len $L_AC 1.0 nIMhr nIEMhr

m1 IEM.HR $T_IEM.HR $Loss_IEM.HR 0 nIEMhr nIEMs1
s IEM.sub $subThick $nFS nIEMs1 nIEMs2
m1 IEM.AR 1 0 0 nIEMs2 nIEMar

#cav AC IM.HR nIMhr IEM.HR nIEMhr

s KC.len $L_KC 1.0 nIEMar nEEMhr
m1 EEM.HR $T_EEM.HR $Loss_EEM.HR 0 nEEMhr dump
#cav KC IEM.HR nIEMs1 EEM.HR nEEMhr

%%% FTend OptSetup

#%%% FTblock RoC
##attr IM.HR Rc -5.2018
##attr IEM.HR Rc 5.2018
##attr EEM.HR Rc 0.5
#%%% FTend

#% SETUP: KC cavity
#s s1 1 n0 nIEM1
#m1 IEM 0.48849 0 0 nIEM1 nIEM2
#attr IEM Rc 5.2018
#s dummySpace 0 nIEM2 nLens1
#lens dummyLens 0.1 nLens1 nLens2
#s KClen 1 nLens2 nEEM1
#m1 EEM 60E-6 0 0 nEEM1 nEEM2
#attr EEM Rc 0.8
#cav KC IEM nIEM2 EEM nEEM1
```

```
%%% FTblock Readout
bp w(x,IM.HR) x w nIMhr
bp w(y,IM.HR) y w nIMhr
bp w0(x,IM.HR) x w0 nIMhr
bp w0(y,IM.HR) y w0 nIMhr
bp z(x,IM.HR) x z nIMhr
bp z(y,IM.HR) y z nIMhr
bp zr(x,IM.HR) x zr nIMhr
bp zr(y,IM.HR) y zr nIMhr
bp g(x,IM.HR) x g nIMhr
bp g(y,IM.HR) y g nIMhr
bp q(x,IM.HR) x q nIMhr
bp q(y,IM.HR) y q nIMhr

bp w(x,IEM.HR) x w nIEMhr
bp w(y,IEM.HR) y w nIEMhr
bp w0(x,IEM.HR) x w0 nIEMhr
bp w0(y,IEM.HR) y w0 nIEMhr
bp z(x,IEM.HR) x z nIEMhr
bp z(y,IEM.HR) y z nIEMhr
bp zr(x,IEM.HR) x zr nIEMhr
bp zr(y,IEM.HR) y zr nIEMhr
bp g(x,IEM.HR) x g nIEMhr
bp g(y,IEM.HR) y g nIEMhr
bp q(x,IEM.HR) x q nIEMhr
bp q(y,IEM.HR) y q nIEMhr

bp w(x,IEM.AR) x w nIEMar
bp w(y,IEM.AR) y w nIEMar
bp w0(x,IEM.AR) x w0 nIEMar
bp w0(y,IEM.AR) y w0 nIEMar
bp z(x,IEM.AR) x z nIEMar
bp z(y,IEM.AR) y z nIEMar
bp zr(x,IEM.AR) x zr nIEMar
bp zr(y,IEM.AR) y zr nIEMar
bp g(x,IEM.AR) x g nIEMar
bp g(y,IEM.AR) y g nIEMar
bp q(x,IEM.AR) x q nIEMar
bp q(y,IEM.AR) y q nIEMar

bp w(x,EEM.HR) x w nEEMhr
bp w(y,EEM.HR) y w nEEMhr
bp w0(x,EEM.HR) x w0 nEEMhr
bp w0(y,EEM.HR) y w0 nEEMhr
bp z(x,EEM.HR) x z nEEMhr
bp z(y,EEM.HR) y z nEEMhr
bp zr(x,EEM.HR) x zr nEEMhr
bp zr(y,EEM.HR) y zr nEEMhr
bp g(x,EEM.HR) x g nEEMhr
bp g(y,EEM.HR) y g nEEMhr
bp q(x,EEM.HR) x q nEEMhr
bp q(y,EEM.HR) y q nEEMhr

#cp AC x w
#cp AC x w0
#cp AC x z
#cp AC x r
#cp AC x q
#
#cp AC x finesse
#cp AC x loss
#cp AC x length
#cp AC x FSR
```

```
#cp AC x FHWM
#cp AC x pole
#
#cp KC x w
#cp KC x w0
#cp KC x z
#cp KC x r
#cp KC x q
#
#cp KC x finesse
#cp KC x loss
#cp KC x length
#cp KC x FSR
#cp KC x FHWM
#cp KC x pole

%%% FTend

trace 2

%%% FTblock xaxis
xaxis AC.len L lin 10 10 2
%%% FTend

yaxis abs
```

Beam jitter coupling in the tunable stability interferometer

Listing A.4: Simtools-based MATLAB® script for steering of the FINESSE beam jitter coupling model.

```
%
%%%%%%%%%%%%%%%%%%%%%%%%%%%%%%%%%%%%%%%%%%%%%%%%%%%%%%%%%%%%%%%%%%%%%%%%%%%%%%
%
% This file is the Finesse run script for the AEI-10m Sub-SQL interferometer
% in the configuration without Khalili cavities, i.e. a simple Michelson
% with FP arm cavities. The skelton of the finesse input file is read in
% from 'AEI10m_finesse_master_3dof_14062011.kat' which is available at:
% https://arran.physics.gla.ac.uk/svn/AEI-PT-locking/
% Please note that the Simtools package is required to run the model.
%
% 31.10.2011 C. Graef (cristian.graef@aei.mpg.de)
%
%%%%%%%%%%%%%%%%%%%%%%%%%%%%%%%%%%%%%%%%%%%%%%%%%%%%%%%%%%%%%%%%%%%%%%%%%%%%%%

% Simulation purpose:
% Beam Jitter Coupling in the AEI 10m subSQL IFO -- static case
%
% -- pure tem00 beam injected
% -- static misalignment of the input optics, i.e. MCol, generates first
%    order mode amplitude
% -- conversion of first order modes to the fundamental mode by static
%    misalignment of the IMs, Finesse asymmetry, loss, ...
% -- shot noise limited sensitivity as a function of parameters that
%    influence beam jitter coupling

clear all;

% set some environment variables to locate dependencies
setSimEnvironment;
```

```
% read in parameters from unique constant file
ps = getSSIGlobalParms();

% read in lookup table for pairs of w_0_opt and L_arm values
lt = getInitWaistRadiusMap();

%% Local modification of parameters specific to the current simulation run

% set arm cavity length for the current simulation run
% note that this will work only for few values for L_arm defined in '
    getInitWaistRadiusMap()'
current_armlength=11.3952;

% overwrite default arm cavity lengths in parameter struct, this assumes
% equal lenghts of both arms
ps.LX=current_armlength;
ps.LY=current_armlength;

% overwrite initial beam waist (aka "PMC waist") in parameter struct
% by extracting the appropriate value from the lookup table
ps.PMC.w=lt(current_armlength);

% Disable rf modulation by setting the modulation idx to a tiny value
ps.fm1.midx=1E-6;

%% Initialize Finesse
FT=FT_init_Finesse('name','kat','path',getenv('KATBINARY'))

%% Read parameters from the intial Finesse input file
blocks=FT_read_blocks_from_file('./AEI10m_finesse_master_BeamJitterTF.kat');

%% Create new block 'commands1' as a container for the 'dynamic' properties
constants = FT_create_new_block('constants');
commands1 = FT_create_new_block('commands1');

%% Commands to be merged to the kat-file
constants = FT_add_line_to_block(constants, '% -----------------');
constants = FT_add_line_to_block(constants, '% Substrates');
constants = FT_add_line_to_block(constants, '% -----------------');
constants = FT_add_line_to_block(constants, strcat('const nsilica', {' '},
    num2str(ps.nFusedSilica, '% 16.14f')));
constants = FT_add_line_to_block(constants, strcat('const sIM', {' '}, num2str
    (ps.SubstrateThickness, '% 16.14f')));
constants = FT_add_line_to_block(constants, strcat('const sEM', {' '}, num2str
    (ps.SubstrateThickness, '% 16.14f')));
constants = FT_add_line_to_block(constants, strcat('const sBS', {' '}, num2str
    (ps.SubstrateThickness_BS, '% 16.14f')));
constants = FT_add_line_to_block(constants, '% ');

constants = FT_add_line_to_block(constants, '% -----------------');
constants = FT_add_line_to_block(constants, '% Lengths');
constants = FT_add_line_to_block(constants, '% -----------------');
constants = FT_add_line_to_block(constants, strcat('const LX1', {' '}, num2str
    (ps.LX, '% 16.14f')));
constants = FT_add_line_to_block(constants, strcat('const LY1', {' '}, num2str
    (ps.LY, '% 16.14f')));
constants = FT_add_line_to_block(constants, strcat('const lx', {' '}, num2str(
    ps.lx, '% 16.14f')));
constants = FT_add_line_to_block(constants, strcat('const ly', {' '}, num2str(
    ps.ly, '% 16.14f')));
constants = FT_add_line_to_block(constants, strcat('const S1', {' '}, num2str(
    ps.lin, '% 16.14f')));
```

```
constants = FT_add_line_to_block(constants, strcat('const S2', {' '}, num2str(
    ps.lin2, '% 16.14f')));
constants = FT_add_line_to_block(constants, '% ');

constants = FT_add_line_to_block(constants, '% ------------------');
constants = FT_add_line_to_block(constants, '% ROCs');
constants = FT_add_line_to_block(constants, '% ------------------');
constants = FT_add_line_to_block(constants, strcat('const RCIMx', {' -'},
    num2str(ps.IMx.ROC, '% 16.14f')));
constants = FT_add_line_to_block(constants, strcat('const RCIMy', {' -'},
    num2str(ps.IMy.ROC, '% 16.14f')));
constants = FT_add_line_to_block(constants, strcat('const RCEMx', {' '},
    num2str(ps.EMx.ROC, '% 16.14f')));
constants = FT_add_line_to_block(constants, strcat('const RCEMy', {' '},
    num2str(ps.EMy.ROC, '% 16.14f')));
constants = FT_add_line_to_block(constants, strcat('const RCIMxAR', {' -'},
    num2str(ps.IMx_AR.ROC, '% 16.14f')));
constants = FT_add_line_to_block(constants, strcat('const RCIMyAR', {' -'},
    num2str(ps.IMy_AR.ROC, '% 16.14f')));
constants = FT_add_line_to_block(constants, strcat('const RC_Mcol', {' '},
    num2str(ps.Mcol.ROC, '% 16.14f')));
constants = FT_add_line_to_block(constants, '% ');

constants = FT_add_line_to_block(constants, '% ------------------');
constants = FT_add_line_to_block(constants, '% Coatings');
constants = FT_add_line_to_block(constants, '% ------------------');

constants = FT_add_line_to_block(constants, strcat('const TBS', {' '}, num2str
    (ps.BS.T, '% 16.14f')));
constants = FT_add_line_to_block(constants, strcat('const LBS', {' '}, num2str
    (ps.BS.L, '% 16.14f')));
constants = FT_add_line_to_block(constants, strcat('const TIMx', {' '},
    num2str(ps.IM.T, '% 16.14f')));
constants = FT_add_line_to_block(constants, strcat('const LIMx', {' '},
    num2str(ps.IM.L, '% 16.14f')));
constants = FT_add_line_to_block(constants, strcat('const TIMy', {' '},
    num2str(ps.IM.T, '% 16.14f')));
constants = FT_add_line_to_block(constants, strcat('const LIMy', {' '},
    num2str(ps.IM.L, '% 16.14f')));
constants = FT_add_line_to_block(constants, strcat('const TEMx', {' '},
    num2str(ps.EM.T, '% 16.14f')));
constants = FT_add_line_to_block(constants, strcat('const LEMx', {' '},
    num2str(ps.EM.L, '% 16.14f')));
constants = FT_add_line_to_block(constants, strcat('const TEMy', {' '},
    num2str(ps.EM.T, '% 16.14f')));
constants = FT_add_line_to_block(constants, strcat('const LEMy', {' '},
    num2str(ps.EM.L, '% 16.14f')));
constants = FT_add_line_to_block(constants, strcat('const RBS_AR', {' '},
    num2str(ps.BS_AR.R, '% 16.14f')));
constants = FT_add_line_to_block(constants, strcat('const LBS_AR', {' '},
    num2str(ps.BS_AR.L, '% 16.14f')));
constants = FT_add_line_to_block(constants, strcat('const RIMxAR', {' '},
    num2str(ps.IM_AR.R, '% 16.14f')));
constants = FT_add_line_to_block(constants, strcat('const LIMxAR', {' '},
    num2str(ps.IM_AR.L, '% 16.14f')));
constants = FT_add_line_to_block(constants, strcat('const RIMyAR', {' '},
    num2str(ps.IM_AR.R, '% 16.14f')));
constants = FT_add_line_to_block(constants, strcat('const LIMyAR', {' '},
    num2str(ps.IM_AR.L, '% 16.14f')));
constants = FT_add_line_to_block(constants, strcat('const REMxAR', {' '},
    num2str(ps.EM_AR.R, '% 16.14f')));
constants = FT_add_line_to_block(constants, strcat('const LEMxAR', {' '},
    num2str(ps.EM_AR.L, '% 16.14f')));
```

```
constants = FT_add_line_to_block(constants, strcat('const REMyAR', {' '},
    num2str(ps.EM_AR.R, '% 16.14f')));
constants = FT_add_line_to_block(constants, strcat('const LEMyAR', {' '},
    num2str(ps.EM_AR.L, '% 16.14f')));
constants = FT_add_line_to_block(constants, '% ');

constants = FT_add_line_to_block(constants, '% -----------------');
constants = FT_add_line_to_block(constants, '% Tunings');
constants = FT_add_line_to_block(constants, '% -----------------');
constants = FT_add_line_to_block(constants, 'const IMxphi 1.2E-4'); %%%
    ATTENTION: the IM tunings are set to compensate for coupling loss due to
    misaligned IMs
constants = FT_add_line_to_block(constants, 'const IMyphi 1.2E-4'); %%% The IM
     tuning of 1.2E-4 deg compensates IM misalignment of 1E-8 rad
constants = FT_add_line_to_block(constants, 'const EMxphi 0');
constants = FT_add_line_to_block(constants, 'const EMyphi 0');
constants = FT_add_line_to_block(constants, strcat('const BSphi', {' '},
    num2str(ps.BS.phi, '% 16.14f')));
constants = FT_add_line_to_block(constants, 'const IMxARphi 0');
constants = FT_add_line_to_block(constants, 'const IMyARphi 0');
constants = FT_add_line_to_block(constants, 'const EMxARphi 0');
constants = FT_add_line_to_block(constants, 'const EMyARphi 0');
constants = FT_add_line_to_block(constants, '% ');

constants = FT_add_line_to_block(constants, '% -----------------');
constants = FT_add_line_to_block(constants, '% Modematching');
constants = FT_add_line_to_block(constants, '% -----------------');
constants = FT_add_line_to_block(constants, strcat('const Mcol_ang', {' '},
    num2str(ps.Mcol.ang, '% 16.14f')));
constants = FT_add_line_to_block(constants, strcat('const i1w', {' '}, num2str
    (ps.PMC.w, '% 16.14f')));
constants = FT_add_line_to_block(constants, '% ');

constants = FT_add_line_to_block(constants, '% -----------------');
constants = FT_add_line_to_block(constants, '% Modulation');
constants = FT_add_line_to_block(constants, '% -----------------');
constants = FT_add_line_to_block(constants, strcat('const fm1', {' '}, num2str
    (ps.fm1.freq, '% 16.14f')));
constants = FT_add_line_to_block(constants, strcat('const midx1', {' '},
    num2str(ps.fm1.midx, '% 16.14f')));
constants = FT_add_line_to_block(constants, '% ');

constants = FT_add_line_to_block(constants, strcat('const amfreq 10'));

%% Settings
commands1 = FT_add_line_to_block(commands1, 'maxtem 10');

%%%%% static misalignment of the arm cavity input mirrors %%%%%
 commands1 = FT_add_line_to_block(commands1, 'attr IMx xbeta 10n');
 commands1 = FT_add_line_to_block(commands1, 'attr IMy xbeta 10n');
%  commands1 = FT_add_line_to_block(commands1, 'attr EMx xbeta 10n');
%  commands1 = FT_add_line_to_block(commands1, 'attr EMy xbeta 10n');

commands1 = FT_add_line_to_block(commands1, 'tem i1 0 0 0 0');
commands1 = FT_add_line_to_block(commands1, 'tem i1 1 0 1 0');

commands1 = FT_add_line_to_block(commands1, 'ad ad1 0 0 $amfreq nPDa');
commands1 = FT_add_line_to_block(commands1, 'ad ad2 0 0 $amfreq nPDa');

commands1 = FT_add_line_to_block(commands1, 'xaxis eom1 f log 10 1M 2000');

commands1 = FT_add_line_to_block(commands1, 'put ad1 f $x1');
commands1 = FT_add_line_to_block(commands1, 'put ad2 f $mx1');
```

```
commands1 = FT_add_line_to_block(commands1, 'scale 2e6');

%%%%% static misalignment of the collimating mirror %%%%%
%commands1 = FT_add_line_to_block(commands1, 'attr Mcol xbeta 1E-5');

%%%%% angular fluctuations of the collimating mirror %%%%%
%commands1 = FT_add_line_to_block(commands1, 'fsig sig1 Mcol xbeta 10 0 10n');

%%%%% amplitude detectors for light converted to tem00 %%%%%
%commands1 = FT_add_line_to_block(commands1, 'ad ad00_pos 0 0 10 nPDa');
%commands1 = FT_add_line_to_block(commands1, 'ad ad00_neg 0 0 10 nPDa');

%% Shot noise limited sensitivity
%commands1 = FT_add_line_to_block(commands1, 'fsig sig1 EMx 10 0 1.666E-13');
%commands1 = FT_add_line_to_block(commands1, 'fsig sig1 EMy 10 180 1.666E-13')
    ;
%commands1 = FT_add_line_to_block(commands1, 'pdS1 PDa 10 max nPDa');
%commands1 = FT_add_line_to_block(commands1, 'pd1 PDa 10 max nPDa');

%commands1 = FT_add_line_to_block(commands1, 'xaxis sig1 f log 10 100k 1000');
%commands1 = FT_add_line_to_block(commands1, 'put PDa f1 $x1');
%commands1 = FT_add_line_to_block(commands1, 'scale meter PDa');

% %% x-arm intra cavity power
% commands1 = FT_add_line_to_block(commands1, 'xaxis* EMy phi lin -0.1 0.1
    10000');
% commands1 = FT_add_line_to_block(commands1, 'pd yArm_DC nEMy1');

%commands1 = FT_add_line_to_block(commands1, 'xaxis LXarm l lin 10.8 11.3952
    200');
%commands1 = FT_add_line_to_block(commands1, 'put LYarm l $x1');

% %%% Tuning of the dark fringe offset via BS phi
% commands1 = FT_add_line_to_block(commands1, 'xaxis BS phi lin 0 10 200');
% commands1 = FT_add_line_to_block(commands1, 'put BSAR1 phi $x1');
% commands1 = FT_add_line_to_block(commands1, 'put BSAR2 phi $x1');

commands1 = FT_add_line_to_block(commands1, 'yaxis abs');
commands1 = FT_add_line_to_block(commands1, 'retrace');

%% Collect blocks necessary for this task from definition kat-file
outbl1(1) = FT_copy_block(blocks, 'AEI10m');
outbl1(2) = constants;
outbl1(3) = commands1;

%% Write the new kat file
katfilename='Full_IFO_out.kat';
FT_write_blocks_into_file(outbl1,katfilename);

Run1=FT_create_new_kat_run();
Run1.filename=katfilename;
Run1=FT_run_kat_simulation(FT,Run1);

%set(0,'DefaultAxesColorOrder',[0 0 255 ; 0 255 0 ; 255 0 0 ; 255 165 0 ; 0
    255 255 ; 255 0 255; 128 128 128 ; 128 0 0 ; 0 128 0 ; 0 0 128; 128 0 128
    ; 128 128 0 ; 0 128 128; 64 0 0; 0 64 0 ; 0 0 64; 64 64 0; 64 0 64; 0 64
    64; 64 64 64 ]./255)
set(0,'DefaultAxesColorOrder',[255 0 0 ; 255 165 0 ; 0 255 255 ; 255 0 255;
    128 128 128 ; 128 0 0 ; 0 128 0 ; 0 0 128; 128 0 128 ; 128 128 0 ; 0 128
    128; 64 0 0; 0 64 0 ; 0 0 64; 64 64 0; 64 0 64; 0 64 64; 64 64 64 ]./255)

% %% arm cavity circulating power
% plot(Run1.data(:,1), Run1.data(:,2))
```

```
% % xlim([200 10000])
% % ylim([1E-20 1E-19])
% grid
% [x i]=max(Run1.data(:,2))
% phase=Run1.data(i,1)

%% shot noise limited sensitivity
h=figure
loglog(Run1.data(:,1), [Run1.data(:,2) Run1.data(:,3)], 'LineWidth',2);
xlabel('Frequency [Hz]','FontSize',12,'FontWeight','bold')
ylabel('TEM10 to TEM00 amplitude TF','FontSize',12,'FontWeight','bold')
%xlim([200 100000])
%ylim([1E-10 1E0])
ylim([1E-5 1E-1])
legend('IM diff., pos. SB','IM diff., neg. SB','Location','SouthWest')
grid

set(h, 'PaperPosition', [0 0 5 3]);

saveas(h,'beam_jitter_tf_11.3952m_im_diff.eps','epsc')
system('ps2pdf -dEPSCrop beam_jitter_tf_11.3952m_im_diff.eps')

% work done, don't leave a mess
system('rm Full_IFO_out.*');
```

Listing A.5: Skeleton FINESSE file for the MATLAB® /Simtools-based model of the tunable stability interferometer to model the coupling of input beam jitter. The function getSSIOpticalParms(.) merges the skeleton FINESSE model with additional parameter and component definitions.

```
%%% FTblock AEI10m
% ----------------------------------------------------------------------
% Finesse input file for the configuration without Khalili cavities
% of the AEI-10m Sub-SQL interferometer.
%
% Description of the file:
% * Started from an 2008-Advanced Virgo inout file (Credit to Mantovani,
%   Freise and Hild).
% * Nomeclature adopted as described on Prototype Labbook page 210.
% * This file can not run on its own, but is rather an input file for the
%   run_master.m file which can be found in the svn repository at:
%   https://arran.physics.gla.ac.uk/svn/AEI-PT-locking
%   Constants are read in via the MATLAB/Simtools runfile
%   from 'getSSIGlobalParams.m' which is available at:
%   https://arran.physics.gla.ac.uk/svn/AEI-PT-locking/trunk/Matlab/SSIlib/
%
% 20.06.2011 C. Graef (cristian.graef@aei.mpg.de), S. Hild (stefan.hild@ligo.
    org)
%            and  S. Huttner (sabina.huttner@glasgow.ac.uk).
% ----------------------------------------------------------------------
%
%%%%%%%%%%%%%%%%%% Laser and Modulation %%%%%%%%%%%%%%%%%%%
%
l i1 5.5555 0 0 nin % These 5.5 W correspond to 5W at the main BS
gauss beam_in i1 nin $i1w 0 % waist at nin with waist size $ilw
%
% Mode matching telescope
s sin $S1 nin nin1
bs Mcol 1 0 0 $Mcol_ang nin1 nin2 dump dump % Collimating mirror on the far
    platform
attr Mcol Rc $RC_Mcol
```

```
s s0 $S2 nin2 nEO1
%
mod eom1 $amfreq $midx1 1 am 0 nEO1 nEO2
s s1 1u nEO2 nInj1
bs Inj .9 .1 0 0 nInj1 nInj2 dump nPDs % This beam splitter is used as pick-
    off
%
s s3 1u nInj2 nbs1
%
%%%%%%%%%%%%%%%%%%%%%%%% Beamsplitter %%%%%%%%%%%%%%%%%%%%%
%
%%                                ^
%%                   to the IMy   |
%%                                |       ,'-.
%%                                |      +     `.
%%                         nbs2   |    ,'        :'
%%         LASER                  |  +i1       +
%%          ---------------->     ,:._  i2 ,'
%%                        nbs1  + \  `-. + nbs3
%%                            ,' i3\   ,' --------------->
%%                           +      \ +     to the IMx
%%                         ,'     i4.'
%%                        `._       ..
%%                           `._ ,' |nbs4
%%                              -   |
%%                                  |
%%                                  |
%%                                  v  OUTPUT
%
bs1 BS $TBS $LBS $BSphi -45 nbs1 nbs2 nbsi1 nbsi3
s sbs1 $sBS $nsilica nbsi1 nbsi2 %the BS substrate
s sbs2 $sBS $nsilica nbsi3 nbsi4
bs2 BSAR1 $RBS_AR $LBS_AR $BSphi -29.195 nbsi2 dump nbs3 nPOBS1
bs2 BSAR2 $RBS_AR $LBS_AR $BSphi 29.195 nbsi4 dump nbs4 nPOSR1
%
s lSRM 1 nbs4 nPDa % length between the AR of BS and PDa
%
%
%%%%%%%%%%%%%%%%%%%%%%%% X Arm %%%%%%%%%%%%%%%%
%
s lx $lx nbs3 nIMx1 % length between the AR of BS and AR of IMx
%
% IMx
bs2 IMxAR $RIMxAR $LIMxAR $IMxARphi 0 nIMx1 nPDMx nIMxi1 dump
s sIMx $sIM $nsilica nIMxi1 nIMxi2
m1 IMx $TIMx $LIMx $IMxphi nIMxi2 nIMx2
attr IMxAR Rc $RCIMxAR
attr IMx Rc $RCIMx
%
s LXarm $LX1 nIMx2 nEMx1
%
% EMx
m1 EMx $TEMx $LEMx $EMxphi nEMx1 nEMxi1
s sEMx  $sEM $nsilica nEMxi1 nEMxi2
m2 EMxAR $REMxAR $LEMxAR $EMxARphi nEMxi2 nEMxo
attr EMx Rc $RCEMx
%
cav x_FP IMx nIMx2 EMx nEMx1
%
%%%%%%%%%%%%%%%%%%%%%%%% Y Arm %%%%%%%%%%%%%%%%
%
s ly $ly nbs2 nIMy1 % length between the AR of BS and AR of IMy
%
```

```
% IMy
bs2 IMyAR $RIMyAR $LIMyAR $IMyARphi 0 nIMy1 nPDMy nIMyi1 dump
s sIMy $sIM $nsilica nIMyi1 nIMyi2
m1 IMy $TIMy $LIMy $IMyphi nIMyi2 nIMy2
attr IMyAR Rc $RCIMyAR
attr IMy Rc $RCIMy
%
s LYarm $LY1 nIMy2 nEMy1
%
% EMy
m1 EMy $TEMy $LEMy $EMyphi nEMy1 nEMyi1
s sEMy  $sEM $nsilica nEMyi1 nEMyi2
m2 EMyAR $REMyAR  $LEMyAR $EMyARphi nEMyi2 nEMyo
attr EMy Rc $RCEMy
%
cav y_FP IMy nIMy2 EMy nEMy1
%
%%% FTend
```

Quantum noise model for the sub-SQL interferometer with balanced homodyne detection

Listing A.6: MATLAB®-based quantum noise model of a Fabry-Perot Michelson interferometer with sub-SQL interferometer parameters.

```
% Quantum noise of a Fabry-Perot Michelson interferometer
% with sub-SQL interferometer parameters
% with balanced homodyne detection for signal readout
%
% 2012-07-17, Christian Graef for the 10m Prototype
%

%% some constants
hbar = 1.05457266912510183*10^(-34);
c = 299792458; % [m/s]
lambda_0=1064E-9; % [m]

m = 0.1; % [kg]
L = 10; % [m]
r_IM = sqrt(0.990695);
r_EM = sqrt(0.999936);
I_0 = 5.5 % [W], optimized input power (no carrier loss in arms assumed)

%% Optical loss: starting configuration w/o KCs
A_loss = 55E-6; % avg. scattering and absorption loss of one mirror
r_cavity = -r_IM + (1-r_IM^2-A_loss)/(1-r_IM*r_EM)*r_EM

%% derived constants
omega_0 = 2*pi * c/lambda_0;
T = 1-r_IM^2
omega_c = T*c/(4*L);
epsilon_loss = 2*(2*A_loss+1-r_EM^2)/T;
I_SQL = m*L^2*omega_c^4/(4*omega_0);

%% Frequency dependent terms
epsilon_loss_SB = @(Omega) 2*epsilon_loss./(1+Omega.^2./omega_c.^2);
h_SQL= @(Omega) sqrt(8*hbar./(m.*Omega.^2.*L.^2));
kappa = @(Omega) (2*(I_0 / I_SQL)*omega_c^4)./(Omega.^2.*(omega_c.^2 + Omega
    .^2));
```

```
kappa_star = @(Omega) kappa(Omega).*(1-0.5.*epsilon_loss_SB(Omega));
kappa_twostar = @(Omega) (2*(I_0*(1- epsilon_loss))/I_SQL*omega_c^4)./(Omega
    .^2.*(omega_c.^2 + Omega.^2)).*(1-0.5.*epsilon_loss_SB(Omega));

%% Noise spectra (zeta is the homodyne angle)
S_h = @(Omega, zeta) h_SQL(Omega).^2 ./(2.* kappa_star(Omega)).*(( (1-
    epsilon_loss_SB(Omega)./2) .* cot(zeta) - kappa_star(Omega)).^2 + (1-
    epsilon_loss_SB(Omega)./2).^2 + epsilon_loss_SB(Omega) + epsilon_loss_SB(
    Omega).*(cot(zeta)).^2 );
S_h_lossless = @(Omega, zeta) (h_SQL(Omega).^2 ./ (2.*kappa(Omega)) .* ((cot(
    zeta) - kappa(Omega)).^2 + 1 ))
S_h_CarrierLossIncluded = @(Omega, zeta) h_SQL(Omega).^2 ./(2.* kappa_twostar(
    Omega)).*(( (1-epsilon_loss_SB(Omega)./2) .* cot(zeta) - kappa_twostar(
    Omega)).^2 + (1-epsilon_loss_SB(Omega)./2).^2 + epsilon_loss_SB(Omega) +
    epsilon_loss_SB(Omega).*(cot(zeta)).^2 );

%% prepare data plotting
myOmega = logspace(1,6,1000);

myS_h_lossless(1,:) = S_h_lossless(myOmega, pi/2);
myS_h_lossless(2,:) = S_h_lossless(myOmega, pi/2-1.06);
myS_h_lossless(3,:) = S_h_lossless(myOmega, pi/2-1.325);
myS_h_lossless(4,:) = S_h_lossless(myOmega, pi/2-1.452);

myS_h(1,:) = S_h(myOmega, pi/2);
myS_h(2,:) = S_h(myOmega, pi/2-1.06);
myS_h(3,:) = S_h(myOmega, pi/2-1.325);
myS_h(4,:) = S_h(myOmega, pi/2-1.452);

myS_h_CLI(1,:) = S_h_CarrierLossIncluded(myOmega, pi/2);
myS_h_CLI(2,:) = S_h_CarrierLossIncluded(myOmega, pi/2-1.06);
myS_h_CLI(3,:) = S_h_CarrierLossIncluded(myOmega, pi/2-1.325);
myS_h_CLI(4,:) = S_h_CarrierLossIncluded(myOmega, pi/2-1.452);

myh_SQL = h_SQL(myOmega);
f=myOmega/(2*pi);

%% plot the spectra in the lossless case
h=figure(1)
loglog(f, L*[ myh_SQL ; sqrt(myS_h_lossless(1,:)); sqrt(myS_h_lossless(2,:));
    sqrt(myS_h_lossless(3,:)); sqrt(myS_h_lossless(4,:))],'LineWidth',2)
xlim([1E1 1E5])
ylim([1E-20 1E-16])
xlabel('Frequency [Hz]','FontWeight','bold')
ylabel('Displacement [m/sqrt(Hz)]','FontWeight','bold')
legend('SQL','QN, \zeta=\pi/2','QN, \zeta(f=150Hz)','QN, \zeta(f=100Hz)','QN,
    \zeta(f=70Hz)')
title('Readout at different homodyne angles, lossless configuration')
grid
set(h, 'PaperPosition', [0 0 6 3.5]);
saveas(h,'subSQL_ifo_bae_via_bhd_lossless.eps','epsc')
system('ps2pdf -dEPSCrop subSQL_ifo_bae_via_bhd_lossless.eps')

%% plot the spectra of the lossy configuration
h=figure(2)
loglog(f, L*[ myh_SQL ; sqrt(myS_h(1,:)); sqrt(myS_h(2,:)); sqrt(myS_h(3,:));
    sqrt(myS_h(4,:))],'LineWidth',2)
xlim([1E1 1E5])
ylim([1E-20 1E-16])
xlabel('Frequency [Hz]','FontWeight','bold')
ylabel('Displacement [m/sqrt(Hz)]','FontWeight','bold')
legend('SQL','QN, \zeta=\pi/2','QN, \zeta(f=150Hz)','QN, \zeta(f=100Hz)','QN,
    \zeta(f=70Hz)')
```

```
title('Readout at different homodyne angles with lossy arm cavities')
grid
set(h, 'PaperPosition', [0 0 6 3.5]);
saveas(h,'subSQL_ifo_bae_via_bhd_lossy.eps','epsc')
system('ps2pdf -dEPSCrop subSQL_ifo_bae_via_bhd_lossy.eps')

%% plot the net fractional SB photon loss in the ACs
h=figure(4)
semilogx(f, epsilon_loss_SB(myOmega),'LineWidth',2)
xlim([1E1 1E5])
xlabel('Frequency [Hz]','FontWeight','bold')
ylabel('Loss coefficient','FontWeight','bold')
title('Net fractional photon loss in the arm cavities')
grid
set(h, 'PaperPosition', [0 0 6 3.5]);
saveas(h,'subSQL_ifo_bae_via_bhd_arm_fract_photon_loss.eps','epsc')
system('ps2pdf -dEPSCrop subSQL_ifo_bae_via_bhd_arm_fract_photon_loss.eps')
```

Grid-based simulations on the RRZN cluster system

Listing A.7: Main routine of the grid-based model of the Fabry-Perot Michelson interferometer with marginally stable arm cavities with sub-SQL interferometer parameters. The model is based on the OSCAR FFT simulation library [186].

```
%
% Grid-based Fabry-Perot Michelson interferometer model
% with marginally stable arm cavities and realistic mirrors
%
% Purpose:
% Modeling the effects of mirrors with realistic surface
% irregularity in the AEI 10m sub-SQL interferometer
%
% This simulation is based on the OSCAR FFT simulation library
% which is available at:
% http://www.mathworks.com/matlabcentral/fileexchange/20607-oscar
%
% The model is intended to run on the
% computer cluster at RRZN, Leibniz Universitaet Hannover
%
% written by Christian Graef for the AEI 10m Prototype
% last changed 2012-09-17
%

clear all; close all; clear classes
addpath(genpath('../../../../../Classes'));
addpath(genpath('../../../../../Functions'));
addpath(genpath('../../../../../SimTools'));

format long

reset(RandStream.getDefaultStream,sum(100*clock))

disp('-----------------------------------------------------------------')
disp('        OSCAR V3  --  The AEI 10m Tunable Stability IFO          ')
disp('  ')

grid_size=
grid_points=
surface_rms=
```

```
loadpath_unperturbed_fields=strcat('/bigwork/nhbfgrae/TSI_FPMI_unperturbed_',
    num2str(grid_points),'_',num2str(grid_size),'m/')
savepath_results=strcat('/bigwork/nhbfgrae/TSI_Loss_at_particular_rms_',
    num2str(grid_points),'_',num2str(grid_size),'m/')

sim.numpix=grid_points;
sim.winsize=grid_size;
sim.optical.w0_init = 417E-6;
sim.optical.P_Laser = 5.5
sim.mirror_radius=24.3E-3;
mirror_dia = 2*sim.mirror_radius;

sim.east_im_rms=surface_rms;
sim.east_em_rms=surface_rms;
sim.north_im_rms=surface_rms;
sim.north_em_rms=surface_rms;
sim.mirror_rms_radius = sim.mirror_radius;

sim.length_east_arm=11.3952;
sim.length_north_arm=11.3952;
d_MCol_BS = 12; % distance MCol beamsplitter
sim.thickness_IM_substrate = 0.0245;
d_BS_NIM = 0.1; % distance BS - north arm input mirror
d_BS_EIM = 0.1; % distance BS - east arm input mirror
d_BS_DP = 0.1; % distance BS - detection at the dark port
BS_AR = 0.5; % Reflectivity beam splitter

G1 = Grid(sim.numpix,sim.winsize);

E_input = E_Field(G1,'w',sim.optical.w0_init);
E_input=Normalise_E(E_input, sim.optical.P_Laser);
Calculate_power(E_input)

% 12m Propagation
E_input = Propagate_E(E_input, 12.0);

% mirror ROC=24m reflection
L1 = Interface(G1,'RoC',24,'CA',0.10,'T',0.0);
[~, E_input] = Transmit_Reflect_Interface(E_input,L1);
E_input = Propagate_E(E_input, 12.5);
Fit_TEM00(E_input);

% coefficients = Decompose_E_Field(E_input);

Input_N = sqrt(BS_AR) * Propagate_E(E_input,d_MCol_BS + d_BS_NIM);
Input_E = 1i* sqrt(1-BS_AR) * Propagate_E(E_input,d_MCol_BS + d_BS_EIM);

% Defining the north arm
N_IM_AR = Interface(G1,'RoC',-1.7755,'CA',0.0486,'T',1,'L',0);
N_IM_HR = Interface(G1,'RoC',5.7,'CA',0.0486,'T',0.009304,'L',0);
north_im_map=generate_synthetic_map(sim.numpix, sim.winsize, sim.mirror_radius
    , sim.mirror_rms_radius, sim.north_im_rms);
N_IM_HR = Add_map_MATRIX(N_IM_HR,north_im_map,'reso',sim.winsize/sim.numpix);
N_IM = Mirror(N_IM_HR,N_IM_AR,sim.thickness_IM_substrate);
N_IM = Add_prop_mat(N_IM,E_input);

N_EM_HR = Interface(G1,'RoC',5.7,'CA',0.0486,'T',64E-6,'L',0);

north_em_map=generate_synthetic_map(sim.numpix, sim.winsize, sim.mirror_radius
    , sim.mirror_rms_radius, sim.north_em_rms);
N_EM_HR = Add_map_MATRIX(N_EM_HR,north_em_map,'reso',sim.winsize/sim.numpix);

North_arm = Cavity1(N_IM,N_EM_HR,sim.length_north_arm,Input_N);
```

```
North_arm.Propagation_mat.Use_DI = true;
North_arm = Cavity_resonance_phase(North_arm);
[North_arm NA_parms]= Calculate_fields_and_parms(North_arm);
sim.north_arm_cavity=NA_parms;
NA_RTL=Calculate_RTL(North_arm)
sim.north_arm_rtl=NA_RTL;
%Check_stability(North_arm)

% % RTL00 calculations
na_unperturbed=load(strcat(loadpath_unperturbed_fields,'North_arm_unperturbed.
    mat'))
NA_RTL00=Calculate_RTL00(North_arm, na_unperturbed.North_arm)
sim.north_arm_rtl00=NA_RTL00;

% Defining the east arm
E_IM_AR = Interface(G1,'RoC',-1.7755,'CA',0.0486,'T',1,'L',0);
E_IM_HR = Interface(G1,'RoC',5.7,'CA',0.0486,'T',0.009304,'L',0);
east_im_map=generate_synthetic_map(sim.numpix, sim.winsize, sim.mirror_radius,
     sim.mirror_rms_radius, sim.east_im_rms);
E_IM_HR = Add_map_MATRIX(E_IM_HR,east_im_map,'reso',sim.winsize/sim.numpix);
E_IM = Mirror(E_IM_HR,E_IM_AR,sim.thickness_IM_substrate); E_IM = Add_prop_mat
    (E_IM,E_input);

E_EM_HR = Interface(G1,'RoC',5.7,'CA',0.0486,'T',64E-6,'L',0);
east_em_map=generate_synthetic_map(sim.numpix, sim.winsize, sim.mirror_radius,
     sim.mirror_rms_radius, sim.east_em_rms);
E_EM_HR = Add_map_MATRIX(E_EM_HR,east_em_map,'reso',sim.winsize/sim.numpix);

East_arm = Cavity1(E_IM,E_EM_HR,sim.length_east_arm,Input_E);
East_arm.Propagation_mat.Use_DI = true;
East_arm = Cavity_resonance_phase(East_arm);
[East_arm EA_parms]= Calculate_fields_and_parms(East_arm); %Calculate_power(
    East_arm.Field_circ);
sim.east_arm_cavity=EA_parms;
EA_RTL=Calculate_RTL(East_arm)
sim.east_arm_rtl=EA_RTL;
% C=Cavity_scan(East_arm)
% Display_scan(C)
EA_RTL=Calculate_RTL(East_arm)
sim.east_arm_rtl=EA_RTL;

% % RTL00 calculations
ea_unperturbed=load(strcat(loadpath_unperturbed_fields,'East_arm_unperturbed.
    mat'))
EA_RTL00=Calculate_RTL00(East_arm, ea_unperturbed.East_arm)
sim.east_arm_rtl00=EA_RTL00;

% Check the phase difference between the two reflected beams
Angle_diff = angle(Calculate_Overlap(North_arm.Field_ref,East_arm.Field_ref));
% Bring the interferometer to the dark fringe
North_arm.Field_ref = North_arm.Field_ref * exp(-1i *(Angle_diff - pi/2));

% Recombine the two beams
Reflected_beam = sqrt(BS_AR) * Propagate_E(North_arm.Field_ref,d_BS_NIM+
    d_MCol_BS) +...
        1i* sqrt(1-BS_AR) * Propagate_E(East_arm.Field_ref,d_BS_EIM+d_MCol_BS)
            ;

Dark_port_beam = 1i* sqrt(1-BS_AR) * Propagate_E(North_arm.Field_ref,d_BS_NIM+
    d_BS_DP) +...
         sqrt(BS_AR)   * Propagate_E(East_arm.Field_ref,d_BS_EIM+d_BS_DP);

Calculate_power(Reflected_beam)
```

```
sim.power.reflected = Calculate_power(Reflected_beam);
Calculate_power(Dark_port_beam)
sim.power.dark_port = Calculate_power(Dark_port_beam);

%%% show fields -- commented out for cluster run
% figure(11)
% subplot(1,2,1)
% E_plot(Reflected_beam); title('Reflected beam')
% subplot(1,2,2)
% E_plot(Dark_port_beam);  title('Dark port')

% Power conservation check
Calculate_power(Reflected_beam) + Calculate_power(Dark_port_beam) +
    Calculate_power(North_arm.Field_trans) + Calculate_power(East_arm.
    Field_trans)
sim.power.sum_refl_dark_trans = Calculate_power(Reflected_beam) +
    Calculate_power(Dark_port_beam) + Calculate_power(North_arm.Field_trans) +
     Calculate_power(East_arm.Field_trans);

% Calculate contrast defect
contrast_defect = 1 - (Calculate_power(Reflected_beam) - Calculate_power(
    Dark_port_beam) )/(Calculate_power(Reflected_beam) + Calculate_power(
    Dark_port_beam) )
sim.contrast_defect = contrast_defect;

jobid_string=getenv('PBS_JOBID');
filename_results=strcat(jobid_string(1:6),'.mat')
full_path_results = strcat(savepath_results, filename_results)
save(full_path_results,'sim')
```

Listing A.8: Python script for automated generation and submission of cluster runs of the grid-based sub-SQL interferometer model.

```
#!/usr/bin/env python

import os
import shutil
import random

no_runs = 10
gridpoints=1024
gridsize=0.06
surf_rms=1.25E-9

# generate 10-digit random numbers for folder names
run_id = range(no_runs)
folder_num_rand_int = []

for k in run_id:
    folder_num_rand_int.append(random.randint(1000000000,9999999999))

workdirstr = str(gridpoints) + '_' + str(gridsize) + 'm'
if not os.path.isdir(workdirstr):
    os.mkdir(workdirstr)

rmsdirstr = workdirstr + '/' + str(surf_rms) + '_rms'
if not os.path.isdir(rmsdirstr):
    os.mkdir(rmsdirstr)

bigwork_results_dir = '/bigwork/nhbfgrae/TSI_ParStudy_'+str(gridpoints)+'_'+
    str(gridsize)+'m'
if not os.path.isdir(bigwork_results_dir):
    os.mkdir(bigwork_results_dir)
```

```
    print "New directory on bigwork created: " + bigwork_results_dir

currworkdir=os.getcwd()

for folder_num in folder_num_rand_int:
    os.mkdir(rmsdirstr+'/'+str(folder_num))
    mlsimfile = open('TSI_FPMI.m')
    l=mlsimfile.readlines()
    mlsimfile.close()
    l[l.index('grid_size=\n')]='grid_size='+str(gridsize)+'\n'
    l[l.index('grid_points=\n')]='grid_points='+str(gridpoints)+'\n'
    l[l.index('surface_rms=\n')]='surface_rms='+str(surf_rms)+'\n'
    runfile=open('oscar_runfile.m','w')
    runfile.write(''.join(l))
    runfile.close()

    shutil.move('oscar_runfile.m', rmsdirstr+'/'+str(folder_num))
    shutil.copy('oscar_run_'+str(gridpoints)+'.sh', rmsdirstr+'/'+str(
        folder_num)+'/oscar_run.sh')
    os.chdir(rmsdirstr+'/'+str(folder_num))
    os.system('qsub oscar_run.sh')
    os.chdir(currworkdir)
```

APPENDIX **B**

Interfacing electronics for the GEO squeezer

In this appendix, schematics of the electronic circuits for interfacing the analog feedback control hardware of GEO squeezed-light laser experiment to the CDS digital system are shown. The schematics of the used analog servo controllers and high-voltage amplifiers were included for completeness.

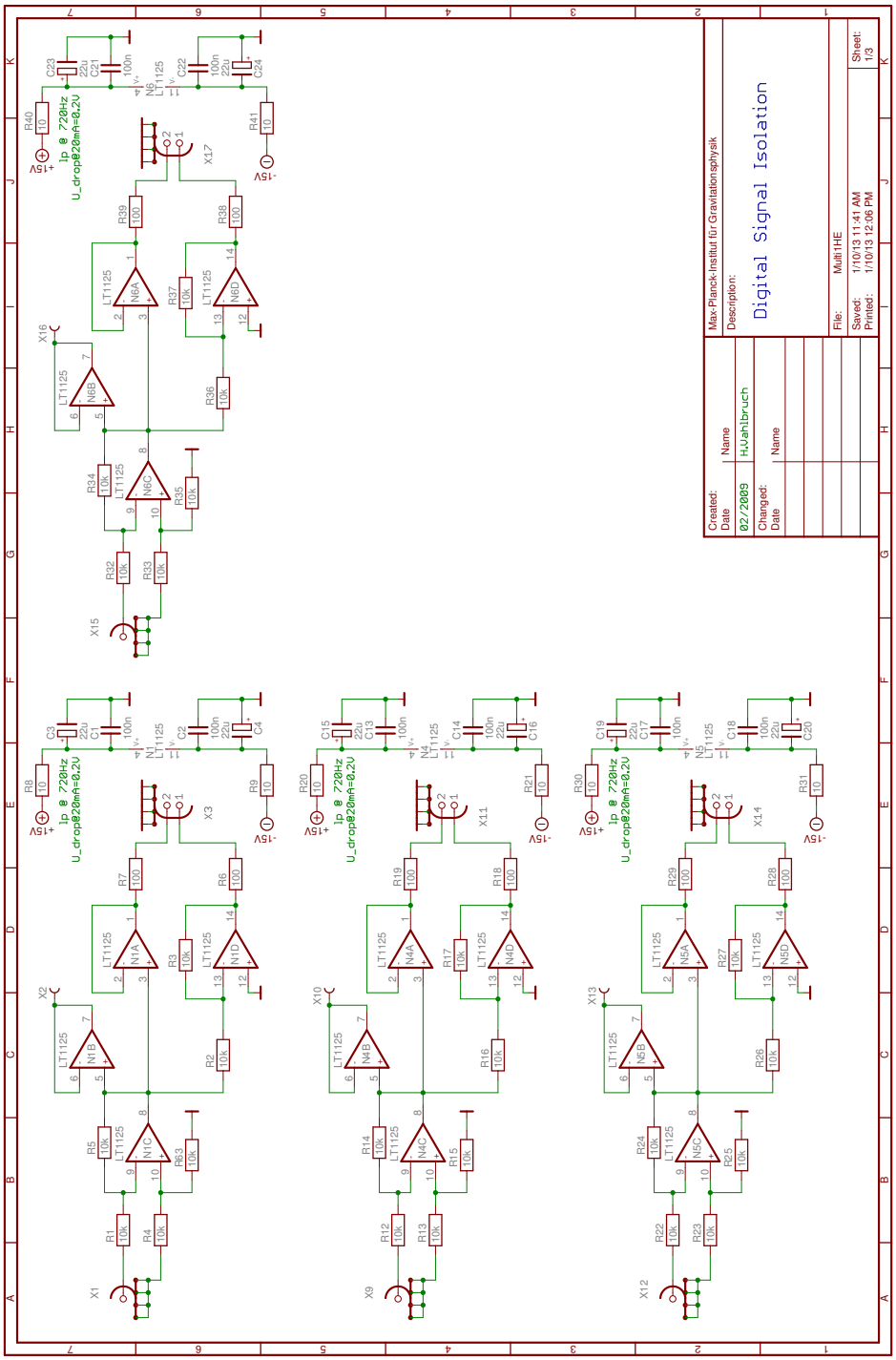

Figure B.1: Digital signal isolation box 1/3.

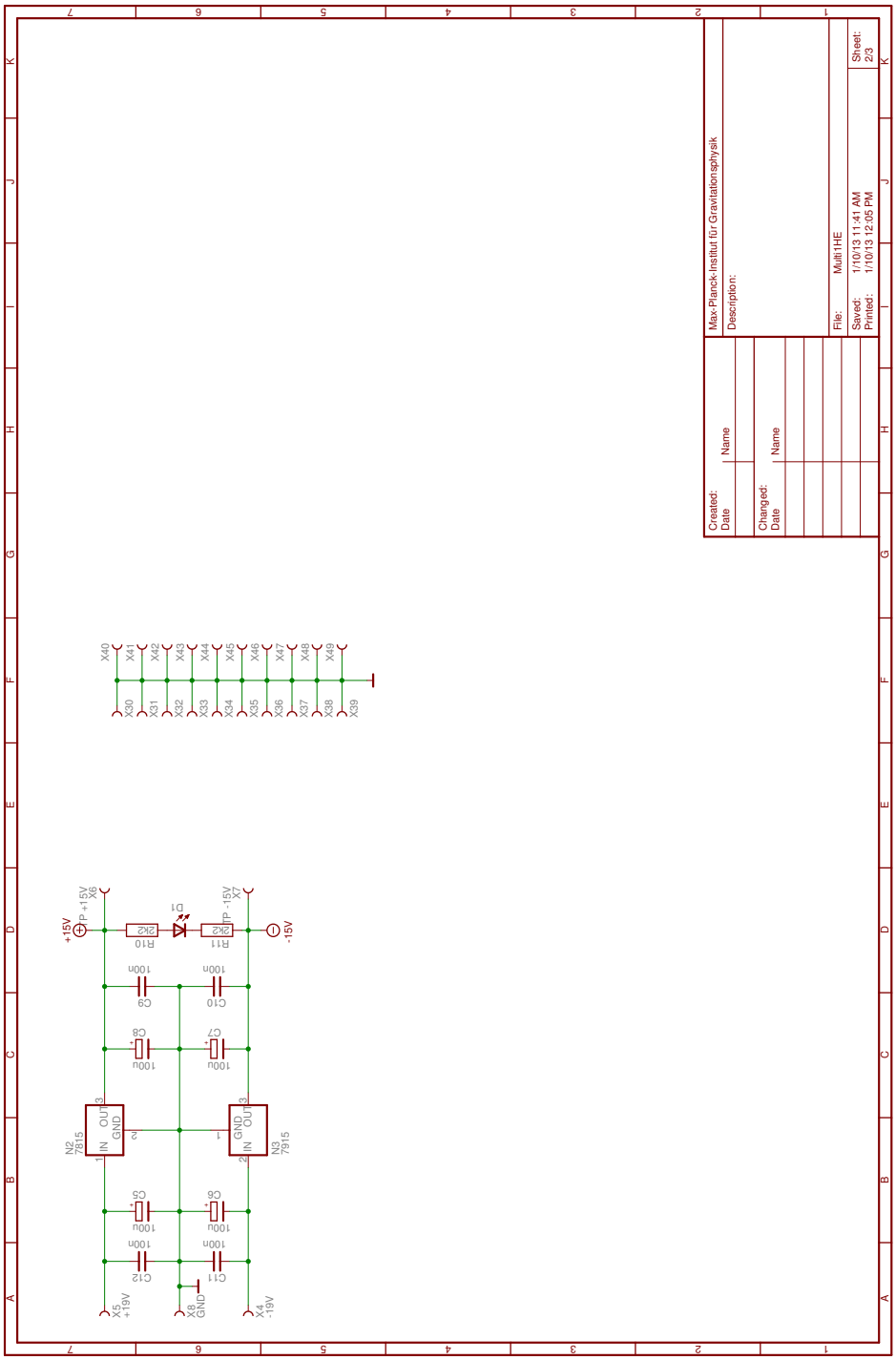

Figure B.2: Digital signal isolation box 2/3.

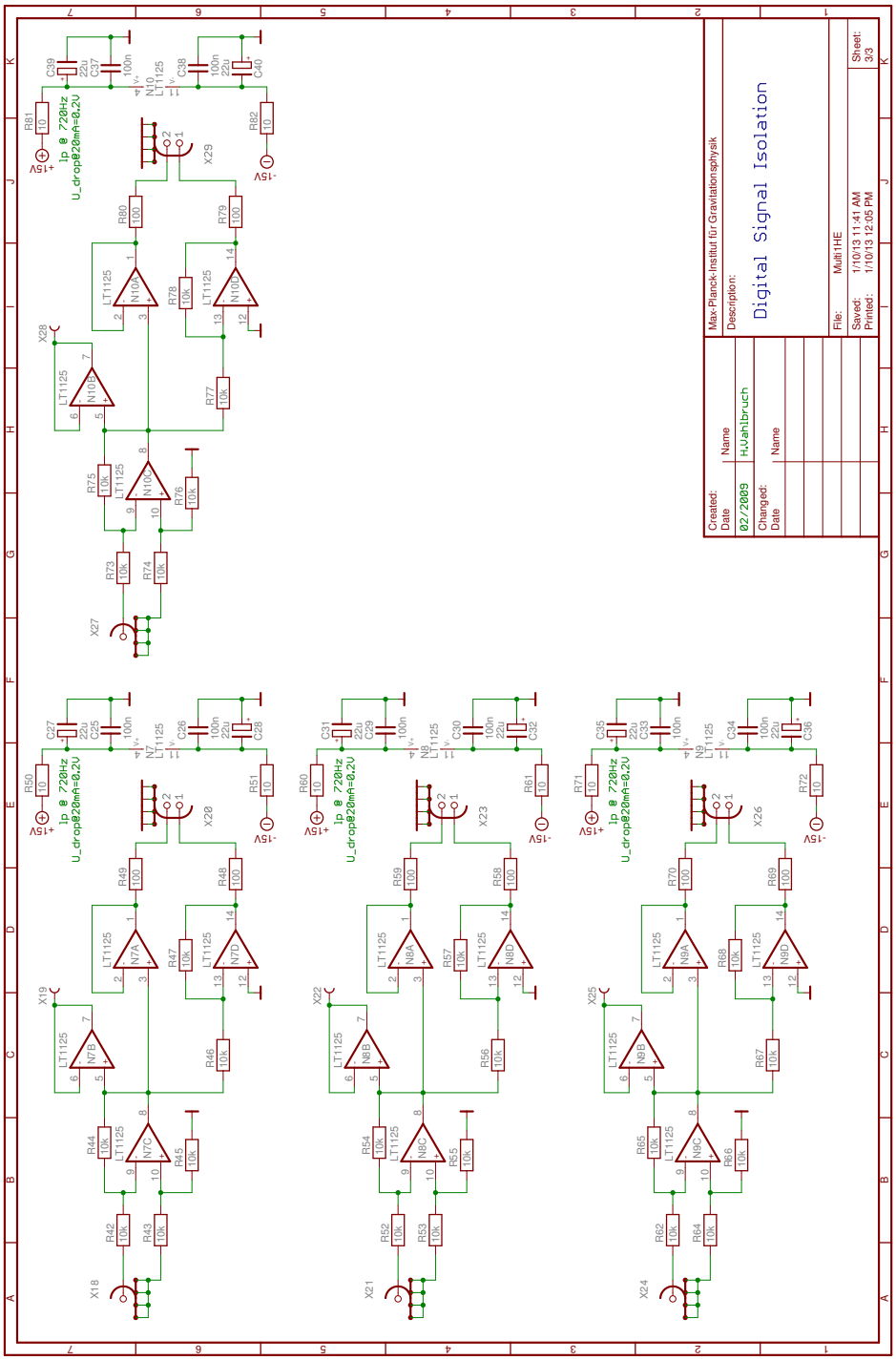

Figure B.3: Digital signal isolation box 3/3.

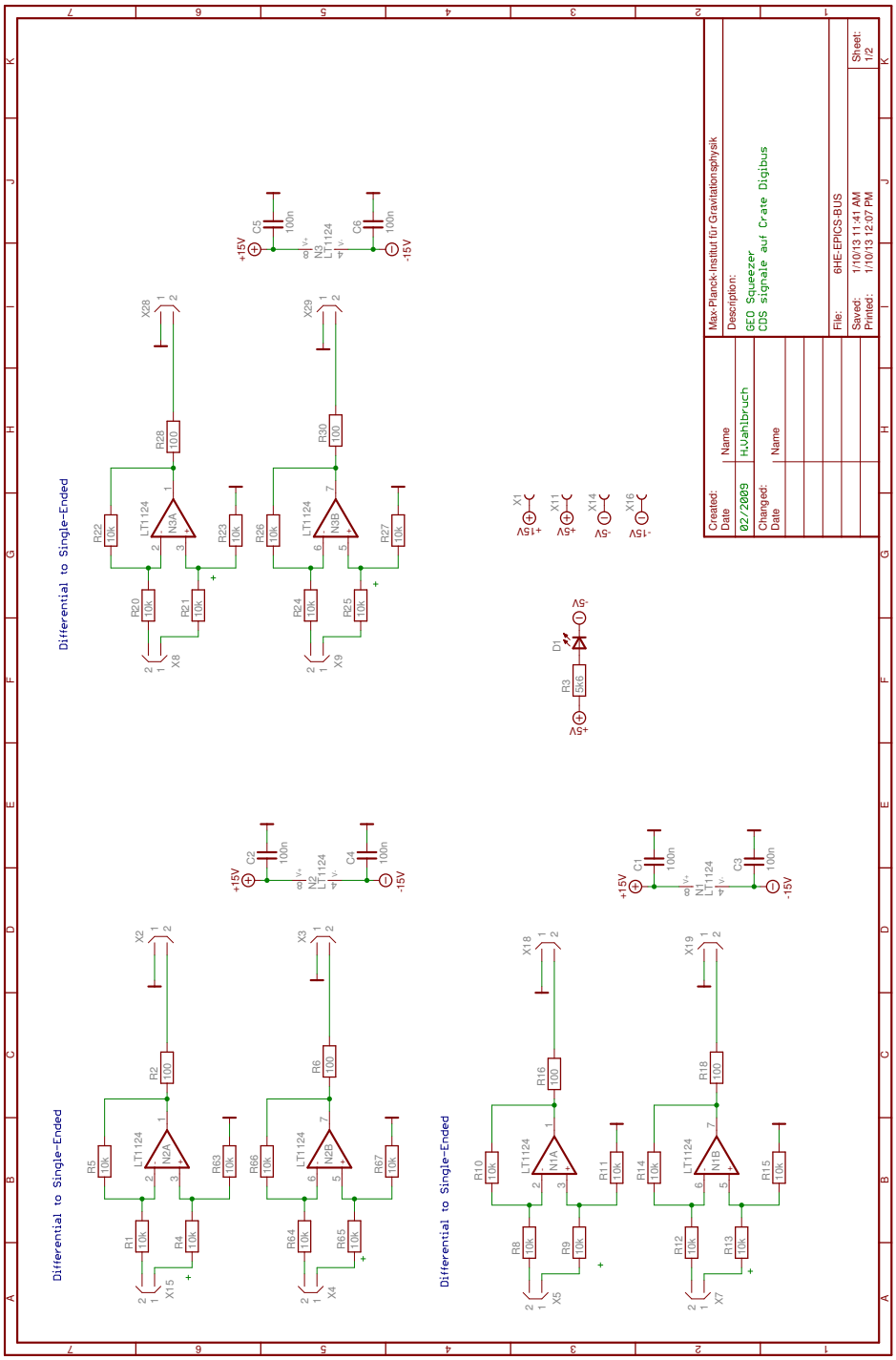

Figure B.4: Digital crate bus CDS interface box 1/2.

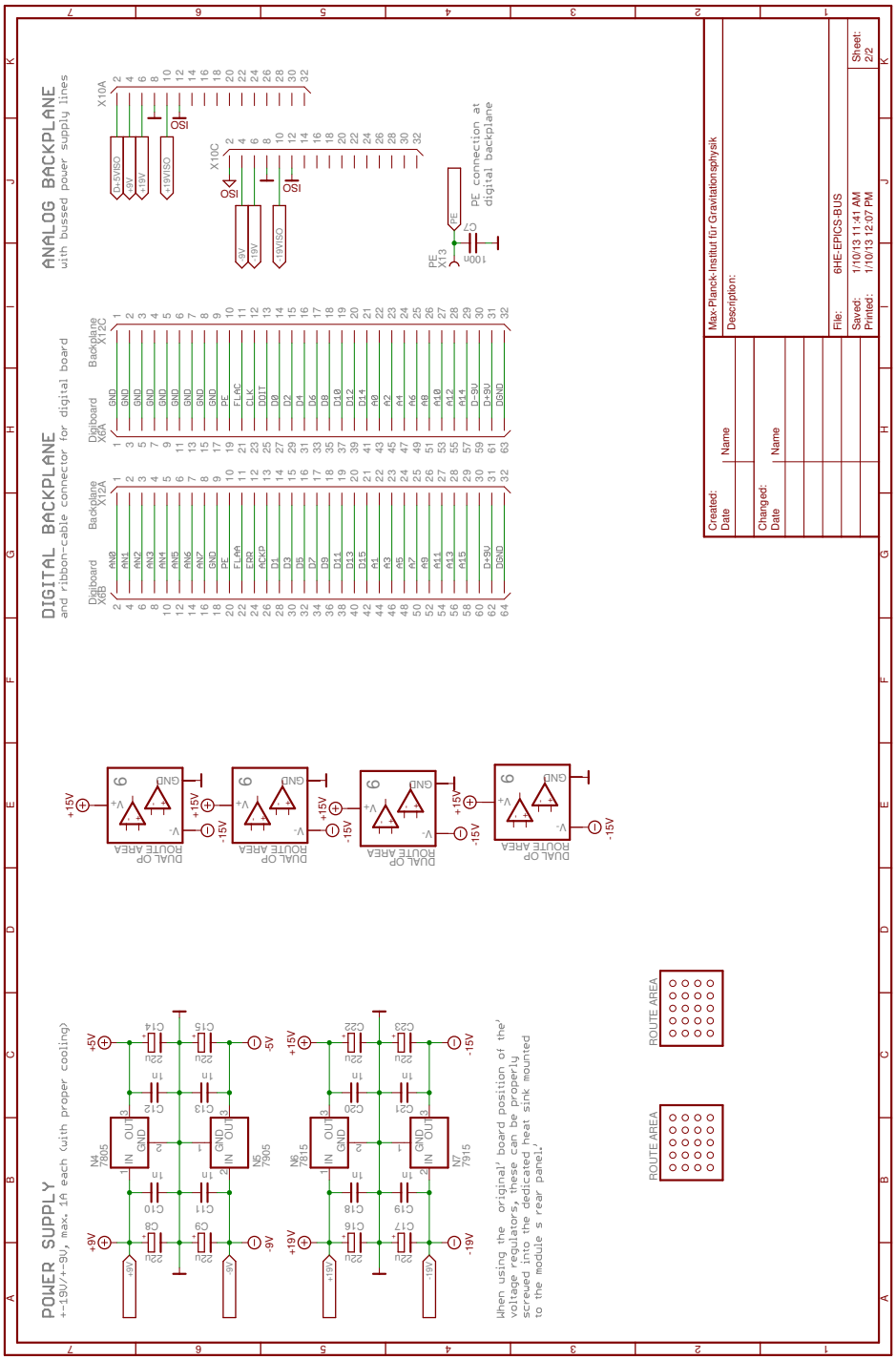

Figure B.5: Digital crate bus CDS interface box 2/2.

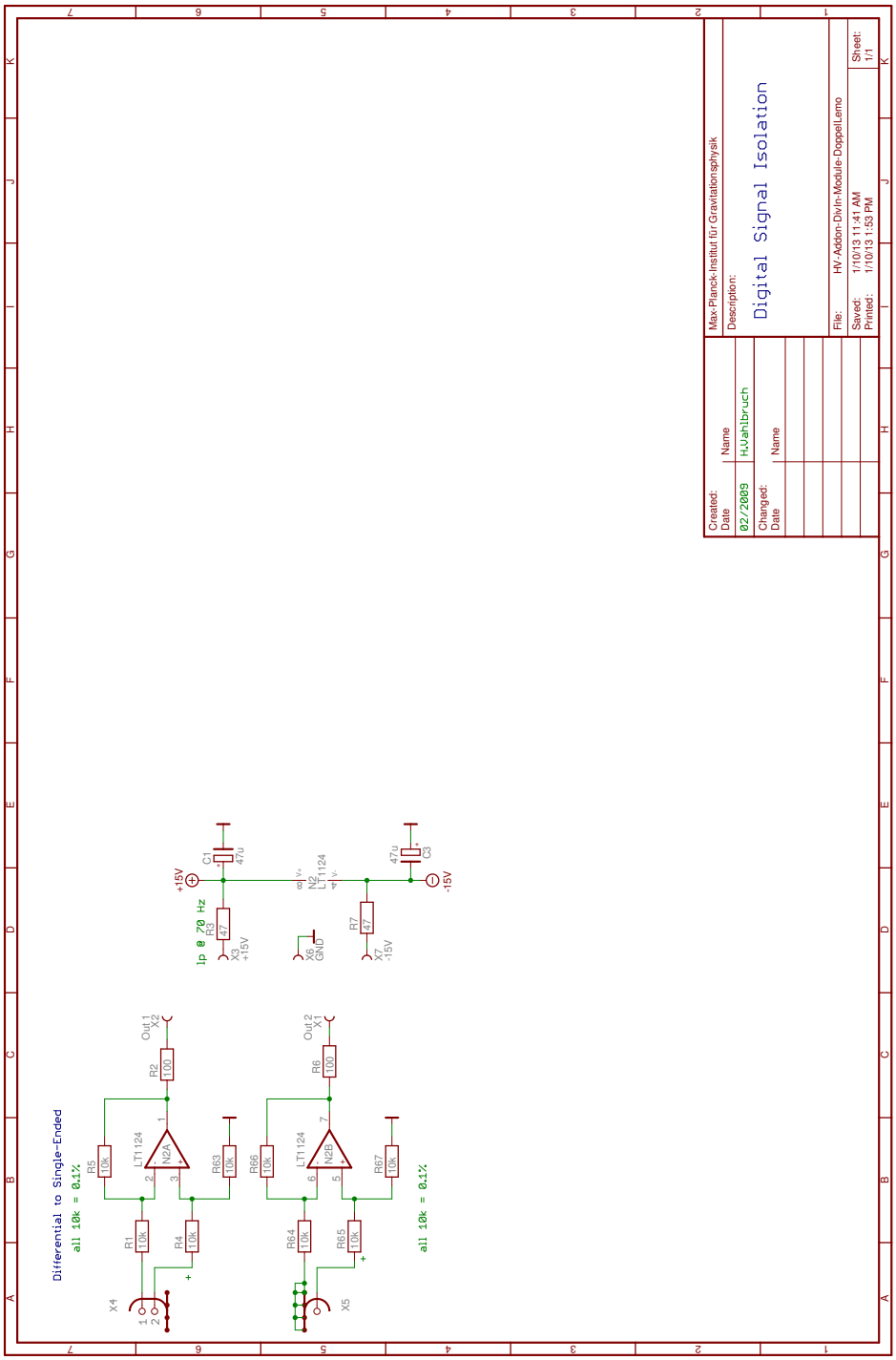

Figure B.6: HV amplifier CDS interface board with summing input.

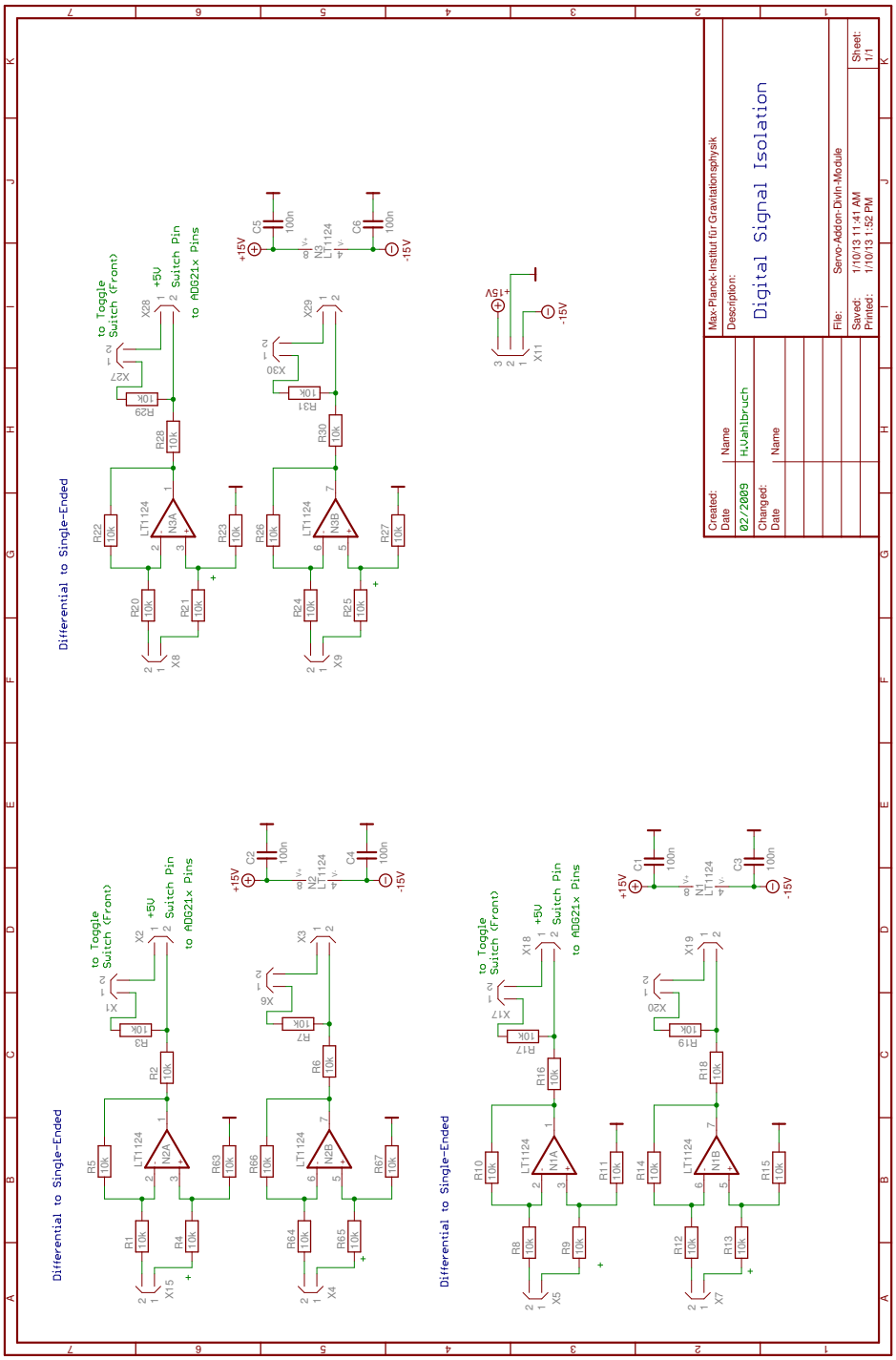

Figure B.7: Standard servo CDS interface board.

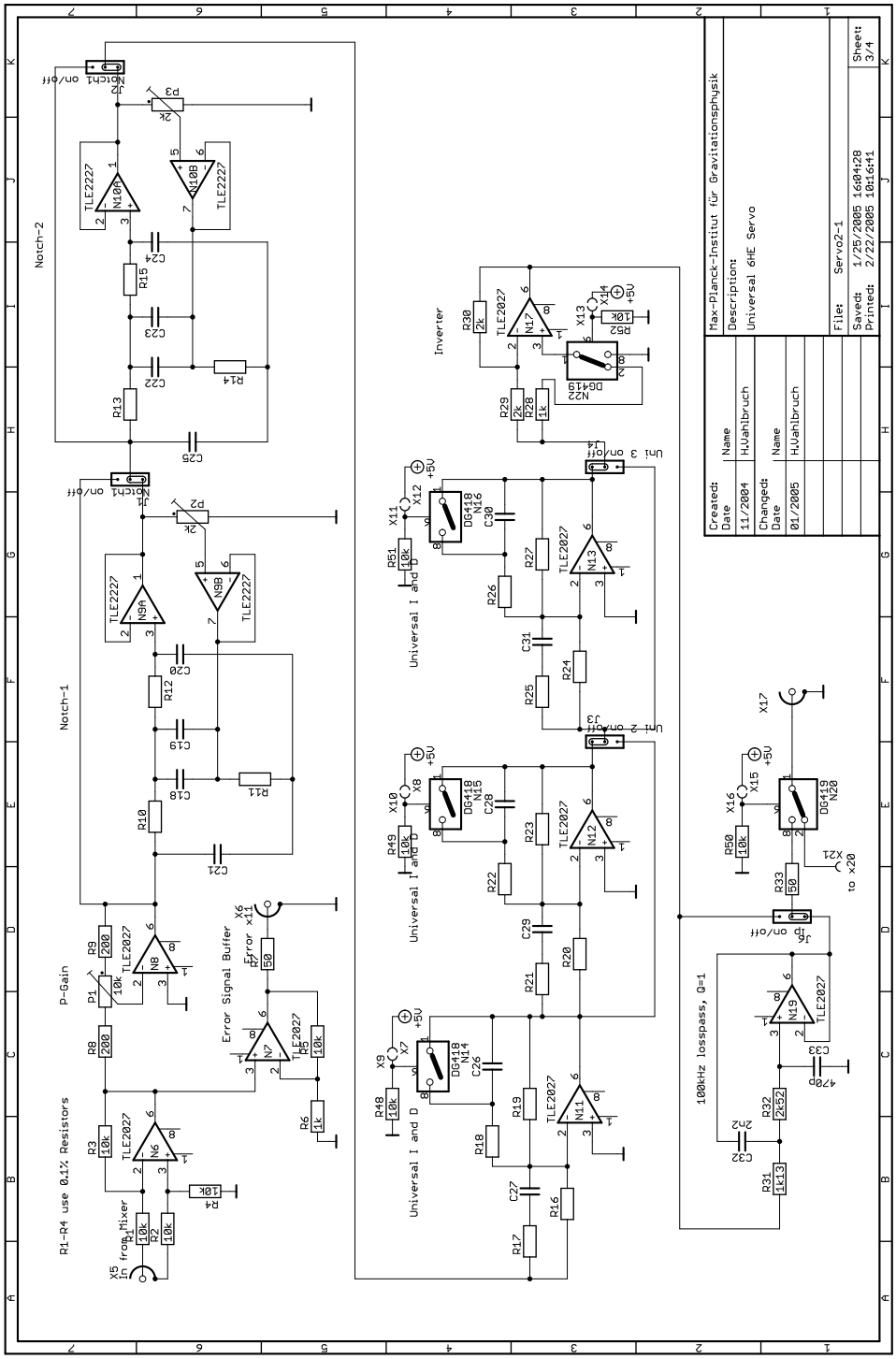

Figure B.8: Universal servo board 1/2.

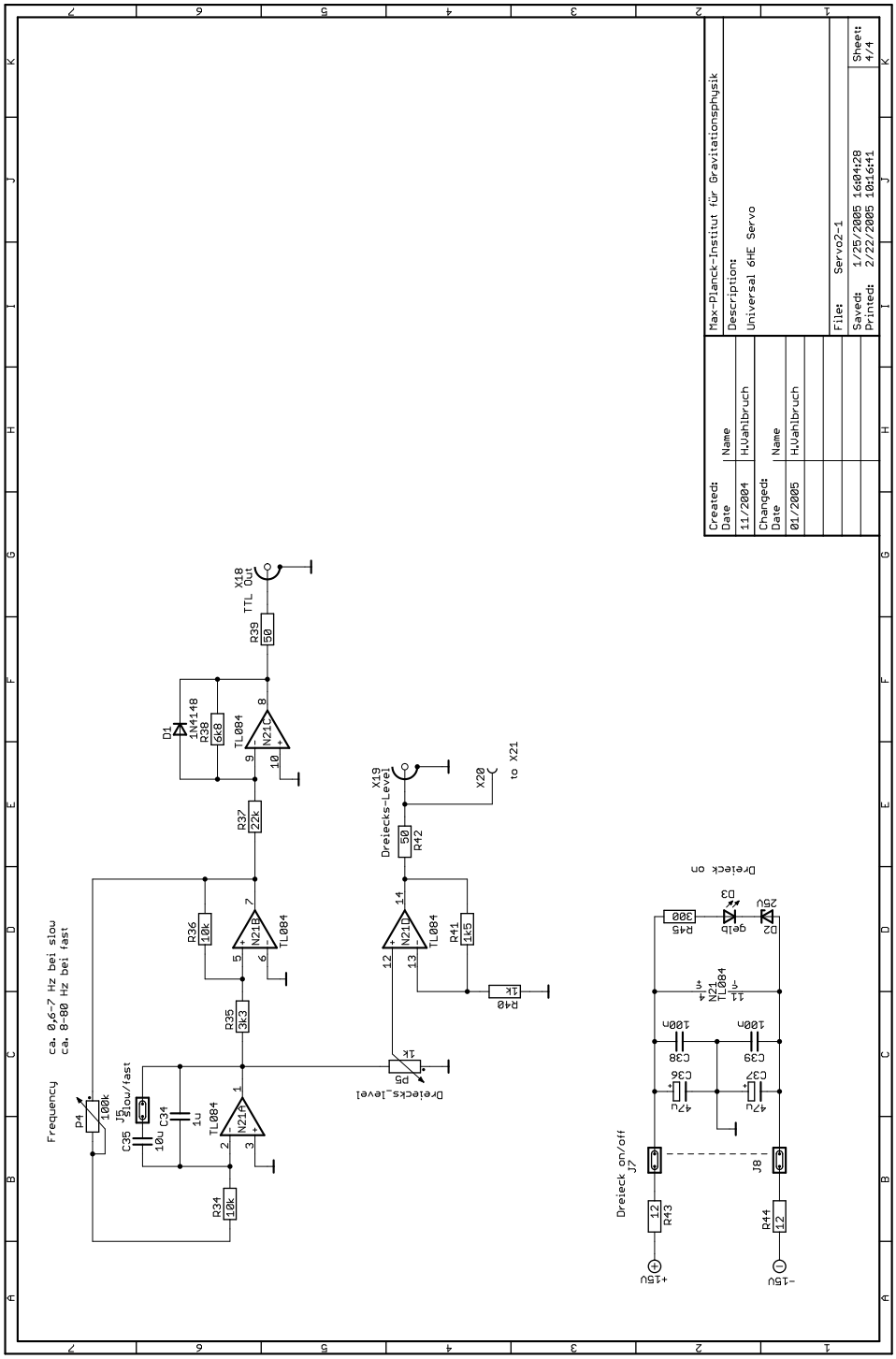

Figure B.9: Universal servo board 2/2.

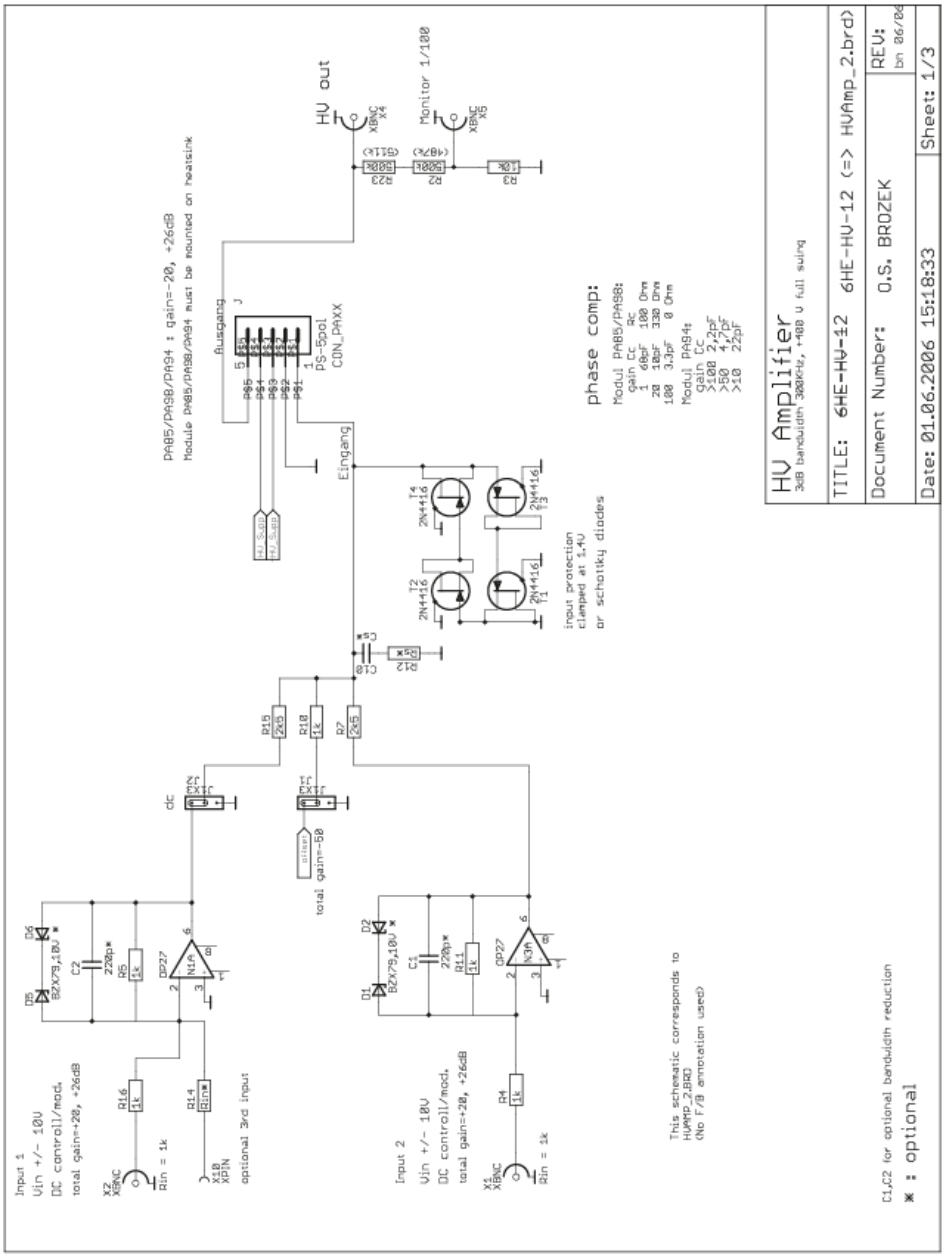

Figure B.10: High-voltage amplifier 1/3.

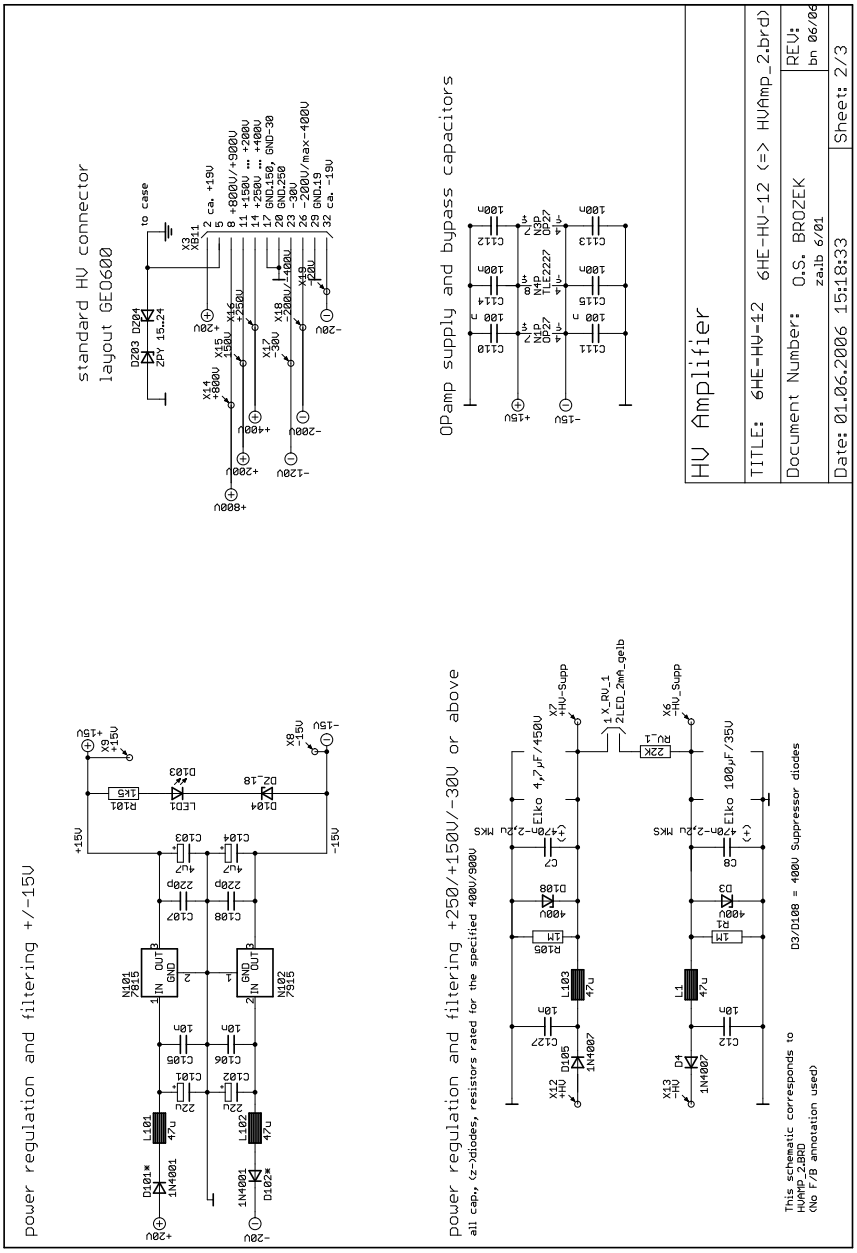

Figure B.11: High-voltage amplifier 2/3.

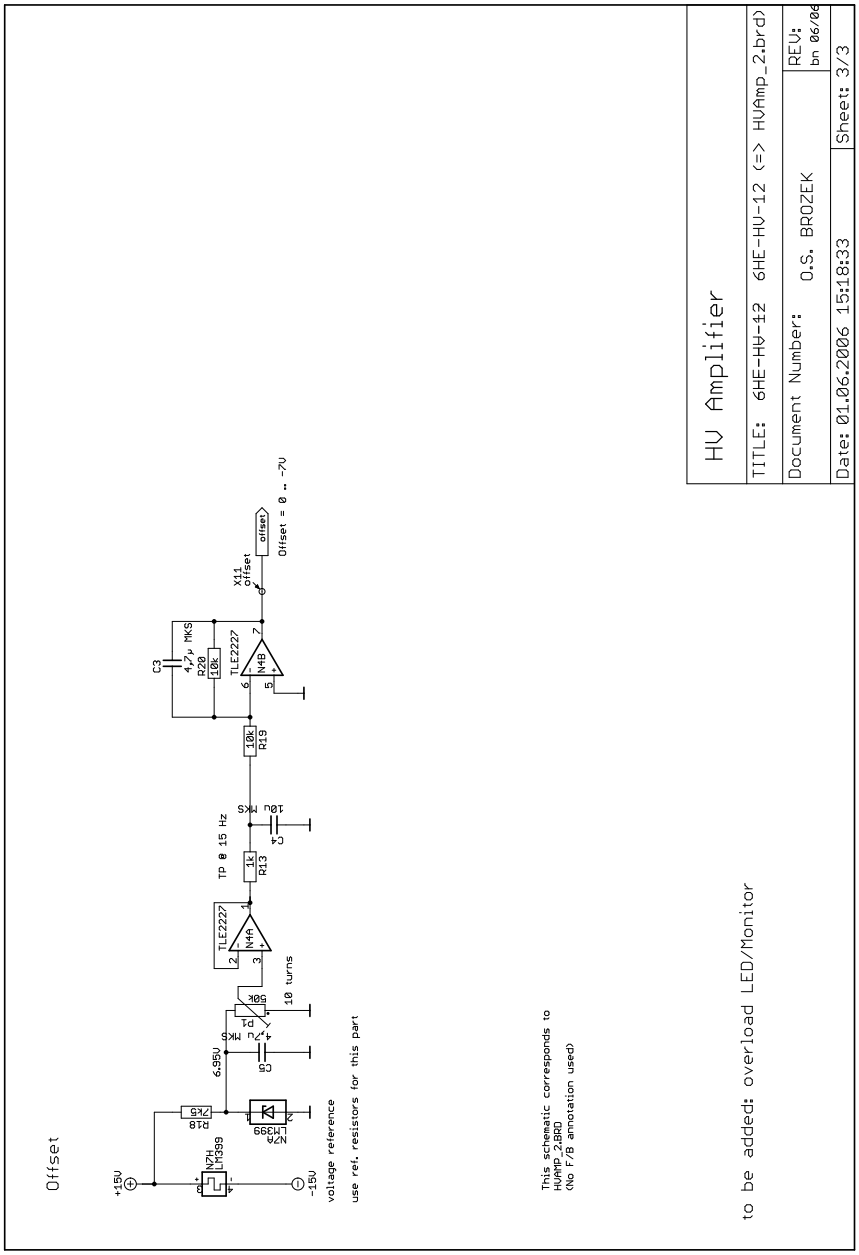

Figure B.12: High-voltage amplifier 3/3.

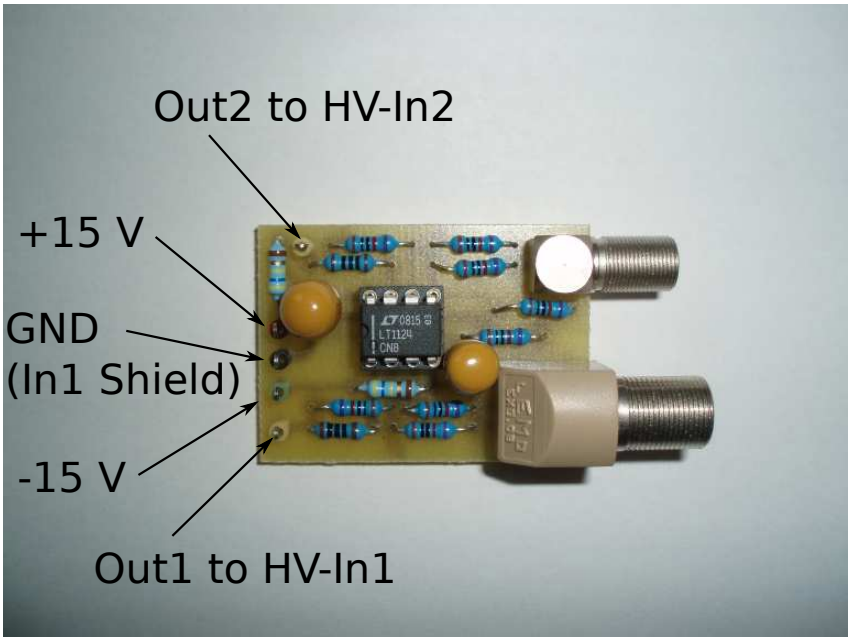

Figure B.13: Photograph of the HV amplifier add-on board with pin allocation.

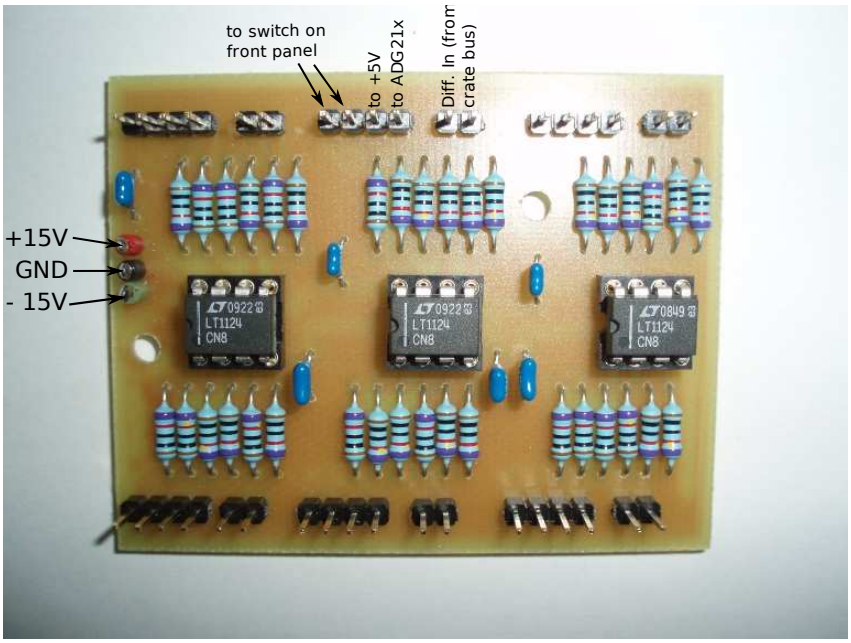

Figure B.14: Photograph of the HV amplifier add-on board with pin allocation.

APPENDIX C

GEO squeezer automation real-time code

In this appendix, the source code of the base routine for real-time control of the optical stages in the GEO squeezed-light laser is given. This code is included in the real-time modules of all lockable components, i.e. the second harmonic generator, the squeezed light source, the Mach-Zehnder interferometer, the mode cleaner cavity for the green pump field, the phase lock of the pump field, the mode cleaner cavity for the local oscillator field and the balanced homodyne detector.

Listing C.1: Base routine "rt-locker.c". During compilation of the real-time control module this code is included by all lockable components in the GEO squeezed light laser.

```
static int sign = 1;
static double ramp_out = 0.0;
static double islocked = 0.0;
static double integrator1 = 0.0;
static double integrator2 = 0.0;
static double closeloop = 0.0;
static int int1_delay_cnt = 0;
static int int2_delay_cnt = 0;
static int lock_stage = 0;
// lock_stage = 0 -> not locked
// lock_stage = 1 -> locking, ramp is on
// lock_stage = 2 -> locking, closeloop is 1
// lock_stage = 3 -> locking, int2 is 1
// lock_stage = 4 -> locked
//

static double reset_out_prevcycle = 1.0;
static double unlock_prevcycle = 1.0;
static double lock_once_prevcycle = 1.0;

const int DEBUG = 0;

if (lock_once && !lock_once_prevcycle){
  sign = 1; /* forces the ramp to increase on start */
  lock_stage = 1;
  if (DEBUG) {
    printk("--- CDS --- lock stage %i\n", lock_stage);
  }
}
```

```
if (lock_in_transmission){
  if (dc_pd > thresh_inLock && lock_stage != 0) islocked = 1.0;
  else{
    islocked = 0.0;
  }
}
else{
  if (dc_pd < thresh_inLock && lock_stage != 0) islocked = 1.0;
  else{
    islocked = 0.0;
  }
}

if (reset_out && !reset_out_prevcycle){
  ramp_out = 0.0;
}

if (unlock && !unlock_prevcycle){
  islocked = 0.0;
  integrator1 = 0.0;
  integrator2 = 0.0;
  closeloop = 0.0;
  ramp_out = 0.0;
  lock_stage = 0;
  if (DEBUG){
    printk("--- CDS --- lock stage %i\n", lock_stage);
    printk("--- CDS --- -------------\n\n", lock_stage);
  }
}

if (lock_stage == 1){
  if (lock_in_transmission){
    if (DEBUG) {
        printk("--- CDS --- dc_pd = %i, thesh_acq = %i\n", (int) dc_pd, (int)
            thresh_acq);
    }

    if (dc_pd < thresh_acq){
      ramp_out += sign*amp*(4*freq/FE_RATE);

      if (ramp_out > amp) sign *= -1, ramp_out = amp;
      if (ramp_out < -amp) sign *= -1, ramp_out = -amp;
    }
    else {
      closeloop = 1.0;
      int1_delay_cnt = 0;
      int2_delay_cnt = 0;
      lock_stage = 2;
      if (DEBUG) {
          printk("--- CDS --- lock stage %i\n", lock_stage);
      }
    }
  }
  else{
    if (dc_pd > thresh_acq){
      ramp_out += sign*amp*(4*freq/FE_RATE);

      if (ramp_out > amp) sign *= -1, ramp_out = amp;
      if (ramp_out < -amp) sign *= -1, ramp_out = -amp;
    }
    else{
      closeloop = 1.0;
      int1_delay_cnt = 0;
```

```
      int2_delay_cnt = 0;
      lock_stage = 2;
      if (DEBUG) {
          printk("--- CDS --- lock stage %i\n", lock_stage);
      }
    }
  }
}
else if (lock_stage == 2){
  if (int2_delay_cnt > switch_delay){
    integrator2 = 1;
    lock_stage = 3;
      if (DEBUG) printk("--- CDS --- lock stage %i\n", lock_stage);
  }
  else
    int2_delay_cnt++;
}
else if (lock_stage == 3){
  if (int1_delay_cnt > switch_delay){
    integrator1 = 1;
    lock_stage = 4;
      if (DEBUG) printk("--- CDS --- lock stage %i\n", lock_stage);
  }
  else
    int1_delay_cnt++;
}

unlock_prevcycle = unlock;
reset_out_prevcycle = reset_out;
lock_once_prevcycle = lock_once;
```

Appendix D

Memorable whiteboard sketches

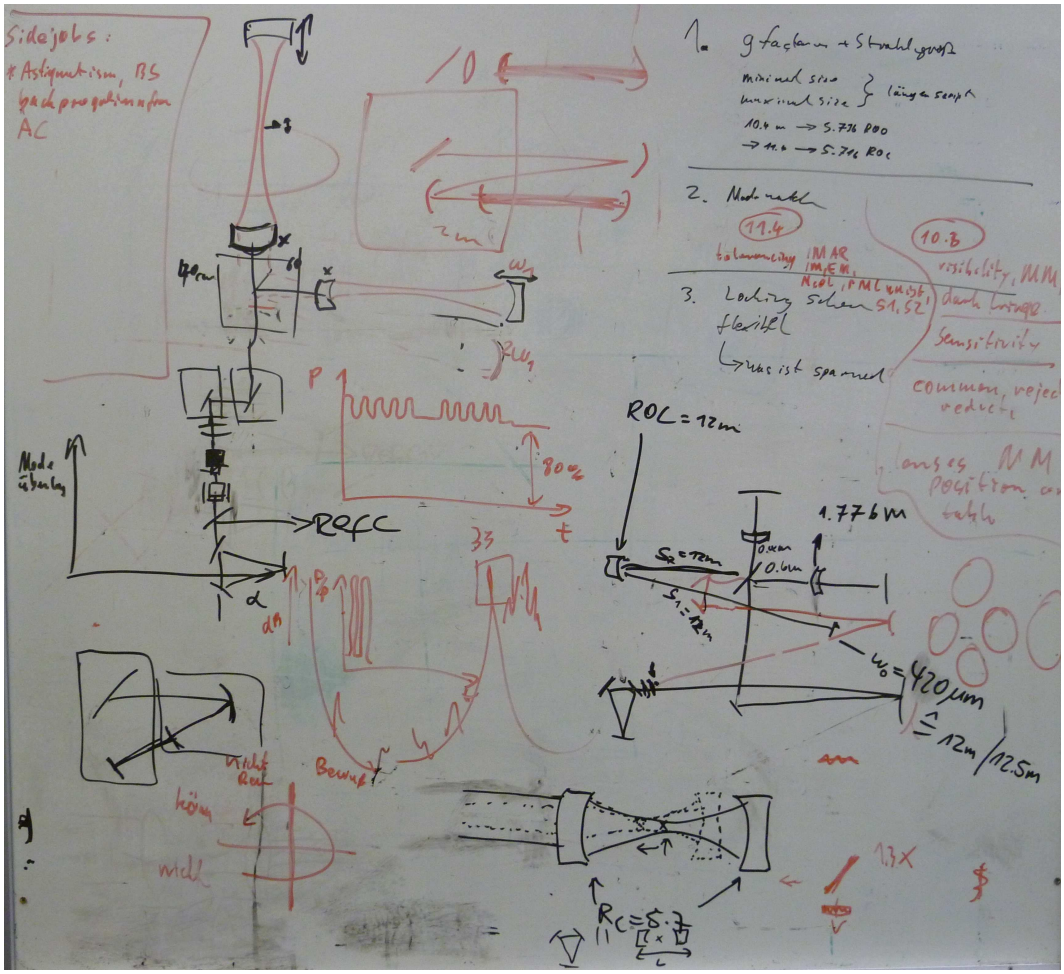

Figure D.1: Development of an optical layout for the Fabry-Perot Michelson interferometer with tunable stability. Glasgow, June 27, 2011.

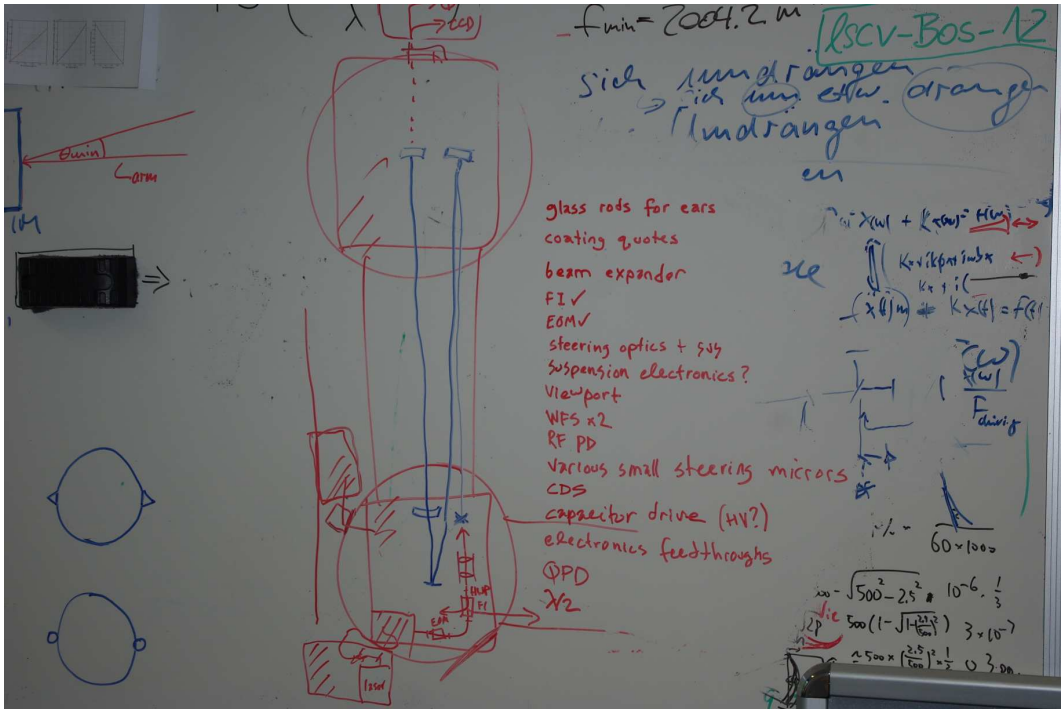

Figure D.2: The single arm test experiment. Hannover, August 29, 2012.

Curriculum vitae

Personal details

Full Name:	Christian Gräf
Date of Birth:	May 8, 1980
Place of Birth:	Hannover

Education and Employment

since 04/2013	Research assistant position at the Institute for Gravitational Research, University of Glasgow, Scotland
01/2009–present	Doctoral studies in the 10 m Prototype group at the Max-Planck-Institute for Gravitational Physics, Leibniz Universität Hannover, Germany
07/2009–03/2013	Scholarship holder of the International Max Planck Research School (IMPRS) on Gravitational Wave Astronomy
04/2009–06/2009	Visiting student of the LIGO group at the Kavli Institute for Astrophysics and Space Research, Massachusetts Institute of Technology, Cambridge, USA
12/2008–06/2009	Scientific assistant position at Leibniz Universität Hannover
09/2008	Degree "Diplom Physiker" awarded by Leibniz Universität Hannover, grade: "with distinction"
10/2002–09/2008	Diploma studies in physics at Leibniz Universität Hannover, Thesis title *"PPKTP-Quetschlichtquelle und Twin-Signal-Recycling"*, Institute for Gravitational Physics, Quantum Interferometry Group
09/2001–06/2002	Community service at Malteser Hilfsdienst gGmbH, Hannover-Anderten
06/2001	Abitur at Fachgymnasium Wirtschaft, Berufsbildende Schule 11, Hannover

Publications

Publications with direct contribution

- C. Gräf, A. Thüring, H. Vahlbruch, K. Danzmann and R. Schnabel "*Length sensing and control of a Michelson interferometer with power recycling and twin signal recycling cavities*," Opt. Express **21**, 5287-5299 (2013)
- S. Hild, S. Leavy, C. Gräf, B. Sorazu "*Smart Charging Technologies for Portable Electronic Devices*," arXiv:1209.5931 [cs.OH] (2012), submitted to IEEE Trans. Smart Grid
- A. Khalaidovski, H. Vahlbruch, N. Lastzka, C. Gräf, K. Danzmann, R. Schnabel "*A Squeezed Light Source for the Gravitational Wave Detector GEO 600*," in: T. Damour, R. T. Jantzen, R. Ruffini (eds.) The Twelfth Marcel Grossmann Meeting on General Relativity, World Scientific 1729–1731 (2012)
- K. Dahl, T. Alig, ..., C. Gräf, ..., B. Willke, K. A. Strain, S. Goßler and K. Danzmann, "*Status of the AEI 10 m prototype*," Class. Quantum Grav. **29**, 145005 (2012)
- C. Gräf, S. Hild, H. Lück, B. Willke, K. A. Strain, S. Goßler and K. Danzmann, "*Optical layout for a 10 m Fabry-Perot Michelson interferometer with tunable stability*," Class. Quantum Grav. **29** 075003 (2012)
- T. Westphal, G. Bergmann, ..., C. Gräf, ..., B. Willke, K. A. Strain, S. Goßler and K. Danzmann, "*Design of the 10 m AEI prototype facility for interferometry studies*," Appl. Phys. B **106**, 551–557 (2012)
- A. Khalaidovski, H. Vahlbruch, N. Lastzka, C. Gräf, K. Danzmann, H. Grote and R. Schnabel, "*Long-term stable squeezed vacuum state of light for gravitational wave detectors*," Class. Quantum Grav. **29** 075001 (2012)
- A. Khalaidovski, H. Vahlbruch, N. Lastzka, C. Gräf, H. Lück, K. Danzmann, H. Grote and R. Schnabel, "*Status of the GEO 600 squeezed-light laser*," J. Phys.: Conf. Ser. **363** 012013 (2012)
- M. Abernathy, F. Acernese, ..., C. Gräf, ..., K. Yamamoto, "*Einstein Gravitational Wave Telescope Conceptual Design*," (2011) `http://www.et-gw.eu/etdsdocument`

- H. Vahlbruch, A. Khalaidovski, N. Lastzka, C. Gräf, K. Danzmann and R. Schnabel, "*The GEO 600 squeezed light source*," Class. Quantum Grav. **27**, 084027 (2010)
- A. Thüring, C. Gräf, H. Vahlbruch, M. Mehmet, K. Danzmann and R. Schnabel, "*Broadband squeezing of quantum noise in a Michelson interferometer with Twin-Signal-Recycling*," Opt. Lett. **34**, 824 (2009)
- C. Gräf, "*PPKTP-Quetschlichtquelle und Twin-Signal-Recycling*," Diplomarbeit Universität Hannover (2008)

Complete list of publications

— 2008 —

- C. Gräf, "*PPKTP Quetschlichtquelle und Twin-Signal-Recycling*," Diplomarbeit Universität Hannover (2008)

— 2009 —

- A. Thüring, C. Gräf, H. Vahlbruch, M. Mehmet, K. Danzmann, and R. Schnabel, "*Broadband squeezing of quantum noise in a Michelson interferometer with Twin-Signal-Recycling*," Opt. Lett. **34**, 824 (2009)

— 2010 —

- S. Goßler, A. Bertolini, M. Born, Y. Chen, K. Dahl, D. Gering, C. Gräf, G. Heinzel, S. Hild, F. Kawazoe, O. Kranz, G. Kühn, H. Lück, K. Mossavi, R. Schnabel, K. Somiya, K. A. Strain, J. R. Taylor, A. Wanner, T. Westphal, B. Willke and K. Danzmann, "*The AEI 10 m Prototype Interferometer*," Class. Quantum Grav. **27**, 084023 (2010)
- H. Vahlbruch, A. Khalaidovski, N. Lastzka, C. Gräf, K. Danzmann, and R. Schnabel, "*The GEO 600 squeezed light source*," Class. Quantum Grav. **27**, 084027 (2010)
- K. Dahl, A. Bertolini, M. Born, Y. Chen, D. Gering, S. Goßler, C. Gräf, G. Heinzel, S. Hild, F. Kawazoe, O. Kranz, G. Kühn, H. Lück, K. Mossavi, R. Schnabel, K. Somiya, K. A. Strain, J. R. Taylor, A. Wanner, T. Westphal, B. Willke and K. Danzmann, "*Towards a Suspension Platform Interferometer for the AEI 10 m Prototype Interferometer*," J. of Phys.: Conf. Series **228**, 012027 (2010)
- F. Kawazoe, A. Bertolini, M. Born, Y. Chen, K. Dahl, D. Gering, S. Goßler, C. Gräf, G. Heinzel, S. Hild, O. Kranz, G. Kühn, H. Lück, K. Mossavi, R. Schnabel, K. Somiya, K. A. Strain, J. R. Taylor, A. Wanner, T. Westphal, B. Willke

and K. Danzmann, "*Designs of the frequency reference cavity for the AEI 10 m Prototype interferometer*," J. of Phys.: Conf. Series **228**, 012028 (2010)

- J. Abadie, B. P. Abbott, ... , C. Gräf, ... , J. Zweizig, The LIGO Scientific Collaboration and the Virgo Collaboration and K. Belczynski, "*Predictions for the rates of compact binary coalescences observable by ground-based gravitational-wave detectors*," Class. Quantum Grav. **27**, 173001 (2010)

- J. Abadie, B. P. Abbott, ... , C. Gräf, ... , J. Zweizig, and The LIGO Scientific Collaboration, "*First search for gravitational waves from the youngest known neutron star*," The Astrophys. J. **722**, 1504 (2010)

- J. Abadie, B. P. Abbott, ... , C. Gräf, ... , J. Zweizig, and The LIGO Scientific Collaboration and The Virgo Collaboration, "*Search for gravitational waves from compact binary coalescence in LIGO and Virgo data from S5 and VSR1*," Phys. Rev. D. **82**, 102001 (2010)

- J. Abadie, B. P. Abbott, ... , C. Gräf, ... , J. Zweizig, "*Calibration of the LIGO gravitational wave detectors in the fifth science run*," Nucl. Inst. Phys. A **624**, 223-240 (2010)

- The LIGO Scientific Collaboration and the Virgo Collaboration: J. Abadie, B. P. Abbott, ... , C. Gräf, ... , J. Zweizig, "*Sensitivity to Gravitational Waves from Compact Binary Coalescences Achieved during LIGO's Fifth and Virgo's First Science Run*," arXiv:1003.2481v3 [gr-qc] (2010)

— 2011 —

- M. Abernathy, F. Acernese, ..., C. Gräf, ..., K. Yamamoto, "*Einstein Gravitational Wave Telescope Conceptual Design*," (2011)
  `http://www.et-gw.eu/etdsdocument`

- S. Hild, M. Abernathy, F. Acernese, ... , C. Gräf, ... , K. Yamamoto, "*Sensitivity studies for third-generation gravitational wave observatories*," Class. Quantum Grav. **28**, 094013 (2011)

- J. Abadie, B. P. Abbott, ... , C. Gräf, ... , K. Yamaoka, "*Search for gravitational wave bursts from six magnetars*," Astrophys. J. Lett. **734**, L35 (2011)

- J. Abadie, B. P. Abbott, ... , C. Gräf, ... , J. Zweizig, and The LIGO Scientific Collaboration and The Virgo Collaboration, "*Search for gravitational waves from binary black hole inspiral, merger, and ringdown*," Phys. Rev. D. **83**, 122005 (2011)

- J. Abadie, B. P. Abbott, ... , C. Gräf, ... , J. Zweizig, and The LIGO Scientific Collaboration, S. Buchner, A. Hotan, J. Palfreyman, "*Beating the Spin-down Limit on Gravitational Wave Emission from the Vela Pulsar*," The Astrophys. J. **737**, 93 (2011)

- LIGO scientific collaboration, J. Abadie, ..., C. Gräf, ... , J. Zweizig, "*A gravitational wave observatory operating beyond the quantum shot-noise limit*," Nature Physics **7**, 962–965 (2011)
- J. Abadie, B. P. Abbott, ... , C. Gräf, ... , J. Zweizig, "*Directional limits on persistent gravitational waves using LIGO S5 science data*," Phys. Rev. Lett. **107** 271102 (2011)

— 2012 —

- C. Gräf, S. Hild, H. Lück, B. Willke, K. A. Strain, S. Goßler and K. Danzmann, "*Optical layout for a 10 m Fabry–Perot Michelson interferometer with tunable stability*," Class. Quantum Grav. **29** 075003 (2012)
- A. Khalaidovski, H. Vahlbruch, N. Lastzka, C. Gräf, K. Danzmann, H. Grote and R. Schnabel, "*Long-term stable squeezed vacuum state of light for gravitational wave detectors*," Class. Quantum Grav. **29** 075001 (2012)
- A. Khalaidovski, H. Vahlbruch, N. Lastzka, C. Gräf, H. Lück, K. Danzmann, H. Grote and R. Schnabel, "*Status of the GEO 600 squeezed–light laser*," J. Phys.: Conf. Ser. **363** 012013 (2012)
- F. Kawazoe, G. Bergmann, A. Bertolini, M. Born, Y. Chen, A. V. Cumming, L. Cunningham, K. Dahl, C. Gräf, G. Hammond, G. Heinzel, S. Hild, S.H. Huttner, R. Jones, S. Köhlenbeck, G. Kühn, H. Lück, K. Mossavi, J. H. Pöld, K. Somiya, A. M. van Veggel, A. Wanner, T. Westphal, B. Willke, K. A. Strain, S. Goßler and K. Danzmann, "*The AEI 10 m Prototype Interferometer frequency control using the reference cavity and its angular control*," J. Phys.: Conf. Ser. **363** 012012 (2012)
- A. Khalaidovski, H. Vahlbruch, N. Lastzka, C. Gräf, K. Danzmann and R. Schnabel, "*A Squeezed Light Source for the Gravitational Wave Detector GEO 600*," in: T. Damour, R.T. Jantzen, R. Ruffini (eds.) The Twelfth Marcel Grossmann Meeting on General Relativity. World Scientific (2012) 1729 – 1731
- K. Dahl, T. Alig, G. Bergmann, A. Bertolini, M. Born, Y. Chen, A. V. Cumming, L. Cunningham, C. Gräf, G. Hammond, G. Heinzel, S. Hild, S. H. Huttner, R. Jones, F. Kawazoe, S. Köhlenbeck, G. Kühn, H. Lück, K. Mossavi, P. Oppermann, J. Pöld, K. Somiya, A. M. van Veggel, A. Wanner, T. Westphal, B. Willke, K. A. Strain, S. Goßler and K. Danzmann, "*Status of the AEI 10 m prototype*," Class. Quantum Grav. **29** 145005 (2012)
- The LIGO Scientific Collaboration and the Virgo Collaboration: J. Abadie, B. P. Abbott, ... , C. Gräf, ... , J. Zweizig, M. Boer, R. Fender, N. Gehrels, A. Klotz, E. O. Ofek, M. Smith,M. Sokolowski, B. W. Stappers, I. Steele, J. Swinbank, R. A. M. J. Wijers, "*Implementation and testing of the first prompt search for electromagnetic counterparts to gravitational wave transients*," Astronomy & Astrophysics **539**, A124 (2012)

- J. Abadie, B. P. Abbott, ... , C. Gräf, ... , J. Zweizig, "*All-sky Search for Periodic Gravitational Waves in the Full S5 LIGO Data*," Phys. Rev. D **85** 022001 (2012)
- T. Westphal, G. Bergmann, ..., C. Gräf, ..., B. Willke, K. A. Strain, S. Goßler and K. Danzmann, "*Design of the 10 m AEI prototype facility for interferometry studies*," Appl. Phys. B **106**, 551–557 (2012)
- J. Abadie, B. P. Abbott, ... , C. Gräf, ... , J. Zweizig, "*Search for gravitational waves from low mass compact binary coalescence in LIGO's sixth science run and Virgo's science runs 2 and 3*," Phys. Rev. D **85** 082002 (2012)
- The LIGO Scientific Collaboration and the Virgo Collaboration: J. Abadie, B. P. Abbott, ... , C. Gräf, ... , J. Zweizig, M. Boer, R. Fender, N. Gehrels, A. Klotz, E. O. Ofek, M. Smith,M. Sokolowski, B. W. Stappers, I. Steele, J. Swinbank, R. A. M. J. Wijers, "*First low-latency LIGO+Virgo search for binary inspirals and their electromagnetic counterparts*," Astronomy & Astrophysics **541**, A155 (2012)
- P. A. Evans, J. K. Fridriksson, N. Gehrels, J. Homan, J. P. Osborne, M. Siegel, A. Beardmore, P. Handbauer, J. Gelbord, J. A. Kennea, M. Smith, Q. Zhu, The LIGO Scientific Collaboration, Virgo Collaboration J. Aasi, J. Abadie, ..., C. Gräf, ... , J. Zweizig, "*Swift follow-up observations of candidate gravitational-wave transient events*," ApJS **203**, 28 (2012)
- The LIGO Scientific Collaboration, Virgo Collaboration: J. Abadie, B. P. Abbott, ..., C. Gräf, ... , J. Zweizig, "*Search for gravitational waves associated with gamma-ray bursts during LIGO science run 6 and Virgo science runs 2 and 3*," ApJ **760**, 12 (2012)
- The ANTARES Collaboration; the LIGO Scientific Collaboration; the Virgo Collaboration, "*A First Search for coincident Gravitational Waves and High Energy Neutrinos using LIGO, Virgo and ANTARES data from 2007*," arXiv:1205.3018 [astro-ph.HE]
- J. Abadie, B. P. Abbott, ... , C. Gräf, ... , J. Zweizig, "*Search for gravitational waves from intermediate mass binary black holes*," Phys. Rev. D **85**, 102004 (2012)
- B. Sathyaprakash, M. Abernathy, F. Acernese, ... , C. Gräf, ... , K. Yamamoto, "*Scientific objectives of Einstein Telescope*," Class. Quantum Grav. **29** 124013 (2012)
- J. Abadie, B. P. Abbott, ... , C. Gräf, ... , J. Zweizig, "*Upper limits on a stochastic gravitational-wave background using LIGO and Virgo interferometers at 600–1000 Hz*," Phys. Rev. D **85**, 122001 (2012)
- J. Abadie, B. P. Abbott, ... , C. Gräf, ... , J. Zweizig, "*All-sky search for gravitational-wave bursts in the second joint LIGO-Virgo run*," Phys. Rev. D **85**, 122007 (2012)

- J. Abadie, B. P. Abbott, ... , C. Gräf, ... , J. Zweizig, M. A. Bizouard, A. Dietz, G. M. Guidi, and M. Was, "*Implications for the origin of GRB 051103 from LIGO observations*," ApJ **755**, 2 (2012)

- J. Aasi, J. Abadie, ... , C. Gräf, ... , J. Zweizig, "*The characterization of Virgo data and its impact on gravitational-wave searches*," Class. Quantum Grav. **29** 155002 (2012)

— 2013 —

- C. Gräf, A. Thüring, H. Vahlbruch, K. Danzmann and R. Schnabel "*Length sensing and control of a Michelson interferometer with power recycling and twin signal recycling cavities*," Opt. Express **21**, 5287-5299 (2013)

- S. Hild, S. Leavy, C. Gräf, B. Sorazu "*Smart Charging Technologies for Portable Electronic Devices*," arXiv:1209.5931 [cs.OH], manuscript submitted to IEEE Transactions on Smart Grid

- The LIGO Scientific Collaboration, Virgo Collaboration: J. Aasi, J. Abadie, ..., C. Gräf, ... , J. Zweizig, "*Search for gravitational waves from binary black hole inspiral, merger, and ringdown in LIGO-Virgo data from 2009–2010*," Phys. Rev. D **87**, 022002 (2013)

- The LIGO Scientific Collaboration, Virgo Collaboration: J. Aasi, J. Abadie, ..., C. Gräf, ... , J. Zweizig, "*Einstein@Home all-sky search for periodic gravitational waves in LIGO S5 data*," Phys. Rev. D **87**, 042001 (2013)

- The LIGO Scientific Collaboration, Virgo Collaboration: J. Aasi, J. Abadie, ..., C. Gräf, ... , J. Zweizig, "*Prospects for Localization of Gravitational Wave Transients by the Advanced LIGO and Advanced Virgo Observatories*," arXiv:1304.0670 [gr-qc]

- The LIGO Scientific Collaboration, Virgo Collaboration: J. Aasi, J. Abadie, ..., C. Gräf, ... , J. Zweizig, "*Parameter estimation for compact binary coalescence signals with the first generation gravitational-wave detector network*," arXiv:1304.1775 [gr-qc]

Acknowledgements

The years I spent as a student at the Albert-Einstein-Institute were not only an extraordinarily instructive but also a very exciting time. I want to seize the opportunity to thank all those people who contributed to my work, in one way or another, and who made the past years as productive and enjoyable as they were for me.

First of all, I want to thank Karsten Danzmann for giving me the opportunity to spend my time as a doctoral student at a truly outstanding institute and for all his generous support.

I feel very fortunate to have been part of the AEI 10 m Prototype team and to be able to make a contribution to the exciting and ambitious sub-SQL interferometer experiment. I want to thank Stefan Goßler for his mentoring and for keeping the project on track. I also want to thank all the other past and present members of the Prototype team I had the pleasure to work with: Gerald Bergmann, Alessandro Bertolini, Michael Born, Katrin Dahl, Tobin Fricke, Manuela Hanke, Fumiko Kawazoe, Sina Köhlenbeck, Gerrit Kühn, Kasem Mossavi, Conor Mow-Lowry, Harald Lück, Patrick Oppermann, Kentaro Somiya, Bob Taylor, Alexander Wanner, Tobias Westphal, Benno Willke and many others. Thanks for all the inspiring discussions and the great time I had working with you. Special thanks go to Stefan Hild for his constant support and encouragement, to Ken Strain for sharing his knowledge in countless occasions and to the Glasgow group for their hospitality during my visits.

I want to thank Peter Fritschel for giving me the opportunity to stay with the LIGO-MIT group for three months, to gain hands-on experience with digital controls in the LASTI prototype. The LIGO-MIT team made this stay an outstanding experience and especially Rich Mittleman, Fabrice Matichard, Chris Wipf and Sheila Dwyer deserve acknowledgement for answering my numerous questions on the digital control system and for being great company.

I want to thank Andreas Freise and his group for being excellent hosts during my stay in Birmingham and for many enlightening discussions on all aspects of numerical interferometer modeling over the past years. I would also like to thank Roland Schilling for always being approachable and for generously sharing his insight in interferometer simulations and Jérôme Degallaix for providing guidance in Fourier-space. I want to thank Oliver Bock for helpful discussions and for providing hardware for GPU computing tests.

I also acknowledge the support of the RRZN cluster system team in the production of part of the results which were presented in Chapter 5 of this work. I would

especially like to thank Paul Cochrane, who offered a helping hand whenever things did not quite work as expected with the computer cluster.

Working on the GEO squeezed-light laser automation was much fun thanks to Nico Lastzka, Henning Vahlbruch, Alexander Khalaidovski. Michael Born and Gerrit Kühn deserve acknowledgement for making sure that the digital control system was always up and running and Andreas Weidner for his support with the interfacing electronics. It was always a pleasure to work "on site" at the GEO detector. Thanks, GEO folks!

I would like to acknowledge the International Max Planck Research School (IMPRS) on Gravitational Wave Astronomy for financial support over the past years.

For proof reading parts of this thesis I want to thank (in alphabetical order) Christoph Affeldt, Tobin Fricke, Stefan Goßler, Hartmut Grote, Stefan Hild, Birthe Klebow, Harald Lück, Christoph Mahrdt and Dirk Schütte. Of course, all remaining errors are in my own responsibility.

Finally, I want to express gratitude to my family for all their support and to Birthe for all her patience, especially over the past few months.

Christian Gräf, May 28, 2013